

**FLOW STRUCTURE GENERATED BY PERPENDICULAR  
BLADE-VORTEX INTERACTION AND IMPLICATIONS FOR  
HELICOPTER NOISE PREDICTION**

Technical report to NASA Langley on  
Research Performed under the Grant NAG-1-1539  
for the period ending 18th January 1996

**Volume 1: MEASUREMENTS**

by

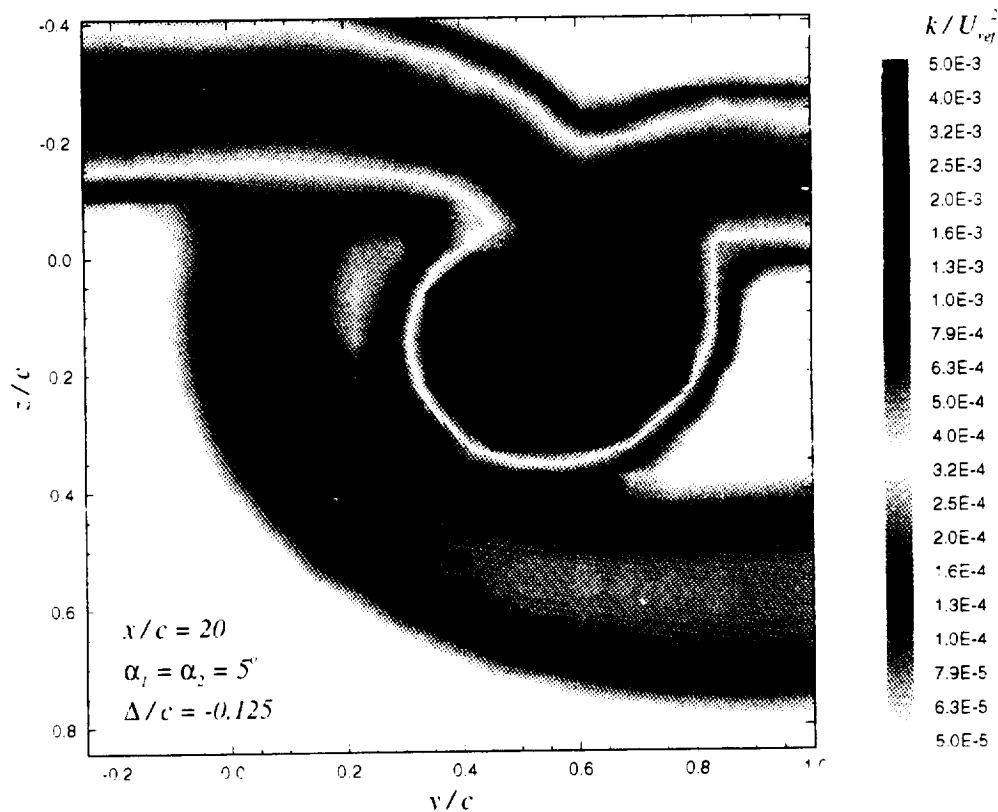
Kenneth S. Wittmer  
(Graduate student)

and

William J. Devenport  
(Principal investigator)

Department of Aerospace and Ocean Engineering  
Virginia Polytechnic Institute and State University  
Blacksburg, VA 24061

January 1996



**ABSTRACT**

The perpendicular interaction of a streamwise vortex with an infinite span helicopter blade was modeled experimentally in incompressible flow. Three-component velocity and turbulence measurements were made using a sub-miniature four sensor hot-wire probe. Vortex core parameters (radius, peak tangential velocity, circulation, and centerline axial velocity deficit) were determined as functions of blade-vortex separation, streamwise position, blade angle of attack, vortex strength, and vortex size. The downstream development of the flow shows that the interaction of the vortex with the blade wake is the primary cause of the changes in the core parameters. The blade sheds negative vorticity into its wake as a result of the induced angle of attack generated by the passing vortex. Instability in the vortex core due to its interaction with this negative vorticity region appears to be the catalyst for the magnification of the size and intensity of the turbulent flowfield downstream of the interaction. In general, the core radius increases while peak tangential velocity decreases with the effect being greater for smaller separations. These effects are largely independent of blade angle of attack; and if these parameters are normalized on their undisturbed values, then the effects of the vortex strength appear much weaker.

Two theoretical models were developed to aid in extending the results to other flow conditions. An empirical model was developed for core parameter prediction which has some rudimentary physical basis, implying usefulness beyond a simple curve fit. An inviscid flow model was also created to estimate the vorticity shed by the interaction blade, and to predict the early stages of its incorporation into the interacting vortex.

## ACKNOWLEDGEMENTS

The authors would like to thank NASA Langley, in particular Tom Brooks and Mike Marcolini, for their support under grant NAG-1-1539. The assistance of Gordie Follin, Mark Engel, Christine Vogel, and Joe Miranda in taking many of the measurements presented here is also gratefully acknowledged.

## NOMENCLATURE

$c$	vortex generator and interaction blade chord length (0.203m)
$G_{uu}$ , $G_{vv}$ , $G_{ww}$	$v_x$ , $v_\theta$ , and $v_r$ velocity autospectra respectively
$h$	height of y-axis origin above floor of wind tunnel
$k$	turbulent kinetic energy
$L$	half-width of wake annulus
$L_w$	length scale of the unrolled-up part of the spiral wake
$P$	turbulent kinetic energy production
$r$	distance from the core center in the y-z plane
$r_l$	vortex core radius corrected for wandering
$r_{lm}$	vortex core radius measured from the core center to the point of peak tangential velocity
$r_{lo}$	initial (undisturbed) vortex core radius corrected for wandering
$Re_c$	Reynolds number based on blade chord
$u$ , $v$ , $w$	fluctuating velocity components in the x, y, and z directions respectively
$U$ , $V$ , $W$	mean velocity components in the x, y, and z directions respectively
$v_x$ , $v_\theta$ , $v_r$	fluctuating velocity components in the core-aligned system
$V_x$ , $V_\theta$ , $V_r$	mean velocity components in the core-aligned system
$U_d$	axial velocity deficit in the vortex core center corrected for wandering effects ( $U_d = (U_{ref} - U_0) / U_{ref}$ )
$U_{dm}$	measured axial velocity deficit in the vortex core center ( $U_{dm} = (U_{ref} - U_{0m}) / U_{ref}$ )
$U_0$	axial velocity in the vortex core center corrected for wandering effects
$U_{0m}$	measured axial velocity in the vortex core center
$U_{ref}$	reference velocity
$U_\infty$	free stream velocity
$U_w$	velocity scale of the unrolled-up part of the spiral wake
$V_{\theta l}$	peak tangential velocity at vortex core edge corrected for wandering
$V_{\theta lm}$	measured peak tangential velocity at vortex core edge



$V_{\theta l0}$	initial (undisturbed) peak tangential velocity at vortex core edge corrected for wandering
$x, y, z$	wind-tunnel fixed coordinates defined in figure 2.2
$\alpha(y)$	local angle of attack (positive about negative y-axis shown in figure 2.2)
$\alpha_1$	angle of attack of the vortex generator (positive about the negative y-axis shown in figure 2.2)
$\alpha_2$	angle of attack of the interaction blade (positive about the negative y-axis shown in figure 2.2)
$\alpha_v(y)$	local angle of attack induced by vortex (positive about the negative y-axis shown in figure 2.2)
$\Delta$	blade-vortex separation distance defined in figure 2.2
$\gamma(y)$	vortex sheet strength ( $d\Gamma_b/dy$ )
$\Gamma(r)$	circulation distribution based on circular paths about the vortex center and assuming axisymmetric flow
$\Gamma_b(y)$	circulation distribution of full-span wing
$\Gamma_f(y)$	final circulation distribution of vortex (used in vortex circulation theory)
$\Gamma_i(y)$	initial circulation distribution of vortex (used in vortex circulation theory)
$\Gamma_0$	root circulation of the vortex generator calculated using lifting line theory
$\Gamma_l$	vortex core circulation defined as $2\pi \cdot r_l \cdot V_{\theta l}$ (corrected for wandering)
$\Gamma_{lm}$	measured vortex core circulation defined as $2\pi \cdot r_{lm} \cdot V_{\theta lm}$
$\tau_a$	axial shear stress magnitude ( $\sqrt{(\overline{uv})^2 + (\overline{uw})^2}$ )
$\Omega_x$	mean streamwise vorticity ( $\partial W/\partial y - \partial V/\partial z$ )
$\Omega_y$	mean streamwise vorticity ( $\partial U/\partial z - \partial W/\partial x$ ; crossed out term ignored)
$\Omega_z$	mean streamwise vorticity ( $\partial V/\partial x - \partial U/\partial y$ ; crossed out term ignored)

## CONTENTS

1. INTRODUCTION	1-1
1.1 Purpose	1-1
1.2 Some rotor flow details	1-1
1.3 Importance for BVI noise	1-2
1.4 Importance for BWI noise	1-3
1.5 Review of previous work	1-4
1.6 Flow over the blade	1-8
1.7 Objectives and approach	1-9
2. APPARATUS AND INSTRUMENTATION	2-1
2.1 Wind tunnel	2-1
2.2 Blades	2-1
2.3 Hot-wire anemometry	2-3
2.4 Helium bubble flow visualization	2-5
3. RESULTS AND DISCUSSION	3-1
3.1 Coordinate system and flow conditions	3-1
3.2 The undisturbed vortex	3-2
3.2.1 Streamwise development	3-3
3.2.2 Angle of attack variations	3-7
3.2.3 Effects of spoiler size	3-8
3.3 Evolution of flow after interaction	3-9
3.3.1 Pressure side passage of $\Delta/c = -0.125$	3-9
3.3.2 Suction side passage of $\Delta/c = 0.125$	3-15

3.4 Effects of blade–vortex separation	3-17
3.4.1 Baseline variation	3-17
3.4.2 Decreased blade angle of attack	3-20
3.4.3 Increased vortex strength	3-22
3.4.4 Increased core radius	3-23
3.4.4.1 Spoiler diameter of $0.2125c$	3-24
3.4.4.2 Spoiler diameter of $0.3125c$	3-27
3.5 Angle of attack variations with fixed blade–vortex separation	3-29
3.5.1 Changing blade angle of attack	3-29
3.5.2 Changing vortex strength and blade angle of attack simultaneously	3-30
3.6 Other velocity measurements	3-31
 4. THEORETICAL MODELING	 4-1
4.1 Correlation of core parameters	4-1
4.1.1 Data summary	4-1
4.1.2 Modeling	4-5
4.2 Vortex circulation theory (VCT)	4-8
4.2.1 Derivation	4-8
4.2.2 Comparison with experimental data	4-11
 5. CONCLUSIONS	 5-1
 6. REFERENCES	 6-1
 7. APPENDIX	 7-1

## 1. INTRODUCTION

### 1.1 Purpose

Much of the noise generated by a helicopter is a consequence of the interaction of its blades with their own vortex wakes. The objective of the work described here is to improve understanding of the effects of perpendicular blade-vortex interactions upon those wakes. Changes in the vortex structure are of interest because of the effects on the whole rotor-plane flow and noise generated by subsequent interactions. Understanding how tip vortices are affected by a perpendicular interactions is therefore critical to the accurate prediction of helicopter noise, rotor aerodynamics and blade loading.

### 1.2 Some rotor flow details

The flowfield produced in and around a helicopter rotor is very complex and is dependent upon numerous parameters—even in steady flight for a particular helicopter configuration—such as the thrust coefficient, advance ratio, and tip-path-plane angle. Each blade is continuously shedding a vortex sheet, which quickly rolls up into a concentrated vortex. There are many opportunities for significant interactions between the main rotor vortices and following blades for many low to moderate flight speed conditions. In hover, Landgrebe [1] shows through smoke flow visualization that the tip vortex initially moves radially towards the hub and has only a very small downward axial movement. It is not until the next blade passes, creating another vortex, that the first vortex is convected downward. In forward flight, experiments have shown that there can be a strong upwash on the upstream part of the rotor disk forcing some vortices above the rotor disk

(Simons *et al.* [2]). An often used method for determining the wake structure of a helicopter rotor for identification of possible blade–vortex interactions is through the lifting line helicopter trim code CAMRAD (Comprehensive Analytical Model of Rotorcraft Aerodynamics and Dynamics) (Johnson [3]). An example of the results obtained from use of this code are presented by Preisser *et al.* [4] which predict that multiple interactions can occur (in agreement with their acoustic measurements) and these interactions can be either above or below following blades.

### 1.3 Importance for BVI noise

Blade–vortex interactions, where the axis of the vortex is nearly parallel to the blade leading edge (see figure 1.1a), result in impulsive blade loading which produces impulsive noise referred to as BVI noise (also as blade slap). BVI noise often occurs in the flight regime where the rotorcraft is near the ground with a frequency content in the middle of the audible range which, combined with its impulsive nature, makes it particularly annoying and highly detectable (George [5]). A majority of the research concerning helicopter noise prediction has concentrated on parallel interactions because experimental (see Hoad [6] in conjunction with Egolf and Landgrebe [7]) and theoretical (see Widnall and Wolf [8] and Hardin and Lamkin [9]) studies have indicated that the intensity of the impulsive noise increases as the tip vortex becomes more nearly parallel to the blade.

An interaction where the vortex axis is nearly perpendicular to the blade leading edge (figure 1.1b) is an important subset of blade–vortex interactions. As previously mentioned, multiple interactions can occur in the rotor plane meaning that if a perpendicular interaction

precedes a noise producing oblique or parallel interaction (as shown in figure 1.2), the effects of the perpendicular interaction on the vortex must be known to subsequently predict the noise resulting from a later interaction. Many theoretical schemes have shown that the prediction of BVI noise is very sensitive to the inputted values of core size, strength, and distribution (see Widnall and Wolf[8], Srinivasan *et al.* [10], Tadghighi *et al.* [11], Lee and Smith [12]) confirming the importance of the effects a previous perpendicular interaction might have on the vortex. Also illustrated in figure 1.2 is the possibility that these perpendicular interactions can occur at different radial locations. Depending upon the advance ratio, perpendicular interactions can occur at any radial location. If the interaction occurs far inboard of the blade tip, the interaction will be subsonic and the interacting blade might be considered locally two-dimensional (depending on the blade loading). For interactions occurring near the tip, the interaction may be transonic and the downstream interaction with the tip vortex shed from the interacting blade will be important as shown in the case of hover by Landgrebe [1].

### 1.4 Importance for BWI noise

Perpendicular interactions are also of importance in the prediction of blade-wake interaction (BWI) noise. This noise source is defined by Brooks *et al.* [13] as the mid-frequency, broadband noise due to blade interaction with turbulent portions of previous blade wakes. They also found that BWI noise dominates the mid-frequency range at flight conditions slightly away from where peak BVI noise occur. Devenport *et al.* [14] studied the turbulence and spectral structure of an undisturbed trailing vortex and incorporated the data into the BWI noise prediction

scheme of Glegg [15]. Their results showed that the turbulence of an undisturbed vortex is insufficient to account for most of the BWI noise generated. A perpendicular interaction (occurring before a noise producing BWI) may alter the turbulent flowfield significantly, and may therefore be a necessary feature for BWI. The present study aims at identifying the effects of a perpendicular interaction on the turbulence and spectral structure in and around the core after interaction to identify if this is indeed the source of the turbulence necessary to produce the measured values of BWI noise.

### 1.5 Review of previous work

Most previous work on perpendicular interactions has been concerned with effects on the aerodynamic characteristics of the blade rather than on the vortex itself. Some of this research was aimed at determining whether perpendicular interactions are directly responsible for noise generation while other research was directed towards determining airloads for performance and structural considerations of helicopters or aircraft with canard configurations. Ham [16] made pressure measurements on a rotating blade experiencing a perpendicular interaction with an independently generated vortex. Discrepancies were seen between theoretical pressure distributions predicted by the lifting surface theory of Johnson [17] and experimental data for blade-vortex separations of less than one-half of the rotor blade chord. The discrepancies were thought to be the result of local separation occurring due to the vortex-induced loading which lead to a non-rotating, perpendicular interaction study (Ham [18]). For this study, an instrumented two-dimensional airfoil was placed seven chord lengths ( $c$ ) downstream of the vortex generator with the planforms of the two blades lying in perpendicular planes. The configuration allowed the blade-vortex

separation to be continuously varied by oscillating the vortex generator in its spanwise direction. Pressure measurements were made at the 10% chord location on the interaction blade to determine the differential pressure induced by the passing vortex. An empirical relation is derived which suggests that the spanwise pressure gradient supplied by the vortex limits, through flow separation, the amount of loading which can be induced on the blade. For typical helicopter rotor blade-vortex interactions, this limits the maximum incremental lift coefficient to less than 0.3. Peak loading induced by the vortex were found to be independent of the frequency of vortex impingement and proportional to vortex strength (he argues that this peak value is dependent on the two thirds power of the vortex circulation). The angle of attack of the interaction blade did not appear to effect the peak loading except to increase the scatter of the data as the angle of attack was increased. Small deviations in yaw of the interaction blade—producing a non-perpendicular interaction—appeared to have a small, unpredictable effect on the peak loading.

Patel and Hancock [19] investigated the perpendicular interaction of a vortex generated by a rectangular wing (13.6% Clark Y airfoil section) lying in the vertical plane with both a wing (same airfoil section and chord) and a flat plate lying in the horizontal plane: both spanned the entire wind tunnel and were located 10 chord lengths downstream of the vortex generator. Oil and smoke flow visualizations were performed for various heights of the vortex above the wing. Surface pressure measurements were also made. The oil flow visualizations shows that the vortex is displaced spanwise as it passes the wing with a separation distance of  $0.5c$ . For a closer separation of  $0.2c$  a secondary separation line (indicated by the edge of a three-dimensional herringbone pattern) occurs and the vortex does not appear to be deflected in the spanwise



direction. At  $0.1c$  it appears that the vortex has caused a local stalling of the airfoil due to the upwash induced by the vortex. With the vortex impinging on the wing, no flow patterns are observed. Smoke flow visualizations were done at an extremely low Reynolds number of about 10,000. Vortex breakdown is observed to occur farther upstream for closer separations. This trend is also seen for the case of the vortex approaching a flat plate at zero angle of attack which leads them to conclude that it is not a pressure gradient effect. They assumed that it is a surface boundary layer effect which causes the instability, but offer no explanation as to how this is propagated upstream ahead of the airfoil. After the broken down vortex passes the wing, they observe a reassembly of the vortex. Pressure measurements are compared with the inviscid theory of Hancock [20] showing only qualitative agreement.

Paterson *et al.* [21] used a configuration similar to Patel and Hancock's [19] where a perpendicular interaction was produced using a fixed 4" chord NACA 0012 generator and a 9" chord full-span NACA 0012 blade whose planforms lie in perpendicular planes. The suction side of the interacting airfoil was instrumented with microphones and the vortex passed approximately  $0.11c$  below the wing (pressure side passage). The noise creating mechanism was concluded to be 'trailing edge noise' due to the interaction between eddies created from localized stall and the airfoil trailing edge. A stall region was found to extend into the spanwise portion of the airfoil where downwash is experienced. This region is characterized as being dominated by low frequency pressure fluctuations.

Phillipe and Armand [22] studied the influence of a trailing vortex on the integrated lift and drag of a rectangular NACA 0012 blade at a Mach number of 0.6 for a constant blade-vortex

separation. The vortex was found to reduce the blade lift and increase drag by as much as 40% in the presence of the vortex.

Seath and Wilson [23] studied interactions with a two-dimensional, rectangular NACA 64A015 blade at zero angle of attack at a chord Reynolds number of 417,000. They observed substantial changes in the pressure distribution on the blade in the vicinity of the vortex. A spanwise drift of the vortex was also seen to occur in a direction consistent with the velocity component which would be induced by an image vortex. Flow visualizations were also performed which show three-dimensional separation and reattachment lines induced by the nearby vortex.

Müller [24] studied the “mid vortex” resulting from the interaction of a vortex with a blade, and studied the “double vortex” produced by a blade with a downward pointing winglet. Main thrust of experiment was to prove the existence of these flow phenomena. The investigation of the “mid vortex” was done with two fixed (non-rotating), blades in perpendicular planes. The disturbing wing created a streamwise vortex which passed to the pressure side of the twisted interaction blade near its tip (a twisted blade was used to approximate the loading of a rotor blade in hover). Flow visualizations and LDV measurements were made in a water tunnel for a chord Reynolds number of 120,000. The LDV measurements clearly showed the “mid vortex” in vorticity contour plots. He also subtracted the disturbing and tip vortices contribution to the velocity field by assuming a Lamb or Oseen-Hammel vortex core tangential field approximation. The trajectories of the three vortices are also presented for a short distance downstream of the blade trailing edge. Based on his measurements and theoretical considerations, he postulates that

the disturbance caused by the vortex on the blade lift distribution causes the local shedding of a “mid vortex” with a strength of one quarter to one third of that of the blade tip vortex.

Kalkhoran *et al.* [25] examined the influence of a trailing vortex on a two-dimensional rectangular NACA 0012 blade at zero incidence for Mach numbers of 0.68–0.9 and blade–vortex separations of 0.1–0.3. Pressure measurements in the flowfield were made at the leading and trailing edges of the interaction blade as well as on the surface of the airfoil. Most of the changes in the pressure distribution on the airfoil were found to be confined to the leading 30% of the chord. These pressure changes were found to be a function of vortex strength and separation distance, but is relatively insensitive to the Reynolds number. The vortex drifted in the spanwise direction as it passed over the blade under the influence of its image in the blade surface. Large unsteady fluctuations in pressure were observed near the vortex center at the blade trailing edge after interaction (this result is most likely caused by buffeting of the vortex due to the nearby separated flow). Two minimum pressure regions were observed in the pressure survey behind the blade for one separation distance, suggesting the possibility of a second vortex. This second vortex may have been formed due to a breakup of the primary vortex or caused by separated flow due to the interaction.

## 1.6 Flow over the blade

Beginning with the above results one can infer some major features of flow over a blade in the presence of a streamwise vortex (figure 1.3). Velocities associated with the vortex change the local angle of attack ( $\alpha$ ) of the blade; increasing it outboard of the vortex center and decreasing it

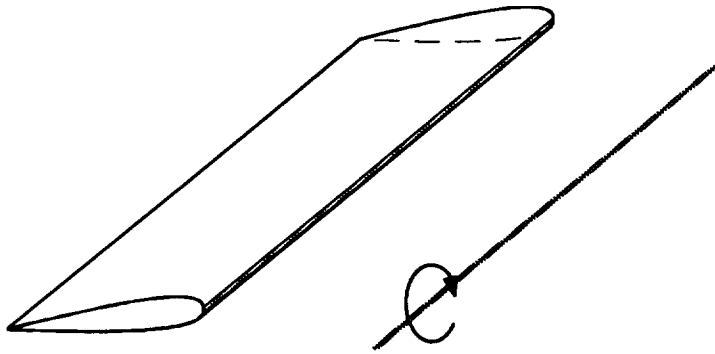
inboard. These changes have a strong influence on the blade boundary layer and wake. Outboard of the vortex center the thickness of the suction-side boundary layer and the resulting wake are increased by the additional angle of attack. If the vortex is sufficiently strong, or the encounter sufficiently close, a local separation may be induced on the suction surface. Conversely, inboard of the vortex center the boundary layer and wake thickness will be decreased by the presence of the vortex. Since the vortex produces a change in angle of attack along the blade span it also induces the formation of streamwise vorticity in the blade boundary layers which is shed into the wake. Inboard and outboard of the core  $\partial\alpha/\partial y$  is positive and thus positive vorticity is shed. In the immediate vicinity of the core negative vorticity is shed. As the vortex passes over the blade it drifts under the influence of its image: inboard for pressure-side passage, outboard for suction-side passage (depicted in figure 1.3). Downstream of the blade it is expected that the vortex will interact with both the blade wake and the blade tip vortex.

### 1.7 Objectives and approach

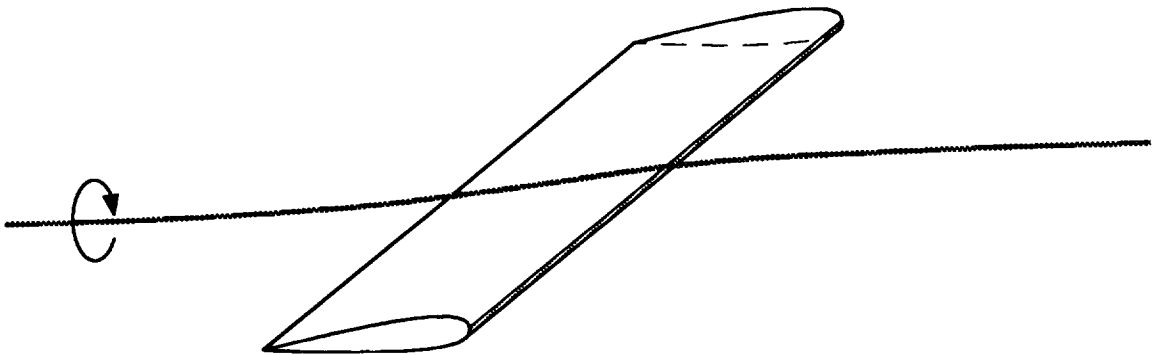
The effects of perpendicular blade vortex interaction on tip vortex wakes remain largely undocumented. To our knowledge, there are no measurements of the turbulence structure resulting from a perpendicular and thus little to base BWI noise predictions on. There is no systematic data documenting the effects of perpendicular interactions upon vortex core size and circulation distribution and thus little to base improved BVI noise predictions on. It is the objective of the present study to provide this needed information. Specifically, to document the effects a perpendicular blade–vortex interaction has upon the vortex core parameters, circulation

distribution, and turbulence structure as a function of the most important independent variables.

In the first part of this study (see Devenport *et al.* [26] and Wittmer *et al.* [27]) the effects of perpendicular interaction in the vicinity of a blade tip were studied. While this study revealed much about the overall form and physics of the interaction, many of the more subtle effects were obscured by the second vortex shed from the blade tip. The present study has therefore concentrated on the effects of perpendicular blade–vortex interactions occurring much further inboard, where the effects of this second tip vortex are negligible. At a given Reynolds number and Mach number, the effects of such interactions are functions of the blade–vortex separation, the vortex strength, its core size, and the blade angle of attack. All these effects are documented here by using an idealized configuration consisting of two blades separated by a streamwise distance and probing the flow they generate with hot wires.



(a) Parallel interaction



(b) Perpendicular interaction

**Figure 1.1** Two types of blade–vortex interactions

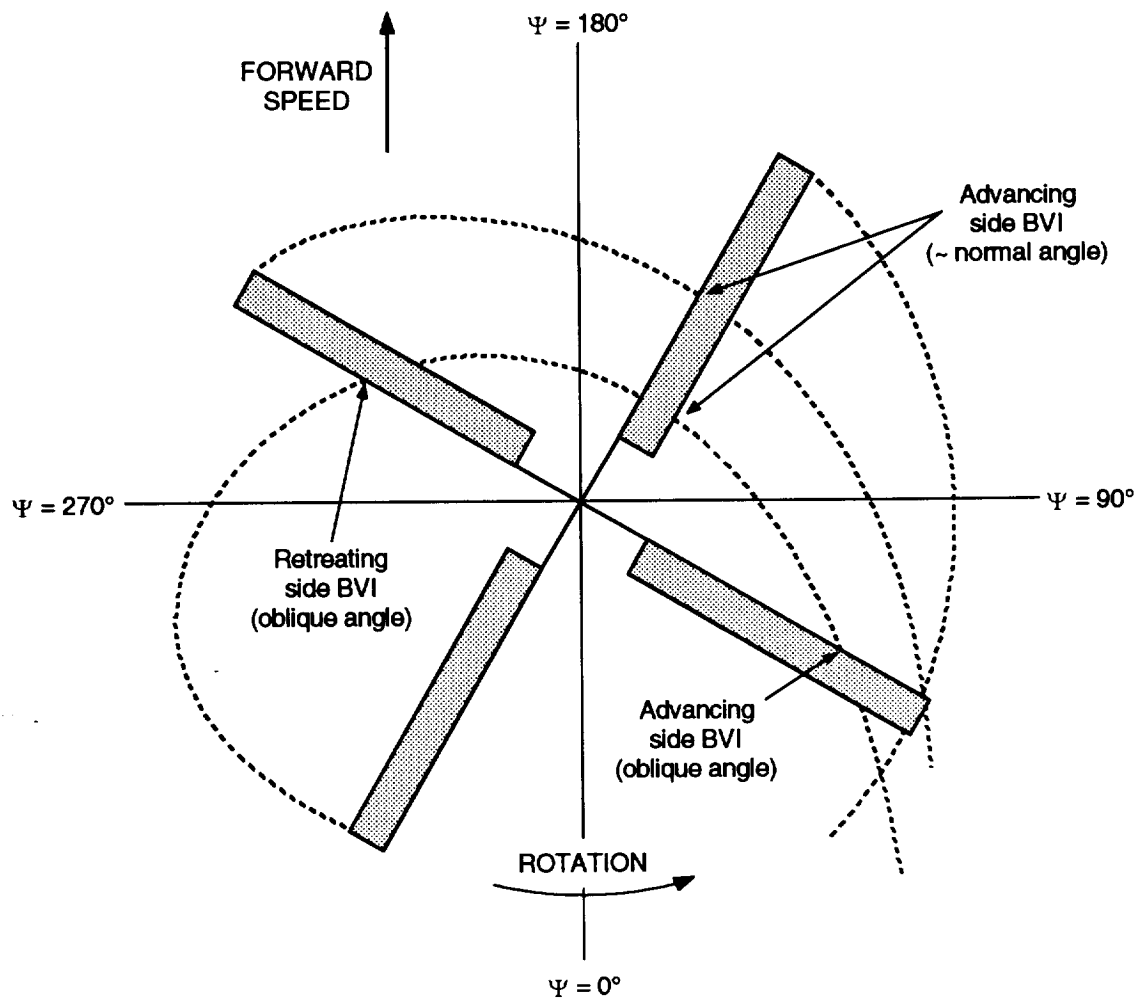


**Figure 1.2** Simplified example of blade and vortex positions in forward flight

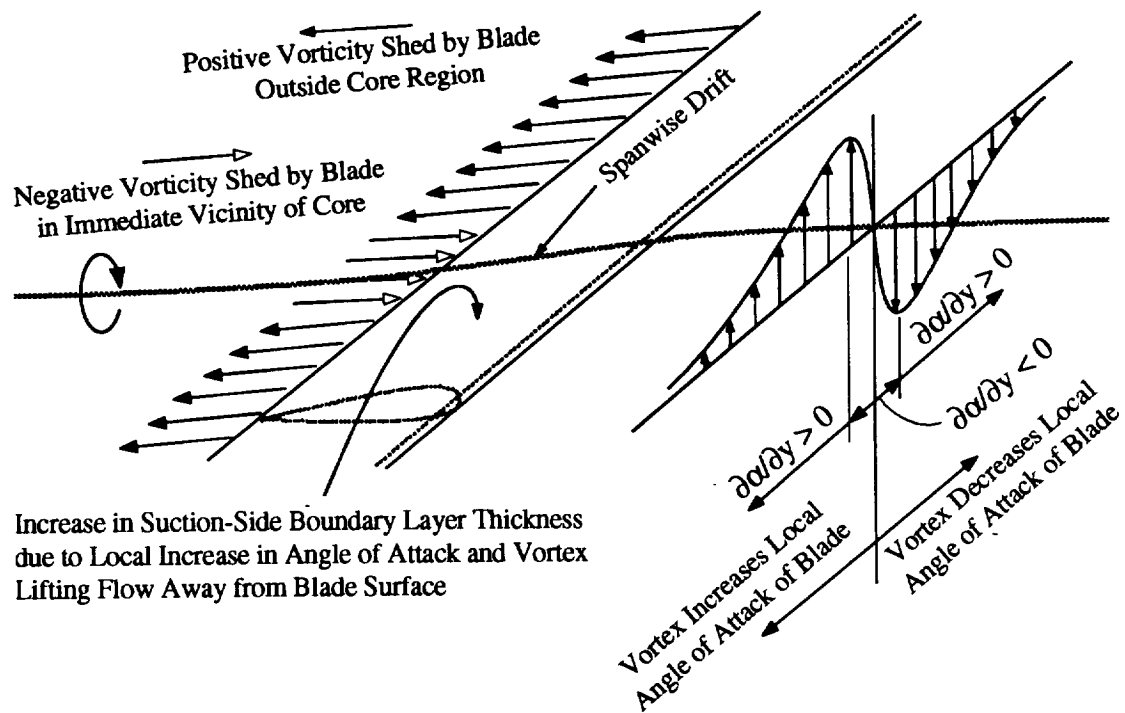


**Figure 1.3** Primary features of a perpendicular blade–vortex interaction



## 2. APPARATUS AND INSTRUMENTATION

### 2.1 Wind Tunnel

Experiments were performed in the Virginia Tech Stability Wind Tunnel (figure 2.1). It is a closed-circuit tunnel powered by a 600 horsepower axial fan with a test section which measures 1.83m×1.83m×7.33m. Flow in the empty test section is closely uniform with a turbulence intensity of less than 0.1% (Choi and Simpson [28]). For speeds between 6 and 30m/s, a slight favorable pressure gradient ( $\partial C_p / \partial x = -0.003/\text{m}$ ) exists along the test section due to boundary layer growth which causes some convergence of the streamlines (Reynolds [29]). Flow angles are small near the middle of the section but increase to about 2° near the walls.

The free stream dynamic pressure and flow temperature are monitored continuously during operation of the wind tunnel. The former is measured using a pitot-static probe located at the upstream end of the test section connected to a Barocell electronic manometer. The latter is sensed using an Omega thermocouple located within the test section boundary layer—there is no significant temperature gradient across the boundary layer.

### 2.2 Blades

Untwisted NACA 0012 blades were used: one to generate the vortex and the other to interact with it. Both had a rectangular planform of 0.203m chord ( $c$ ) and were machined from aluminum with a numerically controlled milling machine. Effective boundary layer trips were placed on both blades. These consisted of 0.5mm diameter glass beads glued in a random pattern

which completely covered the entire span between the 20% and 40% chord locations. The resulting turbulent boundary layers were documented for a range of angles of attack by Devenport *et al.* [14]. The vortex generator blade was mounted vertically as a half wing at the center of the upper wall of the test section entrance with 0.879m protruding into the flow (see figure 2.2). The interaction blade was mounted 14c downstream, completely spanning the test section. A full-span blade was used to eliminate the complicating effects of an additional blade tip vortex.

To vary the strength of the vortex the angle of attack of the generator ( $\alpha_1$ ) could be adjusted. To vary its core size, circular spoilers were attached to the trailing edge of the generator tip. By choosing the spoiler diameter ( $d$ ), core sizes larger than that produced without spoiler can be produced. See appendix by Weisser [30] for a complete description of the usage of circular spoilers for this purpose. To vary the blade-vortex separation distance ( $\Delta$ ) and the strength of the interaction, the z-position and angle of attack ( $\alpha_2$ ), respectively, of the interaction blade could both be varied. The angles of attack of both the vortex generator and interaction blade were adjusted about their quarter chord lines. Positive angle defined as a right-handed rotation about the negative y-axis (see figure 2.2).

The interaction blade was instrumented with 40 static pressure ports and was set at zero angle of attack by equalizing the pressures on both sides. The generator was then placed in the tunnel and set at zero angle of attack by equalizing the pressures on both sides of a removable wing tip holding 48 static pressure ports.

### 2.3 Hot-wire anemometry

A four-sensor hot-wire probe manufactured by Auspex Corporation (type AVOP-4-100) was used to make three-component velocity measurements. The probe consists of two orthogonal X-wire arrays with each wire inclined at a nominal  $45^\circ$  angle to the probe axis (see figure 2.3). Eight tapered prongs ( $75\mu\text{m}$  in diameter at their tips) position the wires some 40mm upstream of the main part of the probe. The sensors are etched tungsten wire of  $5\mu$  diameter with an approximate length of 0.8mm. The measurement volume of the probe is approximately  $0.5\text{mm}^3$ . Each of the hot-wire sensors was operated separately using a Dantec 56C17/56C01 constant temperature anemometer unit. The output voltages from the anemometer bridges were recorded by an IBM AT compatible computer using an Analogic 12 bit HSDAS-12 A/D converter buffered by four  $\times 10$  buck-and-gain amplifiers. The dynamic response of all four channels of the system was measured separately using the method of Wood [31] and found to be adequate to well over 20kHz at a nominal overheat of 1.7.

This type of probe is more normally associated with vorticity measurements (Kovasznay [32]). An initial study by Devenport *et al.* [14] showed it to be better than standard triple and X-array probes for trailing vortex measurements. The triple wire probe was found to be very sensitive to gradient errors of the type found in vortices—axial velocity measurements being contaminated (up to 10%) by the streamwise vorticity. The X-array probe also displayed some sensitivity to streamwise vorticity and produced large uncertainties in Reynolds stress measurements because the velocity components were not measured simultaneously. The four-sensor probe is capable of simultaneous 3-component measurements from a relatively compact

measurement volume and appeared to overcome both of these problems. Note that four-sensor probes which can suffer serious problems in boundary layers (Vukoslavcevic and Wallace [33]), are better suited to wake flows because they contain only weak axial velocity gradients.

The probe was calibrated separately for velocity and angle response. Velocity calibrations were performed in the wind tunnel freestream referenced against the wind tunnel's pitot-static probe. All sensors were calibrated simultaneously by using their measured angles and the flow direction at the calibration location (determined with a seven hole yaw probe) to form a relationship between their effective cooling velocities ( $U_{eff}$ ) and the velocity sensed by the wind tunnel's pitot-static probe. King's law (equation 2.1) is used to relate the voltage  $E$  of each wire to its effective cooling velocity.

$$E^2 = A + B \cdot U_{eff}^n \quad (2.1)$$

Using an exponent  $n$  of 0.45 and determining the constants  $A$  and  $B$  via linear regression from 10 or more calibration points. The accuracy of the curve fit was always better than 1%. The effects of ambient temperature drift were corrected using the method of Bearman [34].

To calibrate the angle response a method similar to that of Mathioudakis and Breugelmans [35] was used. In this method the probe is placed in the potential core of a uniform jet of known flow direction and velocity equal to the wind-tunnel free-stream velocity. The cooling velocities are then measured as the probe is pitched and yawed over all likely angle combinations from  $-45^\circ$  to  $+45^\circ$ . At each angle combination, standard X-array response equations (e.g. Tutu and Chevray [36]) are used to extract rough estimates of  $U$  and  $V$  from the cooling velocities of one pair of sensors and  $U$  and  $W$  from the other. After averaging the two  $U$  estimates (to minimize the

influence of axial vorticity) the quantities  $Q$ ,  $V/Q$ , and  $W/Q$  are calculated, where  $Q = \sqrt{U^2 + V^2 + W^2}$ . Look up tables of the errors in  $Q$ ,  $V/Q$ , and  $W/Q$  are then constructed by comparing them with the true values inferred from the known pitch and yaw angles. Interpolations on these tables are then used to correct instantaneous estimates of  $Q$ ,  $V/Q$ , and  $W/Q$  (and therefore  $U$ ,  $V$ , and  $W$ ) obtained during a measurement. Residual errors can be evaluated by reprocessing the angle calibration data using the look up tables and were found to be very small using tables containing only 400 points each.

This approach is much more accurate than using only standard angle response equations and avoids several difficulties normally associated with the accurate solution of those equations. The calibration process also reveals the acceptance cone of the probe (the region within which a single valued relationship between the cooling velocities and velocity components can be established) thereby preventing non-uniqueness problems. One advantage of the method over others in which look up tables are used (e.g. Browne *et al.* [37], Leuptow *et al.* [38], and Döbbeling *et al.* [39]) is that sophisticated interpolation is not required because the corrections vary only slowly over most of the acceptance cone. One possible drawback is the assumption that the angle calibration is independent of velocity. However, in the trailing vortex flows studied by the authors, absolute velocity variations are small (typically  $< \pm 15\%$ ) and angle calibrations performed over a range of speeds indicated negligible dependence on velocity over this range.

## 2.4 Helium bubble flow visualization

Flow visualizations were performed by seeding the flow with helium-filled soap bubbles produced by a Sage Action Inc. model 5 generator. Being lighter than air, the bubbles centrifuge

into the vortex core, marking it clearly. The bubbles were introduced through a streamlined strut located in the wind tunnel's contraction and illuminated using a Varian arc lamp (model p150s-7) located at the end of the test section. Varying either the strut location or the arc lamp position produced no visible effects on the vortex and its path. It was therefore assumed that they produced no significant disturbances to the flowfield. Both the strut and arc lamp were removed for all velocity measurements.

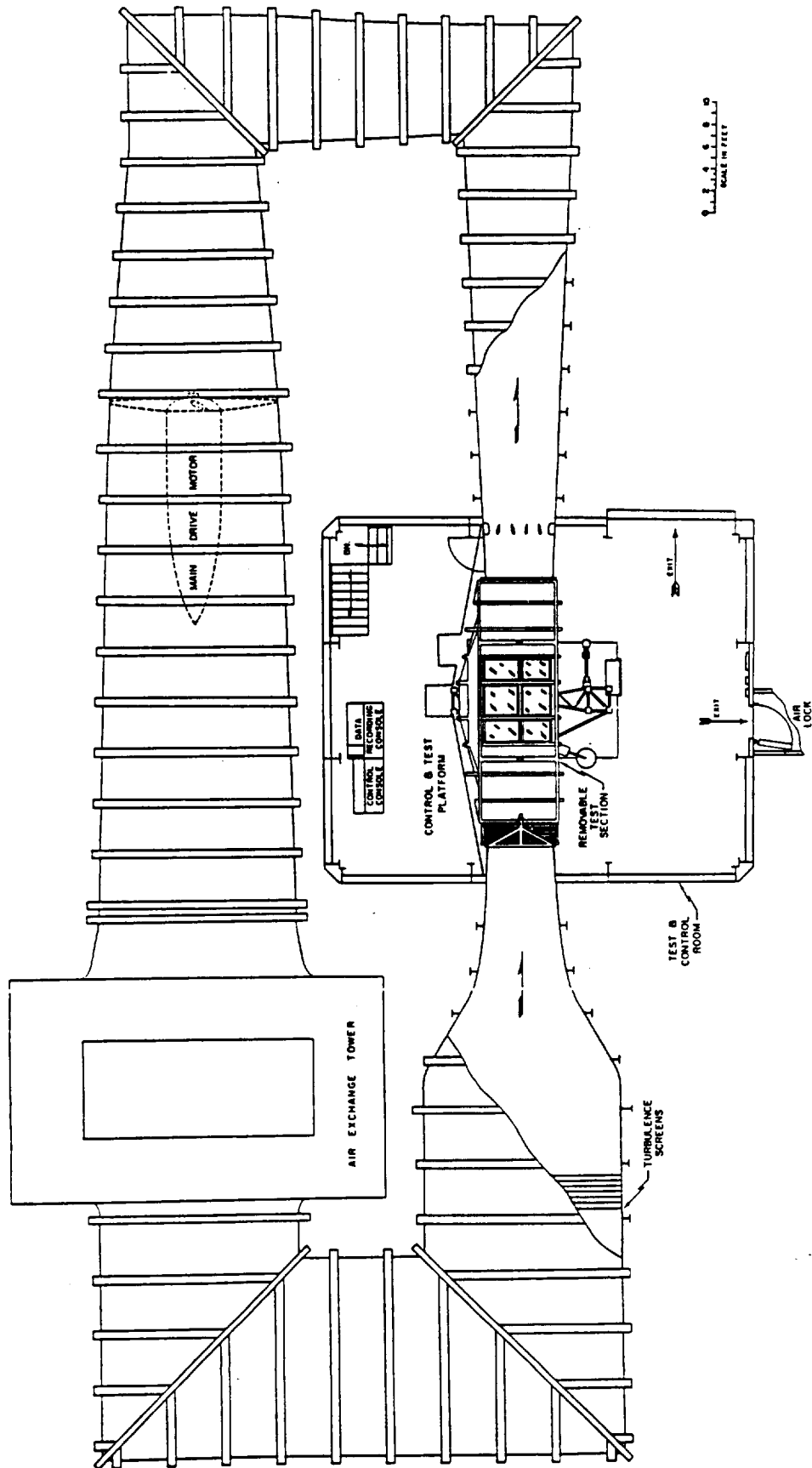
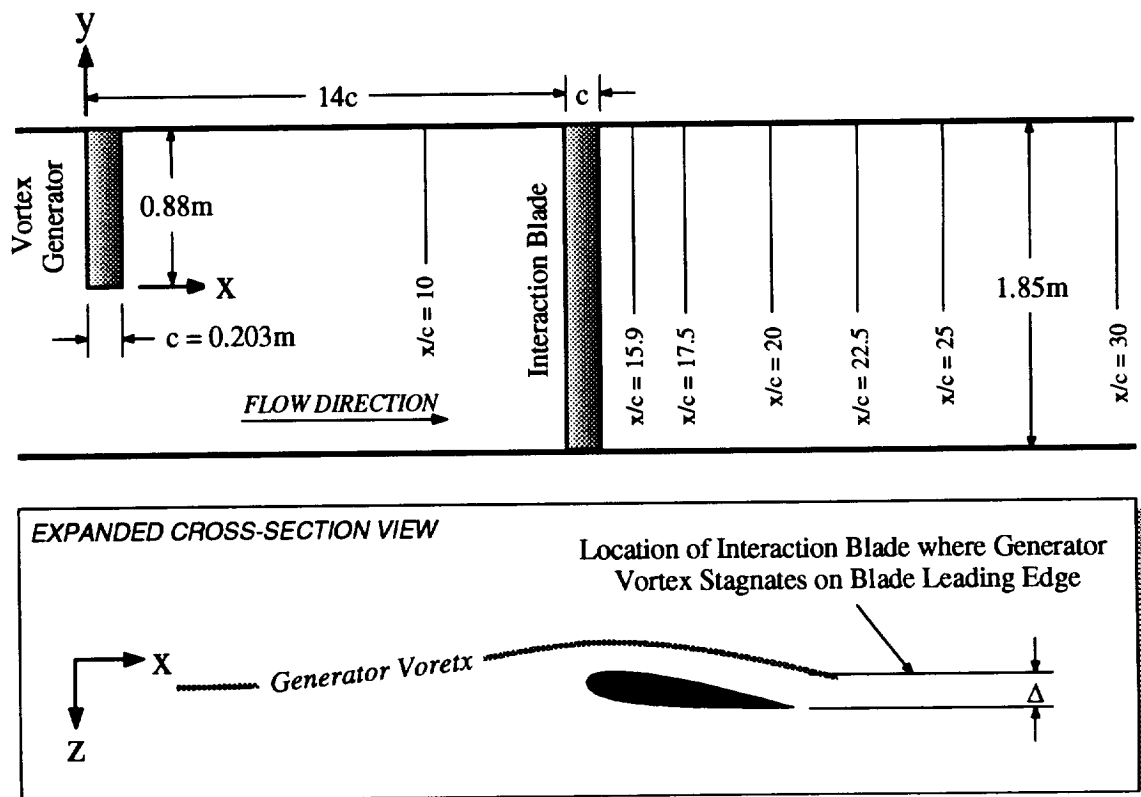
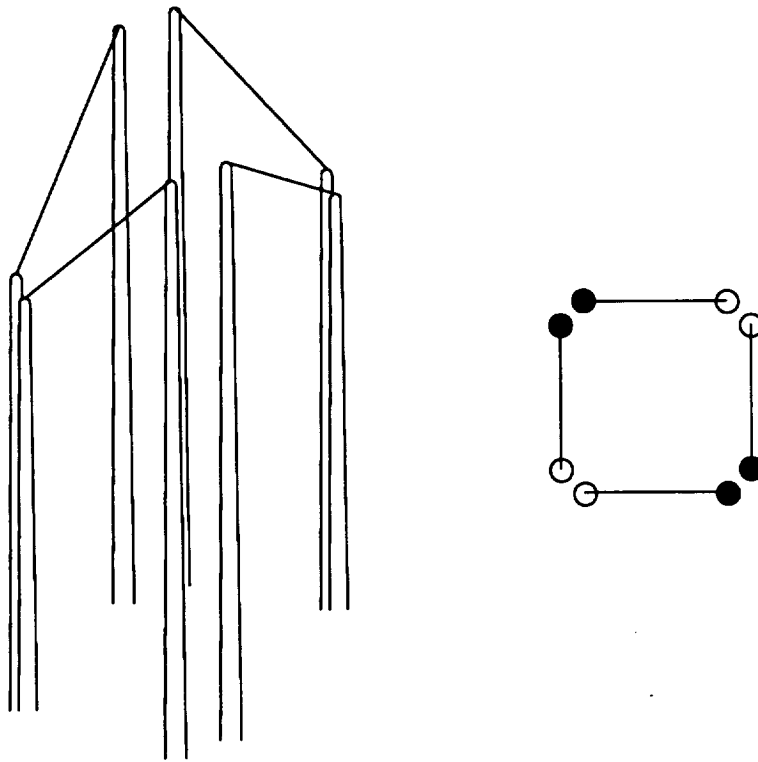


Figure 2.1 Virginia Tech Stability Wind Tunnel



**Figure 2.2** Configuration and coordinate system





**Figure 2.3** Four-sensor hot-wire probe geometry. Isometric view on left, planform view of prong tips on right (solid symbols represent long prongs).

### 3. RESULTS AND DISCUSSION

#### 3.1 Coordinate system and flow conditions

Measurements will be presented in the wind-tunnel aligned coordinate system ( $x, y, z$ ) shown in on figure 2.2. Coordinate  $x$  is measured downstream from the generator leading edge,  $y$  inboard from its tip, and  $z$  from the quarter chord line so as to complete the right-handed system. The mean velocity components  $U, V, W$ ; and the fluctuating velocity components  $u, v, w$ ; are defined in the  $x, y, z$  directions respectively. In this system, the leading edge of the interaction blade is at  $x / c = 14$ . All measurements are presented in non-dimensional form. Most are normalized on the free-stream velocity ( $U_{ref}$ ) indicated by the wind tunnel's pitot-static probe, and blade chord. All measurements were performed at a chord Reynolds number ( $Re_c$ ) of 530,000, corresponding to a free-stream velocity of about 40m/s.

A blade-vortex separation of zero corresponds to the blade  $z$  position where the streamline marking the vortex center stagnates upon the blade's leading edge.  $\Delta$  is negative when the vortex passes on the pressure side of the interaction blade, and positive when it passes on the suction side. Zero  $\Delta$  configurations were determined using helium bubble flow visualizations. Because of the limitations of the flow visualization technique most such determinations had to be made at a chord Reynolds number of 260,000; though this position did appear Reynolds number independent. We were unsuccessful at revealing the vortex core centers using helium bubble flow visualization when either of the two spoilers were attached. In these cases, zero  $\Delta$  was determined retrospectively from grids of velocity measurements.

Some velocity profile measurements are presented in terms of core-aligned mean ( $V_x$ ,  $V_\theta$ ,  $V_r$ ) and fluctuating ( $v_x$ ,  $v_\theta$ ,  $v_r$ ) velocity components. This system is obtained by rotating the wind-tunnel fixed system twice (a rotation about its y-axis, and then a rotation about the resulting z-axis) so that local velocity of the vortex core center is defined solely by  $V_x$ . All profiles were measured along lines parallel to the z axis. Distances in these profiles are expressed in terms of the coordinate  $r$  representing distance from the core center ( $r$  is considered negative if the location is in the negative z-direction from the core center).

Experiments were performed for many combinations of blade-vortex separation, streamwise position, blade angle of attack, vortex strength (controlled by generator angle of attack), and core radius (controlled by spoiler diameter). A full list of conditions and locations is given in tables 3.1, 3.3 and 3.4.

### 3.2 The undisturbed vortex

Velocity measurements were made without the interaction blade to document the undisturbed structure and development of the tip vortex shed by the generator as functions of generator angle of attack and spoiler size. Measurement locations and conditions, and vortex core parameters for these cases are summarized in table 3.1. Most of these data sets have been already analyzed and discussed by Devenport *et al.* [27] and Weisser [30] (see Appendix), so only details relevant to the blade-vortex interaction problem are discussed here. Particular emphasis is placed on measurements made at  $x/c = 10$  since these characterize the inflow to the interaction blade

(mounted at  $x / c = 14$ ) for many of the perpendicular BVI tests presented in following sections. Uncertainty estimates for velocity measurements are given in table 3.2.

### 3.2.1 Streamwise development

To document the streamwise development of the undisturbed vortex, measurements were made at  $x / c = 5, 10, 15, 20, 25$ , and  $30$  the generator at  $5^\circ$  angle of attack and no spoiler attached. Figure 3.1 illustrates the overall form of the vortex in terms of contours of axial normal turbulent stress ( $\overline{u^2} / U_{ref}^2$ ) measured at these six streamwise locations. More detailed views of the flow structure surrounding the vortex core region at  $x / c = 10$  are given by the vectors of: mean cross-flow velocity ( $V / U_{ref}, W / U_{ref}$ ) and mean cross-flow vorticity ( $\Omega_y \cdot c / U_{ref}, \Omega_z \cdot c / U_{ref}$ ); and contours of: mean axial velocity deficit ( $(U_{ref} - U) / U_{ref}$ ), mean axial vorticity ( $\Omega_x \cdot c / U_{ref}$ ), axial normal turbulent stress, summed cross-flow normal turbulent stresses ( $(\overline{v^2} + \overline{w^2}) / U_{ref}^2$ ), turbulent kinetic energy ( $k / U_{ref}^2$ ), and axial shear stress magnitude ( $\tau_a / U_{ref}^2$ ) shown in figure 3.2. The mean cross-flow vorticity vectors were computed ignoring streamwise derivatives. Equations 3.1 and 3.2 contain the definitions of  $k$  and  $\tau_a$ .

$$k = 1/2(\overline{u^2} + \overline{v^2} + \overline{w^2}) \quad (3.1)$$

$$\tau_a = \sqrt{(\overline{uv})^2 + (\overline{uw})^2} \quad (3.2)$$

Mean axial ( $V_x / U_{ref}$ ) and tangential ( $V_\theta / U_{ref}$ ) velocity profiles measured in the  $z$ -direction through the core center are shown in figure 3.3.

Figures 3.1 through 3.3 show the vortex to consist of a small concentrated core surrounded by a circulating velocity field that has wound the wing wake into a spiral. This wake spiral

dominates the turbulence structure outside the core—any region of axisymmetric turbulent flow around the core being small, if present at all. The turbulence measurements made at  $x / c = 10$  (figures 3.2e–h) indicate a variation of turbulence levels along the spiral. Far from the core, the flow is essentially a two-dimensional turbulent wake. Three-dimensional effects become apparent as one moves outboard. Peak turbulence levels first rise, reaching a maximum in the region where the wake begins to curve, and then fall as the core is approached along the spiral. Devenport *et al.* [27] show these variations to be a consequence of the mean rates of strain and lateral curvature suffered by the turbulence. These secondary strain rates, which are in places larger than the peak (primary) axial velocity gradient, appear in velocity spectra to be inhibiting the motions of larger turbulent eddies.

Moving into the core, the apparent turbulence levels increase dramatically (e.g. figure 3.2g). Devenport *et al.* [27] show this to be a consequence of vortex core wandering with an r.m.s. amplitude between 11% and 35% of the vortex core radius, depending on streamwise position. Some clues as to the true turbulence structure in the core region are given by the series of velocity autospectra shown in figure 3.4. These were measured at  $x / c = 10$  along a  $z$ -wise profile from the spiral wake centerline ( $y / c = -0.037$ ,  $z / c = -0.160$ ) to the core center ( $-0.037$ ,  $0.006$ ) (see figure 3.2). At non-dimensional frequencies less than  $f \cdot c / U_{ref} = 20$ , spectral levels rise as the core center is approached because of wandering and other inactive motions of the core. At frequencies greater than  $f \cdot c / U_{ref} = 20$ —where we would expect to see the influence of smaller turbulent structures—spectral levels fall, becoming an order of magnitude smaller at the core center than they are in the wake. Even in the region just outside the core edge where the mean tangential and axial rates of strain reach their maxima (e.g.  $z / c = -0.039$ ), spectral levels in this frequency range

are substantially lower than in the spiral wake. This could indicate that the velocity field of the vortex core may be generating little if any turbulence of its own.

In fact, Devenport *et al.* [27] demonstrate by several means that the core is laminar. They show the rate of evolution of the core mean velocity profiles to be consistent with laminar flow and that small scale turbulence levels in the core are very low. They also argue that the scaling of the high-frequency part of the velocity spectrum at the core center should reveal the scaling and therefore the source of any turbulent velocity fluctuations in the core. They find that the spectrum does not scale on parameters of the core mean-velocity field (implying an absence of any locally generated turbulence) but upon the axial velocity deficit and thickness of the unrolled-up portion of the spiral wake. They conclude that the core is laminar and that the velocity fluctuations within it are generated as the core is buffeted by turbulence in the surrounding spiral wake. Examples of this scaling are shown in figure 3.5 where velocity autospectra measured in the core center at the six streamwise stations are shown normalized on the reference parameters  $U_{ref}$  and  $c$  and on the velocity and length scales of the unrolled-up part of the spiral wake ( $U_w$  and  $L_w$  respectively).

Mean velocities obtained from a  $z$ -wise profile through the core at  $x / c = 10$  are shown in figure 3.3. The tangential ( $V_\theta / U_{ref}$ ) velocity profile is closely antisymmetric about the core center and contains a steep gradient at the core center. The measured peak tangential velocity ( $V_{\theta/m}$ ) is  $0.273U_{ref}$  and the measured core radius ( $r_{1m}$ )—defined as the radius where the peak tangential velocity occurs—is  $0.036c$ . Assuming an axisymmetric core, this implies a measured core circulation of  $0.257\Gamma_0$  where  $\Gamma_0$  is the root circulation of the vortex generator calculated using lifting line theory. The axial ( $V_x$ ) velocity profile is approximately Gaussian in the vicinity of the

core and has a value at the core centerline ( $U_{0m}$ ) of only  $0.847U_{ref}$ . This measured deficit ( $U_{dm}$ ) of  $0.153U_{ref}$  is presumed to be the result of the drag of the vortex generator superimposed on the surplus generated by the low pressure at the core center (see Batchelor [40], Moore and Saffman [41]). Using the method of Devenport *et al.* [27], the profile data in the vicinity of the core can be corrected for wandering effects. This method assumes that the velocity field of the undisturbed vortex core generates little or no turbulence of its own. After correction the core parameters become: core radius,  $r_l = 0.037c$ ; peak tangential velocity,  $V_{\theta l} = 0.286U_{ref}$ ; core circulation,  $\Gamma_l = 0.274\Gamma_0$ ; axial velocity deficit,  $U_d = 0.152U_{ref}$ .

The tangential velocity profile can also be used to calculate a circulation distribution based upon circular paths centered on the vortex core assuming an axisymmetric mean velocity flowfield (see figure 3.6). Since the profiles passed completely through the core, essentially giving two estimates of the tangential velocity at a given radius, the circulation distribution  $\Gamma(r)$  was calculated by equation 3.3.

$$\Gamma(r) = 2\pi \cdot r \cdot \frac{1}{2} (|V_{\theta}(r)| + |V_{\theta}(-r)|) \quad (3.3)$$

As can be seen from the mean streamwise vorticity contours (figure 3.2d), the loose spiral of the blade wake contains a measurable amount of vorticity, showing the limitation of assuming axisymmetric flow. The measured circulation distribution is compared with the predicted circulation distribution of the vortex using Betz's [42] theory (as simplified by Rossow [43] and Donaldson *et al.* [44]) which assumes inviscid two-dimensional flow and complete roll up of the vortex to an axisymmetric state. Lifting line theory was used to estimate the lift distribution of the vortex generator required for the Betz's theory calculation, and the theoretical root circulation ( $\Gamma_0$ )

was used to normalize the curves.  $\Gamma / \Gamma_0$  increases monotonically with radius for both the measured and computed distributions, indicating that the vortex is stable according to Rayleigh's criterion. Outside the core region ( $r / c > 0.1$ ) Betz's theory over-predicts the circulation distribution. Whether this disagreement is a consequence of the assumptions made by Betz or the limitations of the theoretical lift distribution on which the predictions were based is not clear. However, it does appear that the vortex is fully rolled up since measurements made at the other streamwise locations show little variation in circulation distribution with downstream distance.

Figure 3.7 shows the variations of the core parameters (corrected for wandering) with streamwise distance (values listed in table 3.1). Consistent with laminar diffusion none of the parameters varies significantly over the measured streamwise length.

### 3.2.2 Angle of attack variations

Velocity measurements were also made at  $x / c = 10$  with the vortex generator at angles of attack  $2.5^\circ$ ,  $3.75^\circ$ , and  $7.5^\circ$ , with no spoiler attached, to characterize the inflow to the interaction blade as a function of vortex strength. Tangential and axial velocity profiles are plotted in figure 3.8, circulation distributions are shown in figure 3.9, and core parameters corrected for wandering are presented in figure 3.10 and table 3.1. Cross-sectional turbulence measurements were not made in these cases, but turbulence stress profiles and the scaling of velocity spectra measured at the core center (figure 3.11) revealed a very similar structure a to that seen at  $5^\circ$  (i.e. a laminar core in which velocity fluctuations scale on the parameters of the surrounding spiral wake). The measurements show the vortex core size and the peak tangential velocity to increase approximately



in proportion to the angle of attack. The proportion of the circulation contained within the core also increases from  $16.4\%\Gamma_o$  at  $2.5^\circ$  to  $32.8\%\Gamma_o$  at  $7.5^\circ$ . The circulation distributions (figure 3.9) for  $\alpha_i = 3.75^\circ$  and  $7.5^\circ$  are quite similar to the  $5^\circ$  distribution out to  $r/c = 0.25$ . None of the distributions match the Betz's theory very well at locations outside the core region ( $r/c > 0.1$ ) where the theory over predicts all of the distributions.

### 3.2.3 Effects of spoiler size

Velocity measurements were made at  $x/c = 10$  for an angle of attack of  $5^\circ$  with the  $0.2125c$  and  $0.3125c$  diameter spoilers attached to the tip of the generator blade trailing edge to characterize the inflow to the interaction blade at these conditions. Tangential and axial velocity profiles are plotted in figure 3.12, circulation distributions are shown in figure 3.13, and core parameters corrected for wandering are presented in figure 3.14 and table 3.1. Before performing these measurements, much was already known about the structure of these vortex cores from the measurements of Weisser [30] (reported in appendix). Most interestingly, Weisser showed the velocity spectrum at the center of the vortex core to be quite different with spoilers attached, having a much more turbulent character and not scaling on the parameters of the spiral wake (refer also to section 3.4.4). The measurements presented here also show the vortex core to be much larger and weaker with the spoilers attached, as intended. Specifically, adding the  $0.2125c$  diameter spoiler increases the core radius from  $0.037c$  to  $0.178c$  and decreases the peak tangential velocity from  $0.286U_{res}$  to  $0.083U_{res}$ . With the  $0.3125c$  spoiler even larger changes are seen, to  $0.395c$  and  $0.061U_{ref}$  respectively. These greatly enlarged cores encompass much more of the

circulation shed by the generator. Core circulation as a proportion of the total is 38.6% and 62.4% with the spoilers attached—increases of 40% and 128%. The circulation distributions (figure 3.13) are greatly effected by the spoilers, but this is to be expected since Betz's theory is not valid inside the core region (which is the whole plotted  $r/c$  range for  $d/c = 0.3125$ ) where viscous or turbulent diffusion cannot be ignored. Also, the spoiler has an unknown, effect on the lift distribution of the wing making comparison with the Betz's distribution derived using the lifting line theory circulation distribution of the wing of uncertain value.

### 3.3 Evolution of flow after interaction

The leading edge of the interaction blade was located at  $x/c = 14$ ,  $4c$  downstream of the plane where the approach vortex data was taken. To examine the streamwise development of the flow following the interaction, measurements were made at  $x/c = 15.16, 15.95, 17.5, 20, 22.5, 25$ , and  $30$ . Two blade–vortex separations were studied,  $\Delta/c = \pm 0.125$ , with  $\alpha_1 = \alpha_2 = 5^\circ$ , and no spoiler attached to the vortex generator. Measurement locations and conditions, and resulting vortex core parameters for these cases are summarized in table 3.3.

#### 3.3.1 Pressure side passage of $\Delta/c = -0.125$

Figures 3.15–3.21 and plates 3.1–3.3 contain vector and contour plots of the grid data measured in  $y$ - $z$  planes at  $x/c = 15.16, 15.95, 17.5, 20, 22.5, 25$ , and  $30$  respectively. In addition to the quantities plotted for the approach vortex, contours of turbulent kinetic energy production ( $P$

$\cdot c / U_{ref}^3$ ) have been added. Neglecting streamwise derivatives,  $P$  is defined in equation 3.4 in terms of the measured velocity components.

$$P = -\overline{v^2} \cdot \partial V / \partial y - \overline{w^2} \cdot \partial W / \partial z - \overline{uv} \cdot \partial U / \partial y - \overline{uw} \cdot \partial U / \partial z - \overline{vw} \cdot (\partial W / \partial y + \partial V / \partial z) \quad (3.4)$$

Note that some of the quantities are not presented for each downstream location, particularly in cases where the measured values are of the order of the uncertainty.

Initially,  $0.16c$  behind the blade ( $x / c = 15.16$ ), turbulence measurements indicate that the blade wake merely cuts the spiral arm of the vortex (figures 3.15e–g). The cross-flow velocity vectors (figure 3.15a) show the downwash produced by the blade as well as the spanwise flow induced on the blade by the vortex. The cross-flow vorticity vectors shown in figure 3.15b, obtain substantial magnitude due to the large gradients in axial velocity (see figure 3.15c). Turbulent kinetic energy production levels (figure 3.15h) are very high in the blade wake. The extreme gradients in these contours around the vortex core located at  $(0.3, 0.15)$  are most likely a result of vortex core wandering.

Contours of mean streamwise vorticity (figure 3.15d) indicate that the core structure is still compact and the blade wake contains significant amounts of negative vorticity due to the local angle of angle of attack variation produced by the vortex. The negative vorticity region spans over one chord and has a peak level of approximately 35% of the value at the core center. The negative vorticity embedded in the wake induces a difference in the spanwise velocity component across the blade which can be seen in figure 3.15a. This difference produces a dislocation in the spiral wake (figure 13.5e), the negative  $z$  section appearing at a slightly lower/higher  $y$  location than the positive  $z$  section. The tangential velocity profile is similar in form to the inflow profile within the

core region (see figure 3.22b); but when the profile cuts through the blade wake at  $r / c < -0.15$  (see figure 3.22a), it is altered significantly by the negative vorticity contained there. The location of the blade wake is clearly indicated by the axial velocity profile which shows a large axial velocity deficit of at least  $0.435U_{ref}$  (several points are off the scale of the figure) associated with the blade wake, centered at about  $r / c = -0.17$ . The measured peak tangential velocity ( $30.3\%U_{ref}$ ) is  $1.7\%U_{ref}$  more than upstream. The centerline axial velocity deficit has grown by  $3\%U_{ref}$  to  $18.2\%U_{ref}$  and the core radius is almost unchanged. One suspects that these changes are a result of the response of the vortex core to the pressure field surrounding the blade...

Progressing downstream, the vortex begins to distort and interact with the wake. Most noticeable is the tongue of turbulent fluid that forms between the core and wake between  $x / c = 15.95$  (figures 3.16d–f) and  $17.5$  (near  $y / c = 0.55$ ,  $z / c = -0.05$ ; figures 3.17d–f). Turbulent kinetic energy levels in the center of this region at  $x / c = 17.5$  are 2.5 times as large as those in the undisturbed sections of blade wake far from the vortex core. This turbulence appears to be associated with strong negative vorticity (figures 3.16c and 3.17c) and large axial velocity deficit (figures 3.16b and 3.17b).

We suspect this is new turbulence generated by a local instability of the flow. When the region of negative streamwise vorticity in the blade wake is imposed on the vortex, a non-monotonic circulation distribution results (see figure 3.23a); which should be unstable according to Rayleigh's criterion. The production of turbulent kinetic energy at  $x / c = 17.5$  (figure 3.17g) indicates that production in the undisturbed blade wake has decreased compared to levels measured at  $x / c = 15.95$ ; but between the core and the wake exists a region where production levels are

greater than in the blade wake. This supports the conjecture that the region of turbulence outside the core cannot just be considered turbulence originally generated from the blade wake which is being rolled up by the vortex. Peak turbulence levels in the undisturbed portion of the blade wake farthest from the vortex are decreasing with downstream distance as expected; but in the disturbed portion, levels are not decreasing due to a significant amount of TKE production. This local instability has yet to significantly effect the core as indicated by the similarity of the velocity profiles and autospectra measured in the core center (figure 3.24). For a while following the interaction ( $x/c = 15.16$  to  $17.5$ ), the autospectra drops as rapidly at high frequencies ( $f \cdot c / U_{ref} > 6$ ) as in the undisturbed vortex, indicating that the core is still laminar. It is therefore not surprising to see that the tangential velocity profile in the core region changes only slightly between  $x/c = 10$  and  $17.5$  (see figure 3.22a).

Another feature of the flow noticeable at the locations  $x/c = 15.16$ ,  $15.95$ , and  $17.5$  is the fact that the blade wake is thicker and more turbulent outboard (more negative  $y$ ) of the vortex center than inboard. This was predicted from our discussion of the expected flow over the blade in section 1.6 where it was mentioned that outboard of the vortex there is an increase in the local angle of attack on the blade, thereby increasing the thickness of the suction side boundary layer and the resulting wake—possibly to the extent that local separation occurs. Lifting of fluid away from the blade surface by the rotational motion of the vortex may also increase the wake thickness inboard of the vortex center, but this effect is clearly smaller here.

Further downstream, the region of strong new turbulence continues to grow, ultimately engulfing the core and producing a very large region of turbulence surrounding it (see figures 3.18–

21, parts d–f). By  $x / c = 22.5$ , the maximum value of the negative vorticity has diminished to about 10% of its original value at  $x / c = 15.16$  (compare figures 3.15d and 3.19c), presumably due to it being absorbed and canceled by the positive vorticity in and around the core. The distortion and rolling up of the blade wake is seen to continue after  $x / c = 20$ , progressing to a state where the two portions of the blade wake appear to be associated more with the vortex than each other.

The core center autospectra data indicate that a fundamental change in the turbulence structure has occurred. As previously mentioned, spectral levels remain low for non-dimensional frequencies ( $f \cdot c / U_{ref}$ ) greater than 6 for  $x / c = 10$  through 17.5. However, further downstream ( $x / c = 20, 22.5, 25$ , and 30) the roll-off of the spectrum above  $f \cdot c / U_{ref} = 6$  is more gradual with a shape resembling that of the undisturbed (two-dimensional) portion of the interaction blade wake,<sup>1</sup> perhaps signaling that the core has become turbulent. Spectral levels at frequencies above  $f \cdot c / U_{ref} = 20$  are at least an order of magnitude greater than those seen upstream at  $x / c = 15.16, 15.95$ , and 17.5. This change in turbulence structure of the core corresponds directly to the growth of the core radius which is seen to occur shortly after  $x / c = 20$ .

As with the inflow data, the coherent wandering motions of the vortex effect the measured values of the core parameters. Unfortunately, the assumption used for the inflow data that turbulence levels in the core are almost entirely due to wandering is not believed to be valid after the interaction. Normalization of each tangential velocity profile using the measured core radius and peak tangential velocity (figure 3.25) are all of similar shape to the q-vortex profile (see

---

<sup>1</sup> With the interaction blade at 5°, autospectra were measured in a z-wise profile through the interaction blade wake at  $x / c = 30, y / c = 1.5$ . Data presented in figures is for the location where the wake was most turbulent (approximately its center).

equation 3.5) proposed by Lamb and Bachelor [41].

$$\frac{V_{\theta}}{V_{\theta i}} = \frac{r_i}{r} \cdot \left(1 + \frac{1}{2 \cdot \alpha}\right) \cdot \left[1 - \exp\left(-\alpha \cdot \frac{r^2}{r_i^2}\right)\right] \quad \text{where } \alpha = 1.25643 \quad (3.5)$$

If the wandering is assumed to be produced by unsteady changes in the flow direction in the wind tunnel test section, the wandering amplitudes presented by Devenport *et al.* [27] for an isolated vortex can be used instead of assuming a laminar vortex core as done for the undisturbed vortex data. Since the profiles are similar in shape to a q-vortex, the analytical equations derived by Devenport *et al.* [27] can be used to correct the measured core parameters.

The development of the corrected core parameters (core radius, peak tangential velocity, core circulation, and core centerline axial velocity deficit) is manifested in figure 3.26. The core radius remains fairly constant until  $x/c = 20$ , with a small increase seen at  $x/c = 22.5$ , and then increases roughly linearly to a size about 67% larger than the undisturbed value. As previously mentioned,  $x/c = 20$  corresponds to the location where the core is first seen to be turbulent in the velocity spectra. The effects of the interaction upon the tangential velocity field are felt significantly further upstream: there is a slight increase immediately after the interaction, but it decreases steadily after  $x/c = 15.95$  to 37% of the undisturbed value at  $x/c = 30$ . The temporal variation of a Taylor vortex (which also has a similar region of negative vorticity surrounding its core) conducted by Sreedhar and Ragab [45] shows a decay of the peak tangential velocity begins before a growth in core radius, much like what is seen here. These changes result in the core circulation falling quickly between  $x/c = 17.5$  and 22.5; thereafter it begins to level off to a value 61% less than the inflow vortex. An explanation for the leveling off may be that the vortex has

become re-stabilized, as suggested by the circulation distributions (figure 3.23) which by  $x / c = 22.5$  again increase in a monotonic fashion. The TKE production also begins to fall off at this location, ultimately to unmeasurable levels by  $x / c = 30$ . The turbulent flowfield at  $x / c = 25$  and 30 (figures 3.20 and 3.21, parts d–f) is similar to  $x / c = 22.5$ ; showing only a modest increase in size, and gradual decrease in peak turbulence levels.

The results presented indicate that it is the interaction of the vortex with the turbulent blade wake containing negative vorticity that causes it to become unstable. This instability results in a turbulent core of expanding radius, declining peak tangential velocity, and diminished core circulation. It is speculated that in becoming turbulent the core becomes turbulent to diffuse the negative vorticity region, thereby re-stabilizing the vortex. As the flow progresses further downstream, the re-organized, stable vortex serves to suppress the turbulent fluctuations, and levels decay.

### 3.3.2 Suction side passage of $\Delta / c = 0.125$

Velocity profiles were taken through the center of the vortex core for suction side passage of  $\Delta / c = 0.125$  at  $x / c = 15.16, 15.95, 17.5, 20, 22.5, 25$ , and 30. Velocity autospectra was also measured in the vortex core center at all of these locations.

Tangential and axial velocity profiles are plotted in figure 3.27—the  $x / c = 30$  profile is not plotted due to drift associated with a failing sensor, but we believe that the core parameters derived from this profile are reasonably accurate. The profiles appear very similar to those for pressure side passage (figure 3.22) with the obvious difference that the blade wake lies on the other



side of the vortex core. The axial velocity profile at  $x / c = 15.16$  shows the blade wake to be centered at approximately  $r / c = 0.13$  (several points are off the scale of the figure). This is about  $0.04c$  closer to the vortex center than the pressure side passage case. Therefore, the negative vorticity contained in the blade wake is initially closer to the vortex core also evidenced by the tangential velocity profile and the circulation distribution shown in figure 3.28. Velocity autospectra measured in the core center (figure 3.29) indicate that the laminar to turbulent transition of the vortex core occurs at approximately  $x / c = 17.5$ , but the transition is not as distinct as it was for pressure side passage (figure 3.24) which occurred further downstream between  $x / c = 17.5$  and 20. The earlier transition is not surprising considering that the blade wake was initially closer to the vortex core for suction side passage.

Vortex core parameters are presented in figure 3.30 and table 3.3 along with the values for pressure side passage for comparison. Wandering effects were accounted for as described in section 3.3.1 for pressure side passage since the core profiles normalized on core parameters again closely resemble a q-vortex profile (see figure 3.30). The core parameters are plotted in figure 3.31 and show that as in the case for pressure side passage (also shown in figure), the peak tangential velocity increases before a growth in core radius. There is a noticeable decrease in the core radius from  $x / c = 15.16$  to 17.5 which is intriguing because it is similar to the results of the aforementioned investigation of longitudinal vortices using large eddy simulation by Sreedhar and Ragab [45]. Their computational study of the Taylor vortex showed an initial decrease in the core radius which later increased as the core became turbulent. After the initial decrease, the core radius consistently increases after  $x / c = 17.5$ —again correlating directly with the core transition.

The overall trend of the core radii, peak tangential velocity, and implied core circulation data is that the suction side passage has a stronger effect on the vortex. This is likely due to the closer proximity of the blade wake for suction side passage immediately after the vortex passes the blade.

### 3.4 Effects of blade–vortex separation

To examine the effects of the blade–vortex separation, measurements were made at  $x / c = 30$  for separations between  $\pm 0.5c$ . To determine a baseline variation for this study, measurements were made with both the vortex generator and the blade set at angles of attack of  $5^\circ$ , with no spoiler attached to the vortex generator, for both pressure and suction side passages of the vortex. Other configurations were also studied to determine the effects of blade angle of attack, vortex strength, and core radius on the baseline variation. All of the measurement locations and conditions, and resulting vortex core parameters for these cases are summarized in table 3.4.

#### 3.4.1 Baseline variation

Velocity measurements were made for fourteen different blade–vortex separations between  $\pm 0.5c$  at  $x / c = 30$ , with  $\alpha_1 = \alpha_2 = 5^\circ$ , and no spoiler attached to the vortex generator. Velocity profiles (figure 3.32), circulation distributions (figure 3.33), and velocity autospectra (figure 3.34) for pressure and suction side passages are plotted separately (parts a and b of figures respectively).

The velocity profiles (figure 3.32) in the core region ( $r / c < 0.1$ ) appear to be unaffected by the interaction (or lack thereof) for blade–vortex separations greater than  $0.25c$ . Further from the core, the circulation distributions (figure 3.33) for separations of  $\pm 0.375c$  show some effect of

the interaction through lower circulation values—a result of the negative vorticity shed from the blade wake. Core center autospectra (figure 3.34) indicate laminar flow in the cores for  $\Delta / c = \pm 0.5$  and  $\pm 0.375$  by the steep roll-off of the spectra at frequencies  $f \cdot c / U_{ref} > 6$ , with spectral levels being uniformly higher for  $\Delta / c = \pm 0.375$  compared to  $\pm 0.5c$ . The extremely high spectral levels of the summed cross-flow autospectra ( $G_{vv} + G_{ww}$ ) at low frequencies ( $f \cdot c / U_{ref} < 3$ ) are a result of wandering motions of the core. For separations of  $\pm 0.25c$ , the peak tangential velocity is seen to decrease slightly, while the core radius remains constant. At these separations, high frequency axial velocity autospectra ( $G_{uu}$ ) in the core center have increased to roughly 10 times the levels seen for  $\Delta / c = \pm 0.375$ , with the high frequency roll-off being not quite as steep—possibly due to intermittency between laminar and turbulent flow. For separations smaller than  $0.25c$ , the velocity gradient in the core is considerably weakened. This is due to the core becoming turbulent as evidenced by the change in shape of the velocity autospectrum at frequencies above  $f \cdot c / U_{ref} = 3$  to resemble that of the undisturbed (two-dimensional) portion of the turbulent blade wake.

Normalized tangential velocity profiles ( $V_\theta / V_{\theta lm}$  vs.  $r / r_{lm}$ ) are again very similar to a q-vortex (see figure 3.35). Therefore, the method described in section 3.3.1 was used to correct the core parameters for wandering effects (values plotted in figure 3.36 and listed in table 3.4). Figure 3.36 shows that enough separations were considered to define the functional variations. The core radius is not significantly affected for blade vortex separations greater than 0.125 to 0.25 chords; but is greatly increased for smaller separations. The peak tangential velocity at the core edge is more sensitive, there being a significant effect of the interaction for blade vortex separations up to about 0.375 chords. All the effects are very dramatic for small blade–vortex separations. For

example, the peak tangential velocity is less than 20% of its undisturbed value for separations of  $0.0625c$  or less, while the core radius is between 3 and 6 times larger than its undisturbed value in this range—resulting in a loss in core circulation of over 40%. Another feature of these plots is that the core is weakened most for a separation of  $0.0312c$  and the variations are fairly symmetric about this value. This difference was also discussed in section 3.3.2 where it was seen that the blade wake was initially closer to the core center for suction side passage of the vortex which resulted in a weaker vortex core compared to pressure side passage. Several factors may be causing this, each with an unknown contribution. Uncertainty in the zero  $\Delta$  location of the blade may be one; due to changes in the flow angularity of the wind tunnel between the speed where the helium bubble flow visualization was done ( $Re_c \approx 260,000$ ), and the speed at which measurements were taken ( $Re_c = 530,000$ ). The other possible causes are much more complex. The vortex experiences a complex pressure gradient field at close separations, which differs for either pressure or suction side passage, and may lead to vortex bursting, splitting, or other instabilities. The viscous interaction with the blade boundary layer is another effect which will differ depending on which side the vortex passes.

Velocity measurements were made in the y-z plane for  $\Delta / c = 0$  to reveal the cross-sectional structure of the flow field surrounding the core. The resulting vector and contour plots presented in figure 3.37. The shape of the turbulent flowfield (see figures 3.37d–f) is similar to the case of  $\Delta / c = -0.125$  (discussed in section 3.3.1 and shown in figures 3.21d–f) with the blade wake even more distorted by the vortex core. In order for this to occur, the vortex must have maintained a significant amount of its strength after the interaction. Turbulence levels near the

core center for  $\Delta / c = 0$  are roughly one-fourth the levels with  $\Delta / c = -0.125$ . Using insight gained from the downstream development of the flow with  $\Delta / c = \pm 0.125$  (see section 3.3), it is speculated that the core becomes turbulent more quickly for the closer separation of  $\Delta / c = 0$ . The end result is a stable vortex which inhibits the formation of new turbulence. Since this is presumed to occur further upstream, the turbulence created by the previous instability would have had longer to decay. Also apparent is the expected thicker, more turbulent blade wake on the outboard side of the vortex—features discussed in section 3.2.1.

### 3.4.2 Decreased blade angle of attack

To examine the effects of blade angle of attack on the functional variation of core parameters with blade–vortex separation, measurements were made with the blade at zero angle of attack (all other factors the same as the baseline variation). Measurement locations and conditions, and vortex core parameters for these cases are summarized in table 3.4. All passages were with the vortex on the same side of the blade. These passages were all considered to be ‘suction side’ ( $\Delta > 0$ ) passages because the vortex passed on what would have been the suction side of the blade if it were at a positive angle of attack. Since the inflow vortex was found in section 3.2.1 to be non-axisymmetric, this may be of some importance.

Mean velocity profiles (figure 3.38) and circulation distributions (figure 3.39) vary in a fashion similar to those for the baseline variation (see figures 3.32 and 3.33). As the blade–vortex separation is decreased, a decrease in peak tangential velocity occurs before the core radius is seen to increase. Circulation distributions for separations between  $0.375c$  and  $0.0625c$  inclusive, are

similar in shape with the lesser separations decreased by nearly a constant factor compared to greater separations. Core center velocity autospectra (figure 3.40) indicate laminar flow in the core for  $\Delta / c = 0.375$  (by the steep roll-off of the spectra at frequencies  $f \cdot c / U_{ref} > 6$ ), and turbulent flow for all of the closer separations. The extremely high spectral levels of the summed cross-flow autospectra ( $G_{vv} + G_{ww}$ ) at low frequencies ( $f \cdot c / U_{ref} < 3$ ) are a result of wandering motions of the core.

Normalized tangential velocity profiles are shown in figure 3.41. These indicate that for  $\Delta / c = 0.0312$  and 0, the profiles do not compare well with the q-vortex profile. This is of little consequence to unwandering because the velocity gradients associated with the core are so weak that wandering corrections would be insignificant.

The core parameters are plotted as functions of blade-vortex separation in figure 3.42 (values listed in table 3.4) for blade angles of attack of  $0^\circ$  and  $5^\circ$  (the baseline variation). As previously discussed, these data show an increase in vortex core size and a reduction in the peak tangential velocity with decrease in the magnitude of the blade vortex separation. These effects appear to be largely independent of the blade angle of attack. This might be expected since an inviscid analysis (see section 4.2) shows that the vortex sheet shed from the blade is independent of its angle of attack, and changes to the core occur have been shown to occur primarily due to its interaction with the negative part of that sheet. The only significant effects of blade angle of attack are seen in the core radius for blade-vortex separations less than the initial core size ( $0.037c$ ). The profiles here with  $\alpha_2 = 0^\circ$  were very hard to interpret due to a non-axisymmetric core. The flowfield in the vicinity of the core is visible in figure 3.43 for  $\Delta / c = 0$ . The vorticity contours

(figure 3.43c) show this weak and non-axisymmetric. It should be noted that the mean velocities measured were very small—on the order of the uncertainty in the measurements. The differences in core parameters for  $\alpha_2 = 0^\circ$  and  $5^\circ$  are probably insignificant considering the profiles cannot be well defined by so few parameters here and the velocity gradients involved are very small—making it difficult to determine the core radius anyway.

A small grid of velocity measurements was also made with  $\Delta / c = 0.0625$ . The resulting vector and contour plots are shown in figure 3.44.

### 3.4.3 Increased vortex strength

To examine the effects of initial vortex strength on the functional variation of core parameters with blade–vortex separation, measurements were made with the vortex generator at an angle of attack of  $10^\circ$  (all other factors the same as the baseline variation). Measurement locations and conditions, and vortex core parameters for these cases are summarized in table 3.4.

Mean velocity profiles (figure 3.45) and circulation distributions (figure 3.46) vary in a fashion similar to those for the baseline variation (see figures 3.32 and 3.33). Core center velocity autospectra (figure 3.47) indicate laminar flow in the core for  $\Delta / c = 0.5$  and  $0.375$ , and turbulent flow for all of the closer separations (as in the baseline variation). Normalized tangential velocity profiles are shown in figure 3.48. These indicate that for  $\Delta / c = 0$  and to some extent  $\Delta / c = 0.0312$  and  $0.0625$ , the profiles do not compare well with the q-vortex profile. This is of little consequence because the velocity gradients associated with the core are so weak that wandering corrections would be insignificant.

The core parameters as functions blade–vortex separation are shown in figure 3.49 for generator angles of attack of  $10^\circ$  and  $5^\circ$  (the baseline variation). The effects of the interaction appear heavily dependent upon the generator angle of attack. At all blade–vortex separations where a comparison is possible, the core radius and peak tangential velocity are greater with the generator at  $10^\circ$  than at  $5^\circ$ . However, if we normalize these parameters on their undisturbed values ( $r_{10}$  and  $V_{\theta 10}$ ) then the effects of the generator angle of attack appear much weaker (figure 4.50). See section 4.1 for a complete discussion.

#### 3.4.4 Increased core radius

To examine the effects the initial vortex core radius has on the functional variation of the core parameters with blade–vortex separation, measurements were made with either the  $0.2125c$  or  $0.3125c$  diameter circular spoiler attached (all other factors the same as the baseline variation). Mean velocity profiles were made for  $\Delta / c = 0.5, 0.25, 0.125, 0$ , and  $-0.125$ . Grids of mean velocity measurements in the  $y$ - $z$  plane were made for  $\Delta / c = 0.125, 0.0625, 0$ , and  $-0.125$ . Table 3.4 summarizes the measurement locations and conditions, and vortex core parameters for these cases. Included in table 3.4 are core parameters derived from both the velocity profiles and grids.

Core parameters were very difficult to obtain from velocity profiles due to weak, non-axisymmetric cores. Core parameters were obtained from the grid measurements by an ad hoc method devised to produce less scattered values suitable for use in simple flow models requiring a core radius. This method is as follows From the velocity profile of a  $q$  vortex



$$\frac{V_{\theta}}{V_{\theta l}} = \frac{r_l}{r} \cdot \left(1 + \frac{1}{2 \cdot \alpha}\right) \cdot \left[1 - \exp\left(-\alpha \cdot \frac{r^2}{r_l^2}\right)\right] \quad \text{where } \alpha = 1.25643 \quad (3.5)$$

the vorticity ( $\Omega(r)$ ) is

$$\Omega(r) = \frac{1}{r} \cdot \frac{\partial}{\partial r}(r \cdot V_{\theta}) = 2 \cdot \frac{V_{\theta l}}{r_l^2} \cdot \left(\alpha + \frac{1}{2}\right) \cdot \exp\left(-\alpha \cdot \frac{r^2}{r_l^2}\right) \quad (3.6)$$

The ratio between the vorticity at the core edge ( $\Omega(r_l)$ ) and the maximum vorticity occurring at the core center ( $\Omega(0)$ ) is a constant equal to approximately 0.285 (see equation 3.7).

$$\frac{\Omega(r_l)}{\Omega(0)} = \exp(-\alpha) \approx 0.285 \quad (3.7)$$

The core edge (and thus the core radius) is located from a vorticity field contour plot by the contour equal to 28.5% of the maximum vorticity in this case. If we assume that the 28.5% maximum vorticity contour is indicative of the core edge for non-axisymmetric, non-q-vortex cores, a mean core radius can be estimated. It is then assumed that this mean core radius used in conjunction with equation 3.6 will give a reasonable estimate of the peak tangential velocity. The core center axial velocity deficit is simply the deficit value at the location of maximum vorticity.

#### 3.4.4.1 Spoiler diameter of 0.2125c

Measurements were made at  $x/c = 30$  with the 0.2125c diameter circular spoiler attached to the generator tip. This produced a vortex with core radius of 0.178c and peak tangential velocity of  $0.083U_{ref}$  at  $x/c = 10$  (see section 3.2.3). The zero  $\Delta$  blade position was initially assumed to be the same as the location determined without the spoiler attached. Grids of velocity measurements were made at the nominal separations of  $\Delta/c = 0.125, 0.0625, 0$ , and  $-0.125$

(vector and contour plots are figures 3.51–3.54 respectively). After examination of these plots, especially the vorticity plots, no adjustment appeared necessary to the initial blade–vortex separation estimates. The estimated core edge contour is marked by the dashed contour line in each vorticity plot (part c of figures 3.51–3.54) as determined by the method described above in section 3.4.4. The core edge contours are fairly circular for  $\Delta/c = \pm 0.125$ , but to a lesser extent for  $\Delta/c = 0.0625$ —the contours are not at all circular for  $\Delta = 0$ . Of course, the vorticity field of the q-vortex is perfectly axisymmetric, so non-circular contours immediately indicate deviation from this assumption. Nonetheless, core radii values were estimated as an average value.

Although the grids were not large enough to completely encompass the change in orientation of the blade and generator wakes with respect to the vortex, a noticeable deformation of the blade wake can be seen. Peak turbulent kinetic energy levels (figures 3.51–3.54, part f) for all four separations are roughly equal, unlike the cases without the spoiler where a direct comparison can be made. For  $\Delta/c = -0.125$  the peak turbulent kinetic energy level with the spoiler attached is only 25% the level without the spoiler (compare figures 3.54f and 3.21f respectively), but the area of the turbulent region is much larger with the spoiler attached. On the other hand, for  $\Delta/c = 0$  the peak turbulent kinetic energy level without the spoiler is decreased by roughly 25% to approximately the value with the spoiler (compare figures 3.37f and 3.53f respectively)—again, the area of the turbulent region is much larger with the spoiler attached.

Mean velocity profiles (figure 3.55) were taken for  $\Delta/c = 0.5, 0.25, 0.125, 0$ , and  $-0.125$ . The tangential velocity profile for  $\Delta/c = 0$  is of particular interest because there is a peak at  $r/c = -0.25$  and another at  $-0.6$ . As can be seen in the corresponding vorticity field plot (figure 3.53c)

the vortex core is very non-axisymmetric. This is probably the result of the core being split as it passes the blade, and not completely reorganizing. This is not surprising since even the undisturbed core would have completed only about one revolution between  $x/c = 15$  and 30. The core tangential velocity profiles for the further separations are fairly well described by the q-vortex profile as shown in figure 3.56 indicating the core radius and peak tangential velocity are still important parameters. The axial velocity profiles for  $\Delta/c = 0$  and -0.125 show that the peak deficit does not occur at the core center, instead the profiles are quite complex. Comparing the location of peak streamwise vorticity from figures 3.53c and 3.54c with the axial velocity deficit contours in figures 3.53b and 3.54b shows that indeed, the peak deficit partially surrounds the core for these cases. This situation is similar to results discussed in section 3.3 (evolution of flow after interaction) where the area of turbulent kinetic energy production, resulting from the negative vorticity region, had a large axial velocity deficit associated with it.

Core center velocity autospectrum taken at  $\Delta/c = 0.5$  (figure 3.57) shows that the turbulent structure of the core is essentially the same at it was before the interaction with the spectra shifted consistently to lower levels for  $x/c = 30$ ; and is very similar to the undisturbed (two-dimensional) turbulent blade wake for frequencies above  $f \cdot c / U_{ref} = 3$ .

The core parameters as functions blade-vortex separation are shown in figure 3.58 with and without the  $0.2125c$  diameter spoiler attached. Parameters derived from both the profiles and grids with the spoiler are shown (values listed in table 3.4). The data appears very scattered, but the general trend remains the same: decreased blade-vortex separation results in a decrease in peak tangential velocity and increase in core radius.

#### 3.4.4.2 Spoiler diameter of $0.3125c$

Measurements were made at  $x / c = 30$  with the  $0.3125c$  diameter circular spoiler attached to the generator tip. This produced a vortex with core radius of  $0.395c$  and peak tangential velocity of  $0.061U_{ref}$  at  $x / c = 10$  (see section 3.2.3). The zero  $\Delta$  blade position was initially assumed to be the same as the location determined without the spoiler attached. Grids of velocity measurements were made at the nominal separations of  $\Delta / c = 0.125, 0.0625, 0$ , and  $-0.125$  (vector and contour plots are figures 3.59–3.62 respectively). After examination of these plots, no adjustment appeared necessary to the initial blade–vortex separation estimates. The estimated core edge contour is marked by the dashed contour line in each vorticity plot (part c of figures 3.59–3.62) as determined by the method described above in section 3.4.4. The core edge contours are not at all circular for any of the separations where measurements were made indicating a substantial deviation from the q-vortex vorticity field assumption. Nonetheless, core radii values were estimated as an average value.

Although the grids were not large enough to completely encompass the change in orientation of the blade and generator wakes with respect to the vortex, a noticeable deformation of the blade wake can be seen. Peak turbulent kinetic energy levels (figures 3.59–3.62, part f) for all four separations are roughly equal. These peak levels are also comparable to the cases with the smaller  $0.2125c$  diameter spoiler attached (see figures 3.51–3.54), but the area of the turbulent region is much larger with the larger  $0.3125c$  diameter spoiler attached. As seen in the smaller spoiler grid data, the location of peak vorticity is adjacent (and partially surrounds) the location of maximum axial velocity deficit (compare parts b and c of figures 3.59–3.62).

Mean velocity profiles (figure 3.63) were taken for  $\Delta / c = 0.5, 0.25, 0.125, 0$ , and  $-0.125$ . The tangential velocity profiles for  $\Delta / c = 0.125$  and  $0$  show multiple peaks. As can be seen in the corresponding vorticity field plot (figure 3.59c and 3.61c) the vortex core is very non-axisymmetric and is actually split in two for  $\Delta = 0$ . The non-axisymmetry is not surprising since even the undisturbed core would have completed only about one-half a revolution between  $x / c = 15$  and  $30$ . The axial velocity profiles for  $\Delta / c = 0$  and  $-0.125$  show the peak deficit to be centered  $0.6c$  to  $0.5c$  away from the core centerline. Comparing the location of peak streamwise vorticity from figures 3.61c and 3.62c with the axial velocity deficit contours in figures 3.61b and 3.62b shows that indeed, the peak deficit partially surrounds the core for these cases. This situation is similar to results discussed in section 3.3 (evolution of flow after interaction) where the area of turbulent kinetic energy production, resulting from the negative vorticity region, had a large axial velocity deficit associated with it. The core tangential velocity profile for the furthest separation ( $\Delta / c = 0.5$ ) is fairly well described by the q-vortex profile as shown in figure 3.64.

Core center velocity autospectrum taken at  $\Delta / c = 0.5$  (figure 3.65) shows that the turbulent structure of the core is essentially the same at it was before the interaction—the spectrum is shifted consistently to lower levels for  $x / c = 30$ , and is very similar to the undisturbed (two-dimensional) turbulent blade wake for frequencies above  $f \cdot c / U_{ref} = 3$ .

The core parameters as functions blade–vortex separation are shown in figure 3.66 with and without the  $0.3125c$  diameter spoiler attached. Parameters derived from both the profiles and grids with the spoiler are shown (values listed in table 3.4). The data appears very scattered, and no correlation between the variations with and without the spoiler could be obtained (see section

4.1 for more detail). However, the general trend remains the same: decreased blade–vortex separation results in a decrease in peak tangential velocity and increase in core radius.

### 3.5 Angle of attack variations with fixed blade vortex separation

Several measurements were made at  $x / c = 30$  for different angle of attack combinations of the vortex generator and blade with a fixed blade–vortex separation of  $-0.125c$ . Table 3.5 summarizes the measurement locations and conditions, and vortex core parameters for these cases.

#### 3.5.1 Changing blade angle of attack

As discussed in section 3.4.2, the blade angle of attack appeared to have little effect on the variation of the core parameters as a function of the blade–vortex separation. Additional measurements were made at  $x / c = 30$ , for a fixed blade–vortex separation of  $-0.125c$  to confirm this observation. The vortex generator angle of attack remained constant at  $5^\circ$  with no spoiler attached. Blade angles of attack of  $2.5^\circ$ ,  $5^\circ$ , and  $7.5^\circ$  were studied.

The mean velocity profiles (figure 3.67) show that increasing the blade angle of attack does have a small effect on the velocity profiles, causing a reduction in peak tangential velocity and increase in core radius. The normalized tangential velocity profiles (figure 3.68) are well described by the q-vortex profile and therefore the unwandering method of section 3.3.1 was used to correct the core parameters shown in figure 3.69 (values listed in table 3.5). Interestingly, the small effects the blade angle of attack has on the core radius and peak tangential velocity are of equal proportion resulting in nearly identical core circulations. Core center velocity autospectra (figure

3.70) show no change in the turbulence structure has occurred. In fact, levels are nearly the same, and they are consistently an order of magnitude higher than the undisturbed (2-D) portion of the blade wake at  $5^\circ$  for frequencies above  $f \cdot c / U_{ref} = 20$ .

### 3.5.2 Changing vortex strength and blade angle of attack simultaneously

Measurements were also made at  $x / c = 30$  for a range of vortex strengths (controlled by  $\alpha_1$ ) and blade angles of attack ( $\alpha_2$ ) where  $\alpha_1 = \alpha_2$ , and a fixed blade–vortex separation of  $-0.125c$ . Table 3.5 summarizes the measurement locations and conditions, and vortex core parameters for these cases. Angles studied were  $\alpha_1 = \alpha_2 = 2.5^\circ, 3.75^\circ, 5^\circ, 6.25^\circ, 7.5^\circ$ , and  $10^\circ$ .

Mean velocity profiles are shown in figure 3.71, and the normalized tangential velocity profiles shown in figure 3.72. The normalized profiles are well described by the q-vortex profile and therefore the unwandering method of section 3.3.1 was used to correct the core parameters shown in figure 3.73 (values listed in table 3.5). The core parameters show that the core radius is roughly parabolic in shape with a minimum value of  $0.058c$  for  $\alpha_1 = \alpha_2 = 3.75^\circ$  and a value over 5 times as large with  $\alpha_1 = \alpha_2 = 10^\circ$  ( $0.3c$ ). Interestingly enough, the variation in the peak tangential velocity is such that the core circulation remains almost constant. Core center velocity autospectra (figure 3.74) are all of similar shape, however levels increase with increasing angle from  $\alpha_1 = \alpha_2 = 2.5^\circ$  to  $6.25^\circ$ , then decrease for  $\alpha_1 = \alpha_2 = 6.25^\circ$  to  $10^\circ$ .

Grid measurements were also made in the  $y$ - $z$  plane for  $\alpha_1 = \alpha_2 = 2.5^\circ$  and  $7.5^\circ$ —vector and contour plots are presented in figures 3.75 and 3.76. Refer to figure 3.21 for the  $\alpha_1 = \alpha_2 = 5^\circ$  vector and contour plots. These figures show that the increased angles produce a much larger and

more turbulent region of flow. This would be expected since the increased strength of the vortex generator causes more negative vorticity to be shed by the blade and it is the interaction of the vortex with this negative vorticity which is responsible for the turbulent region.

### **3.6 Other velocity measurements**

For some of the measurement locations and conditions discussed in the previous sections, velocity autospectra data was taken at locations along a z-wise profile through the core center. This data is presented in figures 3.77–3.80. Measurement locations and conditions and a guide to the figure numbering is contained in table 3.6.



$x/c$	$\alpha_i(^{\circ})$	$d/c$	$r_1/c$	$V_{\theta 1}/U_{ref}$	$\Gamma_1/\Gamma_0$	$U_d/U_{ref}$
5	5	none	0.036	0.286	0.267	0.165
10	5	none	0.037	0.286	0.275	0.152
15	5	none	0.036	0.277	0.260	0.141
20	5	none	0.040	0.278	0.287	0.153
25	5	none	0.033	0.275	0.236	0.147
30	5	none	0.036	0.263	0.248	0.160
10	2.5	none	0.019	0.166	0.164	0.144
10	3.75	none	0.021	0.231	0.167	0.160
10	5	none	0.037	0.286	0.275	0.152
10	7.5	none	0.045	0.422	0.328	0.085
10	5	none	0.037	0.286	0.275	0.152
10	5	0.2125	0.178	0.083	0.386	0.130
10	5	0.3125	0.395	0.061	0.625	0.104

**Table 3.1** Measurement locations and conditions, and core parameters of undisturbed vortices

	wake regions	core edge	core center
$U / U_{ref}$	0.015	0.015	0.014
$V / U_{ref}$	0.025	0.025	0.024
$W / U_{ref}$	0.025	0.024	0.023
$\overline{u^2} / U_{ref}^2$	$3.1 \times 10^{-6}$	$1.4 \times 10^{-5}$	$4.3 \times 10^{-5}$
$\overline{v^2} / U_{ref}^2$	$9.5 \times 10^{-6}$	$1.5 \times 10^{-5}$	$1.7 \times 10^{-4}$
$\overline{w^2} / U_{ref}^2$	$9.9 \times 10^{-6}$	$2.0 \times 10^{-5}$	$1.6 \times 10^{-4}$
$\overline{uv} / U_{ref}^2$	$4.3 \times 10^{-6}$	$1.4 \times 10^{-5}$	$1.2 \times 10^{-4}$
$\overline{vw} / U_{ref}^2$	$4.5 \times 10^{-6}$	$2.3 \times 10^{-5}$	$5.2 \times 10^{-5}$
$\overline{uw} / U_{ref}^2$	$2.9 \times 10^{-6}$	$8.5 \times 10^{-6}$	$1.0 \times 10^{-4}$

Table 3.2 Typical uncertainties in hot-wire measurements

$x/c$	$\alpha_1(^{\circ})$	$\alpha_2(^{\circ})$	$d/c$	$\Delta/c$	$r_1/c$	$V_{\theta 1}/U_{ref}$	$\Gamma_1/\Gamma_0$	$U_d/U_{ref}$
10	5		none		0.037	0.286	0.275	0.152
15.16	5	5	none	-0.125	0.035	0.303	0.279	0.182
15.95	5	5	none	-0.125	0.036	0.318	0.296	0.149
17.5	5	5	none	-0.125	0.036	0.294	0.275	0.144
20	5	5	none	-0.125	0.035	0.232	0.215	0.167
22.5	5	5	none	-0.125	0.039	0.177	0.179	0.160
25	5	5	none	-0.125	0.047	0.139	0.173	0.138
30	5	5	none	-0.125	0.061	0.105	0.168	0.111
10	5		none		0.037	0.286	0.275	0.152
15.16	5	5	none	0.125	0.036	0.310	0.289	0.173
15.95	5	5	none	0.125	0.033	0.297	0.255	0.159
17.5	5	5	none	0.125	0.031	0.264	0.251	0.178
20	5	5	none	0.125	0.036	0.179	0.168	0.181
22.5	5	5	none	0.125	0.05	0.121	0.158	0.153
25	5	5	none	0.125	0.055	0.104	0.149	0.132
30	5	5	none	0.125	0.062	0.065	0.105	0.130

**Table 3.3** Measurement locations and conditions, and core parameters for investigation of downstream development after interaction

$x/c$	$\alpha_1(^{\circ})$	$\alpha_2(^{\circ})$	$d/c$	$\Delta/c$	grid	$r_1/c$	$V_{\theta 1}/U_{ref}$	$\Gamma_1/\Gamma_0$	$U_d/U_{ref}$
30	5	5	none	-0.5		0.035	0.305	0.275	0.131
30	5	5	none	-0.375		0.037	0.294	0.283	0.138
30	5	5	none	-0.25		0.037	0.256	0.250	0.140
30	5	5	none	-0.125		0.061	0.105	0.168	0.111
30	5	5	none	-0.0625		0.109	0.056	0.158	0.076
30	5	5	none	-0.0312		0.139	0.039	0.143	0.066
30	5	5	none	0		0.174	0.023	0.105	0.048
30	5	5	none	0.0312		0.199	0.021	0.107	0.027
30	5	5	none	0.0625		0.159	0.034	0.140	0.041
30	5	5	none	0.0938		0.101	0.039	0.102	0.072
30	5	5	none	0.125		0.062	0.065	0.105	0.130
30	5	5	none	0.25		0.038	0.237	0.235	0.142
30	5	5	none	0.375		0.036	0.291	0.272	0.136
30	5	5	none	0.5		0.034	0.302	0.270	0.131
30	5	0	none	0.375		0.037	0.267	0.260	0.148
30	5	0	none	0.25		0.038	0.221	0.222	0.153
30	5	0	none	0.125		0.071	0.081	0.149	0.106
30	5	0	none	0.0938		0.109	0.050	0.142	0.074
30	5	0	none	0.0625		0.146	0.033	0.127	0.057
30	5	0	none	0.0312		0.595	0.022	0.342	0.021
30	5	0	none	0		0.580	0.021	0.311	0.048
30	10	5	none	0.5		0.053	0.498	0.342	0.030
30	10	5	none	0.375		0.053	0.426	0.293	0.070
30	10	5	none	0.25		0.053	0.298	0.205	0.214
30	10	5	none	0.125		0.119	0.103	0.160	0.144
30	10	5	none	0.0938		0.141	0.081	0.149	0.124
30	10	5	none	0.0625		0.200	0.054	0.141	0.090
30	10	5	none	0.0312		0.250	0.041	0.132	0.042
30	10	5	none	0		0.450	0.043	0.253	0.039
30	5	5	0.2125	0.5		0.216	0.072	0.409	0.087
30	5	5	0.2125	0.25		0.189	0.057	0.283	0.085
30	5	5	0.2125	0.125		0.194	0.039	0.199	0.058
30	5	5	0.2125	0.125	✓	0.246	0.039	0.251	0.073
30	5	5	0.2125	0.0625	✓	0.260	0.031	0.211	0.056
30	5	5	0.2125	0		0.465	0.024	0.286	0.034
30	5	5	0.2125	0	✓	0.444	0.023	0.267	0.047
30	5	5	0.2125	-0.125		0.456	0.029	0.351	0.030
30	5	5	0.2125	-0.125	✓	0.248	0.032	0.208	0.078
30	5	5	0.3125	0.5		0.375	0.047	0.459	0.074
30	5	5	0.3125	0.25		0.420	0.025	0.269	0.063
30	5	5	0.3125	0.125		0.680	0.017	0.309	0.056
30	5	5	0.3125	0.125	✓	0.596	0.024	0.374	0.060
30	5	5	0.3125	0.0625	✓	0.649	0.022	0.373	0.058
30	5	5	0.3125	0		0.680	0.017	0.309	0.025
30	5	5	0.3125	0	✓	0.656	0.023	0.395	0.035
30	5	5	0.3125	-0.125		0.440	0.020	0.230	0.016
30	5	5	0.3125	-0.125	✓	0.577	0.024	0.362	0.058

**Table 3.4** Measurement locations and conditions, and core parameters for investigation of blade-vortex separation effects. If column marked 'grid' is checked, then core parameters were derived from grid data; otherwise they were derived from profile data.

$x/c$	$\alpha_1$ (°)	$\alpha_2$ (°)	$d/c$	$\Delta/c$	$r_1/c$	$V_{\theta 1}/U_{ref}$	$\Gamma_1/\Gamma_0$	$U_d/U_{ref}$
30	5	2.5	none	-0.125	0.052	0.123	0.167	0.116
30	5	5	none	-0.125	0.061	0.105	0.168	0.111
30	5	7.5	none	-0.125	0.068	0.093	0.164	0.098
30	2.5	2.5	none	-0.125	0.058	0.056	0.170	0.065
30	3.75	3.75	none	-0.125	0.055	0.093	0.178	0.092
30	5	5	none	-0.125	0.061	0.105	0.168	0.111
30	6.25	6.25	none	-0.125	0.072	0.110	0.166	0.114
30	7.5	7.5	none	-0.125	0.104	0.093	0.168	0.111
30	10	10	none	-0.125	0.300	0.054	0.212	0.055

**Table 3.5** Measurement locations and conditions, and core parameters for study of angle of attack effects with fixed blade–vortex separation

$x/c$	$\alpha_1(^{\circ})$	$\alpha_2(^{\circ})$	$d/c$	$\Delta/c$	figure
30	5	0	none	0.375	3.77a
30	5	0	none	0.25	3.77b
30	5	0	none	0.125	3.77c
30	5	0	none	0.0938	3.77d
30	5	0	none	0.0625	3.77e
30	5	0	none	0.0312	3.77f
30	5	0	none	0	3.77g
30	10	5	none	0.5	3.78a
30	10	5	none	0.25	3.78b
30	10	5	none	0.125	3.78c
30	10	5	none	0.0625	3.78d
10	5		0.2125		3.79a
30	5	5	0.2125	0.5	3.79b
10	5		0.3125		3.80a
30	5	5	0.3125	0.5	3.80b

**Table 3.6** Measurement locations and conditions, and figure numbers of autospectra data taken along  $z$ -wise profiles through core center

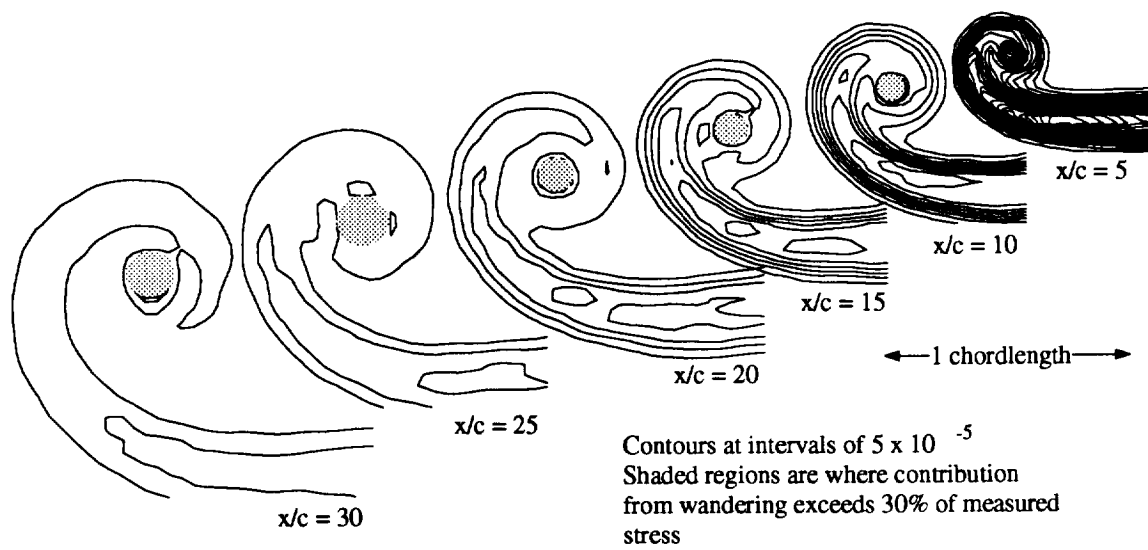


**Figure 3.1** Contours of axial normal turbulent stress ( $\overline{u^2} / U_{ref}^2$ ) measured with the interaction blade removed:  $\alpha_I = 5^\circ$ , no spoiler.

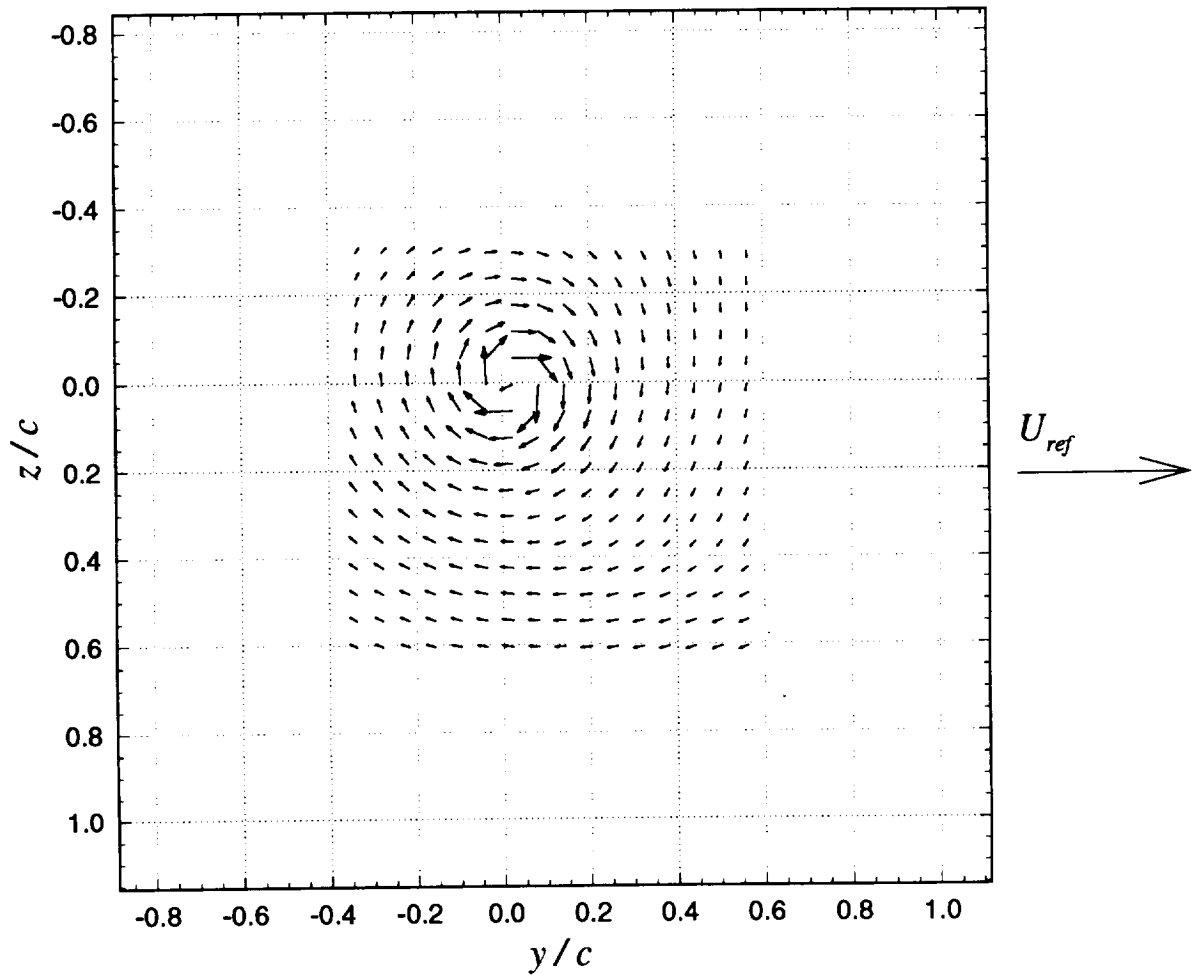


**Figure 3.2a** Mean cross-flow velocity ( $V/U_{ref}$ ,  $W/U_{ref}$ ) vectors:  $x/c = 10$ ,  $\alpha_l = 5^\circ$ , no spoiler



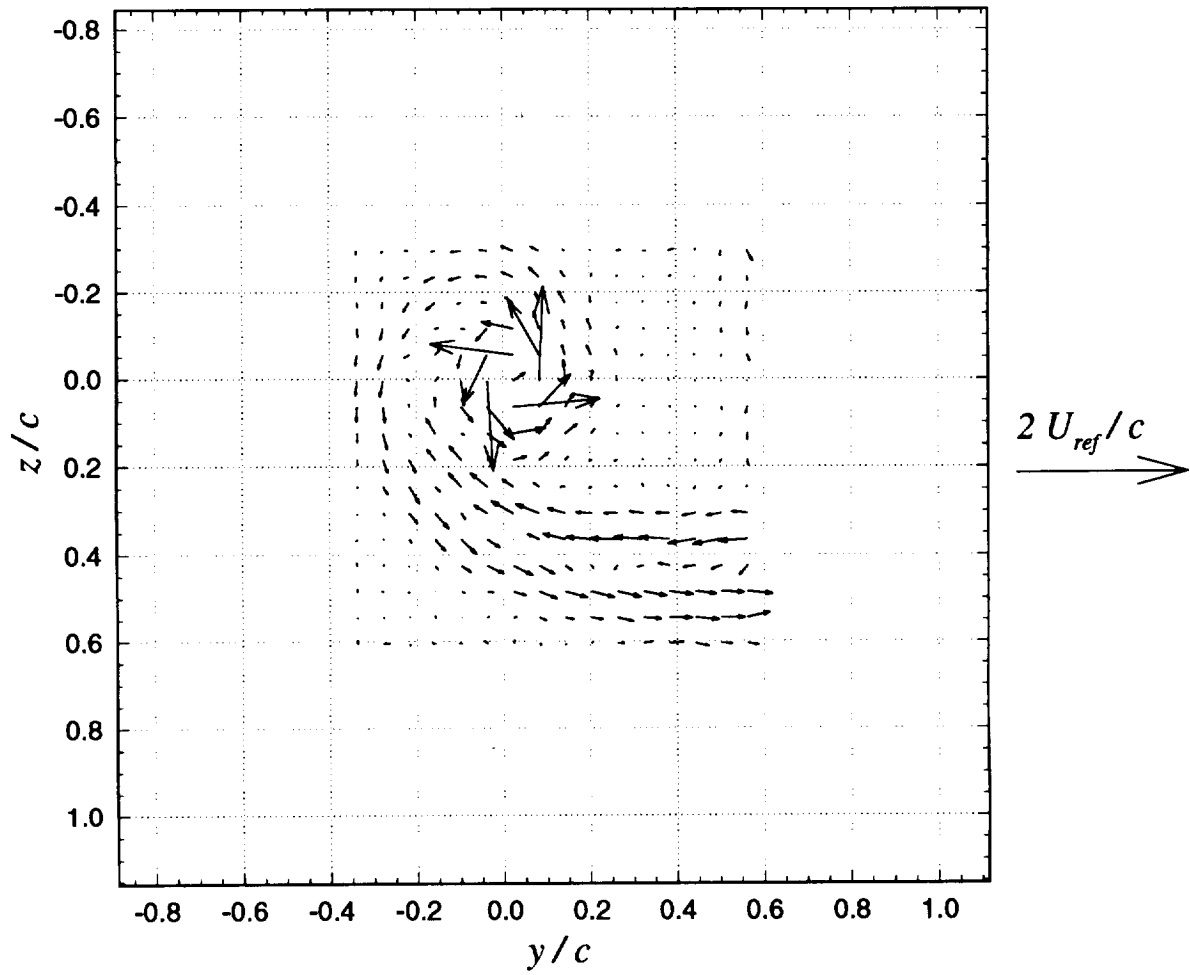


**Figure 3.2b** Mean cross-flow vorticity vectors ( $\Omega_y \cdot c / U_{ref}$ ,  $\Omega_z \cdot c / U_{ref}$ ):  $x/c = 10$ ,  $\alpha_l = 5^\circ$ , no spoiler

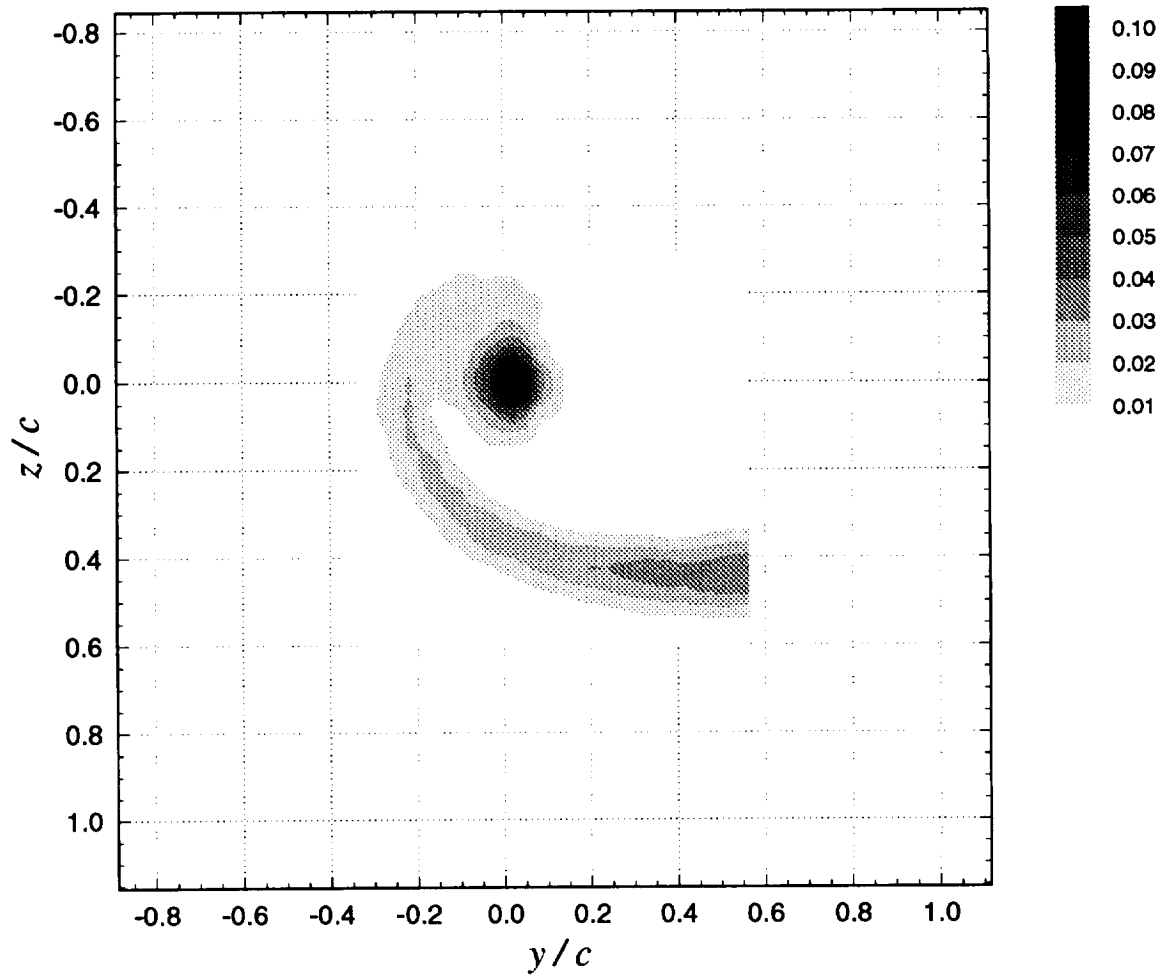


**Figure 3.2c** Contours of mean axial velocity deficit  $((U_{ref} - U) / U_{ref})$ :  $x/c = 10$ ,  $\alpha_l = 5^\circ$ , no spoiler

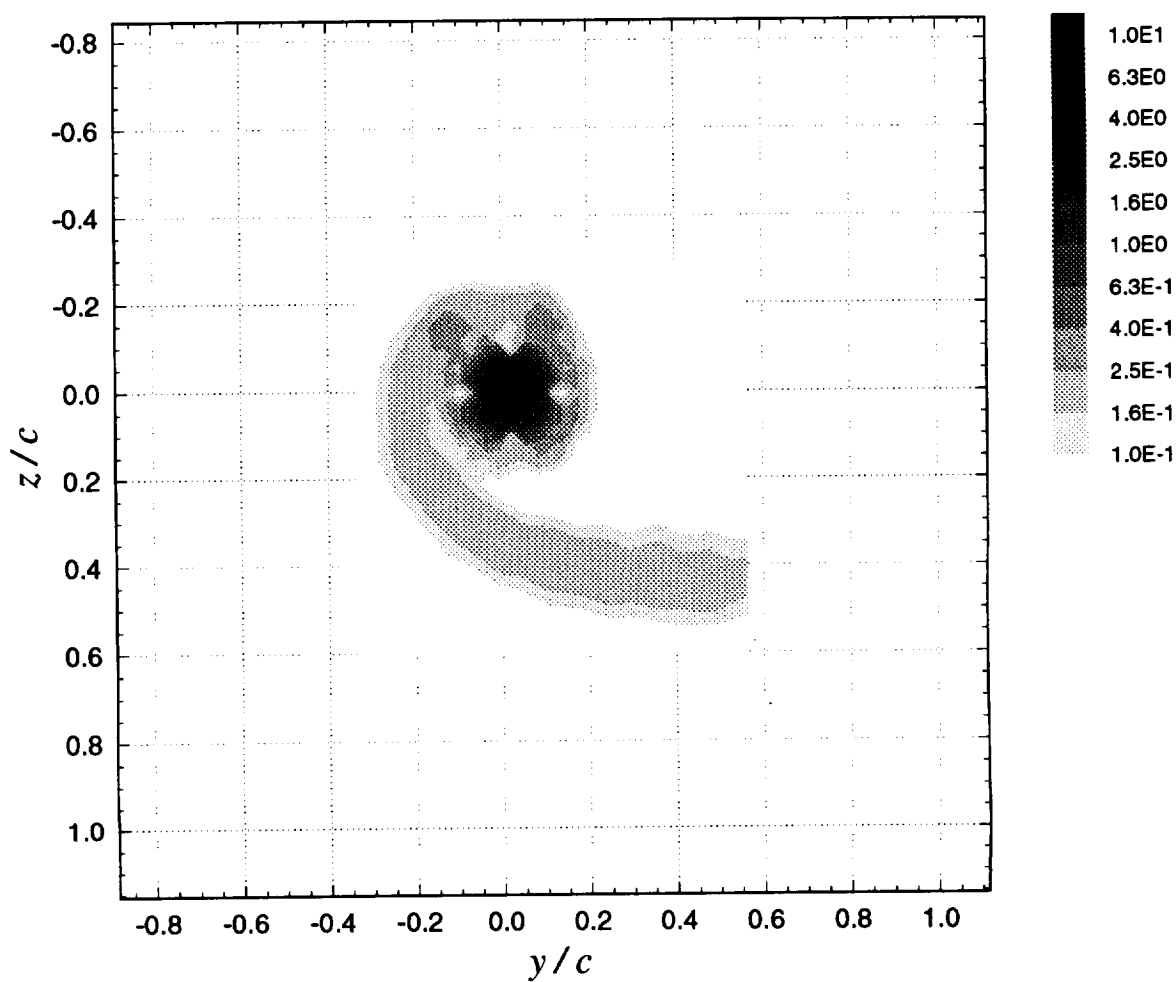


**Figure 3.2d** Contours of mean axial vorticity ( $\Omega_x \cdot c / U_{ref}$ ):  $x/c = 10$ ,  $\alpha_l = 5^\circ$ , no spoiler

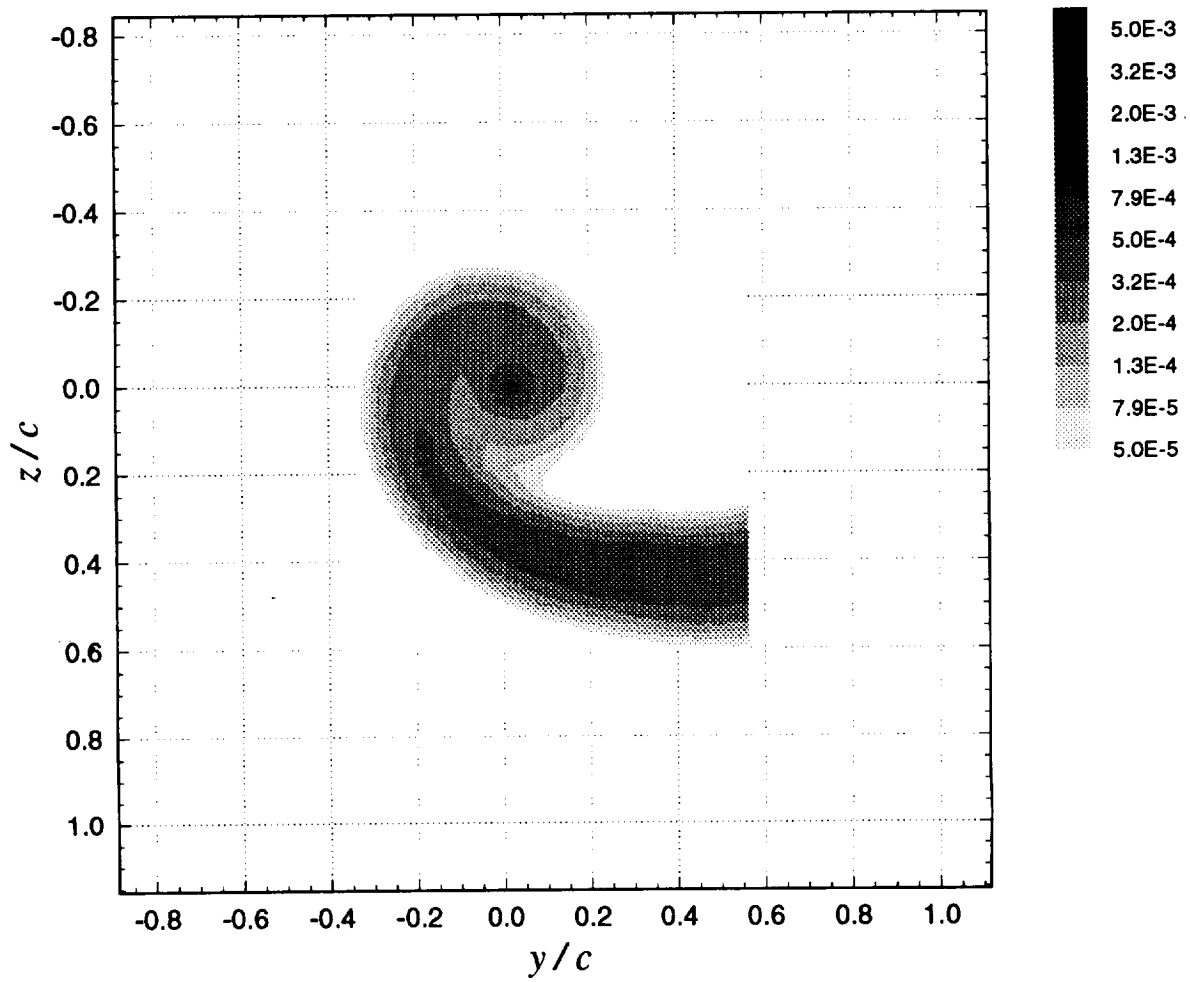


**Figure 3.2e** Contours of axial normal turbulent stress ( $\overline{u^2} / U_{ref}^2$ ):  $x/c = 10$ ,  $\alpha_l = 5^\circ$ , no spoiler

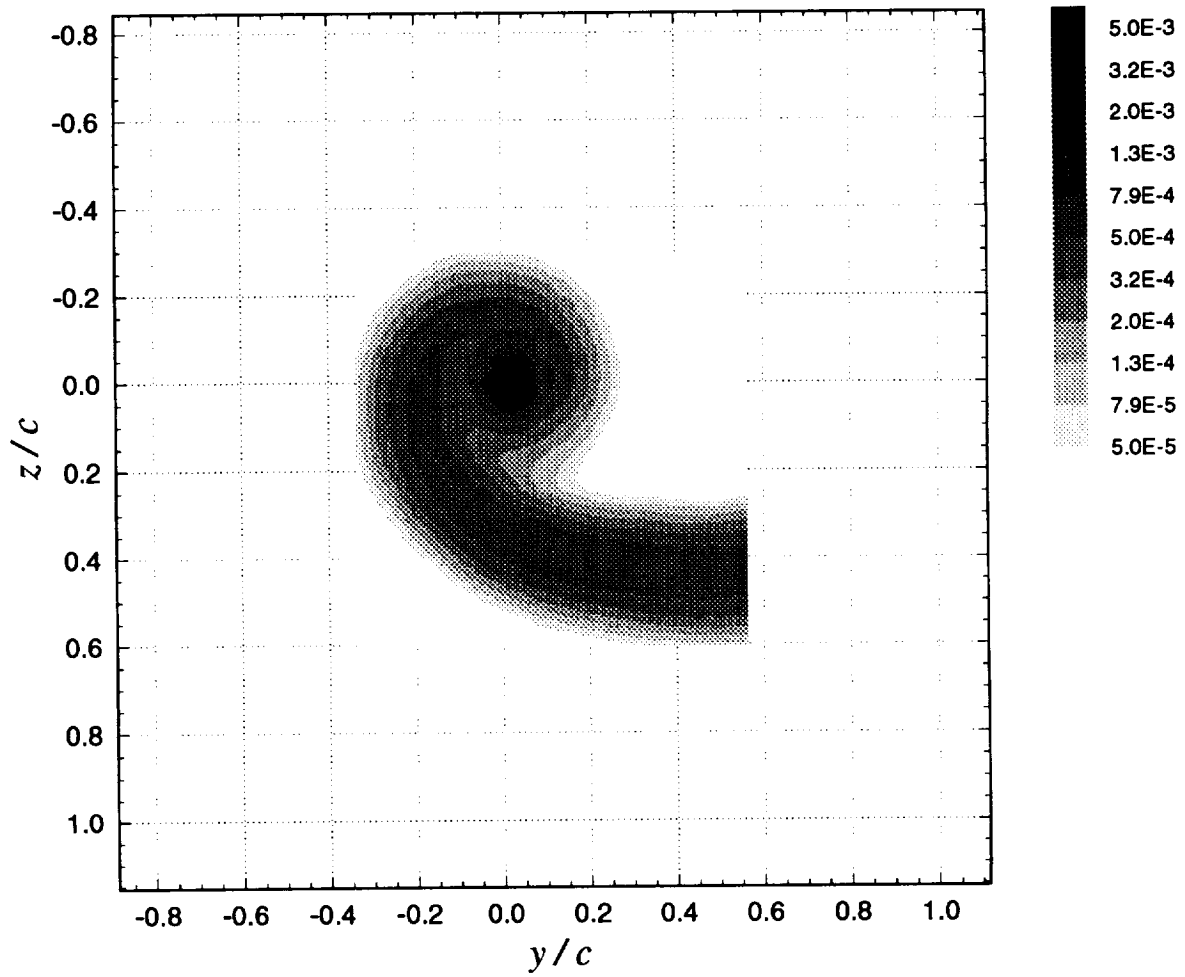


**Figure 3.2f** Contours of summed cross-flow normal turbulent stresses ( $(\overline{v^2} + \overline{w^2}) / U_{ref}^2$ ):  $x/c = 10$ ,  $\alpha_l = 5^\circ$ , no spoiler

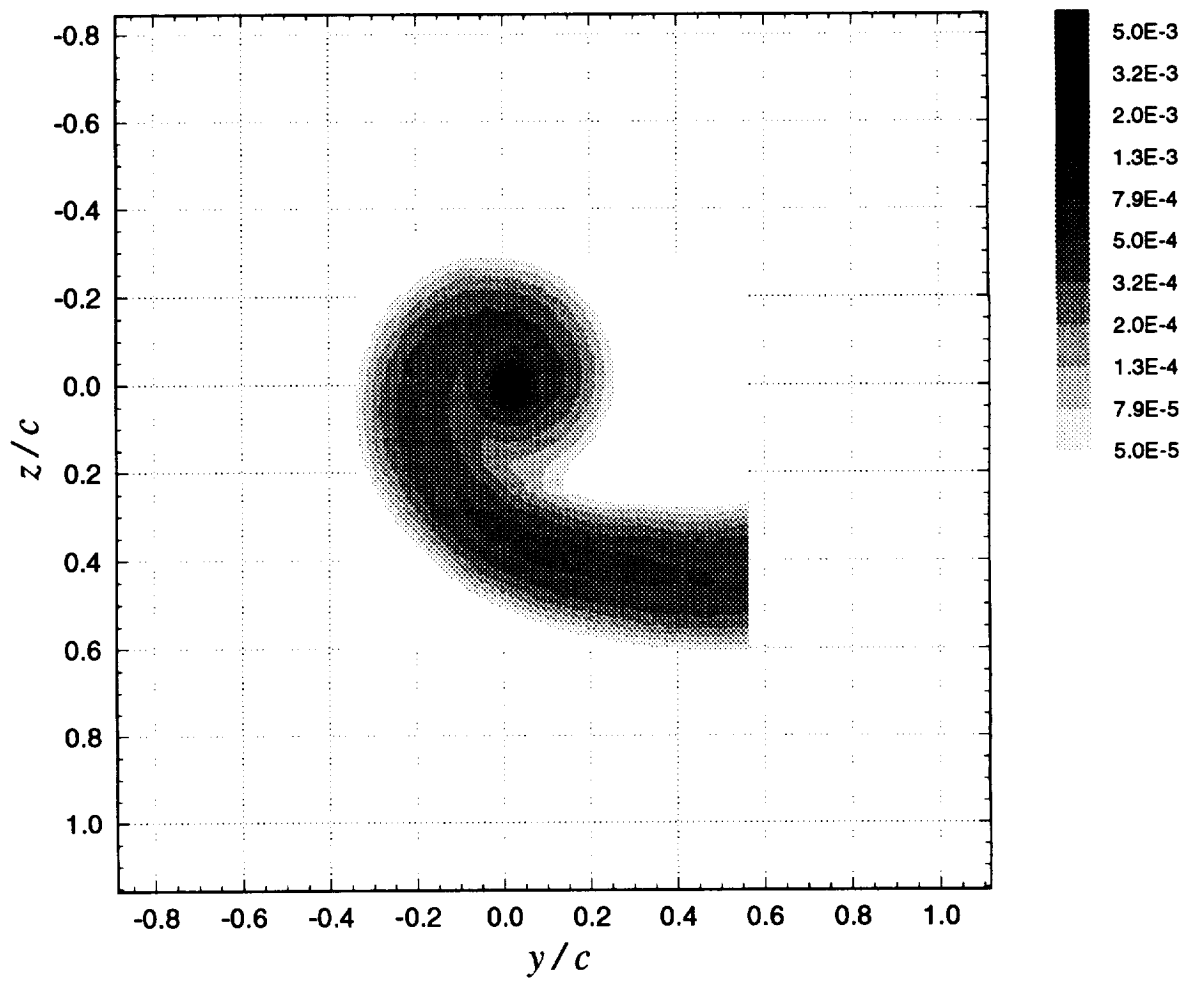


**Figure 3.2g** Contours of turbulent kinetic energy ( $k / U_{ref}^2$ ):  $x / c = 10$ ,  $\alpha_l = 5^\circ$ , no spoiler

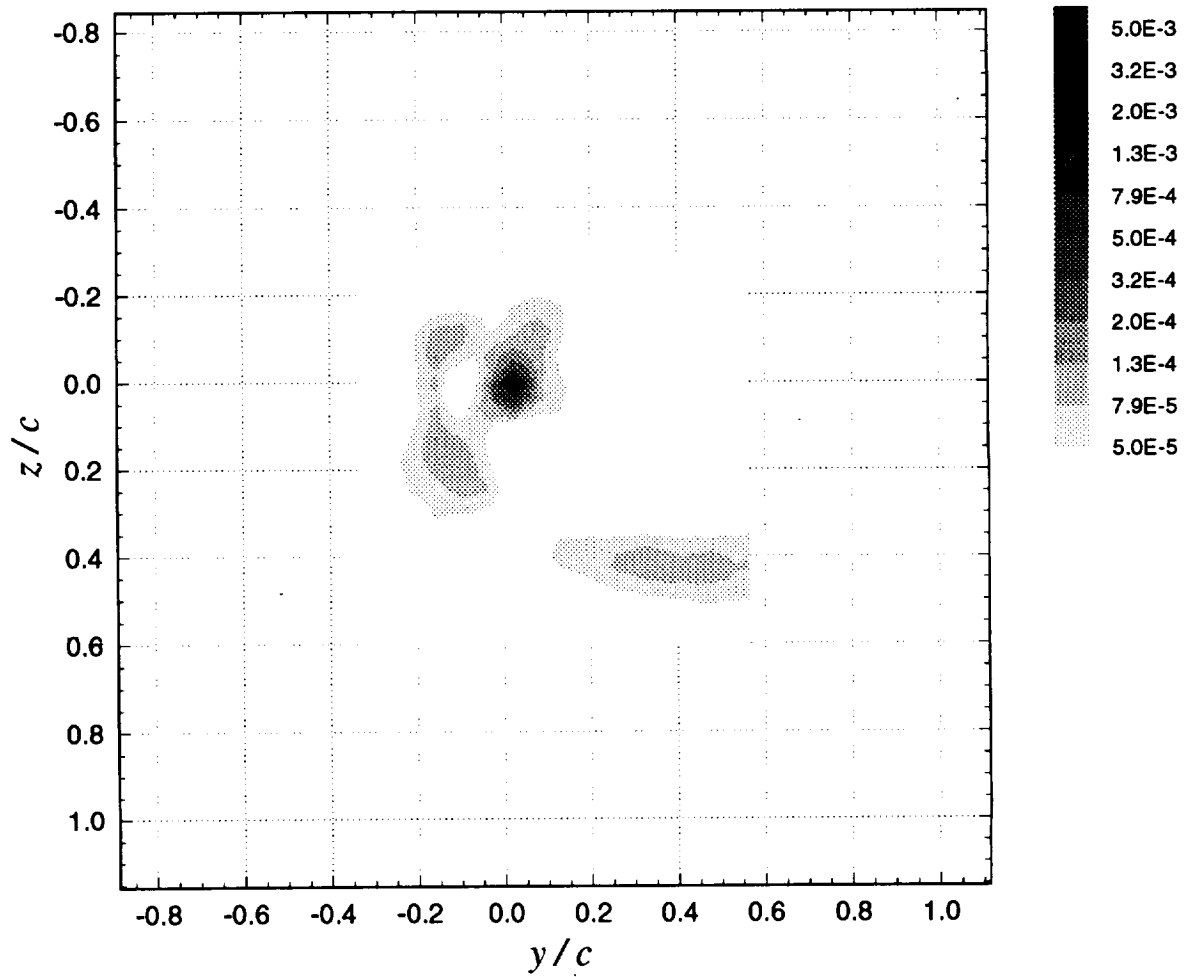


**Figure 3.2h** Contours of axial shear stress magnitude ( $\tau_a / U_{ref}^2$ ):  $x/c = 10$ ,  $\alpha_l = 5^\circ$ , no spoiler

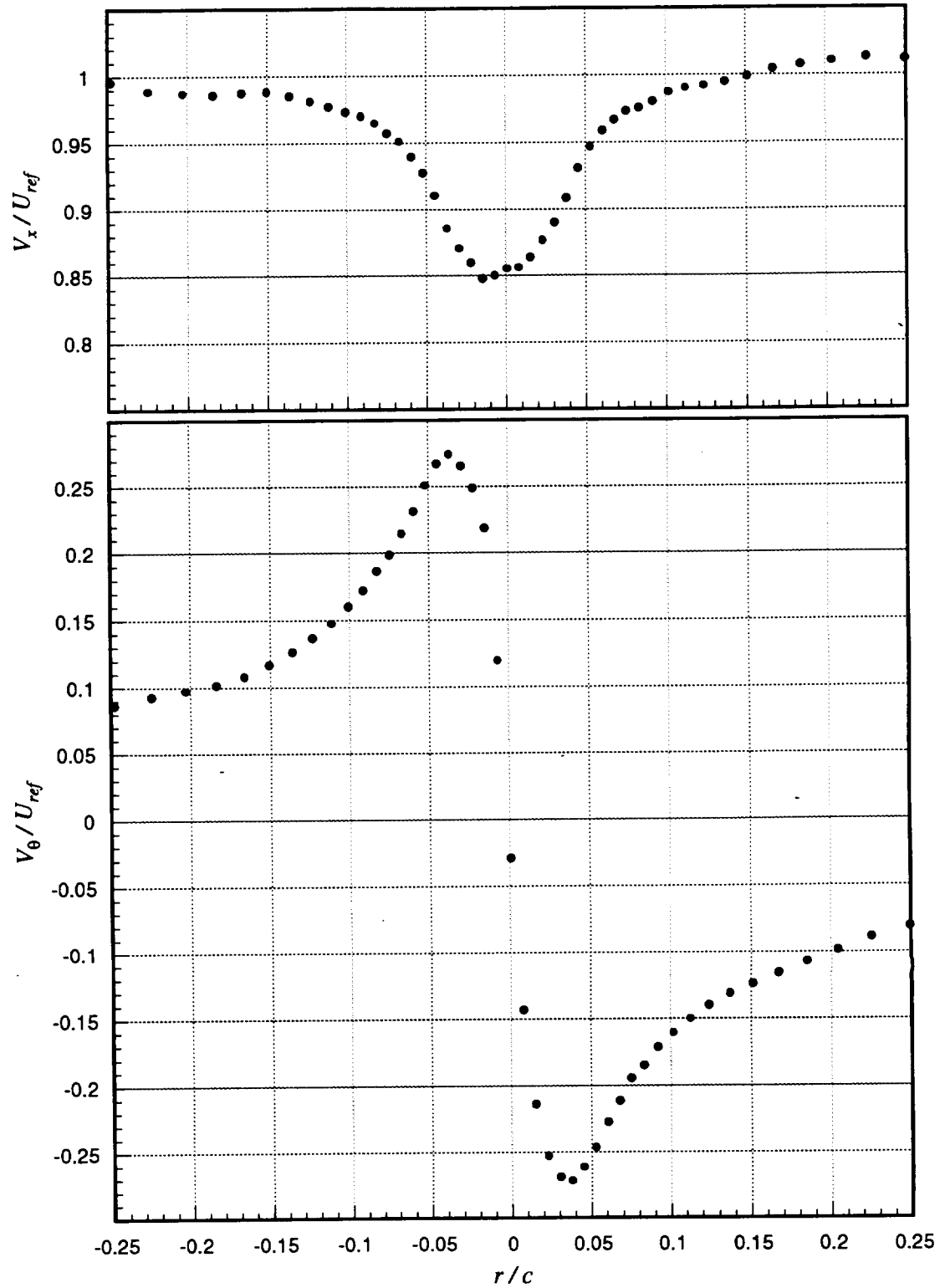


**Figure 3.3** Mean axial ( $V_x$ ) and tangential ( $V_\theta$ ) velocities measured along a  $z$ -wise profile through the vortex core center:  $x/c = 10$ ,  $\alpha_l = 5^\circ$ , no spoiler



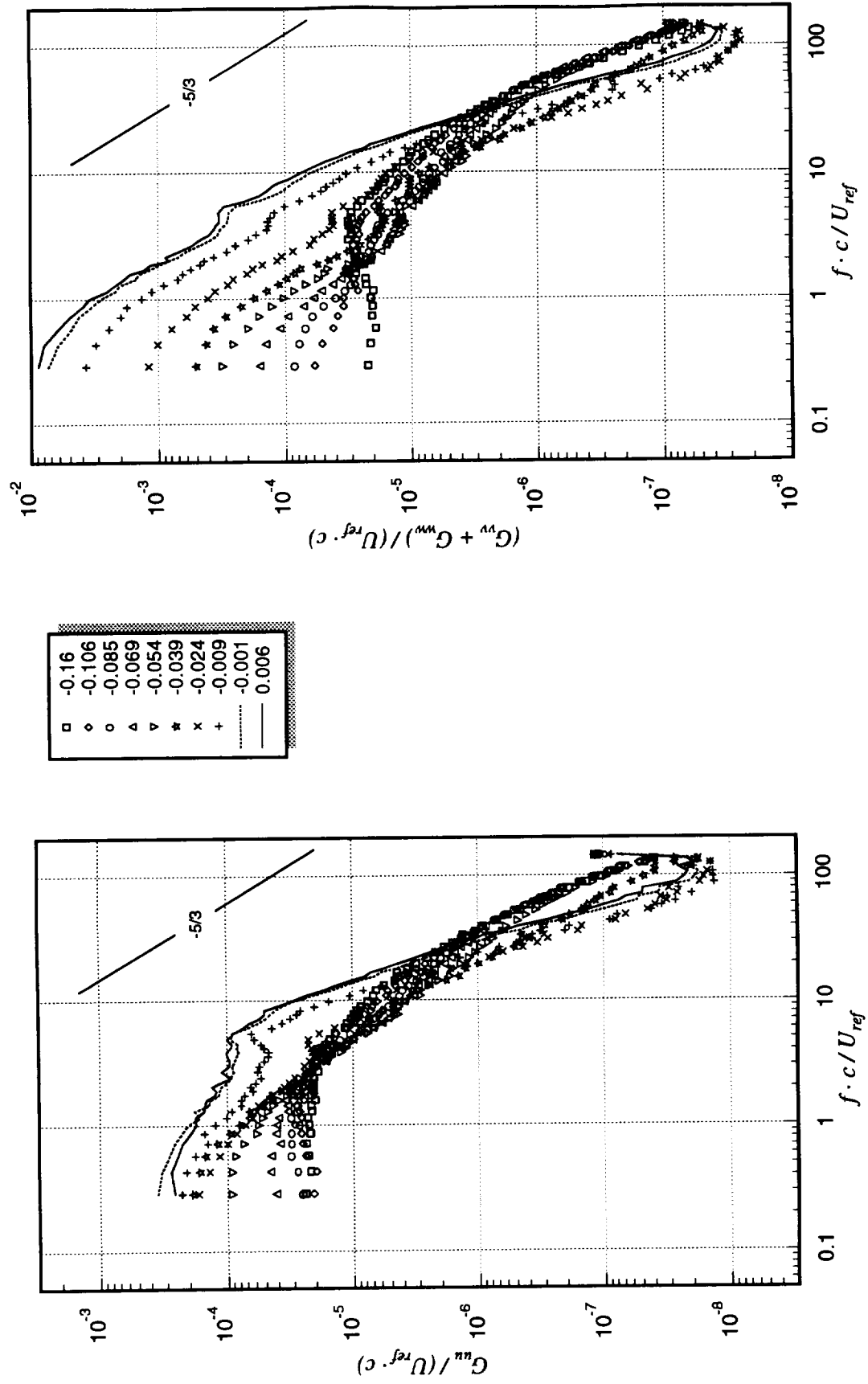


**Figure 3.4** Velocity autospectra measured along the line  $y/c = -0.037$ ;  $x/c = 10$ ,  $\alpha_I = 5^\circ$ , no spoiler. Legend lists  $z/c$  locations (core center at 0.006).

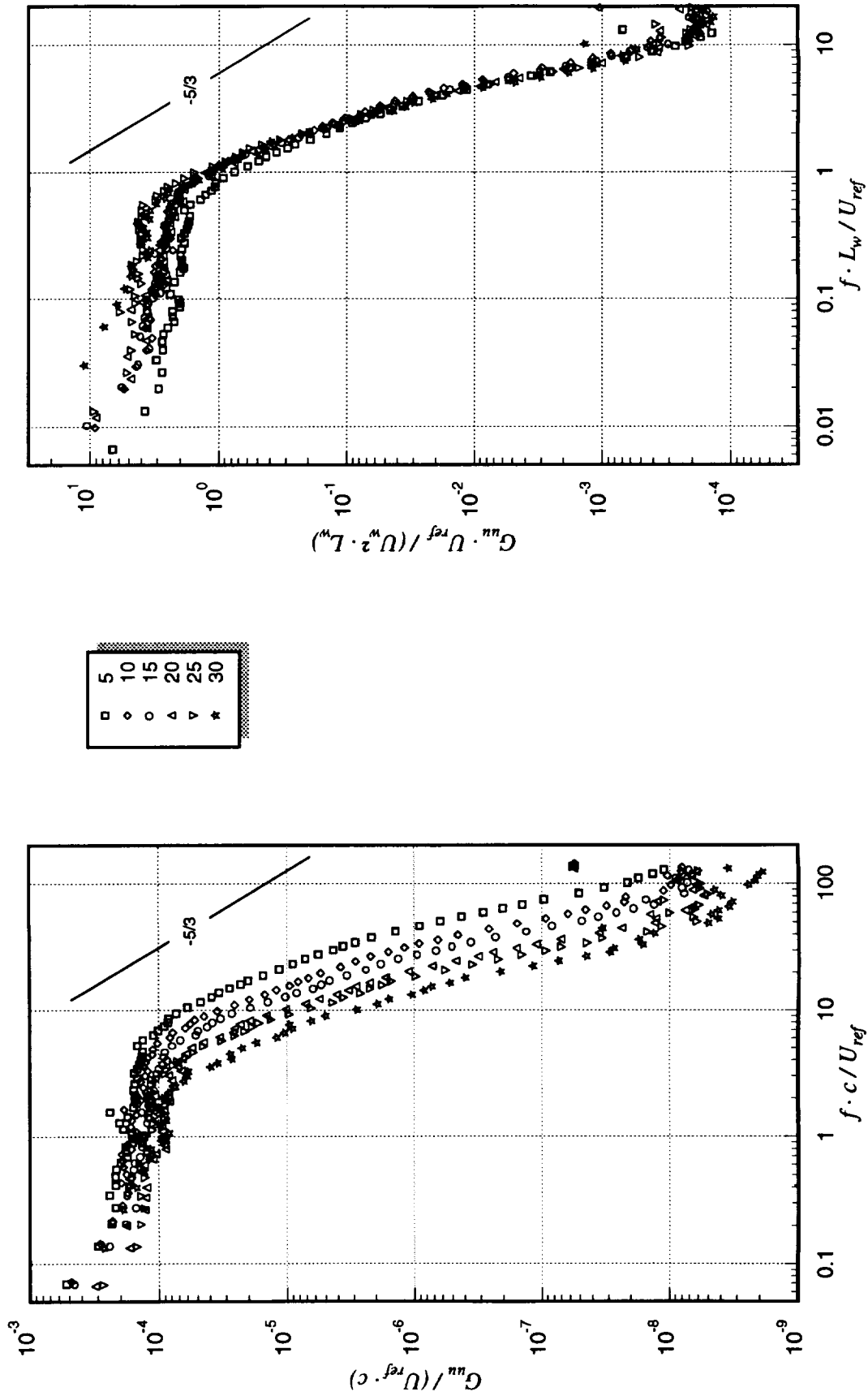


**Figure 3.5** Core center axial velocity autospectra as a function of downstream distance ( $x$ ) with different normalizations:  $\alpha_1 = 5^\circ$ , no spoiler. Legend lists  $x/c$  locations.

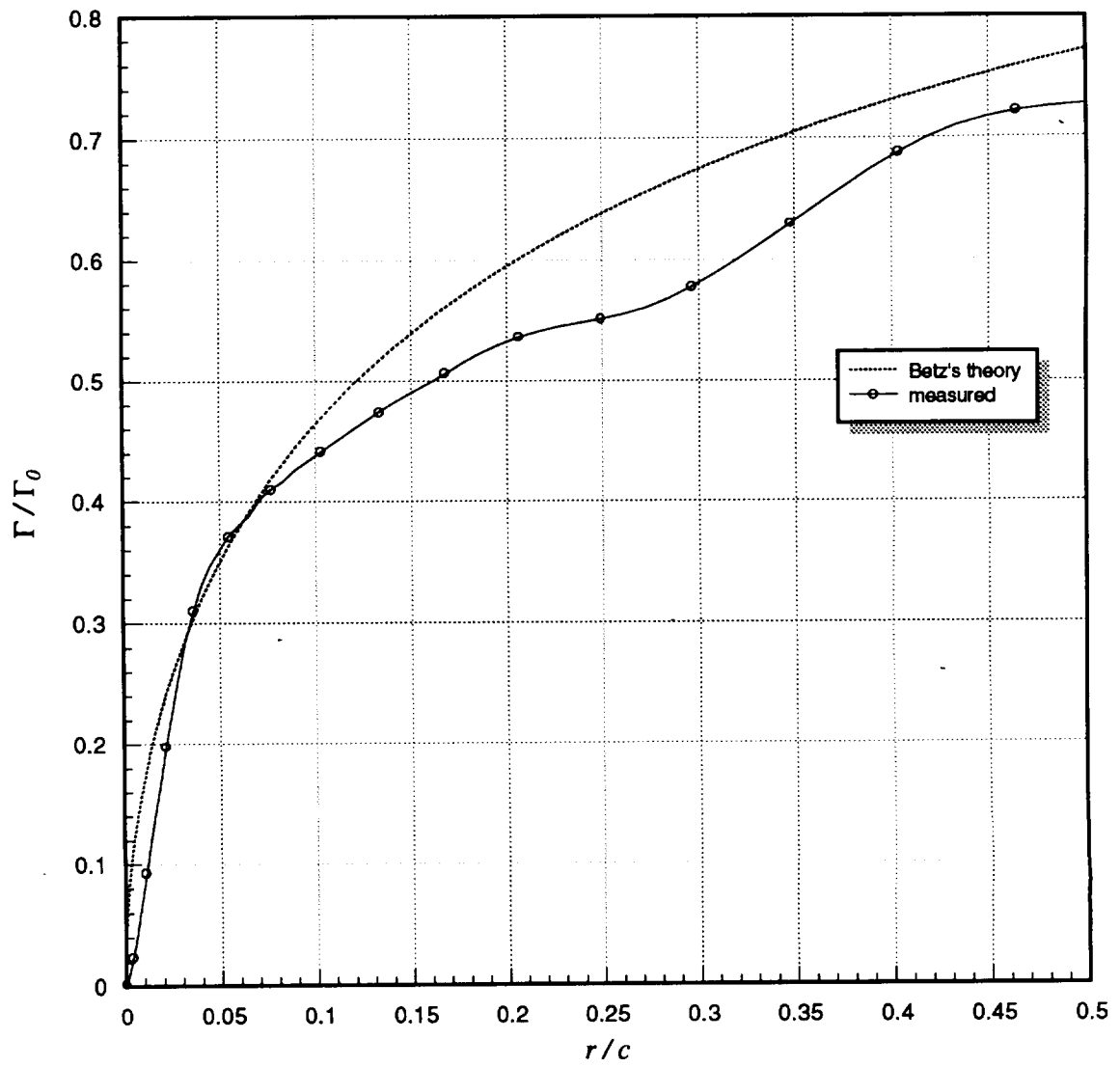


**Figure 3.6** Circulation distributions assuming axisymmetric flow:  $\alpha_l = 5^\circ$ , no spoiler. Measured distribution at  $x/c = 10$ .

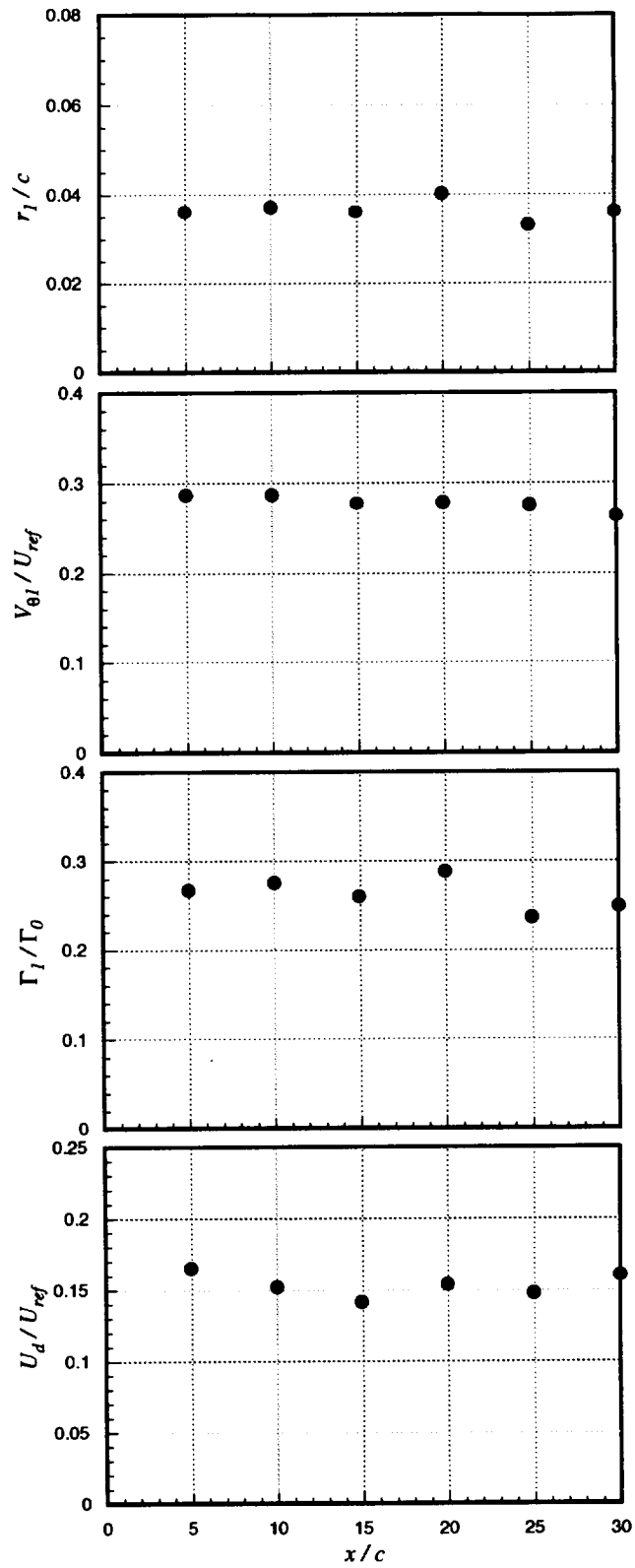


**Figure 3.7** Core parameters (radius,  $r_l$ ; peak tangential velocity,  $V_{\theta l}$ ; circulation,  $\Gamma_l$ ; and axial velocity deficit,  $U_d$ ) as a function of downstream distance ( $x$ ) for undisturbed vortex:  $\alpha_l = 5^\circ$ , no spoiler

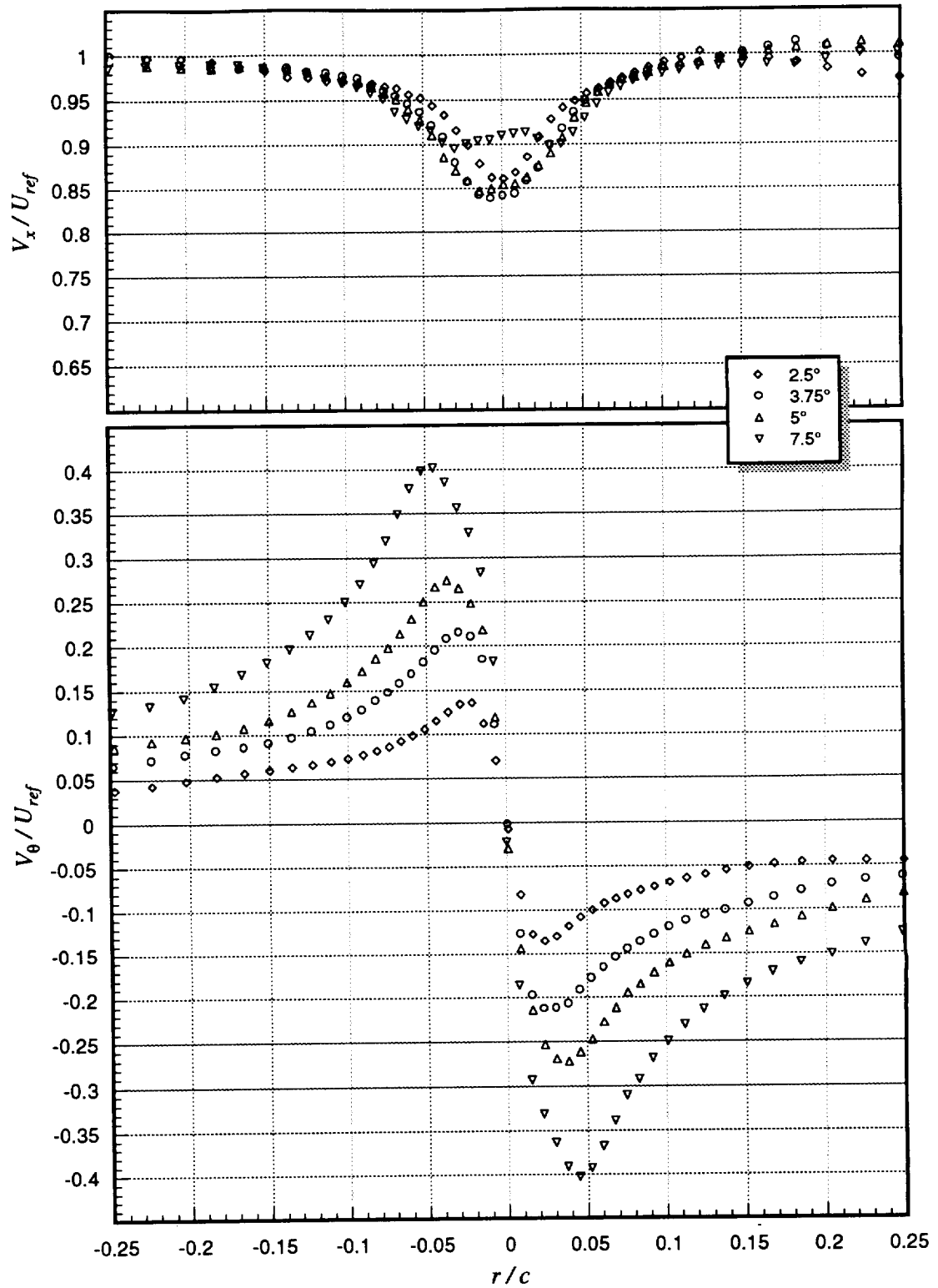


**Figure 3.8** Mean axial ( $V_x$ ) and tangential ( $V_\theta$ ) velocities (measured along  $z$ -wise profiles through the vortex core center) as a function of generator angle of attack ( $\alpha_l$ ):  $x/c = 10$ , no spoiler. Legend lists  $\alpha_l$  values.

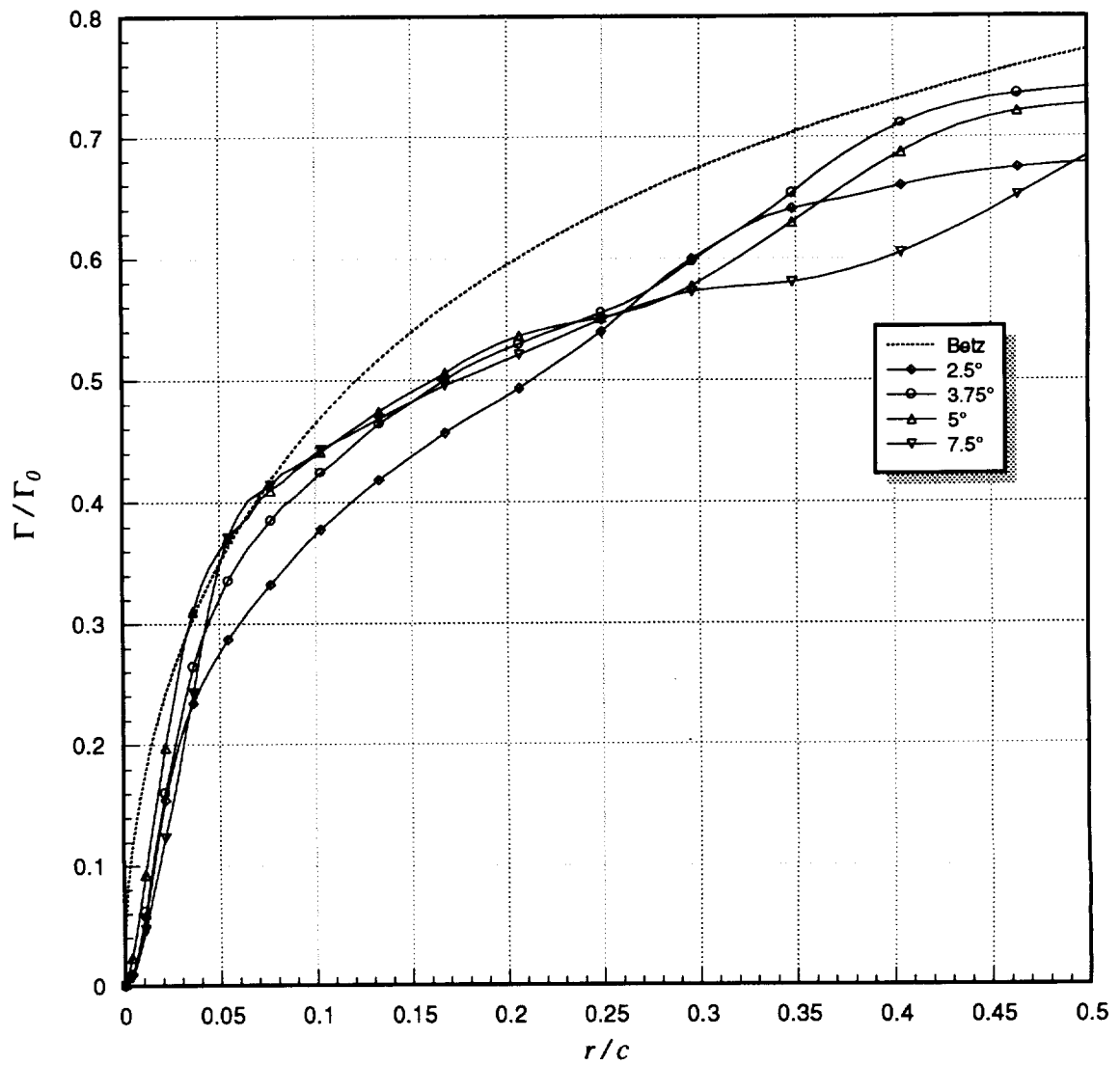


**Figure 3.9** Circulation distributions (assuming axisymmetric flow) as a function of generator angle of attack ( $\alpha_l$ ):  $x/c = 10$ , no spoiler. Legend lists  $\alpha_l$  values.

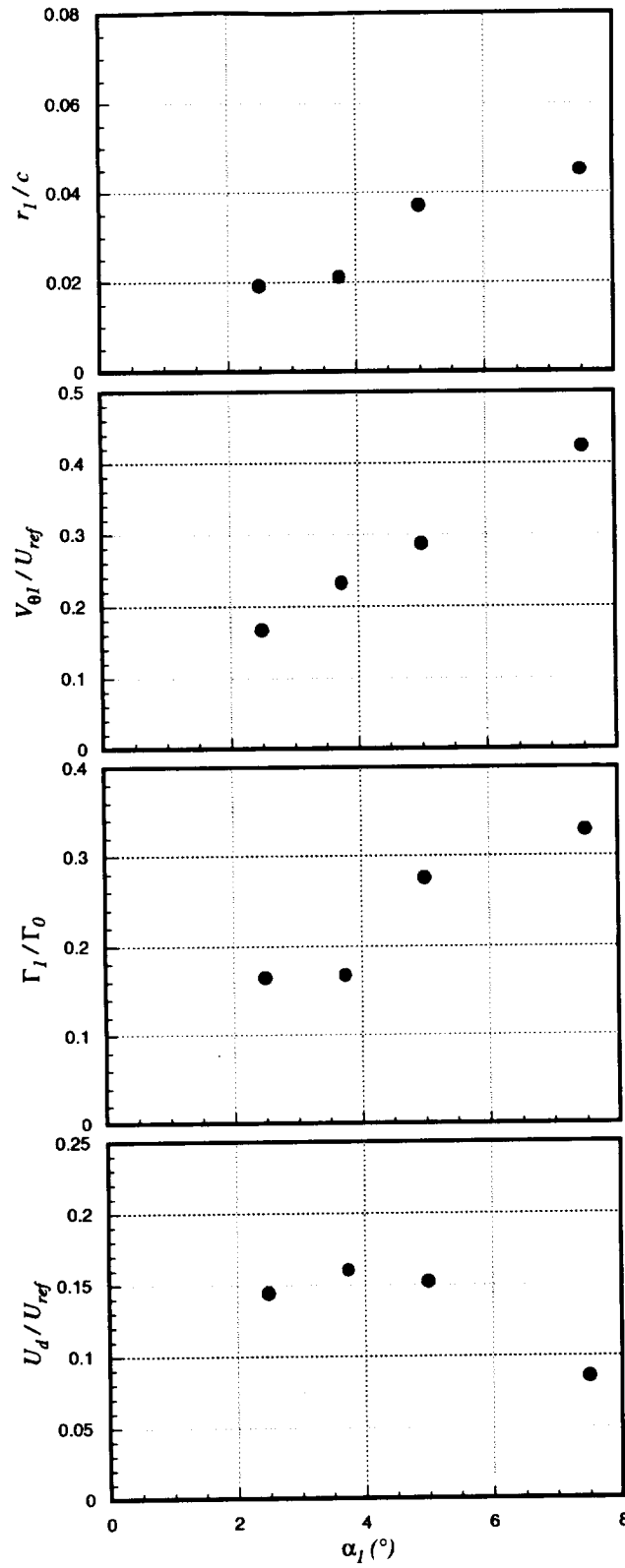


**Figure 3.10** Core parameters (radius,  $r_I$ ; peak tangential velocity,  $V_{\theta I}$ ; circulation,  $\Gamma_I$ ; and axial velocity deficit,  $U_d$ ) as a function of generator angle of attack ( $\alpha_I$ ):  $x/c = 10$ , no spoiler

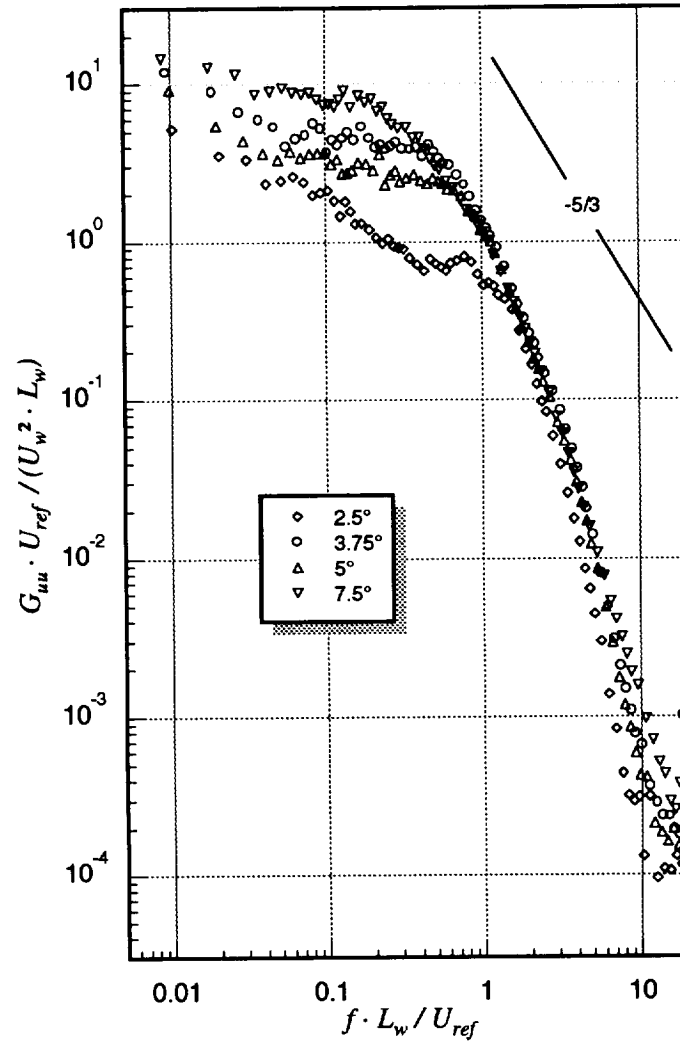


**Figure 3.11** Core center axial velocity autospectra as a function of generator angle of attack ( $\alpha_I$ ):  $x/c = 10$ , no spoiler. Legend lists  $\alpha_I$  values.



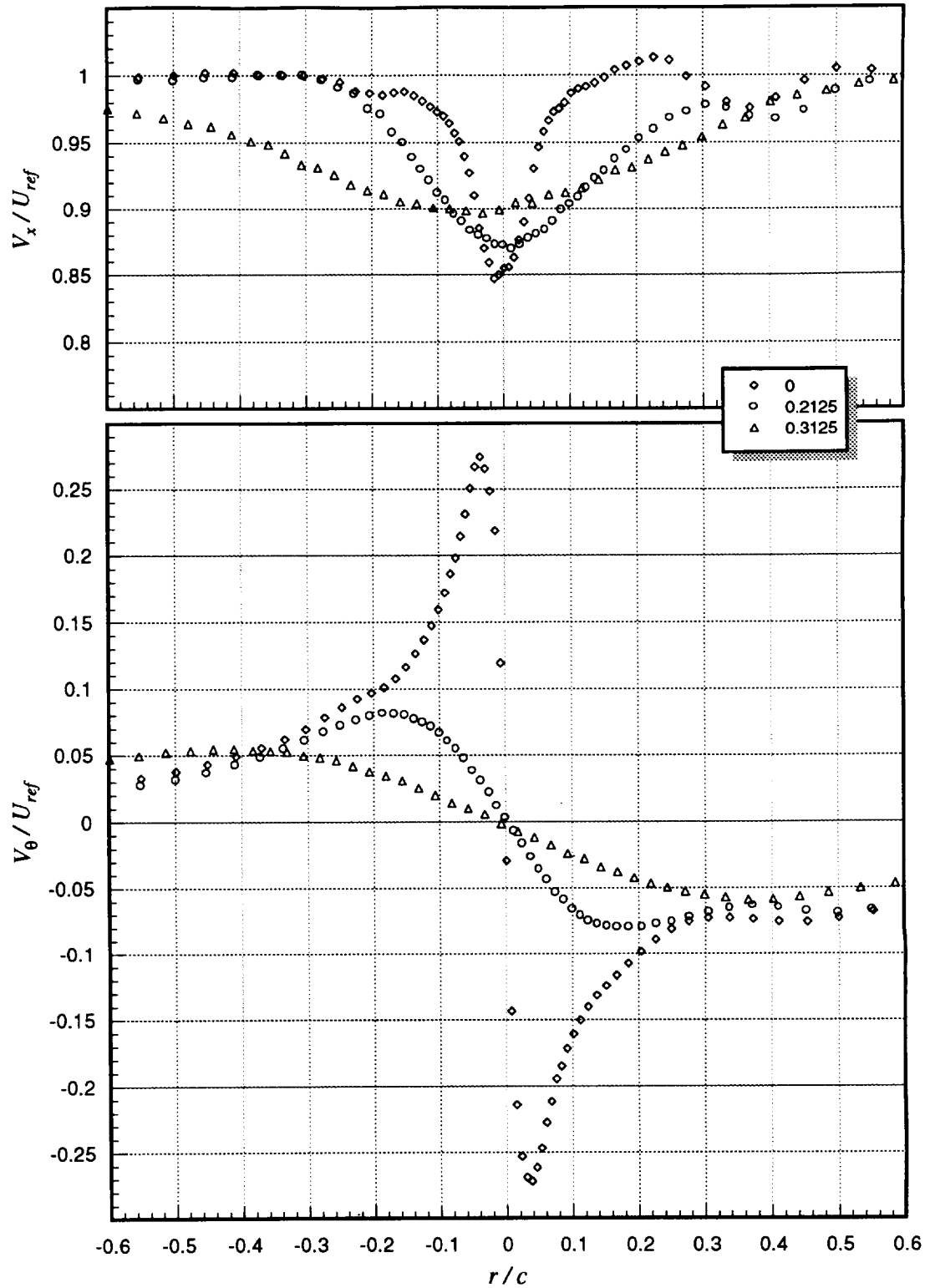


**Figure 3.12** Mean axial ( $V_x$ ) and tangential ( $V_\theta$ ) velocities (measured along  $z$ -wise profiles through the vortex core center) as a function of spoiler diameter ( $d$ ):  $x/c = 10$ , no spoiler. Legend lists  $d/c$  values.

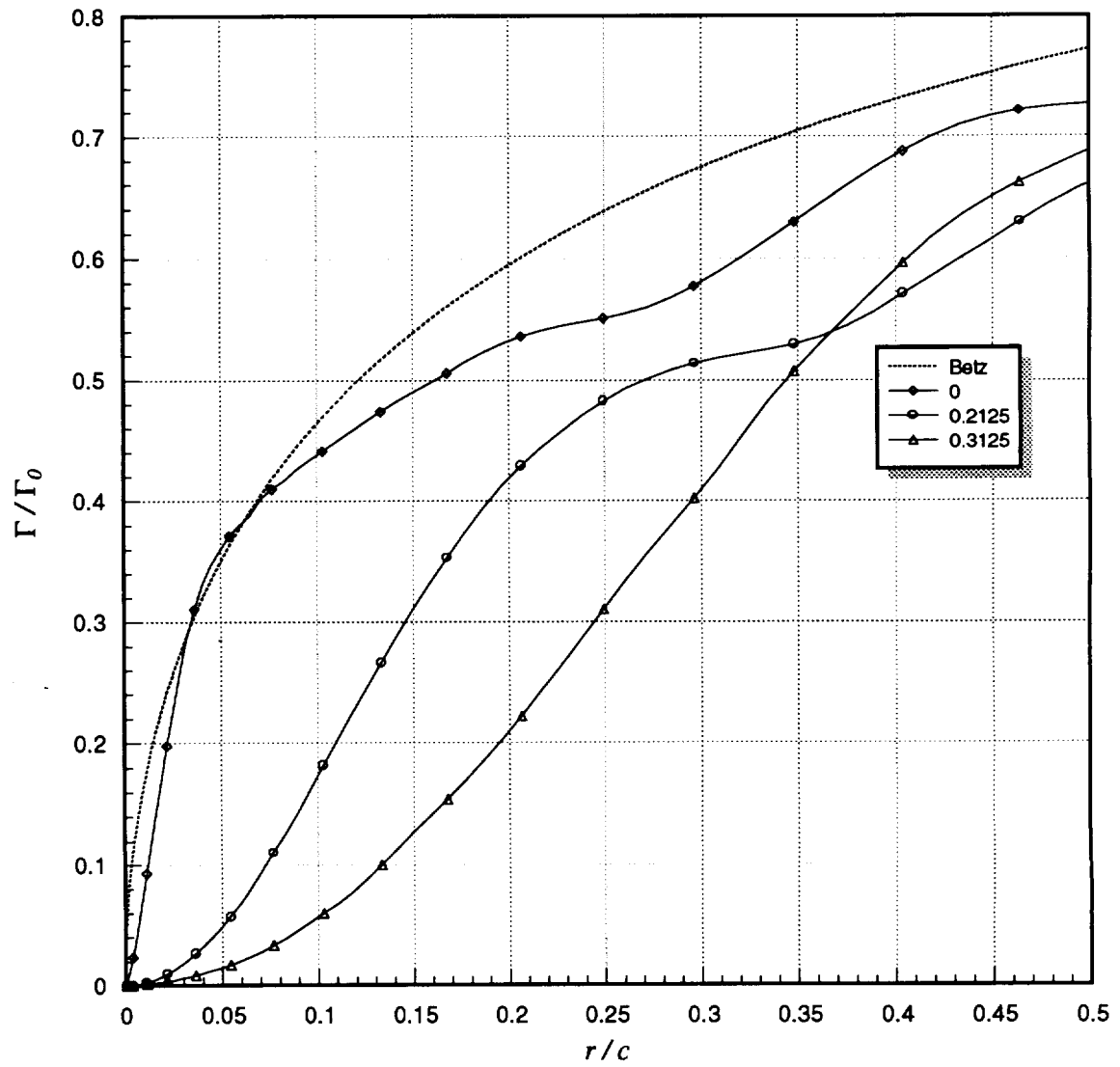


**Figure 3.13** Circulation distributions (assuming axisymmetric flow) as a function of spoiler diameter ( $d$ ):  $x/c = 10$ ,  $\alpha_l = 5^\circ$ . Legend lists  $d/c$  values.

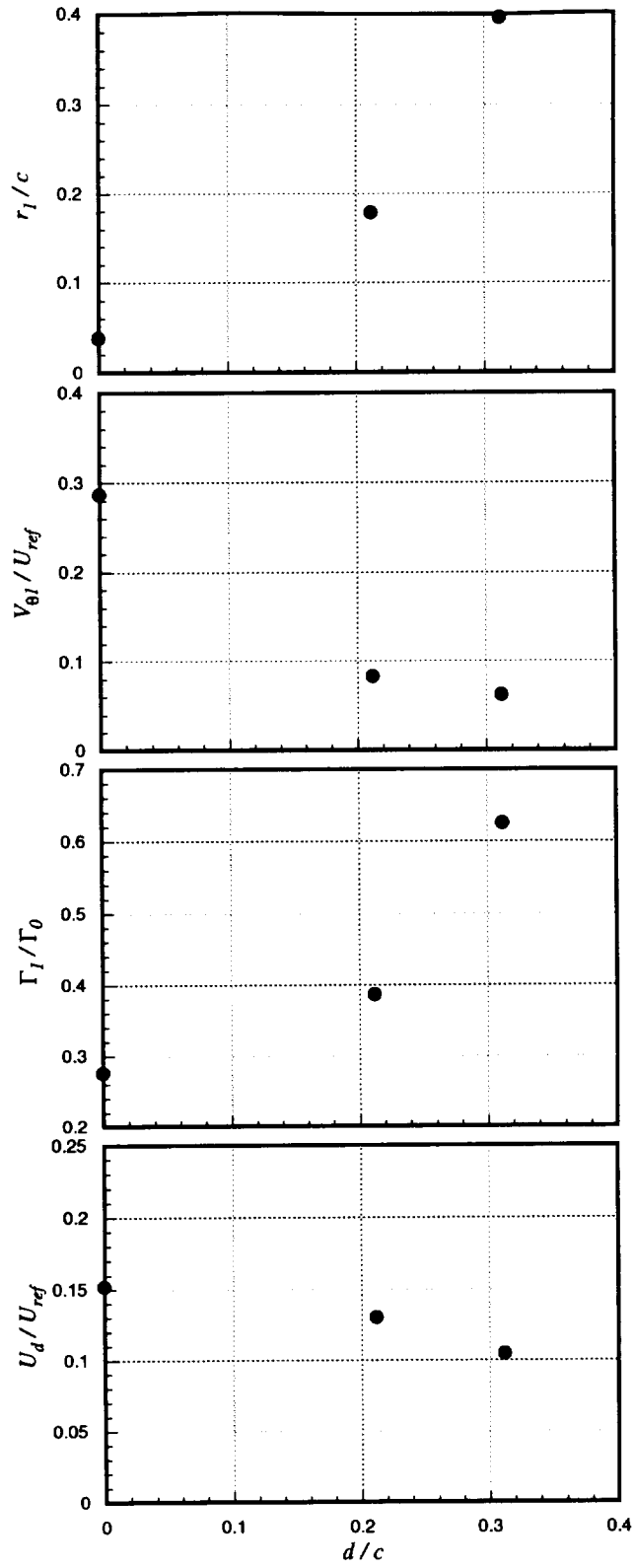


**Figure 3.14** Core parameters (radius,  $r_l$ ; peak tangential velocity,  $V_{\theta l}$ ; circulation,  $\Gamma_l$ ; and axial velocity deficit,  $U_d$ ) as a function of spoiler diameter ( $d$ ):  $x/c = 10$ ,  $\alpha_l = 5^\circ$

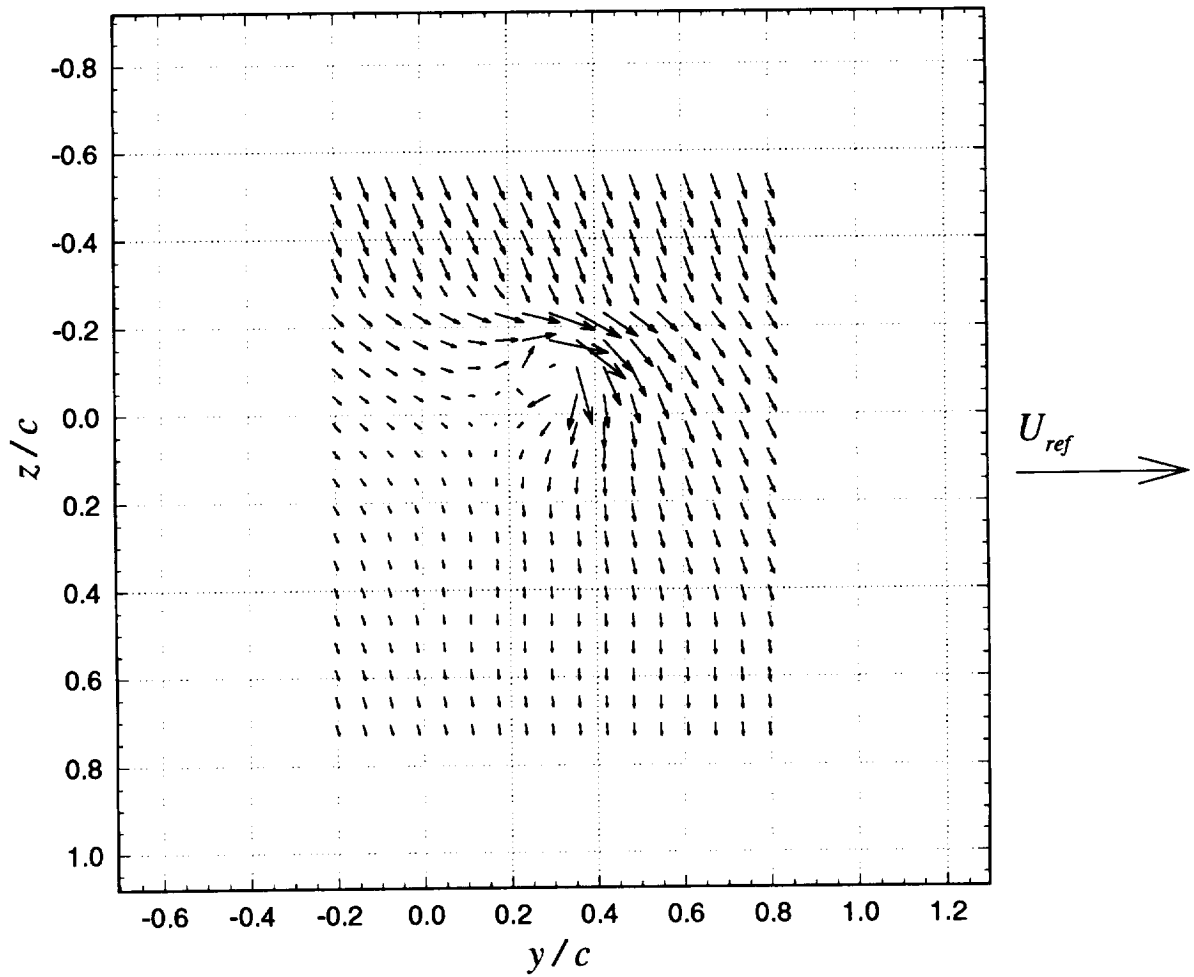


**Figure 3.15a** Mean cross-flow velocity ( $V/U_{ref}$ ,  $W/U_{ref}$ ) vectors for pressure side passage of  $\Delta/c = -0.125$ :  $x/c = 15.16$ ,  $\alpha_1 = 5^\circ$ ,  $\alpha_2 = 5^\circ$ , no spoiler

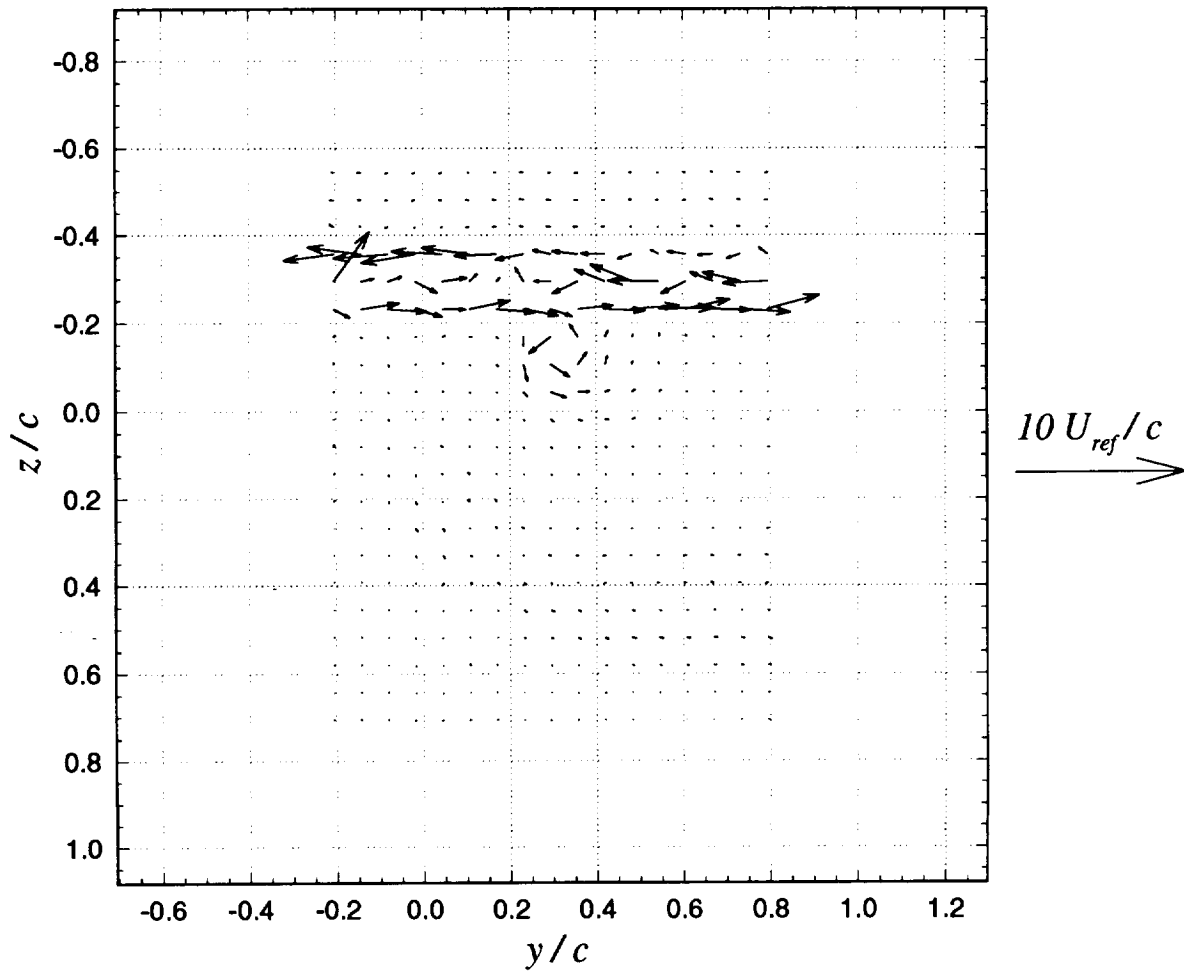


**Figure 3.15b** Mean cross-flow vorticity vectors ( $\Omega_y \cdot c / U_{ref}$ ,  $\Omega_z \cdot c / U_{ref}$ ) for pressure side passage of  $\Delta / c = -0.125$ :  $x / c = 15.16$ ,  $\alpha_1 = 5^\circ$ ,  $\alpha_2 = 5^\circ$ , no spoiler

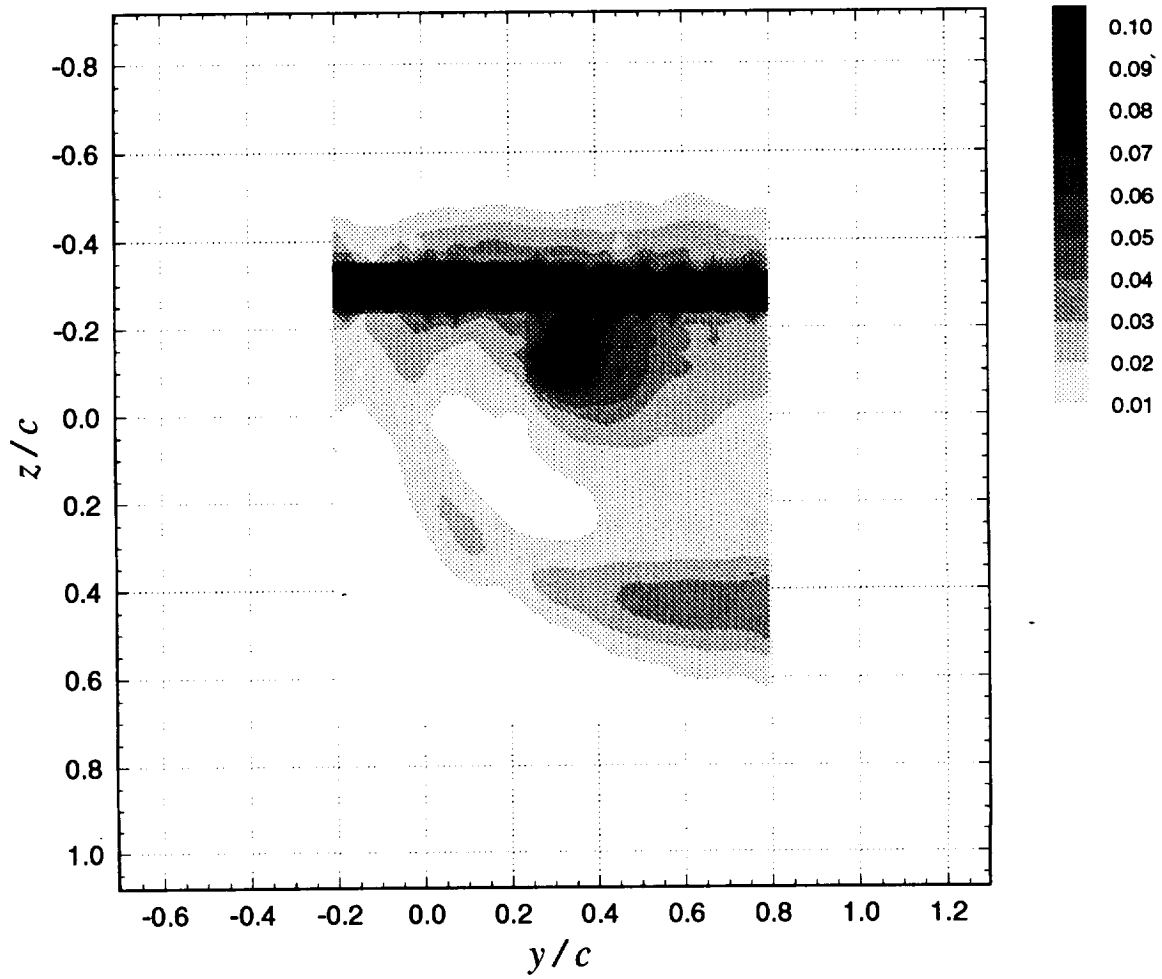


**Figure 3.15c** Contours of mean axial velocity deficit  $(U_{ref} - U) / U_{ref}$  for pressure side passage of  $\Delta/c = -0.125$ :  $x/c = 15.16$ ,  $\alpha_1 = 5^\circ$ ,  $\alpha_2 = 5^\circ$ , no spoiler

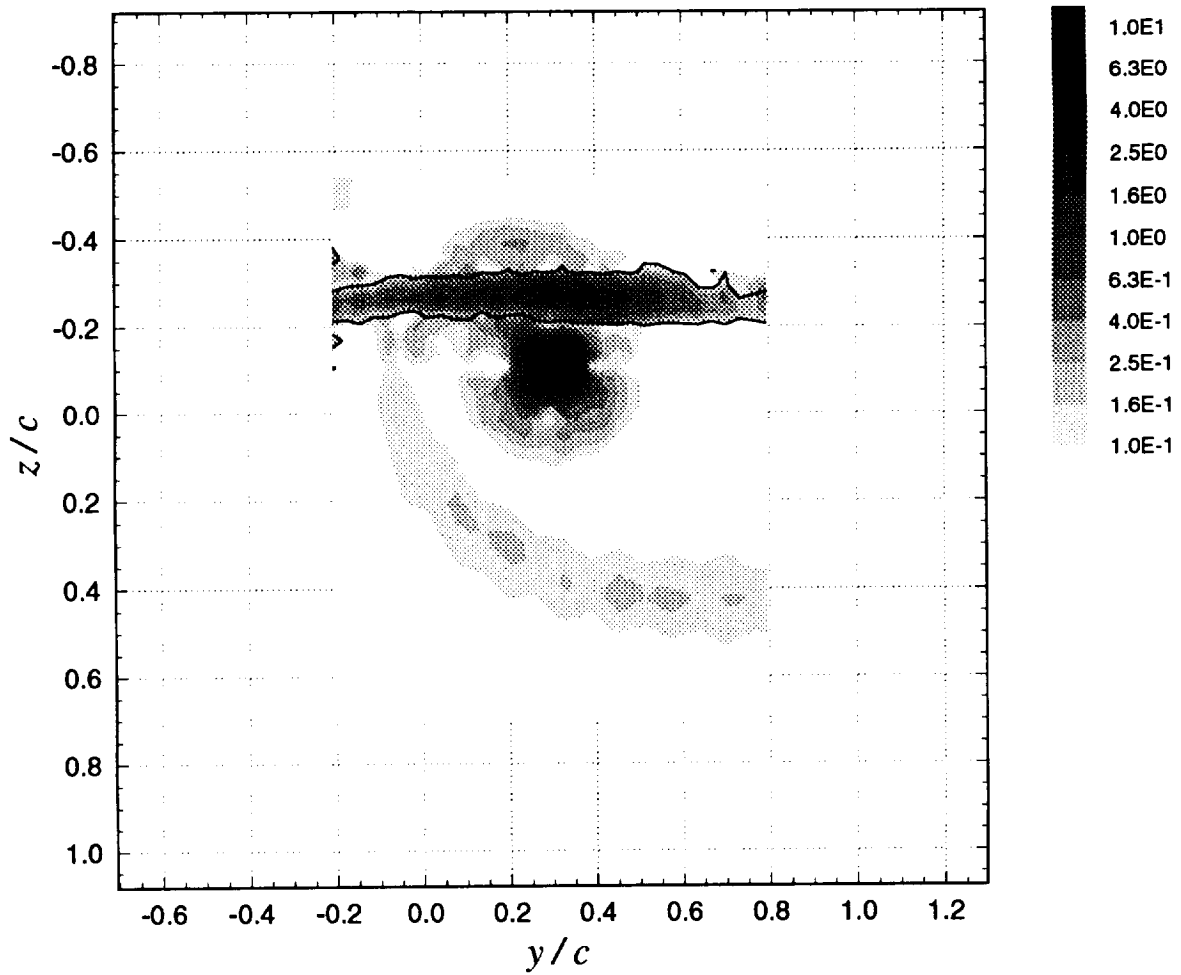


**Figure 3.15d** Contours of mean axial vorticity ( $\Omega_x \cdot c / U_{ref}$ ) for pressure side passage of  $\Delta/c = -0.125$ :  $x/c = 15.16$ ,  $\alpha_1 = 5^\circ$ ,  $\alpha_2 = 5^\circ$ , no spoiler. Legend lists  $|\Omega_x \cdot c / U_{ref}|$  values. Negative values of  $\Omega_x \cdot c / U_{ref}$  are contained within the solid contour lines.

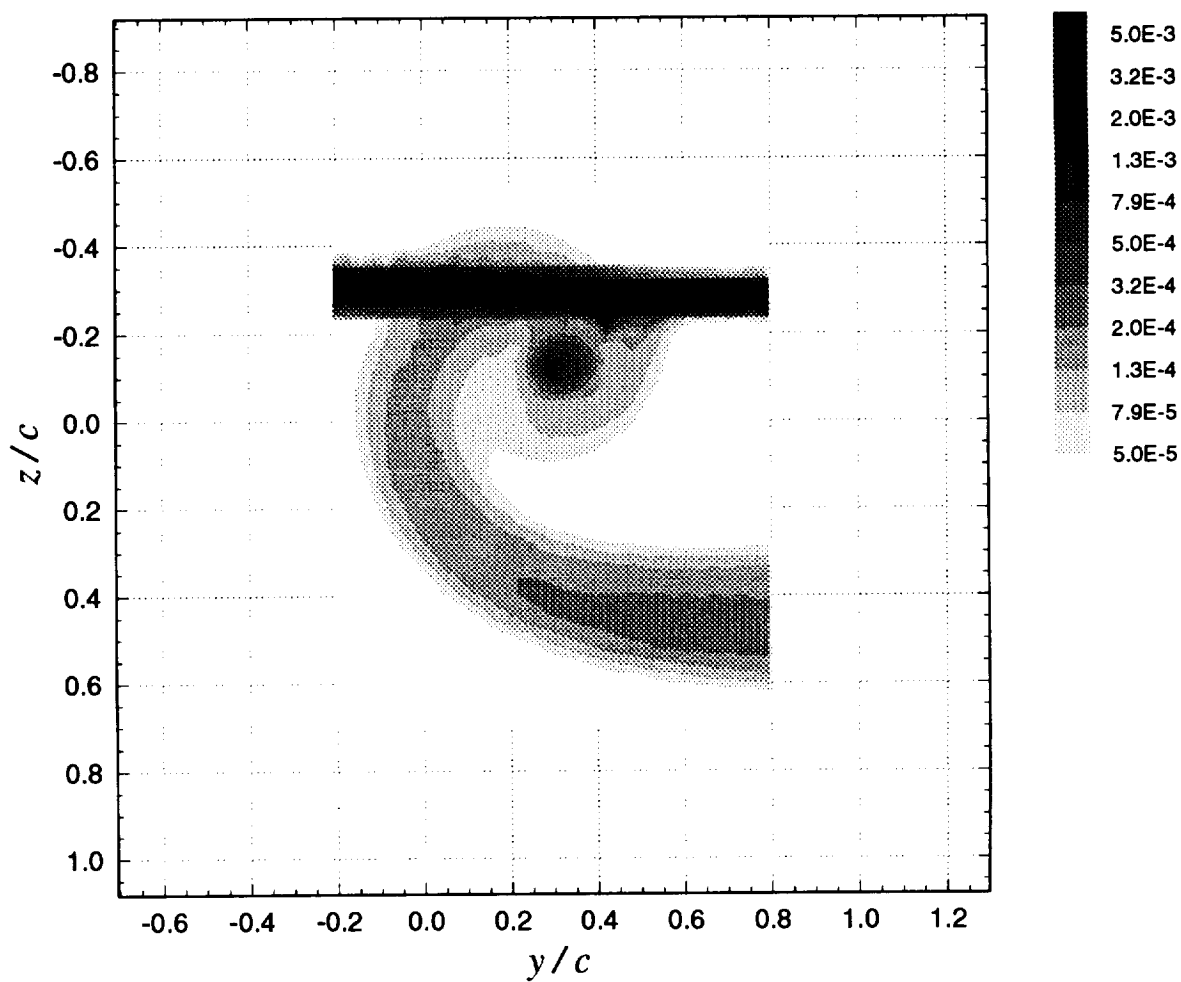


**Figure 3.15e** Contours of axial normal turbulent stress ( $\overline{u^2} / U_{ref}^2$ ) for pressure side passage of  $\Delta/c = -0.125$ :  $x/c = 15.16$ ,  $\alpha_1 = 5^\circ$ ,  $\alpha_2 = 5^\circ$ , no spoiler



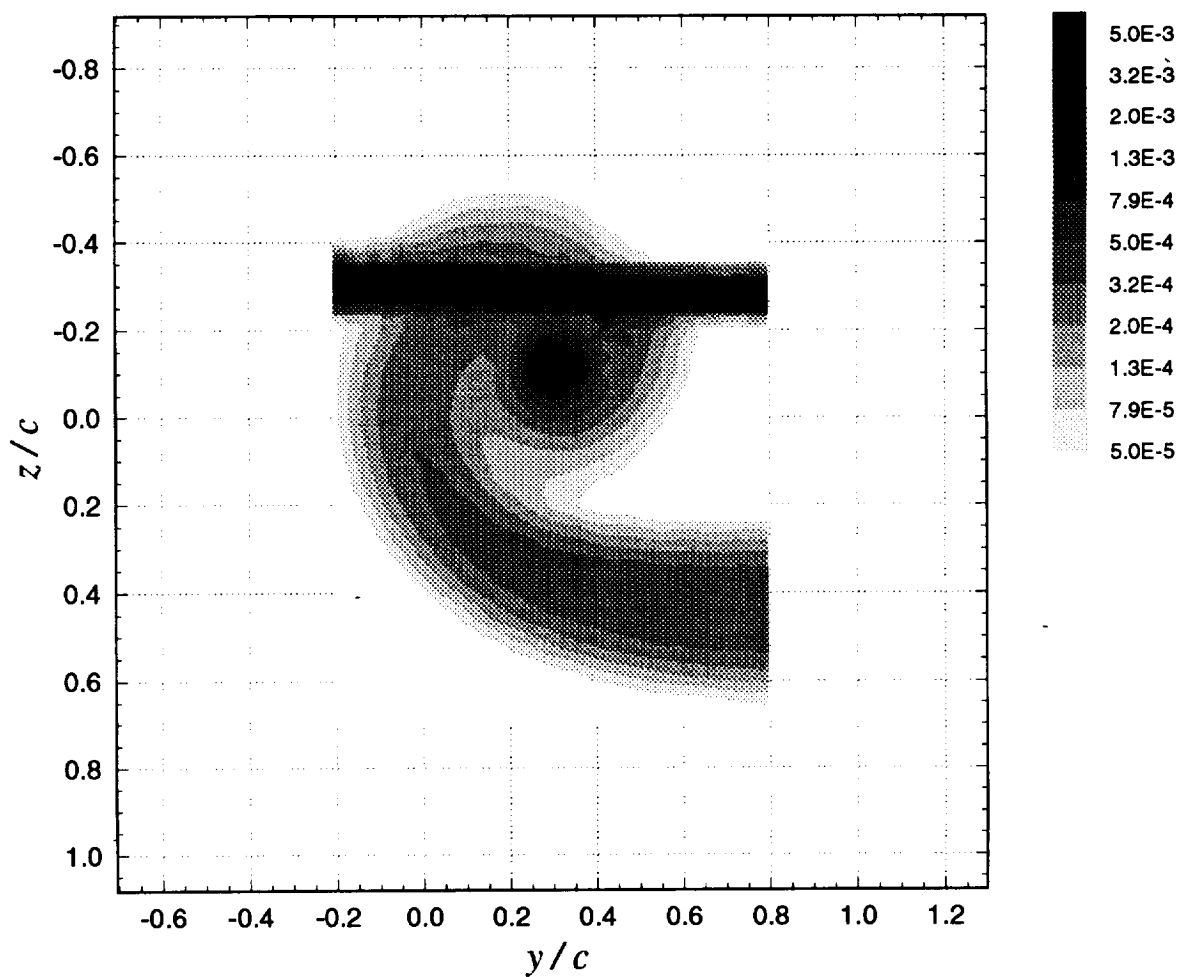


**Figure 3.15f** Contours of summed cross-flow normal turbulent stresses  $(\overline{v^2} + \overline{w^2}) / U_{ref}^2$  for pressure side passage of  $\Delta/c = -0.125$ :  $x/c = 15.16$ ,  $\alpha_1 = 5^\circ$ ,  $\alpha_2 = 5^\circ$ , no spoiler

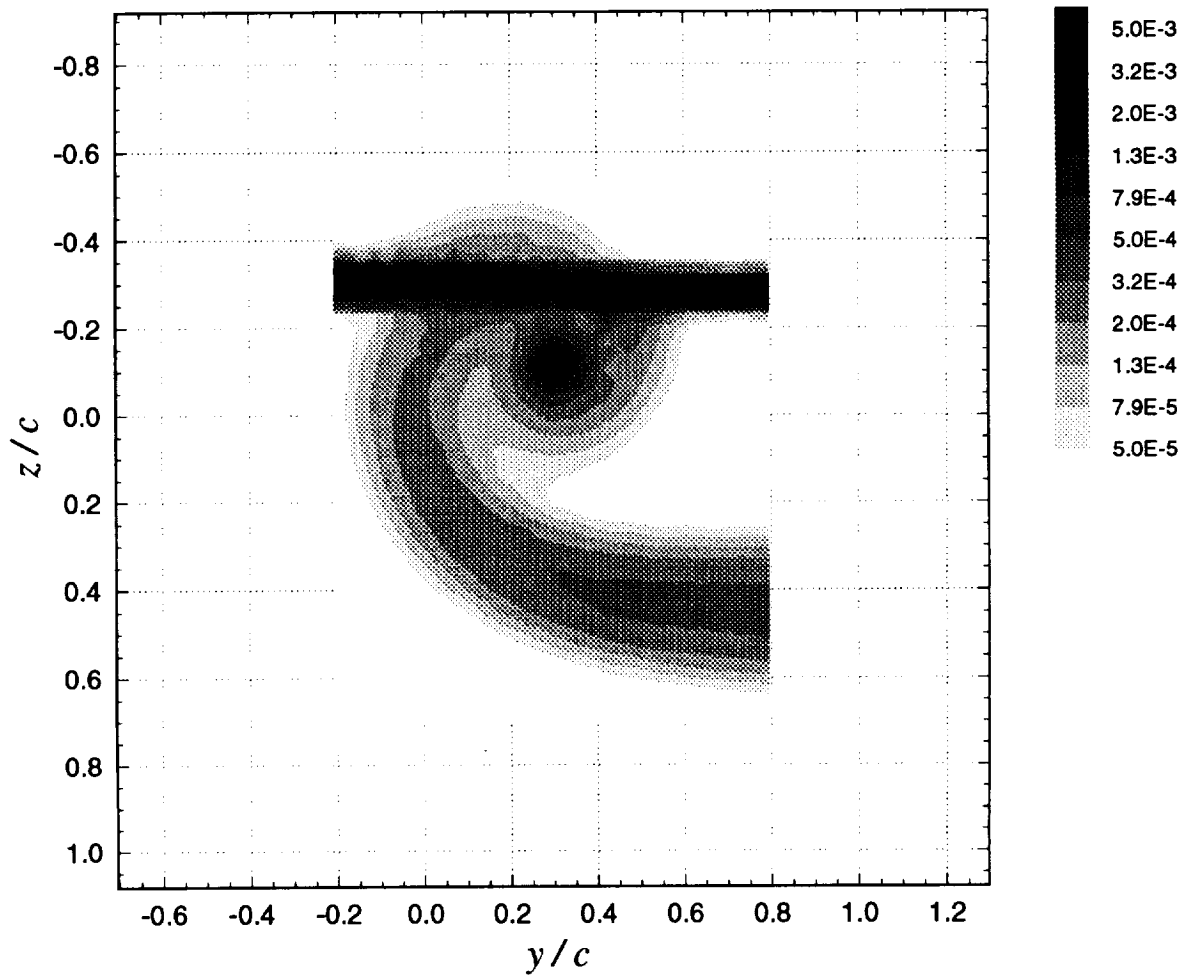


**Figure 3.15g** Contours of turbulent kinetic energy ( $k / U_{ref}^2$ ):  $x / c = 15.16$ ,  $\alpha_l = 5^\circ$ , no spoiler

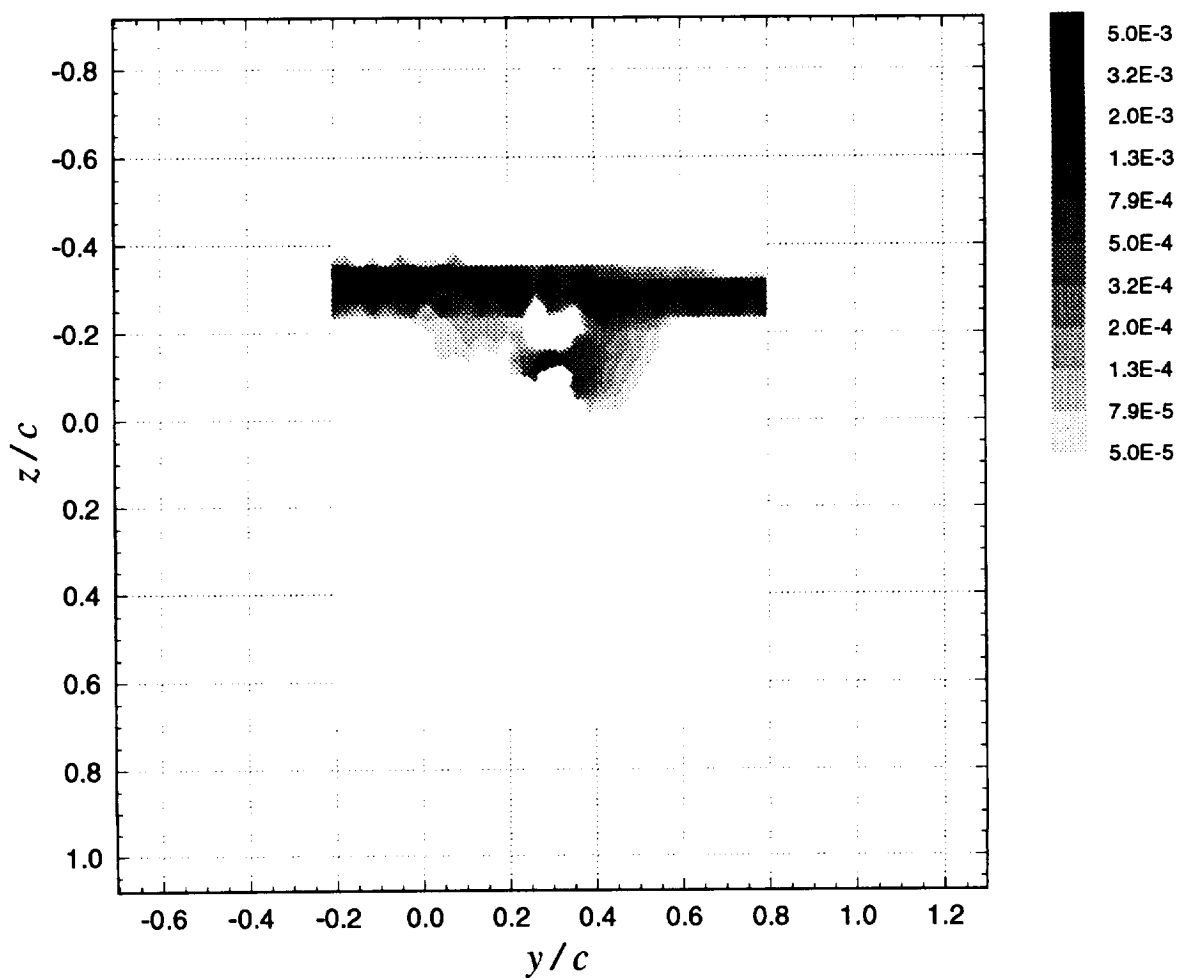


**Figure 3.15h** Contours of turbulent kinetic energy production ( $P \cdot c / U_{ref}^3$ ) for pressure side passage of  $\Delta/c = -0.125$ :  $x/c = 15.16$ ,  $\alpha_1 = 5^\circ$ ,  $\alpha_2 = 5^\circ$ , no spoiler

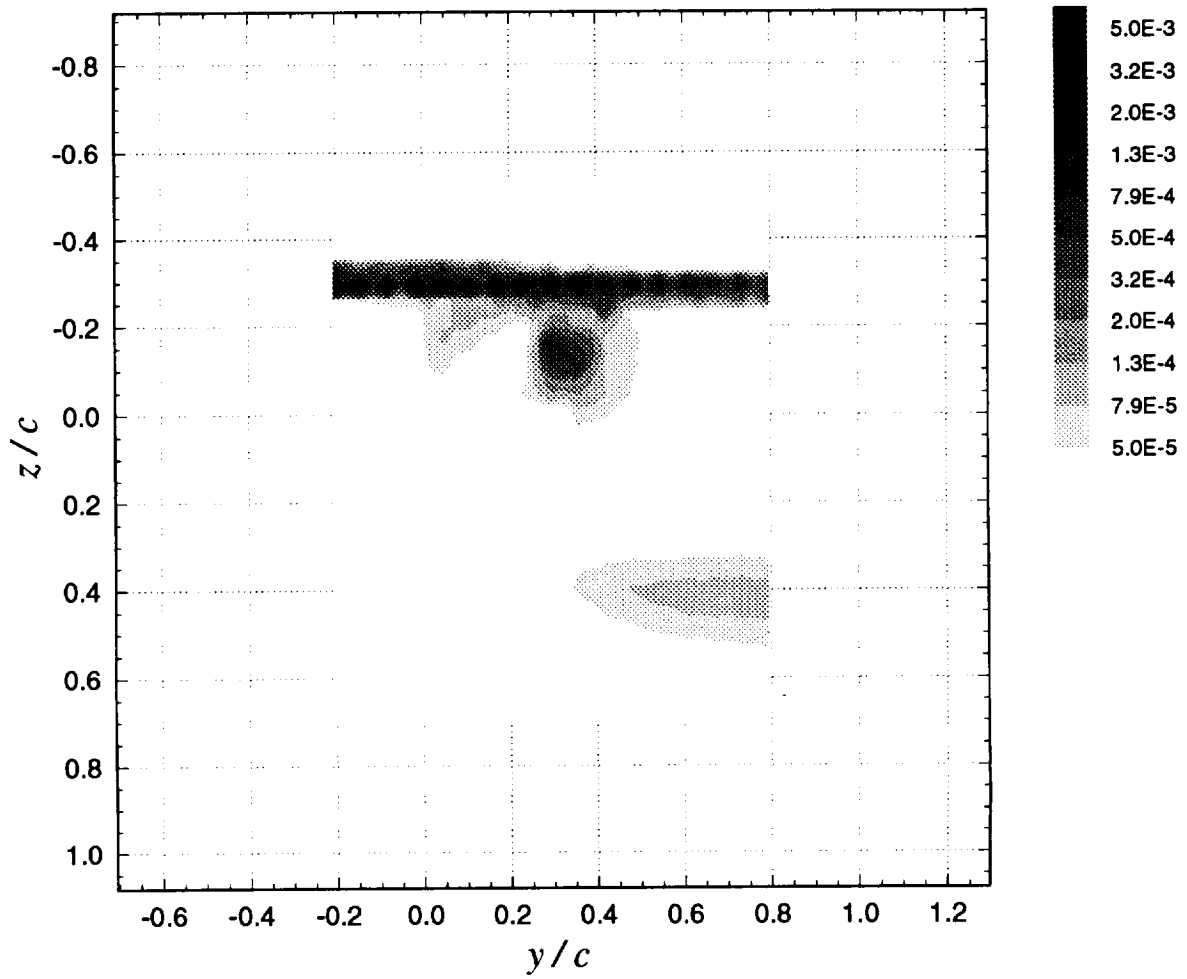


**Figure 3.15i** Contours of axial shear stress magnitude ( $\tau_a / U_{ref}^2$ ) for pressure side passage of  $\Delta / c = -0.125$ :  $x / c = 15.16$ ,  $\alpha_1 = 5^\circ$ ,  $\alpha_2 = 5^\circ$ , no spoiler

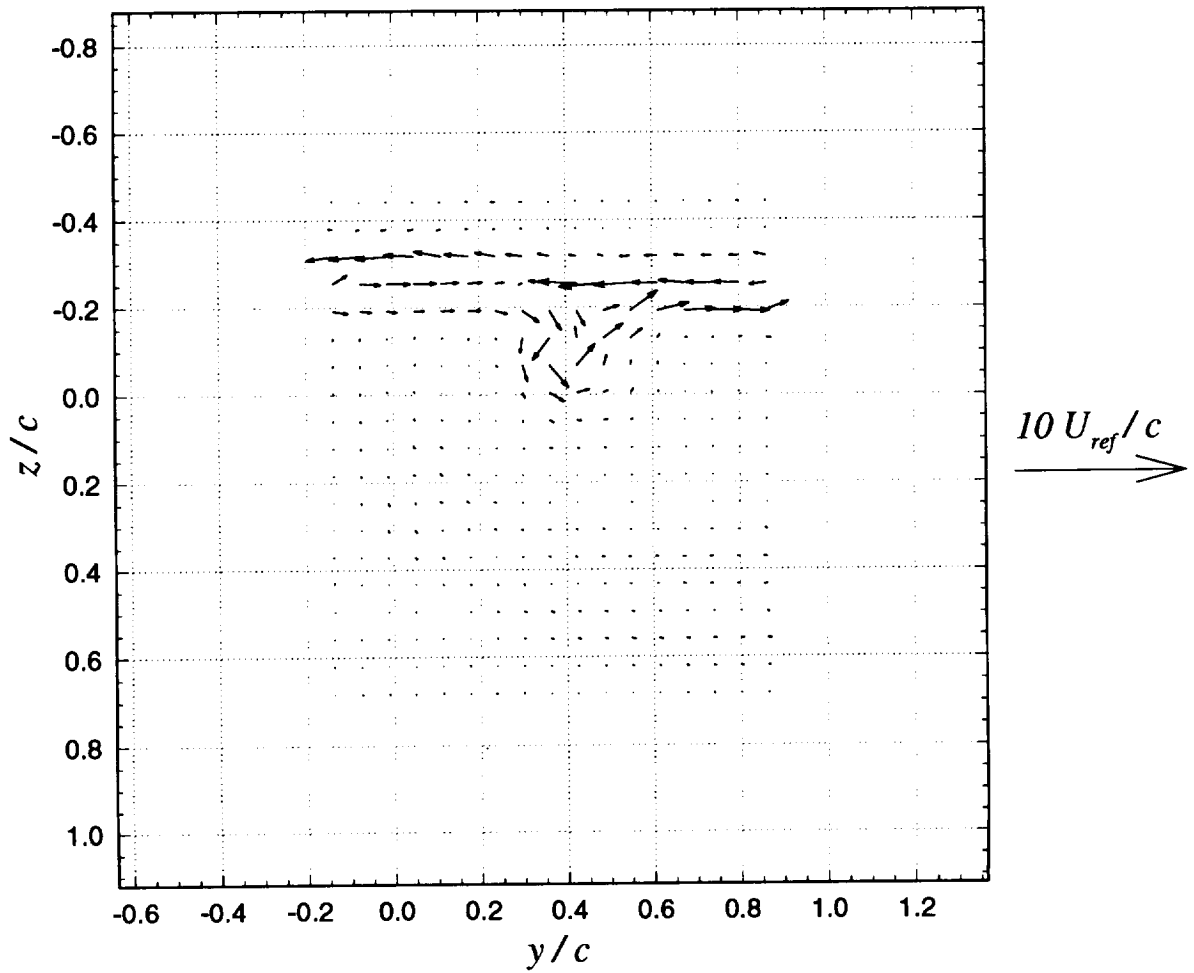


**Figure 3.16a** Mean cross-flow vorticity vectors ( $\Omega_y \cdot c / U_{ref}$ ,  $\Omega_z \cdot c / U_{ref}$ ) for pressure side passage of  $\Delta/c = -0.125$ :  $x/c = 15.95$ ,  $\alpha_1 = 5^\circ$ ,  $\alpha_2 = 5^\circ$ , no spoiler

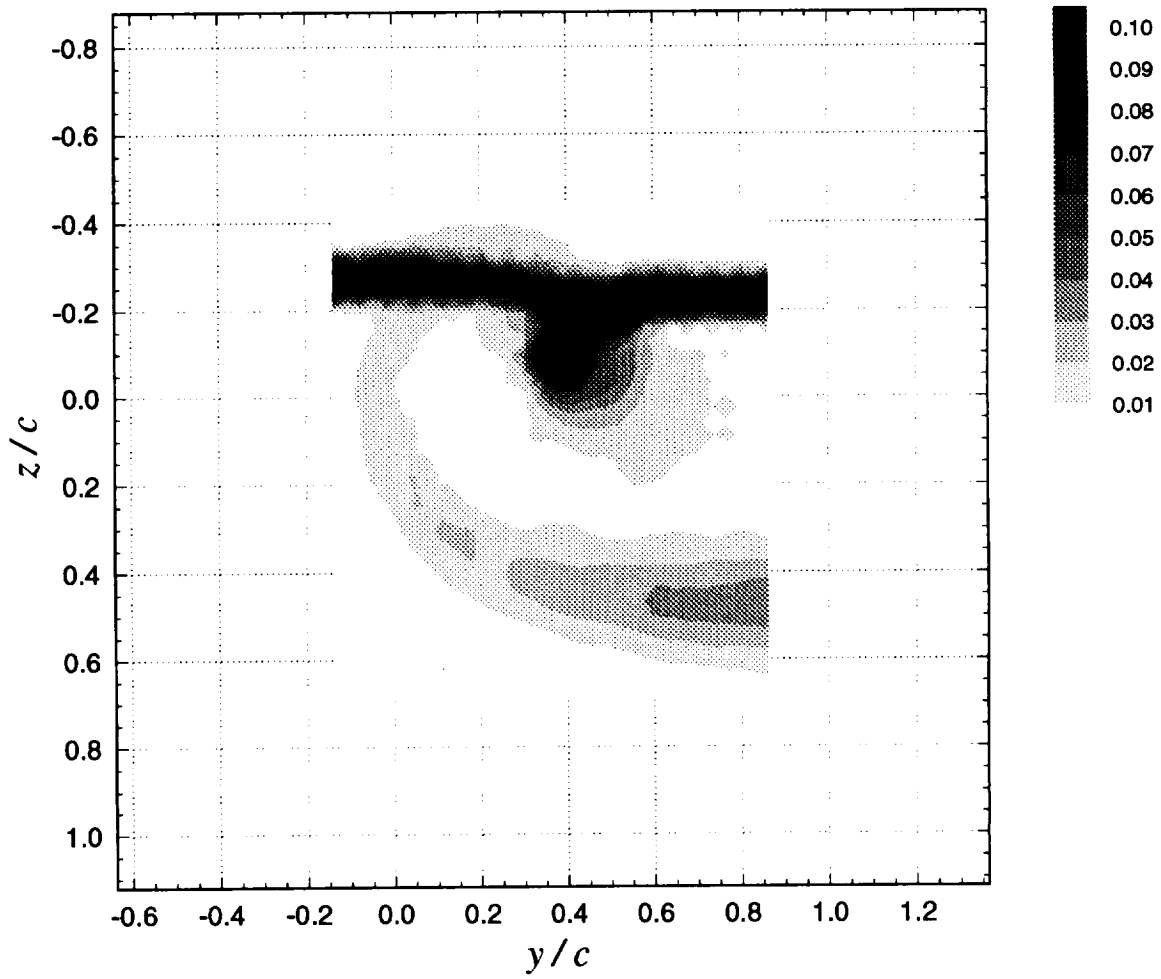


**Figure 3.16b** Contours of mean axial velocity deficit  $((U_{ref} - U) / U_{ref})$  for pressure side passage of  $\Delta/c = -0.125$ :  $x/c = 15.95$ ,  $\alpha_1 = 5^\circ$ ,  $\alpha_2 = 5^\circ$ , no spoiler

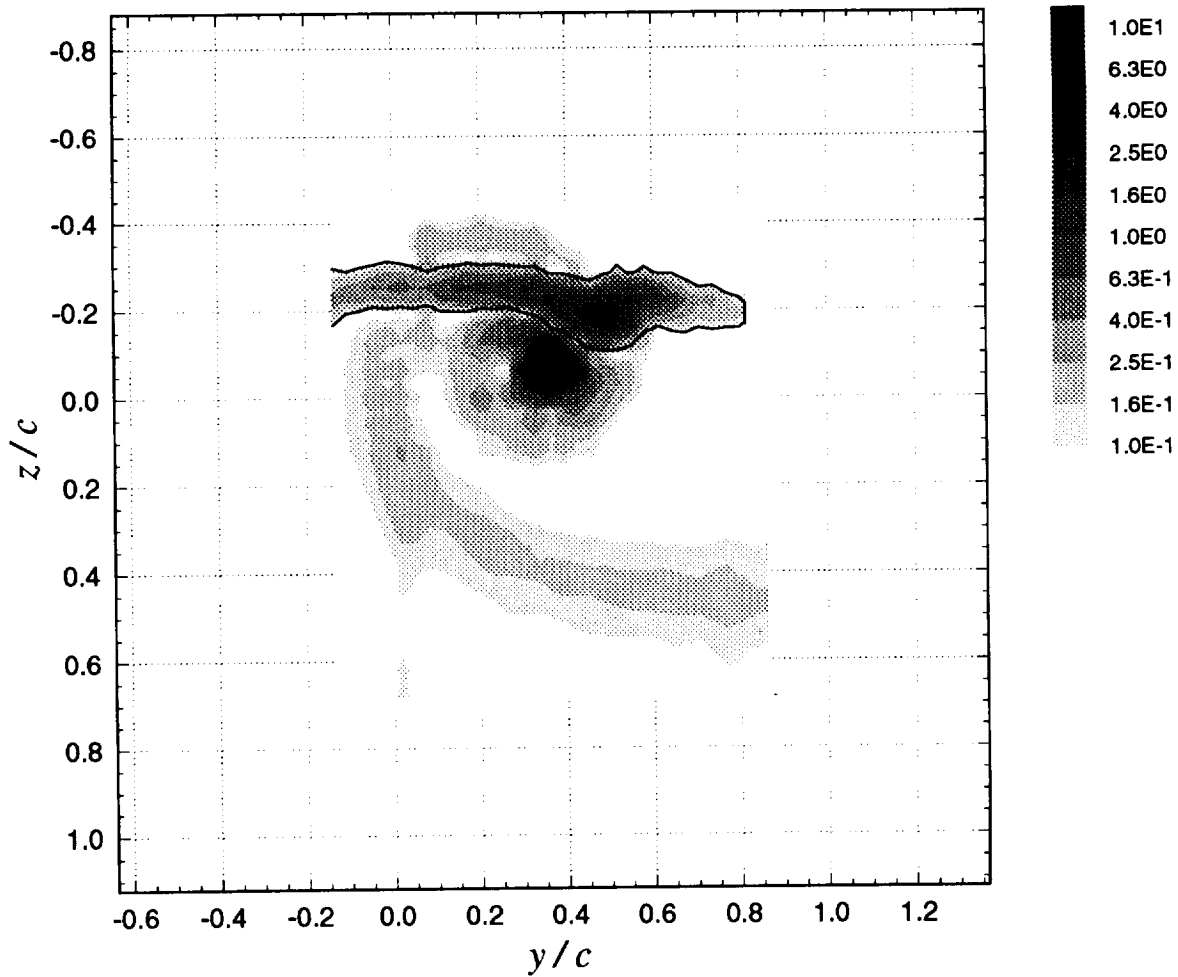


**Figure 3.16c** Contours of mean axial vorticity ( $\Omega_x \cdot c / U_{ref}$ ) for pressure side passage of  $\Delta/c = -0.125$ :  $x/c = 15.95$ ,  $\alpha_1 = 5^\circ$ ,  $\alpha_2 = 5^\circ$ , no spoiler. Legend lists  $|\Omega_x \cdot c / U_{ref}|$  values. Negative values of  $\Omega_x \cdot c / U_{ref}$  are contained within the solid contour lines.

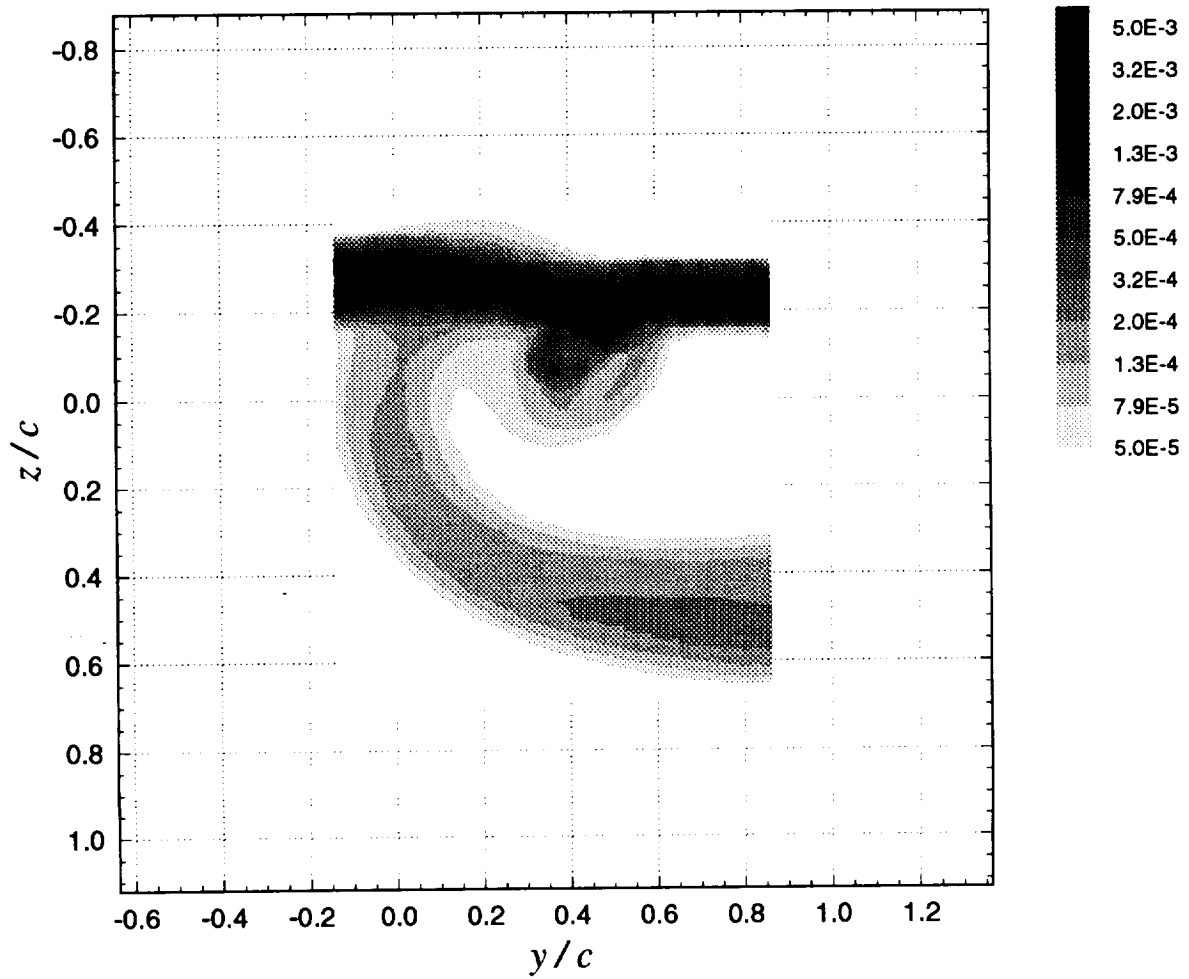


**Figure 3.16d** Contours of axial normal turbulent stress ( $\overline{u^2} / U_{ref}^2$ ) for pressure side passage of  $\Delta/c = -0.125$ :  $x/c = 15.95$ ,  $\alpha_1 = 5^\circ$ ,  $\alpha_2 = 5^\circ$ , no spoiler



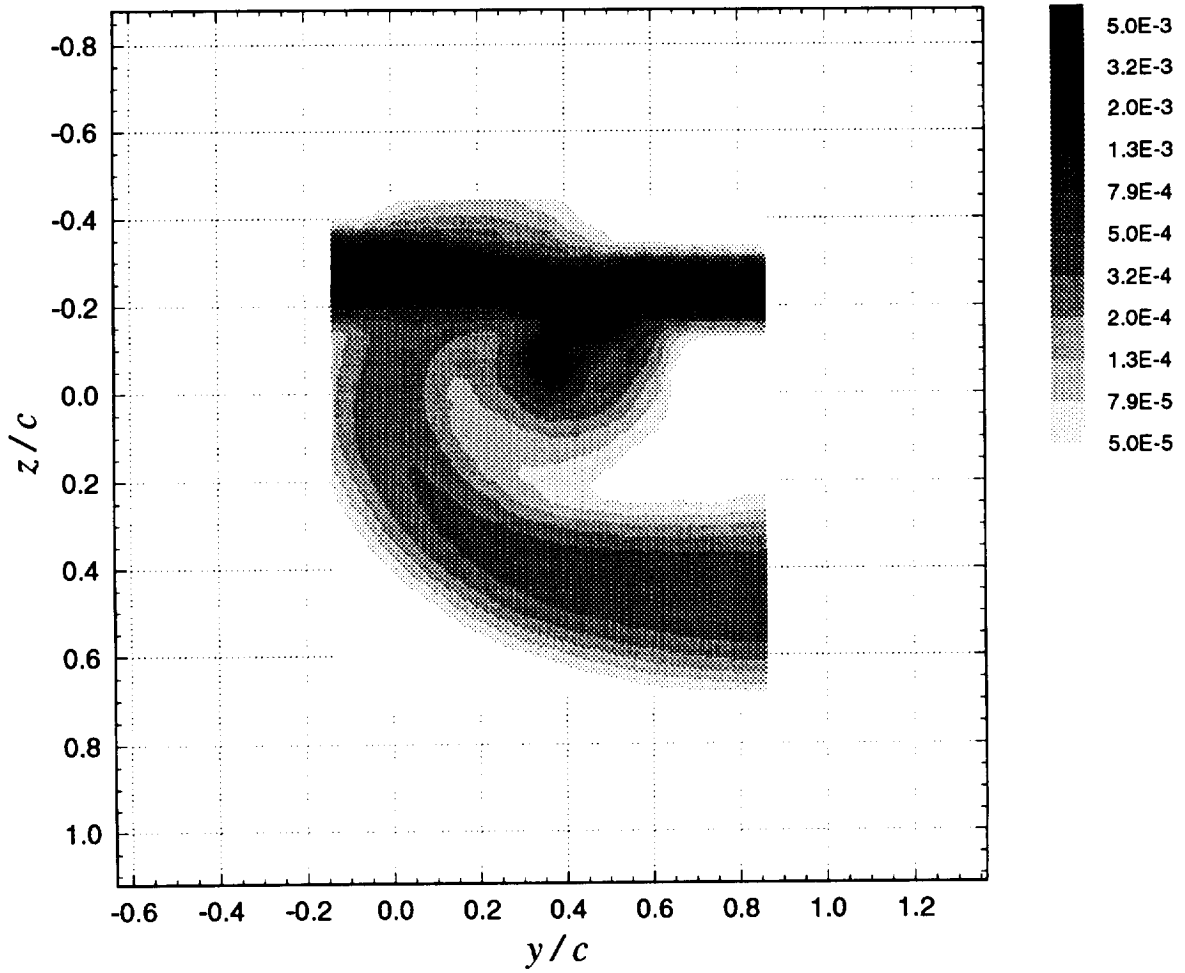


**Figure 3.16e** Contours of summed cross-flow normal turbulent stresses  $(\overline{v^2} + \overline{w^2}) / U_{ref}^2$  for pressure side passage of  $\Delta/c = -0.125$ :  $x/c = 15.95$ ,  $\alpha_1 = 5^\circ$ ,  $\alpha_2 = 5^\circ$ , no spoiler

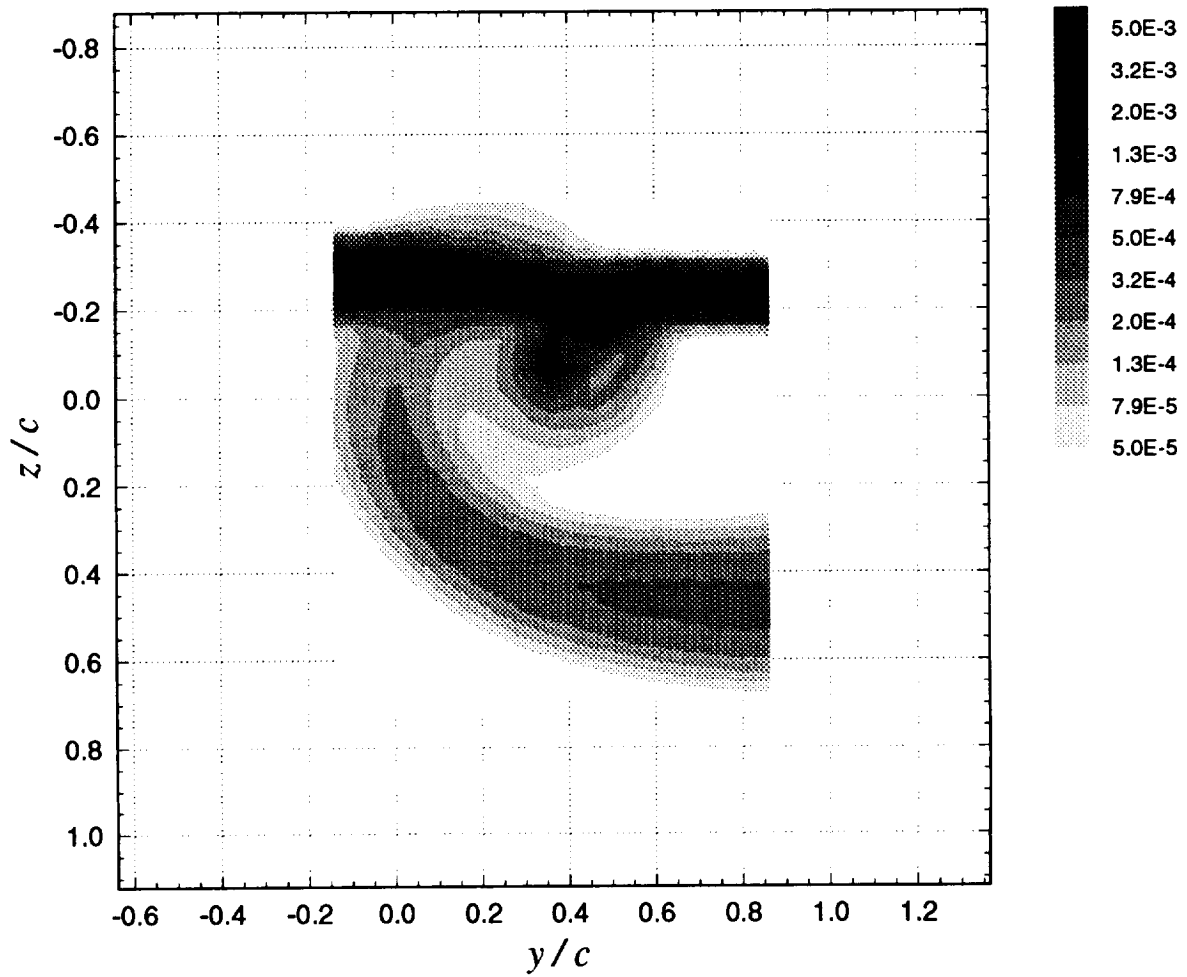


**Figure 3.16f** Contours of turbulent kinetic energy ( $k / U_{ref}^2$ ):  $x / c = 15.95$ ,  $\alpha_l = 5^\circ$ , no spoiler

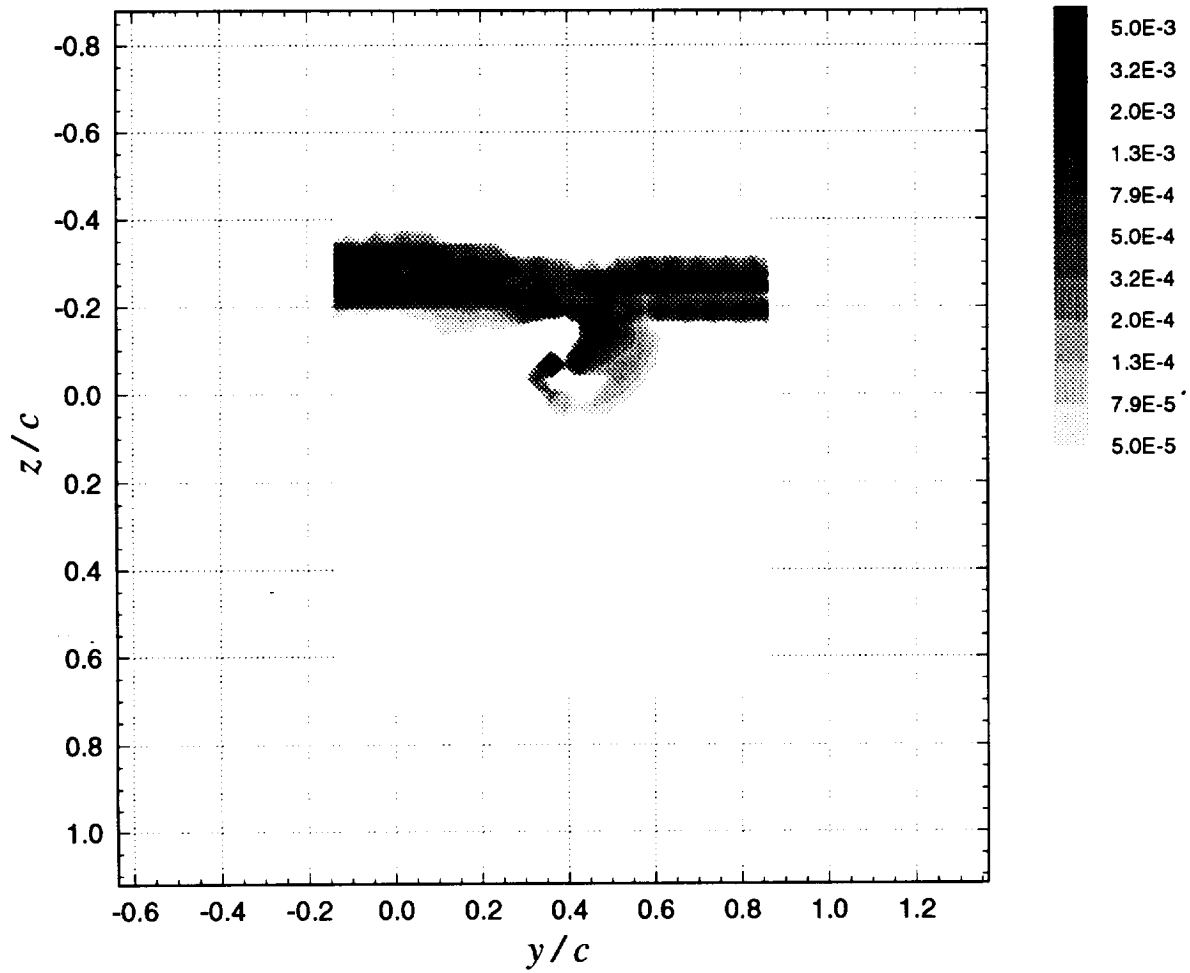


**Figure 3.16g** Contours of turbulent kinetic energy production ( $P \cdot c / U_{ref}^3$ ) for pressure side passage of  $\Delta/c = -0.125$ :  $x/c = 15.95$ ,  $\alpha_1 = 5^\circ$ ,  $\alpha_2 = 5^\circ$ , no spoiler

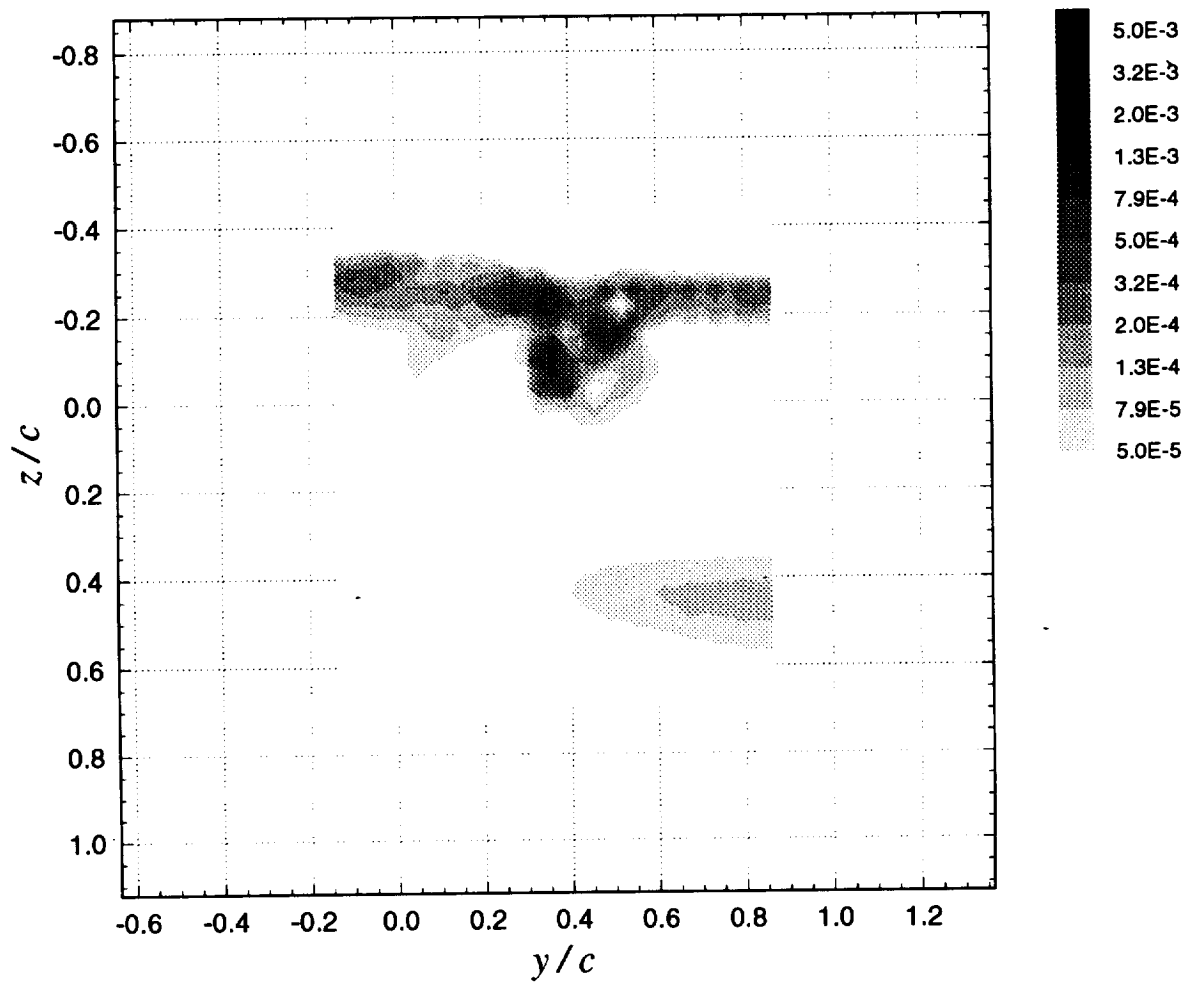


**Figure 3.16h** Contours of axial shear stress magnitude ( $\tau_a / U_{ref}^2$ ) for pressure side passage of  $\Delta/c = -0.125$ :  $x/c = 15.95$ ,  $\alpha_1 = 5^\circ$ ,  $\alpha_2 = 5^\circ$ , no spoiler

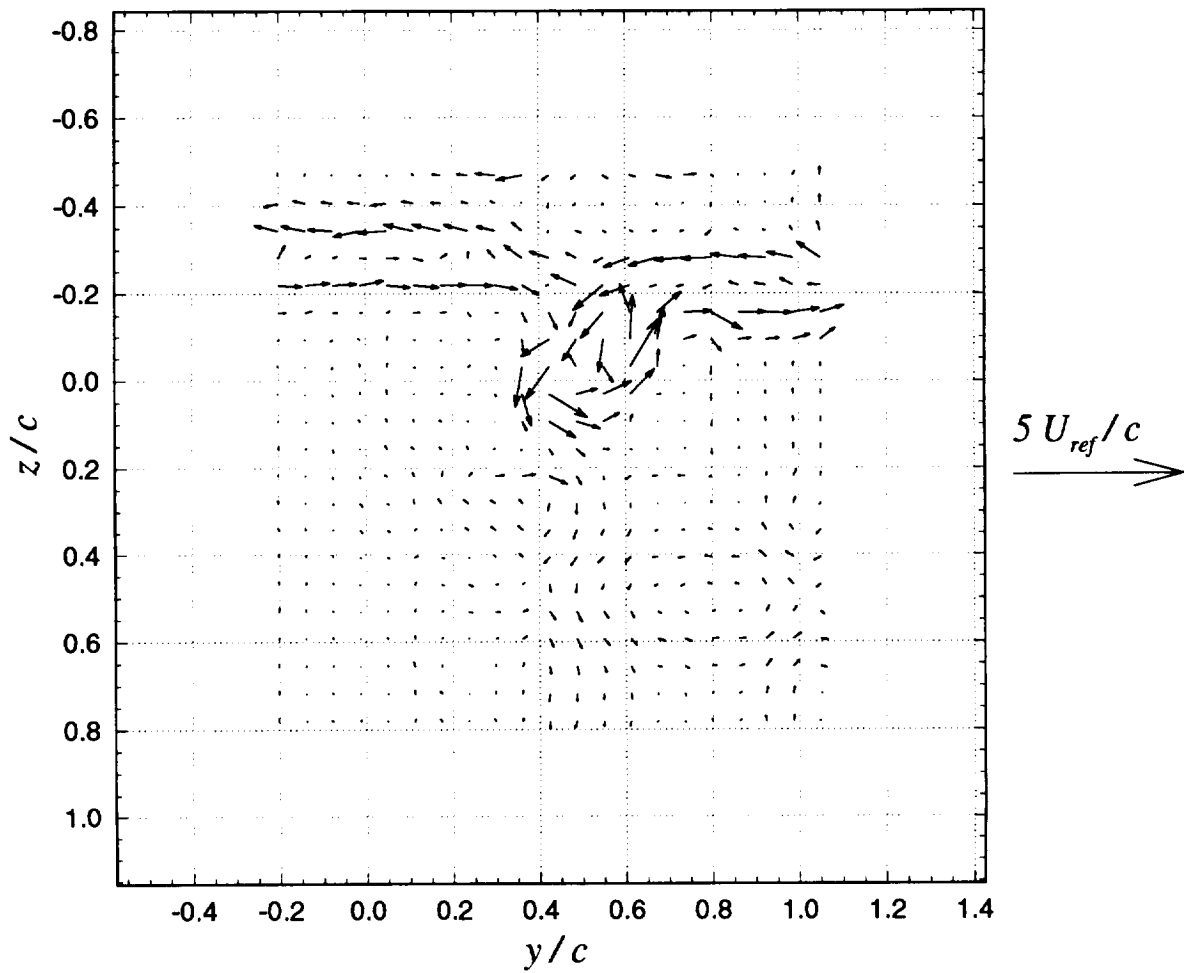


**Figure 3.17a** Mean cross-flow vorticity vectors ( $\Omega_y \cdot c / U_{ref}$ ,  $\Omega_z \cdot c / U_{ref}$ ) for pressure side passage of  $\Delta / c = -0.125$ :  $x / c = 17.5$ ,  $\alpha_1 = 5^\circ$ ,  $\alpha_2 = 5^\circ$ , no spoiler

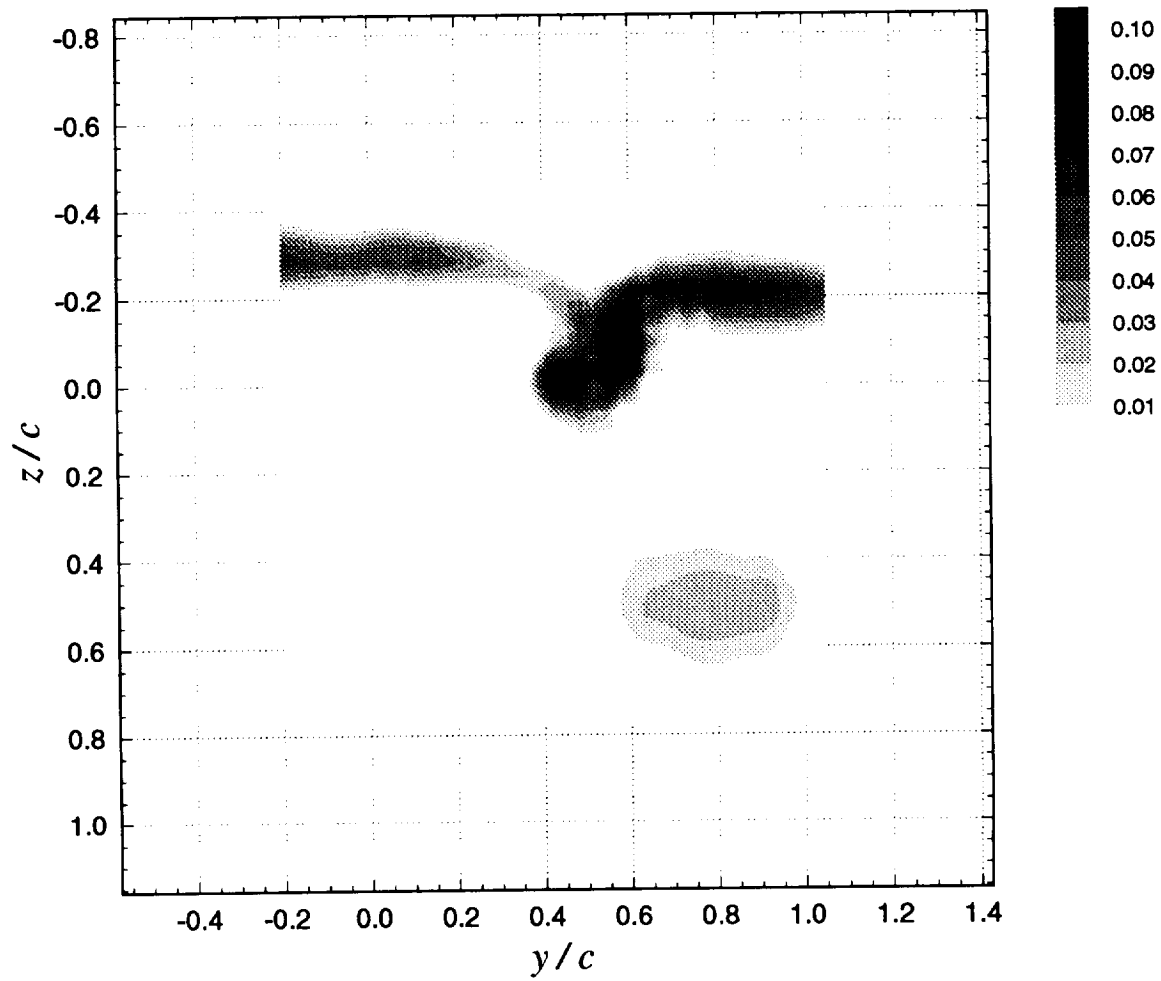


**Figure 3.17b** Contours of mean axial velocity deficit  $((U_{ref} - U) / U_{ref})$  for pressure side passage of  $\Delta/c = -0.125$ :  $x/c = 17.5$ ,  $\alpha_1 = 5^\circ$ ,  $\alpha_2 = 5^\circ$ , no spoiler

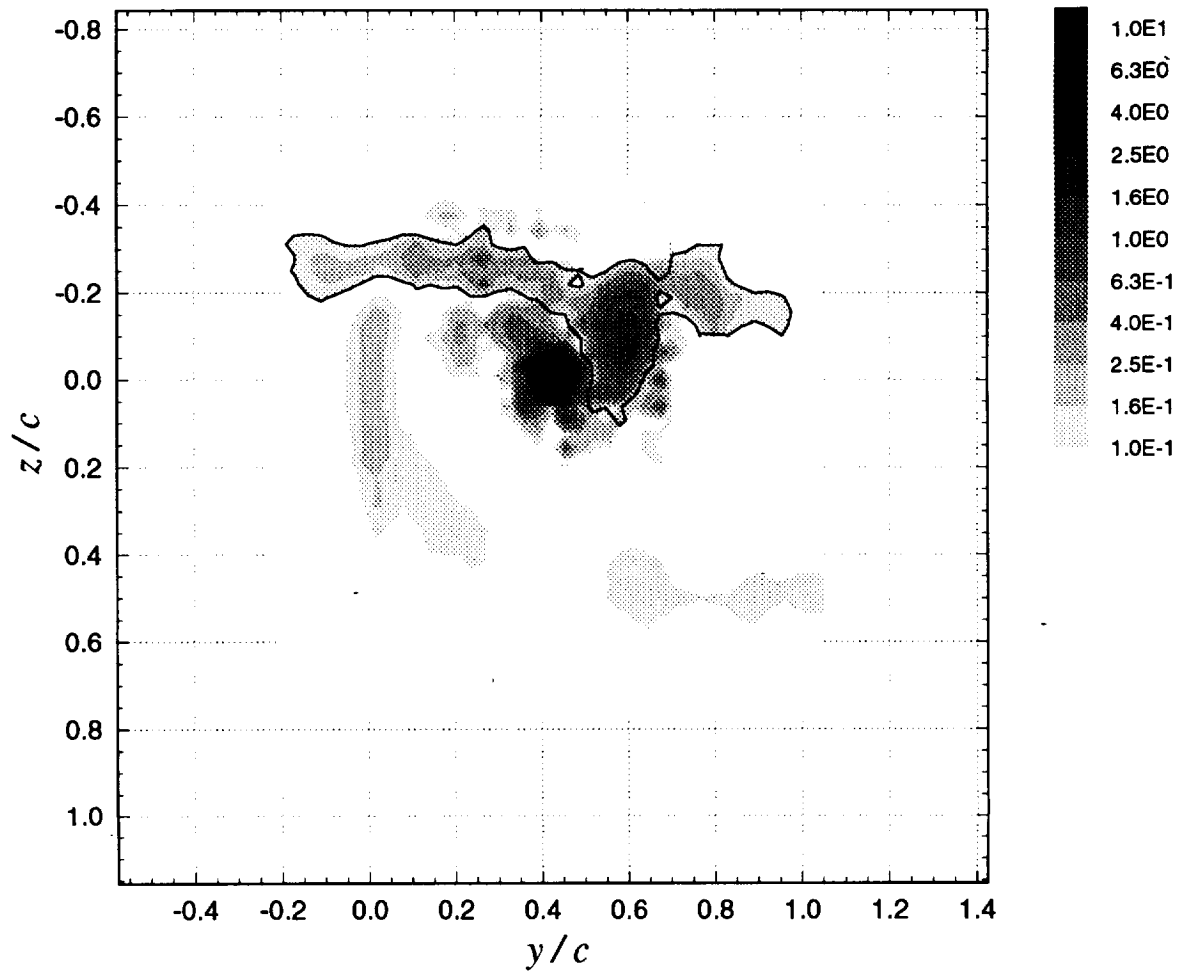


**Figure 3.17c** Contours of mean axial vorticity ( $\Omega_x \cdot c / U_{ref}$ ) for pressure side passage of  $\Delta/c = -0.125$ :  $x/c = 17.5$ ,  $\alpha_1 = 5^\circ$ ,  $\alpha_2 = 5^\circ$ , no spoiler. Legend lists  $|\Omega_x \cdot c / U_{ref}|$  values. Negative values of  $\Omega_x \cdot c / U_{ref}$  are contained within the solid contour lines.

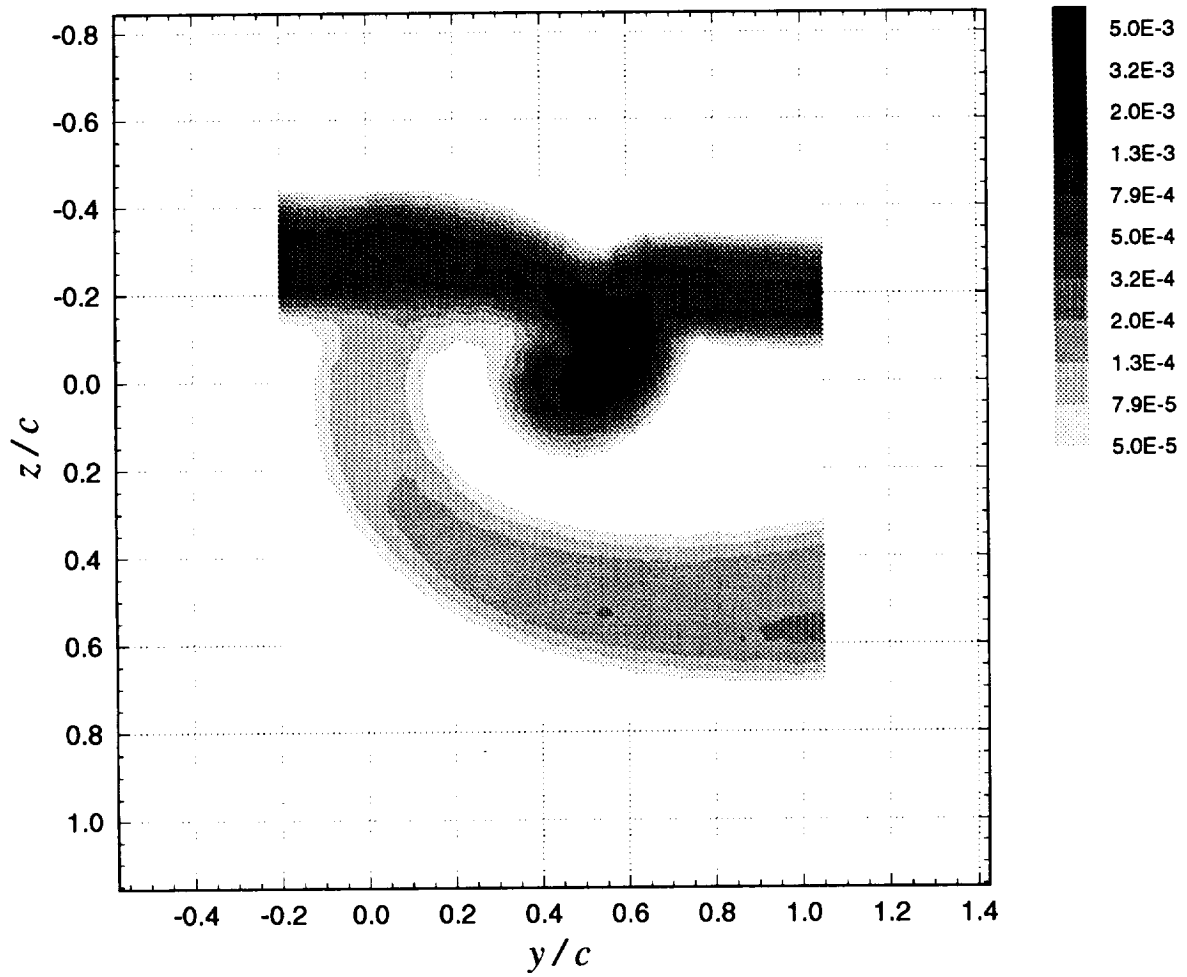


**Figure 3.17d** Contours of axial normal turbulent stress ( $\overline{u^2} / U_{ref}^2$ ) for pressure side passage of  $\Delta/c = -0.125$ :  $x/c = 17.5$ ,  $\alpha_1 = 5^\circ$ ,  $\alpha_2 = 5^\circ$ , no spoiler



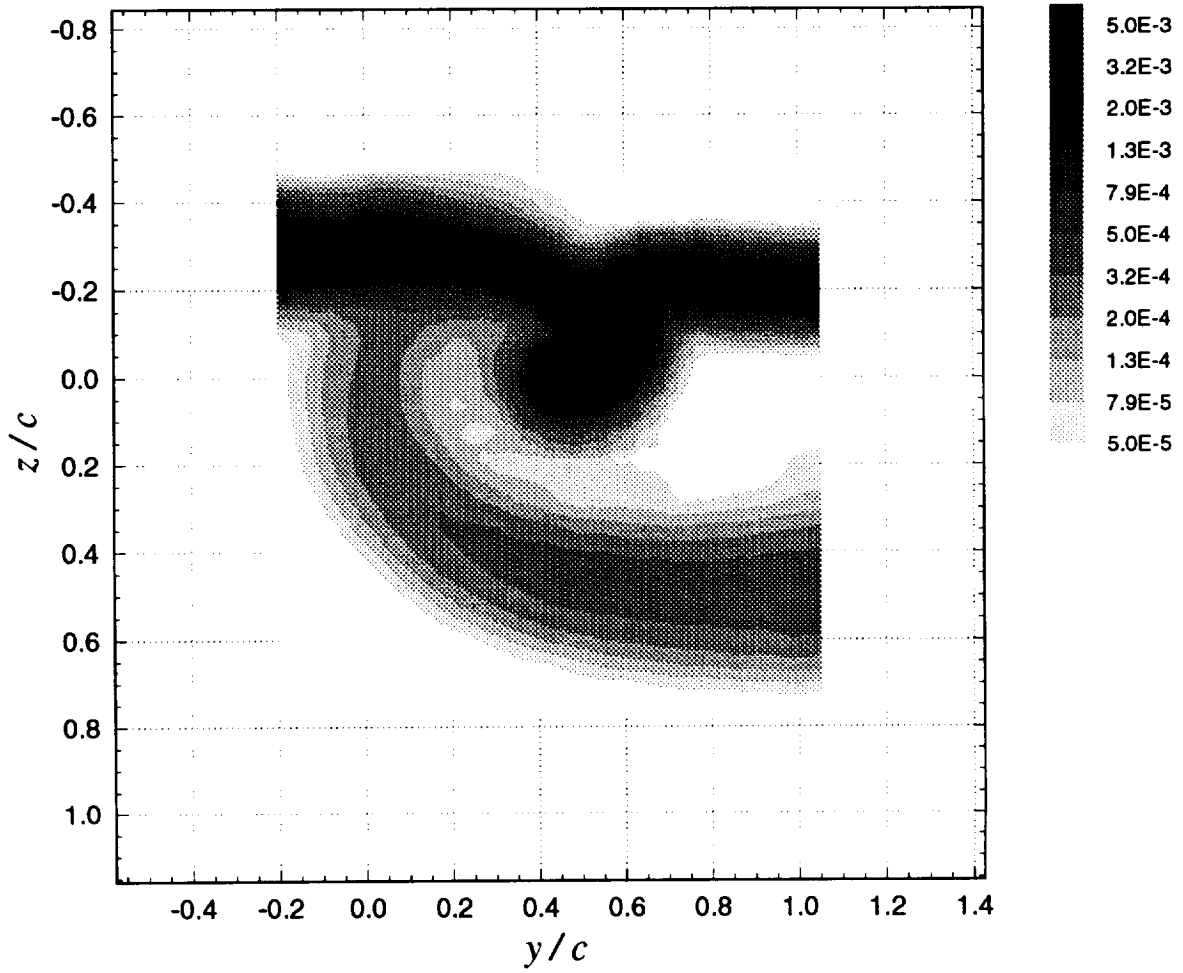


**Figure 3.17e** Contours of summed cross-flow normal turbulent stresses  $(\overline{v^2} + \overline{w^2}) / U_{ref}^2$  for pressure side passage of  $\Delta/c = -0.125$ :  $x/c = 17.5$ ,  $\alpha_1 = 5^\circ$ ,  $\alpha_2 = 5^\circ$ , no spoiler

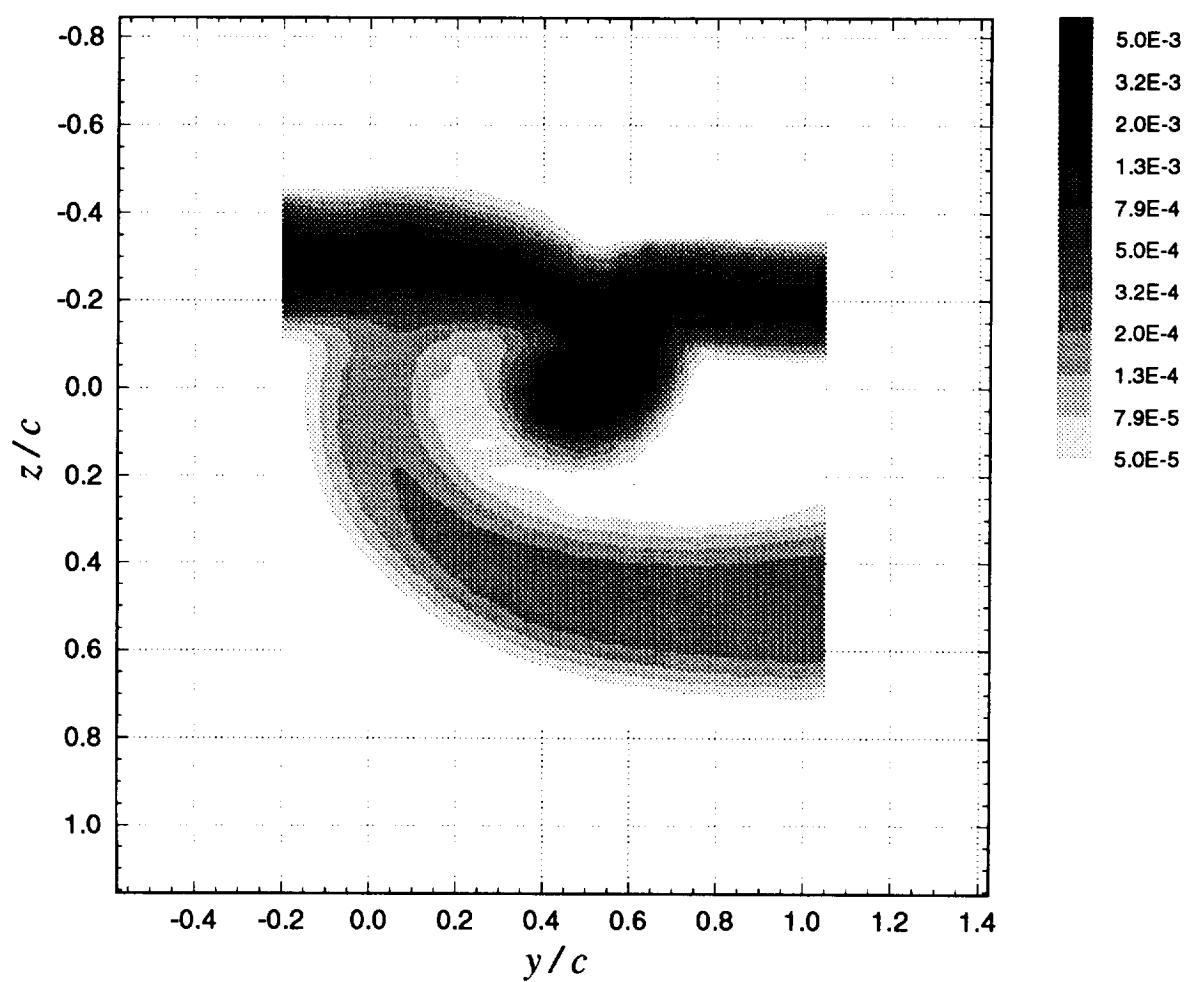


**Figure 3.17f** Contours of turbulent kinetic energy ( $k / U_{ref}^2$ ):  $x/c = 17.5$ ,  $\alpha_l = 5^\circ$ , no spoiler

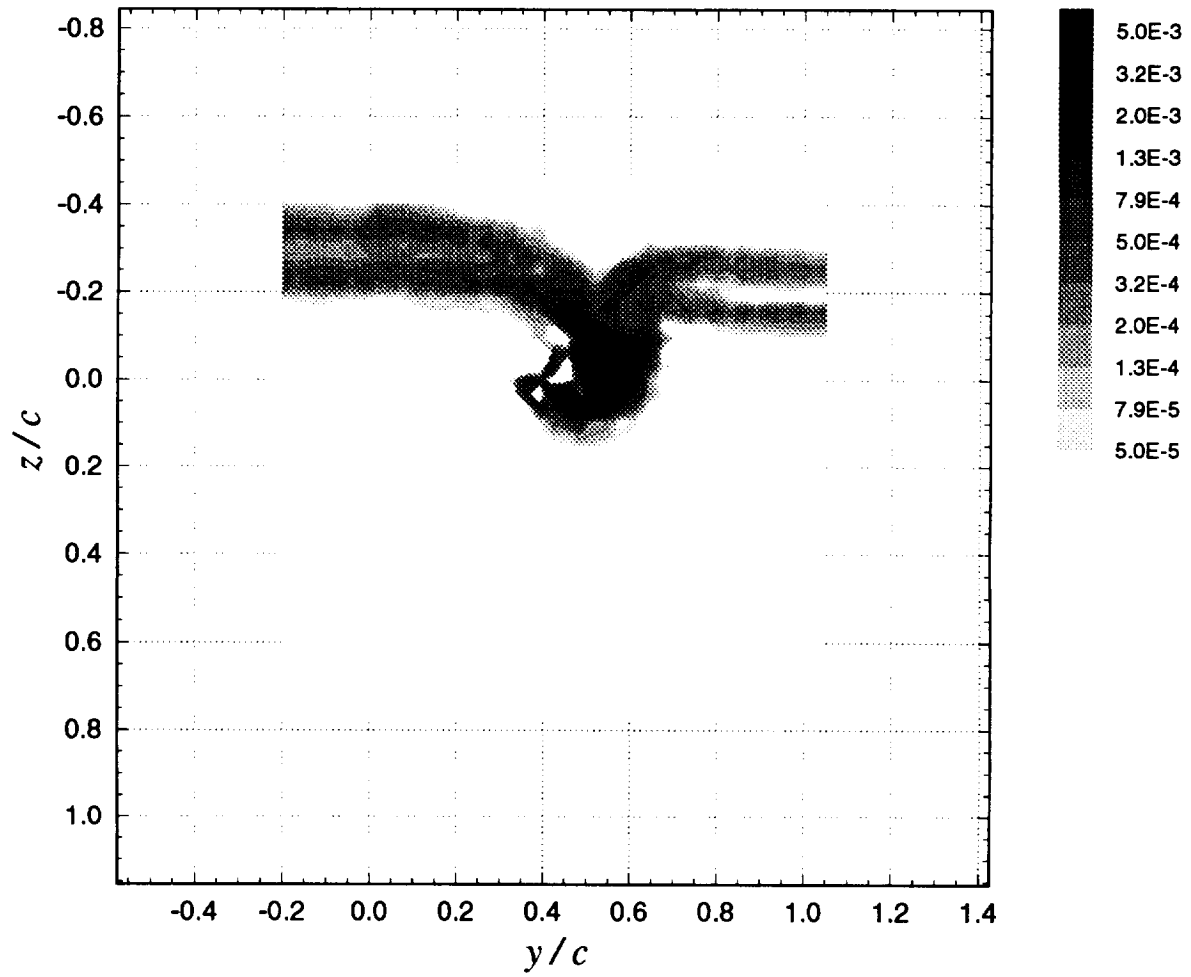


**Figure 3.17g** Contours of turbulent kinetic energy production ( $P \cdot c / U_{ref}^3$ ) for pressure side passage of  $\Delta/c = -0.125$ :  $x/c = 17.5$ ,  $\alpha_1 = 5^\circ$ ,  $\alpha_2 = 5^\circ$ , no spoiler

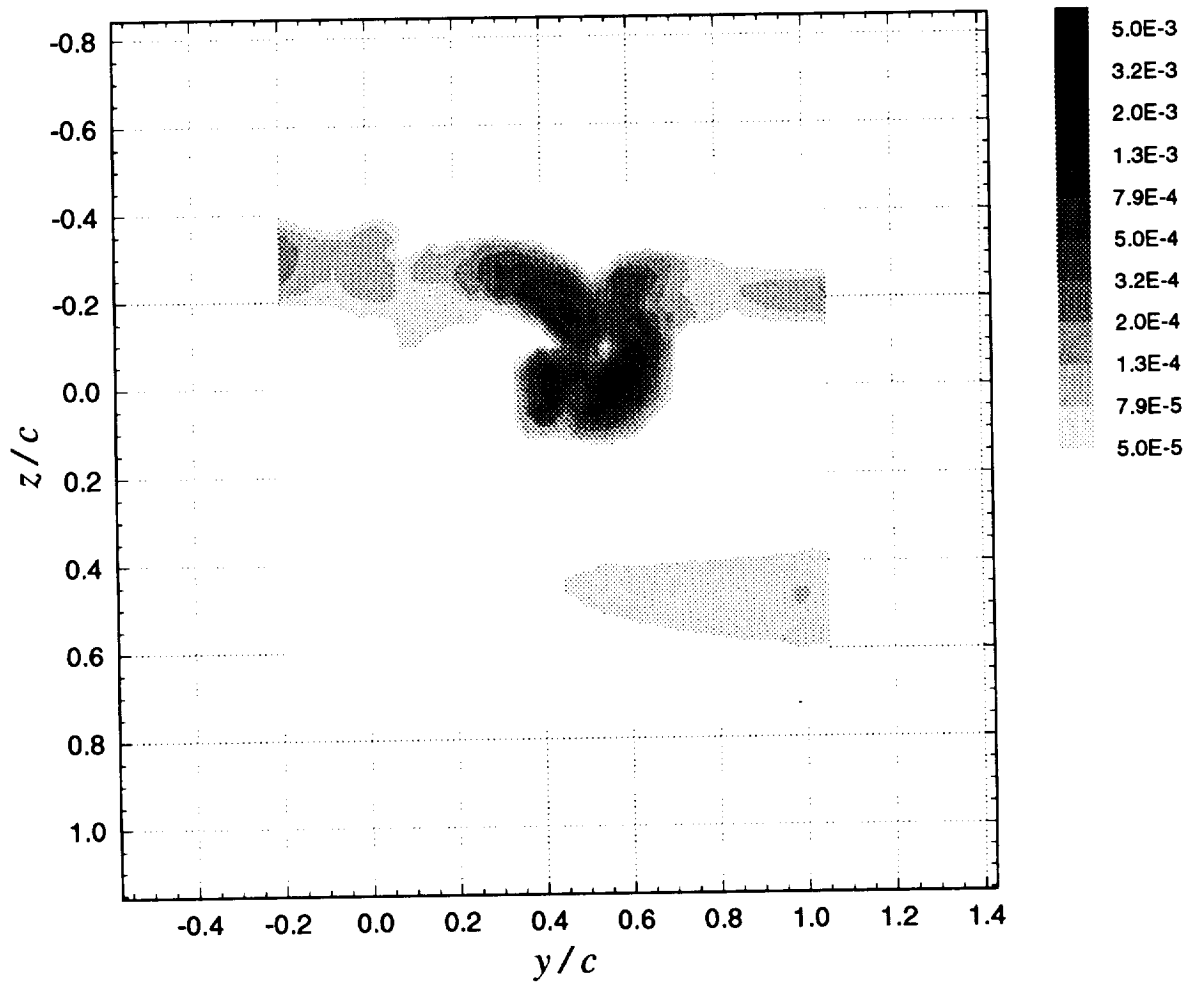


**Figure 3.17h** Contours of axial shear stress magnitude ( $\tau_a / U_{ref}^2$ ) for pressure side passage of  $\Delta/c = -0.125$ :  $x/c = 17.5$ ,  $\alpha_1 = 5^\circ$ ,  $\alpha_2 = 5^\circ$ , no spoiler

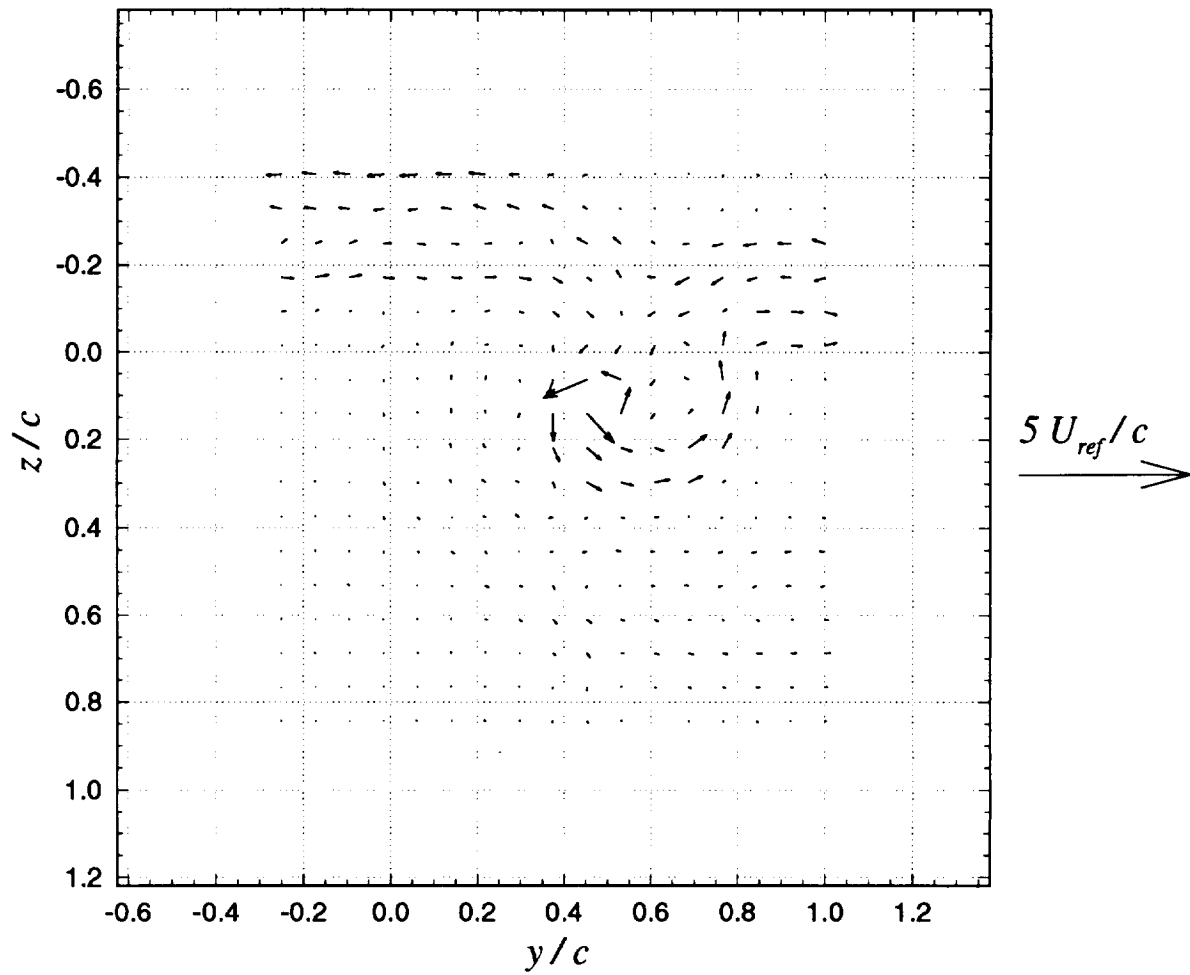


**Figure 3.18a** Mean cross-flow vorticity vectors ( $\Omega_y \cdot c / U_{ref}$ ,  $\Omega_z \cdot c / U_{ref}$ ) for pressure side passage of  $\Delta/c = -0.125$ :  $x/c = 20$ ,  $\alpha_1 = 5^\circ$ ,  $\alpha_2 = 5^\circ$ , no spoiler

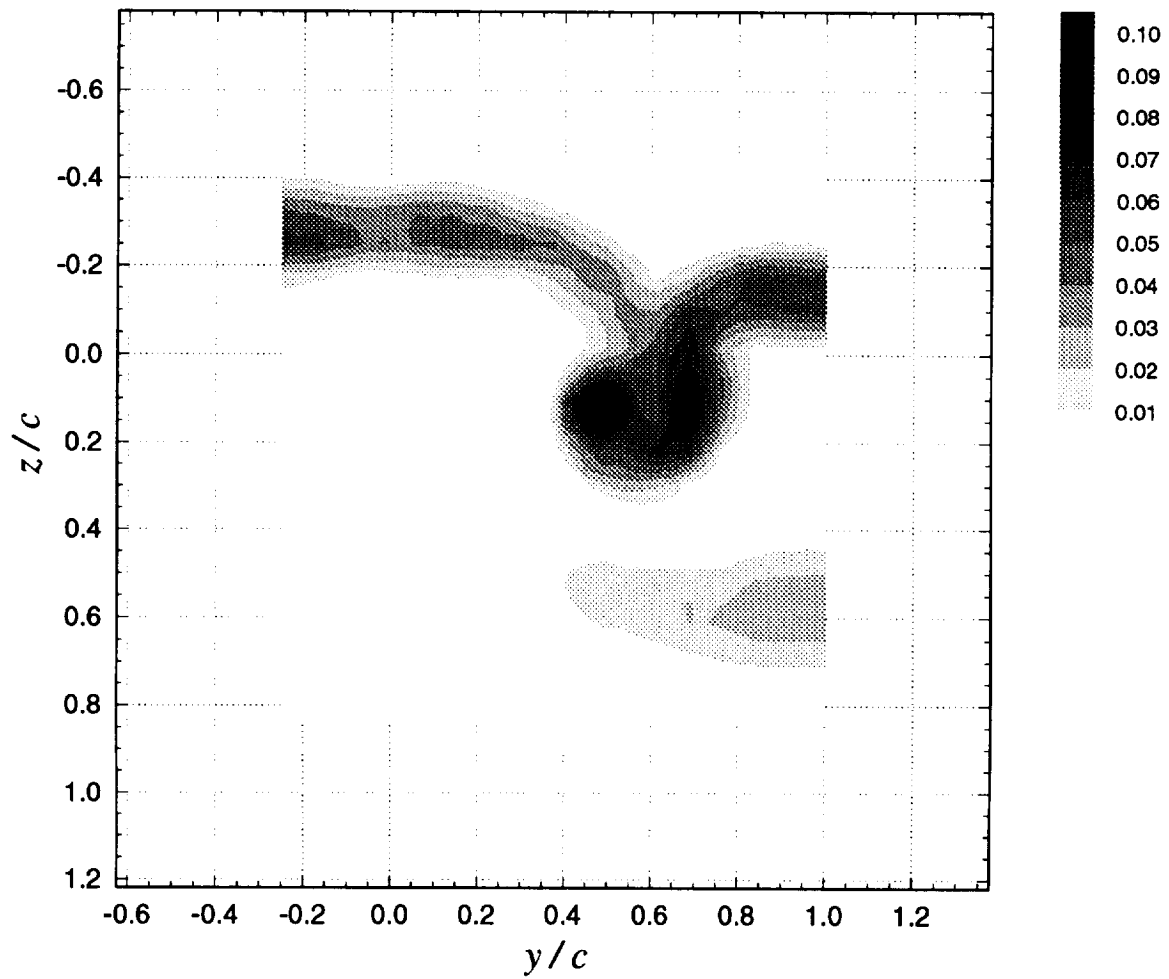


**Figure 3.18b** Contours of mean axial velocity deficit  $((U_{ref} - U) / U_{ref})$  for pressure side passage of  $\Delta/c = -0.125$ :  $x/c = 20$ ,  $\alpha_1 = 5^\circ$ ,  $\alpha_2 = 5^\circ$ , no spoiler

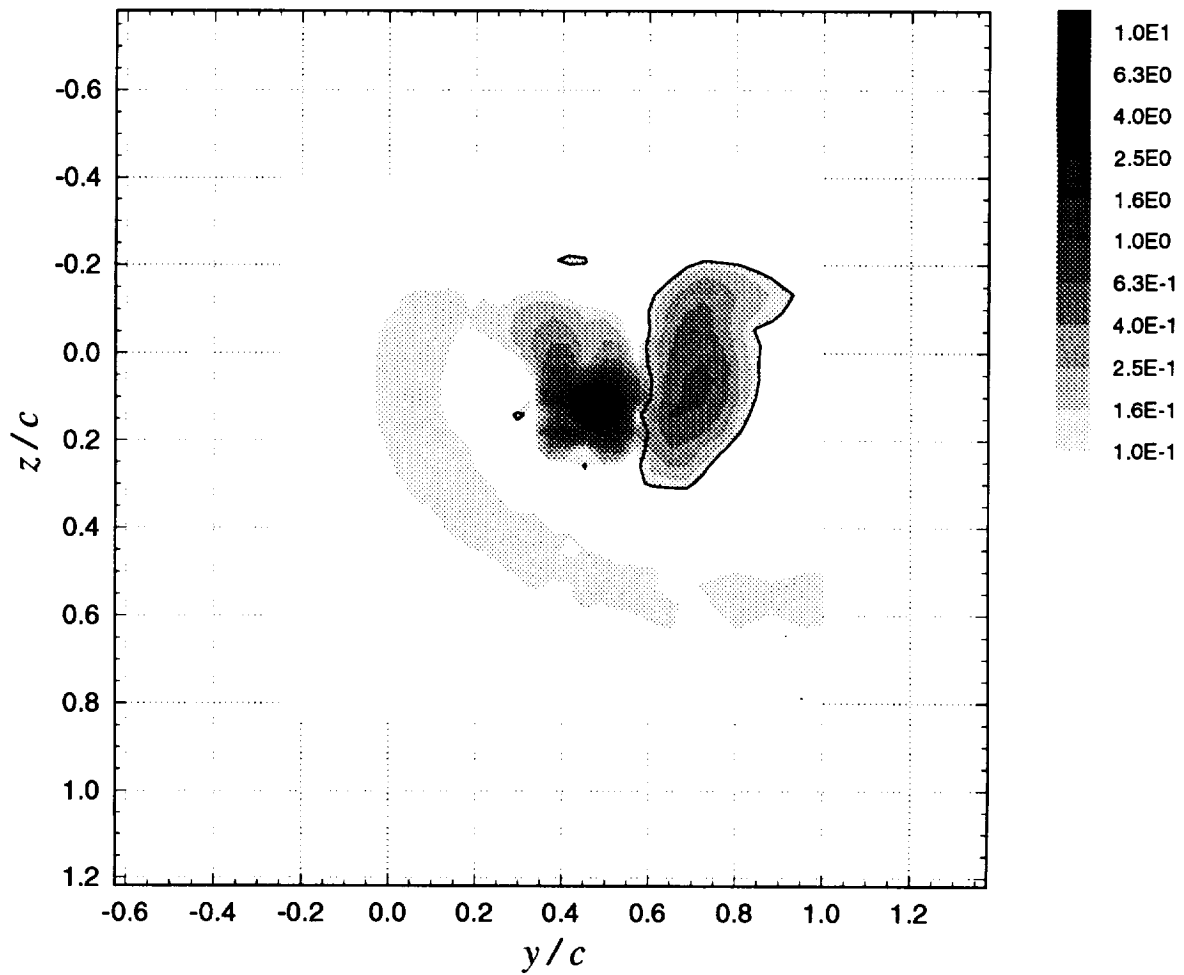


**Figure 3.18c** Contours of mean axial vorticity ( $\Omega_x \cdot c / U_{ref}$ ) for pressure side passage of  $\Delta/c = -0.125$ :  $x/c = 20$ ,  $\alpha_1 = 5^\circ$ ,  $\alpha_2 = 5^\circ$ , no spoiler. Legend lists  $|\Omega_x \cdot c / U_{ref}|$  values. Negative values of  $\Omega_x \cdot c / U_{ref}$  are contained within the solid contour lines.

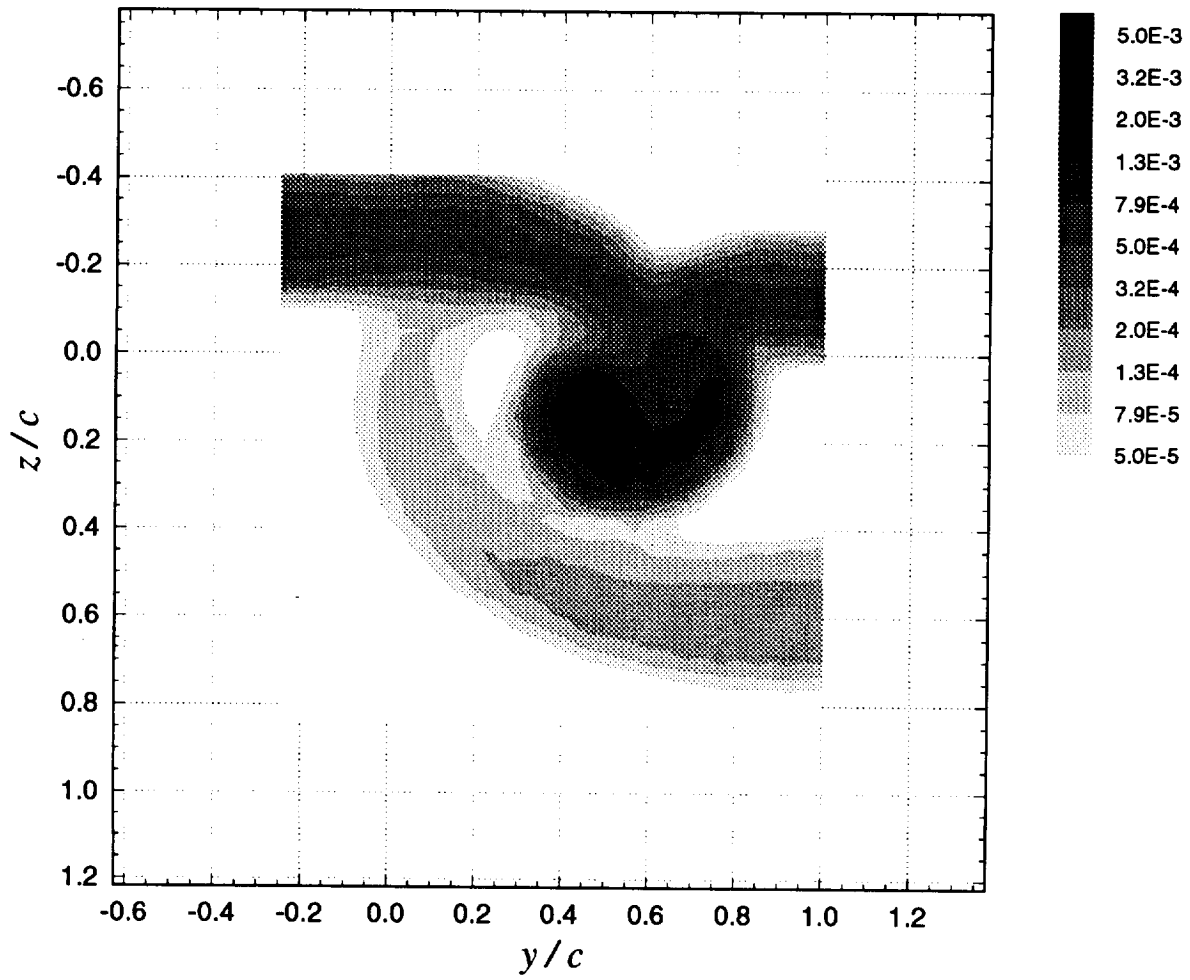


**Figure 3.18d** Contours of axial normal turbulent stress ( $\overline{u^2} / U_{ref}^2$ ) for pressure side passage of  $\Delta/c = -0.125$ :  $x/c = 20$ ,  $\alpha_1 = 5^\circ$ ,  $\alpha_2 = 5^\circ$ , no spoiler



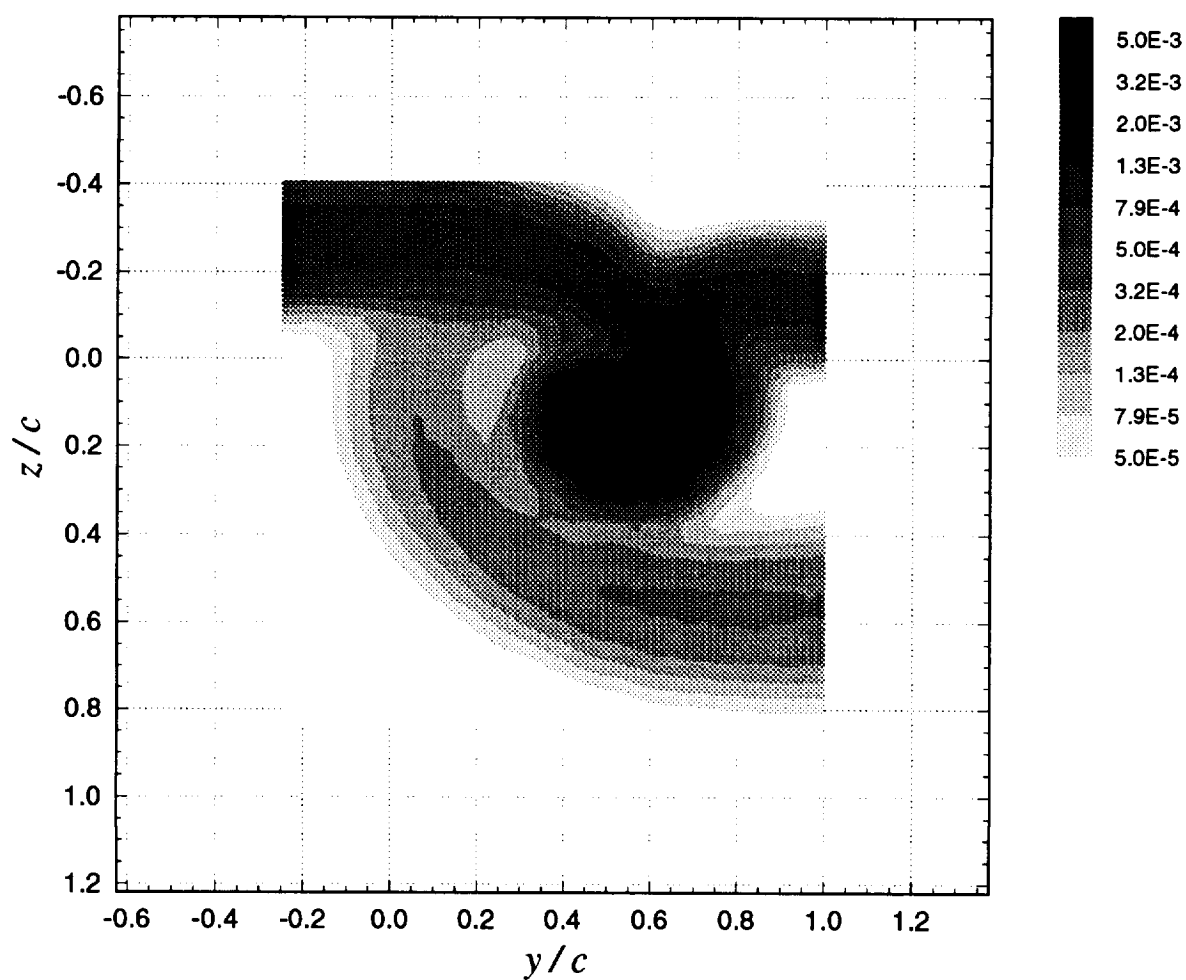


**Figure 3.18e** Contours of summed cross-flow normal turbulent stresses  $(\overline{v^2} + \overline{w^2}) / U_{ref}^2$  for pressure side passage of  $\Delta/c = -0.125$ :  $x/c = 20$ ,  $\alpha_1 = 5^\circ$ ,  $\alpha_2 = 5^\circ$ , no spoiler

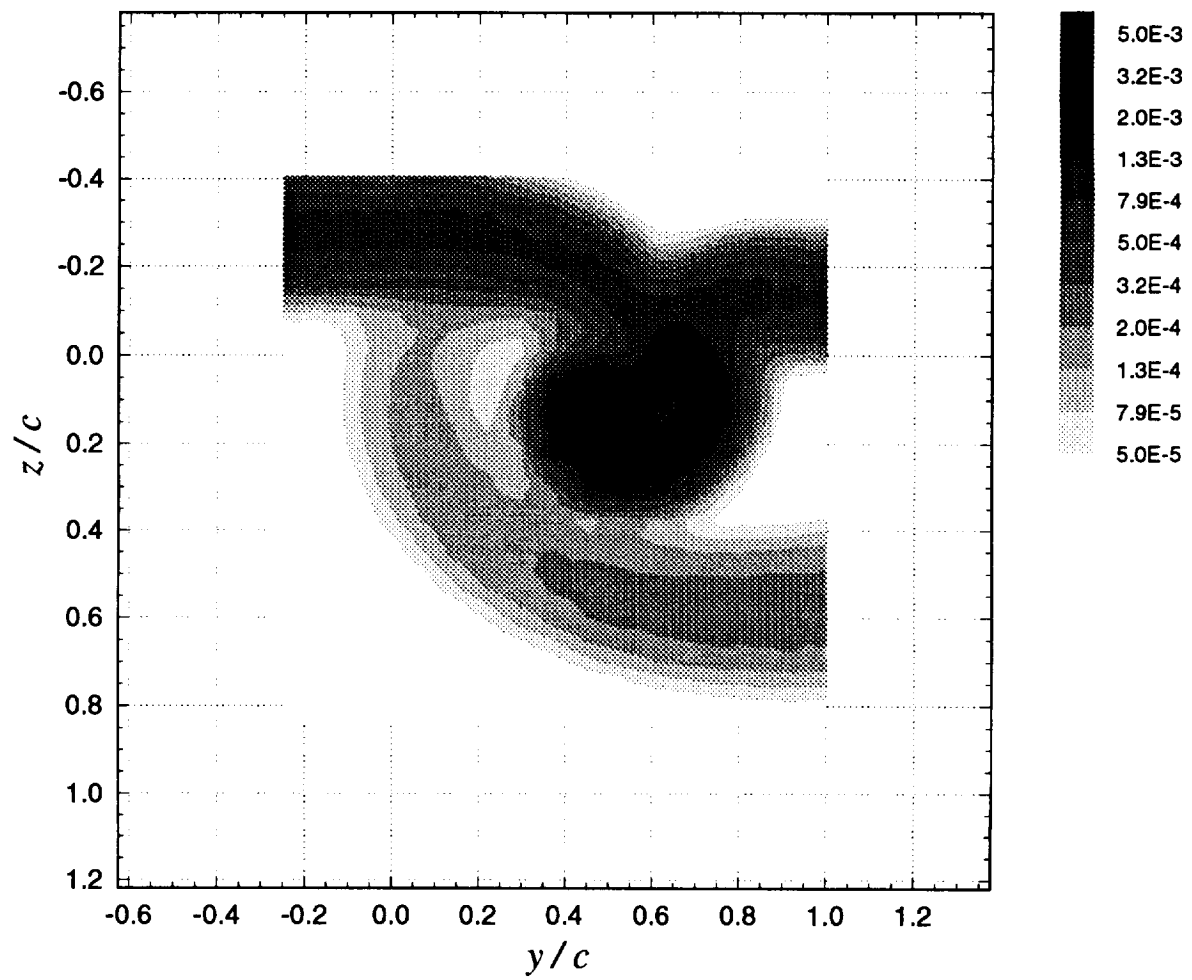


**Figure 3.18f** Contours of turbulent kinetic energy ( $k / U_{ref}^2$ ):  $x / c = 20$ ,  $\alpha_l = 5^\circ$ , no spoiler

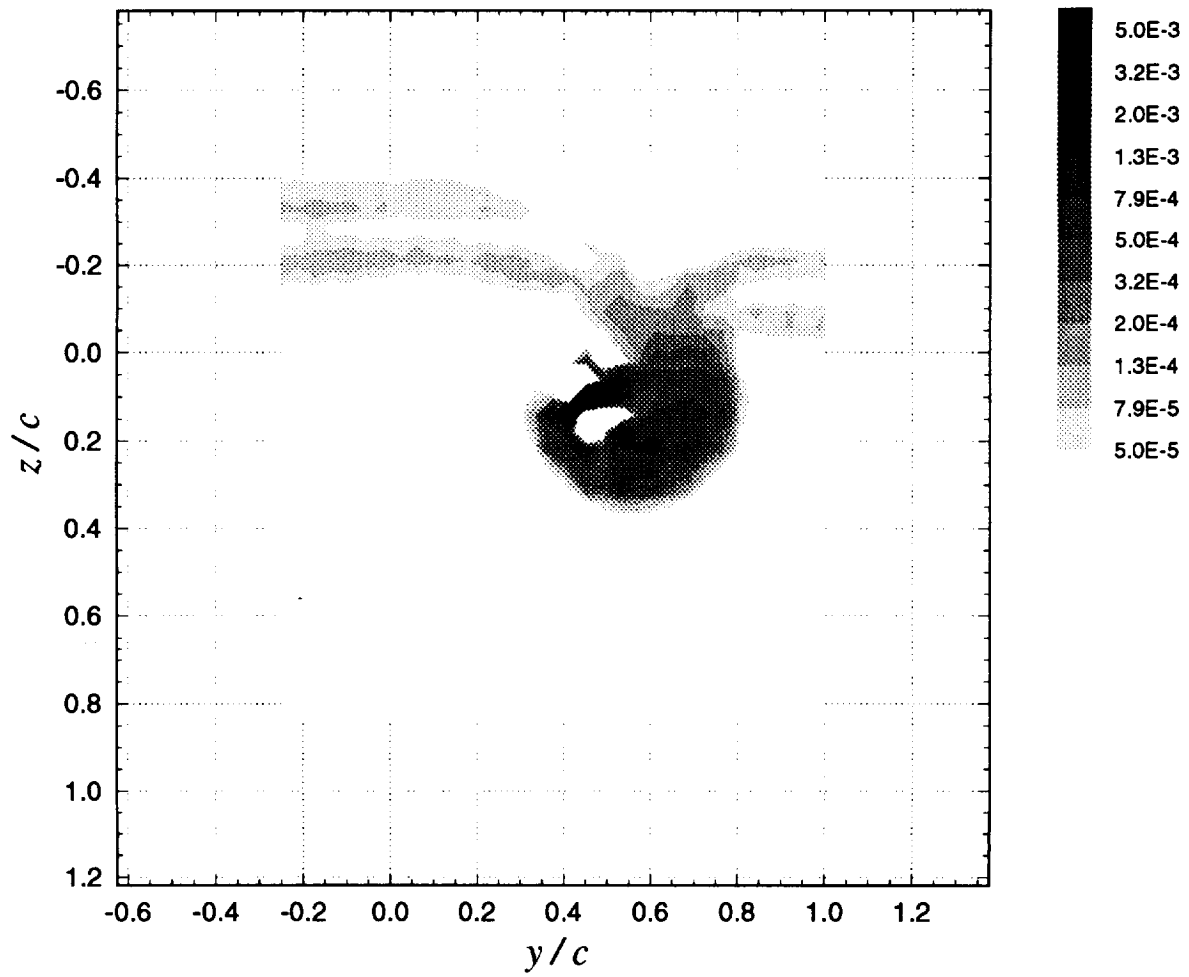


**Figure 3.18g** Contours of turbulent kinetic energy production ( $P \cdot c / U_{ref}^3$ ) for pressure side passage of  $\Delta/c = -0.125$ :  $x/c = 20$ ,  $\alpha_1 = 5^\circ$ ,  $\alpha_2 = 5^\circ$ , no spoiler

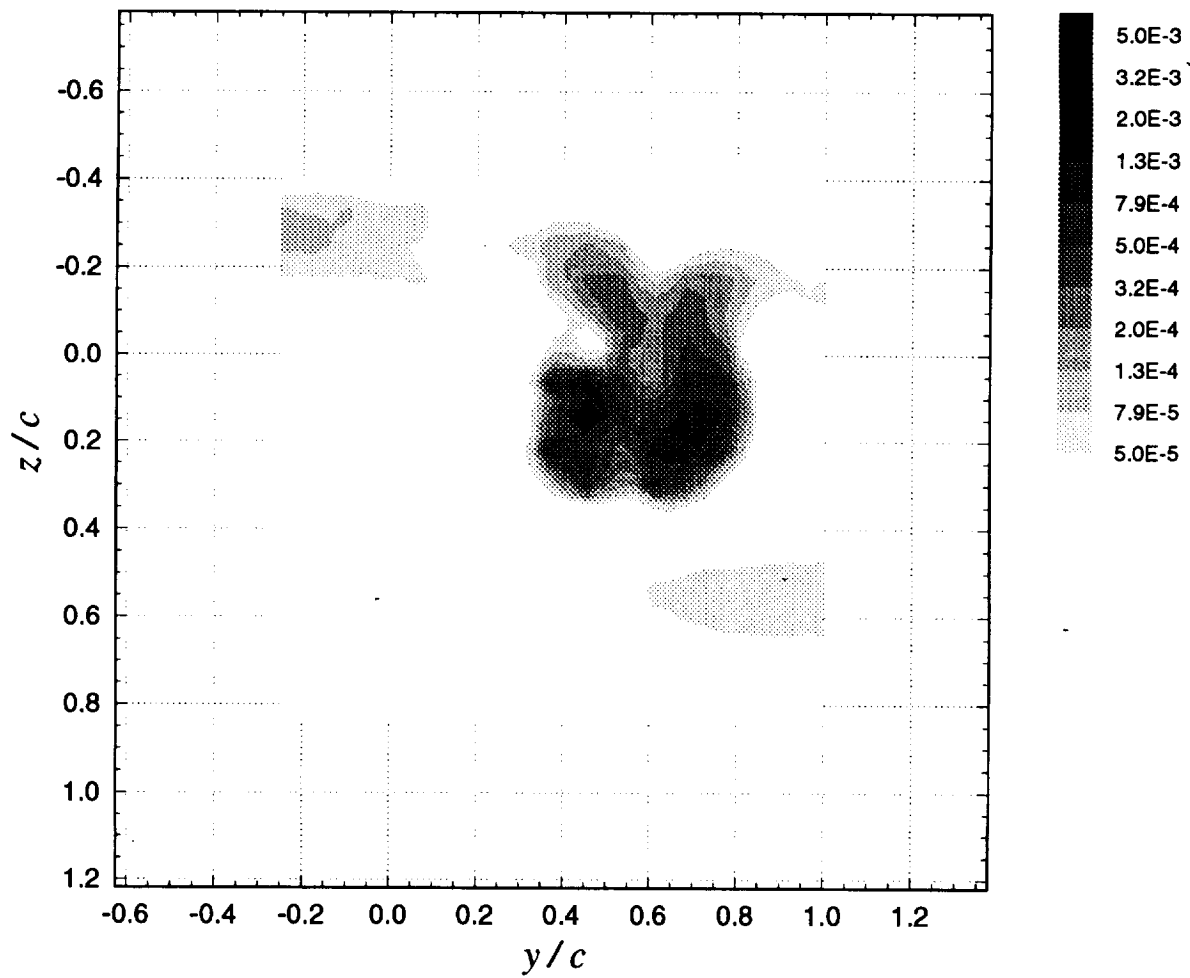


**Figure 3.18h** Contours of axial shear stress magnitude  $(\tau_a / U_{ref}^2)$  for pressure side passage of  $\Delta/c = -0.125$ :  $x/c = 20$ ,  $\alpha_1 = 5^\circ$ ,  $\alpha_2 = 5^\circ$ , no spoiler

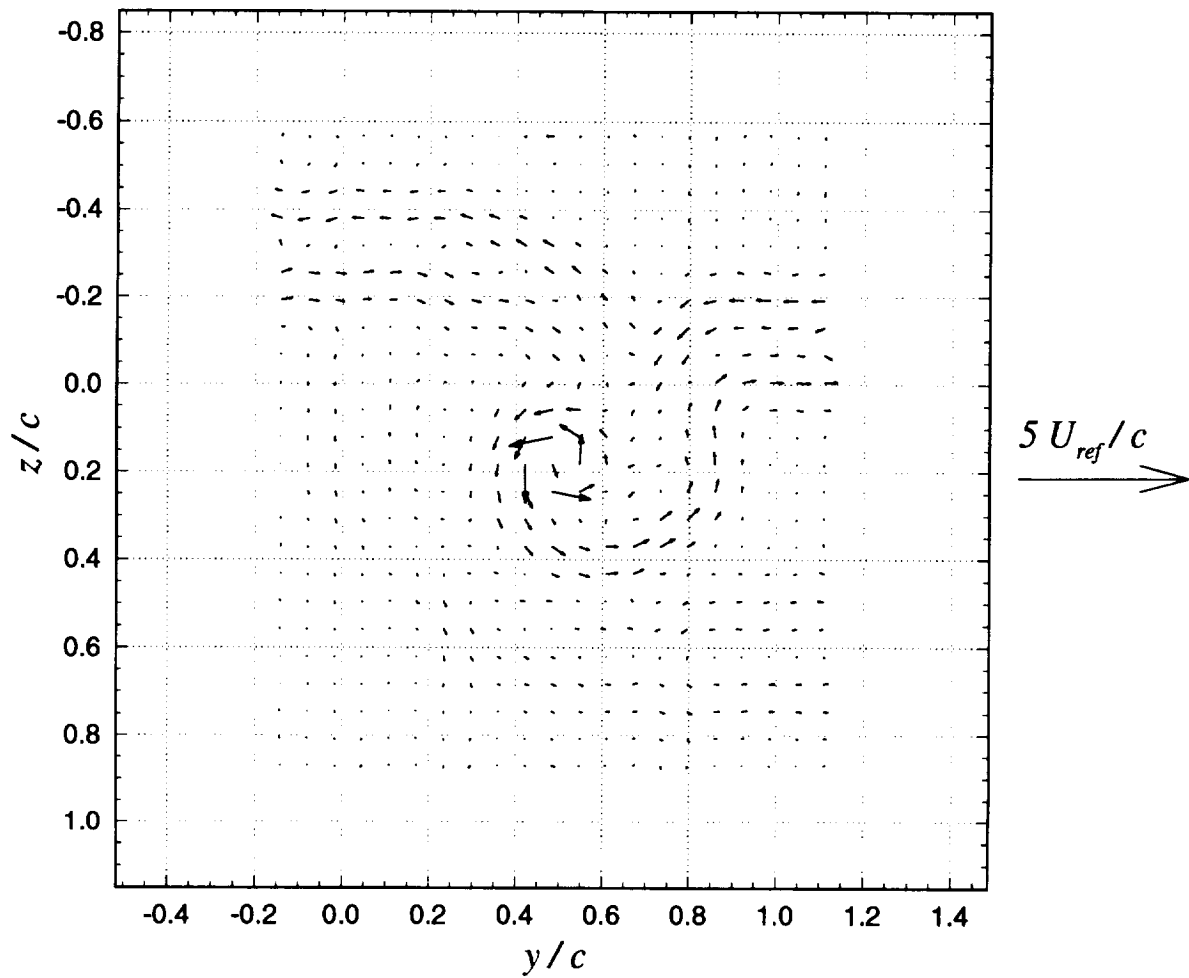


**Figure 3.19a** Mean cross-flow vorticity vectors ( $\Omega_y \cdot c / U_{ref}$ ,  $\Omega_z \cdot c / U_{ref}$ ) for pressure side passage of  $\Delta / c = -0.125$ :  $x / c = 22.5$ ,  $\alpha_1 = 5^\circ$ ,  $\alpha_2 = 5^\circ$ , no spoiler

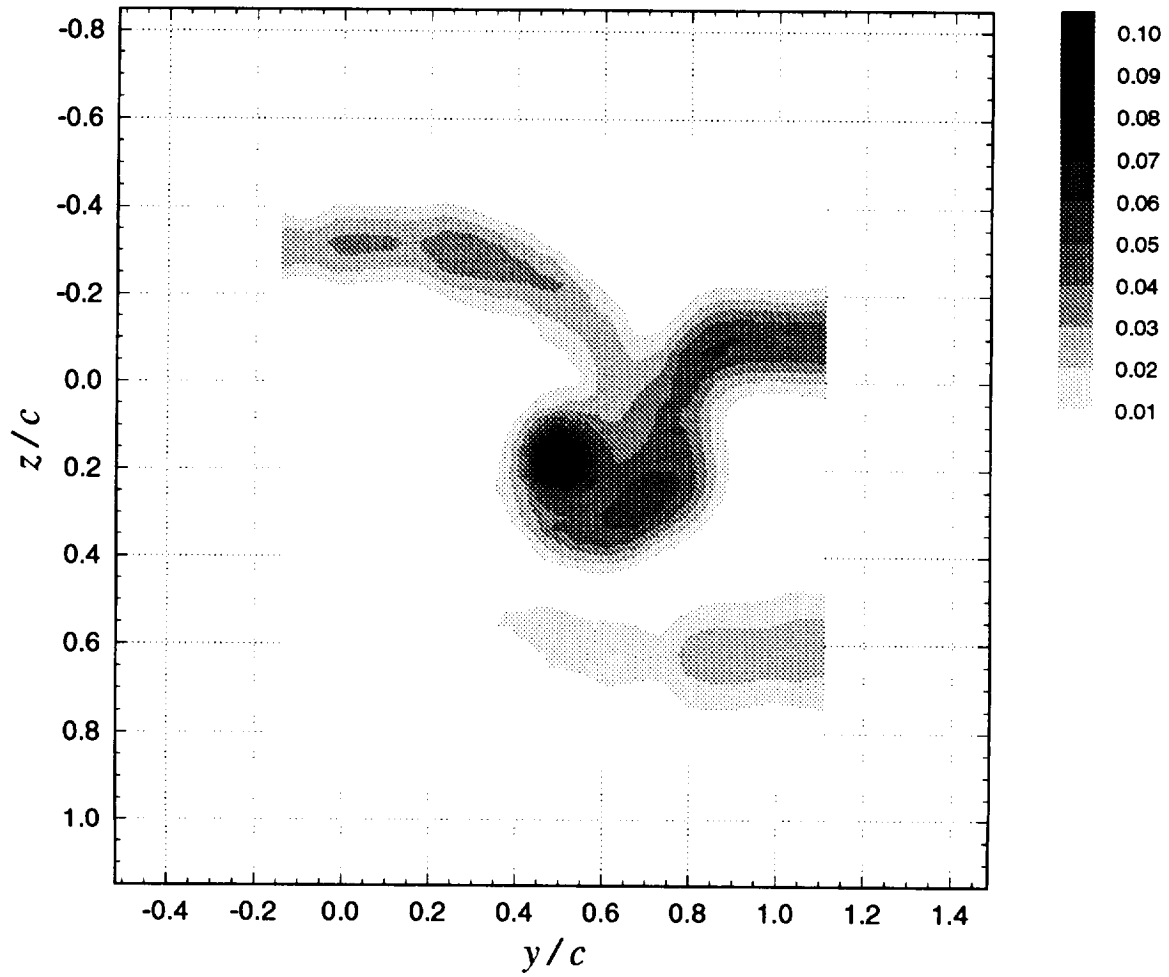


**Figure 3.19b** Contours of mean axial velocity deficit  $((U_{ref} - U) / U_{ref})$  for pressure side passage of  $\Delta/c = -0.125$ :  $x/c = 22.5$ ,  $\alpha_l = 5^\circ$ ,  $\alpha_2 = 5^\circ$ , no spoiler

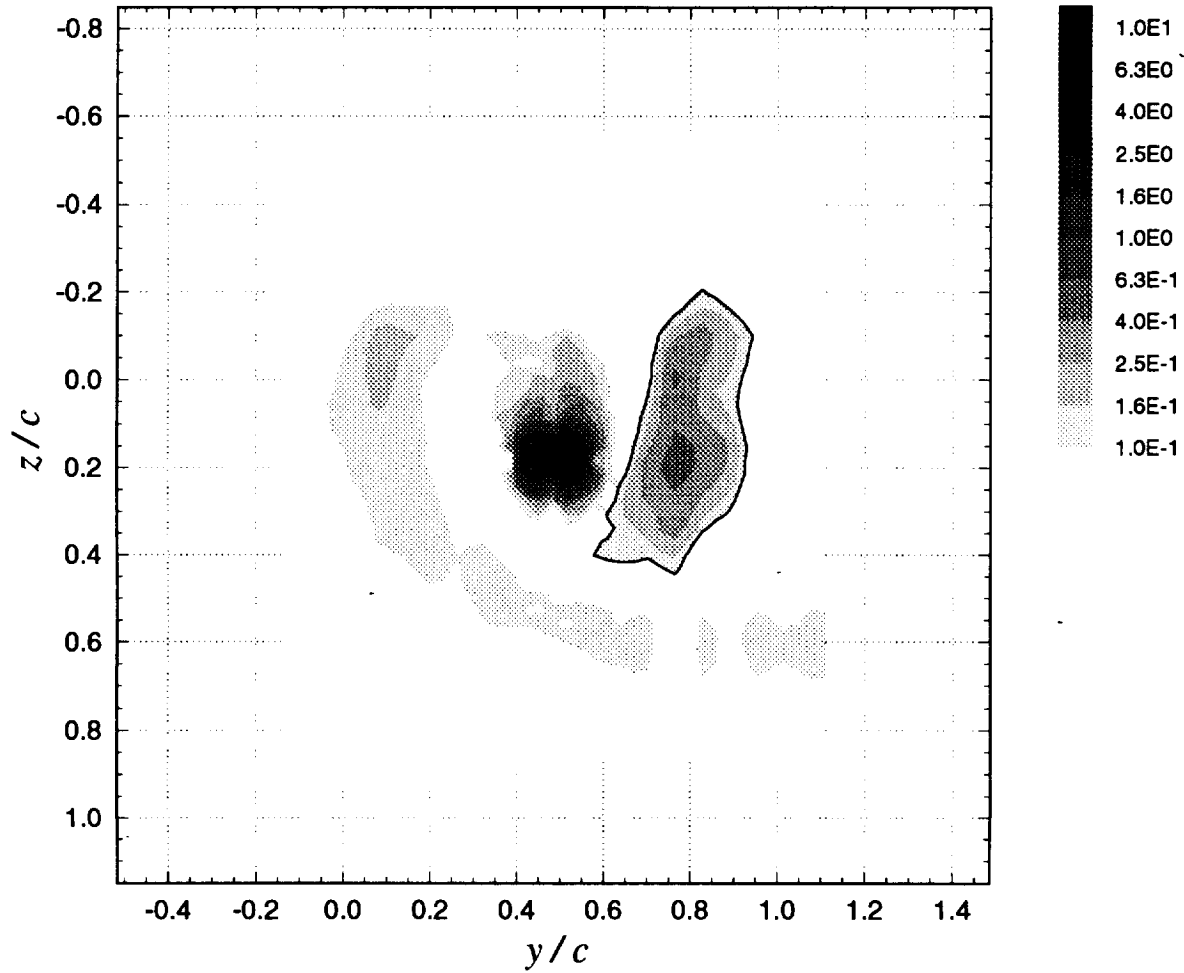


**Figure 3.19c** Contours of mean axial vorticity ( $\Omega_x \cdot c / U_{ref}$ ) for pressure side passage of  $\Delta/c = -0.125$ :  $x/c = 22.5$ ,  $\alpha_1 = 5^\circ$ ,  $\alpha_2 = 5^\circ$ , no spoiler. Legend lists  $|\Omega_x \cdot c / U_{ref}|$  values. Negative values of  $\Omega_x \cdot c / U_{ref}$  are contained within the solid contour lines.

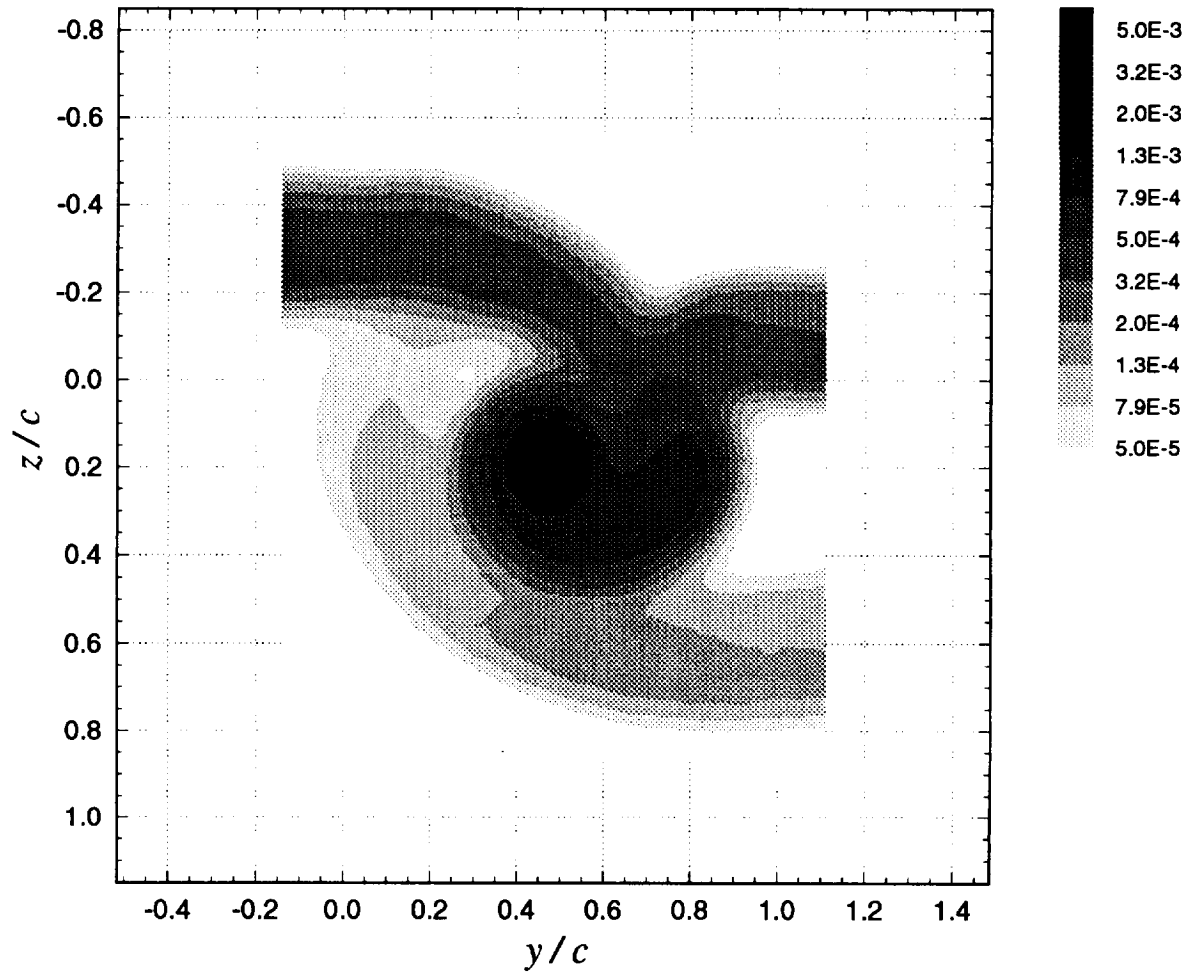


**Figure 3.19d** Contours of axial normal turbulent stress ( $\overline{u^2} / U_{ref}^2$ ) for pressure side passage of  $\Delta/c = -0.125$ :  $x/c = 22.5$ ,  $\alpha_1 = 5^\circ$ ,  $\alpha_2 = 5^\circ$ , no spoiler



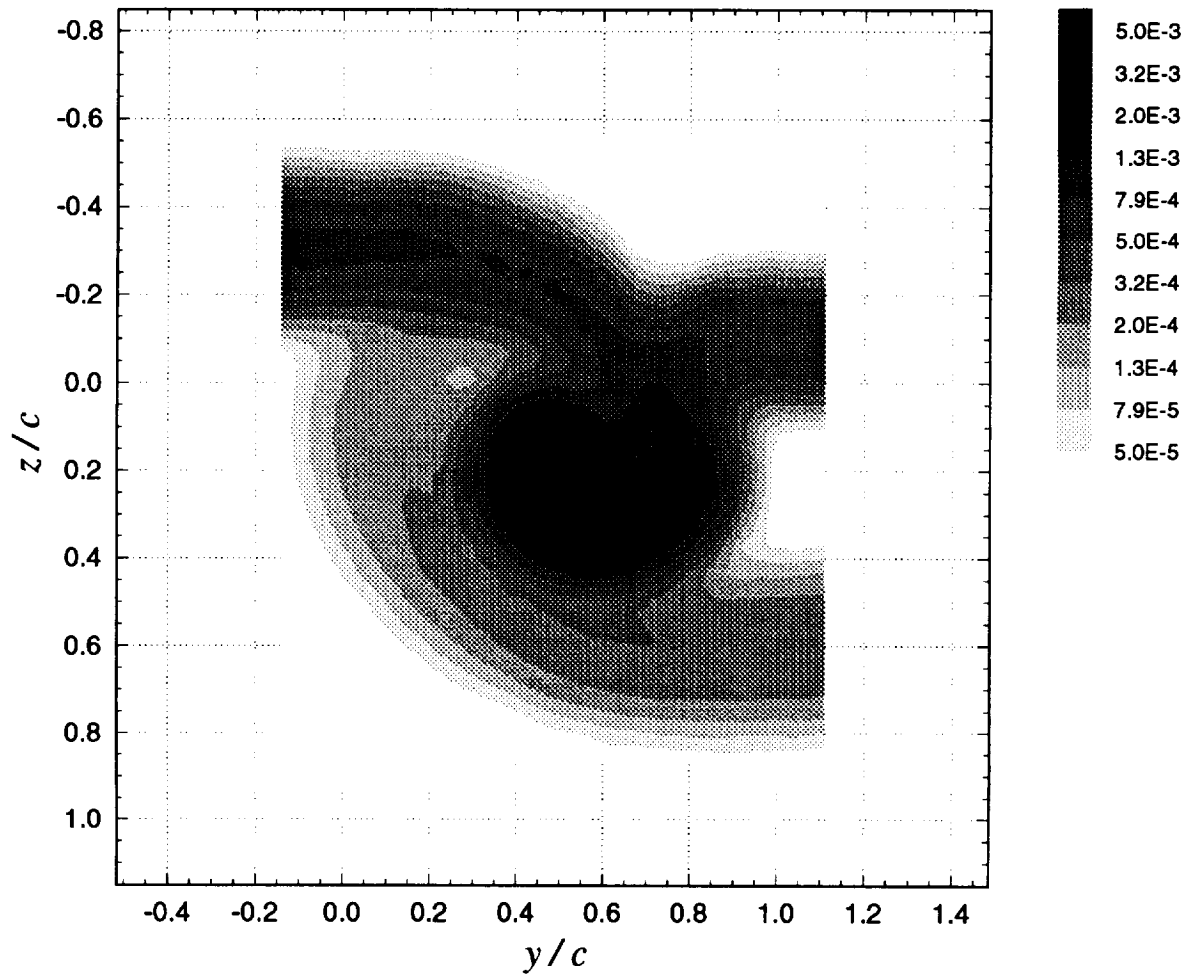


**Figure 3.19e** Contours of summed cross-flow normal turbulent stresses  $(\overline{v^2} + \overline{w^2}) / U_{ref}^2$  for pressure side passage of  $\Delta/c = -0.125$ :  $x/c = 22.5$ ,  $\alpha_1 = 5^\circ$ ,  $\alpha_2 = 5^\circ$ , no spoiler

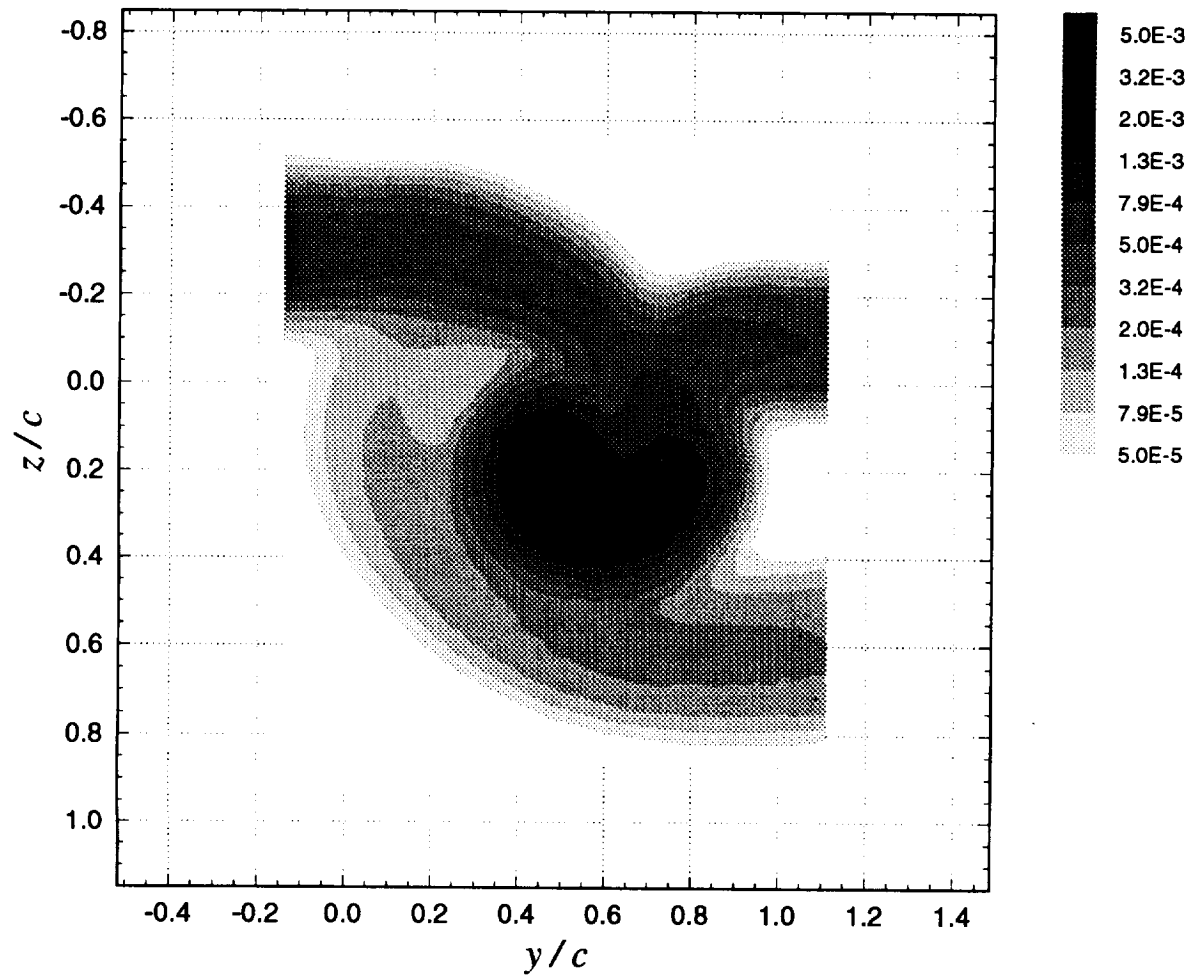


**Figure 3.19f** Contours of turbulent kinetic energy ( $k / U_{ref}^2$ ):  $x / c = 22.5$ ,  $\alpha_l = 5^\circ$ , no spoiler

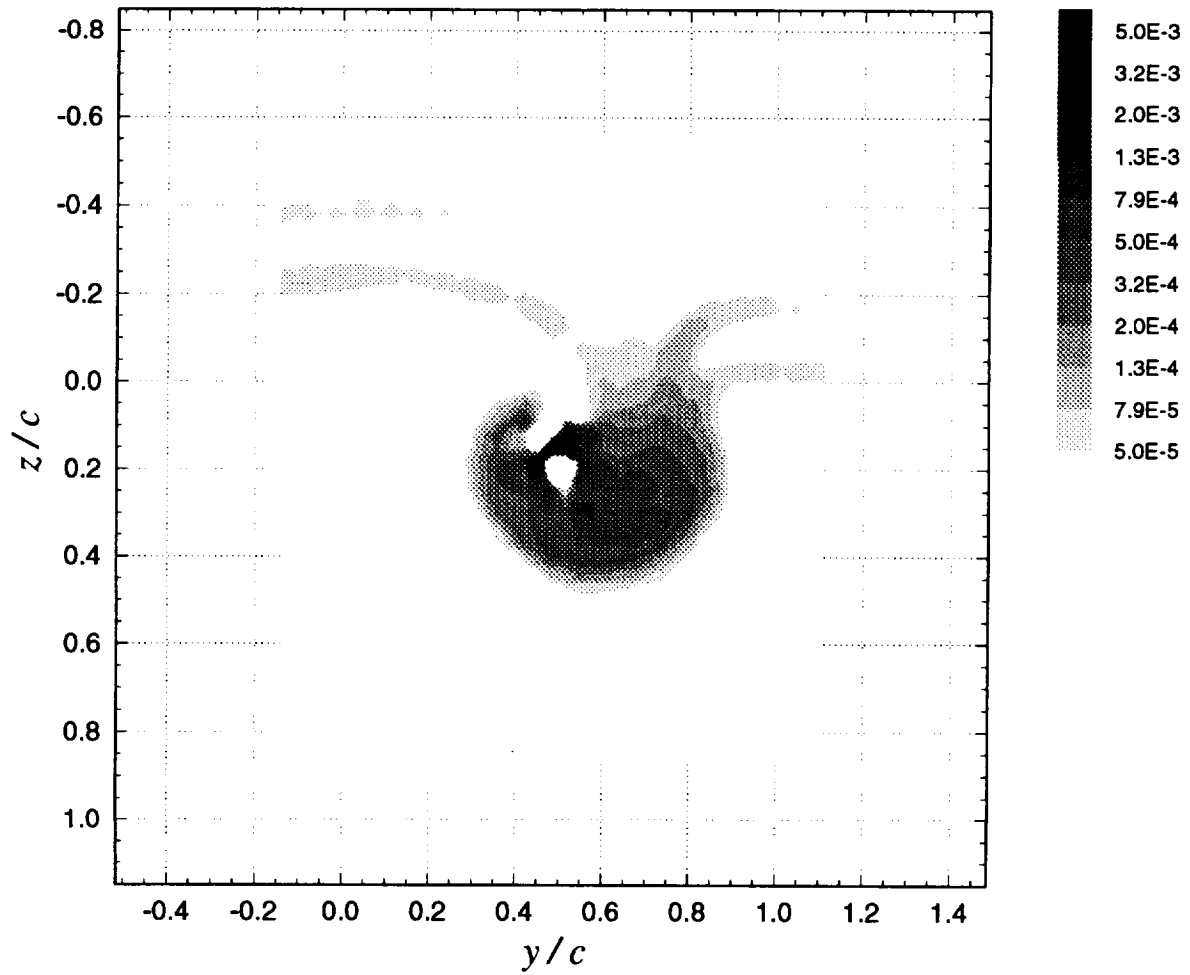


**Figure 3.19g** Contours of turbulent kinetic energy production ( $P \cdot c / U_{ref}^3$ ) for pressure side passage of  $\Delta/c = -0.125$ :  $x/c = 22.5$ ,  $\alpha_1 = 5^\circ$ ,  $\alpha_2 = 5^\circ$ , no spoiler

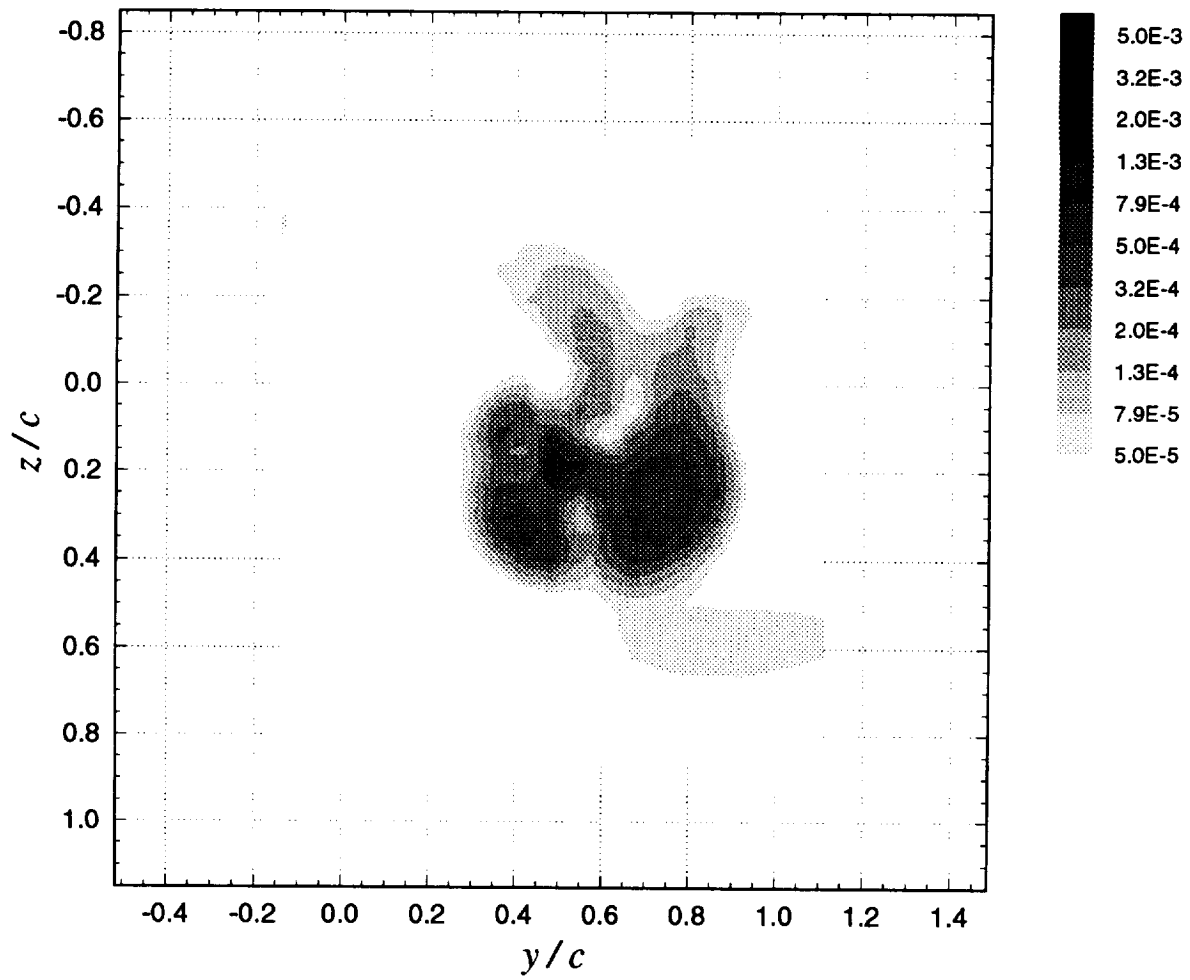


**Figure 3.19h** Contours of axial shear stress magnitude  $(\tau_a / U_{ref})$  for pressure side passage of  $\Delta/c = -0.125$ :  $x/c = 22.5$ ,  $\alpha_1 = 5^\circ$ ,  $\alpha_2 = 5^\circ$ , no spoiler

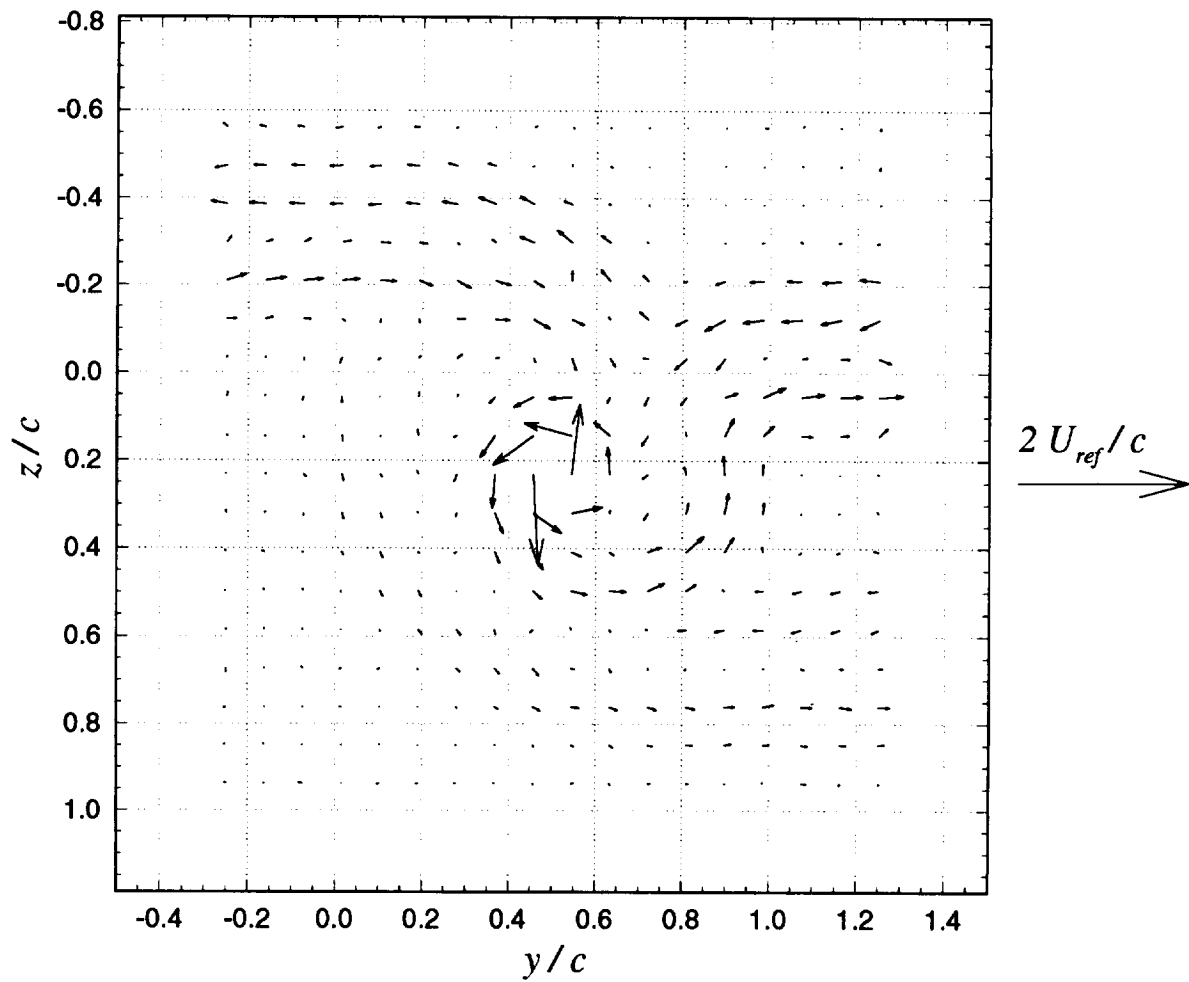


**Figure 3.20a** Mean cross-flow vorticity vectors ( $\Omega_y \cdot c / U_{ref}$ ,  $\Omega_z \cdot c / U_{ref}$ ) for pressure side passage of  $\Delta / c = -0.125$ :  $x / c = 25$ ,  $\alpha_1 = 5^\circ$ ,  $\alpha_2 = 5^\circ$ , no spoiler

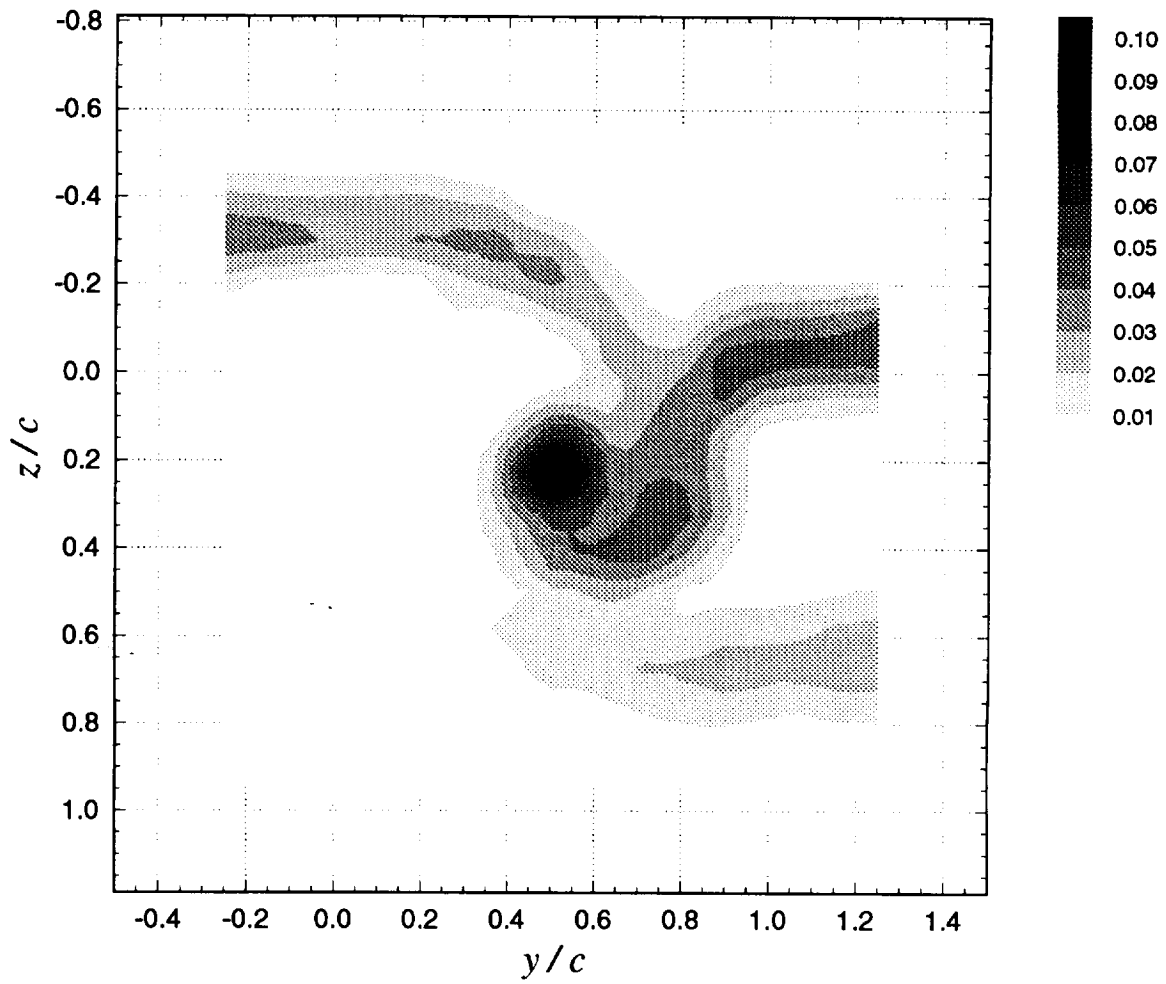


**Figure 3.20b** Contours of mean axial velocity deficit  $((U_{ref} - U) / U_{ref})$  for pressure side passage of  $\Delta/c = -0.125$ :  $x/c = 25$ ,  $\alpha_1 = 5^\circ$ ,  $\alpha_2 = 5^\circ$ , no spoiler

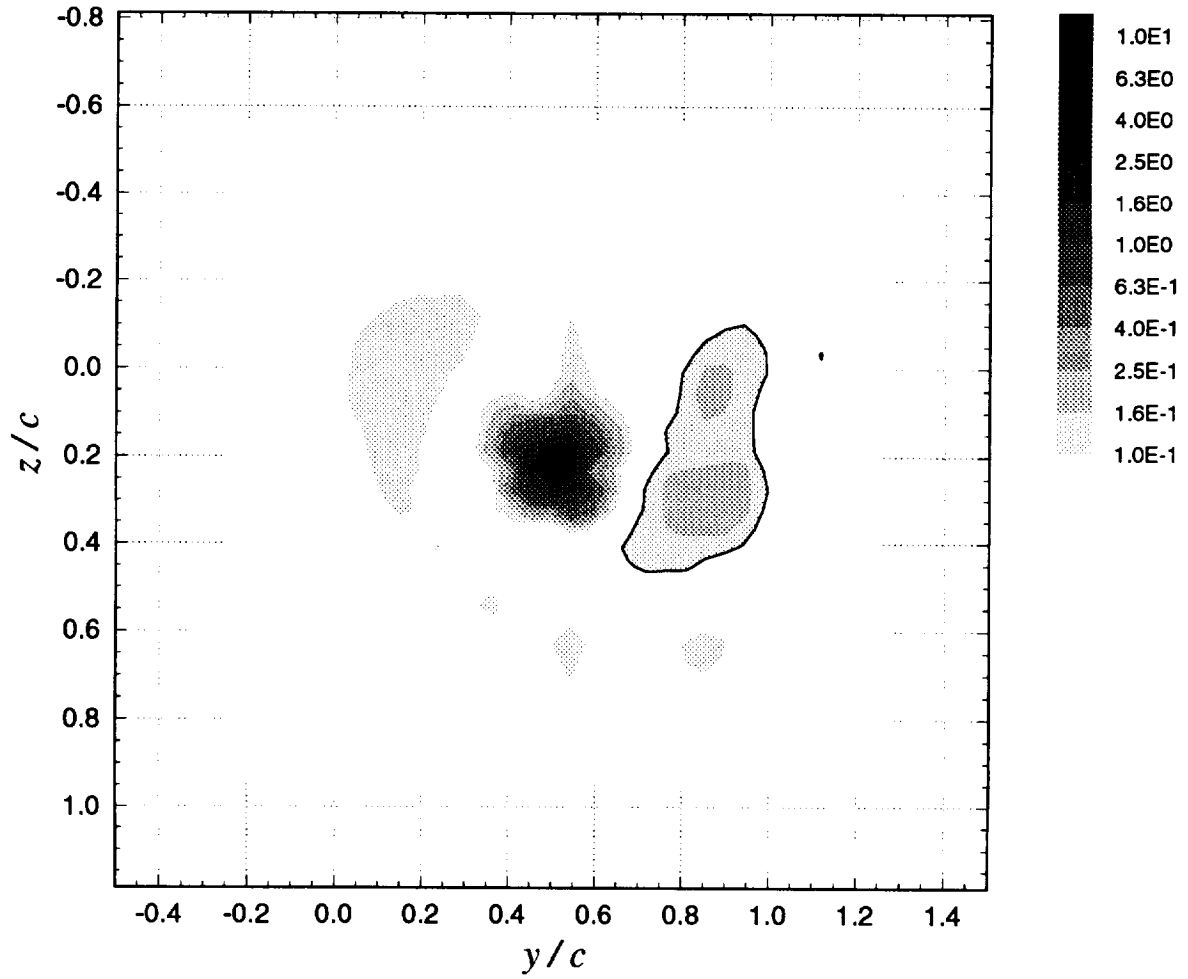


**Figure 3.20c** Contours of mean axial vorticity ( $\Omega_x \cdot c / U_{ref}$ ) for pressure side passage of  $\Delta/c = -0.125$ :  $x/c = 25$ ,  $\alpha_1 = 5^\circ$ ,  $\alpha_2 = 5^\circ$ , no spoiler. Legend lists  $|\Omega_x \cdot c / U_{ref}|$  values. Negative values of  $\Omega_x \cdot c / U_{ref}$  are contained within the solid contour lines.

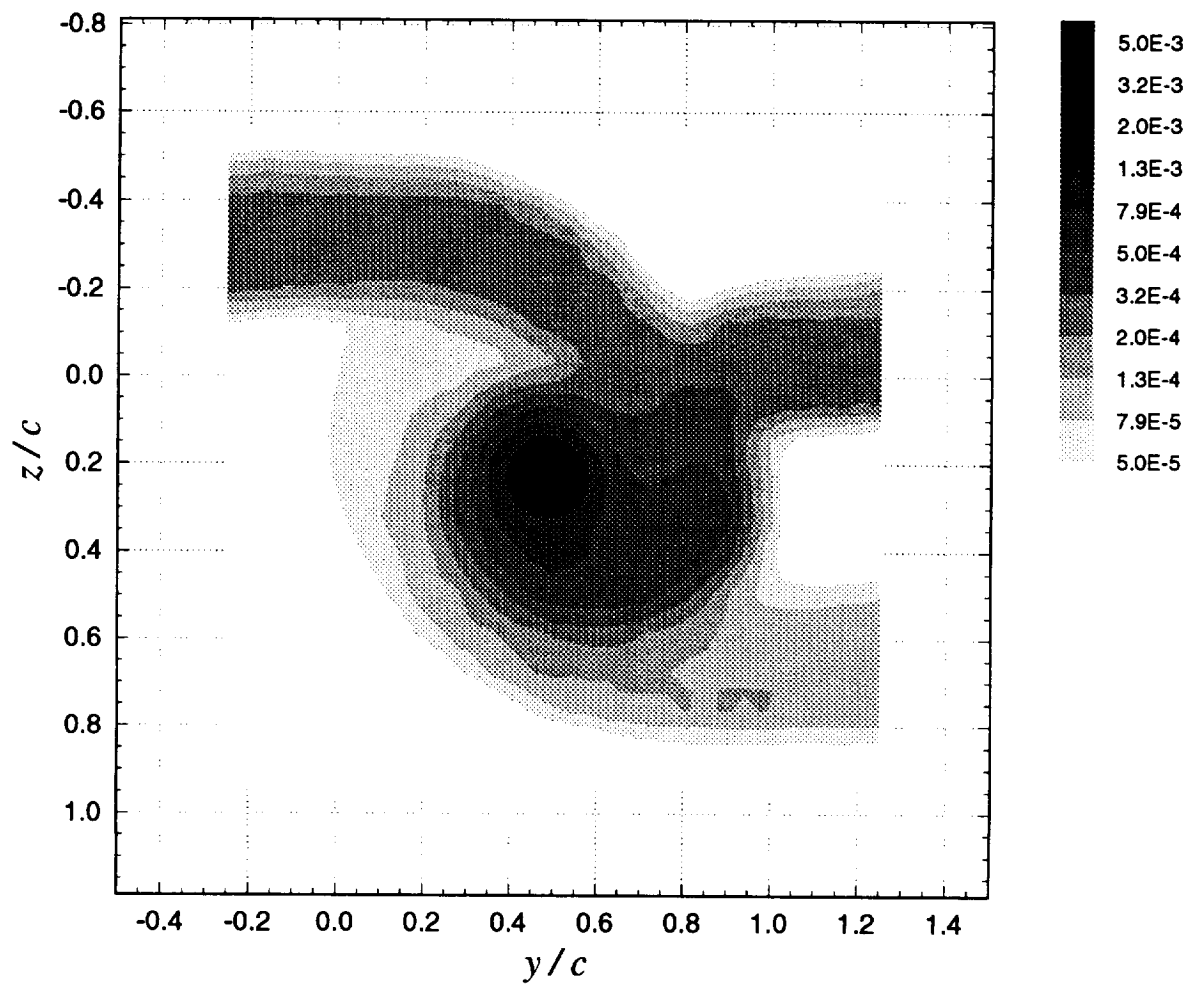


**Figure 3.20d** Contours of axial normal turbulent stress ( $\overline{u^2} / U_{ref}^2$ ) for pressure side passage of  $\Delta/c = -0.125$ :  $x/c = 25$ ,  $\alpha_1 = 5^\circ$ ,  $\alpha_2 = 5^\circ$ , no spoiler



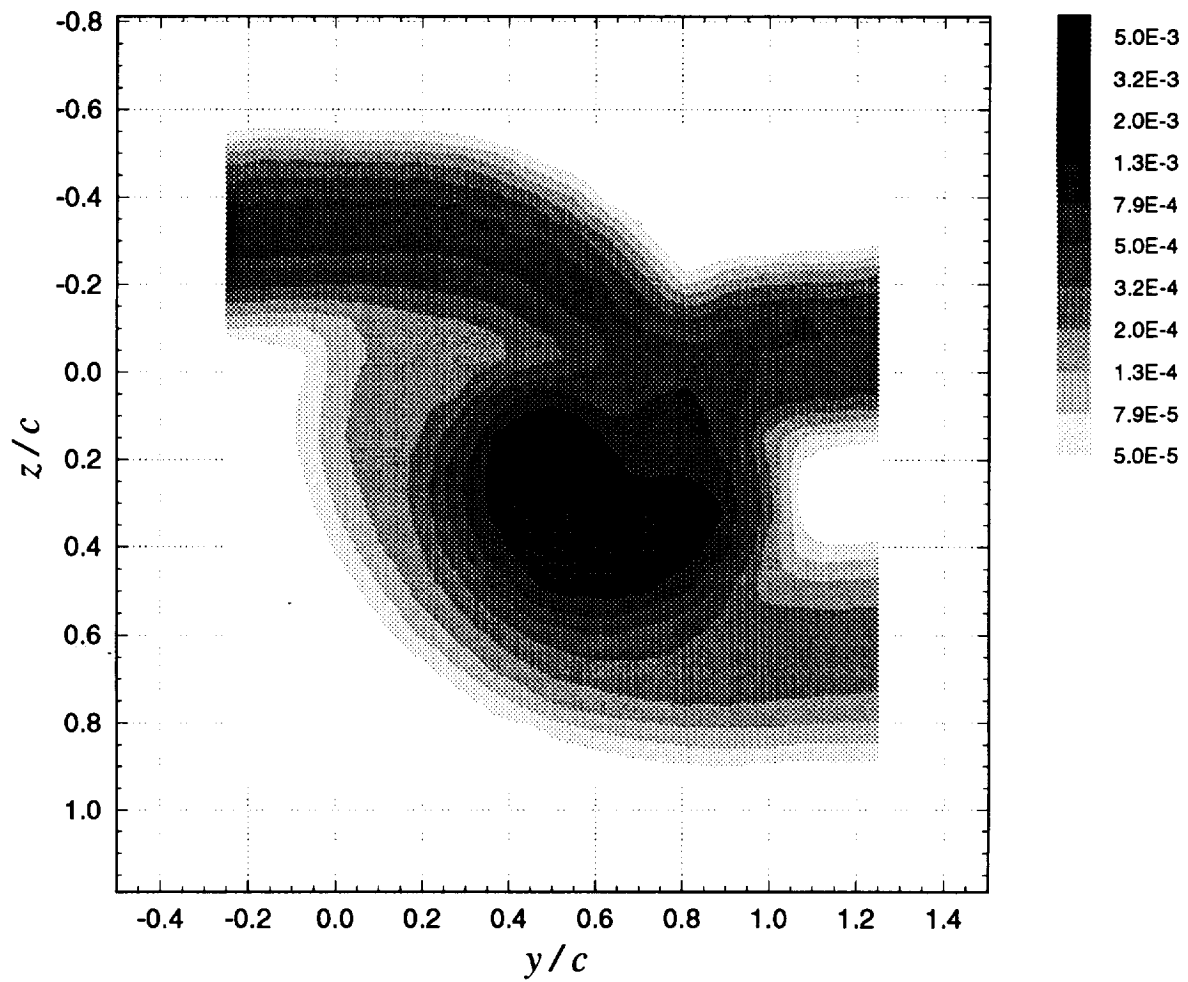


**Figure 3.20e** Contours of summed cross-flow normal turbulent stresses  $(\overline{v^2} + \overline{w^2}) / U_{ref}^2$  for pressure side passage of  $\Delta/c = -0.125$ :  $x/c = 25$ ,  $\alpha_1 = 5^\circ$ ,  $\alpha_2 = 5^\circ$ , no spoiler

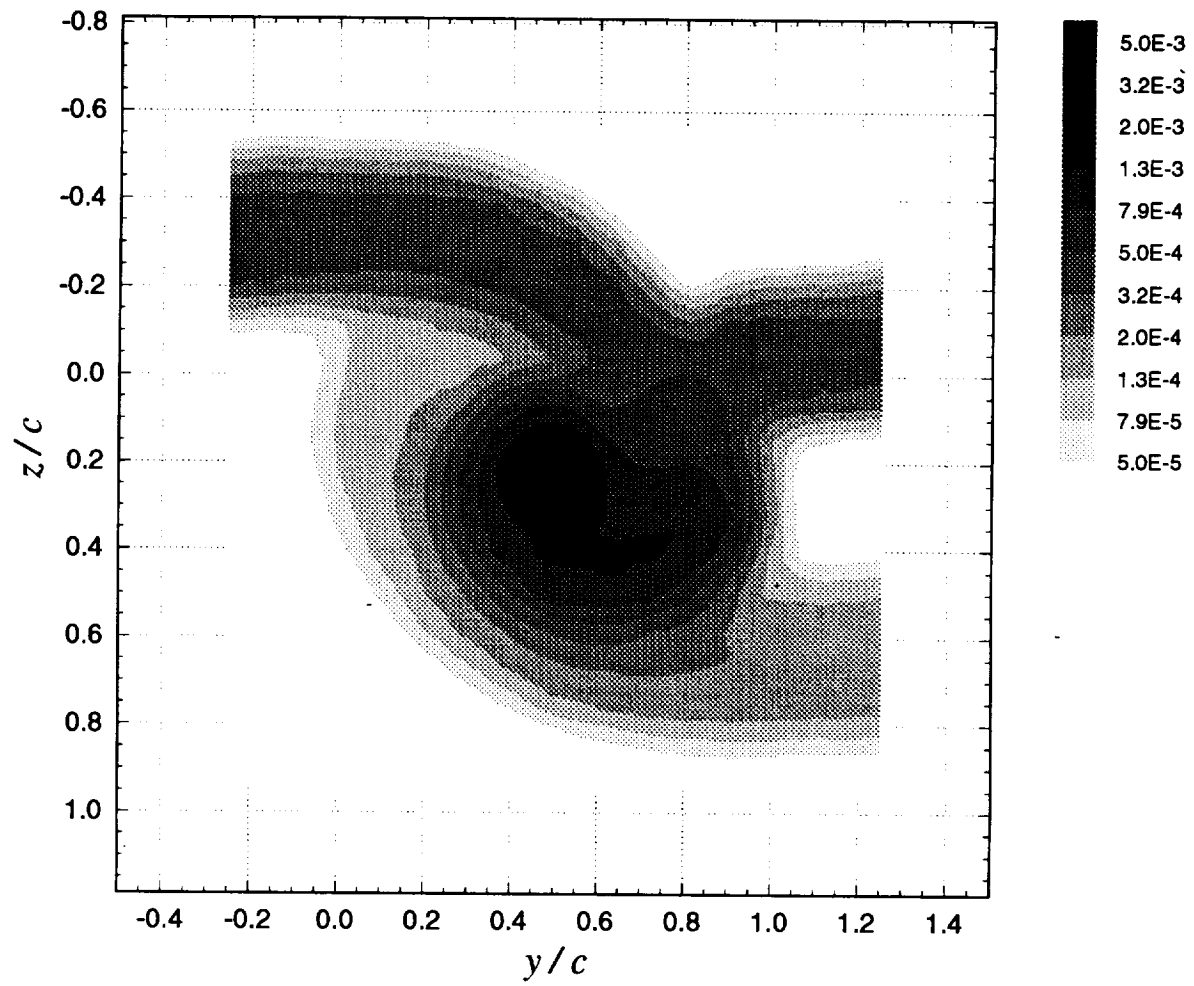


**Figure 3.20f** Contours of turbulent kinetic energy ( $k / U_{ref}^2$ ):  $x / c = 25$ ,  $\alpha_l = 5^\circ$ , no spoiler

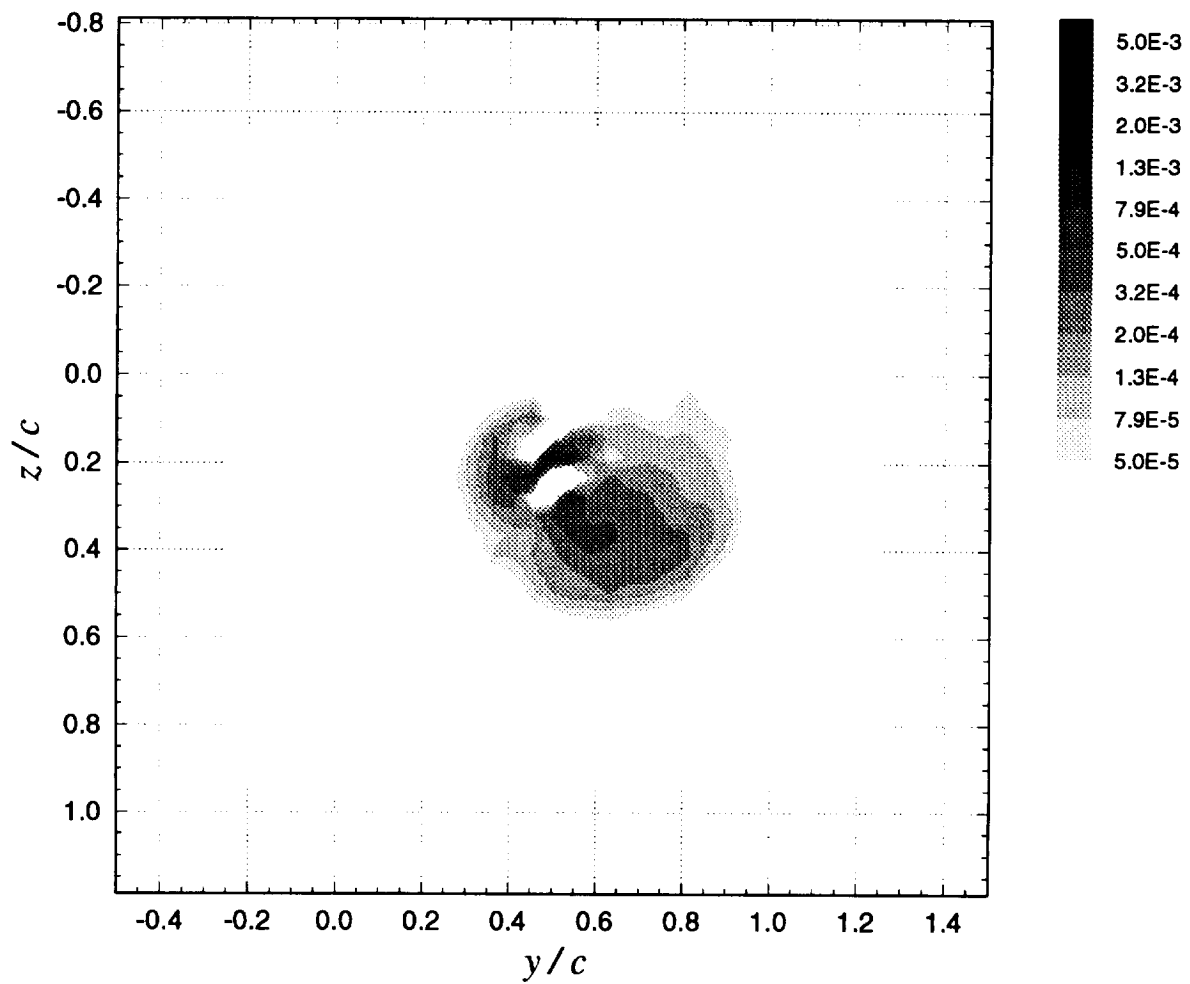


**Figure 3.20g** Contours of turbulent kinetic energy production ( $P \cdot c / U_{ref}^3$ ) for pressure side passage of  $\Delta/c = -0.125$ :  $x/c = 25$ ,  $\alpha_1 = 5^\circ$ ,  $\alpha_2 = 5^\circ$ , no spoiler

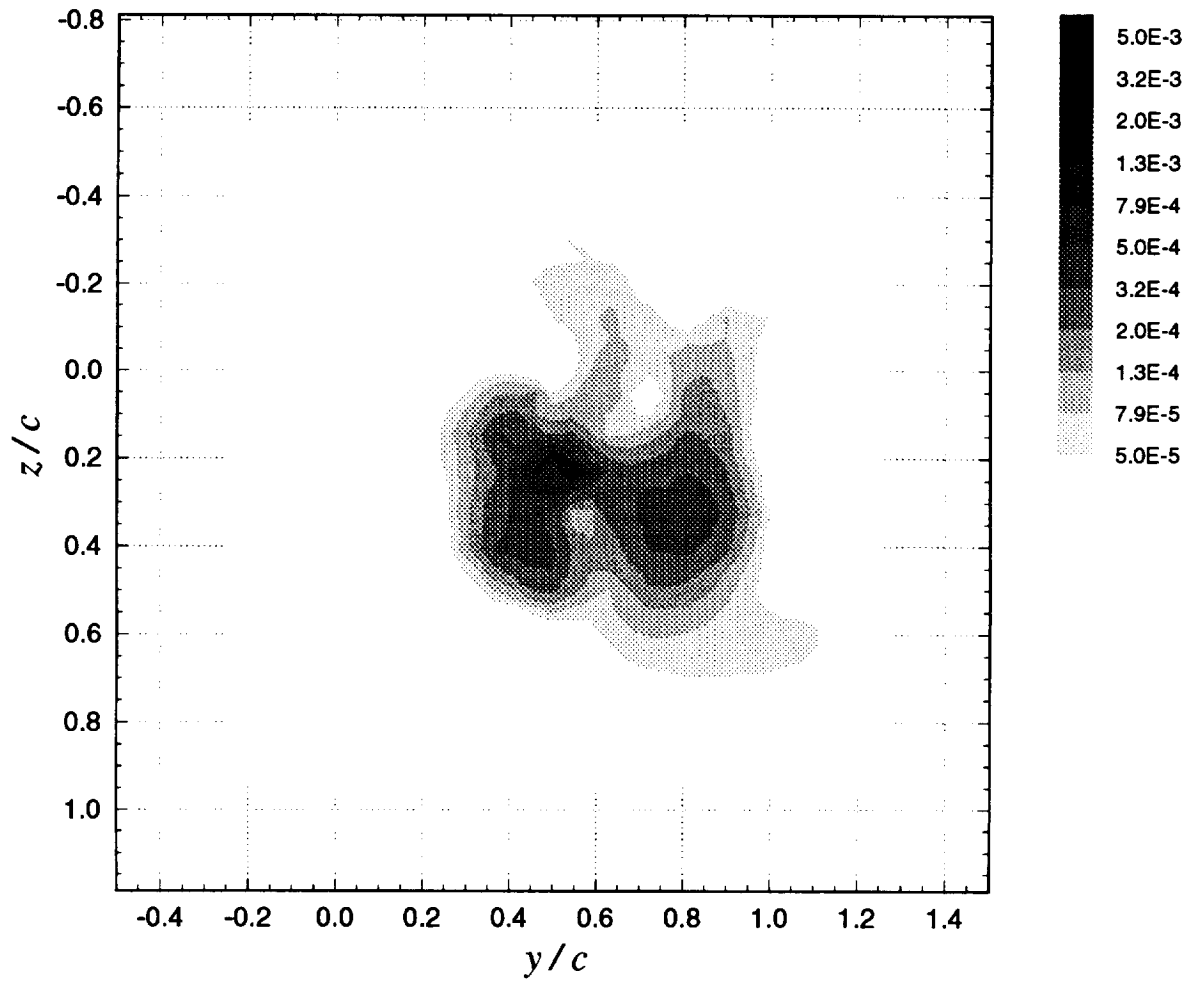


**Figure 3.20h** Contours of axial shear stress magnitude ( $\tau_a / U_{ref}^2$ ) for pressure side passage of  $\Delta/c = -0.125$ :  $x/c = 25$ ,  $\alpha_1 = 5^\circ$ ,  $\alpha_2 = 5^\circ$ , no spoiler

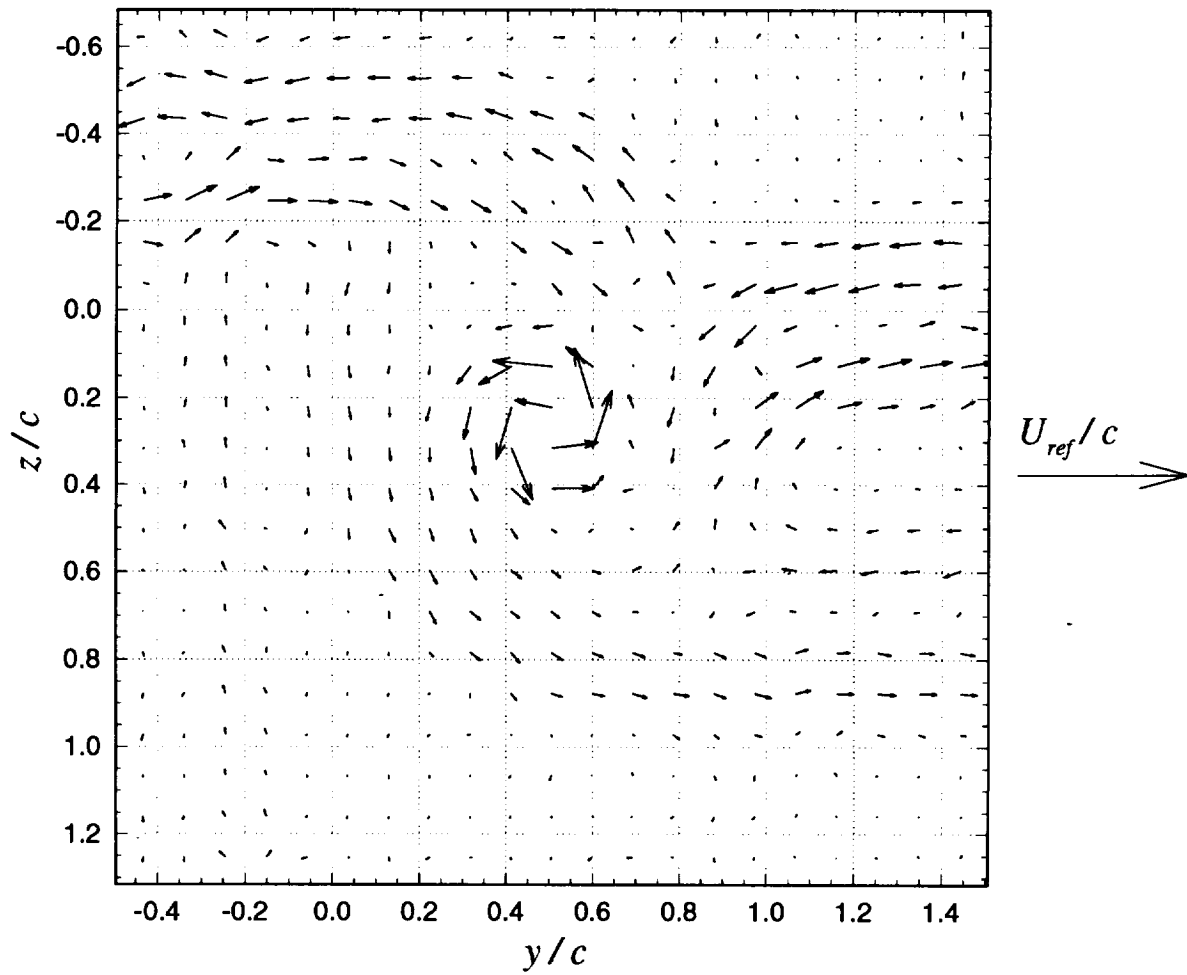


**Figure 3.21a** Mean cross-flow vorticity vectors ( $\Omega_y \cdot c / U_{ref}$ ,  $\Omega_z \cdot c / U_{ref}$ ) for pressure side passage of  $\Delta/c = -0.125$ :  $x/c = 30$ ,  $\alpha_1 = 5^\circ$ ,  $\alpha_2 = 5^\circ$ , no spoiler

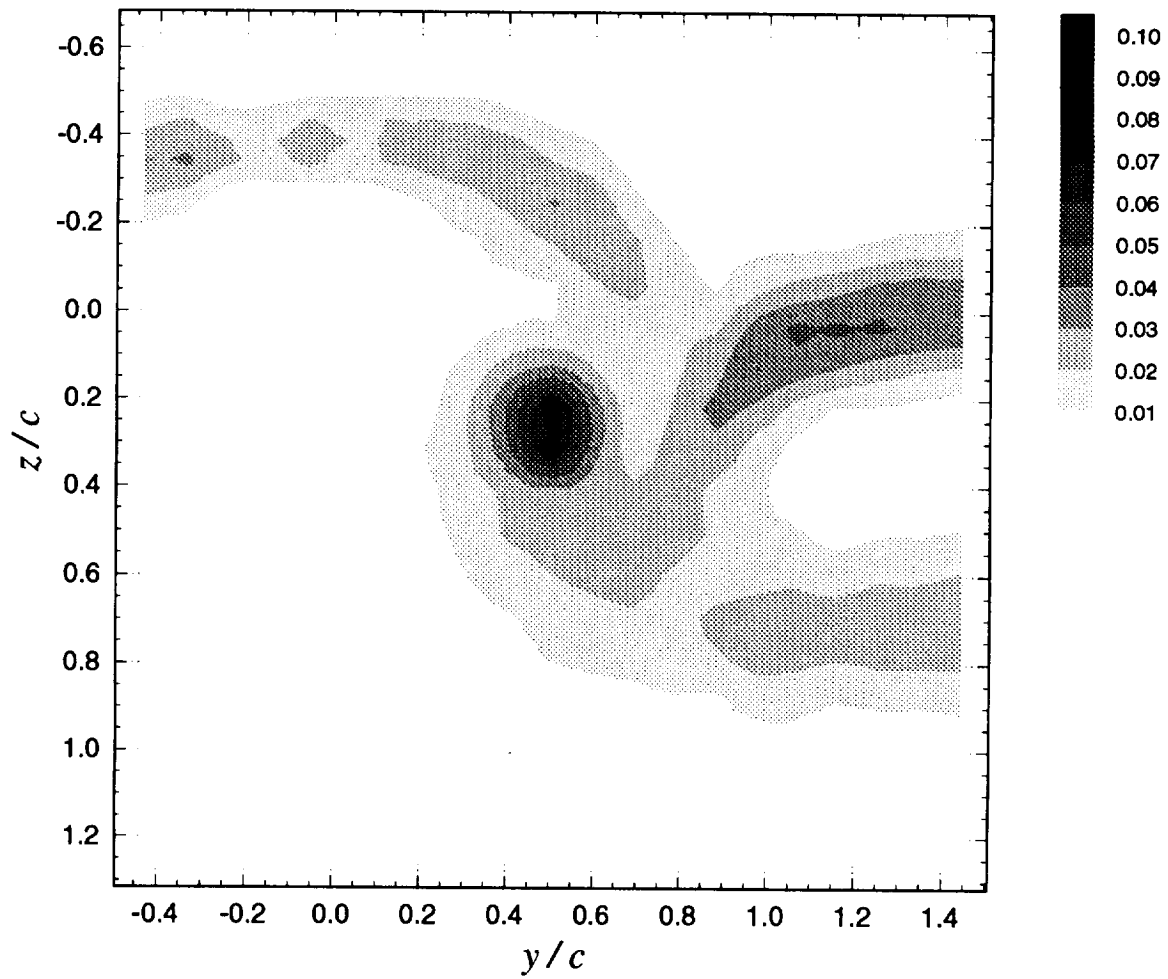


**Figure 3.21b** Contours of mean axial velocity deficit  $((U_{ref} - U) / U_{ref})$  for pressure side passage of  $\Delta/c = -0.125$ :  $x/c = 30$ ,  $\alpha_1 = 5^\circ$ ,  $\alpha_2 = 5^\circ$ , no spoiler

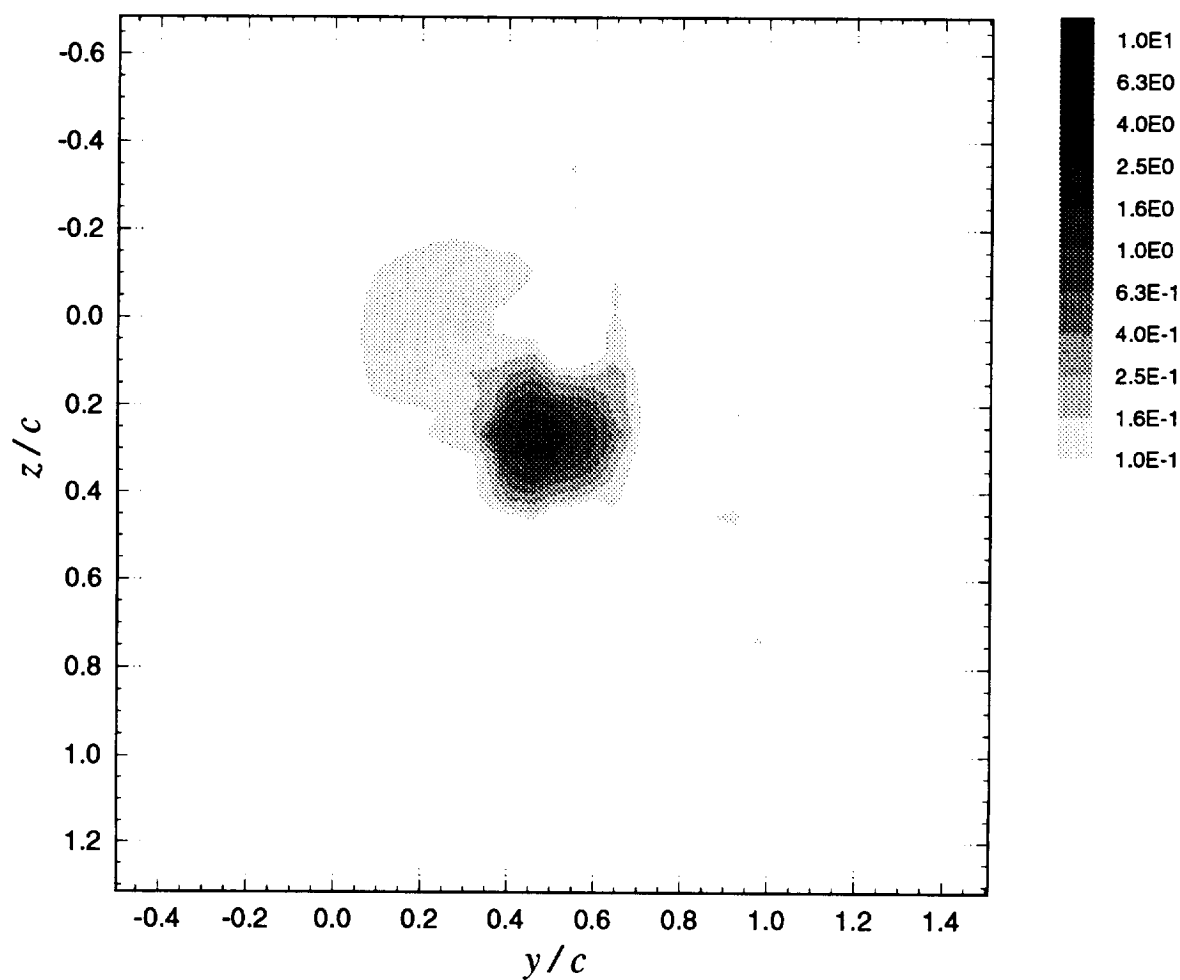


**Figure 3.21c** Contours of mean axial vorticity ( $\Omega_x \cdot c / U_{ref}$ ) for pressure side passage of  $\Delta/c = -0.125$ :  $x/c = 30$ ,  $\alpha_1 = 5^\circ$ ,  $\alpha_2 = 5^\circ$ , no spoiler

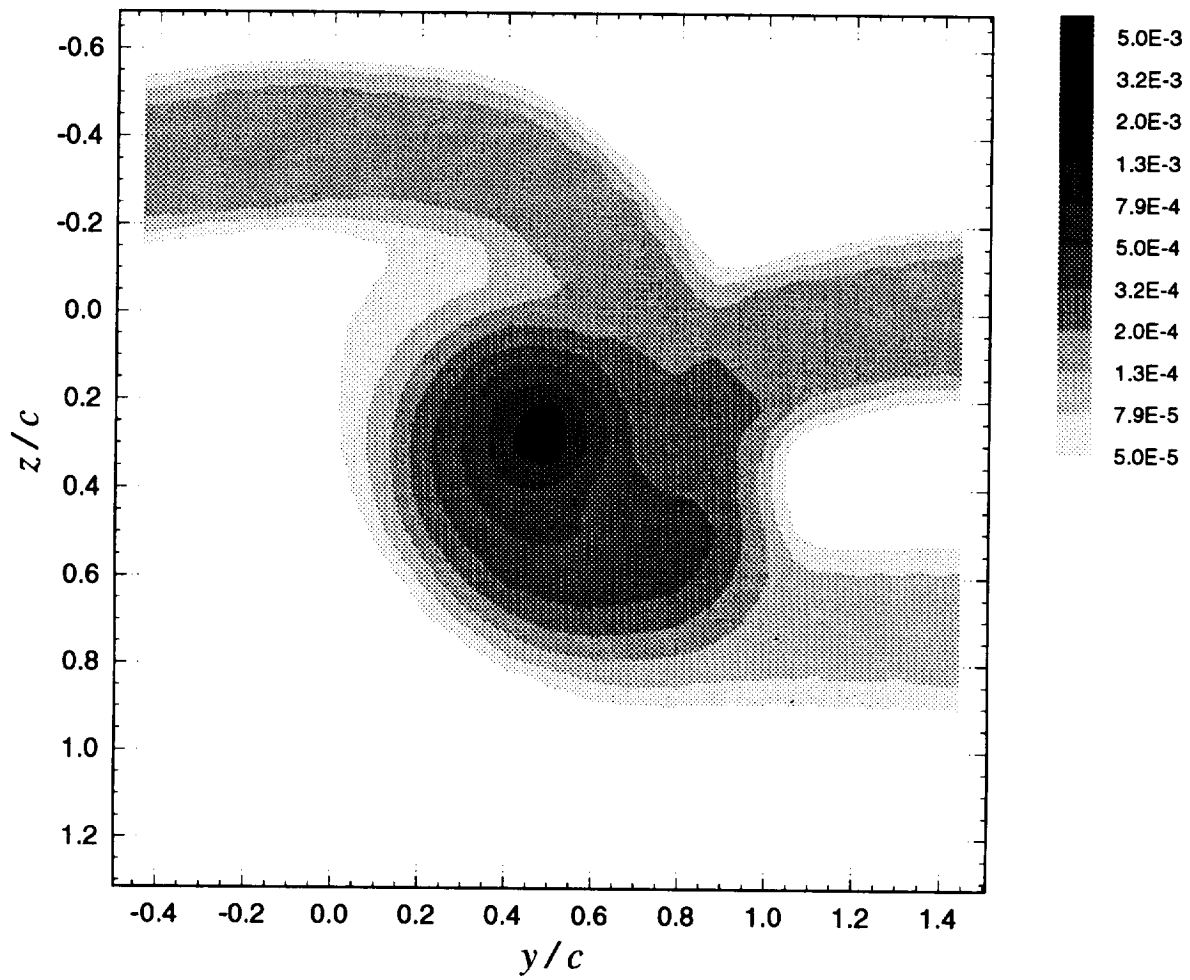


**Figure 3.21d** Contours of axial normal turbulent stress ( $\overline{u^2} / U_{ref}^2$ ) for pressure side passage of  $\Delta/c = -0.125$ :  $x/c = 30$ ,  $\alpha_1 = 5^\circ$ ,  $\alpha_2 = 5^\circ$ , no spoiler



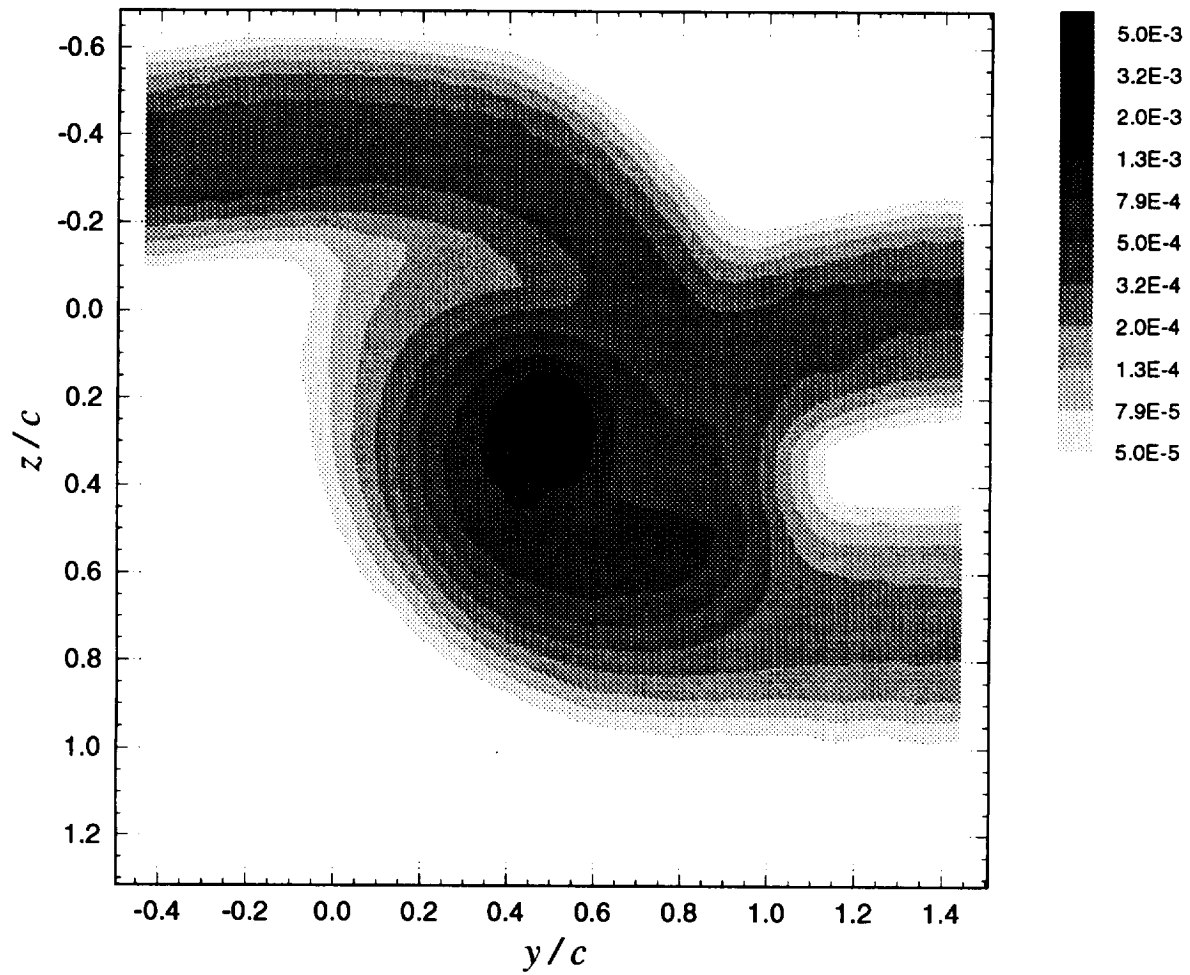


**Figure 3.21e** Contours of summed cross-flow normal turbulent stresses  $(\overline{v^2} + \overline{w^2}) / U_{ref}^2$  for pressure side passage of  $\Delta/c = -0.125$ :  $x/c = 30$ ,  $\alpha_1 = 5^\circ$ ,  $\alpha_2 = 5^\circ$ , no spoiler

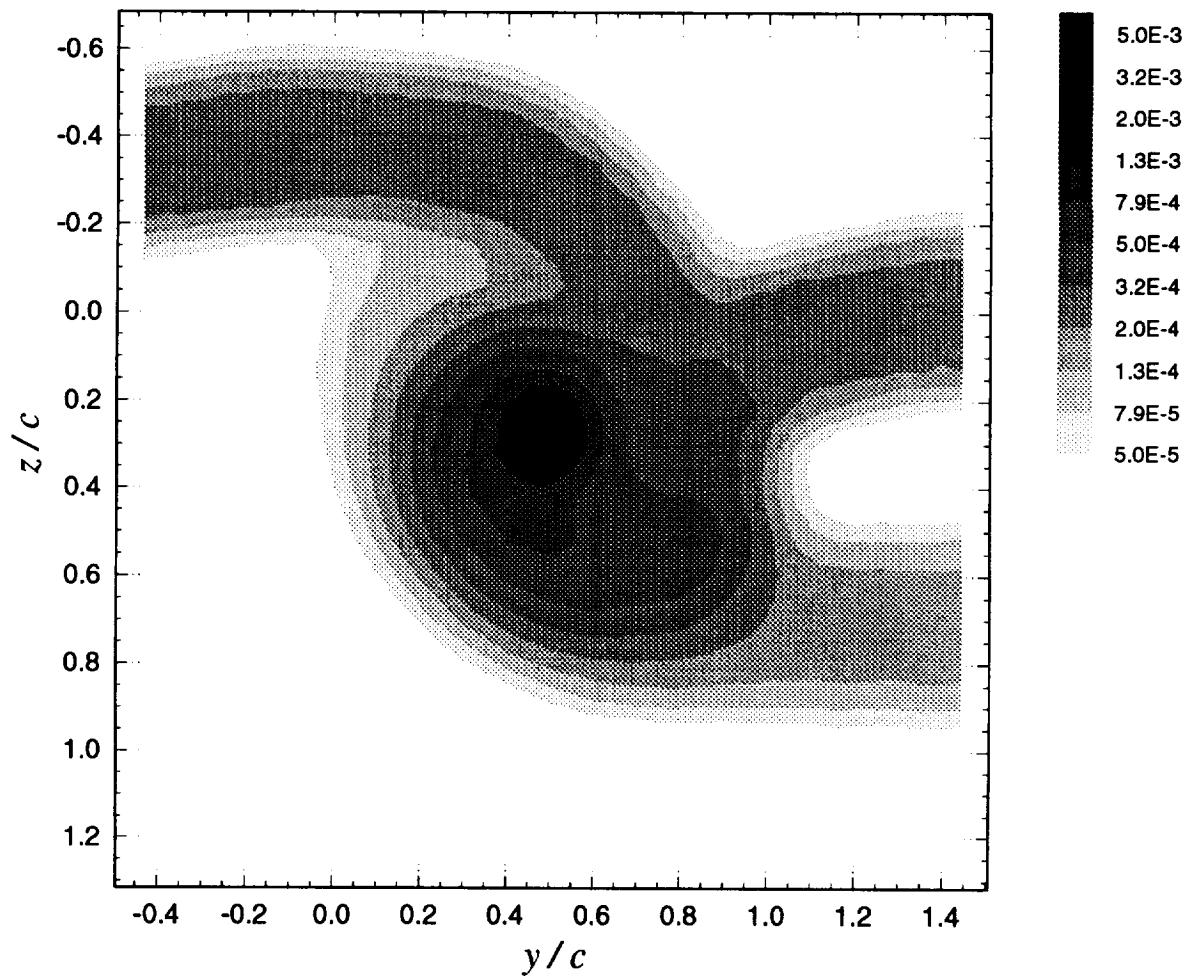


**Figure 3.21f** Contours of turbulent kinetic energy ( $k / U_{ref}^2$ ) for pressure side passage of  $\Delta / c = -0.125$ :  $x / c = 30$ ,  $\alpha_1 = 5^\circ$ ,  $\alpha_2 = 5^\circ$ , no spoiler

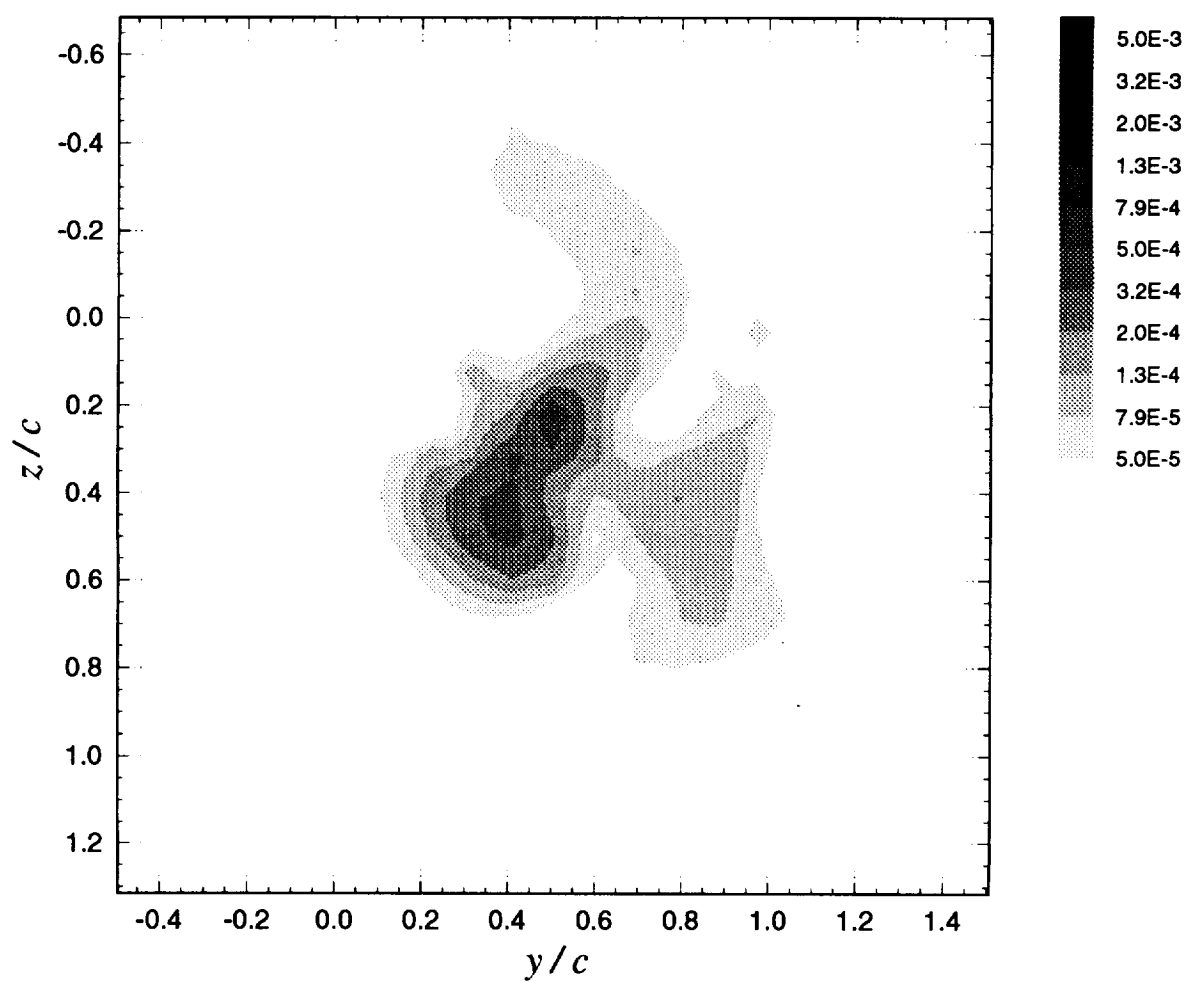


**Figure 3.21g** Contours of axial shear stress magnitude ( $\tau_a / U_{ref}^2$ ) for pressure side passage of  $\Delta/c = -0.125$ :  $x/c = 30$ ,  $\alpha_1 = 5^\circ$ ,  $\alpha_2 = 5^\circ$ , no spoiler

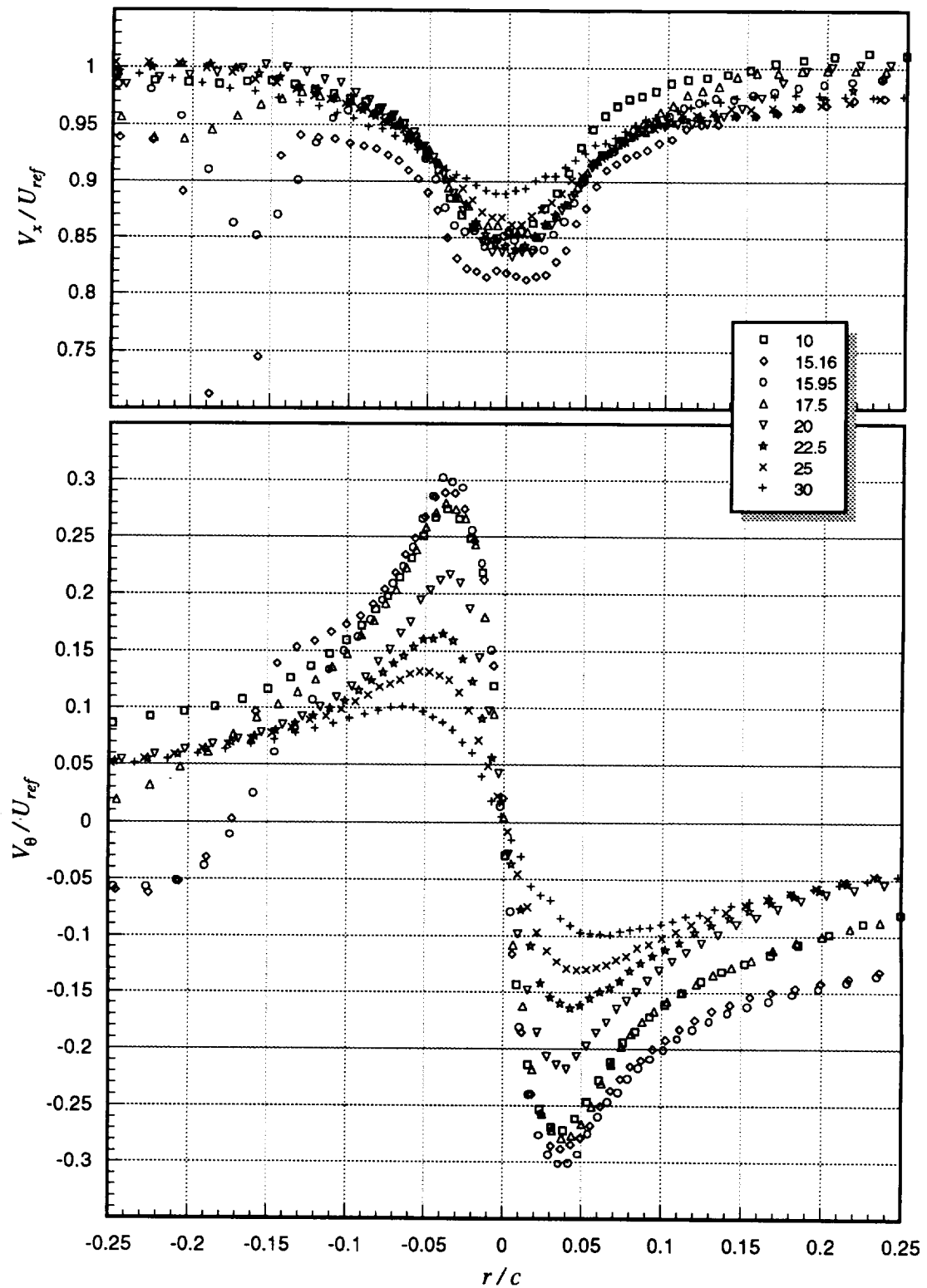


**Figure 3.22a** Mean axial ( $V_x$ ) and tangential ( $V_\theta$ ) velocities (measured along  $z$ -wise profiles through the vortex core center) as a function of downstream distance ( $x$ ) for pressure side passage of  $\Delta/c = -0.125$ :  $x/c = 30$ ,  $\alpha_1 = 5^\circ$ ,  $\alpha_2 = 5^\circ$ , no spoiler. Legend lists  $x/c$  values.

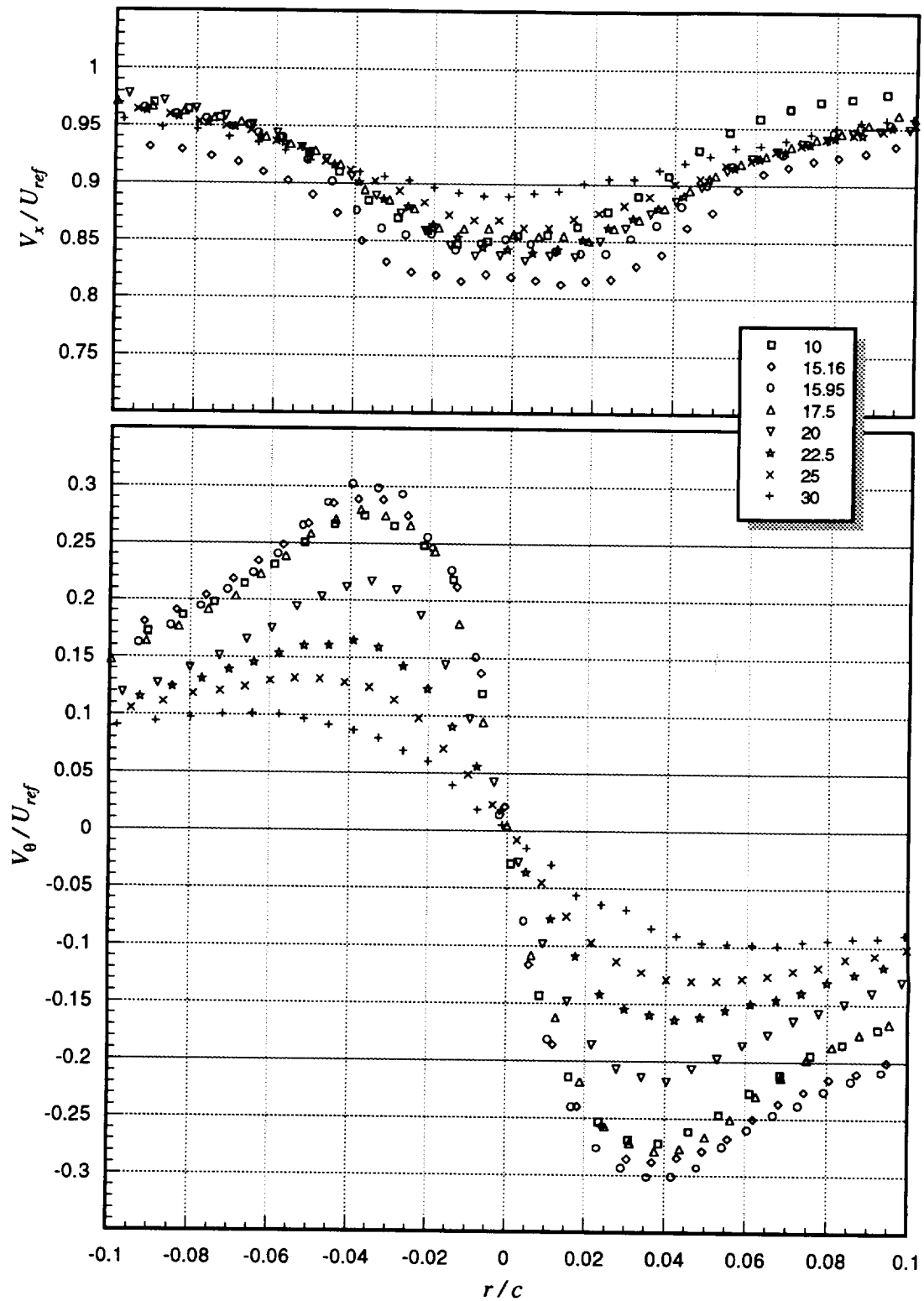


**Figure 3.22b** Mean axial ( $V_x$ ) and tangential ( $V_\theta$ ) velocities (measured along  $z$ -wise profiles through the vortex core center) as a function of downstream distance ( $x$ ) for pressure side passage of  $\Delta/c = -0.125$ :  $x/c = 30$ ,  $\alpha_1 = 5^\circ$ ,  $\alpha_2 = 5^\circ$ , no spoiler. Legend lists  $x/c$  values.

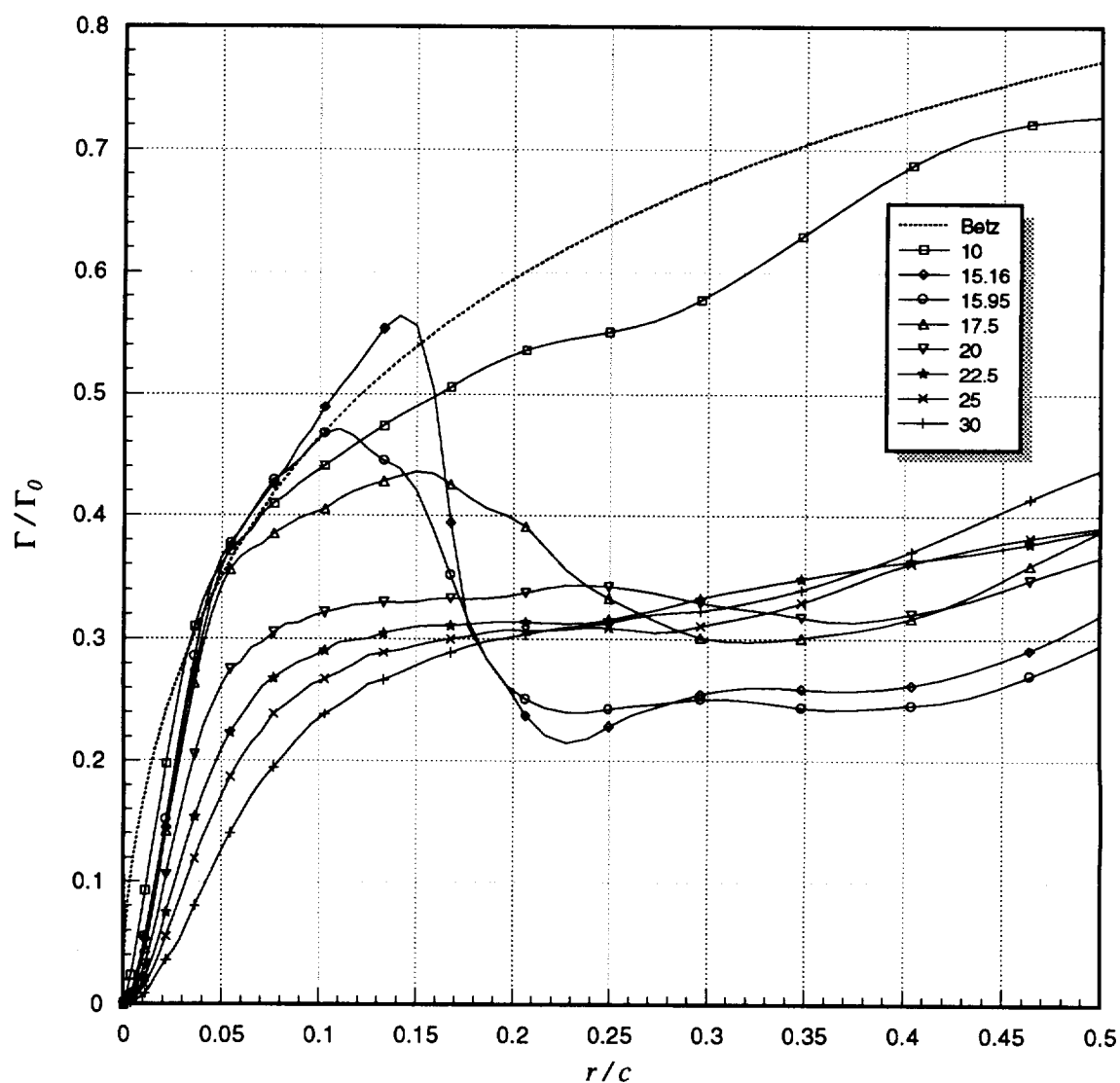


**Figure 3.23a** Circulation distributions (assuming axisymmetric flow) as a function of downstream distance ( $x$ ) for pressure side passage of  $\Delta/c = -0.125$ :  $x/c = 30$ ,  $\alpha_1 = 5^\circ$ ,  $\alpha_2 = 5^\circ$ , no spoiler. Legend lists  $x/c$  values.

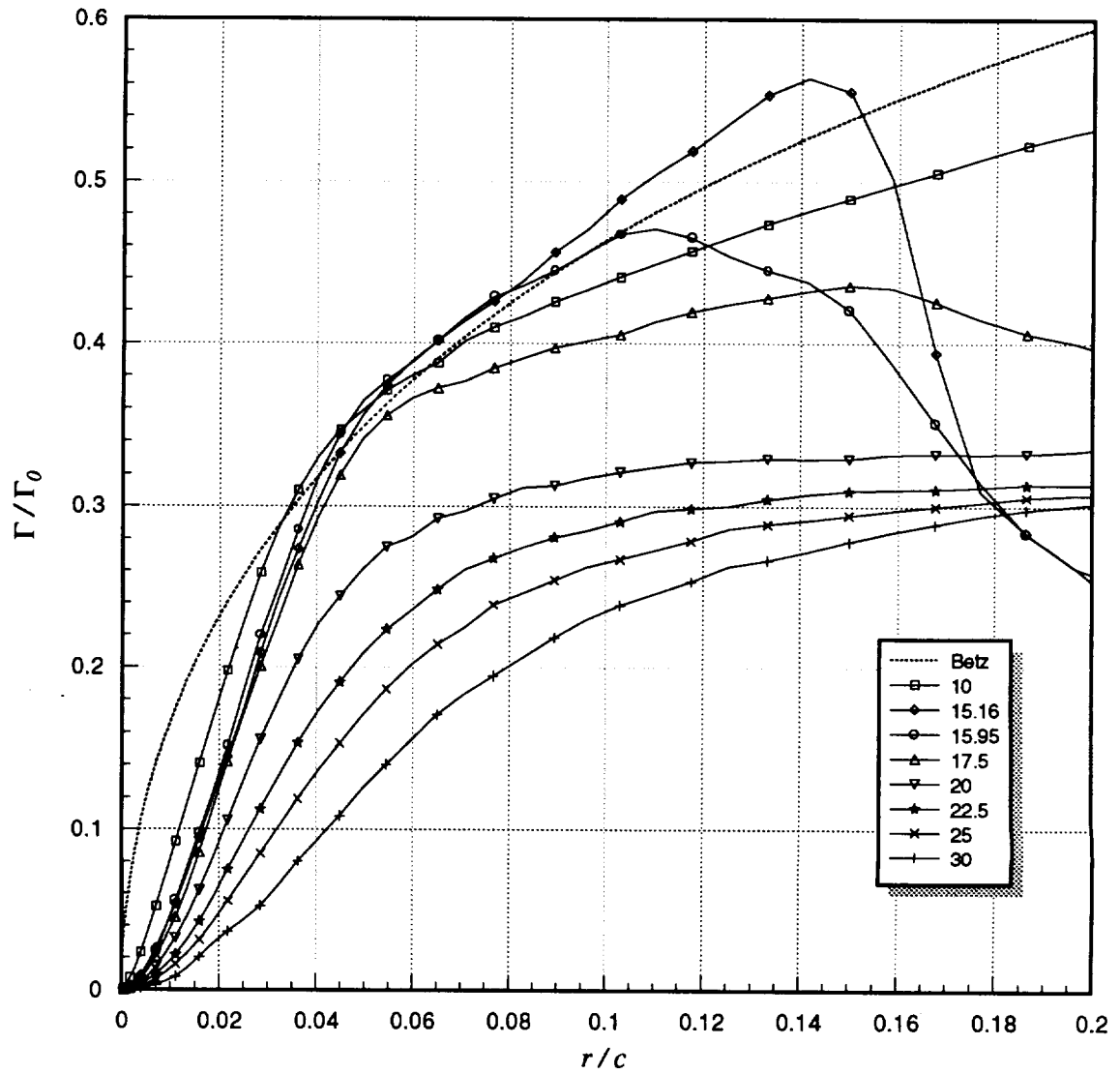


**Figure 3.23b** Circulation distributions (assuming axisymmetric flow) as a function of downstream distance ( $x$ ) for pressure side passage of  $\Delta/c = -0.125$ :  $x/c = 30$ ,  $\alpha_1 = 5^\circ$ ,  $\alpha_2 = 5^\circ$ , no spoiler. Legend lists  $x/c$  values.

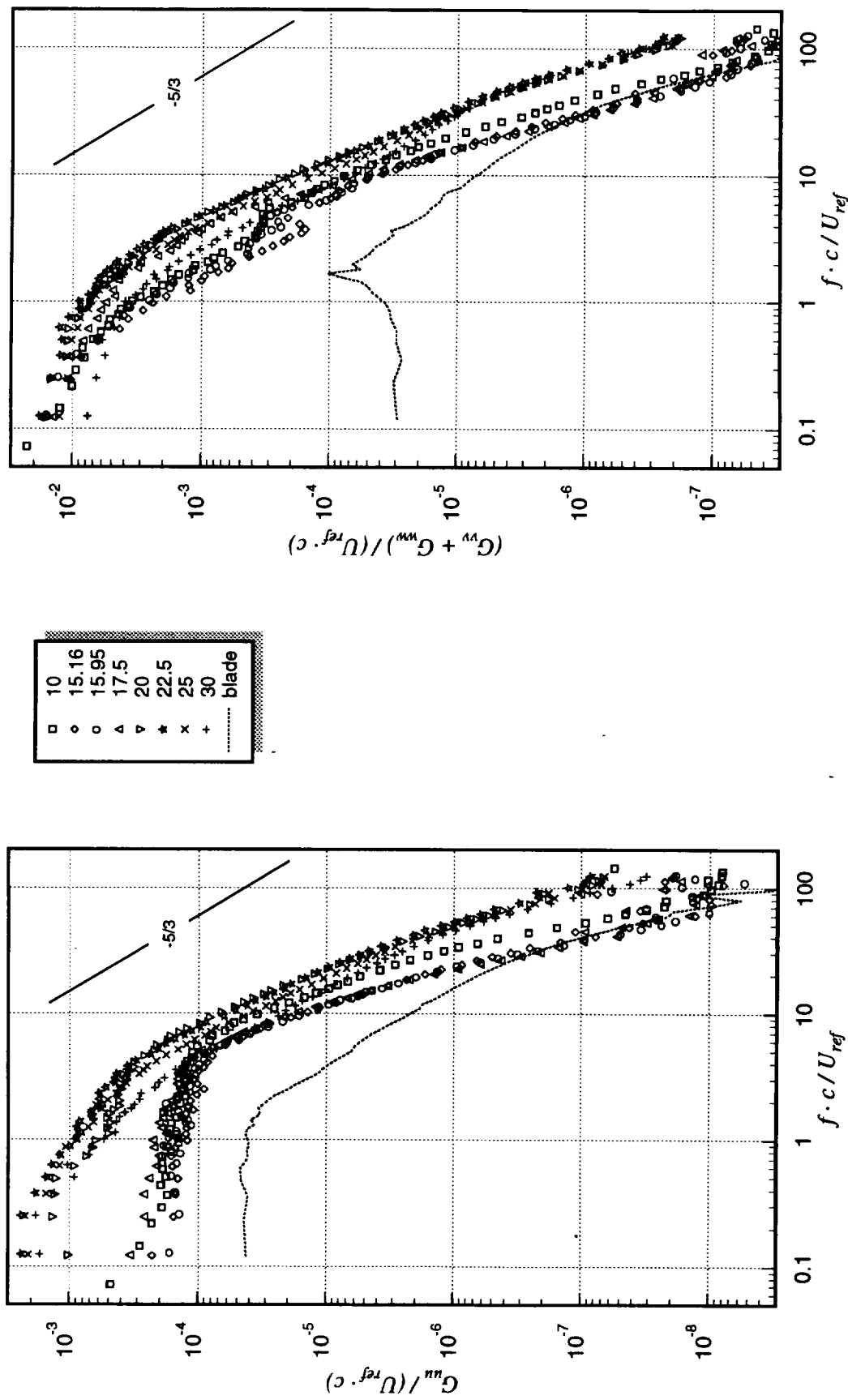
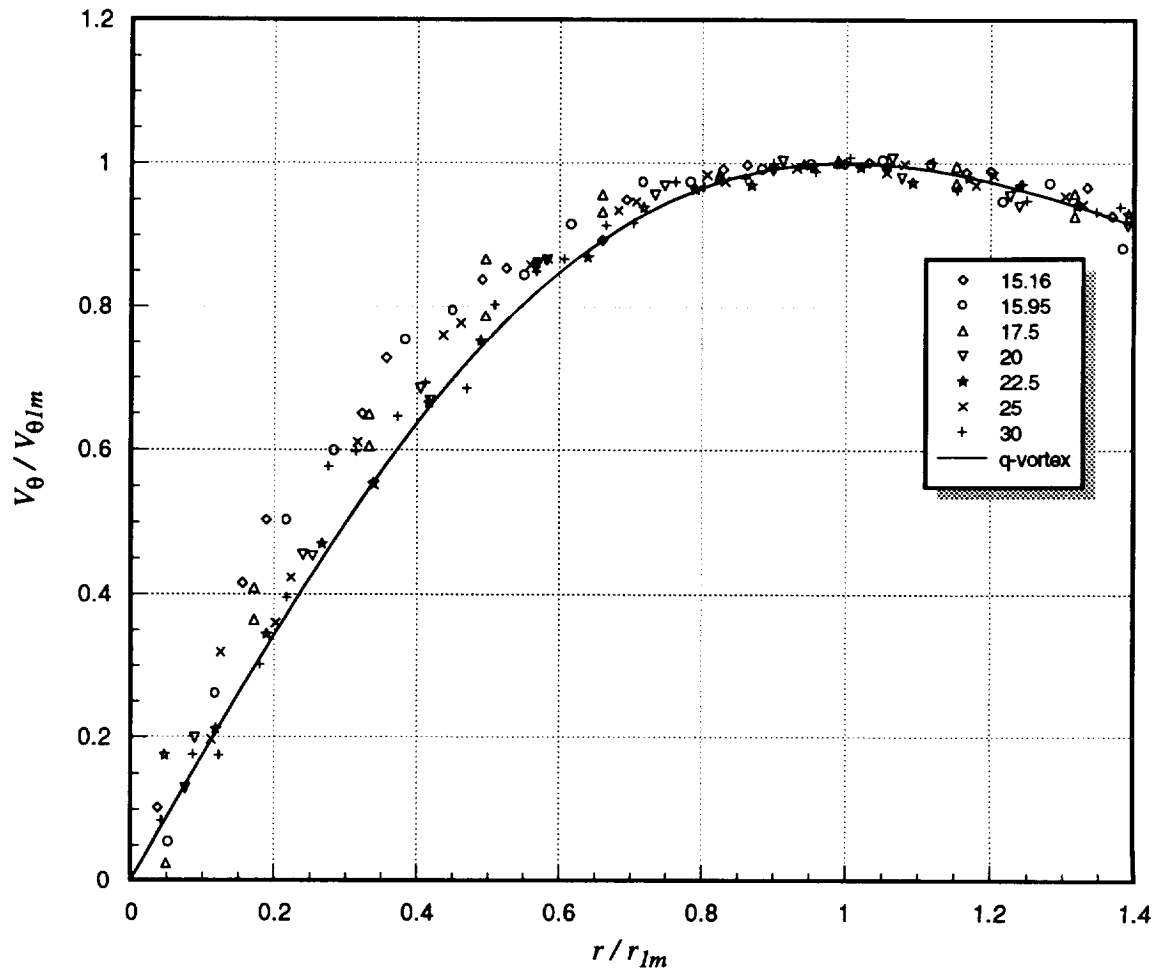
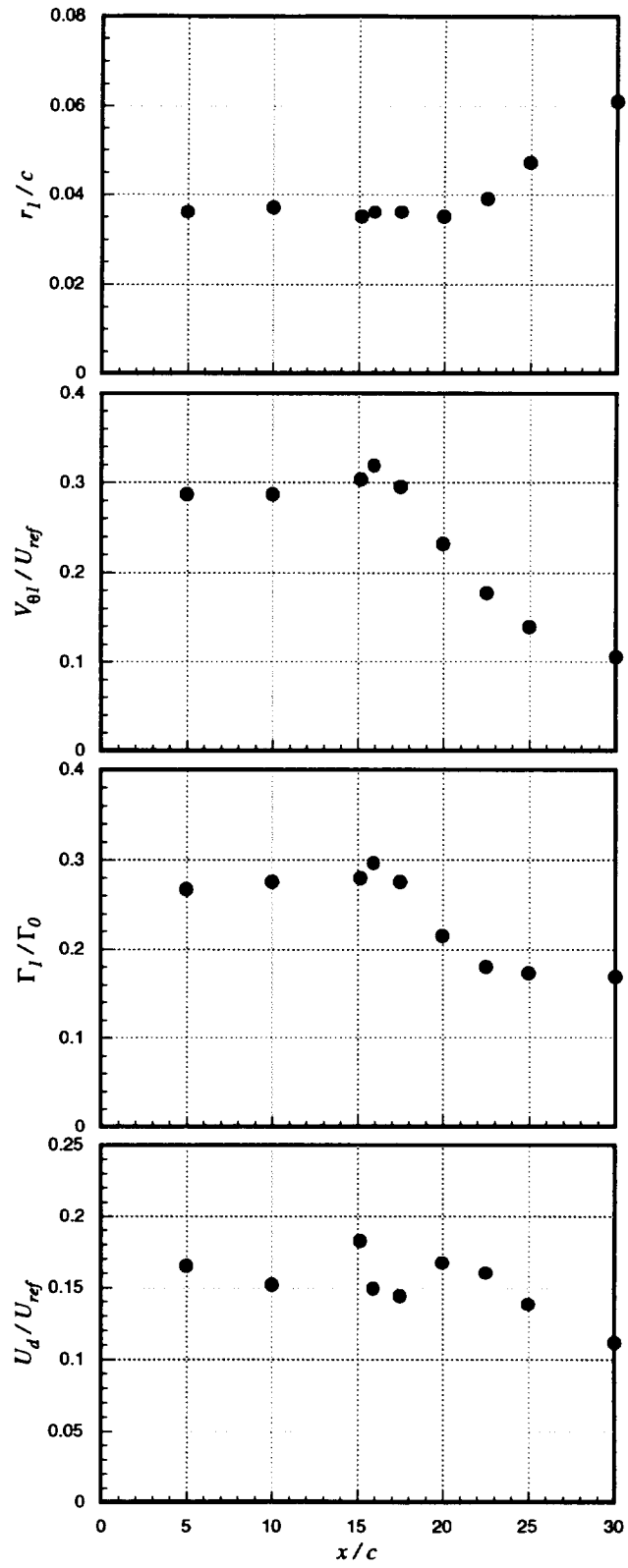


Figure 3.24 Core center velocity autospectra as a function of downstream distance ( $x$ ) for pressure side passage of  $\Delta/c = -0.125$ :  $\alpha_1 = 5^\circ$ ,  $\alpha_2 = 5^\circ$ , no spoiler. Legend lists  $x/c$  locations. Autospectra measured in undisturbed portion of interaction blade wake at  $x/c = 30$  also included (marked as “blade” in legend).





**Figure 3.25** Mean tangential ( $V_\theta$ ) velocities (measured along  $z$ -wise profiles through the vortex core center), normalized on measured peak tangential velocity ( $V_{\theta,m}$ ), as a function of downstream distance ( $x$ ) for pressure side passage of  $\Delta/c = -0.125$ :  $\alpha_1 = 5^\circ$ ,  $\alpha_2 = 5^\circ$ , no spoiler. Legend lists  $x/c$  values.



**Figure 3.26** Core parameters (radius,  $r_I$ ; peak tangential velocity,  $V_{\theta I}$ ; circulation,  $\Gamma_I$ ; and axial velocity deficit,  $U_d$ ) as a function of downstream distance ( $x$ ) for pressure side passage of  $\Delta/c = -0.125$ :  $\alpha_1 = 5^\circ$ ,  $\alpha_2 = 5^\circ$ , no spoiler

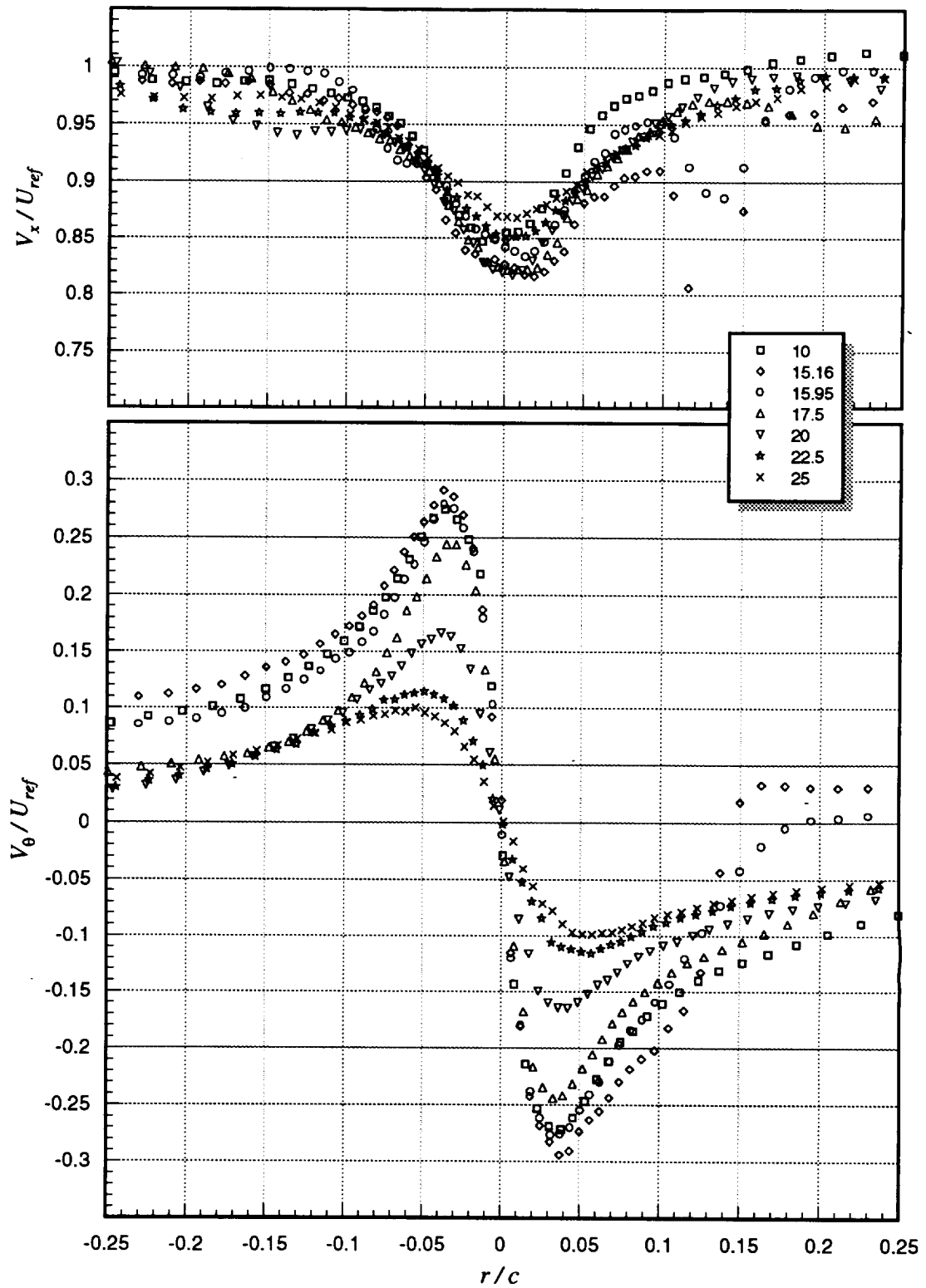


**Figure 3.27a** Mean axial ( $V_x$ ) and tangential ( $V_\theta$ ) velocities (measured along  $z$ -wise profiles through the vortex core center) as a function of downstream distance ( $x$ ) for suction side passage of  $\Delta/c = 0.125$ :  $x/c = 30$ ,  $\alpha_1 = 5^\circ$ ,  $\alpha_2 = 5^\circ$ , no spoiler. Legend lists  $x/c$  values.

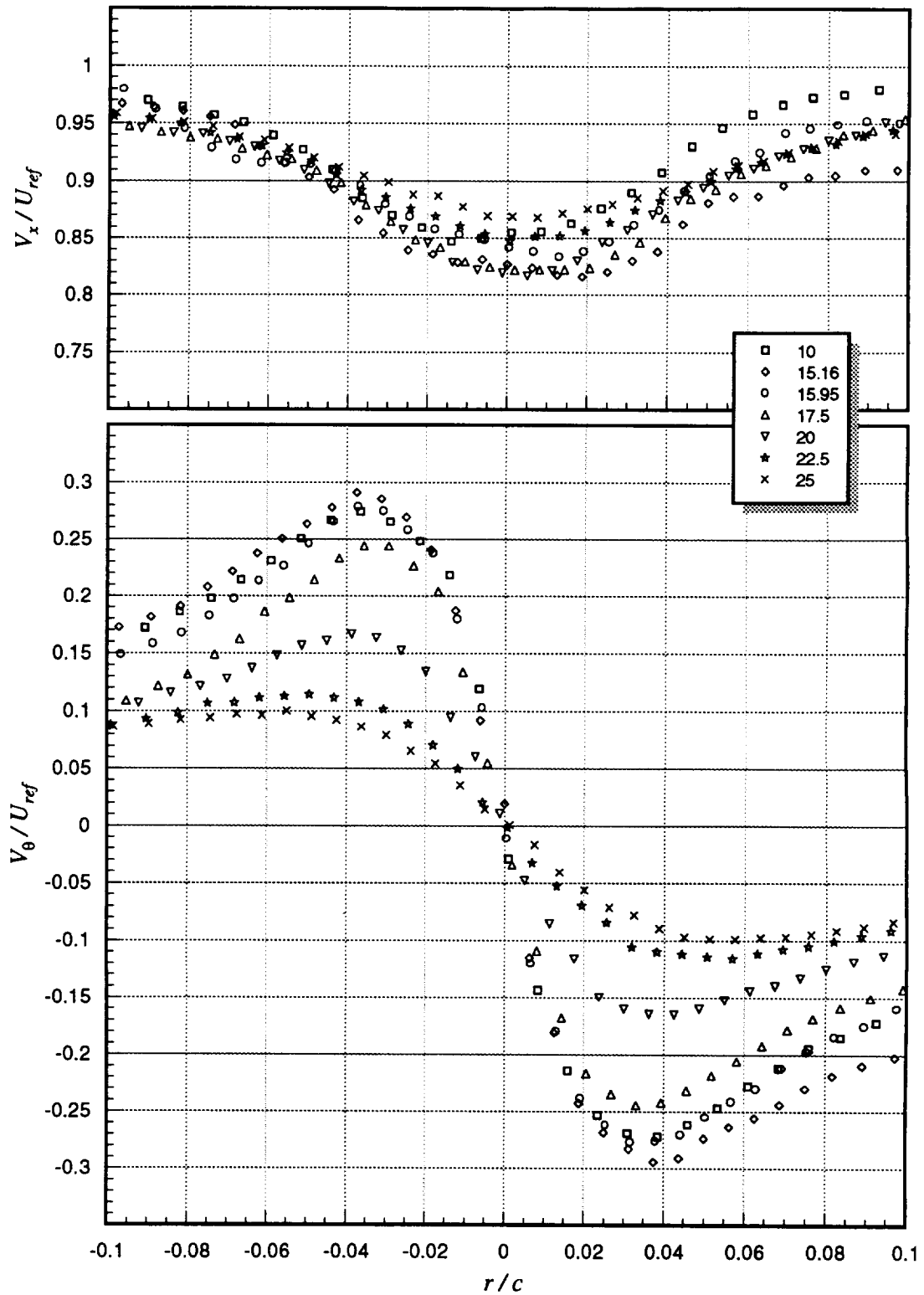


**Figure 3.27b** Mean axial ( $V_x$ ) and tangential ( $V_\theta$ ) velocities (measured along  $z$ -wise profiles through the vortex core center) as a function of downstream distance ( $x$ ) for suction side passage of  $\Delta/c = 0.125$ :  $x/c = 30$ ,  $\alpha_1 = 5^\circ$ ,  $\alpha_2 = 5^\circ$ , no spoiler. Legend lists  $x/c$  values.

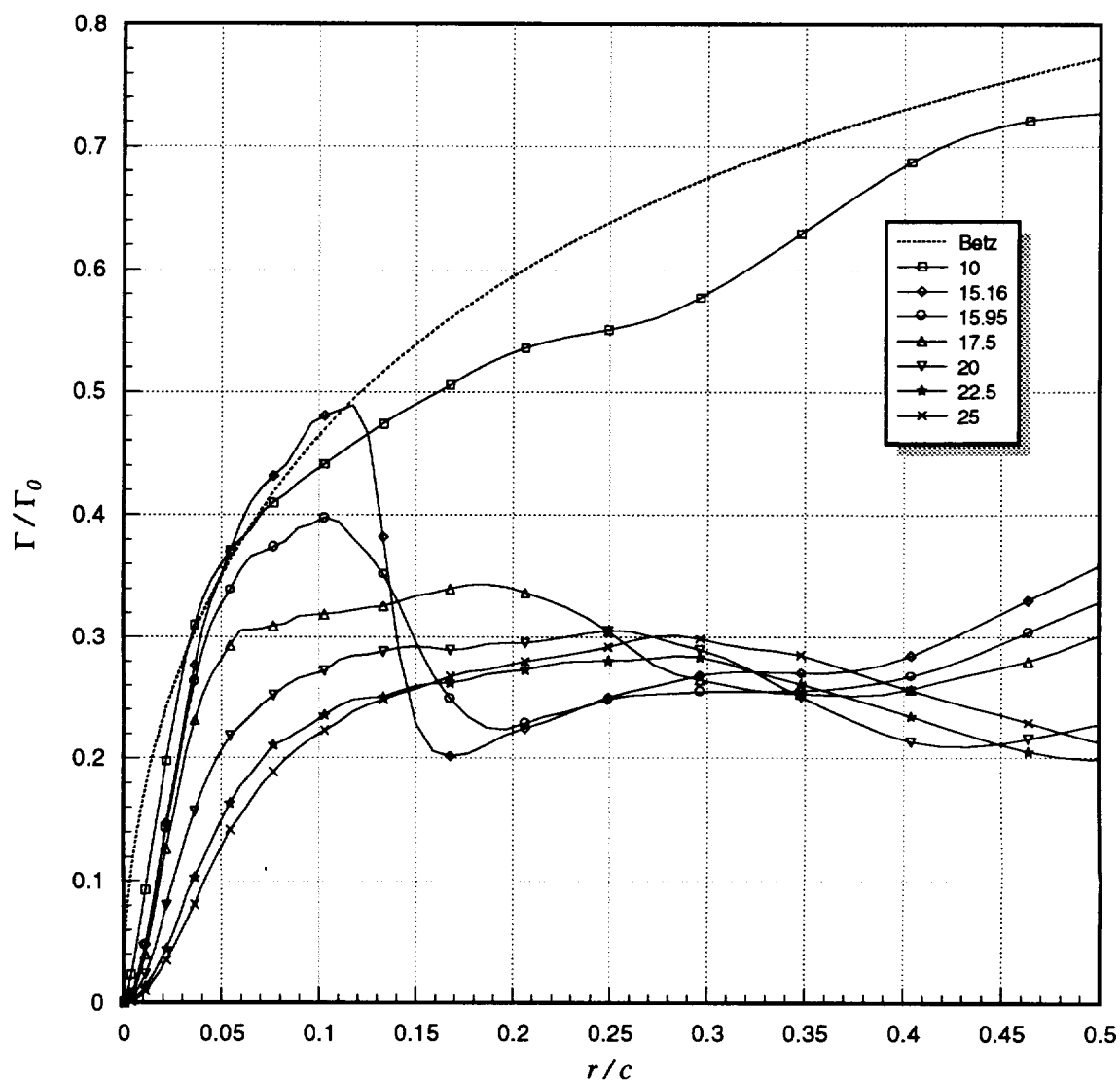


**Figure 3.28a** Circulation distributions (assuming axisymmetric flow) as a function of downstream distance ( $x$ ) for suction side passage of  $\Delta/c = 0.125$ :  $x/c = 30$ ,  $\alpha_1 = 5^\circ$ ,  $\alpha_2 = 5^\circ$ , no spoiler. Legend lists  $x/c$  values.

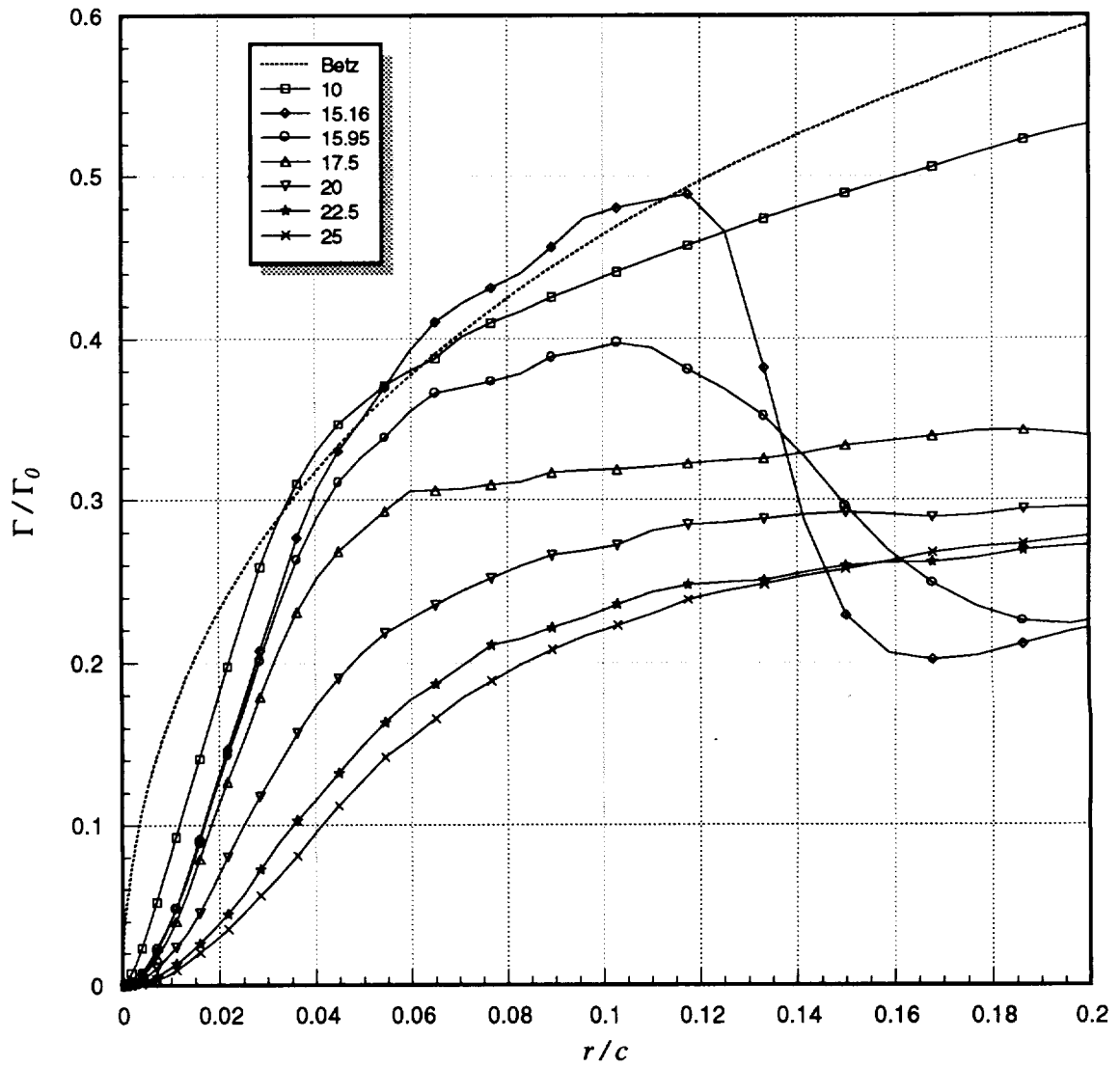


**Figure 3.28b** Circulation distributions (assuming axisymmetric flow) as a function of downstream distance ( $x$ ) for suction side passage of  $\Delta/c = 0.125$ :  $x/c = 30$ ,  $\alpha_1 = 5^\circ$ ,  $\alpha_2 = 5^\circ$ , no spoiler. Legend lists  $x/c$  values.

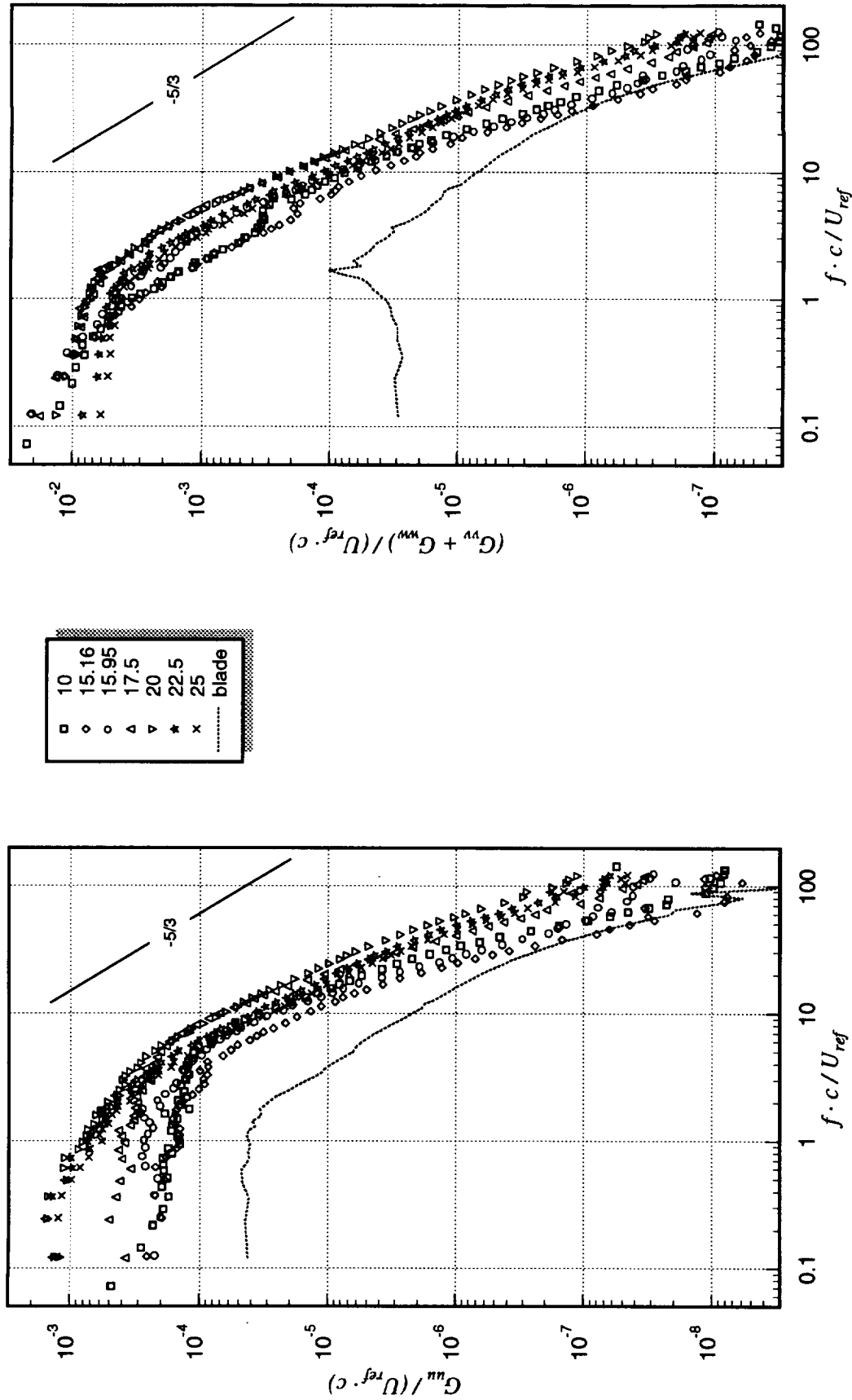


**Figure 3.29** Core center velocity autospectra as a function of downstream distance ( $x$ ) for suction side passage of  $\Delta/c = 0.125$ ;  $\alpha_1 = 5^\circ$ ,  $\alpha_2 = 5^\circ$ , no spoiler. Legend lists  $x/c$  locations. Autospectra measured in undisturbed portion of interaction blade wake at  $x/c = 30$  also included (marked as “blade” in legend).

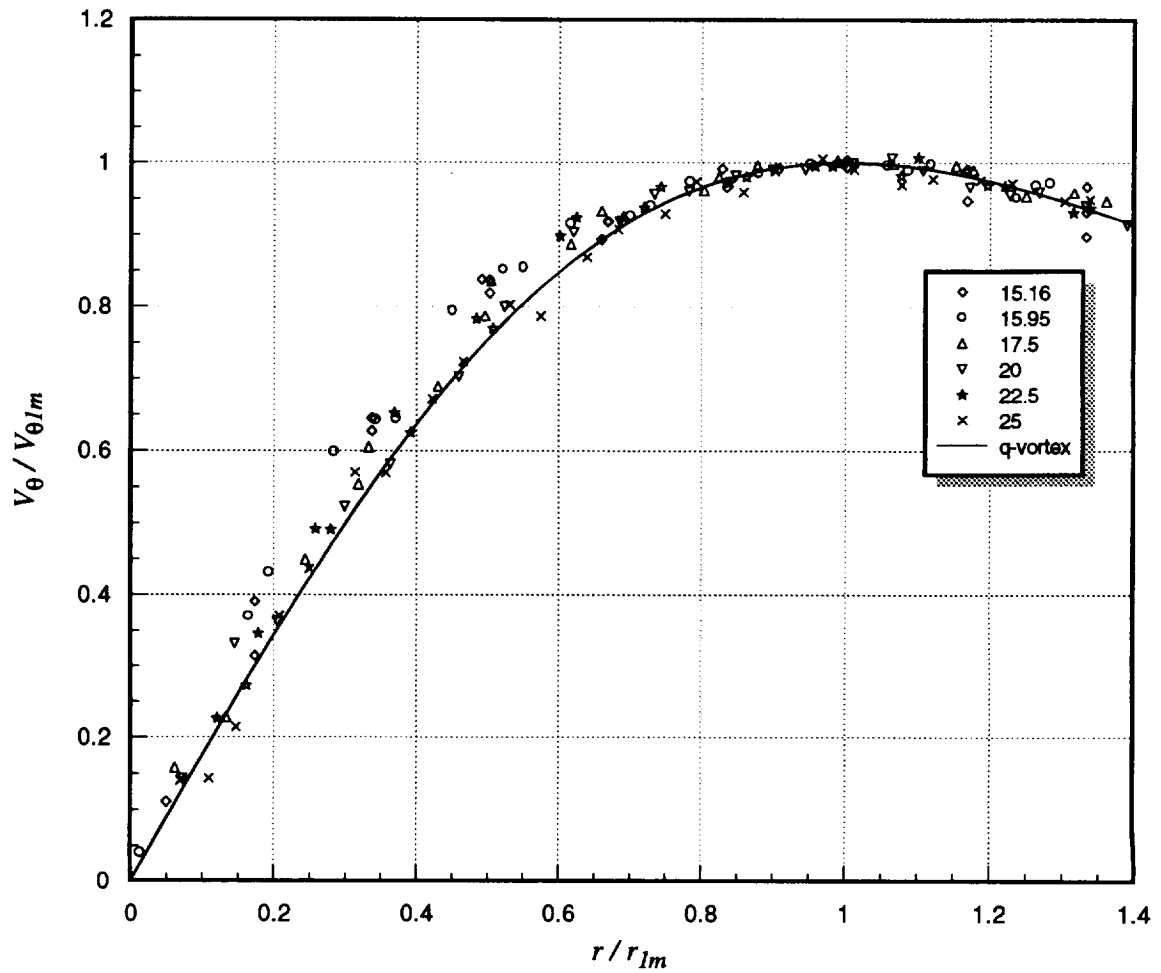


**Figure 3.30** Mean tangential ( $V_\theta$ ) velocities (measured along  $z$ -wise profiles through the vortex core center), normalized on measured peak tangential velocity ( $V_{\theta 1m}$ ), as a function of downstream distance ( $x$ ) for suction side passage of  $\Delta/c = 0.125$ :  $\alpha_1 = 5^\circ$ ,  $\alpha_2 = 5^\circ$ , no spoiler. Legend lists  $x/c$  values.



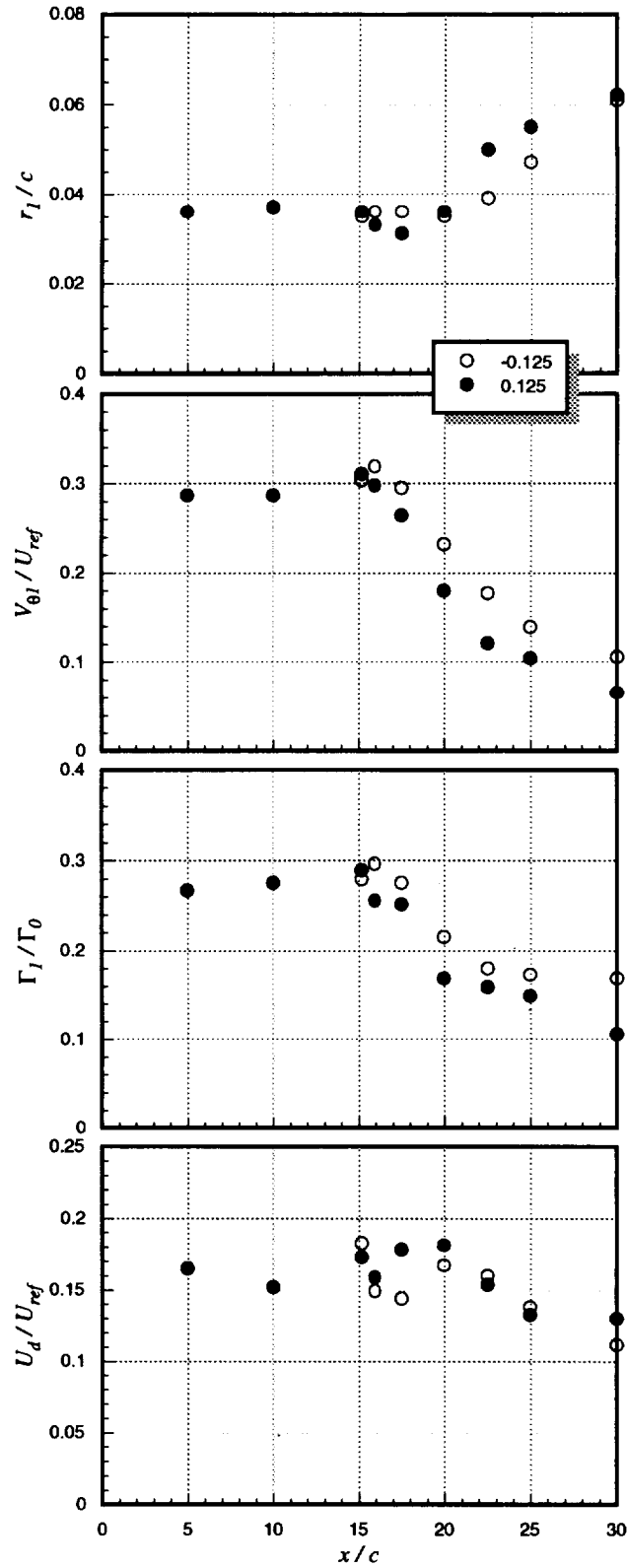


**Figure 3.31** Core parameters (radius,  $r_I$ ; peak tangential velocity,  $V_{\theta I}$ ; circulation,  $\Gamma_I$ ; and axial velocity deficit,  $U_d$ ) as a function of downstream distance ( $x$ ) for both suction ( $\Delta/c = 0.125$ ) and pressure side ( $\Delta/c = -0.125$ ) passage:  $\alpha_1 = 5^\circ$ ,  $\alpha_2 = 5^\circ$ , no spoiler. Legend lists  $\Delta/c$  values.

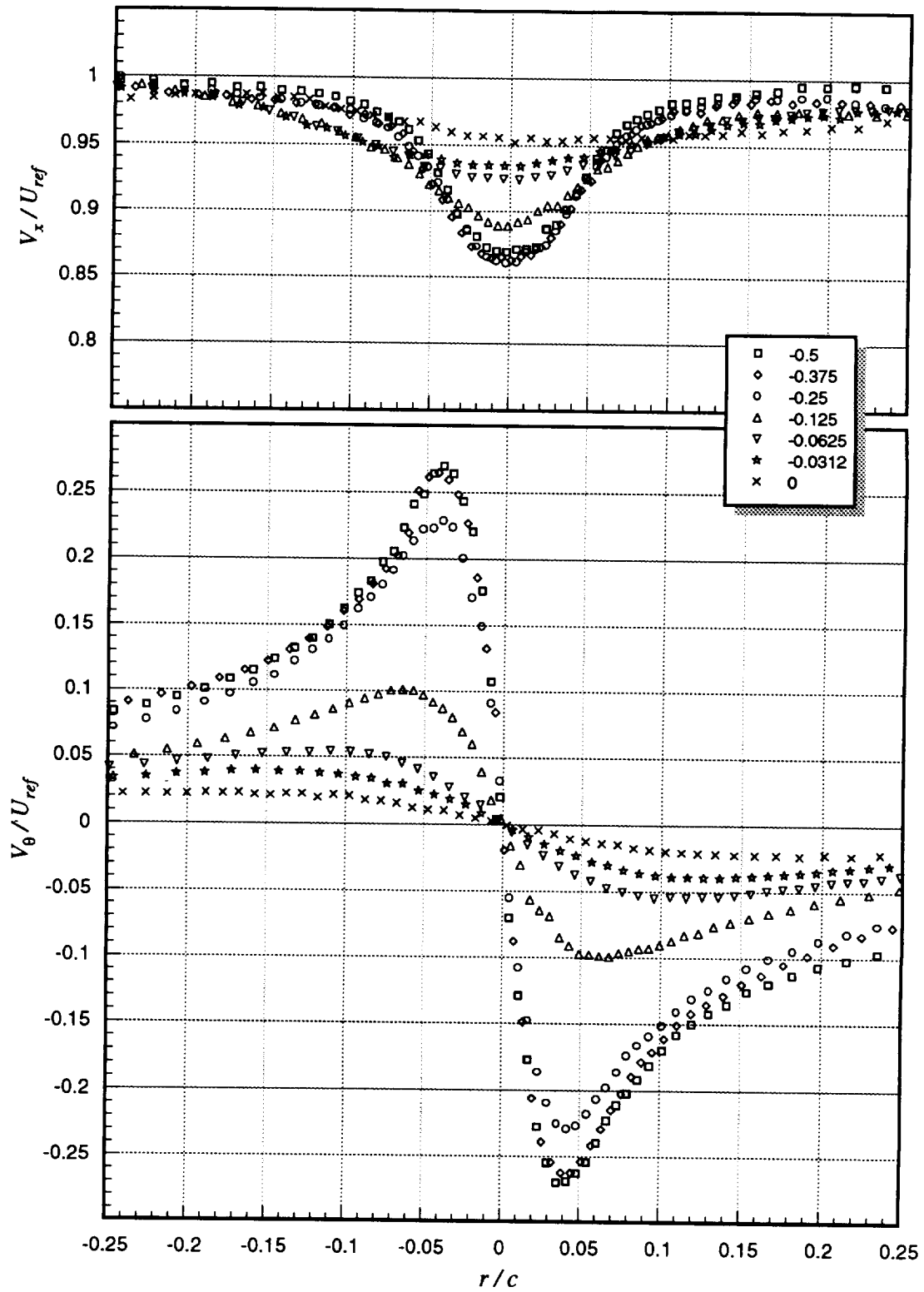


**Figure 3.32a** Mean axial ( $V_x$ ) and tangential ( $V_\theta$ ) velocities (measured along  $z$ -wise profiles through the vortex core center) as a function of blade–vortex separation ( $\Delta$ ) for pressure side passages:  $x/c = 30$ ,  $\alpha_1 = 5^\circ$ ,  $\alpha_2 = 5^\circ$ , no spoiler. Legend lists  $\Delta/c$  values.

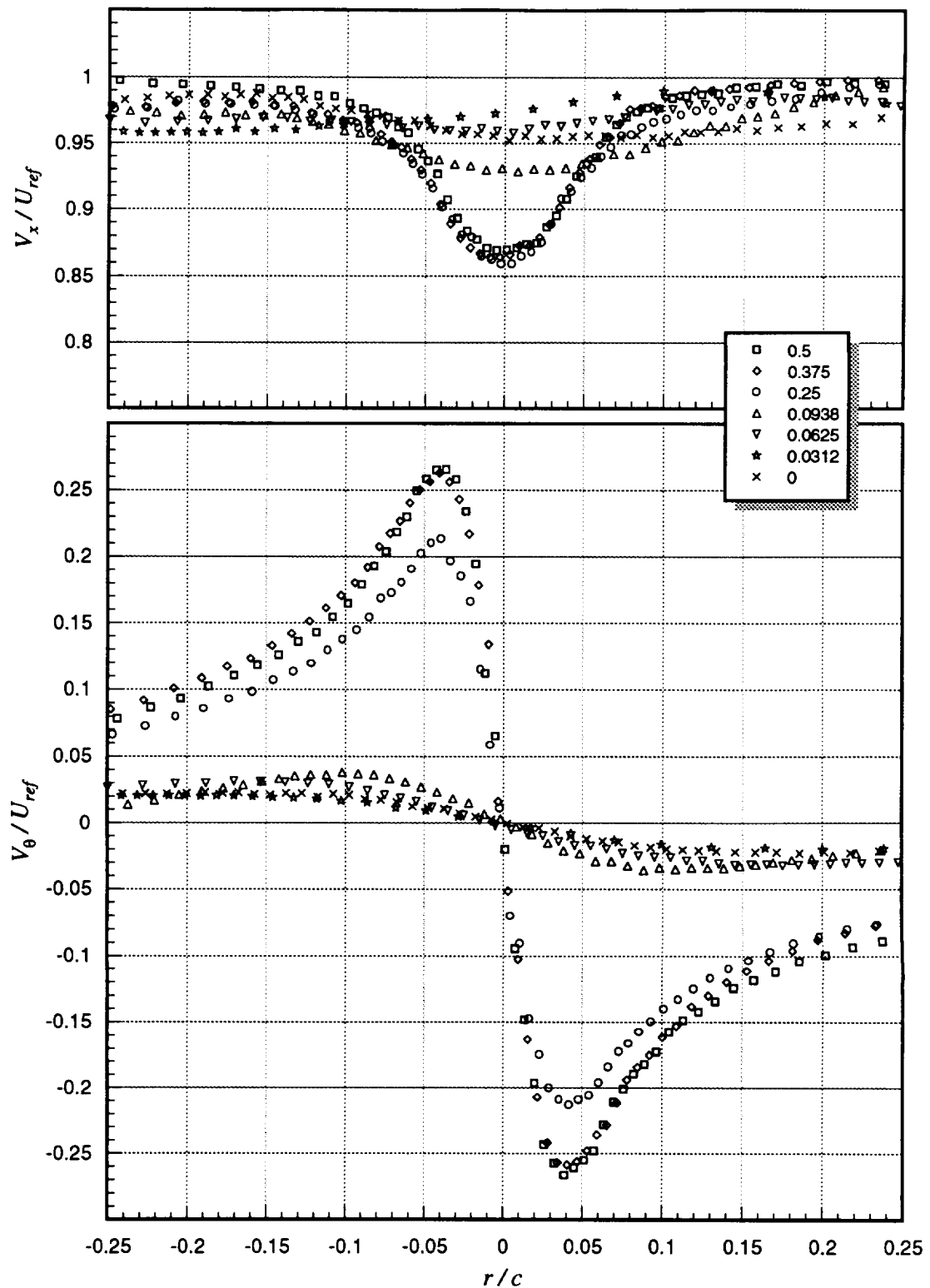


**Figure 3.32b** Mean axial ( $V_x$ ) and tangential ( $V_\theta$ ) velocities (measured along  $z$ -wise profiles through the vortex core center) as a function of blade–vortex separation ( $\Delta$ ) for suction side passages:  $x/c = 30$ ,  $\alpha_1 = 5^\circ$ ,  $\alpha_2 = 5^\circ$ , no spoiler. Legend lists  $\Delta/c$  values.

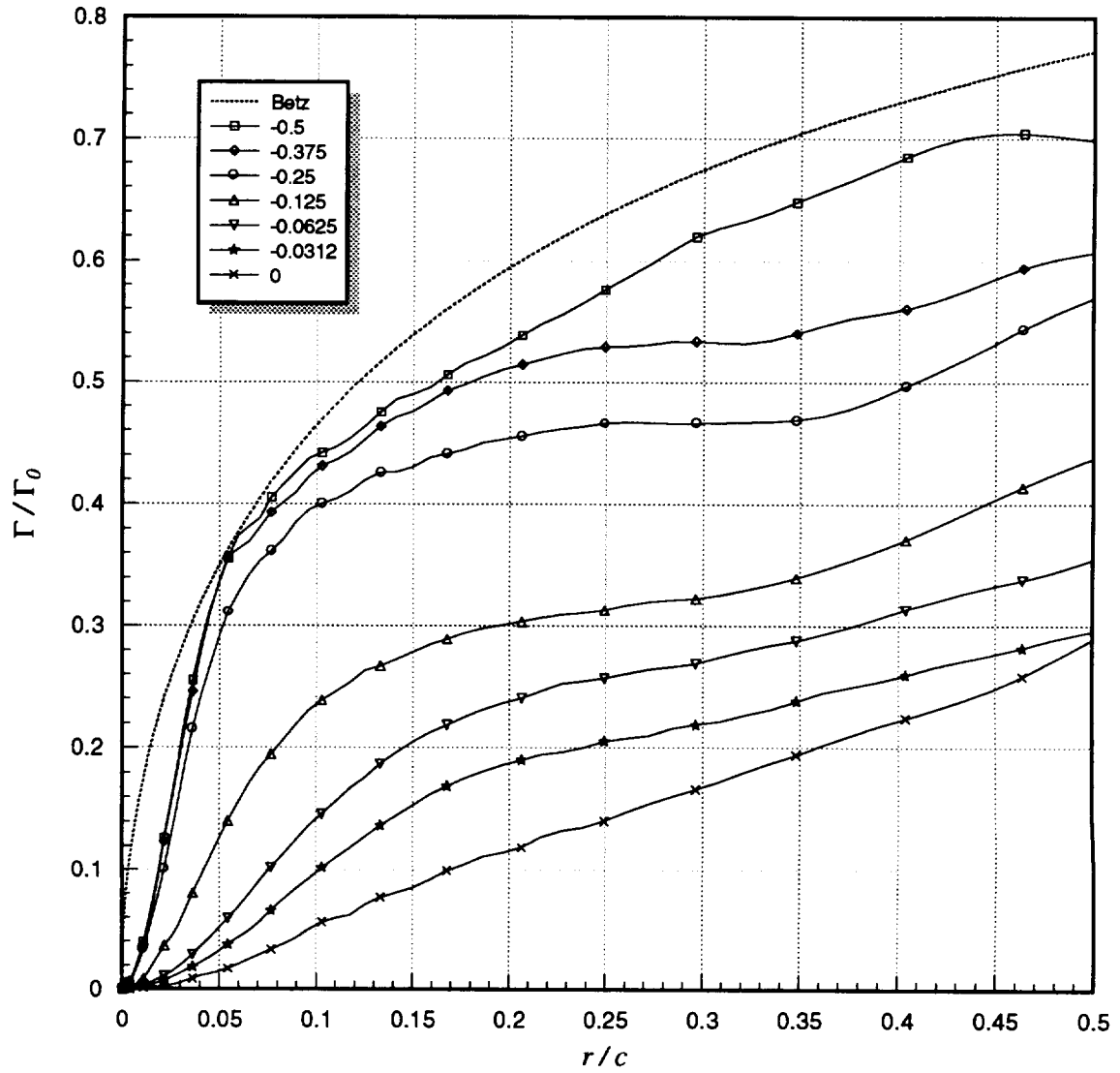


**Figure 3.33a** Circulation distributions (assuming axisymmetric flow) as a function of blade–vortex separation ( $\Delta$ ) for pressure side passages:  $x/c = 30$ ,  $\alpha_1 = 5^\circ$ ,  $\alpha_2 = 5^\circ$ , no spoiler. Legend lists  $\Delta/c$  values.

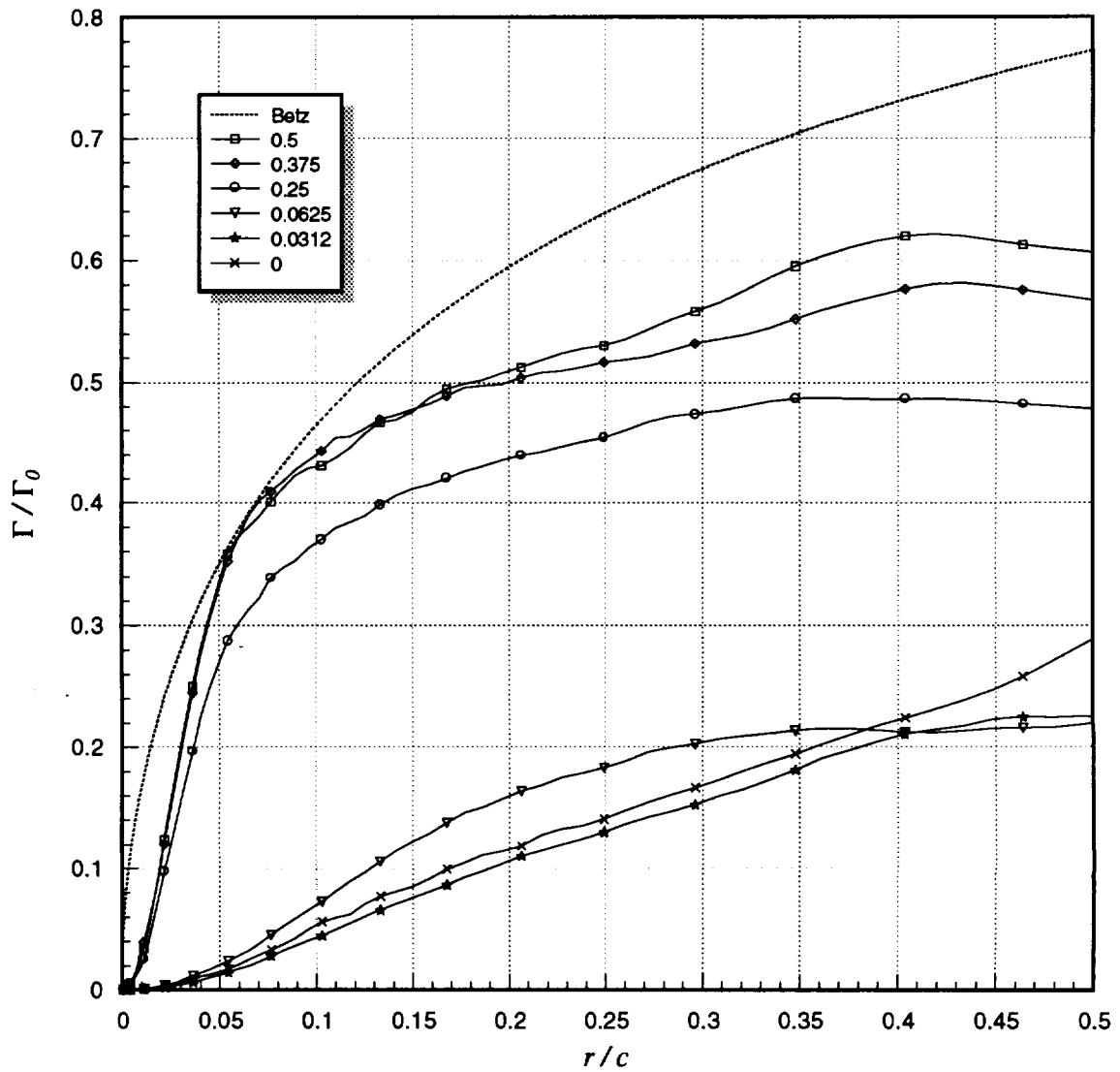


**Figure 3.33b** Circulation distributions (assuming axisymmetric flow) as a function of blade-vortex separation ( $\Delta$ ) for suction side passages:  $x/c = 30$ ,  $\alpha_1 = 5^\circ$ ,  $\alpha_2 = 5^\circ$ , no spoiler. Legend lists  $\Delta/c$  values.

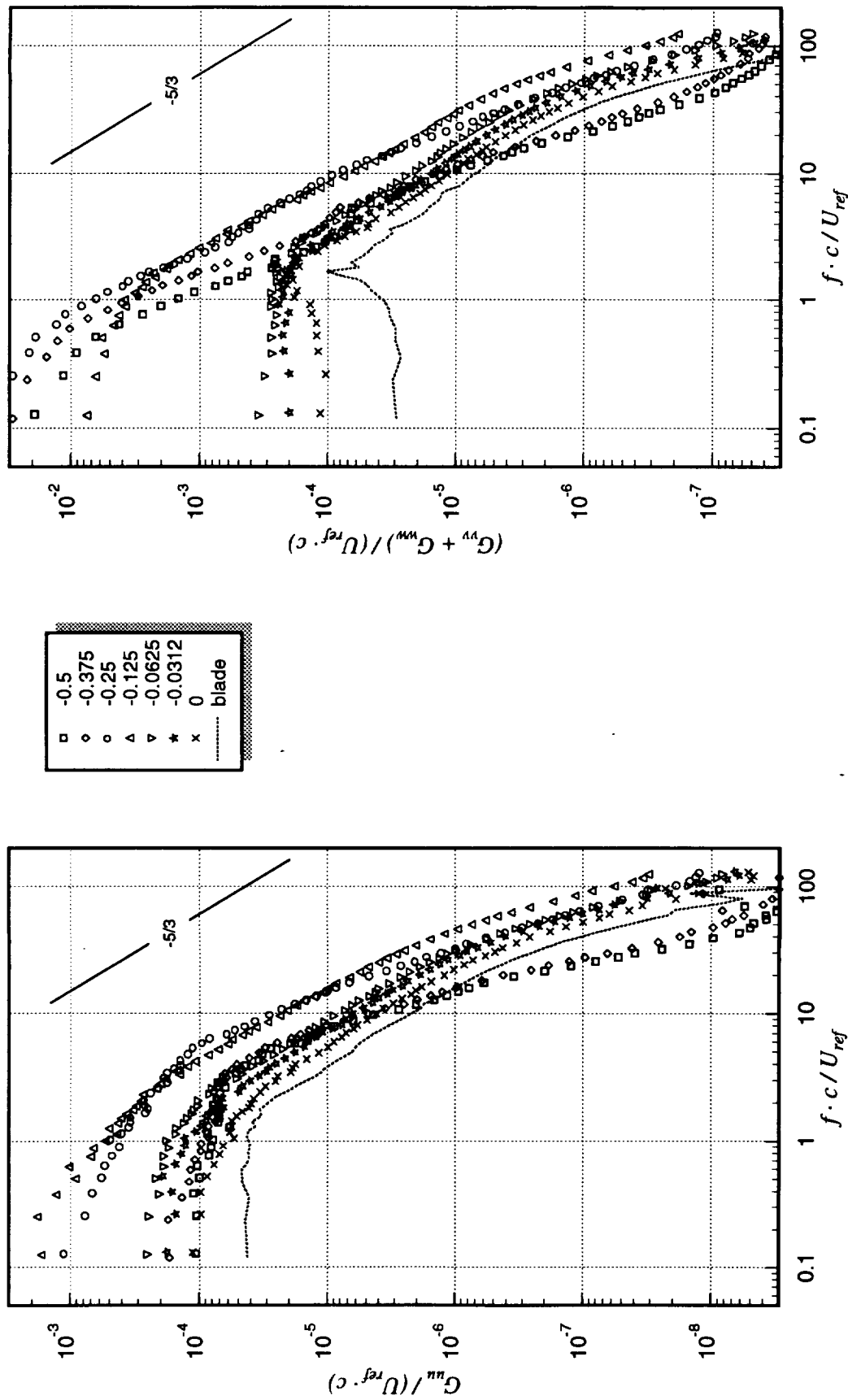


**Figure 3.34a** Core center velocity autospectra as a function of blade–vortex separation ( $\Delta$ ) for pressure side passages:  $x / c = 30$ ,  $\alpha_1 = 5^\circ$ ,  $\alpha_2 = 5^\circ$ , no spoiler. Legend lists  $\Delta / c$  values. Autospectra measured in undisturbed portion of interaction blade wake at  $x / c = 30$  also included (marked as “blade” in legend).

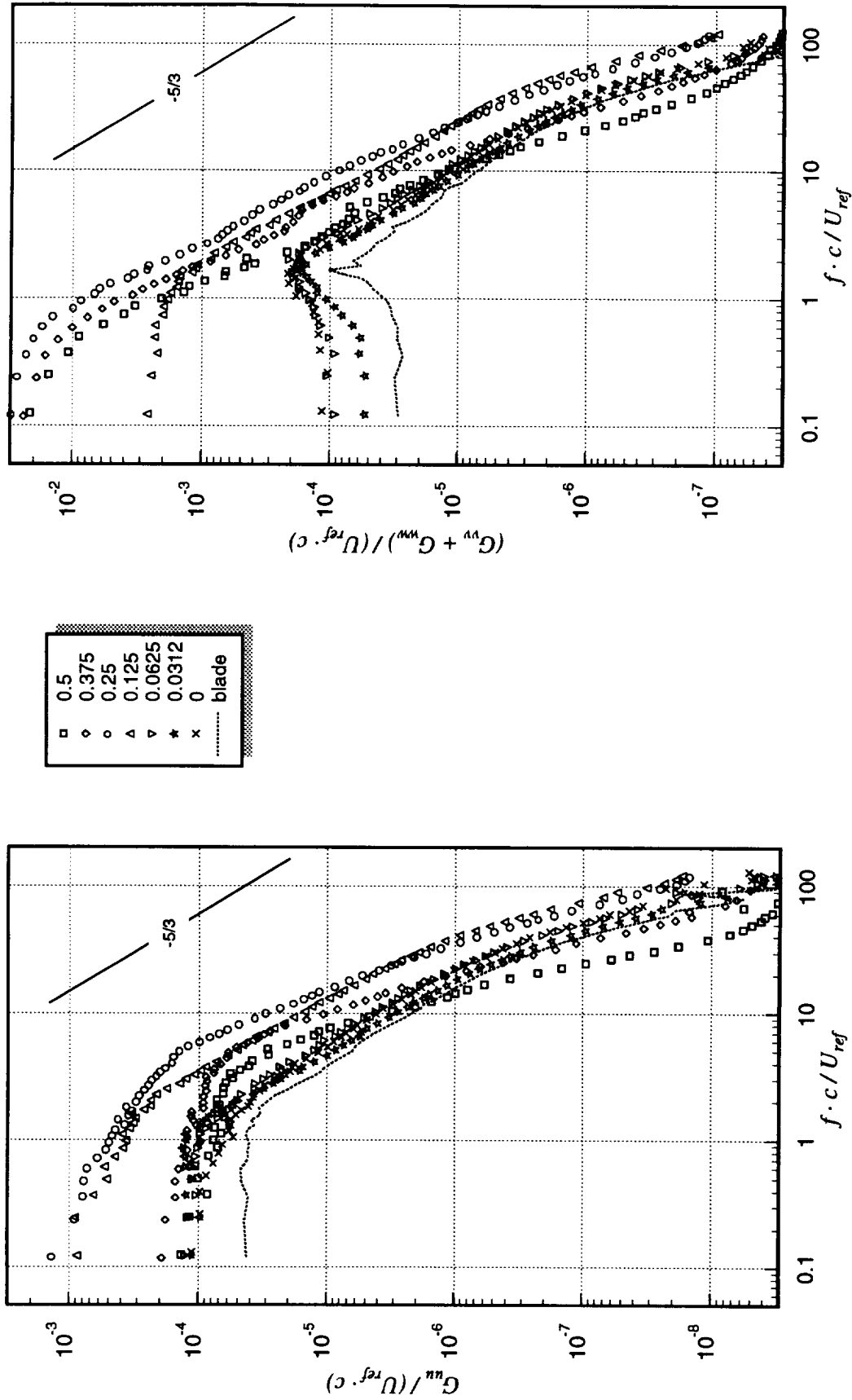


**Figure 3.34b** Core center velocity autospectra as a function of blade–vortex separation ( $\Delta$ ) for suction side passages:  $x/c = 30$ ,  $\alpha_1 = 5^\circ$ ,  $\alpha_2 = 5^\circ$ , no spoiler. Legend lists  $\Delta/c$  values. Autospectra measured in undisturbed portion of interaction blade wake at  $x/c = 30$  also included (marked as “blade” in legend).

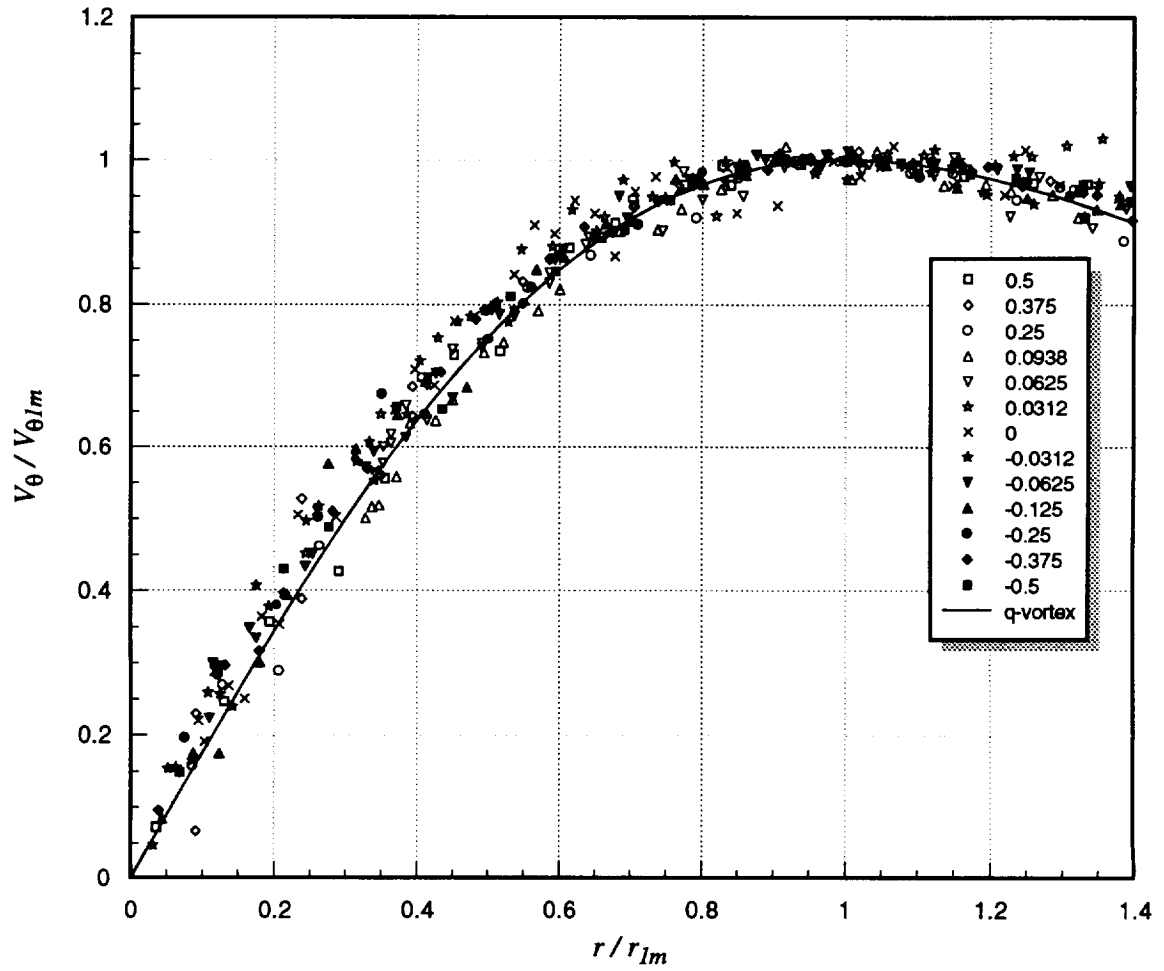


**Figure 3.35** Mean tangential ( $V_\theta$ ) velocities (measured along  $z$ -wise profiles through the vortex core center), normalized on measured peak tangential velocity ( $V_{\theta 1m}$ ), as a function of blade–vortex separation ( $\Delta$ ):  $x/c = 30$ ,  $\alpha_1 = 5^\circ$ ,  $\alpha_2 = 5^\circ$ , no spoiler. Legend lists  $\Delta/c$  values.



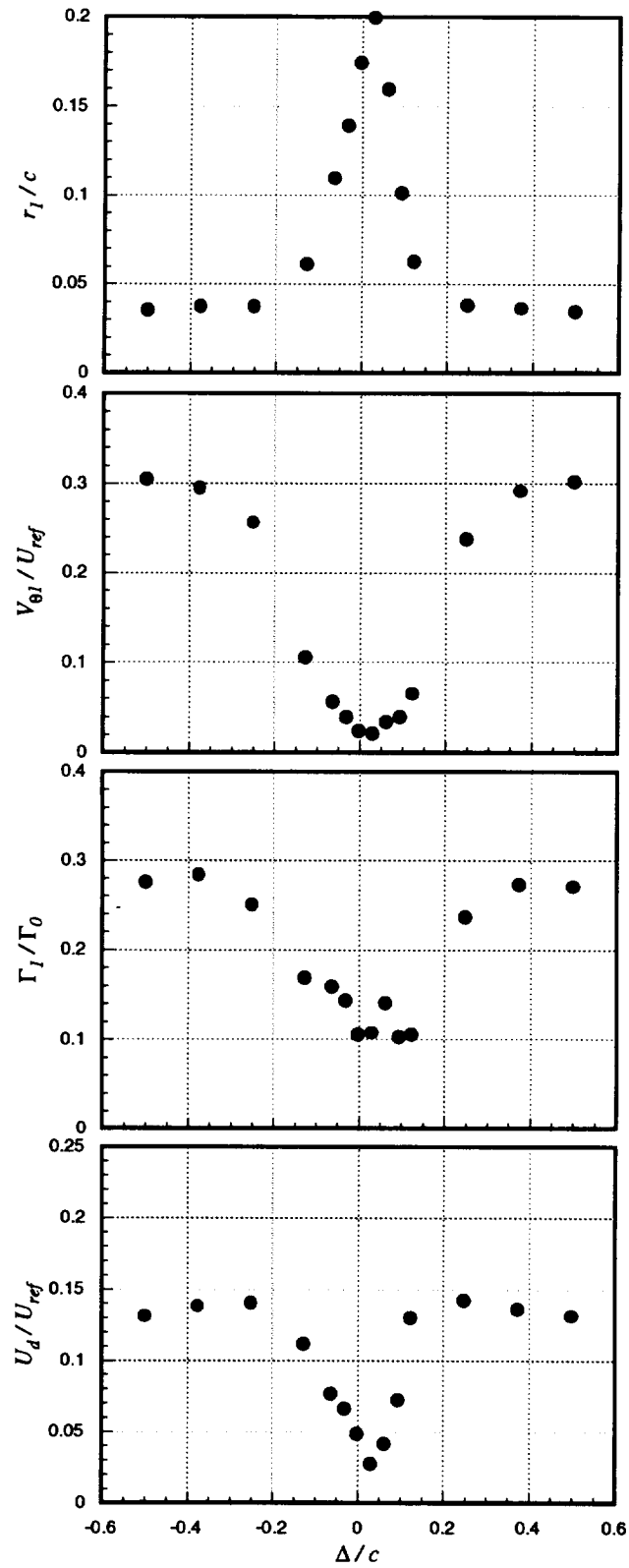


**Figure 3.36** Core parameters (radius,  $r_I$ ; peak tangential velocity,  $V_{\theta I}$ ; circulation,  $\Gamma_I$ ; and axial velocity deficit,  $U_d$ ) as a function of blade-vortex separation ( $\Delta$ ):  $x/c = 30$ ,  $\alpha_1 = 5^\circ$ ,  $\alpha_2 = 5^\circ$ , no spoiler

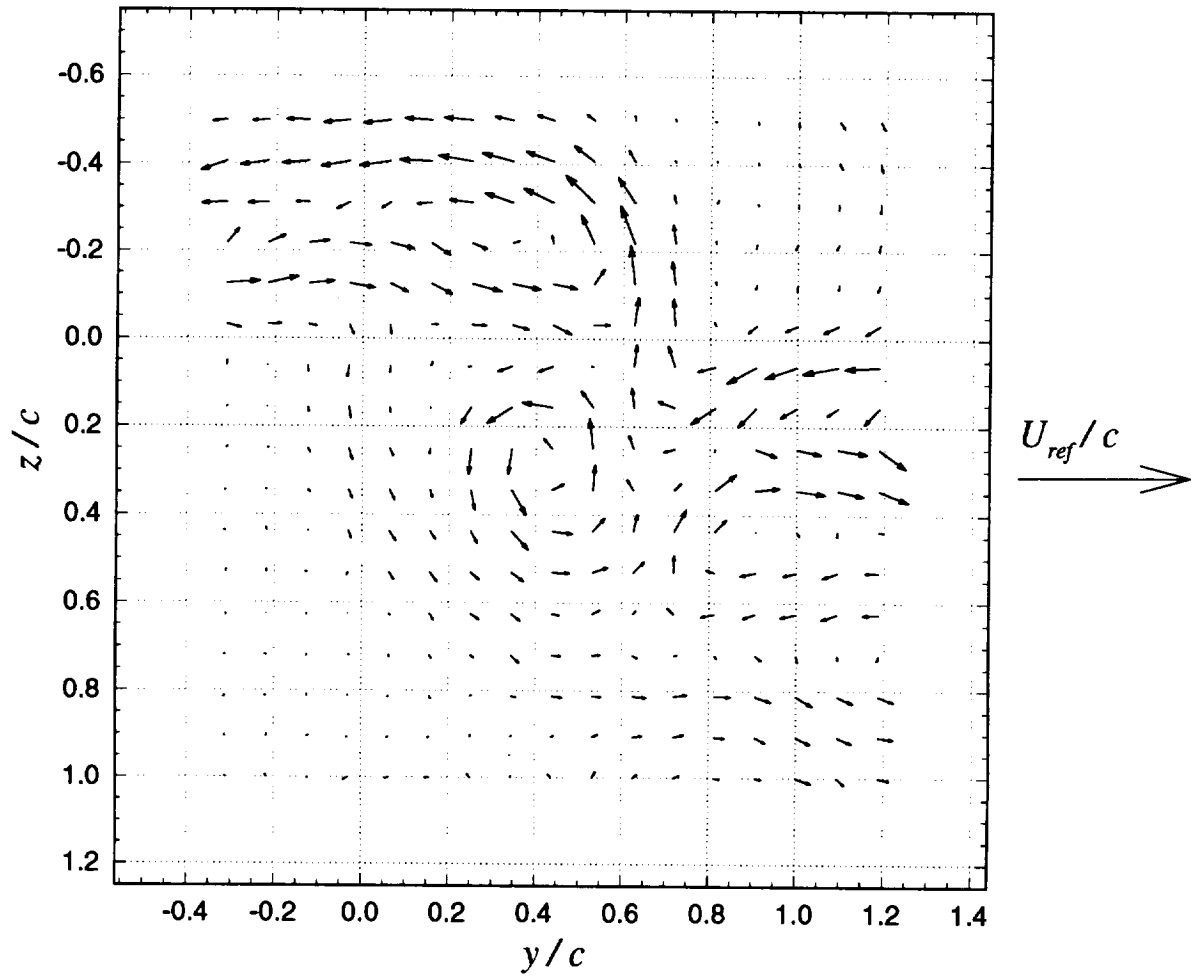


**Figure 3.37a** Mean cross-flow vorticity vectors ( $\Omega_y \cdot c / U_{ref}$ ,  $\Omega_z \cdot c / U_{ref}$ ) for vortex centerline stagnating on blade leading edge ( $\Delta = 0$ ):  $x/c = 30$ ,  $\alpha_1 = 5^\circ$ ,  $\alpha_2 = 5^\circ$ , no spoiler

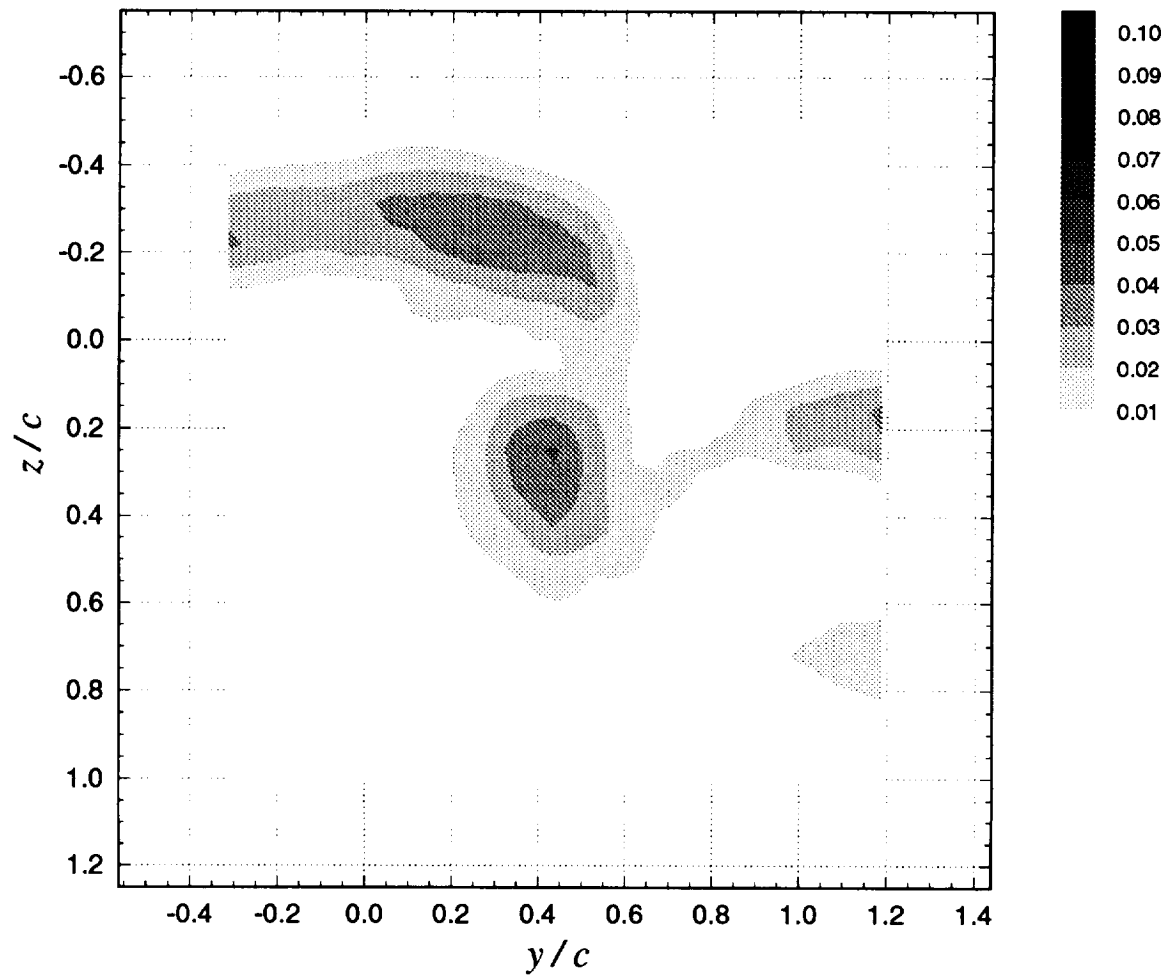


**Figure 3.37b** Contours of mean axial velocity deficit  $((U_{ref} - U) / U_{ref})$  for vortex centerline stagnating on blade leading edge ( $\Delta = 0$ ):  $x/c = 30$ ,  $\alpha_1 = 5^\circ$ ,  $\alpha_2 = 5^\circ$ , no spoiler

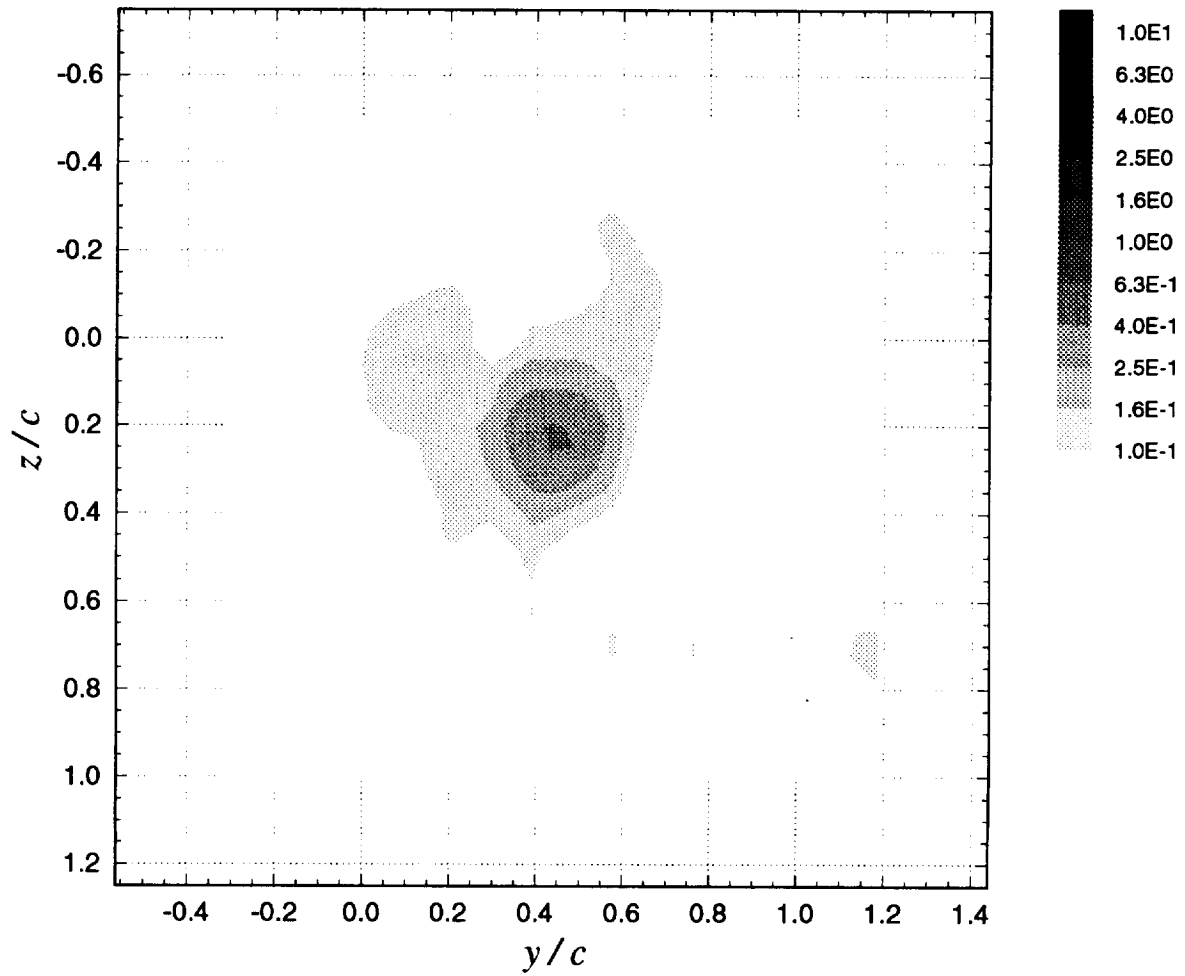


**Figure 3.37c** Contours of mean axial vorticity ( $\Omega_x \cdot c / U_{ref}$ ) for vortex centerline stagnating on blade leading edge ( $\Delta = 0$ ):  $x/c = 30$ ,  $\alpha_1 = 5^\circ$ ,  $\alpha_2 = 5^\circ$ , no spoiler

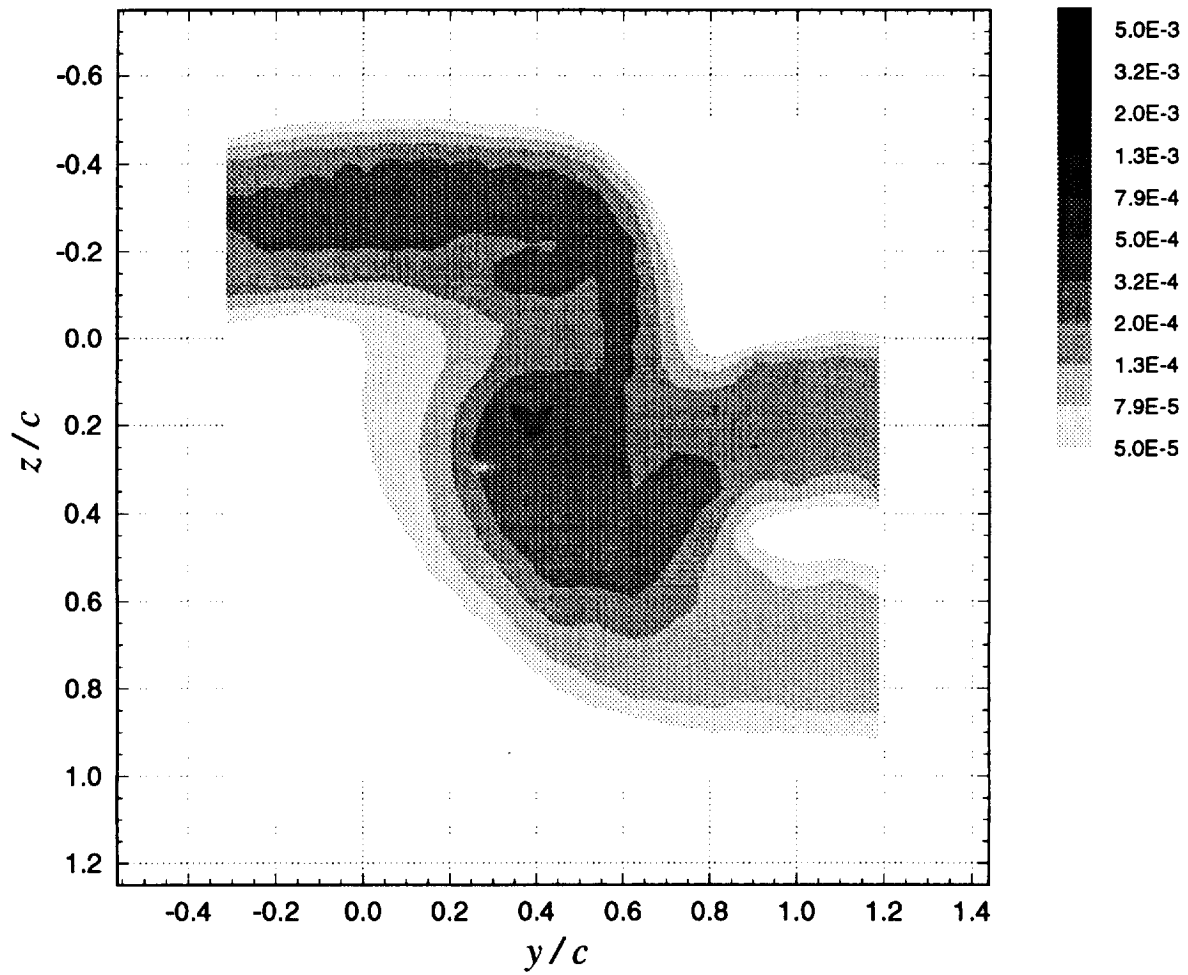


**Figure 3.37d** Contours of axial normal turbulent stress ( $\overline{u'^2} / U_{ref}^2$ ) for vortex centerline stagnating on blade leading edge ( $\Delta = 0$ ):  $x/c = 30$ ,  $\alpha_1 = 5^\circ$ ,  $\alpha_2 = 5^\circ$ , no spoiler

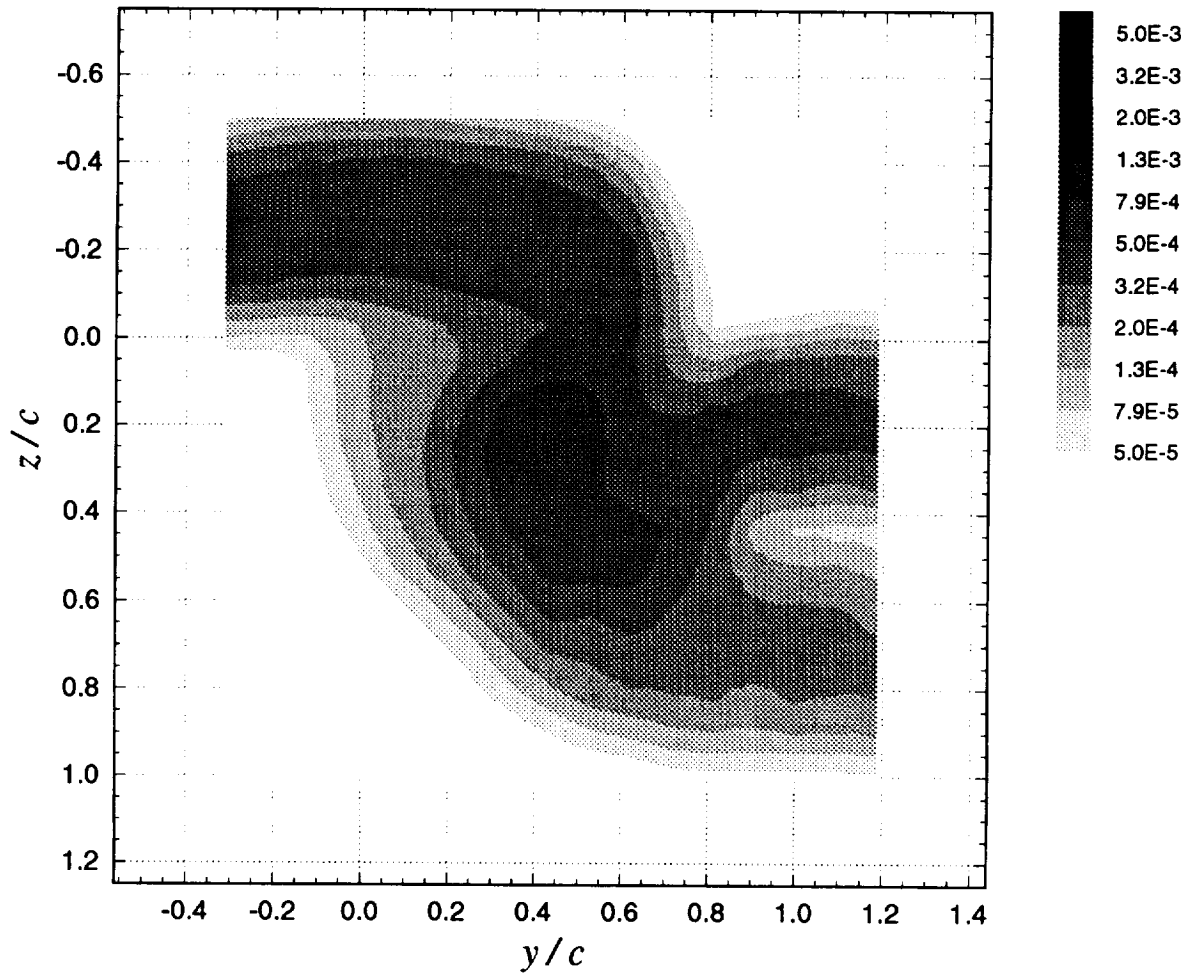


**Figure 3.37e** Contours of summed cross-flow normal turbulent stresses  $(\overline{v^2} + \overline{w^2}) / U_{ref}^2$  for vortex centerline stagnating on blade leading edge ( $\Delta = 0$ ):  $x/c = 30$ ,  $\alpha_1 = 5^\circ$ ,  $\alpha_2 = 5^\circ$ , no spoiler

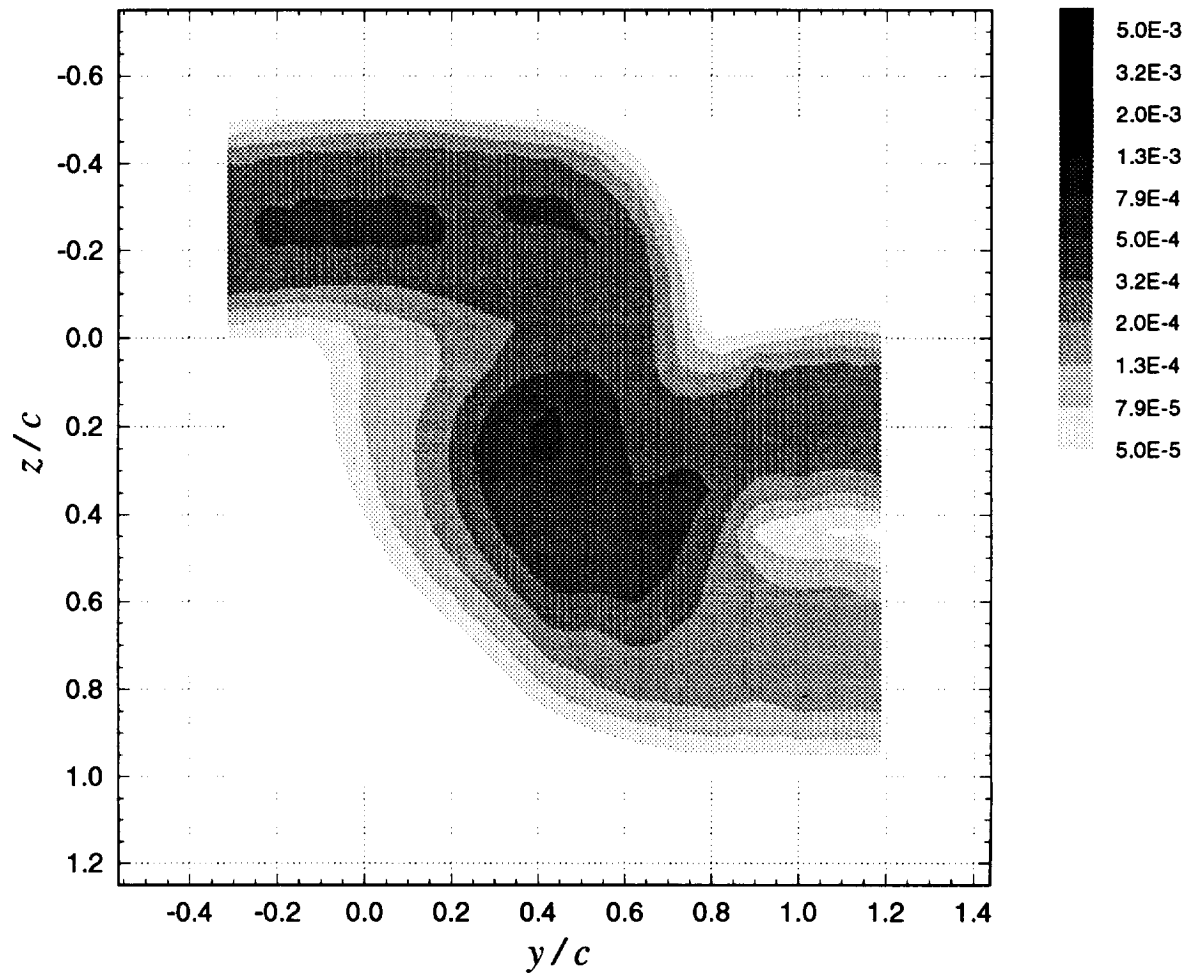


**Figure 3.37f** Contours of turbulent kinetic energy ( $k / U_{ref}^2$ ) for vortex centerline stagnating on blade leading edge ( $\Delta = 0$ ):  $x/c = 30$ ,  $\alpha_1 = 5^\circ$ ,  $\alpha_2 = 5^\circ$ , no spoiler

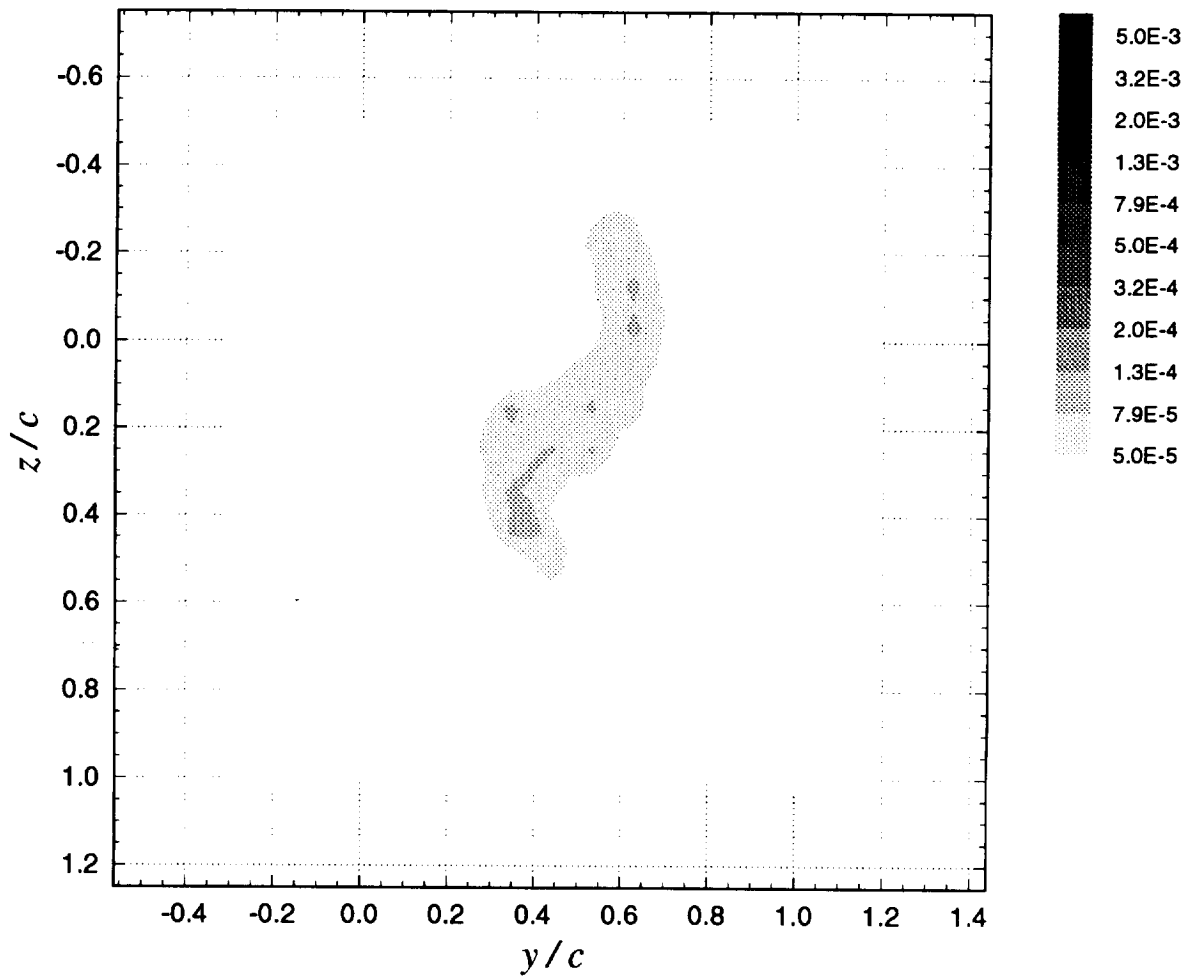


**Figure 3.37g** Contours of axial shear stress magnitude  $(\tau_a / U_{ref}^2)$  for vortex centerline stagnating on blade leading edge ( $\Delta = 0$ ):  $x/c = 30$ ,  $\alpha_1 = 5^\circ$ ,  $\alpha_2 = 5^\circ$ , no spoiler



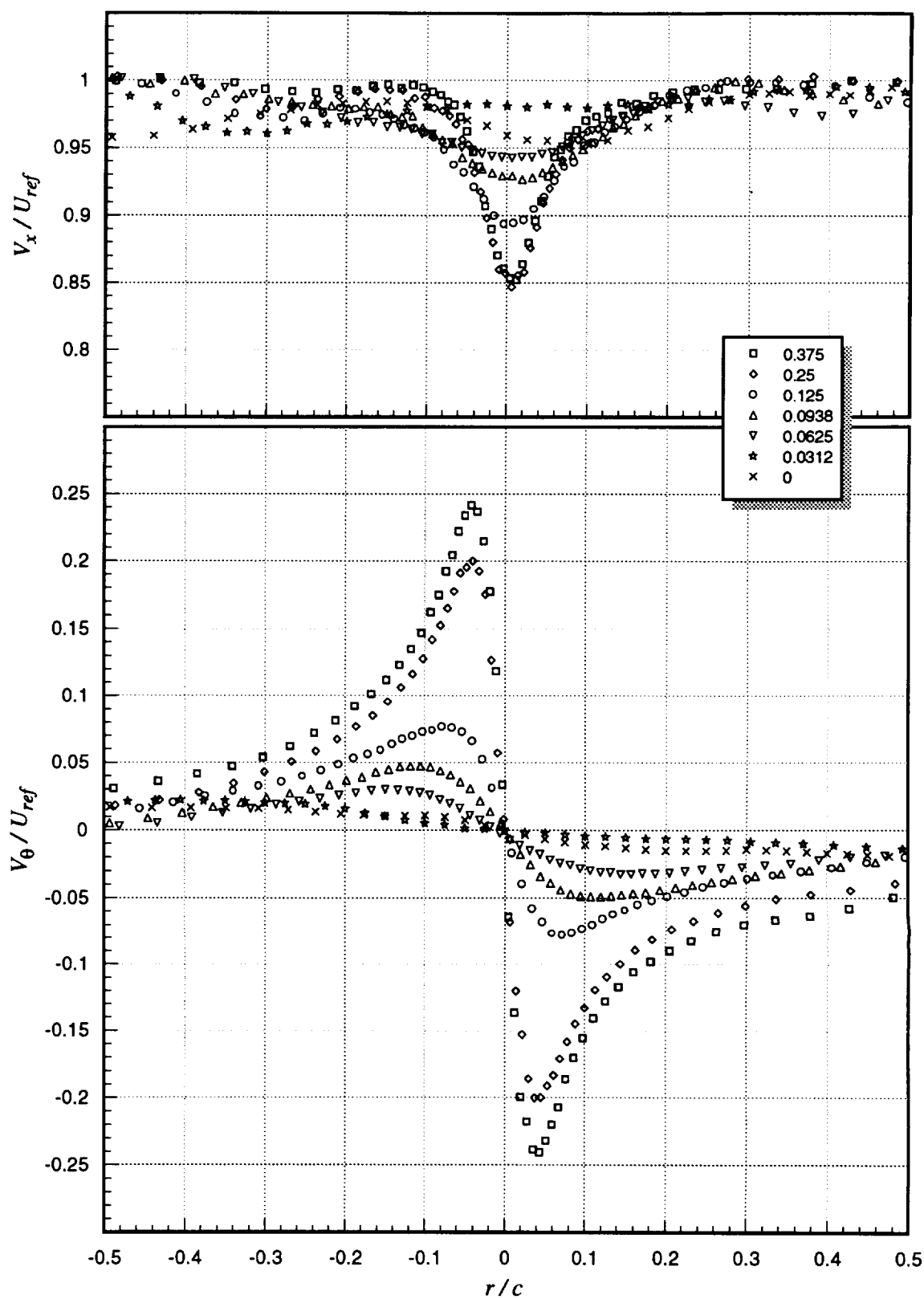


**Figure 3.38** Mean axial ( $V_x$ ) and tangential ( $V_\theta$ ) velocities (measured along  $z$ -wise profiles through the vortex core center) as a function of blade–vortex separation ( $\Delta$ ) for ‘suction side’ passages:  $x/c = 30$ ,  $\alpha_1 = 5^\circ$ ,  $\alpha_2 = 0^\circ$ , no spoiler. Legend lists  $\Delta/c$  values.

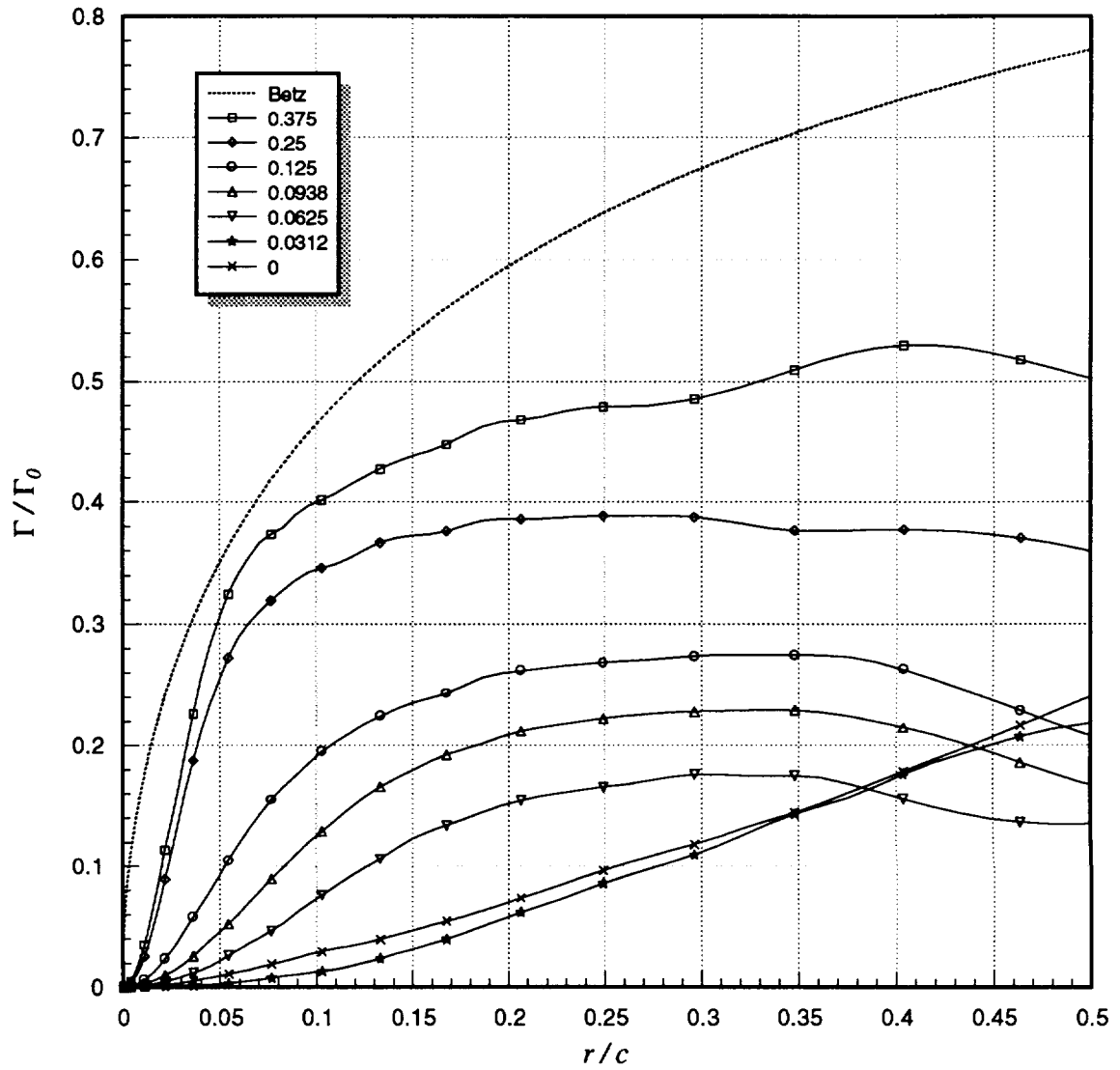


**Figure 3.39** Circulation distributions (assuming axisymmetric flow) as a function of blade-vortex separation ( $\Delta$ ) for 'suction side' passages:  $x/c = 30$ ,  $\alpha_1 = 5^\circ$ ,  $\alpha_2 = 0^\circ$ , no spoiler. Legend lists  $\Delta/c$  values.

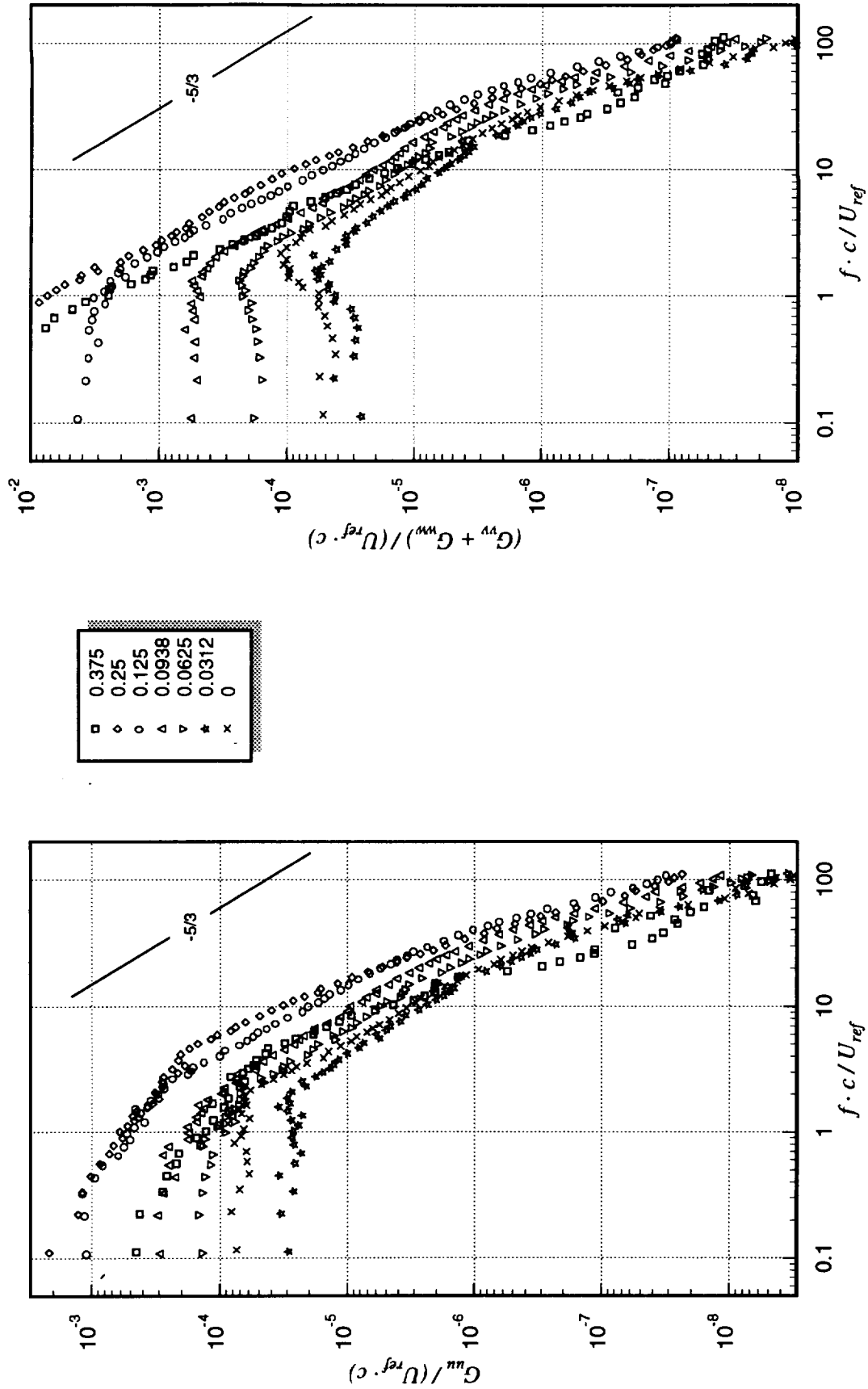


**Figure 3.40** Core center velocity autospectra as a function of blade-vortex separation ( $\Delta$ ) for 'suction side' passages:  $x/c = 30$ ,  $\alpha_1 = 5^\circ$ ,  $\alpha_2 = 0^\circ$ , no spoiler. Legend lists  $\Delta/c$  values.

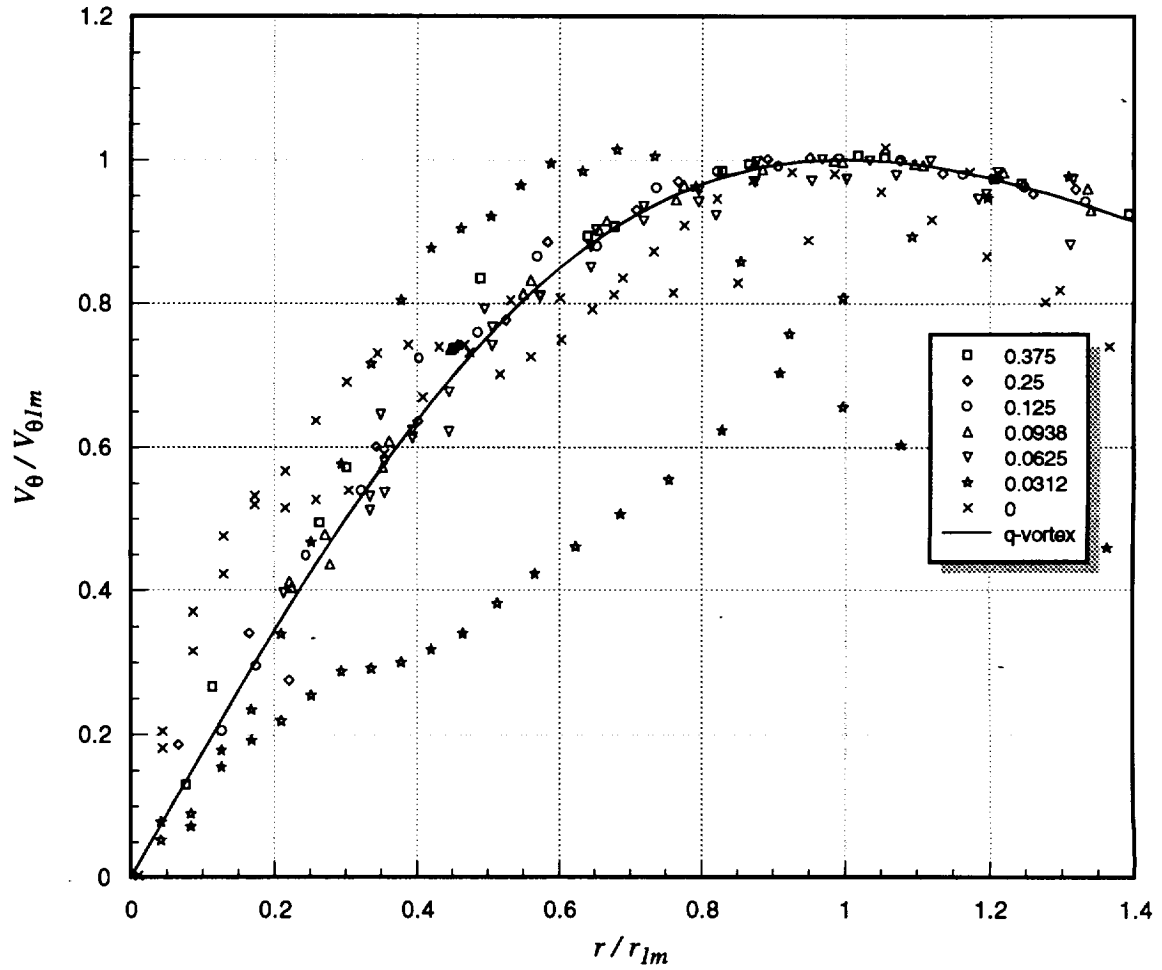


**Figure 3.41** Mean tangential ( $V_\theta$ ) velocities (measured along  $z$ -wise profiles through the vortex core center), normalized on measured peak tangential velocity ( $V_{\theta lm}$ ), as a function of blade–vortex separation ( $\Delta$ ):  $x/c = 30$ ,  $\alpha_1 = 5^\circ$ ,  $\alpha_2 = 0^\circ$ , no spoiler. Legend lists  $\Delta/c$  values.

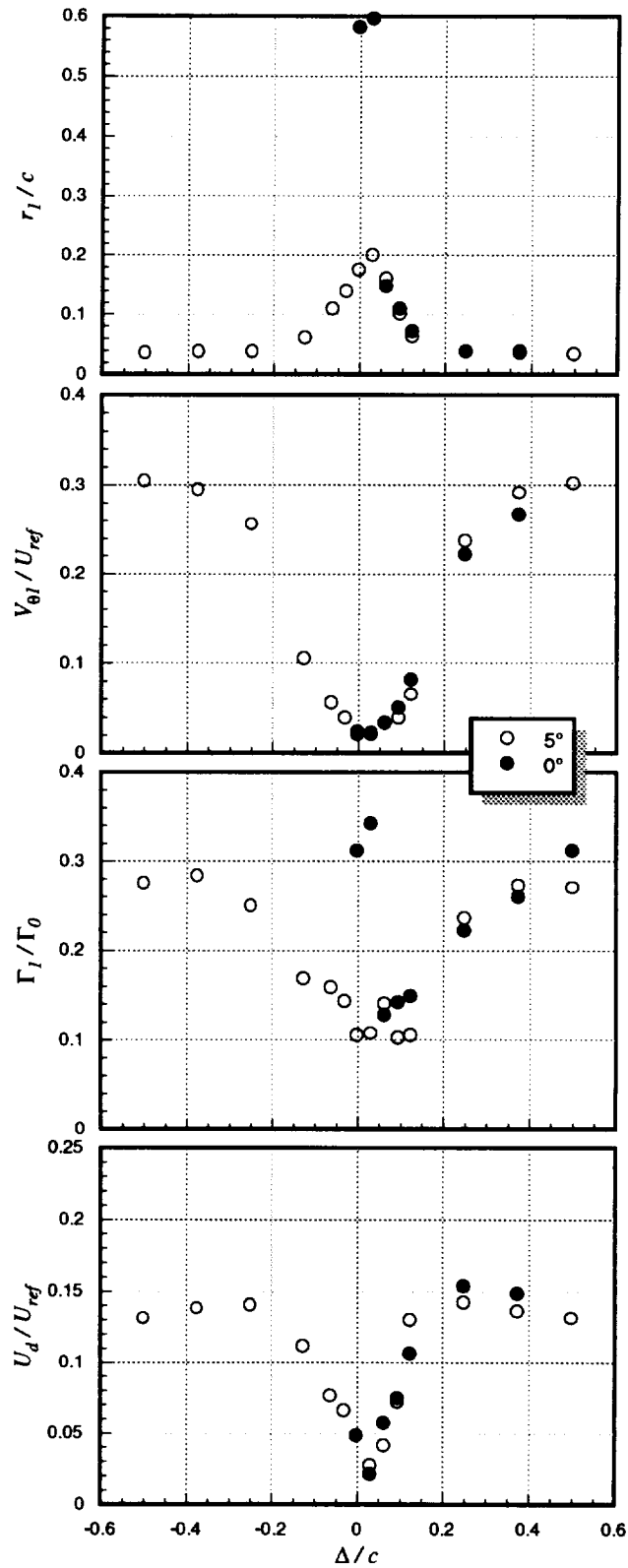


**Figure 3.42** Core parameters (radius,  $r_1$ ; peak tangential velocity,  $V_{\theta 1}$ ; circulation,  $\Gamma_1$ ; and axial velocity deficit,  $U_d$ ) as a function of blade–vortex separation ( $\Delta$ ) for different blade angles of attack ( $\alpha_2$ ):  $x/c = 30$ ,  $\alpha_1 = 5^\circ$ , no spoiler. Legend lists  $\alpha_2$  values.

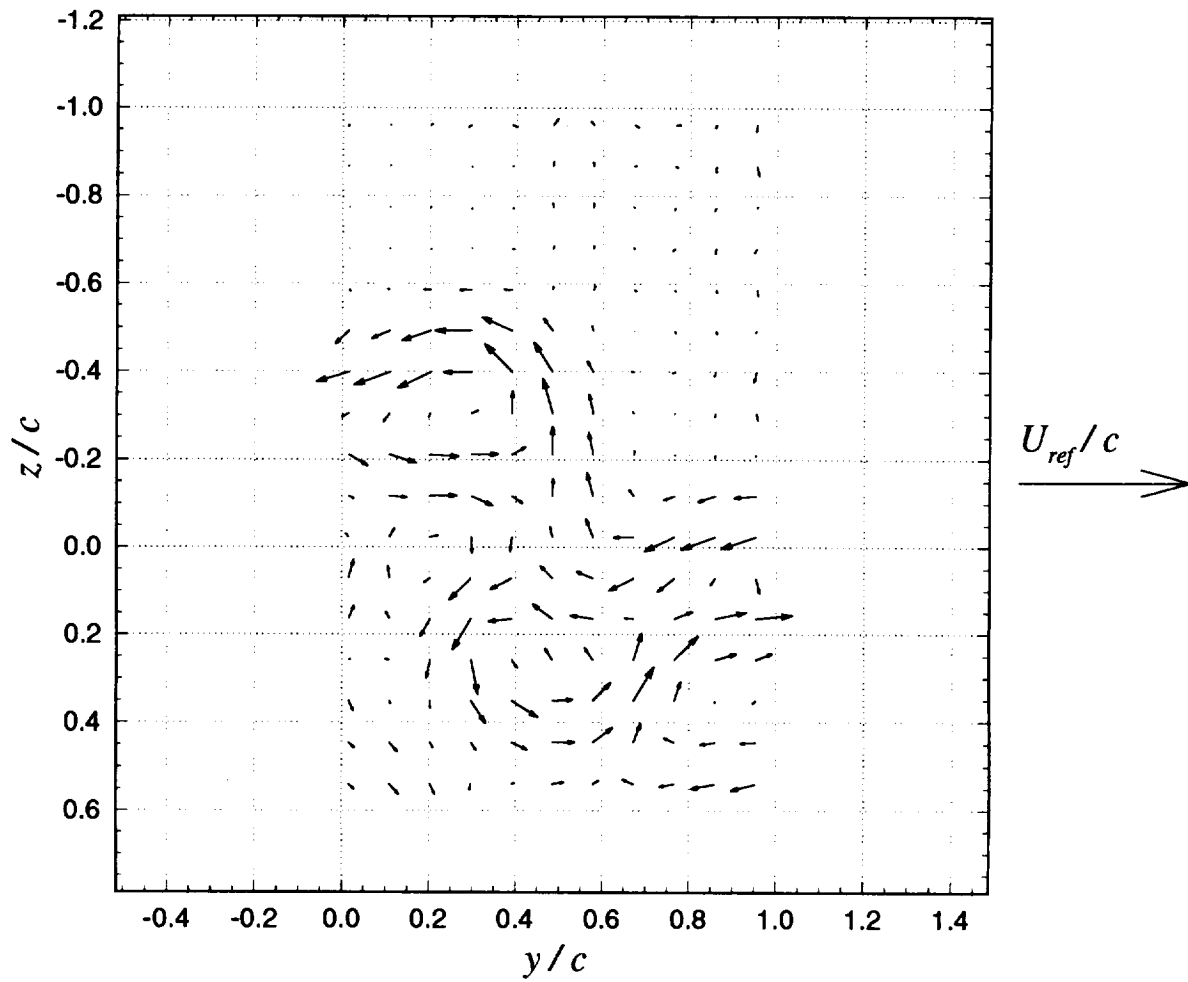


**Figure 3.43a** Mean cross-flow vorticity vectors ( $\Omega_y \cdot c / U_{ref}$ ,  $\Omega_z \cdot c / U_{ref}$ ) for vortex centerline stagnating on blade leading edge ( $\Delta = 0$ ):  $x/c = 30$ ,  $\alpha_1 = 5^\circ$ ,  $\alpha_2 = 0^\circ$ , no spoiler

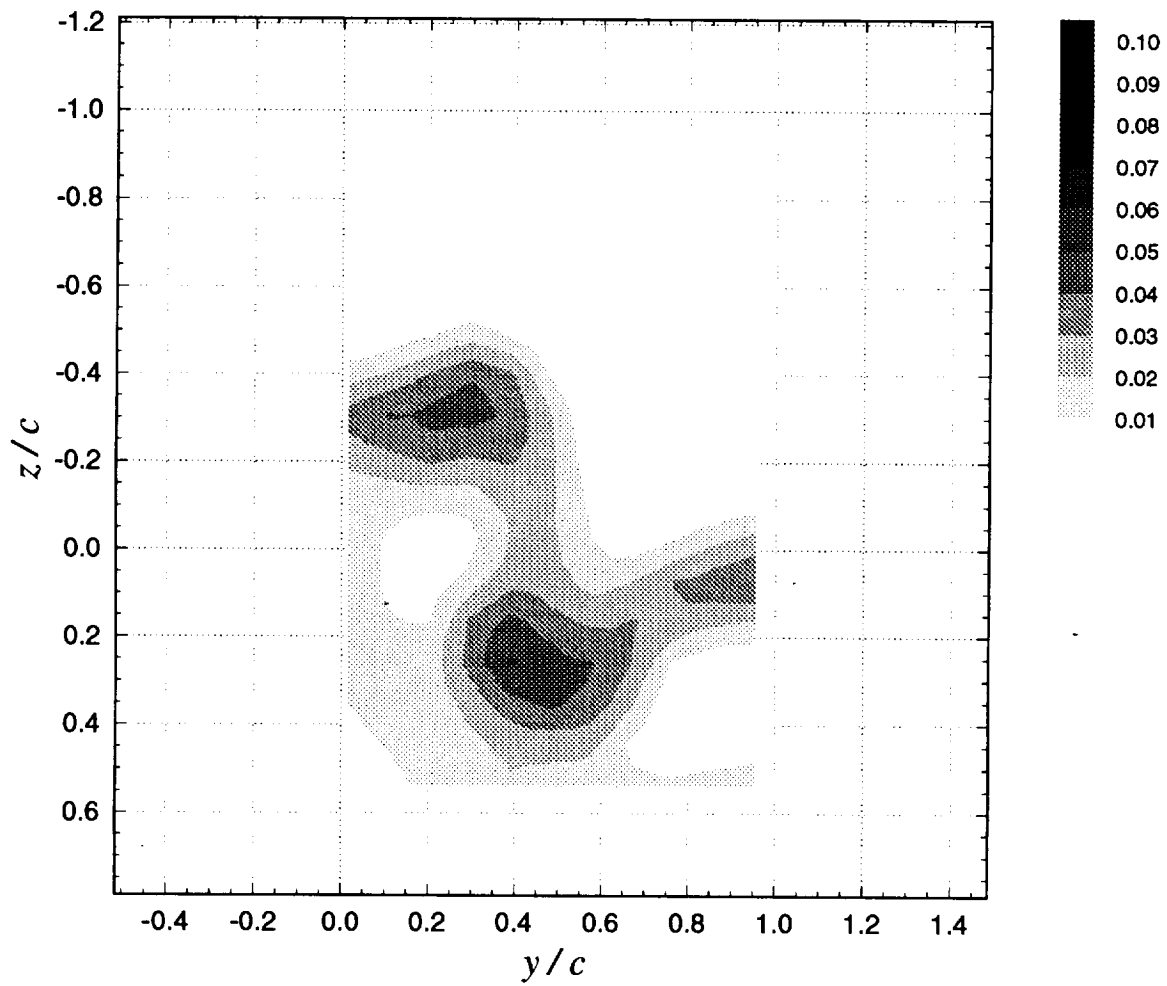


**Figure 3.43b** Contours of mean axial velocity deficit  $((U_{ref} - U) / U_{ref})$  for vortex centerline stagnating on blade leading edge ( $\Delta = 0$ ):  $x/c = 30$ ,  $\alpha_1 = 5^\circ$ ,  $\alpha_2 = 0^\circ$ , no spoiler

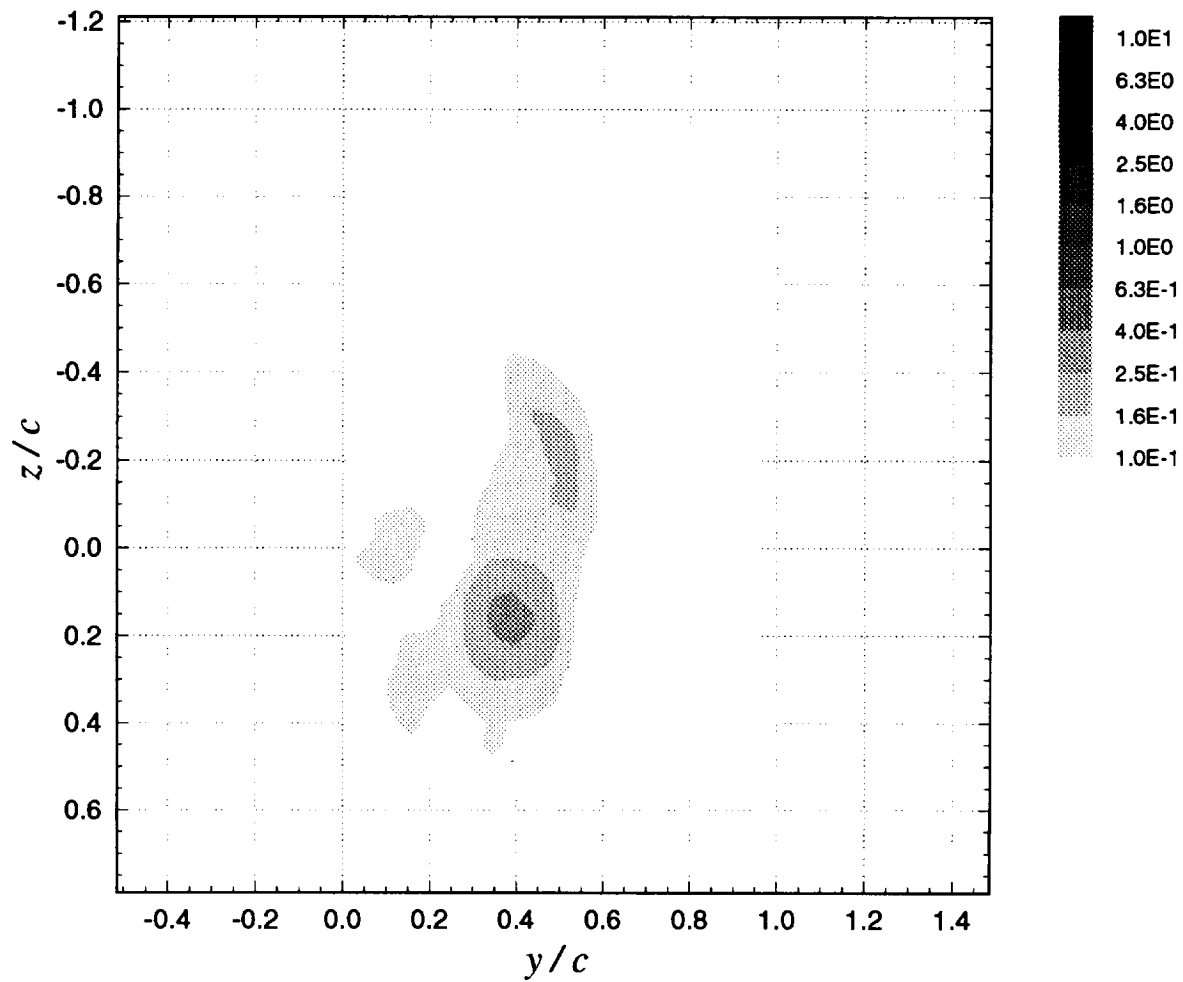


**Figure 3.43c** Contours of mean axial vorticity ( $\Omega_x \cdot c / U_{ref}$ ) for vortex centerline stagnating on blade leading edge ( $\Delta = 0$ ):  $x/c = 30$ ,  $\alpha_l = 5^\circ$ ,  $\alpha_2 = 0^\circ$ , no spoiler



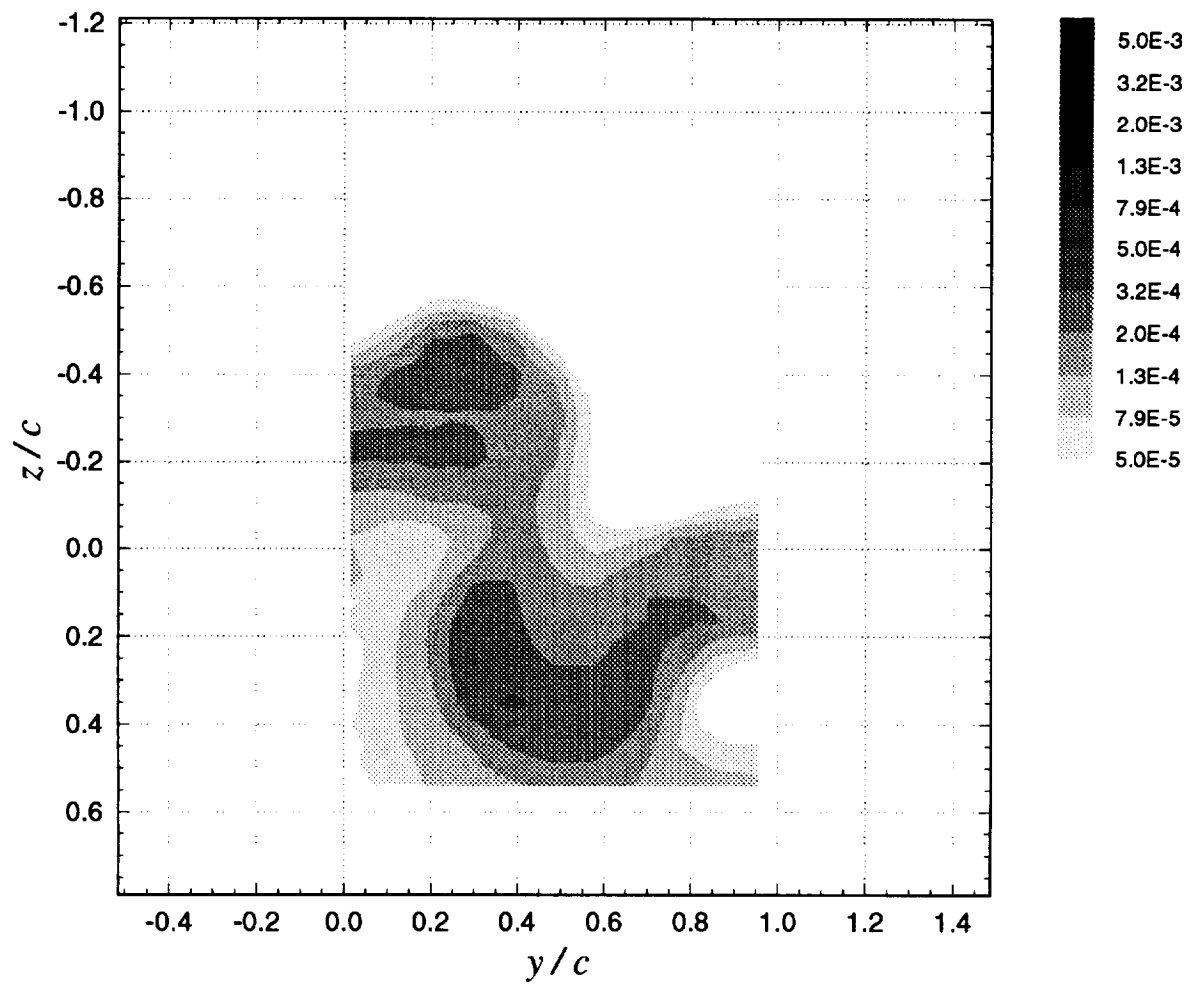


**Figure 3.43d** Contours of axial normal turbulent stress ( $\overline{u^2} / U_{ref}^2$ ) for vortex centerline stagnating on blade leading edge ( $\Delta = 0$ ):  $x/c = 30$ ,  $\alpha_1 = 5^\circ$ ,  $\alpha_2 = 0^\circ$ , no spoiler

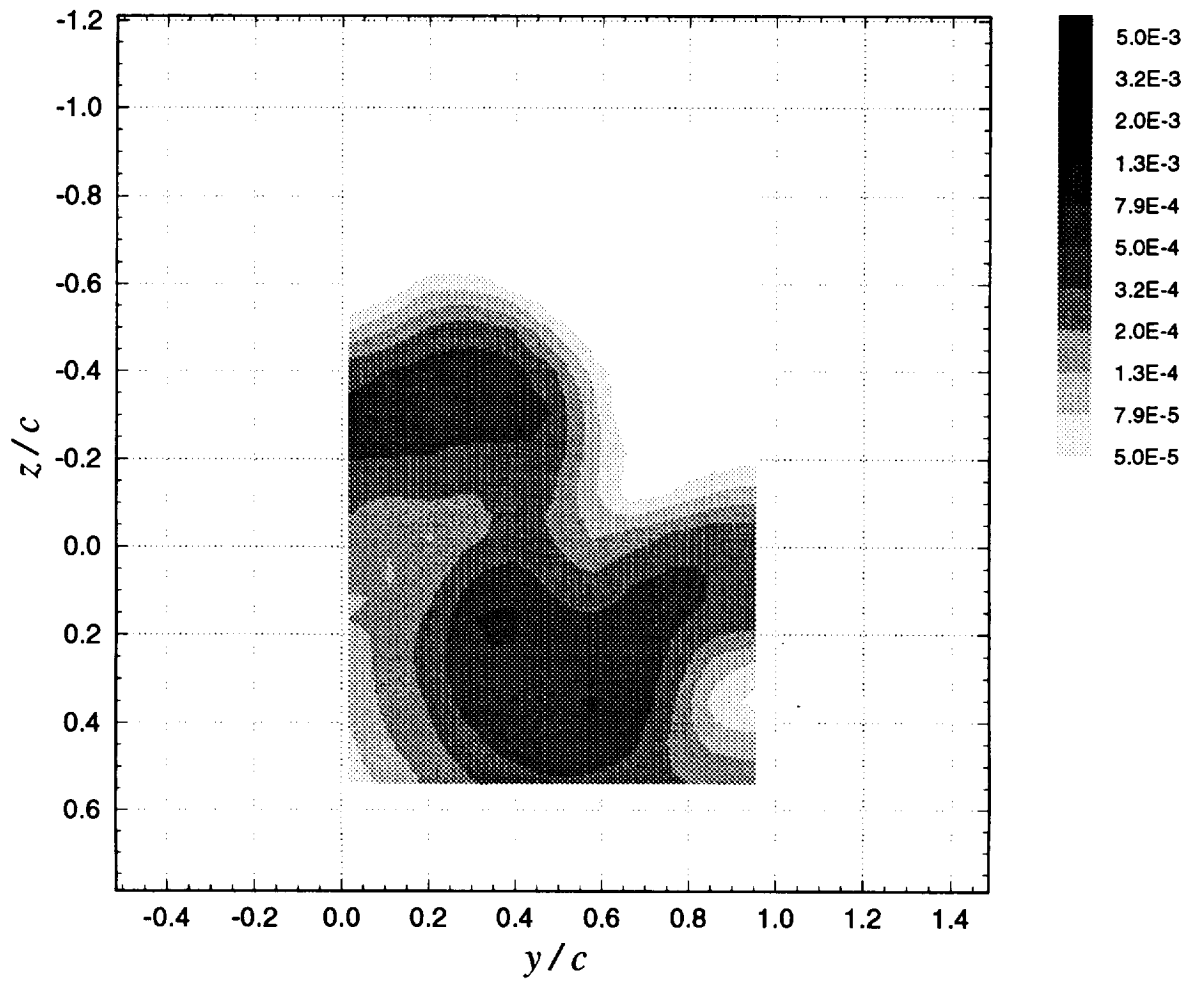


**Figure 3.43e** Contours of summed cross-flow normal turbulent stresses  $(\overline{v^2} + \overline{w^2}) / U_{ref}^2$  for vortex centerline stagnating on blade leading edge ( $\Delta = 0$ ):  $x/c = 30$ ,  $\alpha_1 = 5^\circ$ ,  $\alpha_2 = 0^\circ$ , no spoiler

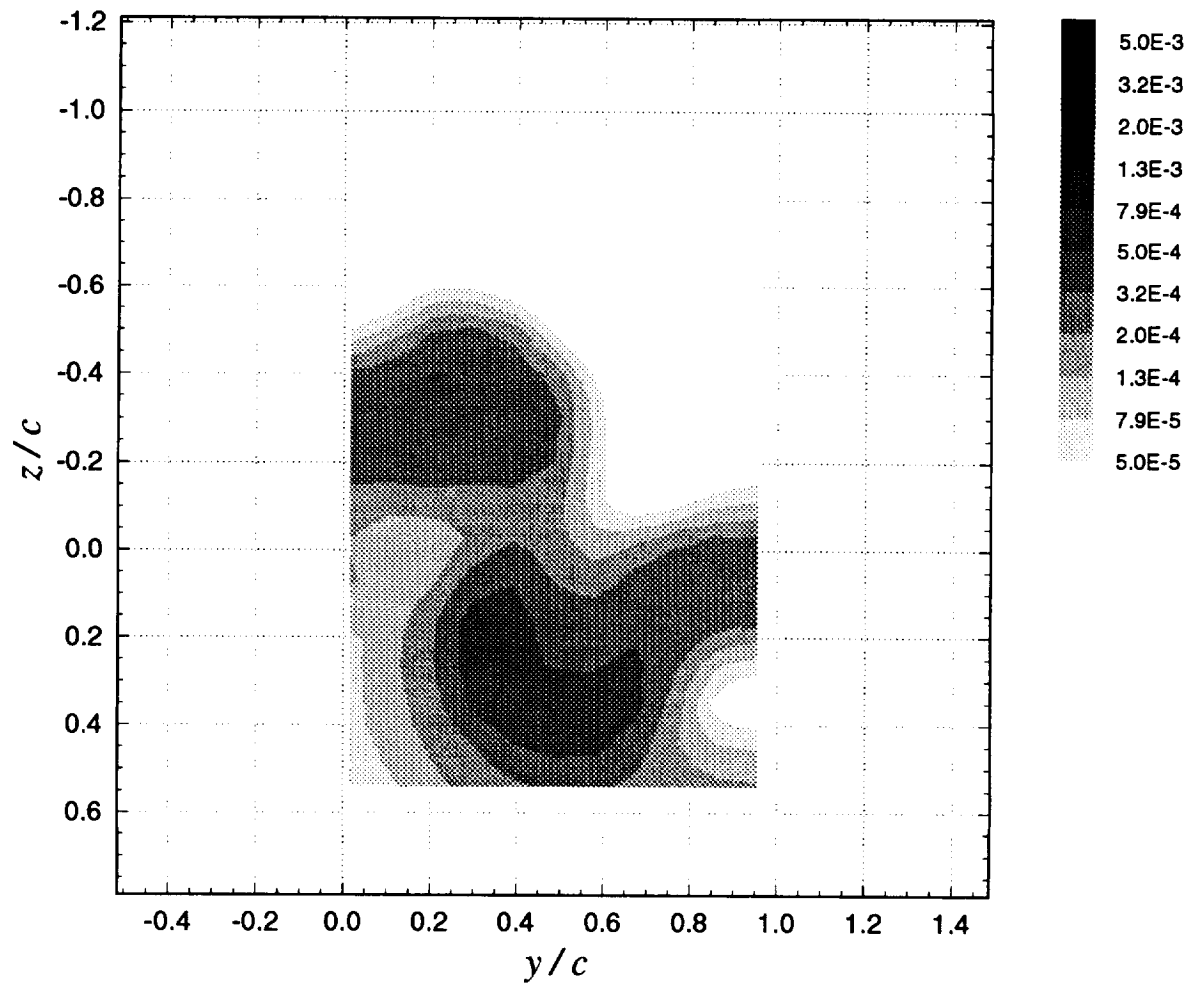


**Figure 3.43f** Contours of turbulent kinetic energy ( $k / U_{ref}^2$ ) for vortex centerline stagnating on blade leading edge ( $\Delta = 0$ ):  $x / c = 30$ ,  $\alpha_1 = 5^\circ$ ,  $\alpha_2 = 0^\circ$ , no spoiler

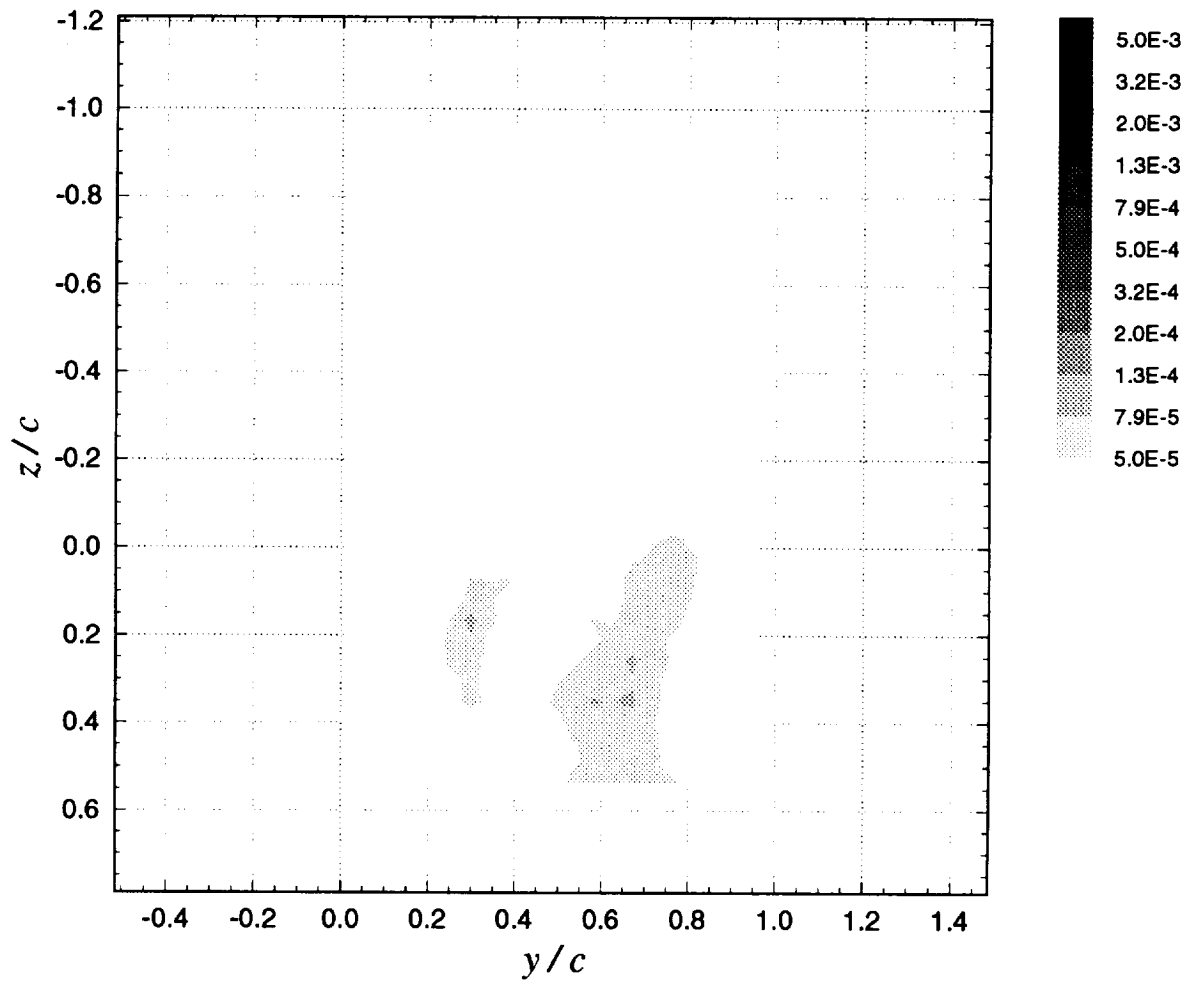


**Figure 3.43g** Contours of axial shear stress magnitude ( $\tau_a / U_{ref}^2$ ) for vortex centerline stagnating on blade leading edge ( $\Delta = 0$ ):  $x / c = 30$ ,  $\alpha_l = 5^\circ$ ,  $\alpha_2 = 0^\circ$ , no spoiler

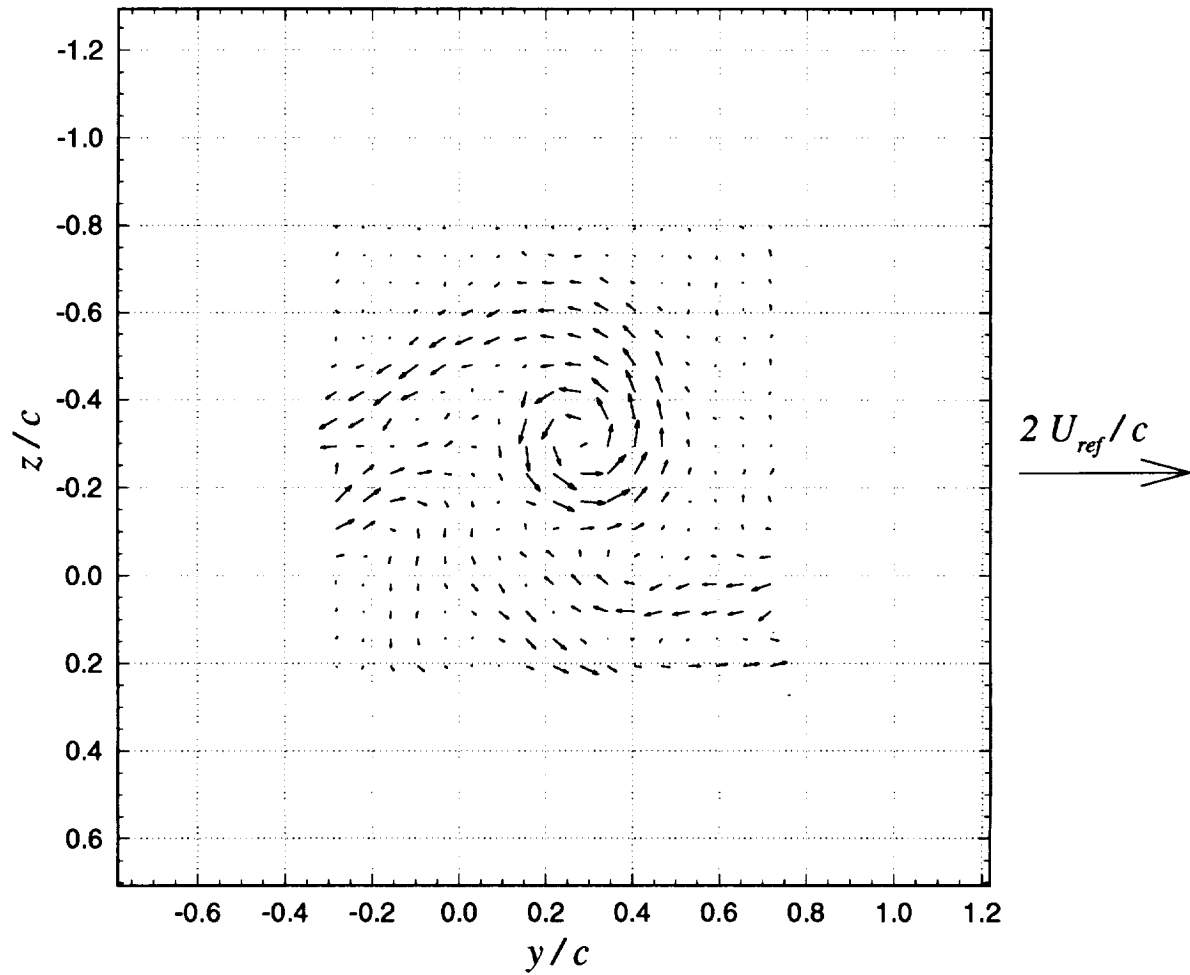


**Figure 3.44a** Mean cross-flow vorticity vectors ( $\Omega_y \cdot c / U_{ref}$ ,  $\Omega_z \cdot c / U_{ref}$ ) for suction side passage of  $\Delta / c = 0.0625$ :  $x / c = 30$ ,  $\alpha_l = 5^\circ$ ,  $\alpha_2 = 0^\circ$ , no spoiler

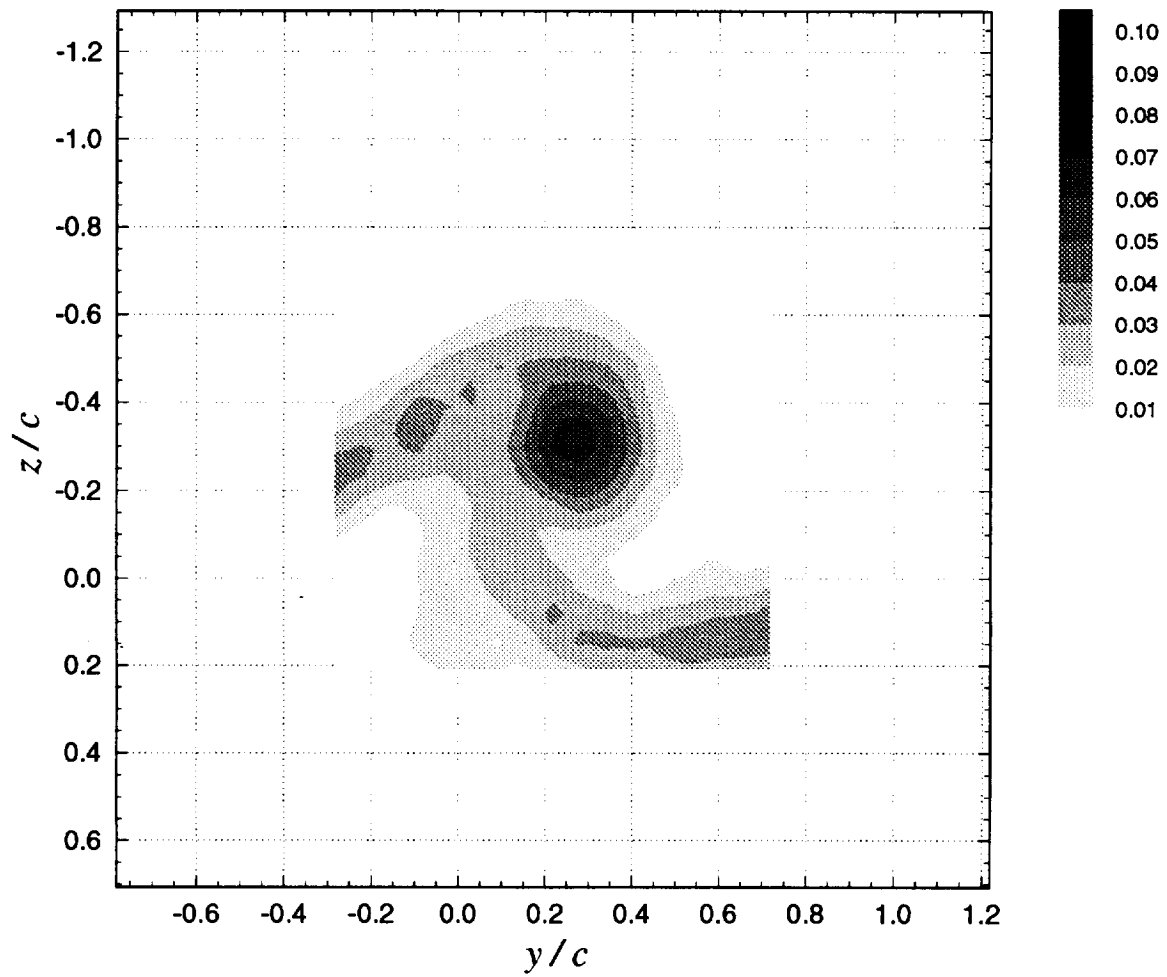


**Figure 3.44b** Contours of mean axial velocity deficit  $((U_{ref} - U) / U_{ref})$  for suction side passage of  $\Delta/c = 0.0625$ :  $x/c = 30$ ,  $\alpha_l = 5^\circ$ ,  $\alpha_2 = 0^\circ$ , no spoiler

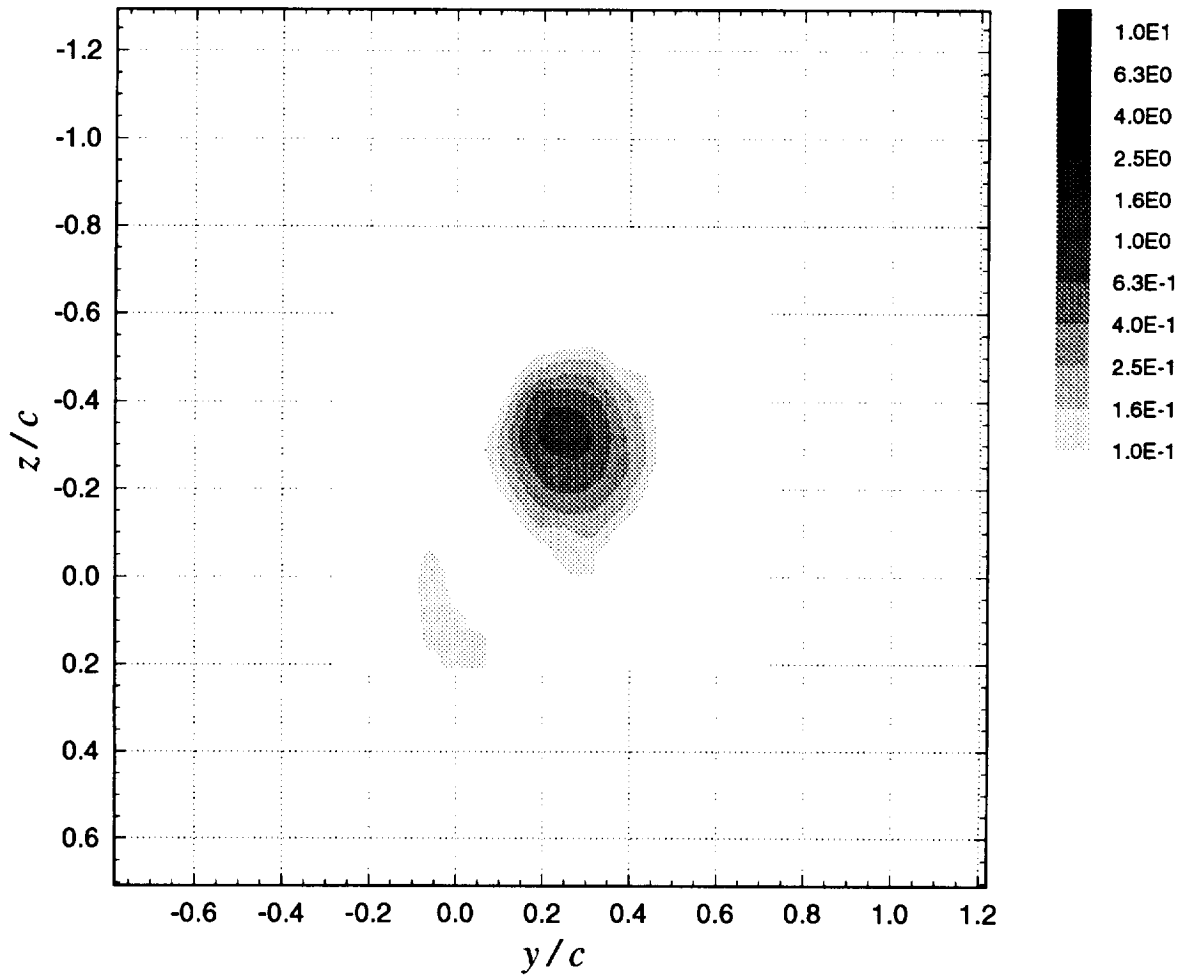


**Figure 3.44c** Contours of mean axial vorticity ( $\Omega_x \cdot c / U_{ref}$ ) for suction side passage of  $\Delta/c = 0.0625$ :  $x/c = 30$ ,  $\alpha_1 = 5^\circ$ ,  $\alpha_2 = 0^\circ$ , no spoiler

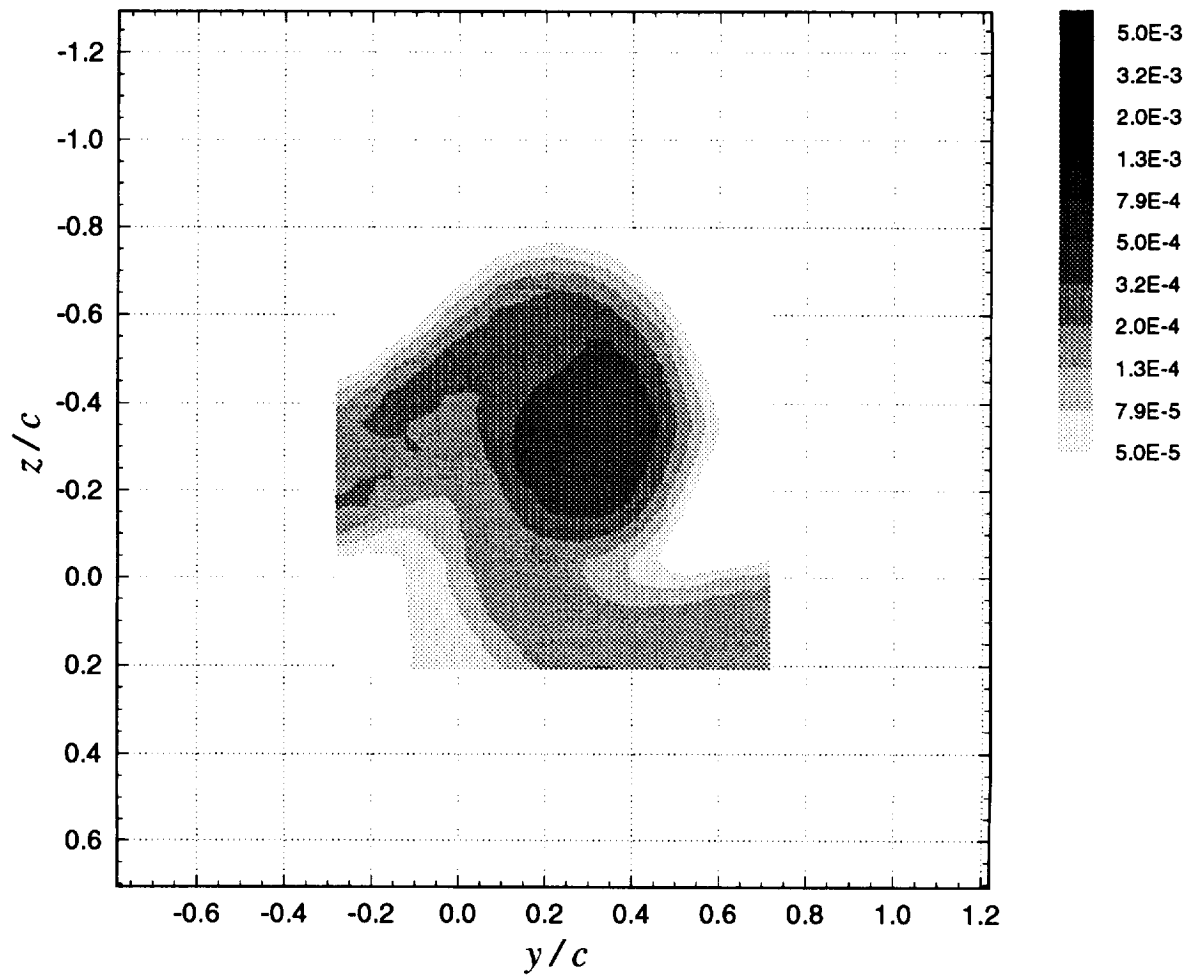


**Figure 3.44d** Contours of axial normal turbulent stress ( $\overline{u^2} / U_{ref}^2$ ) for suction side passage of  $\Delta/c = 0.0625$ :  $x/c = 30$ ,  $\alpha_1 = 5^\circ$ ,  $\alpha_2 = 0^\circ$ , no spoiler



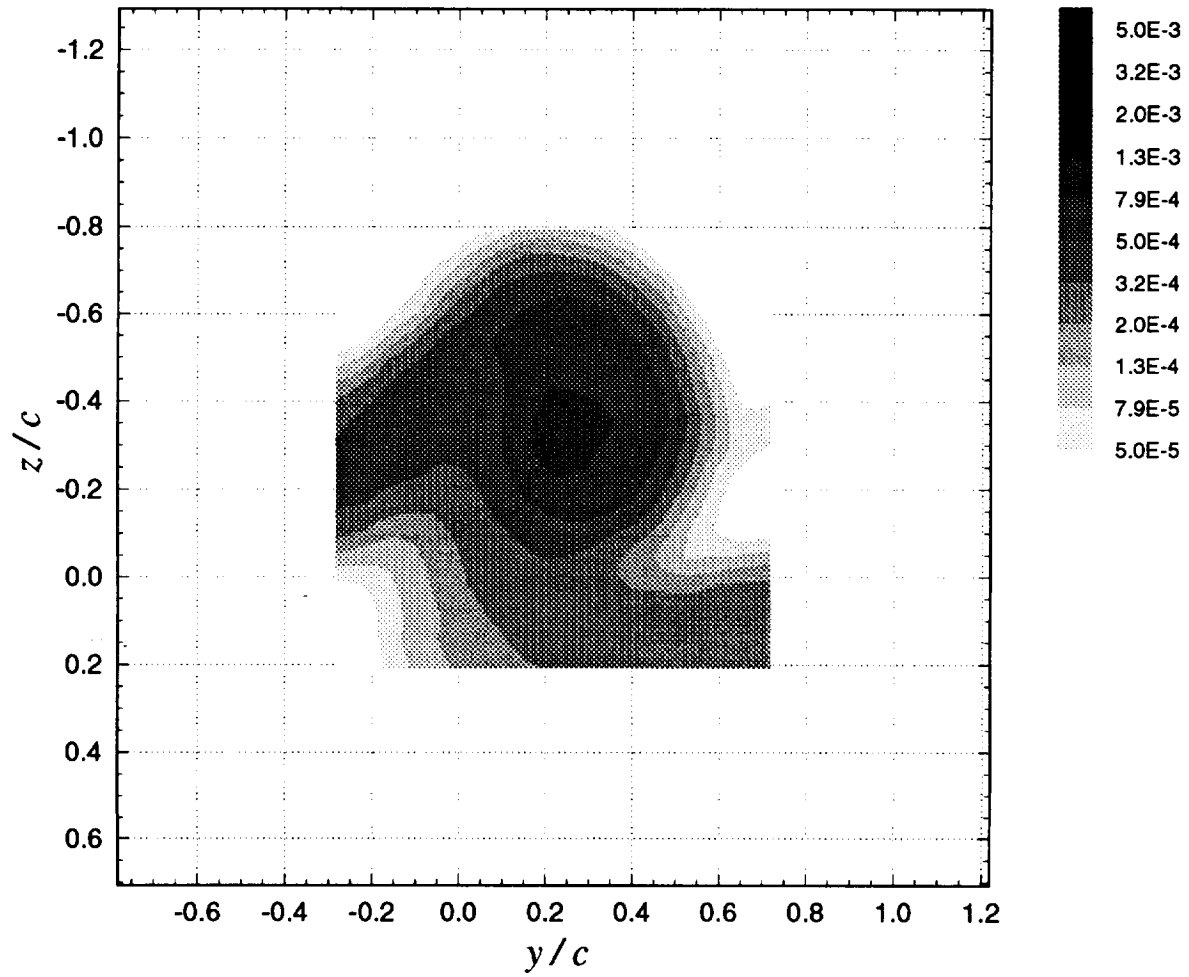


**Figure 3.44e** Contours of summed cross-flow normal turbulent stresses  $(\overline{v^2} + \overline{w^2}) / U_{ref}^2$  for suction side passage of  $\Delta/c = 0.0625$ :  $x/c = 30$ ,  $\alpha_1 = 5^\circ$ ,  $\alpha_2 = 0^\circ$ , no spoiler

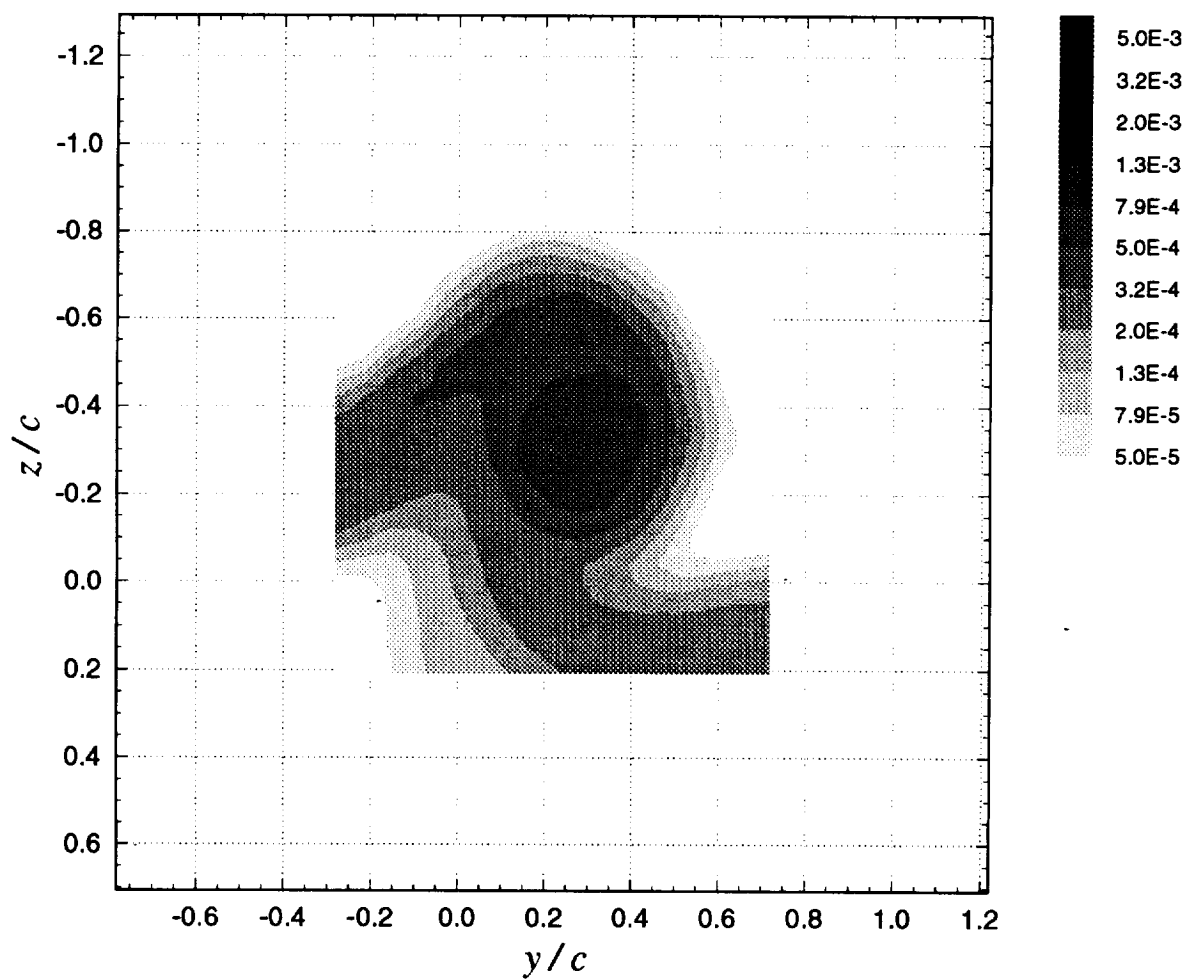


**Figure 3.44f** Contours of turbulent kinetic energy ( $k / U_{ref}^2$ ) for suction side passage of  $\Delta/c = 0.0625$ :  $x/c = 30$ ,  $\alpha_l = 5^\circ$ ,  $\alpha_2 = 0^\circ$ , no spoiler

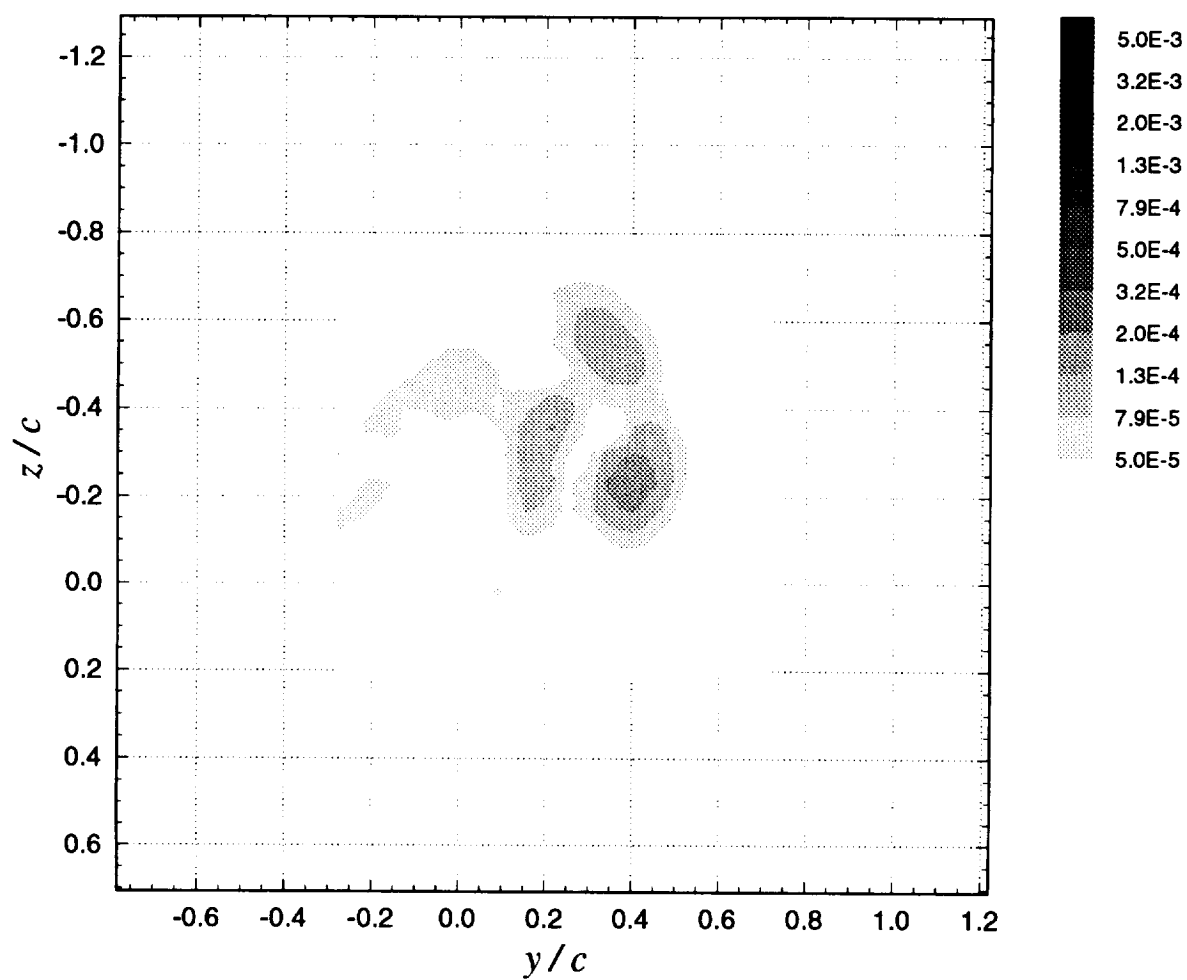


**Figure 3.44g** Contours of axial shear stress magnitude ( $\tau_a / U_{ref}^2$ ) for suction side passage of  $\Delta/c = 0.0625$ :  $x/c = 30$ ,  $\alpha_1 = 5^\circ$ ,  $\alpha_2 = 0^\circ$ , no spoiler

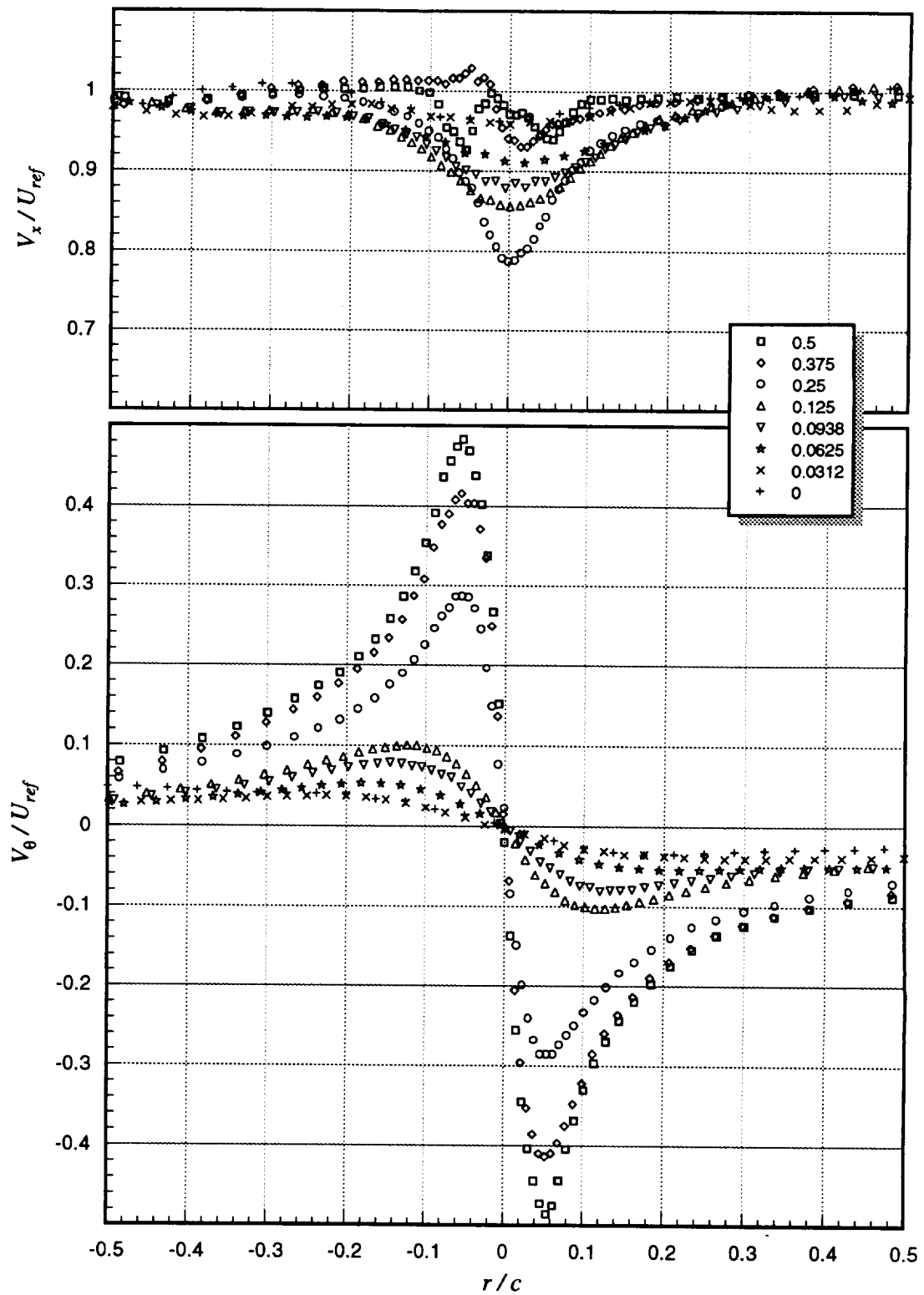


**Figure 3.45** Mean axial ( $V_x$ ) and tangential ( $V_\theta$ ) velocities (measured along  $z$ -wise profiles through the vortex core center) as a function of blade–vortex separation ( $\Delta$ ) for suction side passages:  $x/c = 30$ ,  $\alpha_1 = 10^\circ$ ,  $\alpha_2 = 5^\circ$ , no spoiler. Legend lists  $\Delta/c$  values.

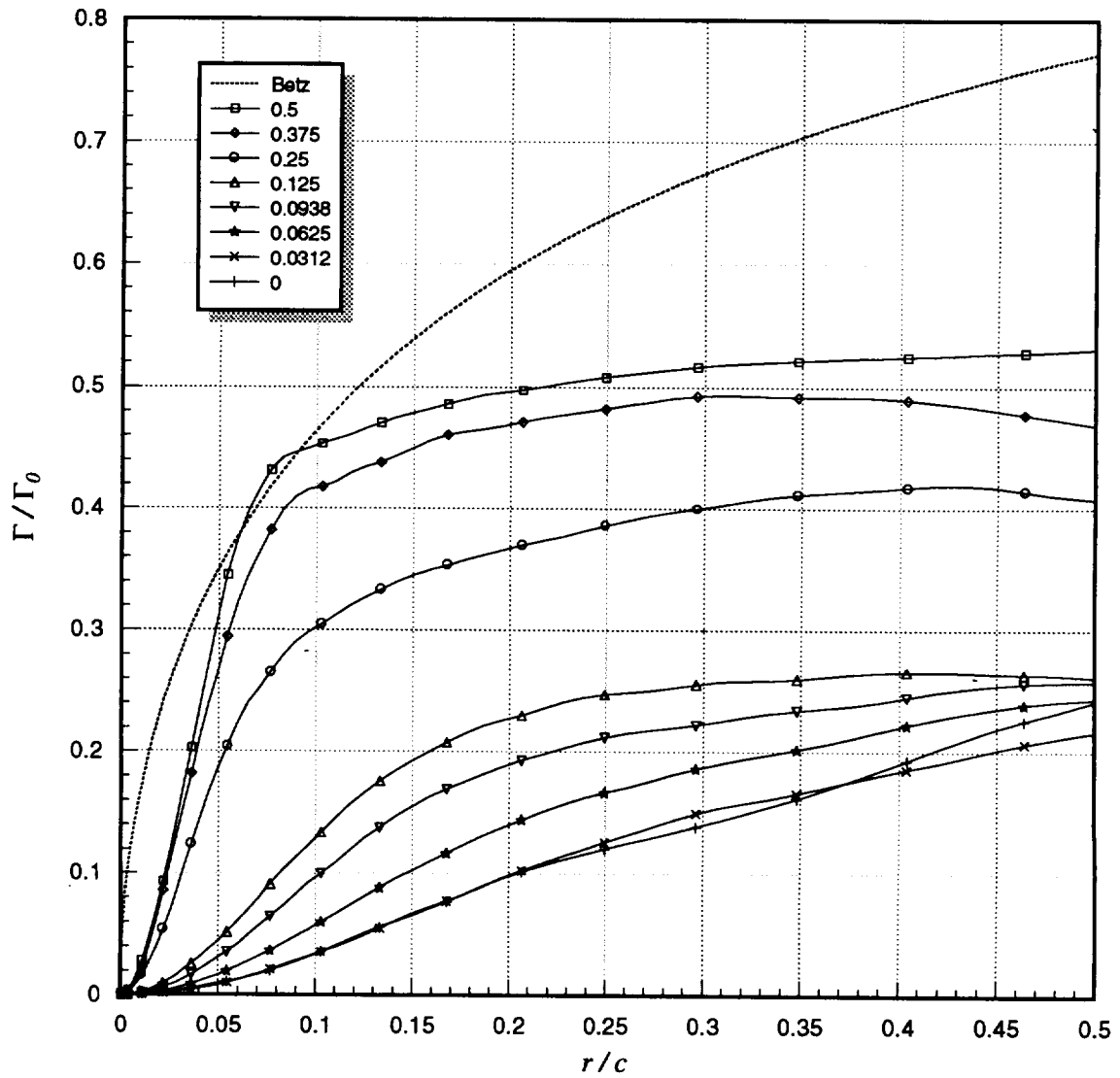


**Figure 3.46** Circulation distributions (assuming axisymmetric flow) as a function of blade-vortex separation ( $\Delta$ ) for suction side passages:  $x/c = 30$ ,  $\alpha_1 = 10^\circ$ ,  $\alpha_2 = 5^\circ$ , no spoiler. Legend lists  $\Delta/c$  values.

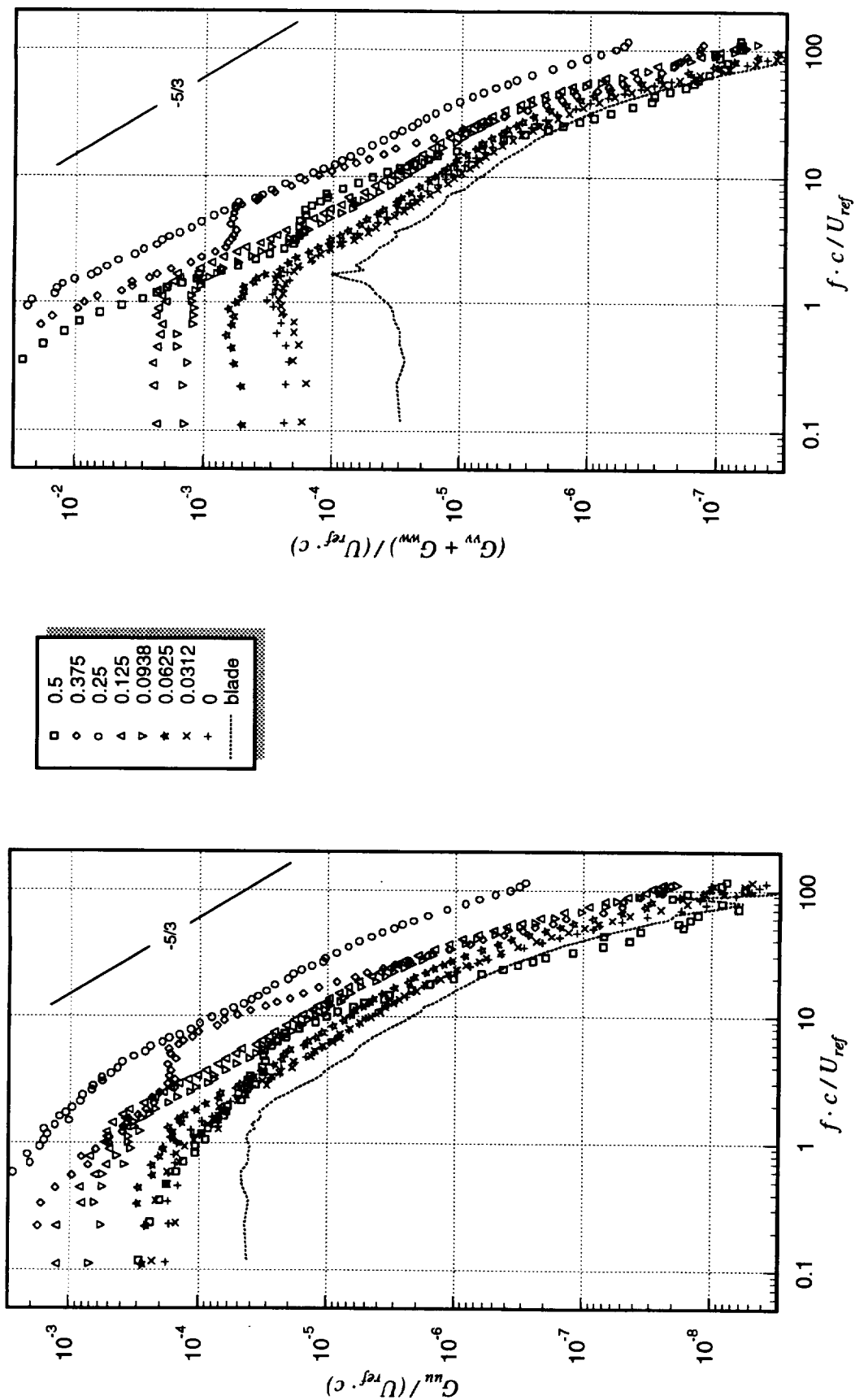
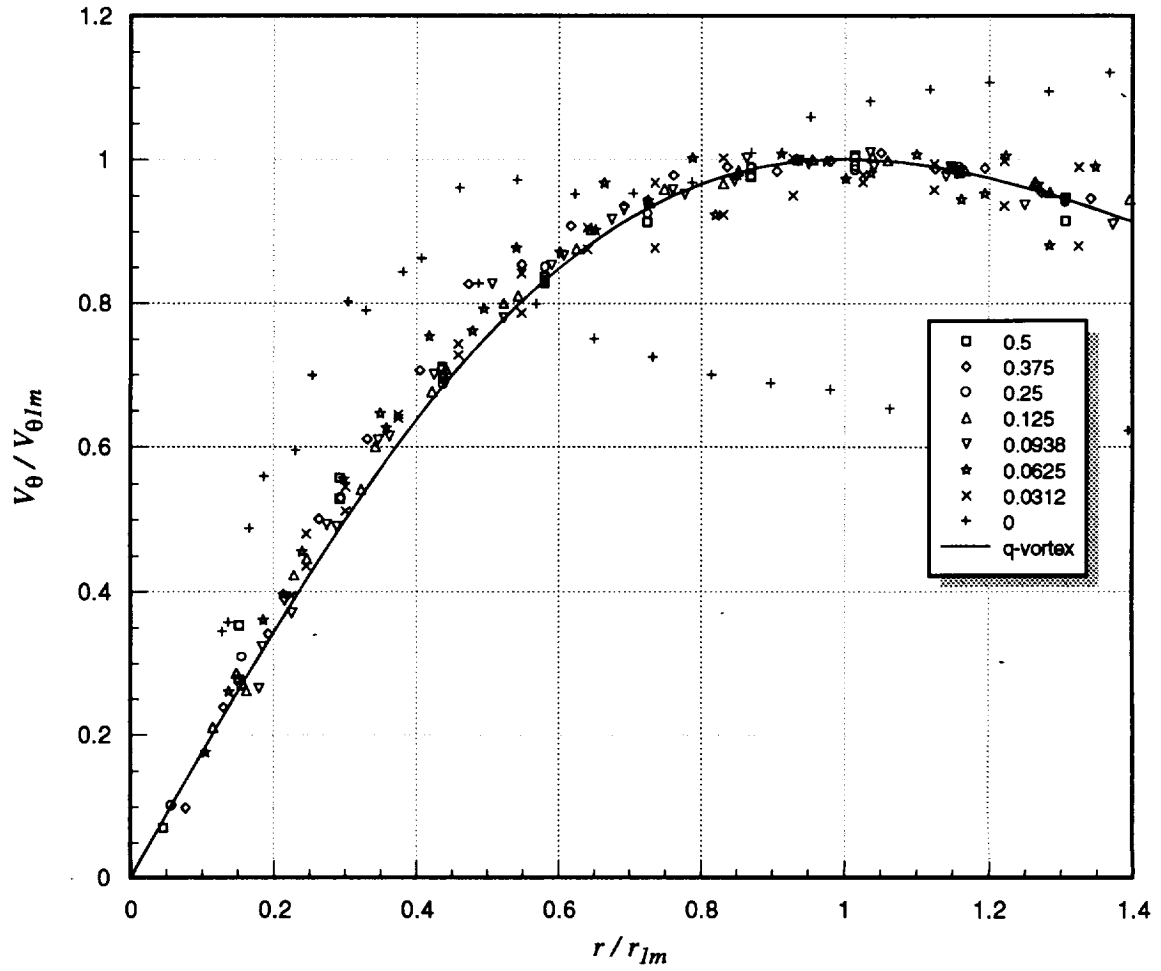
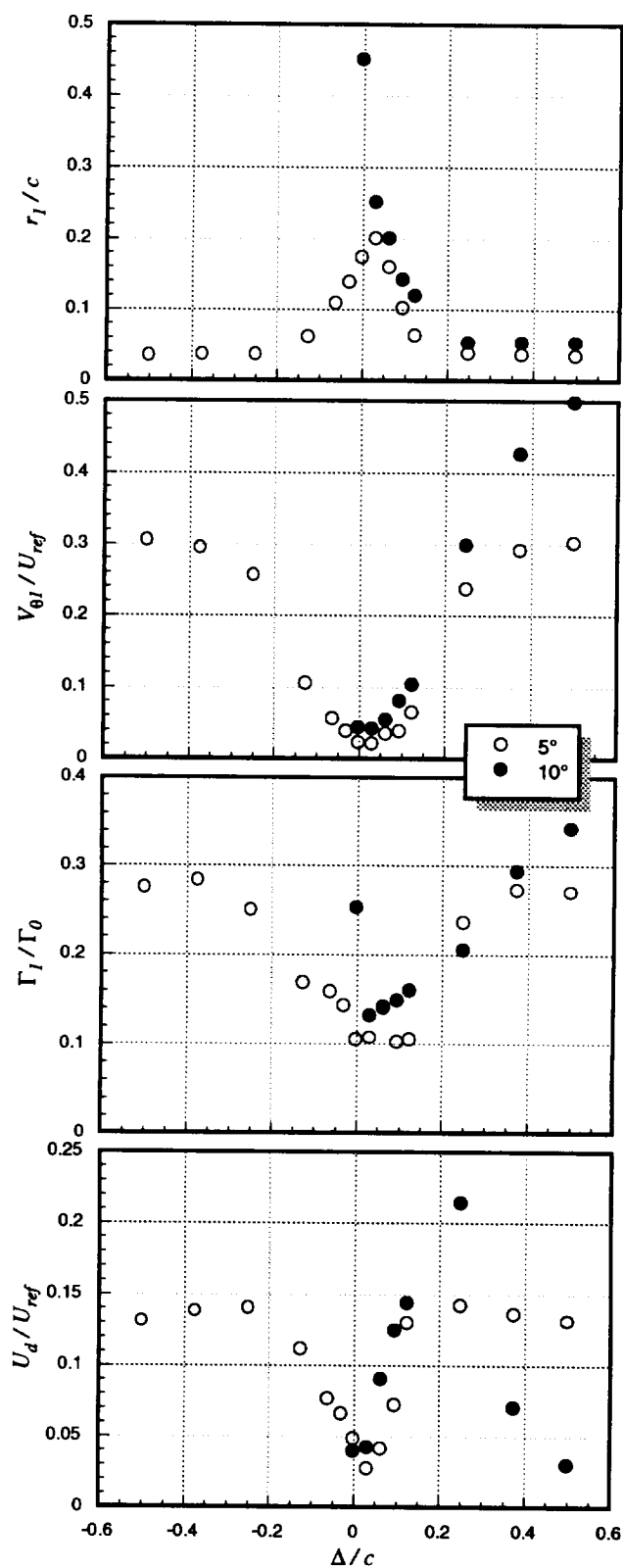


Figure 3.47 Core center velocity autospectra as a function of blade–vortex separation ( $\Delta$ ) for suction side passages:  $x/c = 30$ ,  $\alpha_1 = 10^\circ$ ,  $\alpha_2 = 5^\circ$ , no spoiler. Legend lists  $\Delta/c$  values. Autospectra measured in undisturbed portion of interaction blade wake at  $x/c = 30$  also included (marked as “blade” in legend).



**Figure 3.48** Mean tangential ( $V_\theta$ ) velocities (measured along  $z$ -wise profiles through the vortex core center), normalized on measured peak tangential velocity ( $V_{\theta 1m}$ ), as a function of blade–vortex separation ( $\Delta$ ):  $x/c = 30$ ,  $\alpha_1 = 10^\circ$ ,  $\alpha_2 = 5^\circ$ , no spoiler. Legend lists  $\Delta/c$  values.



**Figure 3.49** Core parameters (radius,  $r_I$ ; peak tangential velocity,  $V_{\theta I}$ ; circulation,  $\Gamma_I$ ; and axial velocity deficit,  $U_d$ ) as a function of blade-vortex separation ( $\Delta$ ) for different initial vortex strengths (controlled by  $\alpha_1$ ):  $x/c = 30$ ,  $\alpha_2 = 5^\circ$ , no spoiler. Legend lists  $\alpha_1$  values.



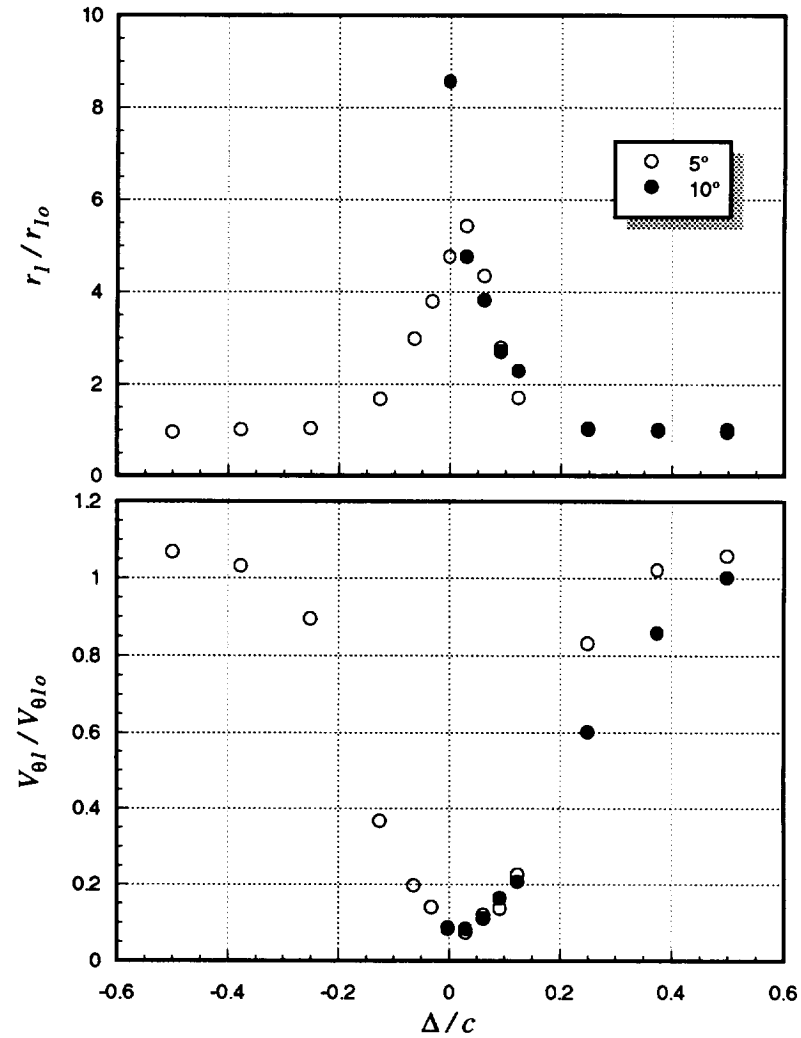


**Figure 3.50** Normalized core parameters (radius,  $r_1/r_{1o}$ ; and peak tangential velocity,  $V_{\theta 1}/V_{\theta 1o}$ ) as a function of blade-vortex separation ( $\Delta$ ) for different initial vortex strengths (controlled by generator angle of attack,  $\alpha_1$ ):  $x/c = 30$ ,  $\alpha_2 = 5^\circ$ , no spoiler. Legend lists  $\alpha_1$  values.

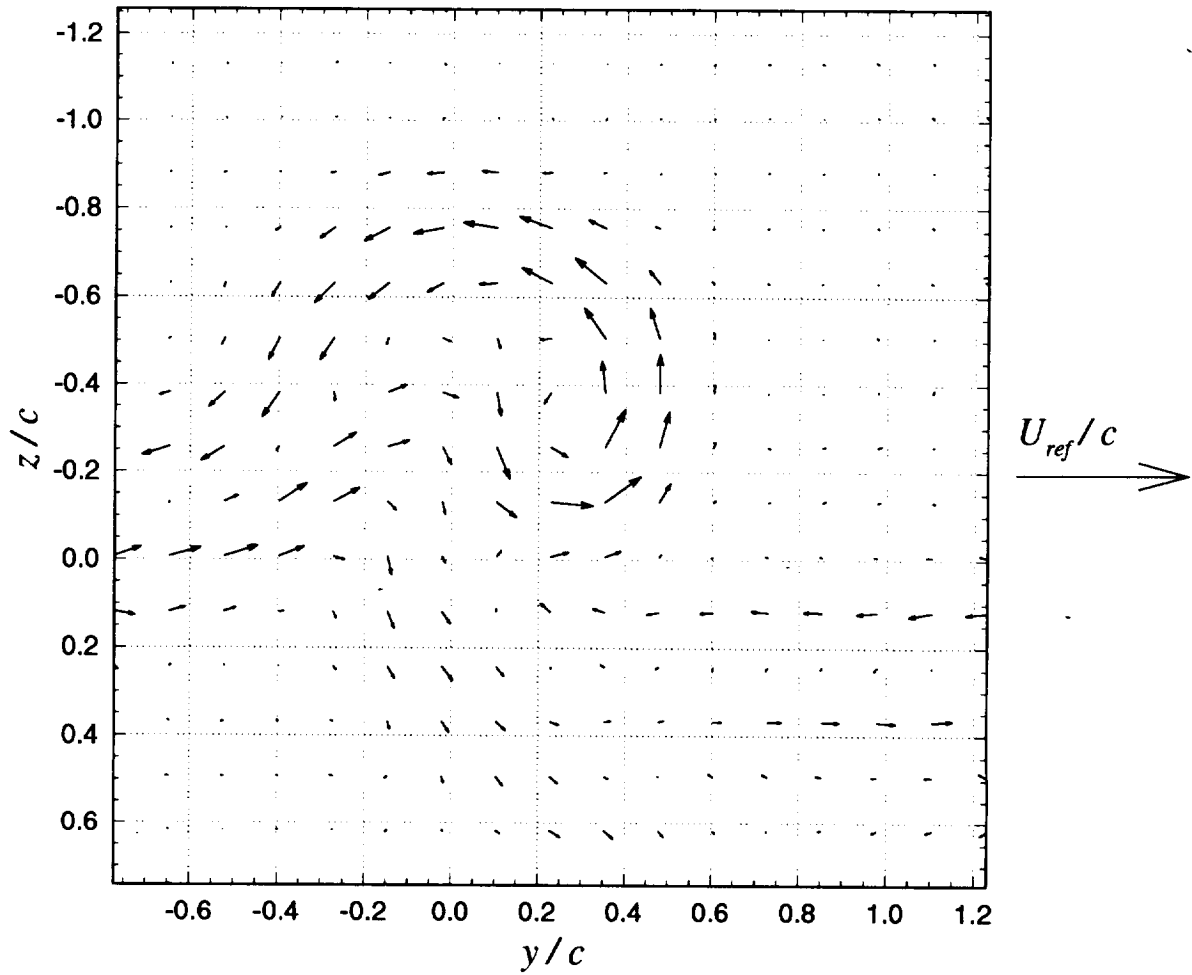


**Figure 3.51a** Mean cross-flow vorticity vectors ( $\Omega_y \cdot c / U_{ref}$ ,  $\Omega_z \cdot c / U_{ref}$ ) for suction side passage of  $\Delta/c = 0.125$ :  $x/c = 30$ ,  $\alpha_1 = 5^\circ$ ,  $\alpha_2 = 5^\circ$ ,  $d/c = 0.2125$

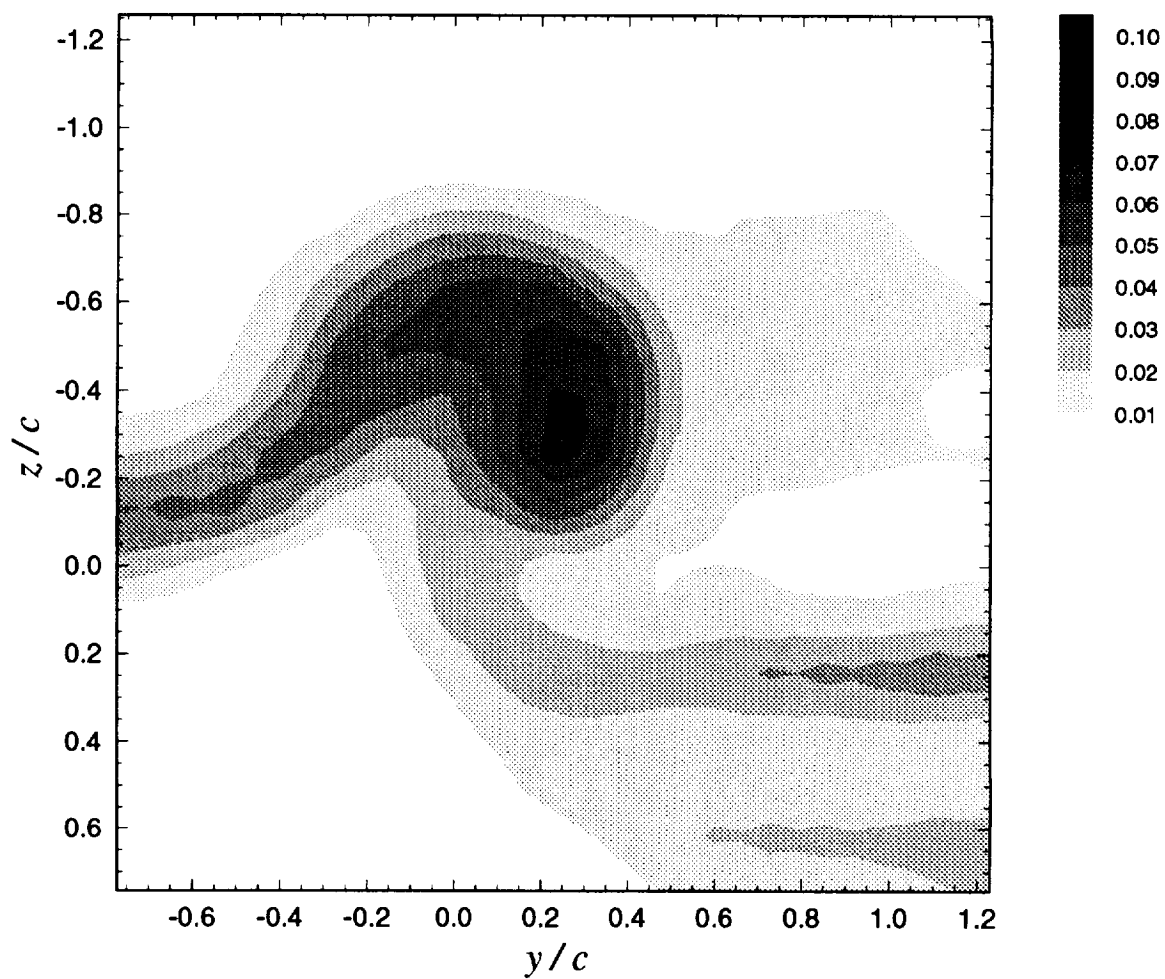


**Figure 3.51b** Contours of mean axial velocity deficit  $(U_{ref} - U) / U_{ref}$  for suction side passage of  $\Delta/c = 0.125$ :  $x/c = 30$ ,  $\alpha_1 = 5^\circ$ ,  $\alpha_2 = 5^\circ$ ,  $d/c = 0.2125$

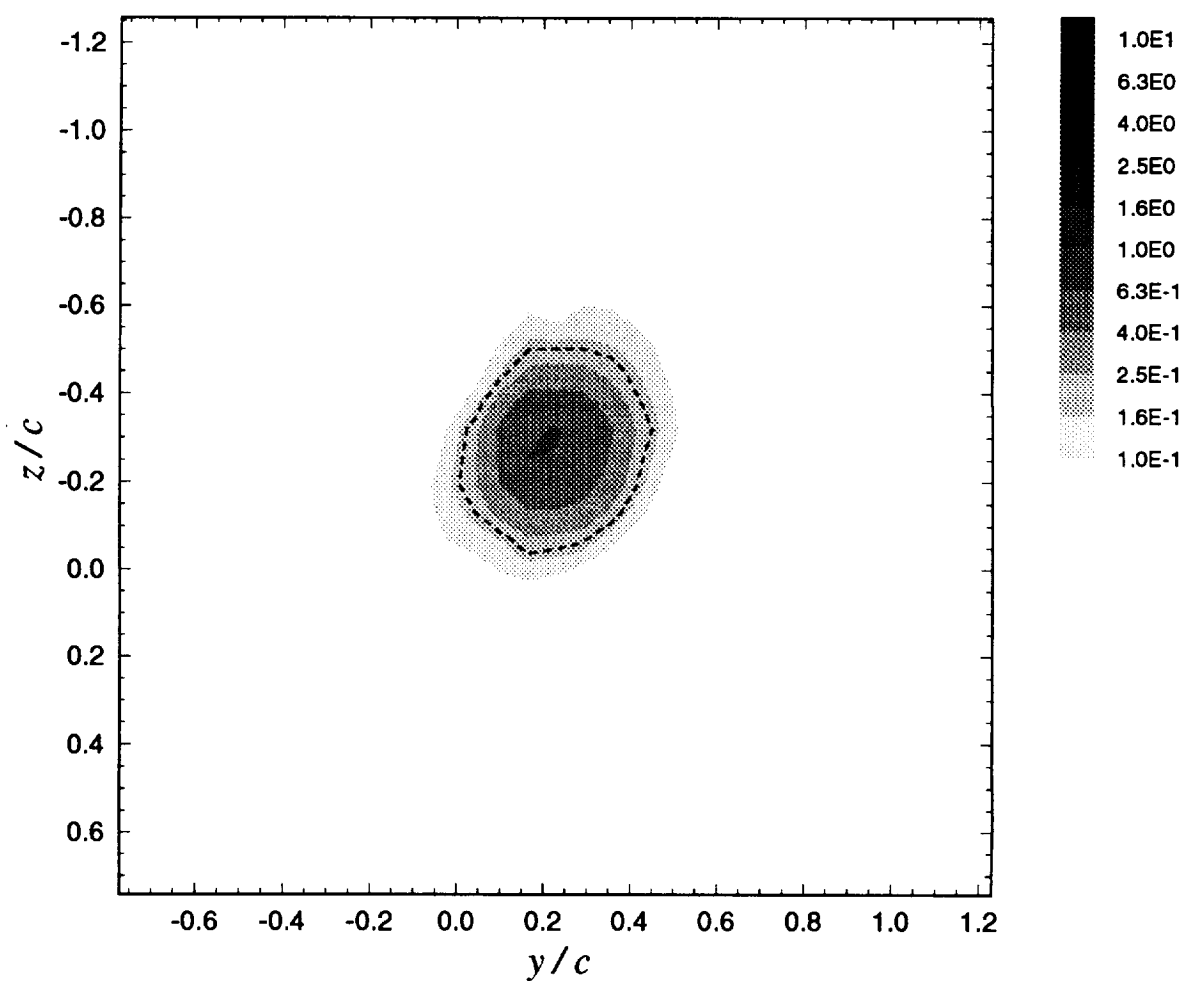


**Figure 3.51c** Contours of mean axial vorticity ( $\Omega_x \cdot c / U_{ref}$ ) for suction side passage of  $\Delta / c = 0.125$ :  $x / c = 30$ ,  $\alpha_1 = 5^\circ$ ,  $\alpha_2 = 5^\circ$ ,  $d / c = 0.2125$ . Dashed contour line is core edge estimate.

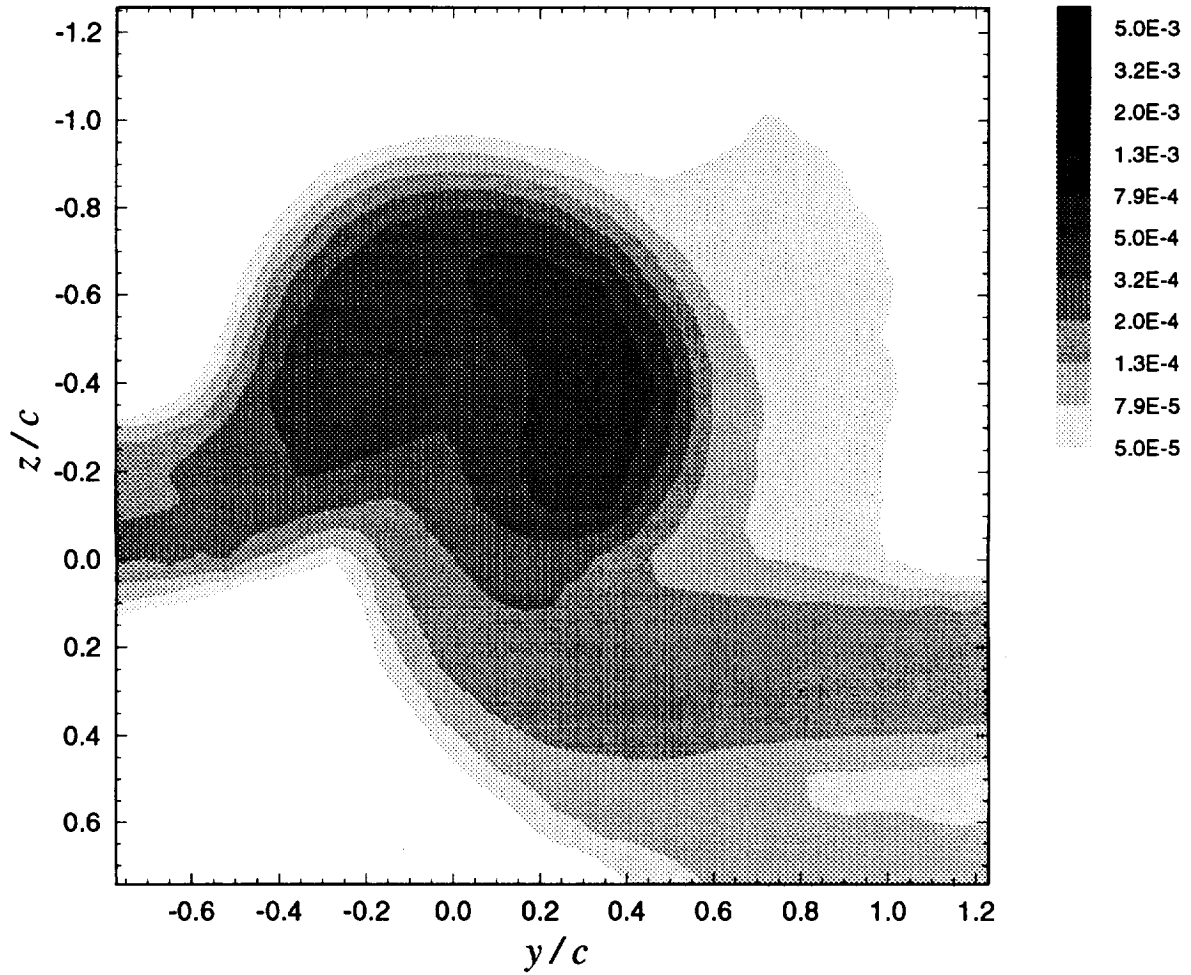


**Figure 3.51d** Contours of axial normal turbulent stress ( $\overline{u'^2} / U_{ref}^2$ ) for suction side passage of  $\Delta/c = 0.125$ :  $x/c = 30$ ,  $\alpha_1 = 5^\circ$ ,  $\alpha_2 = 5^\circ$ ,  $d/c = 0.2125$

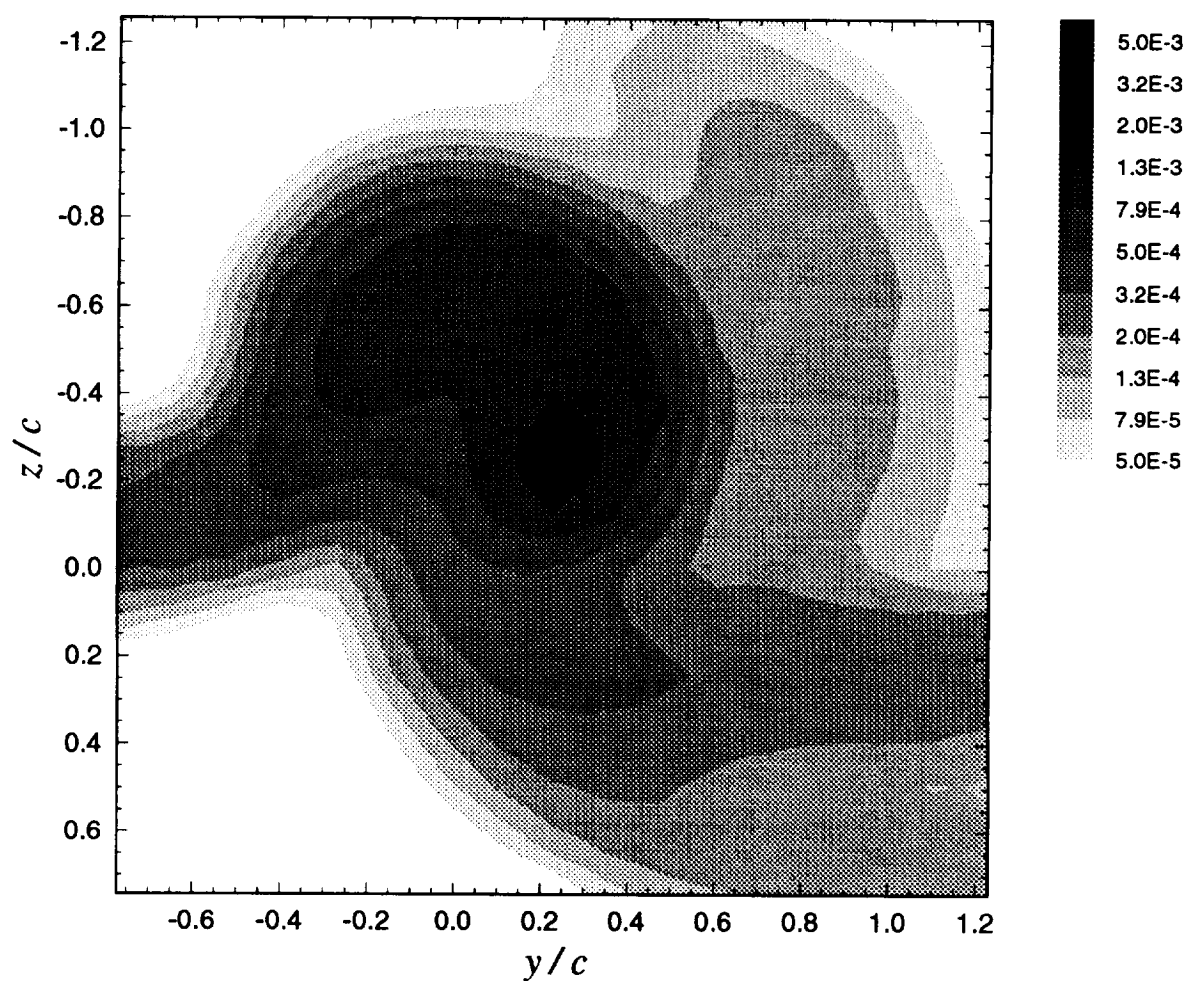


**Figure 3.51e** Contours of summed cross-flow normal turbulent stresses  $(\overline{v^2} + \overline{w^2}) / U_{ref}^2$  for suction side passage of  $\Delta/c = 0.125$ :  $x/c = 30$ ,  $\alpha_1 = 5^\circ$ ,  $\alpha_2 = 5^\circ$ ,  $d/c = 0.2125$

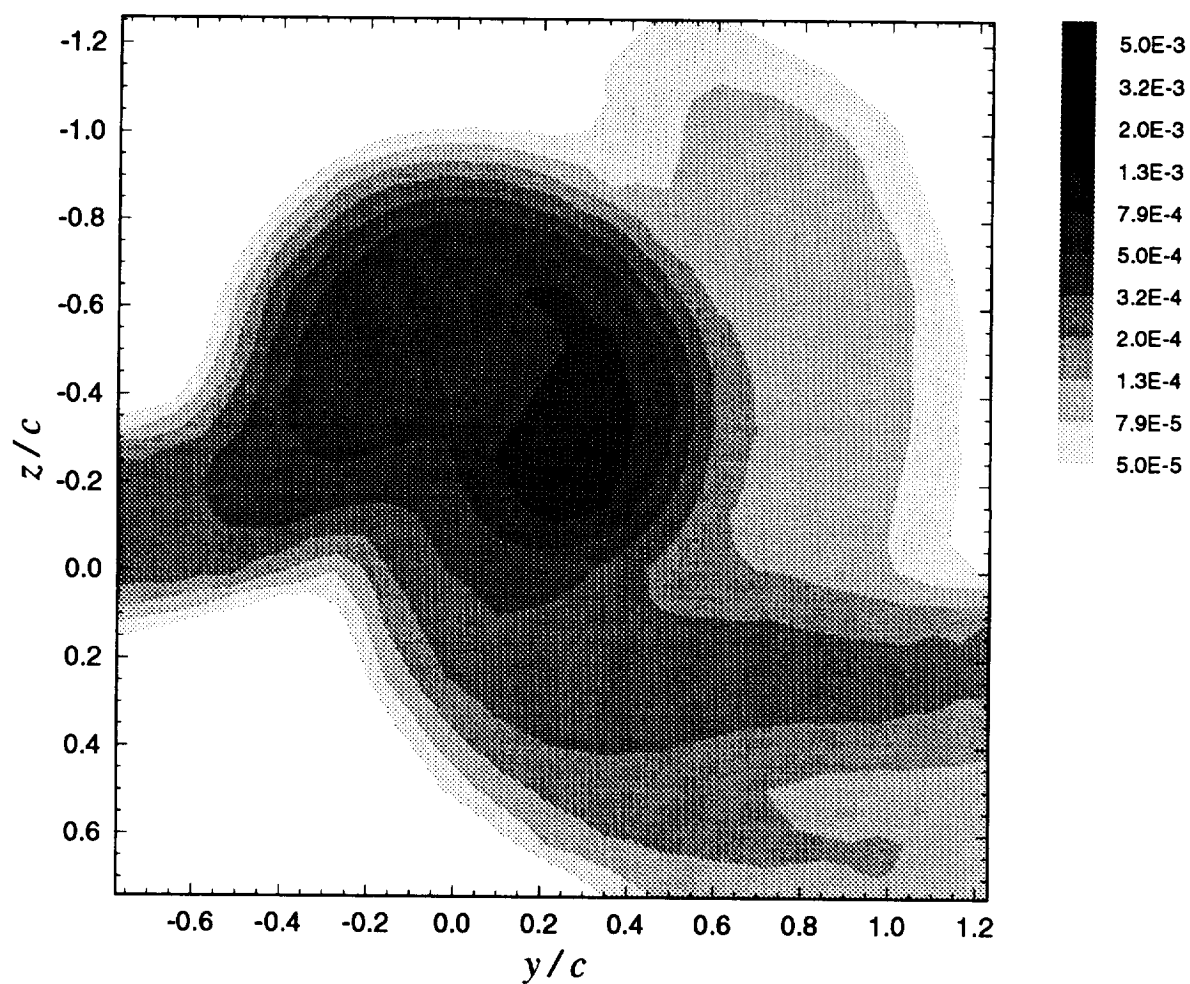


**Figure 3.51f** Contours of turbulent kinetic energy ( $k / U_{ref}^2$ ) for suction side passage of  $\Delta/c = 0.125$ :  $x/c = 30$ ,  $\alpha_1 = 5^\circ$ ,  $\alpha_2 = 5^\circ$ ,  $d/c = 0.2125$

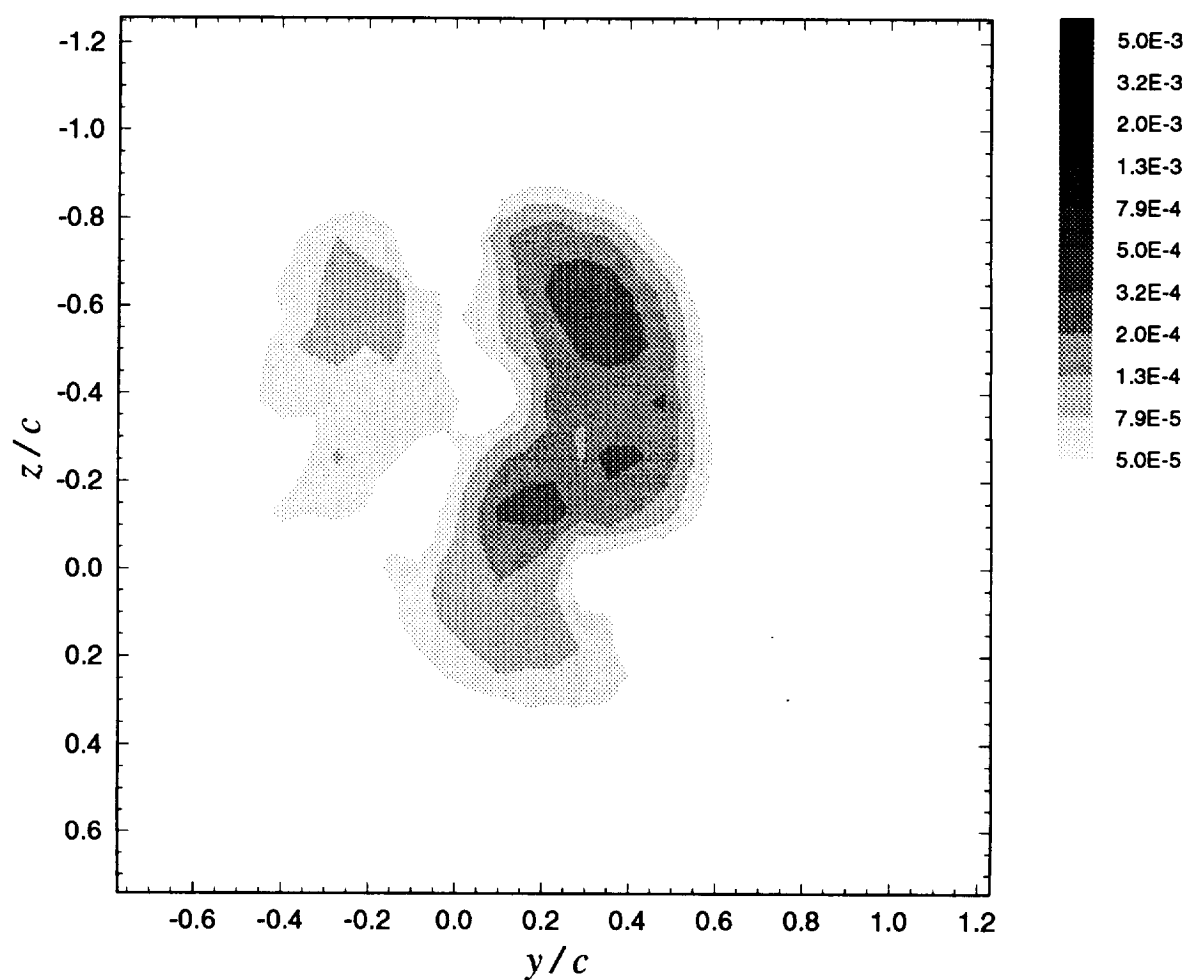


**Figure 3.51g** Contours of axial shear stress magnitude  $(\tau_a / U_{ref}^2)$  for suction side passage of  $\Delta/c = 0.125$ :  $x/c = 30$ ,  $\alpha_1 = 5^\circ$ ,  $\alpha_2 = 5^\circ$ ,  $d/c = 0.2125$



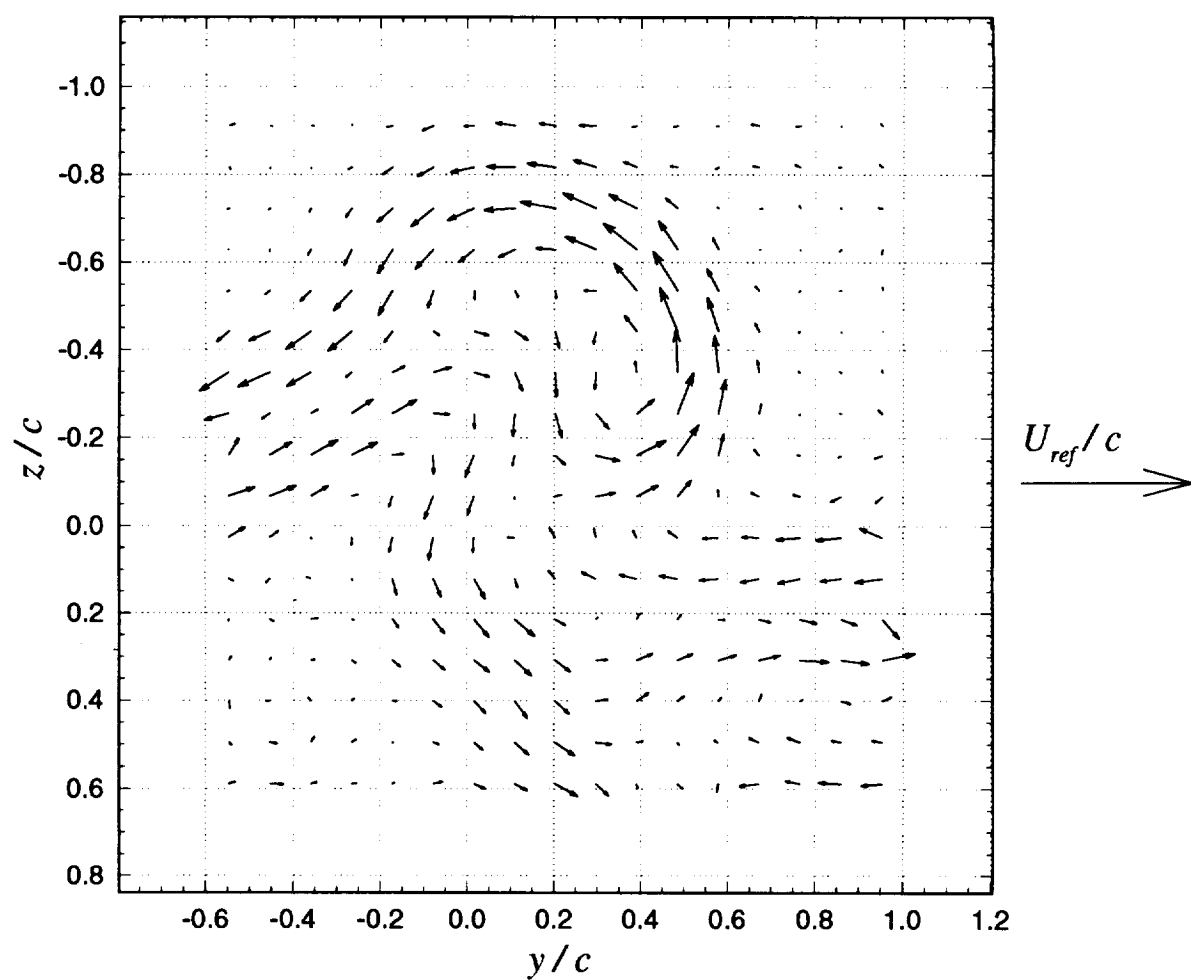


**Figure 3.52a** Mean cross-flow vorticity vectors ( $\Omega_y \cdot c / U_{ref}$ ,  $\Omega_z \cdot c / U_{ref}$ ) for suction side passage of  $\Delta/c = 0.0625$ :  $x/c = 30$ ,  $\alpha_1 = 5^\circ$ ,  $\alpha_2 = 5^\circ$ ,  $d/c = 0.2125$

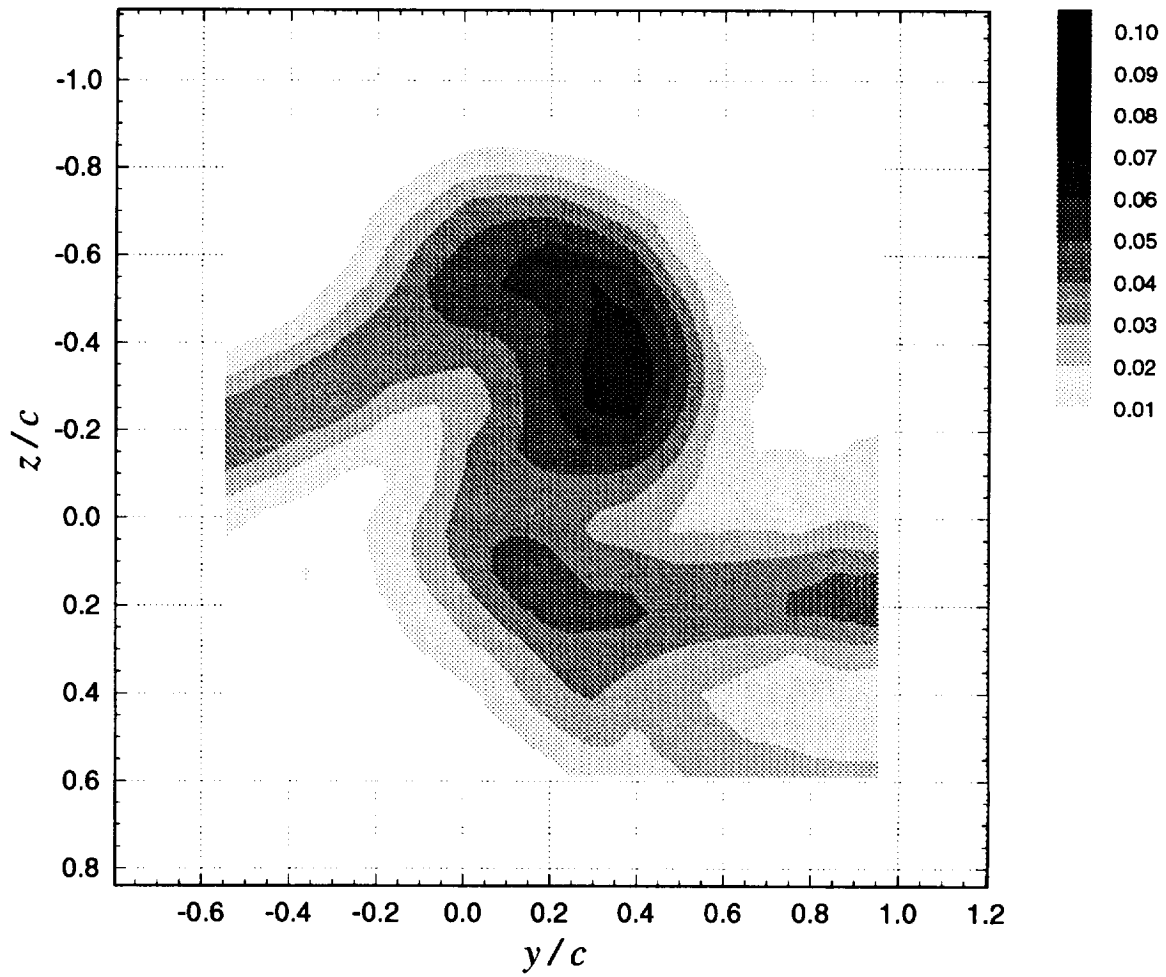


**Figure 3.52b** Contours of mean axial velocity deficit  $((U_{ref} - U) / U_{ref})$  for suction side passage of  $\Delta/c = 0.0625$ :  $x/c = 30$ ,  $\alpha_1 = 5^\circ$ ,  $\alpha_2 = 5^\circ$ ,  $d/c = 0.2125$

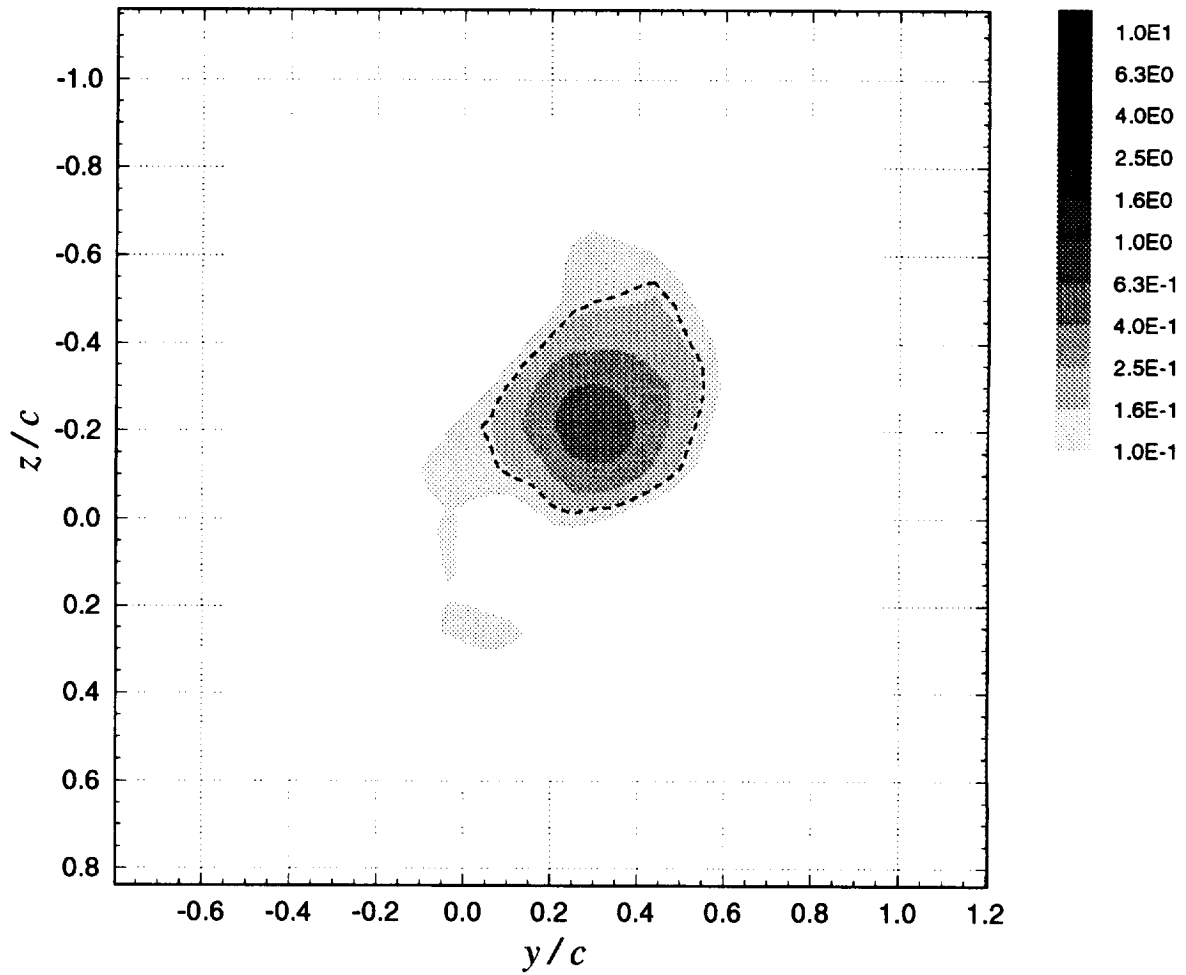


**Figure 3.52c** Contours of mean axial vorticity ( $\Omega_x \cdot c / U_{ref}$ ) for suction side passage of  $\Delta/c = 0.0625$ :  $x/c = 30$ ,  $\alpha_1 = 5^\circ$ ,  $\alpha_2 = 5^\circ$ ,  $d/c = 0.2125$ . Dashed contour line is core edge estimate.

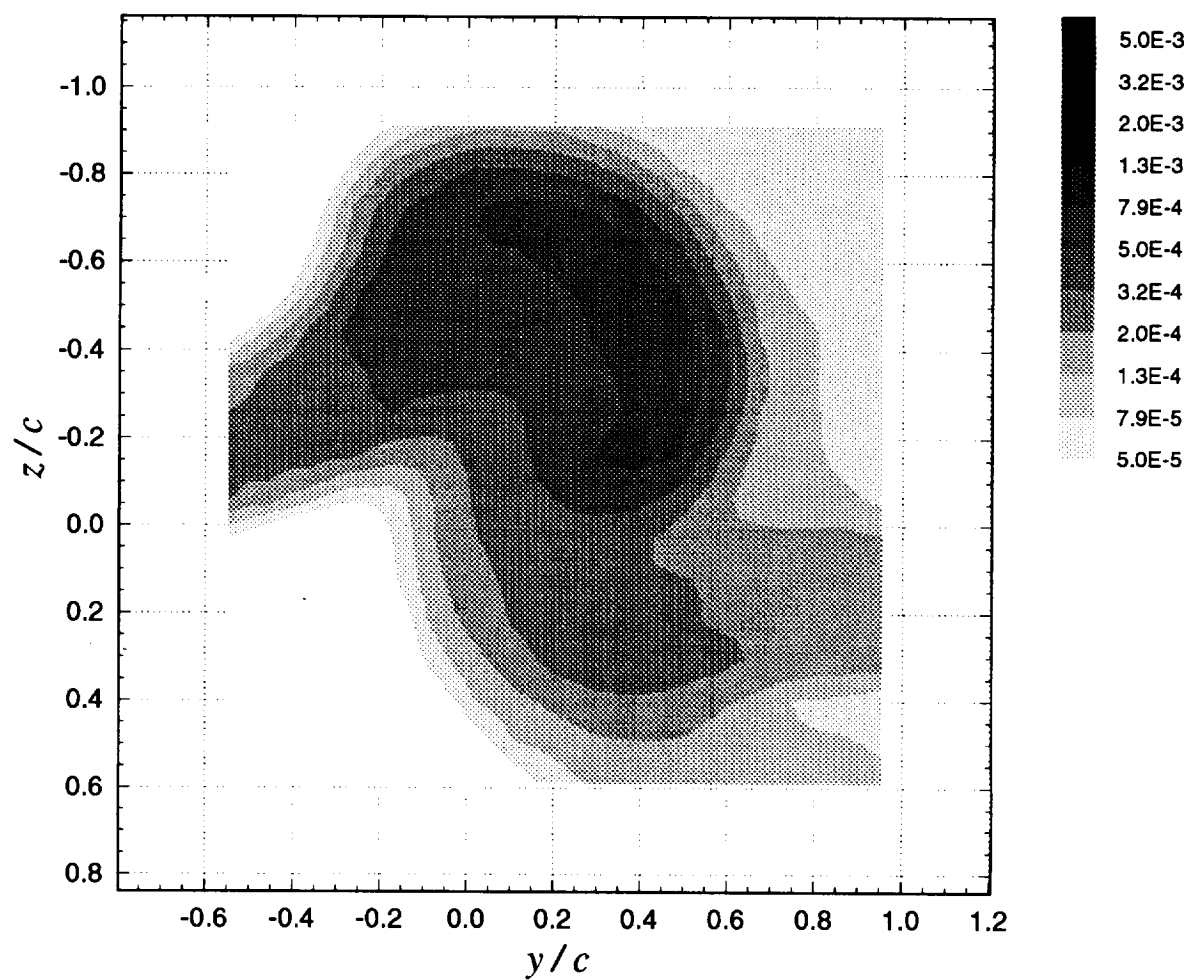


**Figure 3.52d** Contours of axial normal turbulent stress ( $\overline{u^2} / U_{ref}^2$ ) for suction side passage of  $\Delta/c = 0.0625$ :  $x/c = 30$ ,  $\alpha_1 = 5^\circ$ ,  $\alpha_2 = 5^\circ$ ,  $d/c = 0.2125$

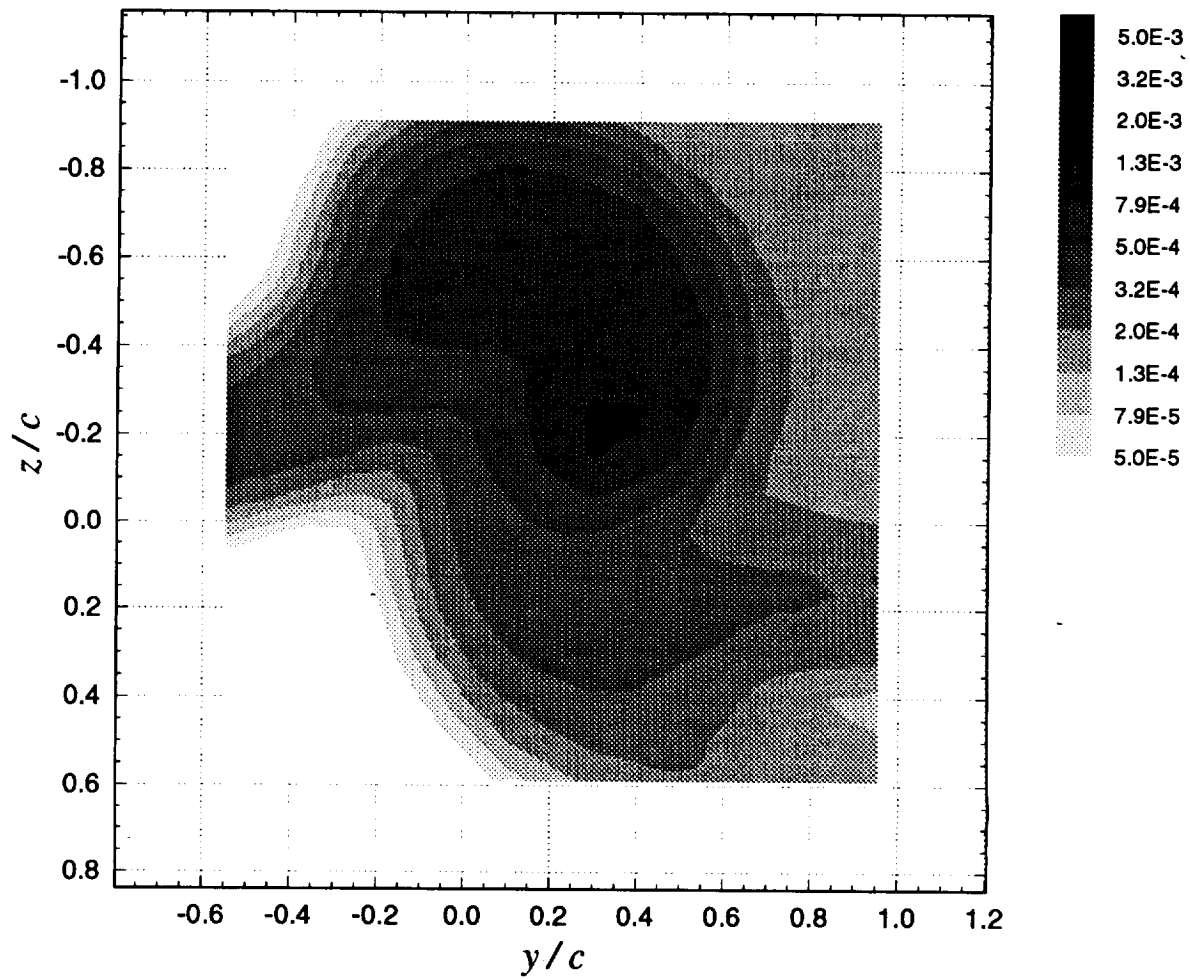


**Figure 3.52e** Contours of summed cross-flow normal turbulent stresses  $(\overline{v^2} + \overline{w^2}) / U_{ref}^2$  for suction side passage of  $\Delta/c = 0.0625$ :  $x/c = 30$ ,  $\alpha_1 = 5^\circ$ ,  $\alpha_2 = 5^\circ$ ,  $d/c = 0.2125$

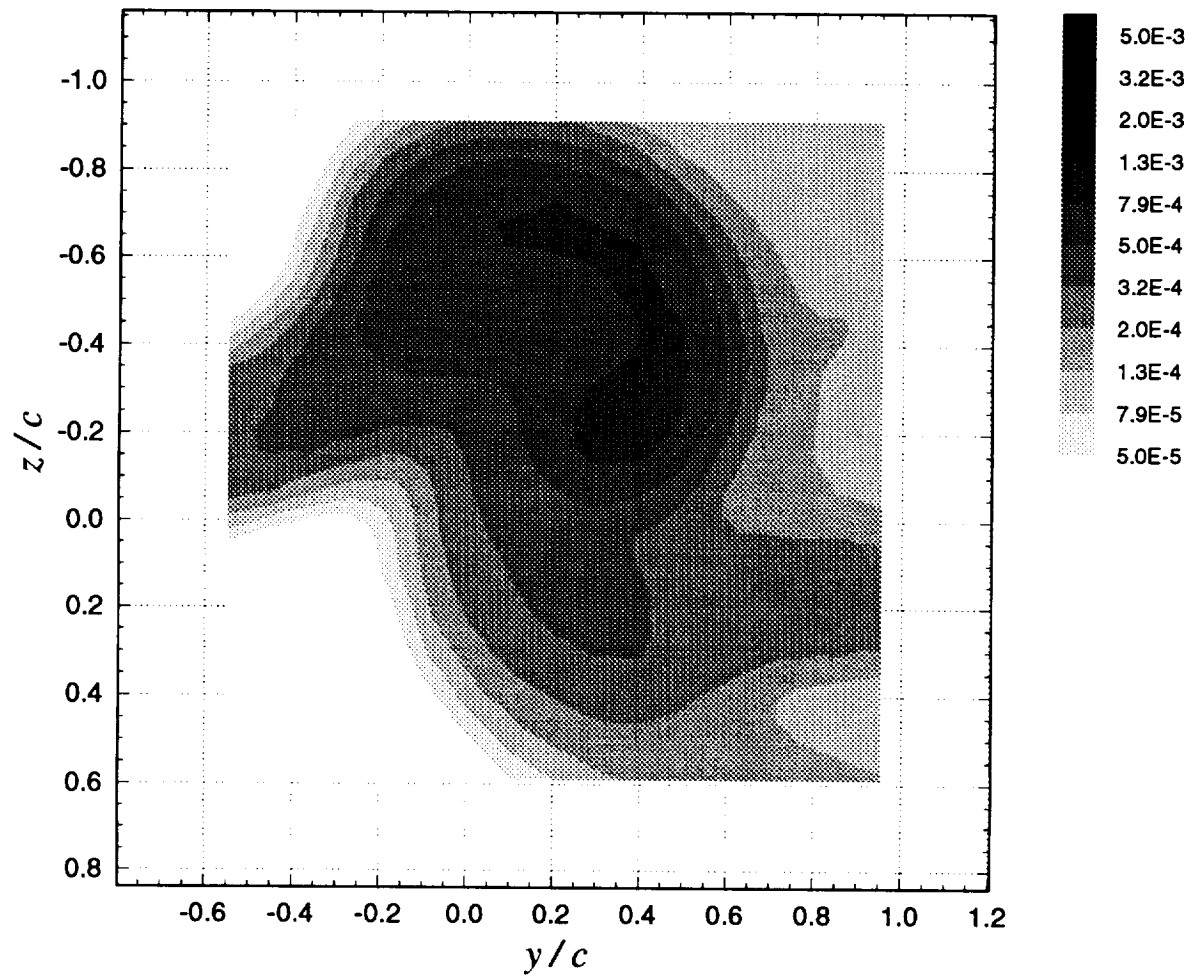


**Figure 3.52f** Contours of turbulent kinetic energy ( $k / U_{ref}^2$ ) for suction side passage of  $\Delta/c = 0.0625$ :  $x/c = 30$ ,  $\alpha_1 = 5^\circ$ ,  $\alpha_2 = 5^\circ$ ,  $d/c = 0.2125$

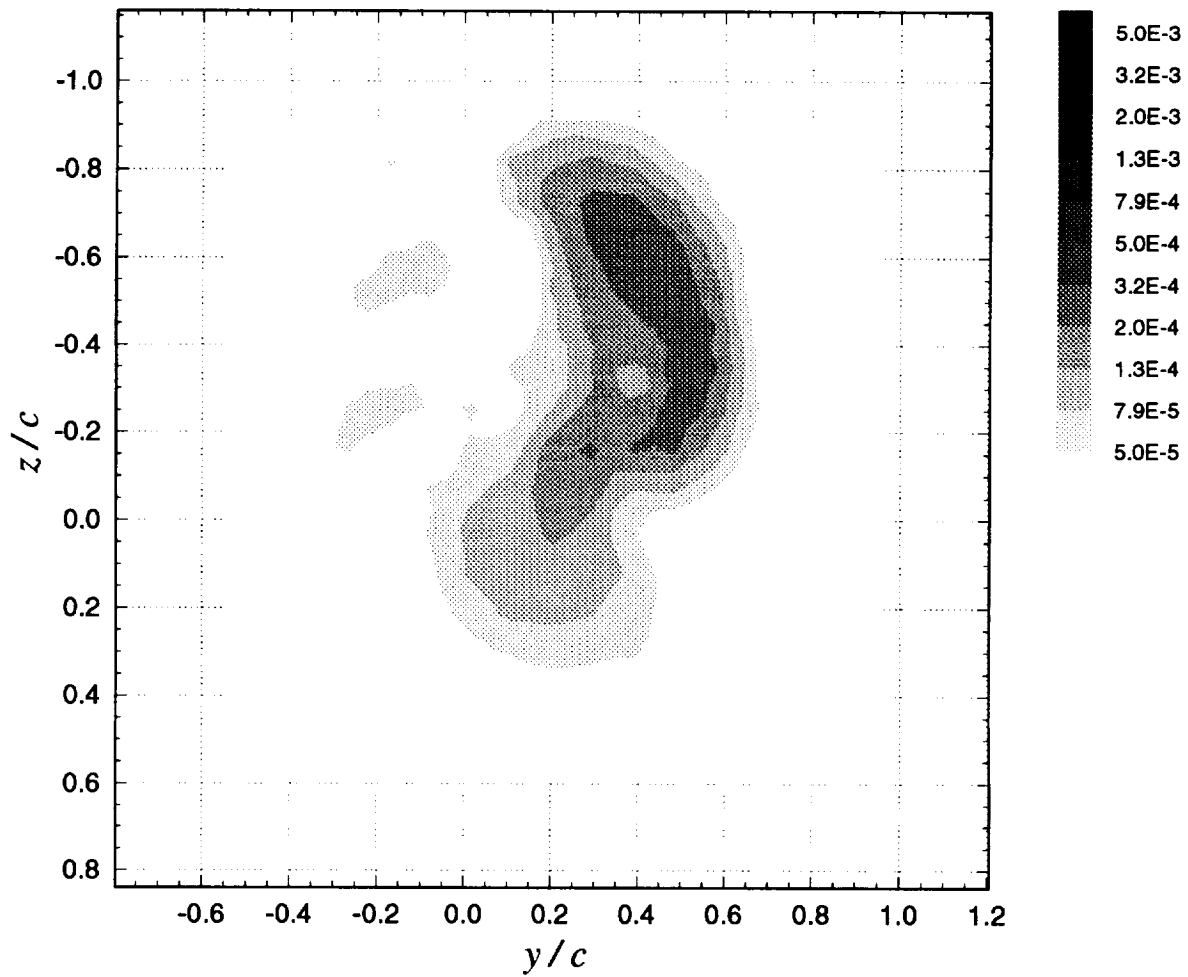


**Figure 3.52g** Contours of axial shear stress magnitude  $(\tau_a / U_{ref}^2)$  for suction side passage of  $\Delta/c = 0.0625$ :  $x/c = 30$ ,  $\alpha_1 = 5^\circ$ ,  $\alpha_2 = 5^\circ$ ,  $d/c = 0.2125$

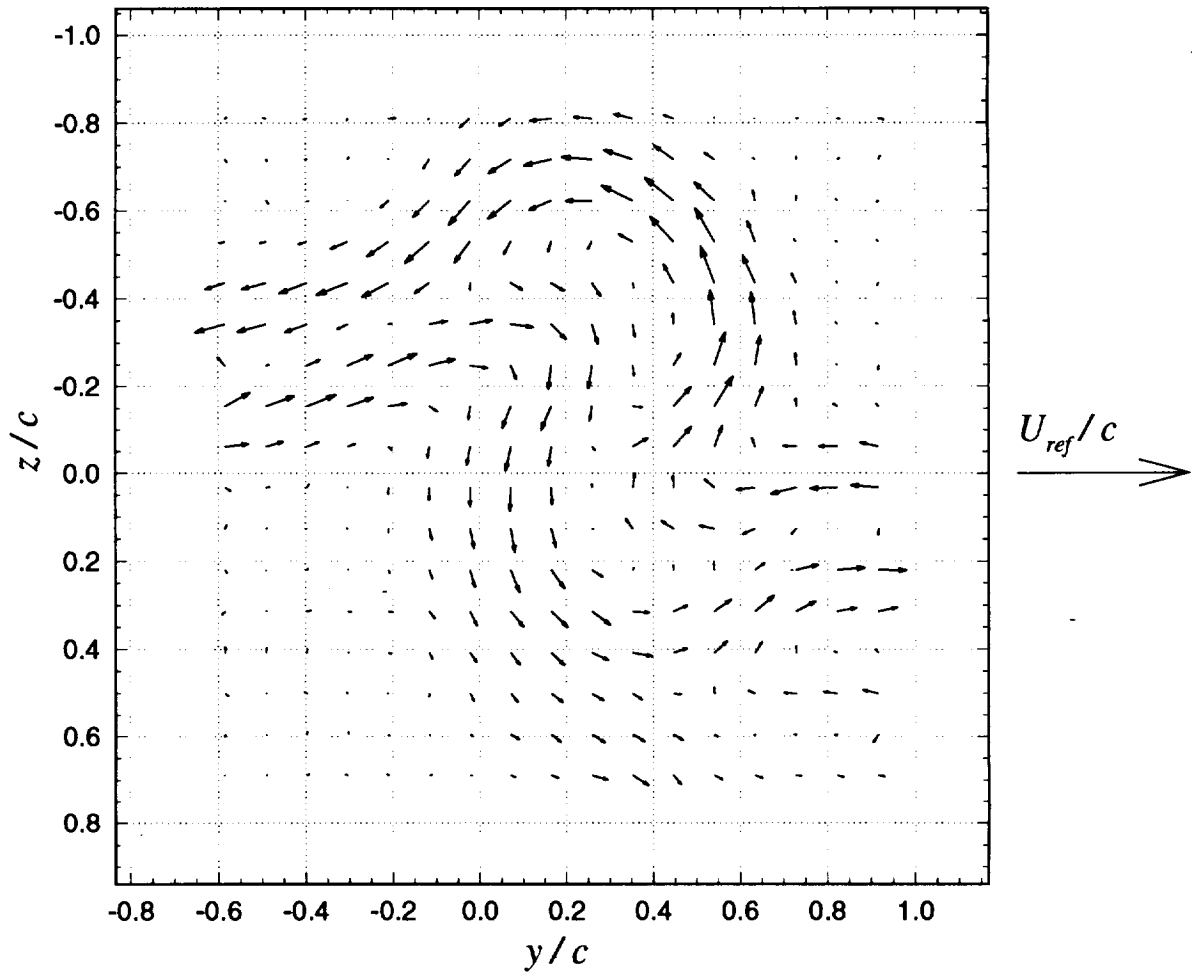


**Figure 3.53a** Mean cross-flow vorticity vectors ( $\Omega_y \cdot c / U_{ref}$ ,  $\Omega_z \cdot c / U_{ref}$ ) for vortex centerline stagnating on blade leading edge ( $\Delta = 0$ ):  $x/c = 30$ ,  $\alpha_1 = 5^\circ$ ,  $\alpha_2 = 5^\circ$ ,  $d/c = 0.2125$



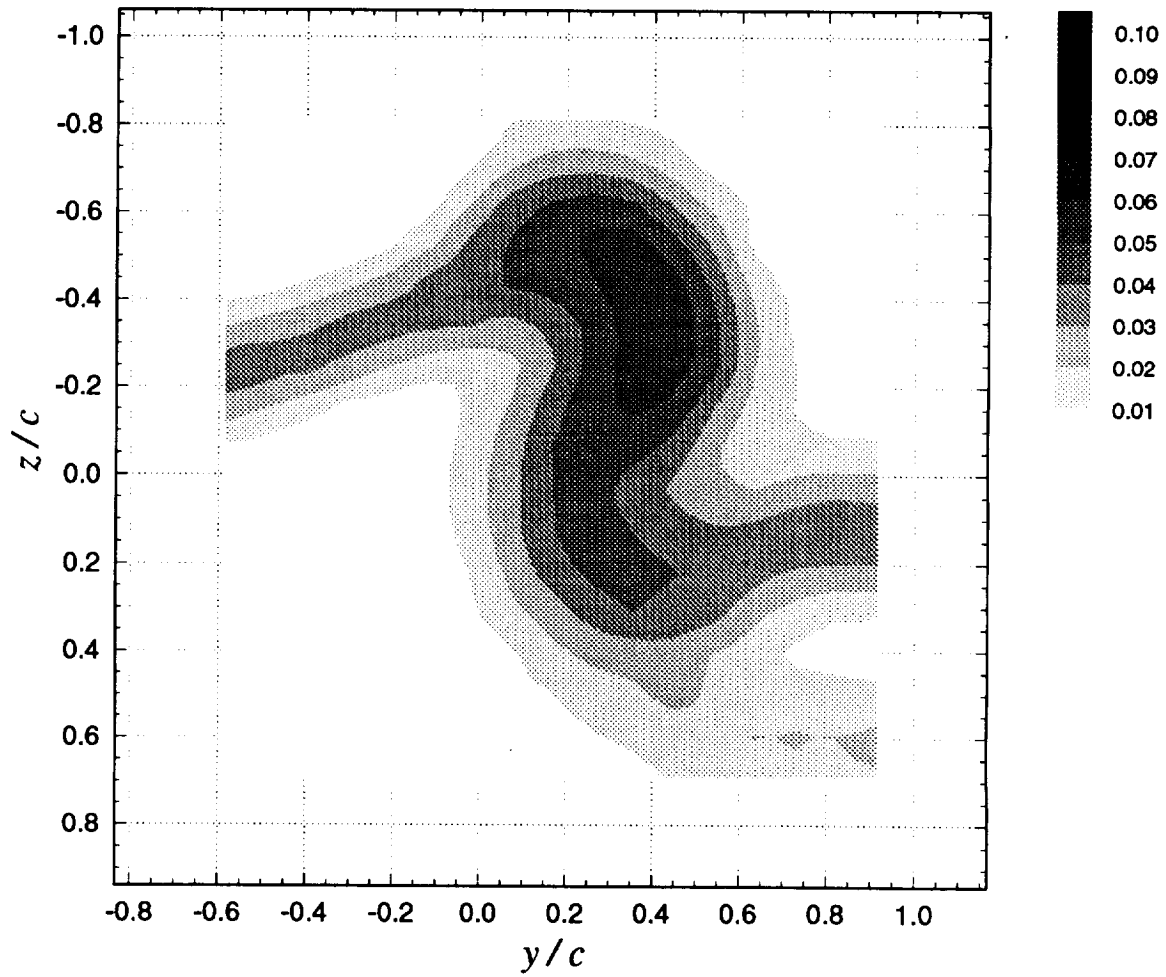


**Figure 3.53b** Contours of mean axial velocity deficit  $((U_{ref} - U) / U_{ref})$  for vortex centerline stagnating on blade leading edge ( $\Delta = 0$ ):  $x/c = 30$ ,  $\alpha_1 = 5^\circ$ ,  $\alpha_2 = 5^\circ$ ,  $d/c = 0.2125$

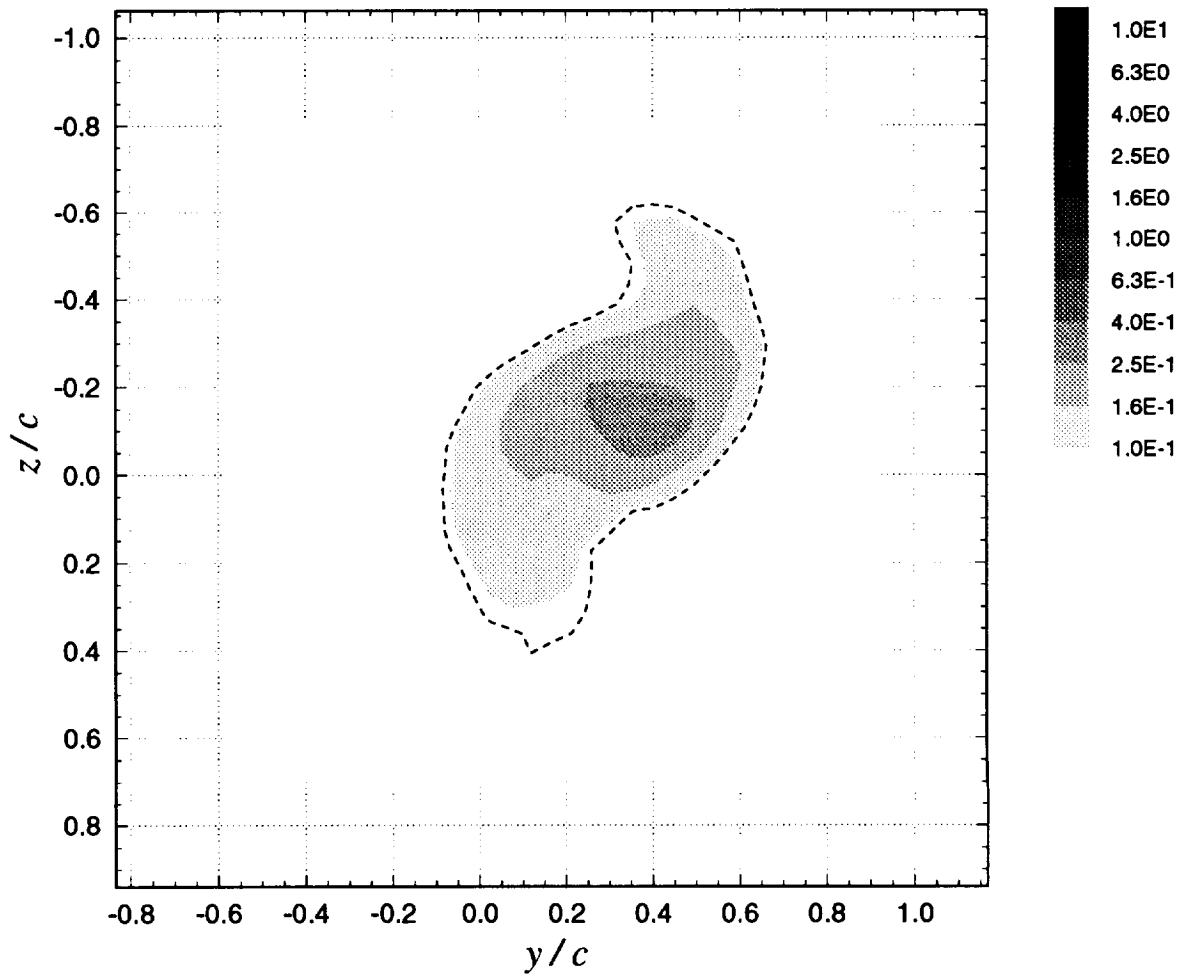


**Figure 3.53c** Contours of mean axial vorticity ( $\Omega_x \cdot c / U_{ref}$ ) for vortex centerline stagnating on blade leading edge ( $\Delta = 0$ ):  $x/c = 30$ ,  $\alpha_1 = 5^\circ$ ,  $\alpha_2 = 5^\circ$ ,  $d/c = 0.2125$ . Dashed contour line is core edge estimate.

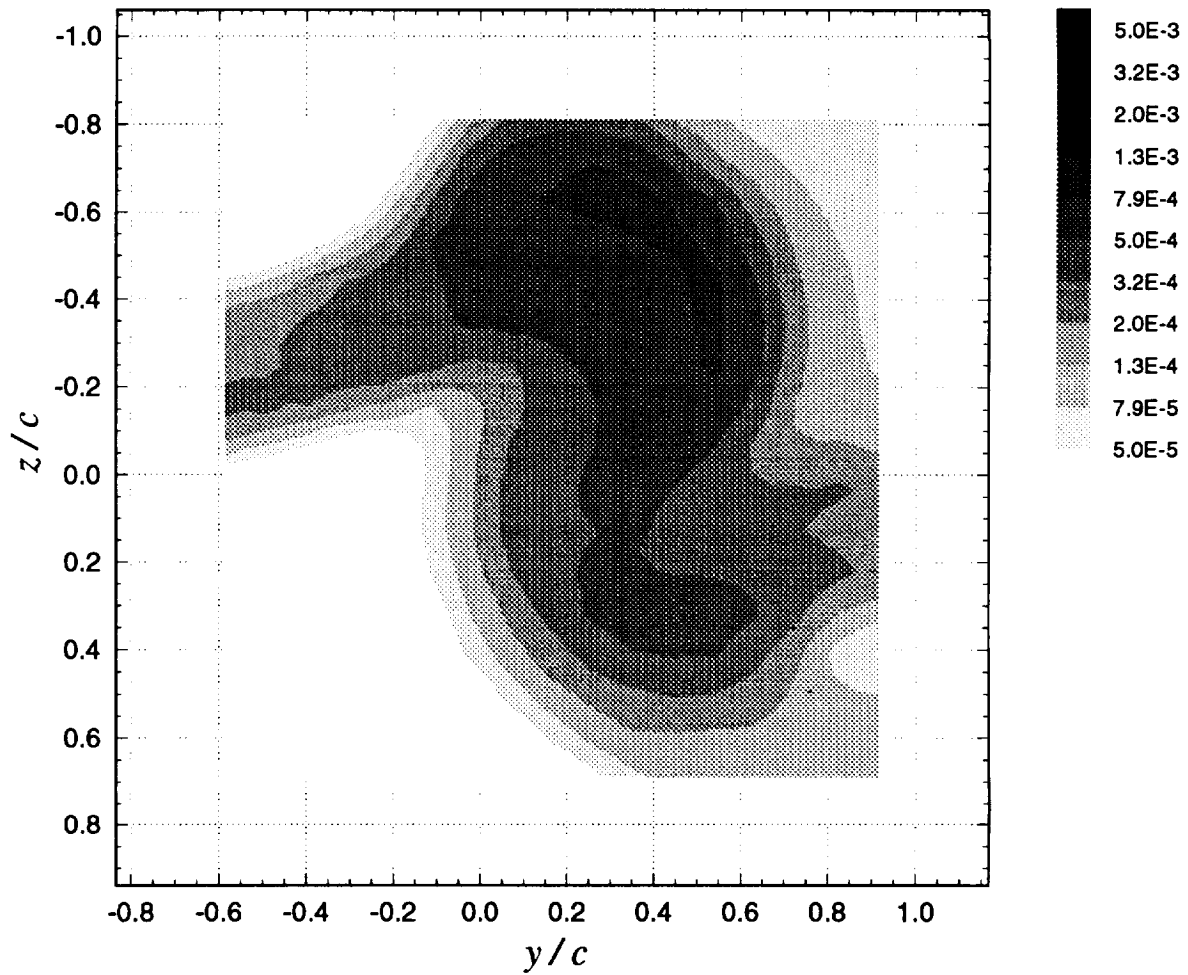


**Figure 3.53d** Contours of axial normal turbulent stress  $\overline{u^2} / U_{ref}^2$  for vortex centerline stagnating on blade leading edge ( $\Delta = 0$ ):  $x/c = 30$ ,  $\alpha_1 = 5^\circ$ ,  $\alpha_2 = 5^\circ$ ,  $d/c = 0.2125$

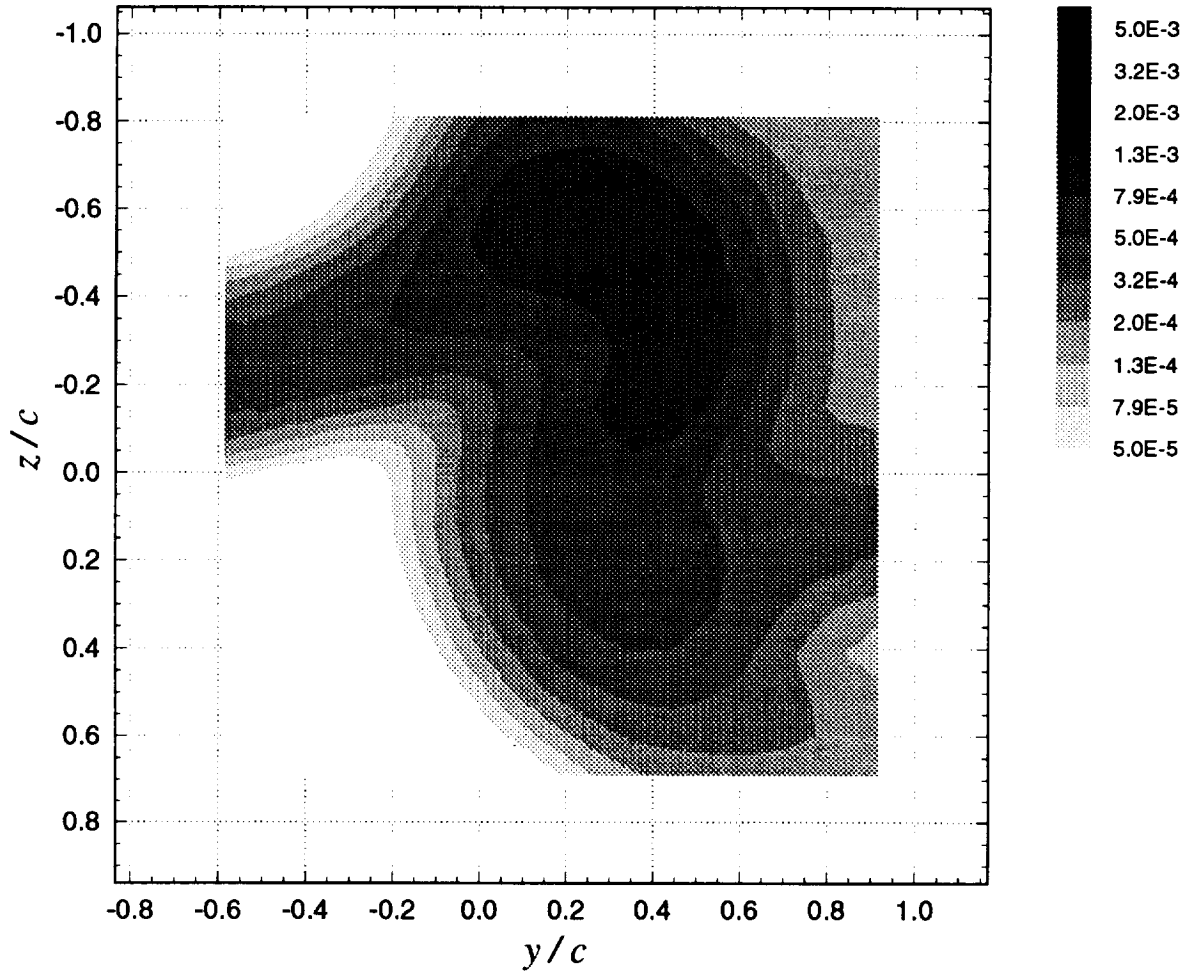


**Figure 3.53e** Contours of summed cross-flow normal turbulent stresses  $(\overline{v^2} + \overline{w^2}) / U_{ref}^2$  for vortex centerline stagnating on blade leading edge ( $\Delta = 0$ ):  $x/c = 30$ ,  $\alpha_1 = 5^\circ$ ,  $\alpha_2 = 5^\circ$ ,  $d/c = 0.2125$

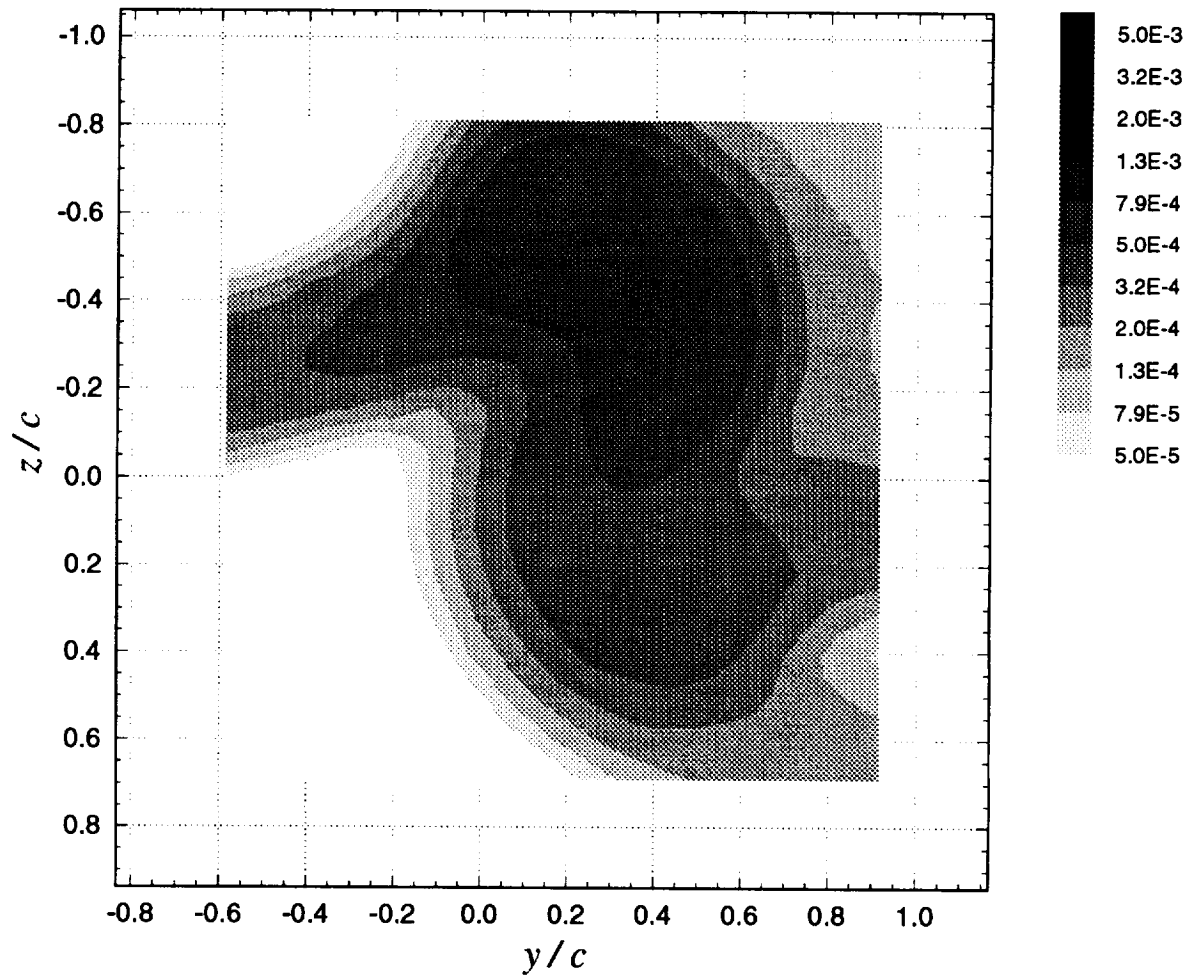


**Figure 3.53f** Contours of turbulent kinetic energy ( $k / U_{ref}^2$ ) for vortex centerline stagnating on blade leading edge ( $\Delta = 0$ ):  $x/c = 30$ ,  $\alpha_1 = 5^\circ$ ,  $\alpha_2 = 5^\circ$ ,  $d/c = 0.2125$

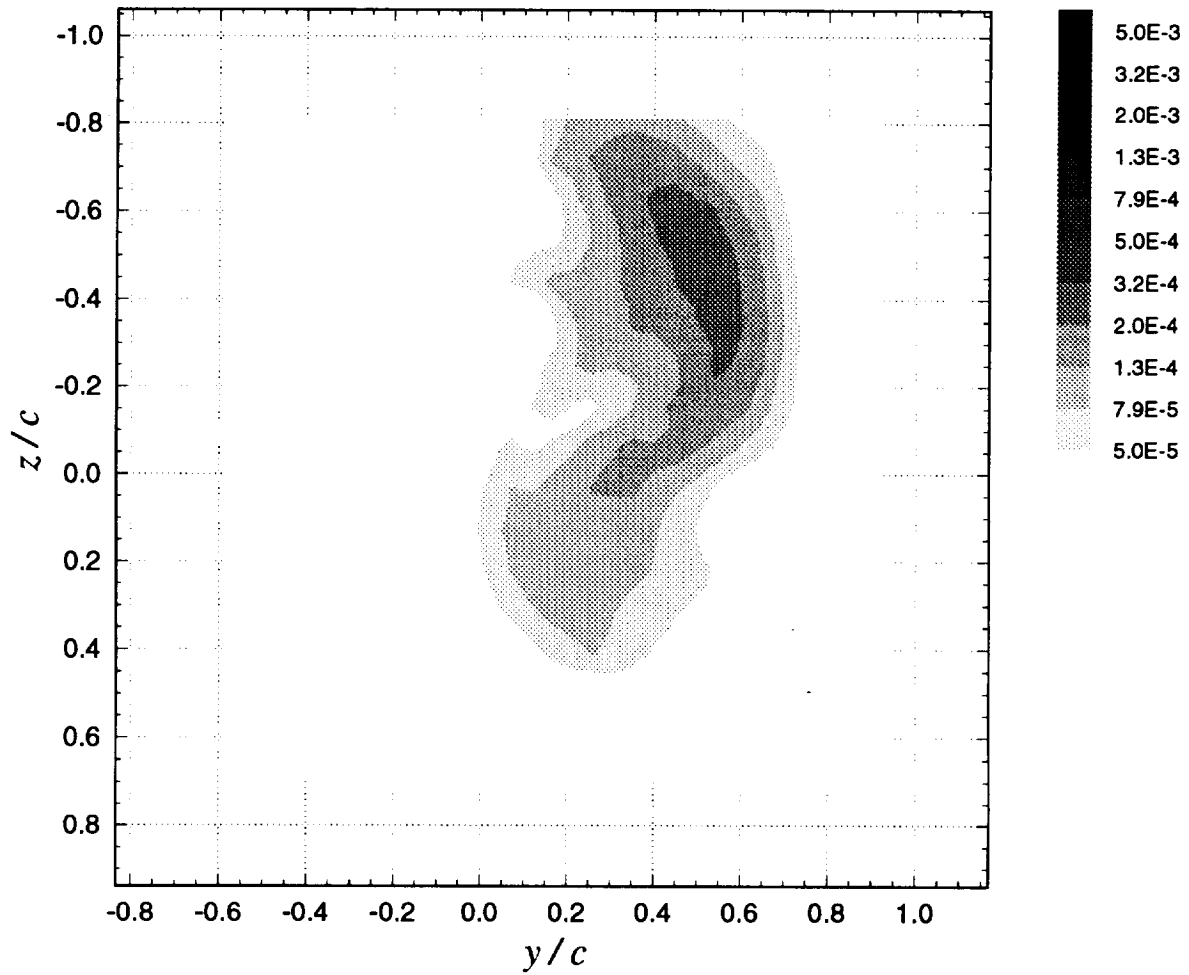


**Figure 3.53g** Contours of axial shear stress magnitude ( $\tau_a / U_{ref}^2$ ) for vortex centerline stagnating on blade leading edge ( $\Delta = 0$ ):  $x/c = 30$ ,  $\alpha_1 = 5^\circ$ ,  $\alpha_2 = 5^\circ$ ,  $d/c = 0.2125$

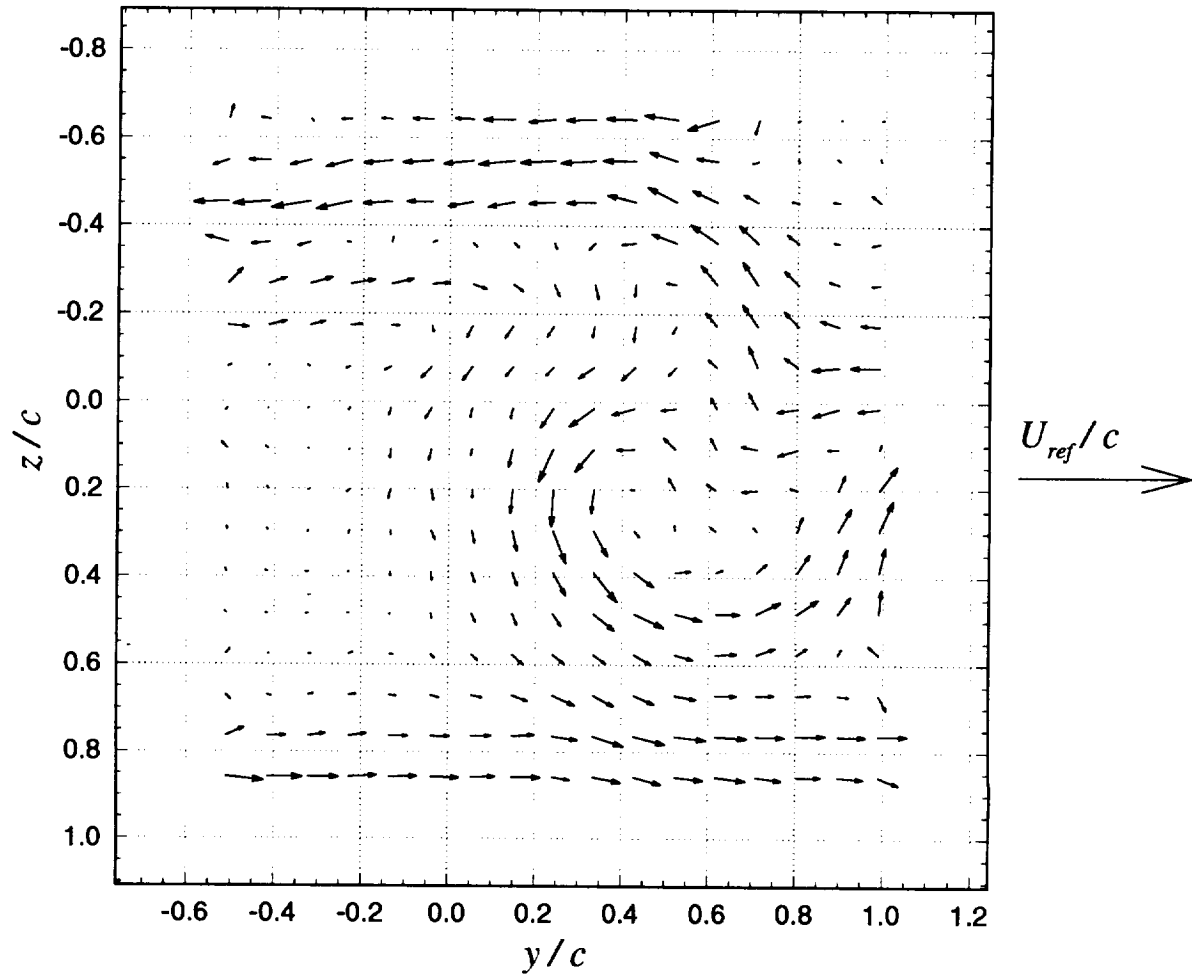


**Figure 3.54a** Mean cross-flow vorticity vectors ( $\Omega_y \cdot c / U_{ref}$ ,  $\Omega_z \cdot c / U_{ref}$ ) for suction side passage of  $\Delta / c = -0.0625$ :  $x / c = 30$ ,  $\alpha_1 = 5^\circ$ ,  $\alpha_2 = 5^\circ$ ,  $d / c = 0.2125$

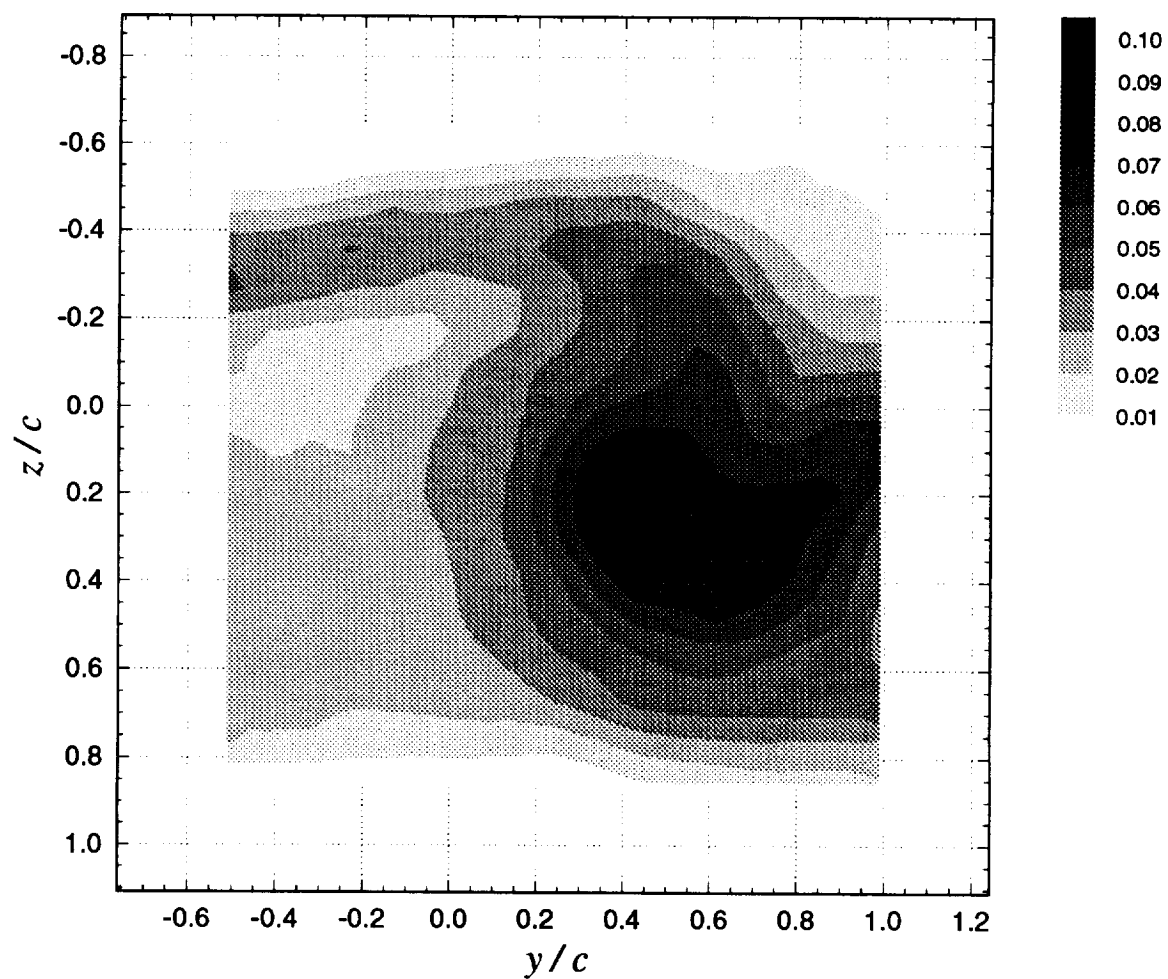


**Figure 3.54b** Contours of mean axial velocity deficit  $((U_{ref} - U) / U_{ref})$  for suction side passage of  $\Delta/c = -0.0625$ :  $x/c = 30$ ,  $\alpha_1 = 5^\circ$ ,  $\alpha_2 = 5^\circ$ ,  $d/c = 0.2125$



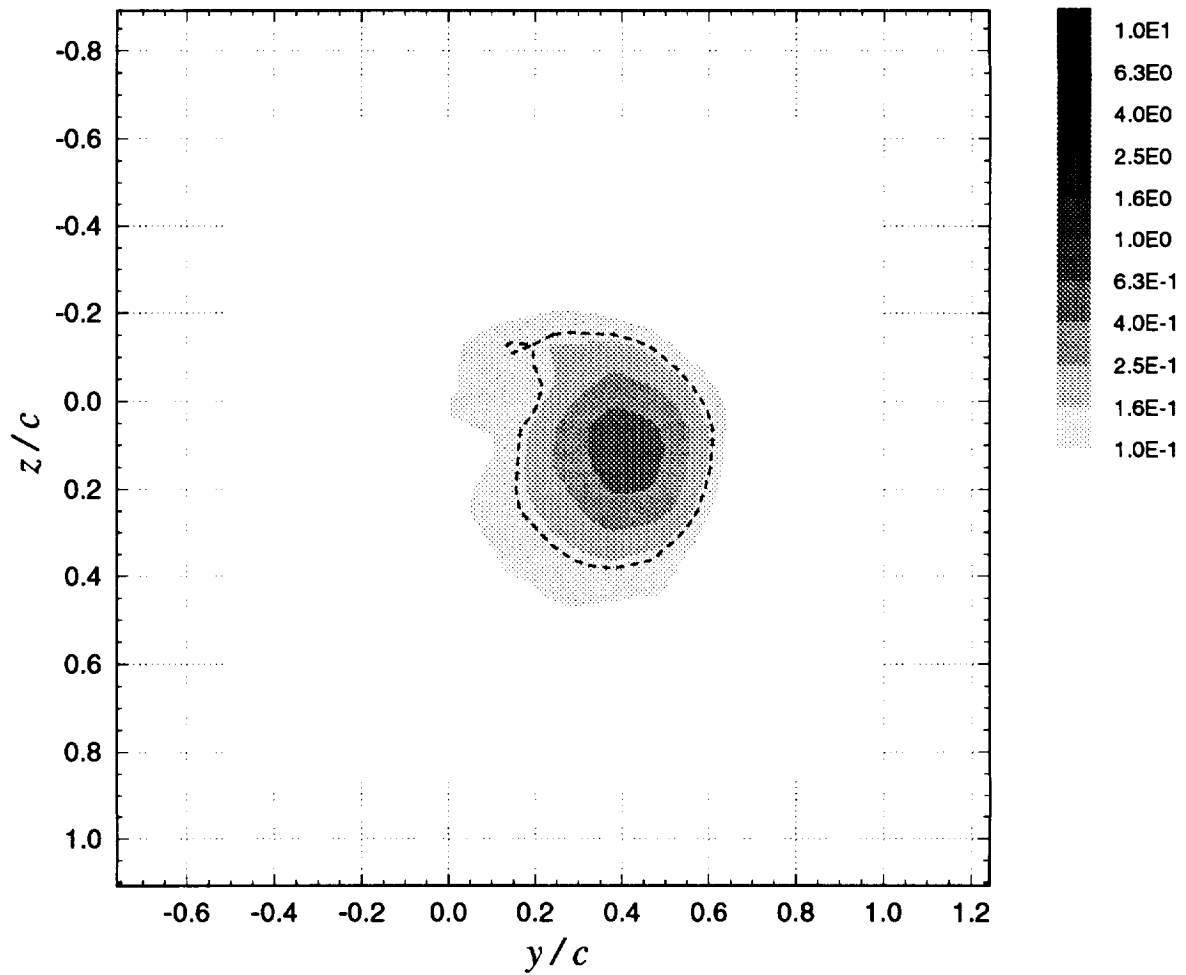


**Figure 3.54c** Contours of mean axial vorticity ( $\Omega_x \cdot c / U_{ref}$ ) for suction side passage of  $\Delta / c = -0.0625$ :  $x / c = 30$ ,  $\alpha_1 = 5^\circ$ ,  $\alpha_2 = 5^\circ$ ,  $d / c = 0.2125$ . Dashed contour line is core edge estimate.

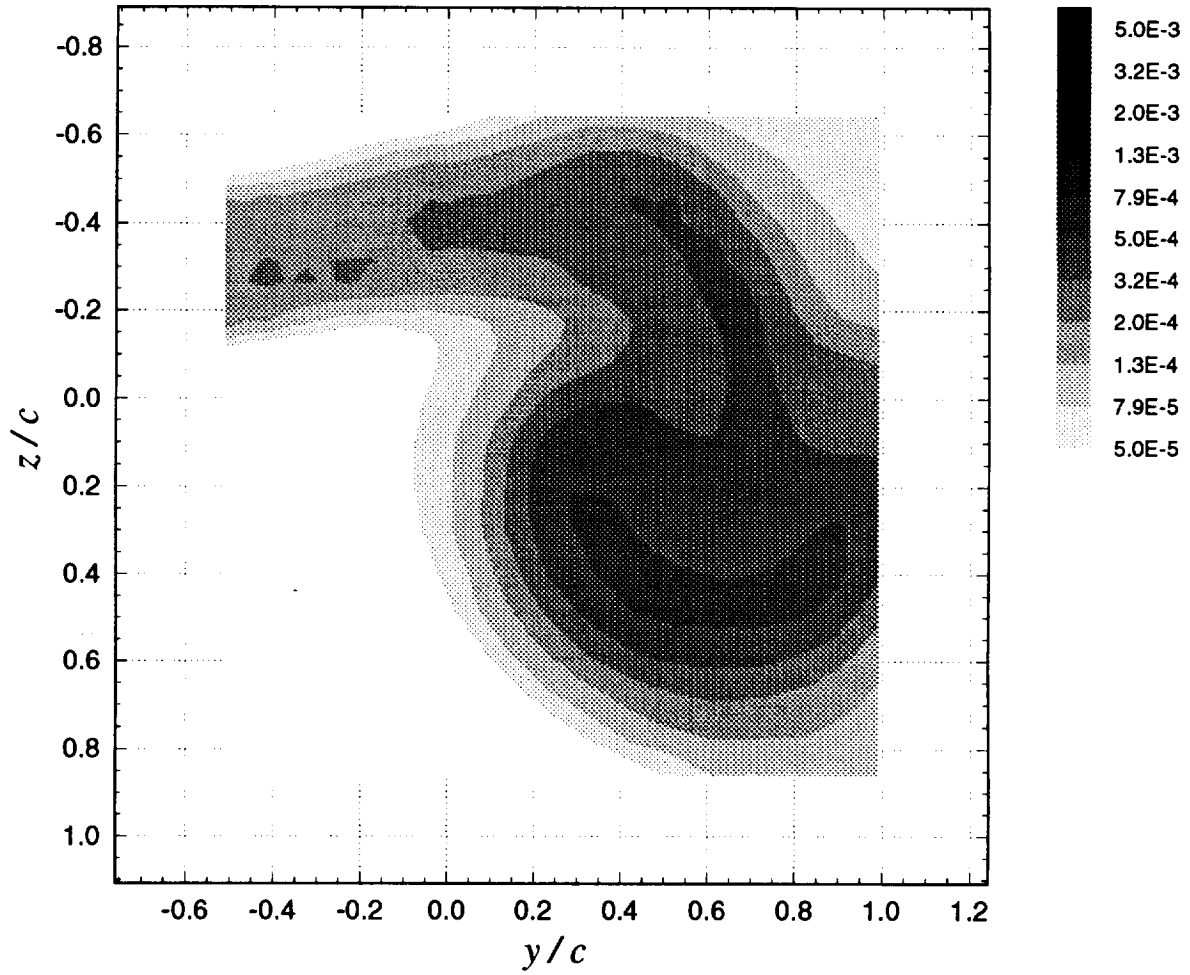


**Figure 3.54d** Contours of axial normal turbulent stress  $(\overline{u^2} / U_{ref}^2)$  for suction side passage of  $\Delta/c = -0.0625$ :  $x/c = 30$ ,  $\alpha_1 = 5^\circ$ ,  $\alpha_2 = 5^\circ$ ,  $d/c = 0.2125$

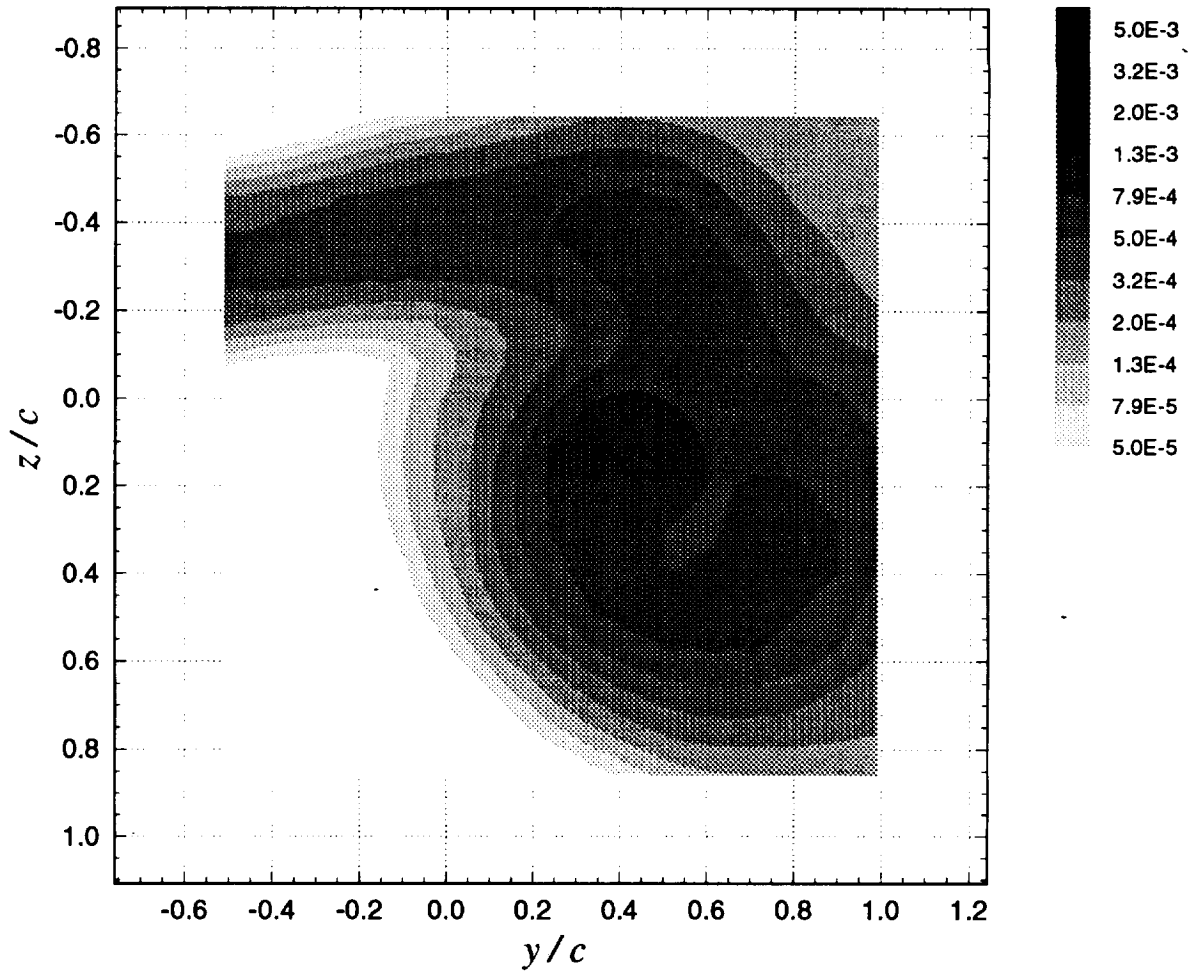


**Figure 3.54e** Contours of summed cross-flow normal turbulent stresses ( $(\overline{v^2} + \overline{w^2}) / U_{ref}^2$ ) for suction side passage of  $\Delta/c = -0.0625$ :  $x/c = 30$ ,  $\alpha_1 = 5^\circ$ ,  $\alpha_2 = 5^\circ$ ,  $d/c = 0.2125$

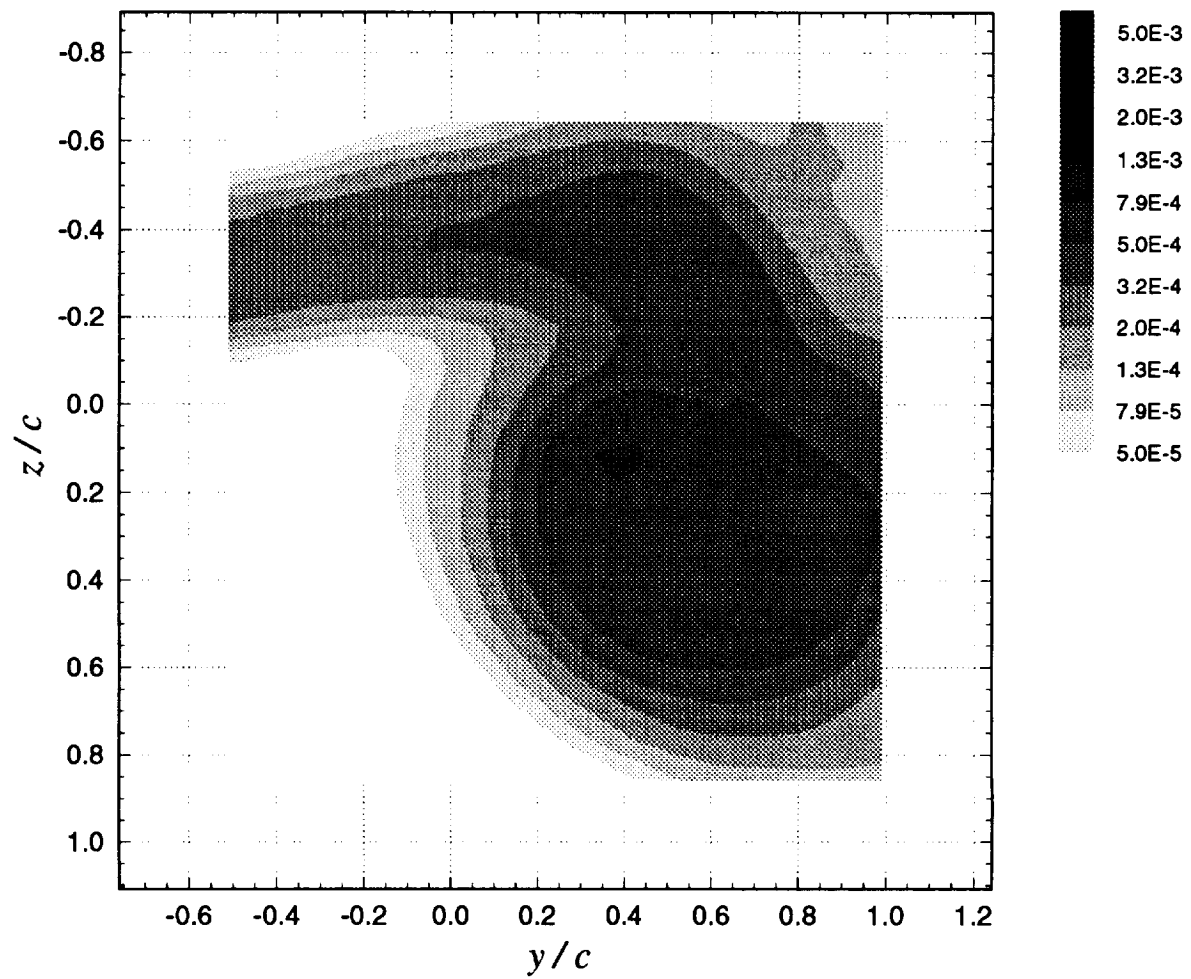


**Figure 3.54f** Contours of turbulent kinetic energy ( $k / U_{ref}^2$ ) for suction side passage of  $\Delta / c = -0.0625$ :  $x / c = 30$ ,  $\alpha_1 = 5^\circ$ ,  $\alpha_2 = 5^\circ$ ,  $d / c = 0.2125$

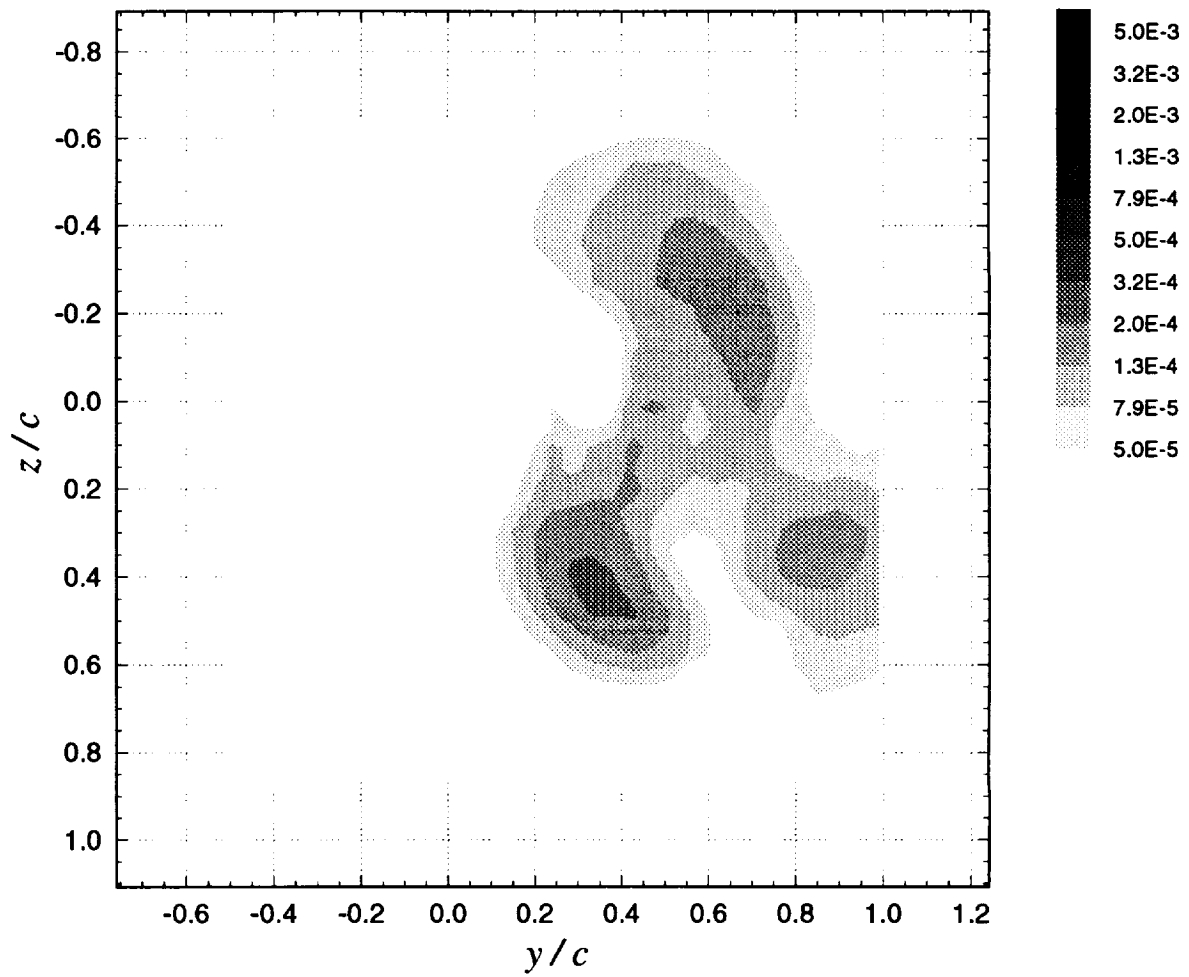


**Figure 3.54g** Contours of axial shear stress magnitude  $(\tau_a / U_{ref}^2)$  for suction side passage of  $\Delta/c = -0.0625$ :  $x/c = 30$ ,  $\alpha_1 = 5^\circ$ ,  $\alpha_2 = 5^\circ$ ,  $d/c = 0.2125$

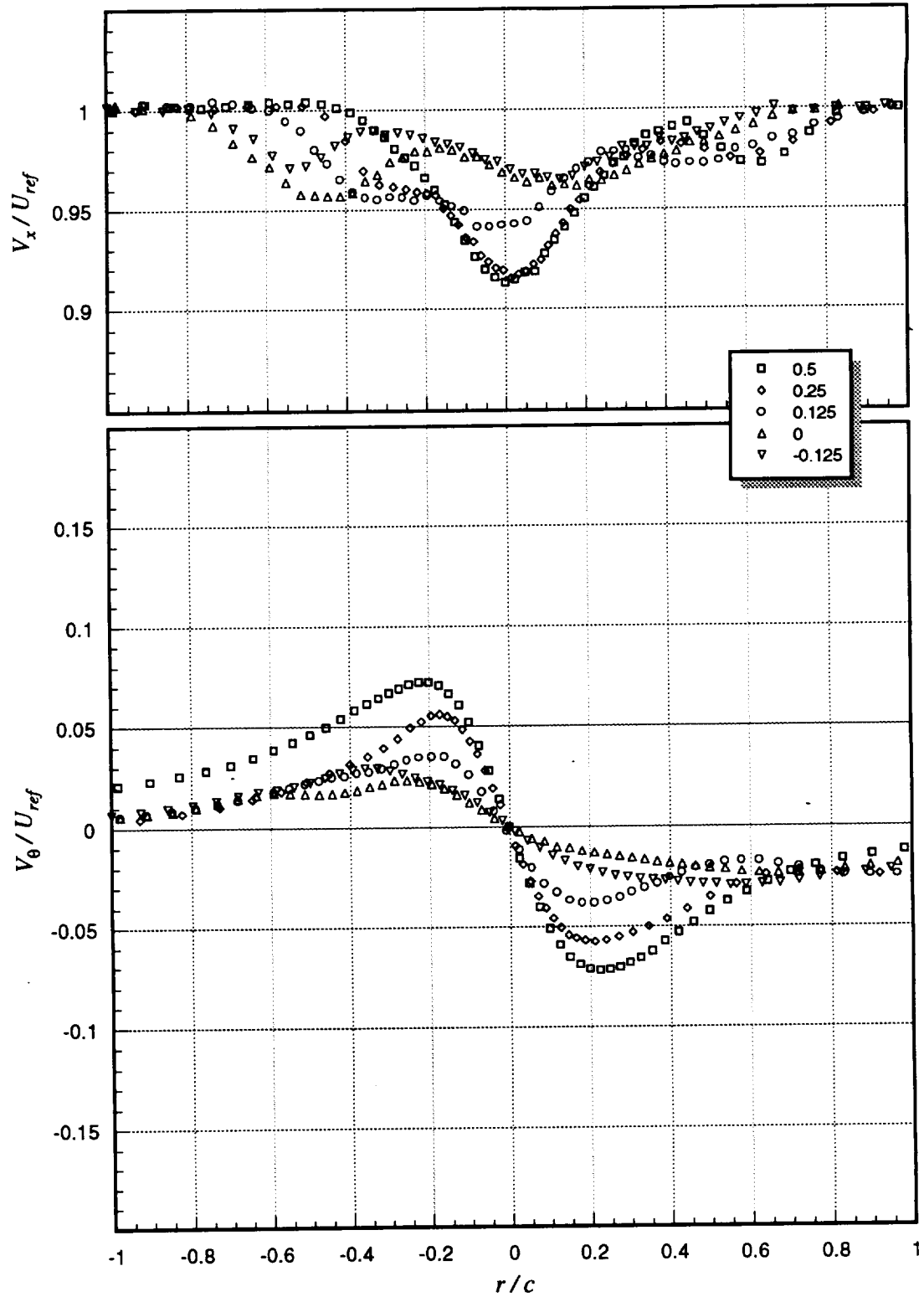


**Figure 3.55** Mean axial ( $V_x$ ) and tangential ( $V_\theta$ ) velocities (measured along  $z$ -wise profiles through the vortex core center) as a function of blade-vortex separation ( $\Delta$ ):  $x/c = 30$ ,  $\alpha_1 = 5^\circ$ ,  $\alpha_2 = 5^\circ$ ,  $d/c = 0.2125$ . Legend lists  $\Delta/c$  values.

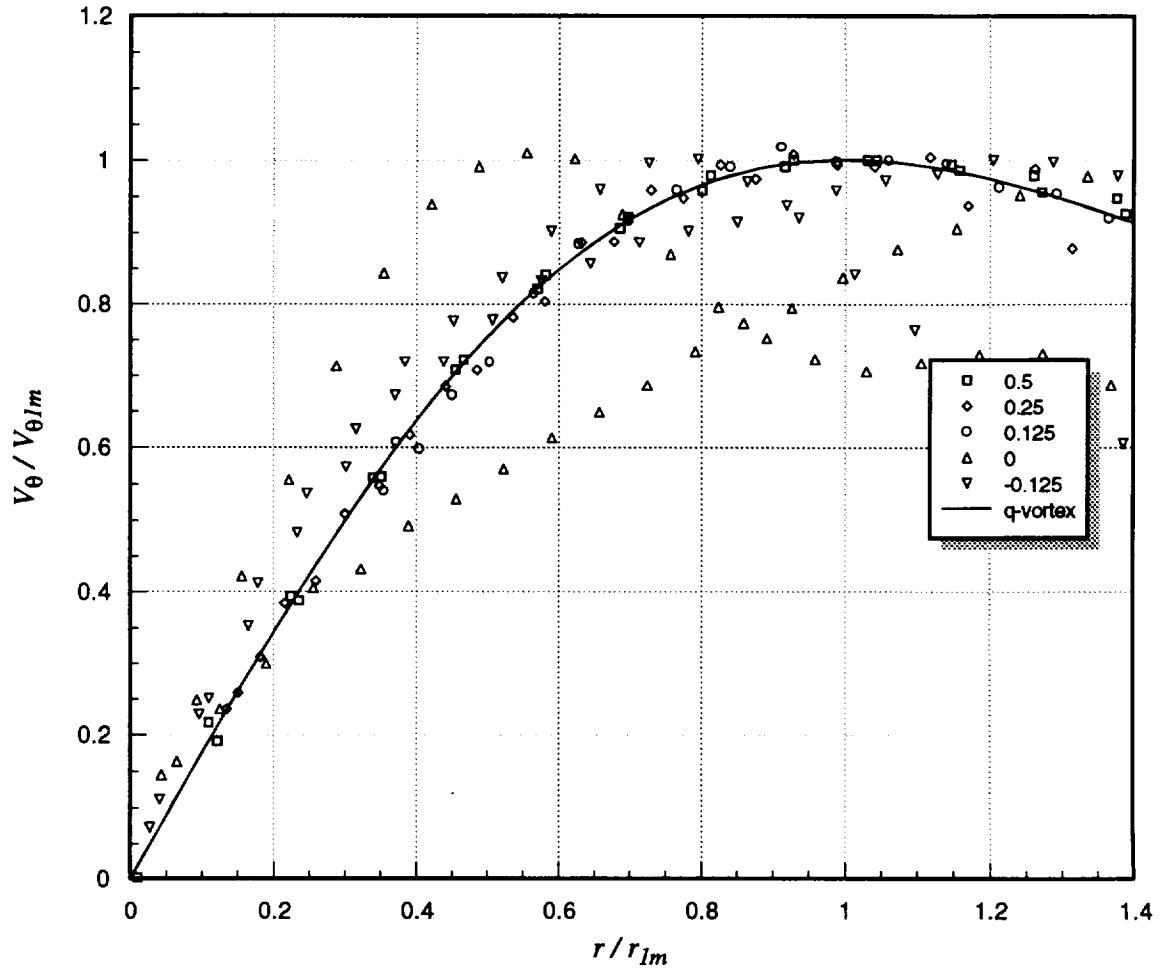


**Figure 3.56** Mean tangential ( $V_\theta$ ) velocities (measured along  $z$ -wise profiles through the vortex core center), normalized on measured peak tangential velocity ( $V_{\theta 1m}$ ), as a function of blade–vortex separation ( $\Delta$ ):  $x/c = 30$ ,  $\alpha_1 = 5^\circ$ ,  $\alpha_2 = 5^\circ$ ,  $d/c = 0.2125$ . Legend lists  $\Delta/c$  values.

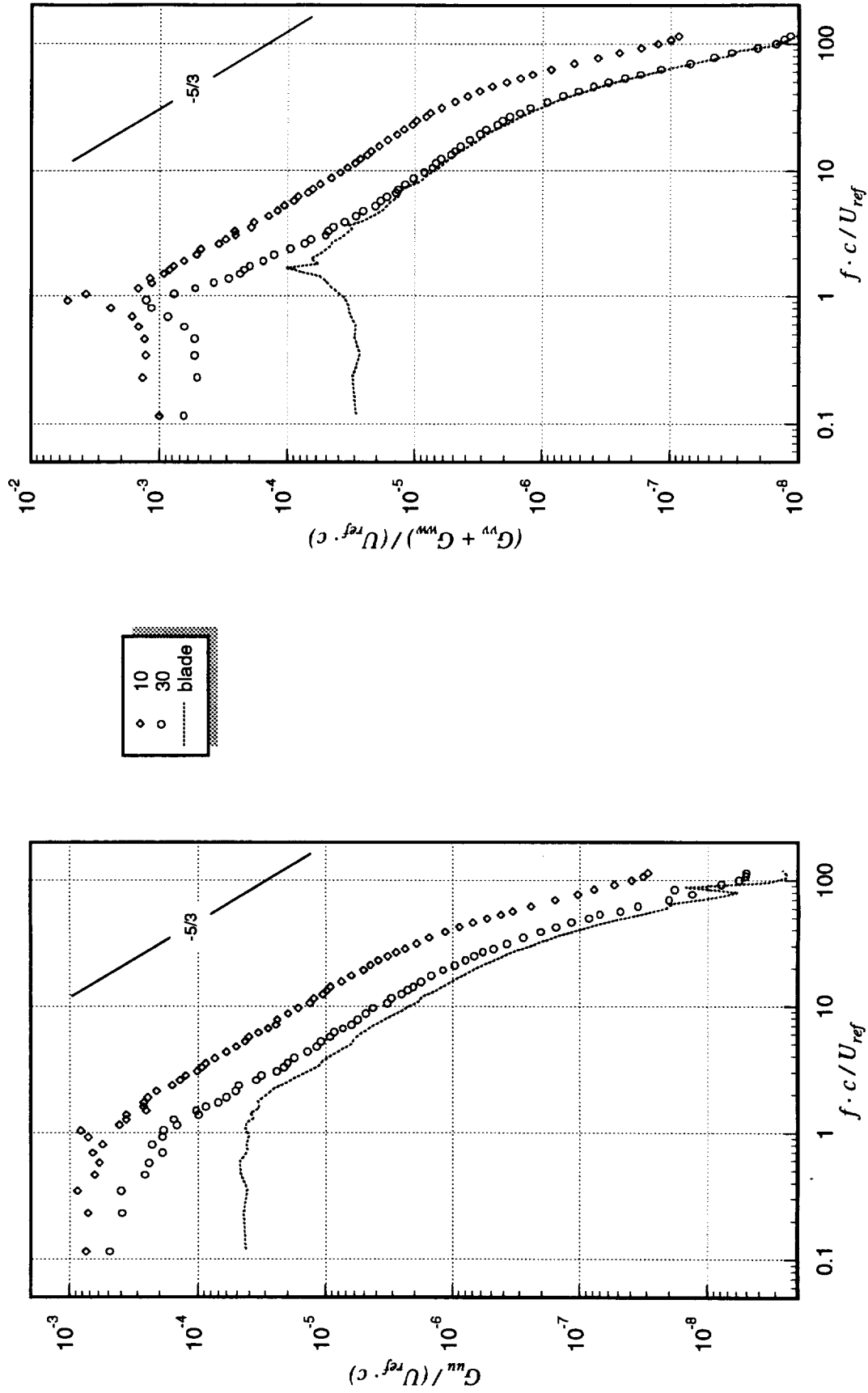


**Figure 3.57** Core center velocity autospectra for undisturbed vortex ( $x/c = 10$ ) and for suction side passage of  $\Delta/c = 0.5$  measured at  $x/c = 30$ :  $\alpha_1 = 5^\circ$ ,  $\alpha_2 = 5^\circ$ ,  $d/c = 0.2125$ . Legend lists  $x/c$  values. Autospectra measured in undisturbed portion of interaction blade wake at  $x/c = 30$  also included (marked as “blade” in legend).



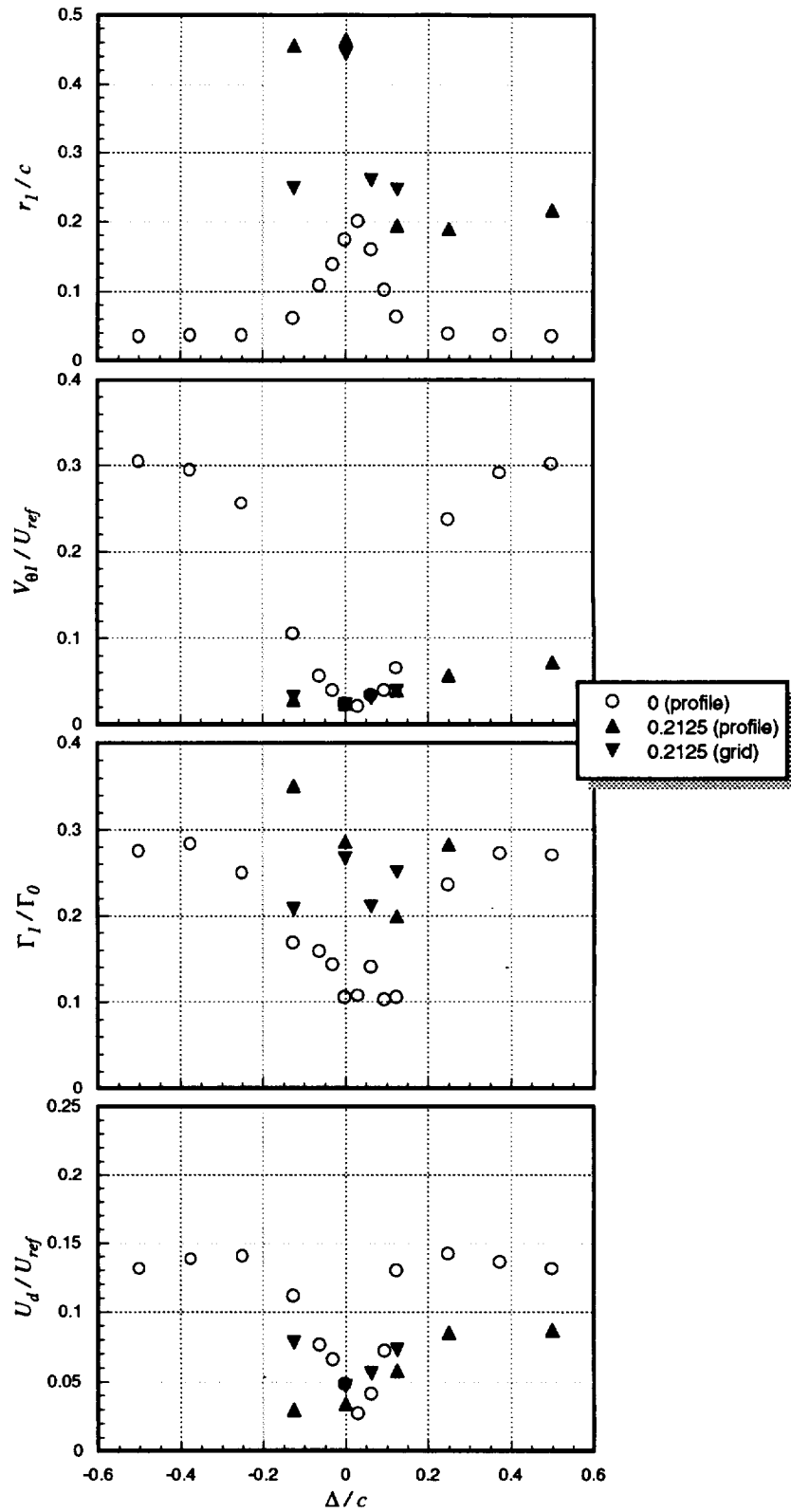


**Figure 3.58** Core parameters (radius,  $r_1$ ; peak tangential velocity,  $V_{\theta 1}$ ; circulation,  $\Gamma_1$ ; and axial velocity deficit,  $U_d$ ) as a function of blade-vortex separation ( $\Delta$ ) for different spoiler diameters ( $d$ ):  $x/c = 30$ ,  $\alpha_1 = 5^\circ$ ,  $\alpha_2 = 5^\circ$ . Legend lists  $d/c$  values (source of parameters also specified).

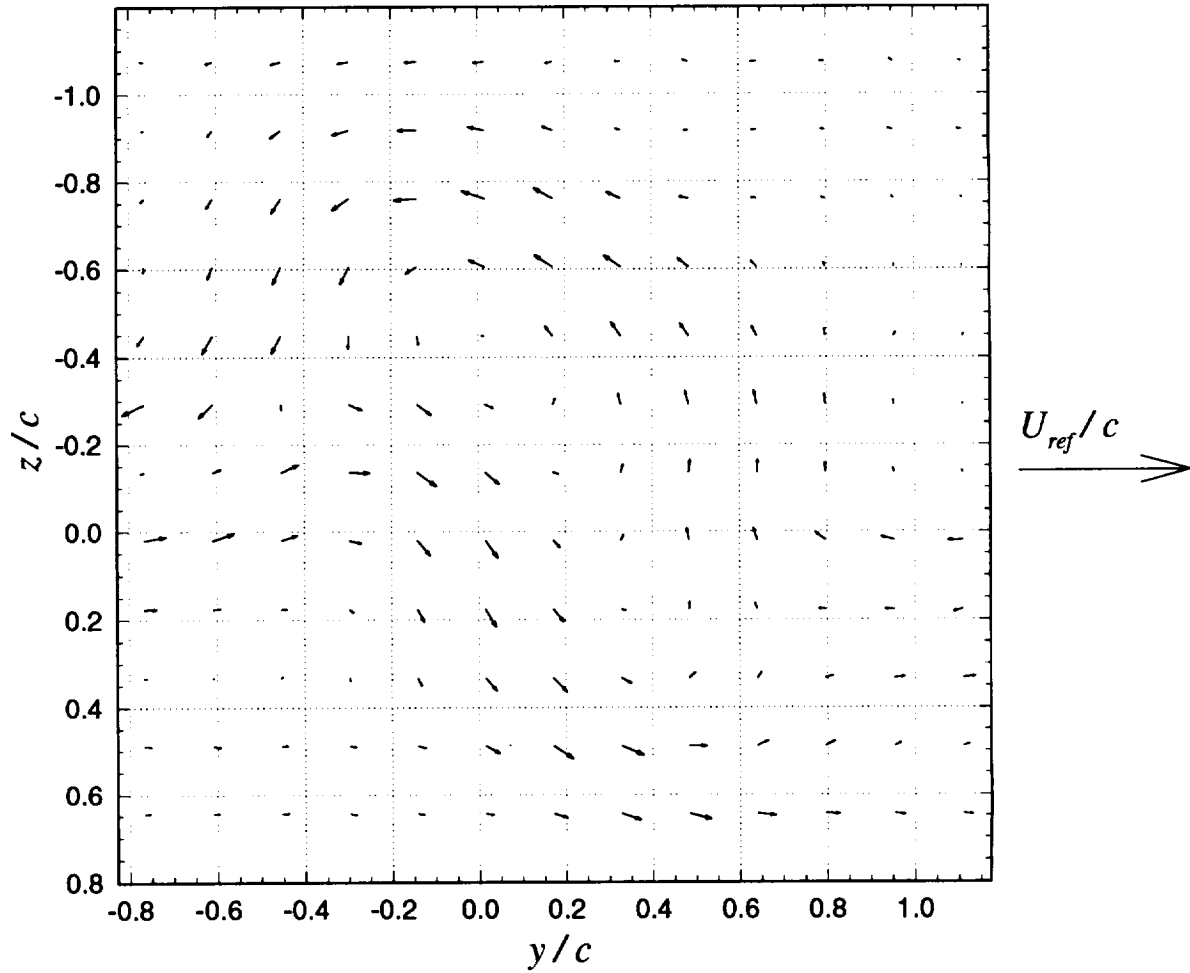


**Figure 3.59a** Mean cross-flow vorticity vectors ( $\Omega_y \cdot c / U_{ref}$ ,  $\Omega_z \cdot c / U_{ref}$ ) for suction side passage of  $\Delta/c = 0.125$ :  $x/c = 30$ ,  $\alpha_1 = 5^\circ$ ,  $\alpha_2 = 5^\circ$ ,  $d/c = 0.3125$

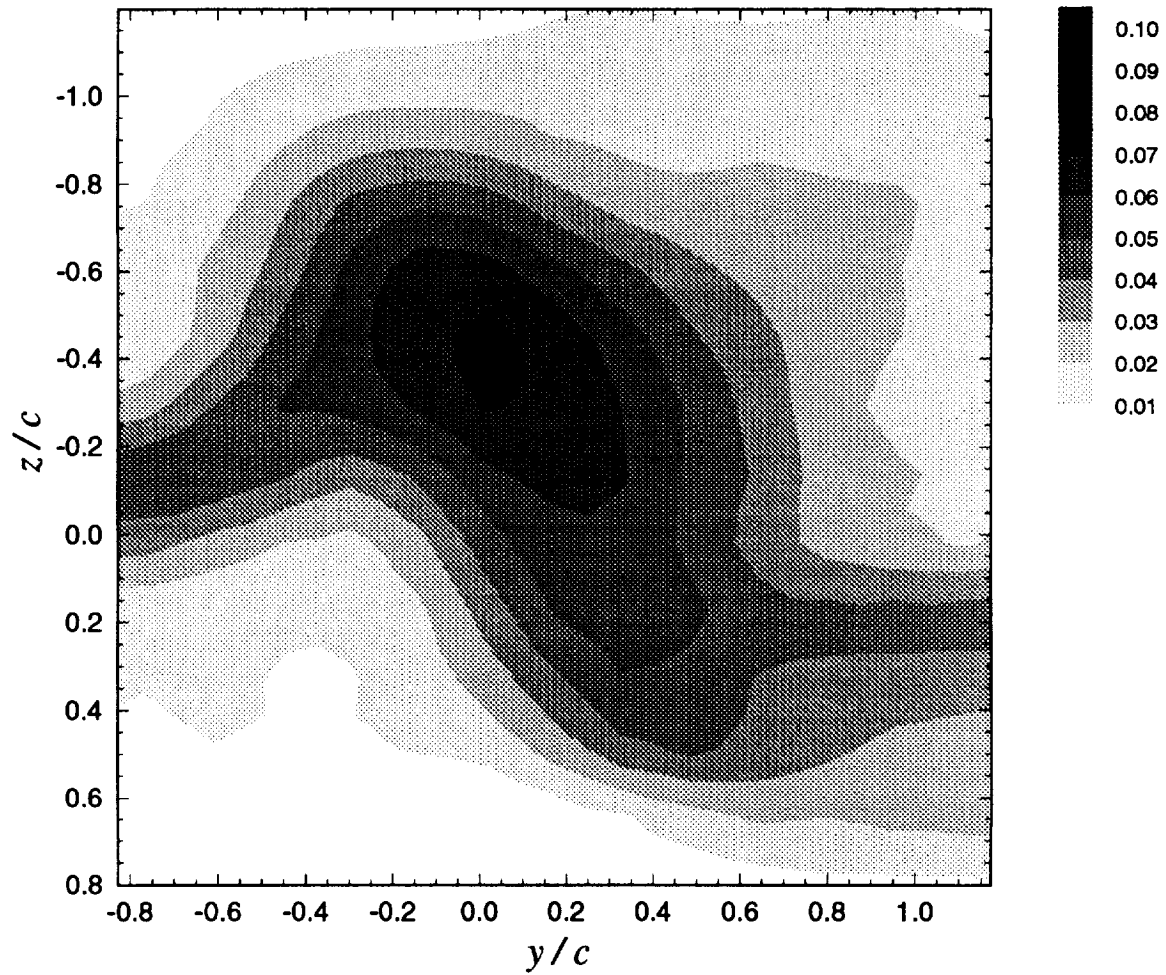


**Figure 3.59b** Contours of mean axial velocity deficit  $((U_{ref} - U) / U_{ref})$  for suction side passage of  $\Delta/c = 0.125$ :  $x/c = 30$ ,  $\alpha_1 = 5^\circ$ ,  $\alpha_2 = 5^\circ$ ,  $d/c = 0.3125$

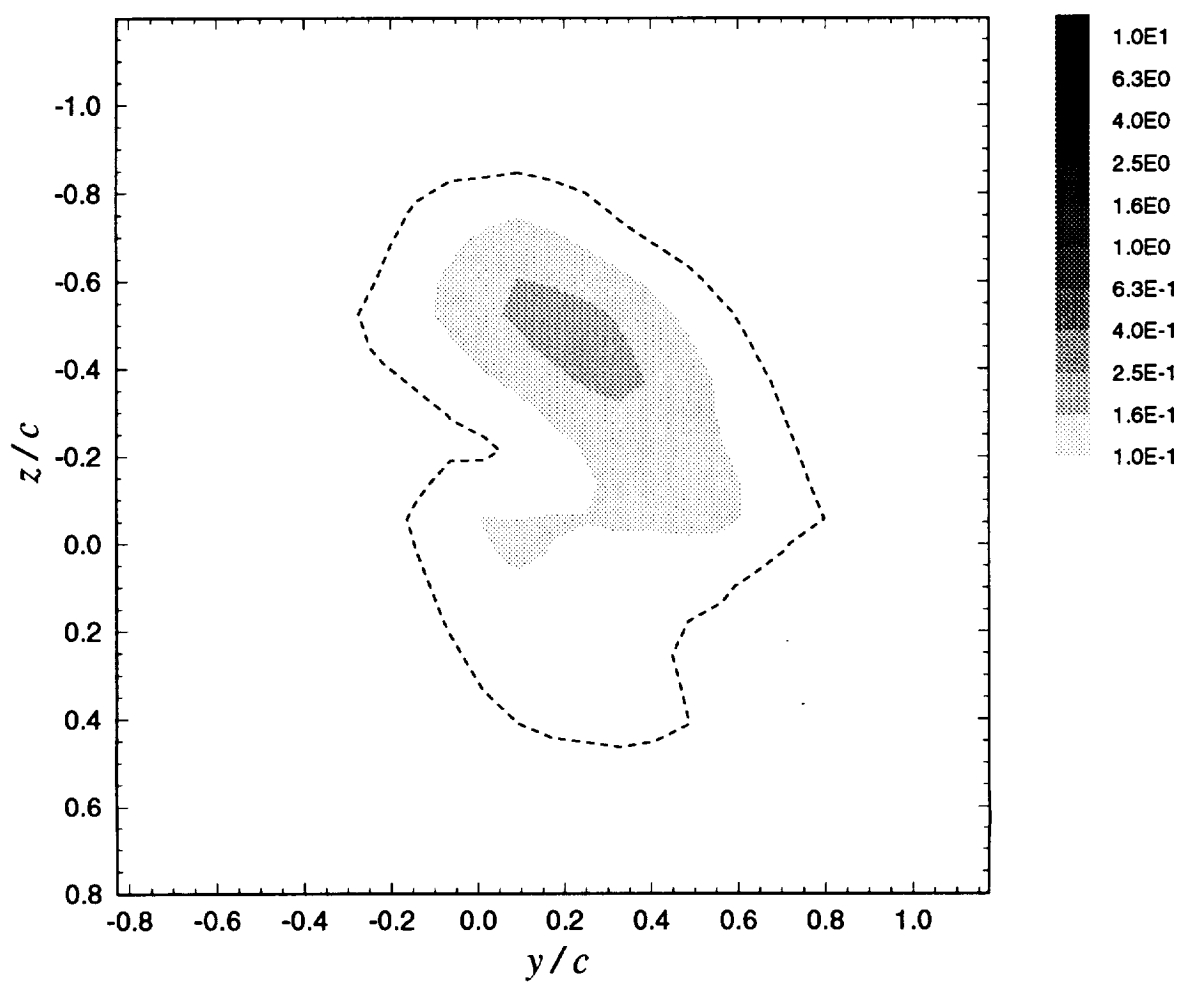


**Figure 3.59c** Contours of mean axial vorticity ( $\Omega_x \cdot c / U_{ref}$ ) for suction side passage of  $\Delta / c = 0.125$ :  $x / c = 30$ ,  $\alpha_1 = 5^\circ$ ,  $\alpha_2 = 5^\circ$ ,  $d / c = 0.3125$ . Dashed contour line is core edge estimate.

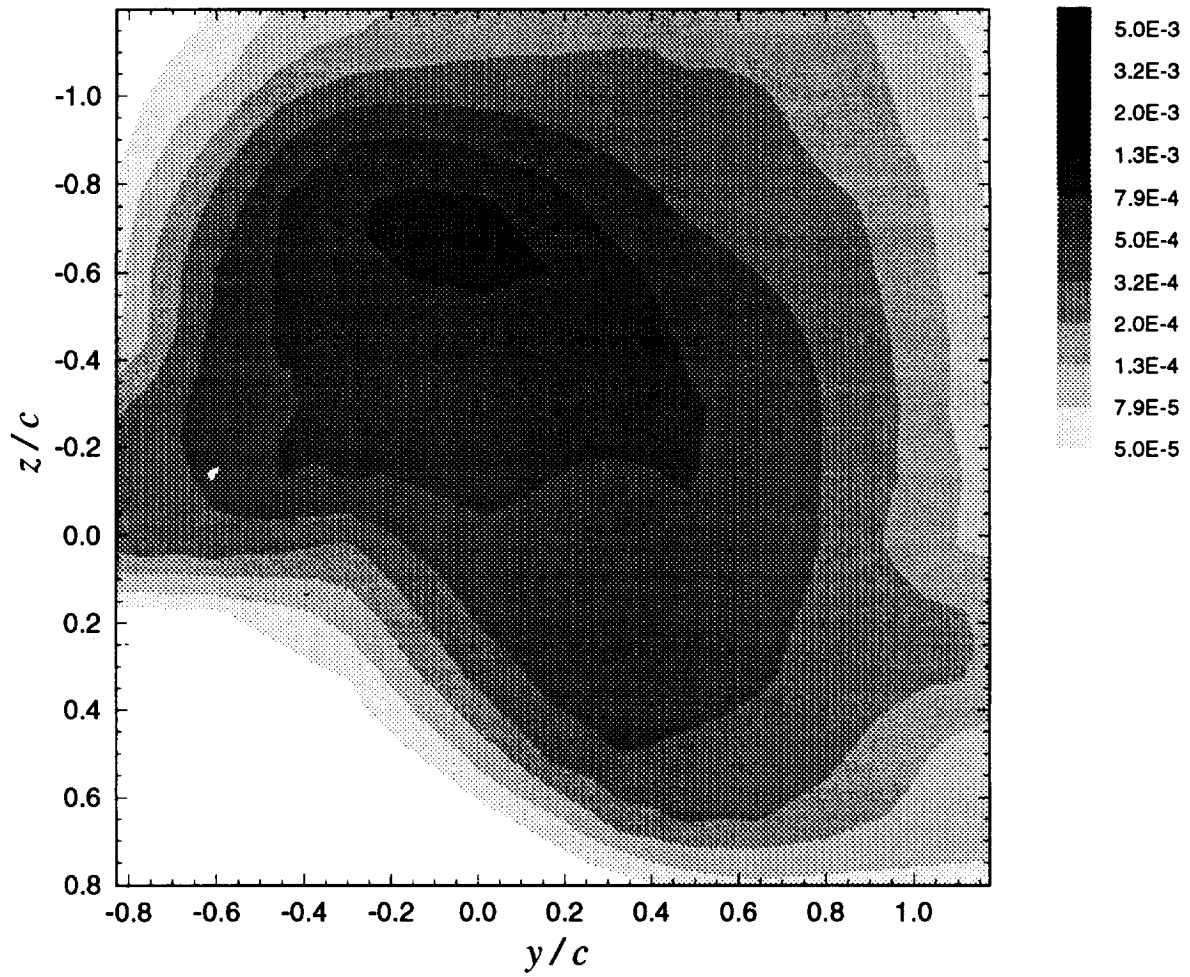


**Figure 3.59d** Contours of axial normal turbulent stress ( $\overline{u^2} / U_{ref}^2$ ) for suction side passage of  $\Delta/c = 0.125$ :  $x/c = 30$ ,  $\alpha_1 = 5^\circ$ ,  $\alpha_2 = 5^\circ$ ,  $d/c = 0.3125$

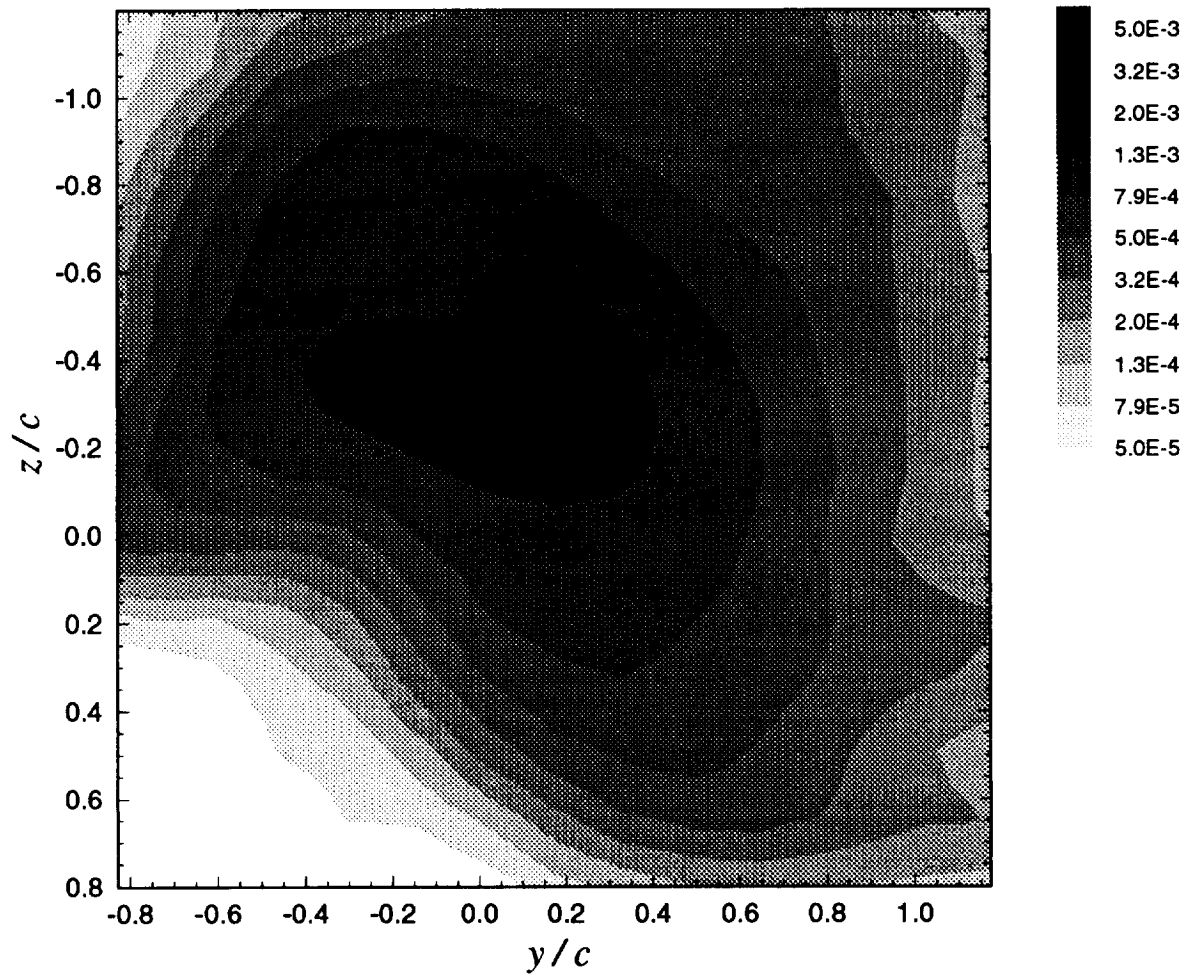


**Figure 3.59e** Contours of summed cross-flow normal turbulent stresses  $(\overline{v^2} + \overline{w^2}) / U_{ref}^2$  for suction side passage of  $\Delta/c = 0.125$ :  $x/c = 30$ ,  $\alpha_1 = 5^\circ$ ,  $\alpha_2 = 5^\circ$ ,  $d/c = 0.3125$

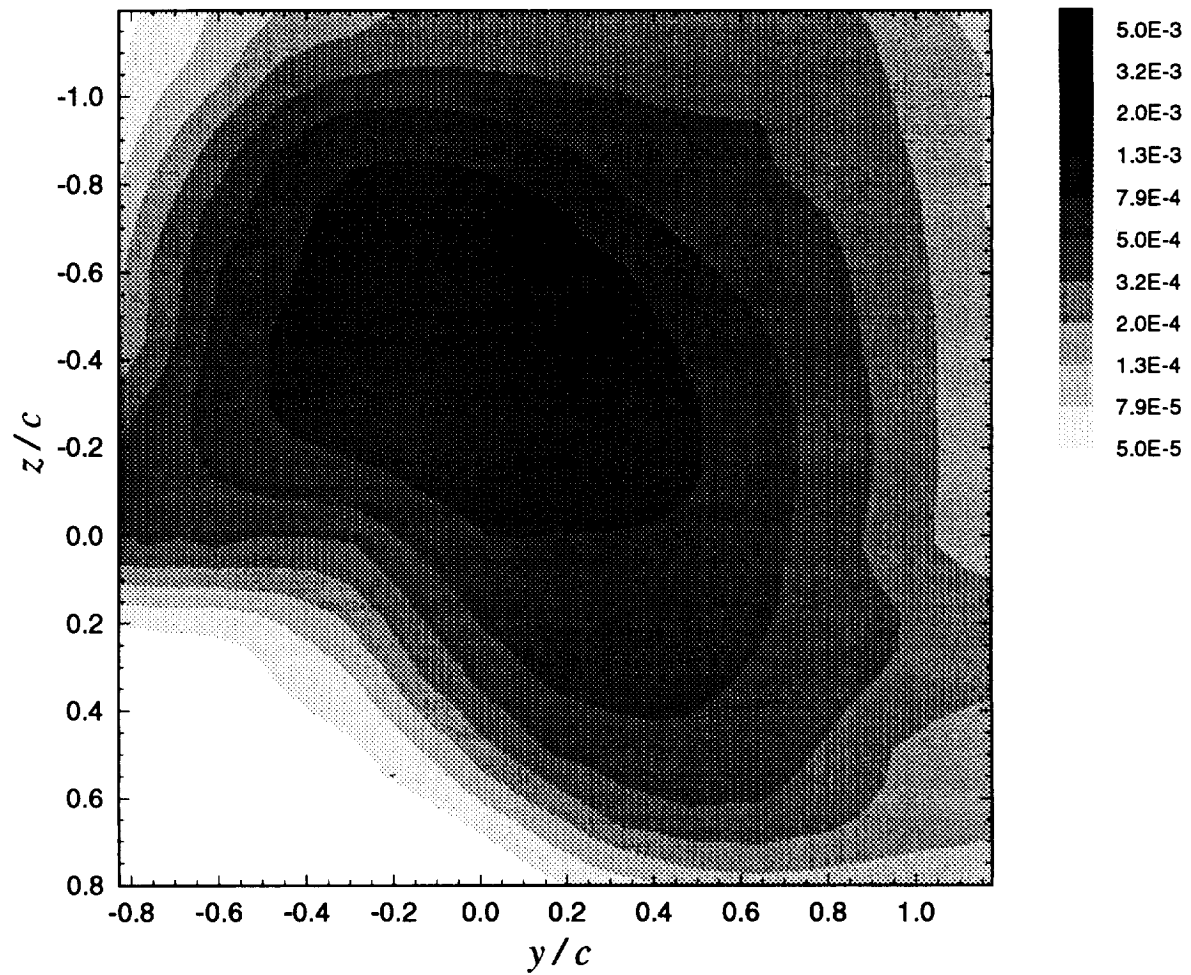


**Figure 3.59f** Contours of turbulent kinetic energy ( $k / U_{ref}^2$ ) for suction side passage of  $\Delta / c = 0.125$ :  $x / c = 30$ ,  $\alpha_1 = 5^\circ$ ,  $\alpha_2 = 5^\circ$ ,  $d / c = 0.3125$

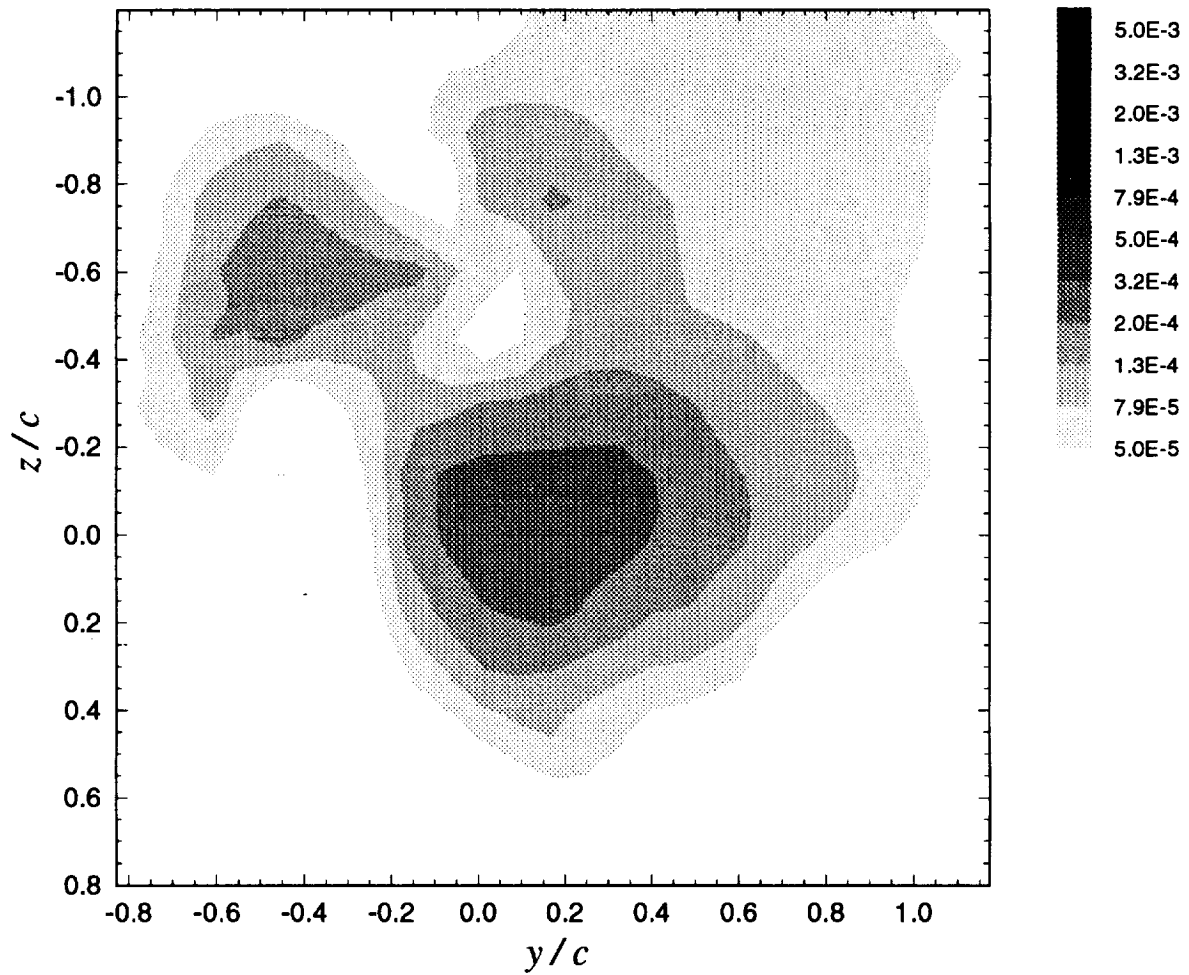


**Figure 3.59g** Contours of axial shear stress magnitude ( $\tau_a / U_{ref}^2$ ) for suction side passage of  $\Delta/c = 0.125$ :  $x/c = 30$ ,  $\alpha_1 = 5^\circ$ ,  $\alpha_2 = 5^\circ$ ,  $d/c = 0.3125$



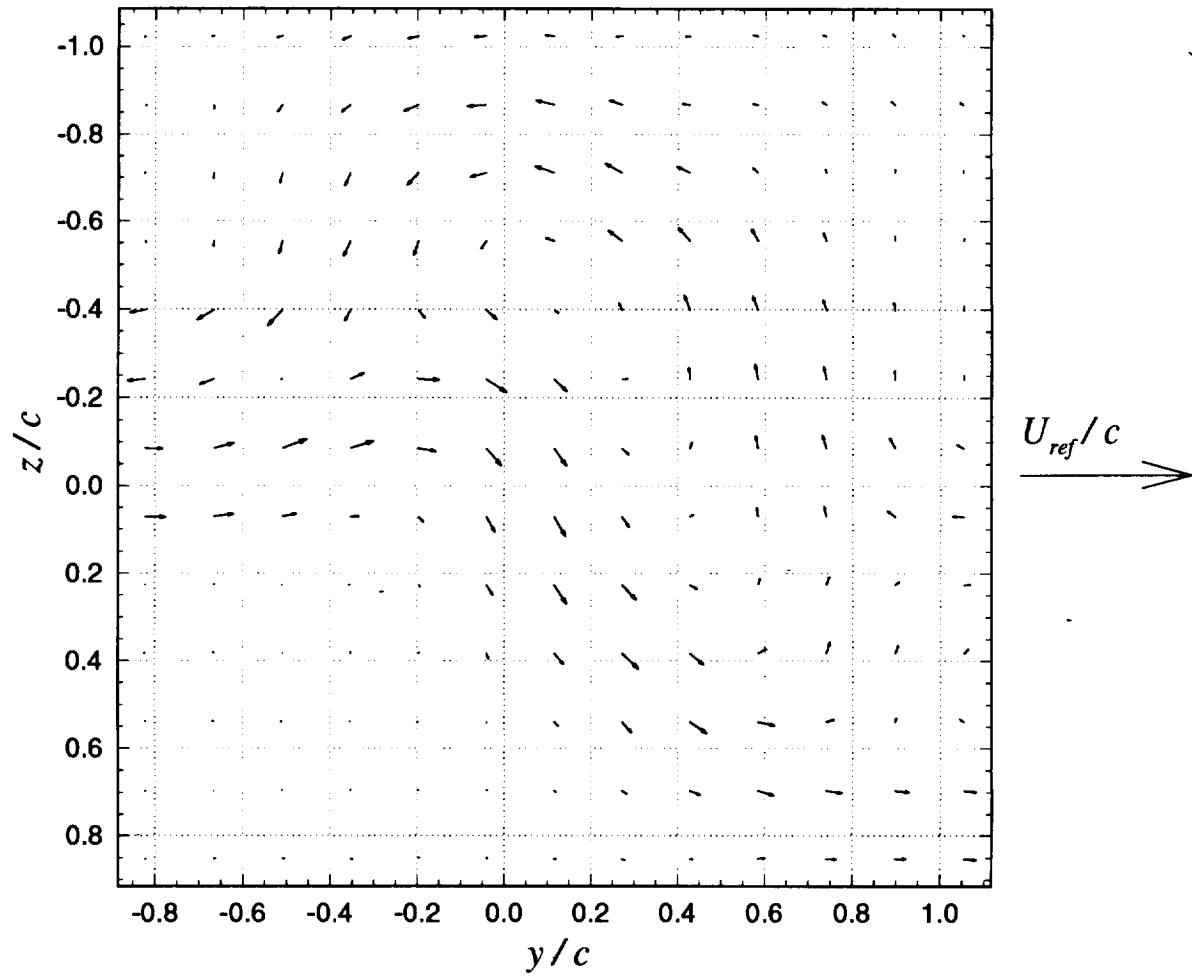


**Figure 3.60a** Mean cross-flow vorticity vectors ( $\Omega_y \cdot c / U_{ref}$ ,  $\Omega_z \cdot c / U_{ref}$ ) for suction side passage of  $\Delta/c = 0.0625$ :  $x/c = 30$ ,  $\alpha_1 = 5^\circ$ ,  $\alpha_2 = 5^\circ$ ,  $d/c = 0.3125$

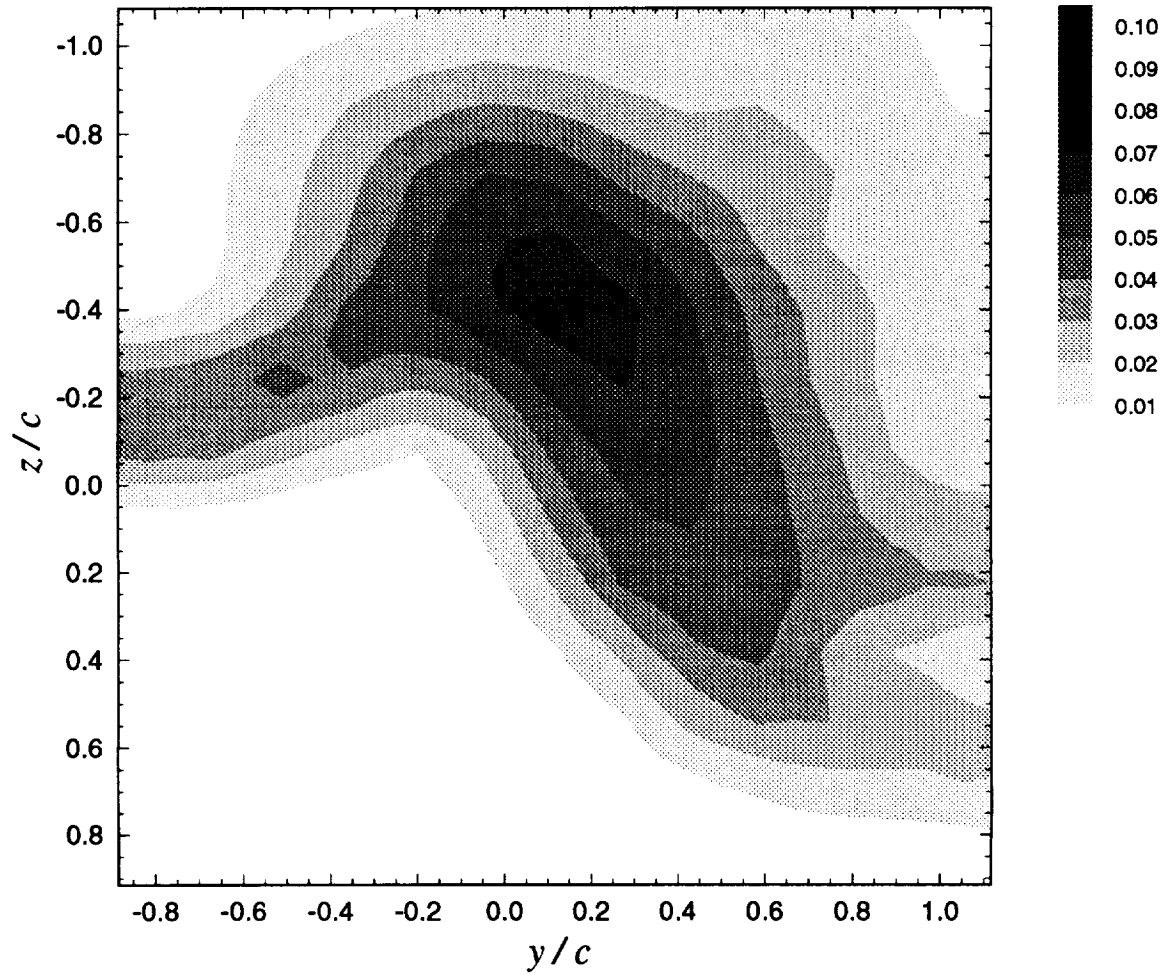


**Figure 3.60b** Contours of mean axial velocity deficit  $(U_{ref} - U) / U_{ref}$  for suction side passage of  $\Delta/c = 0.0625$ :  $x/c = 30$ ,  $\alpha_1 = 5^\circ$ ,  $\alpha_2 = 5^\circ$ ,  $d/c = 0.3125$

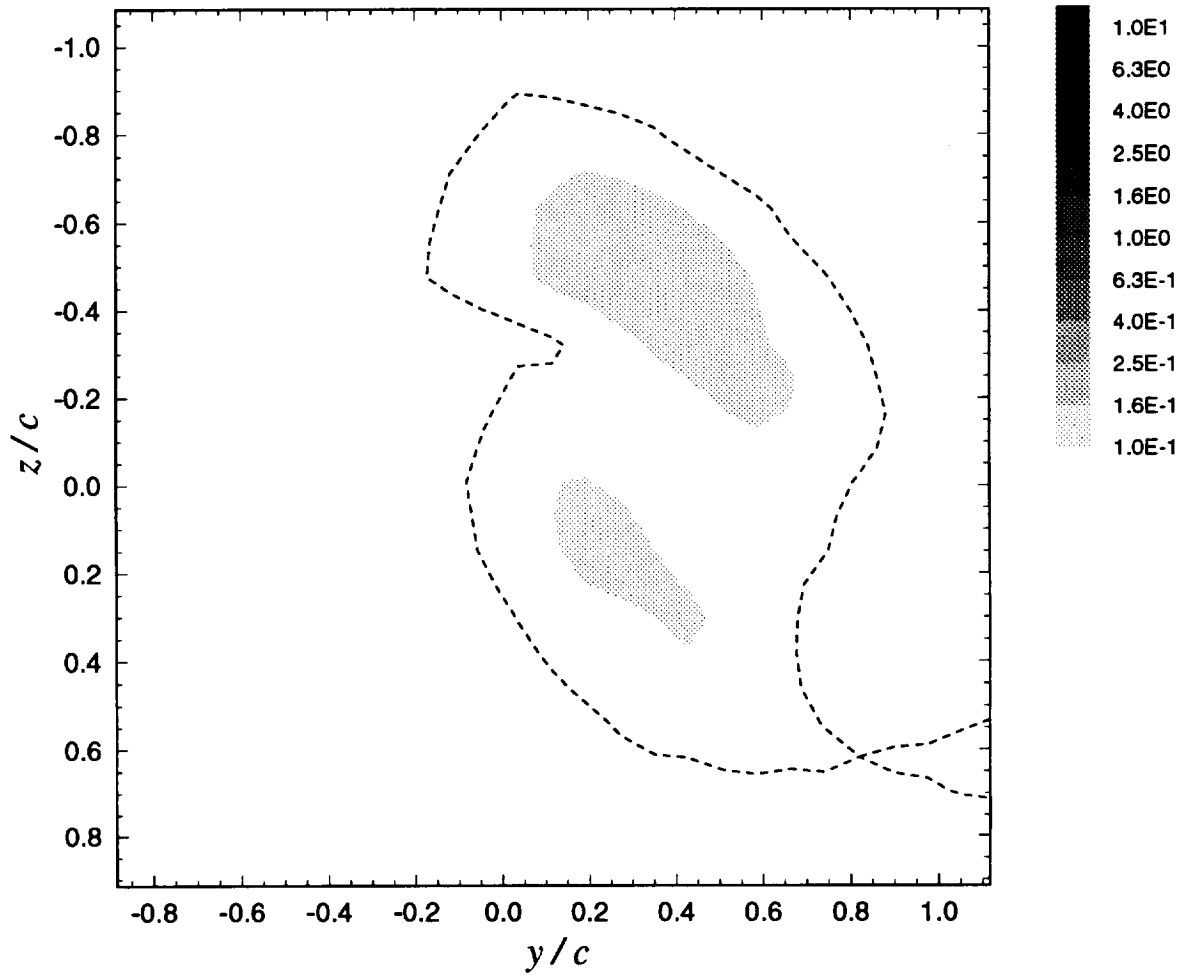


**Figure 3.60c** Contours of mean axial vorticity ( $\Omega_x \cdot c / U_{ref}$ ) for suction side passage of  $\Delta/c = 0.0625$ :  $x/c = 30$ ,  $\alpha_1 = 5^\circ$ ,  $\alpha_2 = 5^\circ$ ,  $d/c = 0.3125$ . Dashed contour line is core edge estimate.

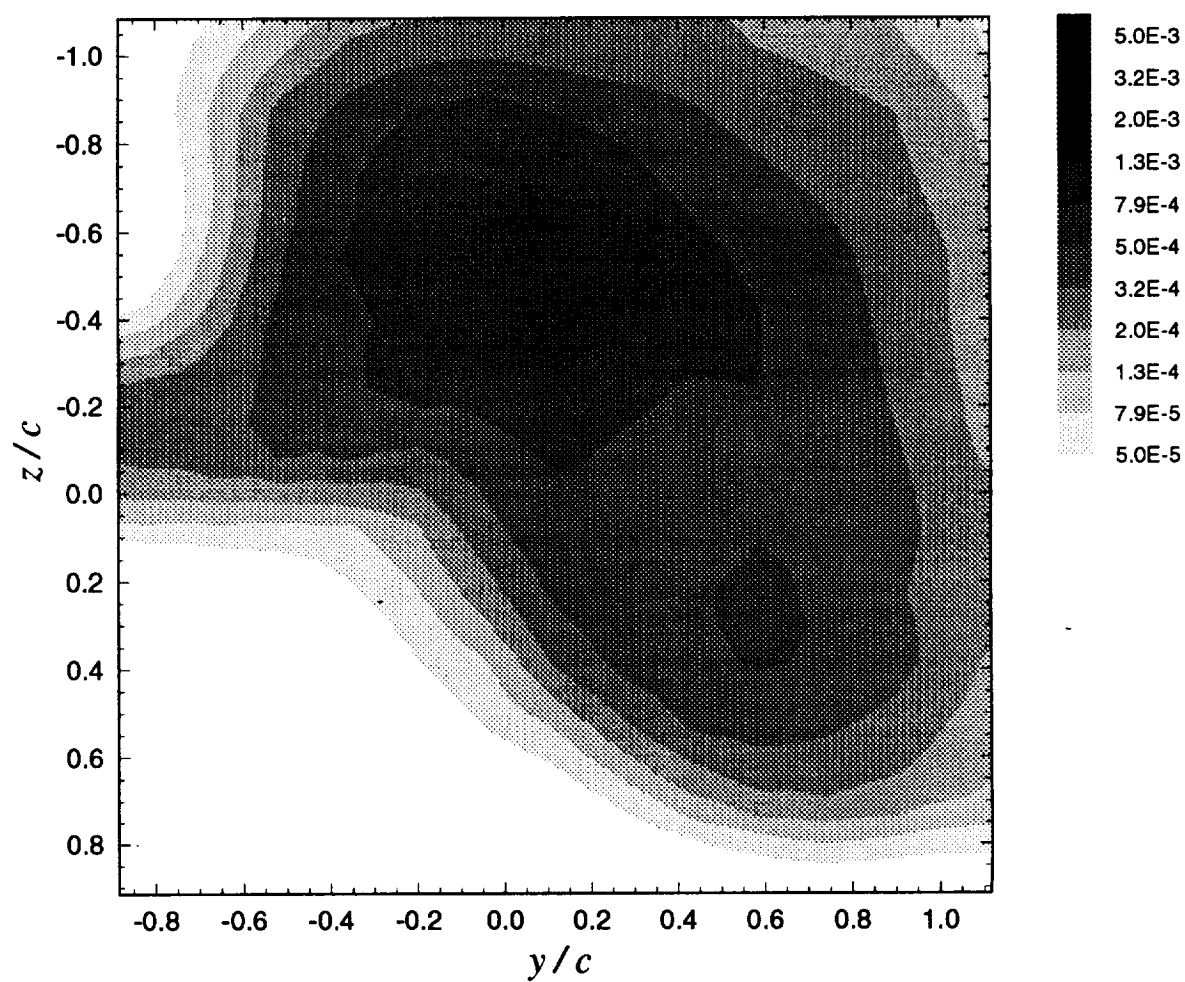


**Figure 3.60d** Contours of axial normal turbulent stress ( $\overline{u'^2} / U_{ref}^2$ ) for suction side passage of  $\Delta/c = 0.0625$ :  $x/c = 30$ ,  $\alpha_1 = 5^\circ$ ,  $\alpha_2 = 5^\circ$ ,  $d/c = 0.3125$

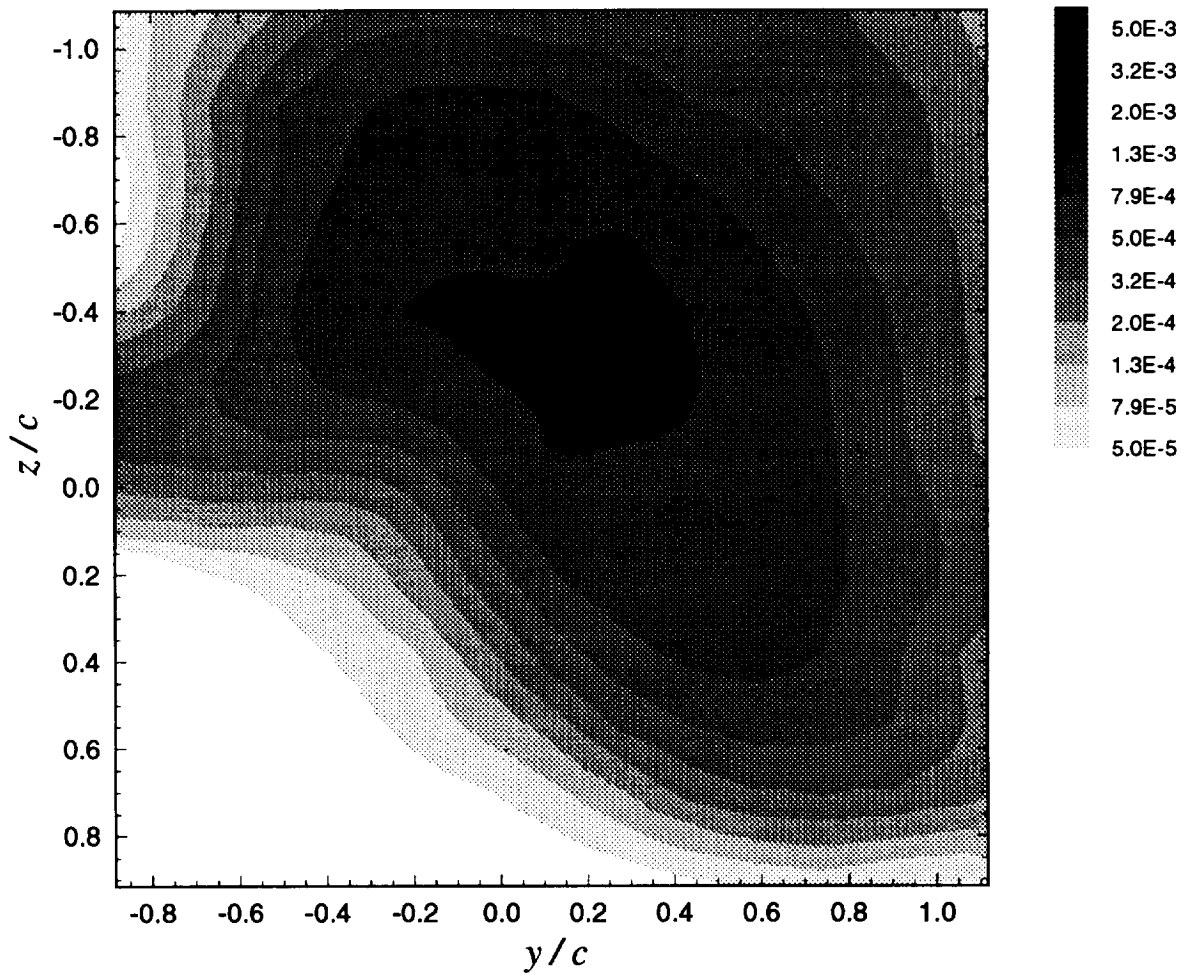


**Figure 3.60e** Contours of summed cross-flow normal turbulent stresses  $(\overline{v^2} + \overline{w^2}) / U_{ref}^2$  for suction side passage of  $\Delta/c = 0.0625$ :  $x/c = 30$ ,  $\alpha_1 = 5^\circ$ ,  $\alpha_2 = 5^\circ$ ,  $d/c = 0.3125$

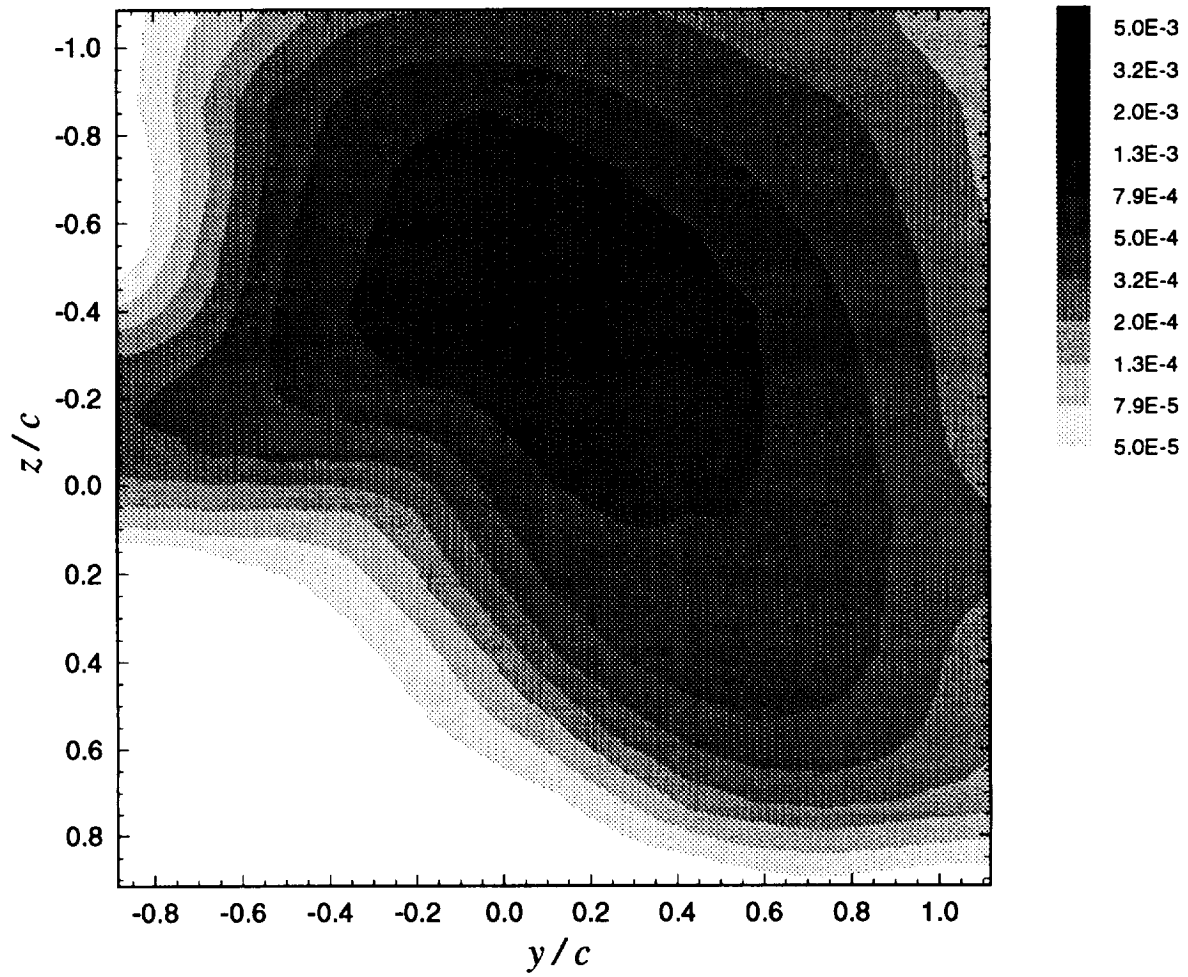


**Figure 3.60f** Contours of turbulent kinetic energy ( $k / U_{ref}^2$ ) for suction side passage of  $\Delta / c = 0.0625$ :  $x / c = 30$ ,  $\alpha_1 = 5^\circ$ ,  $\alpha_2 = 5^\circ$ ,  $d / c = 0.3125$

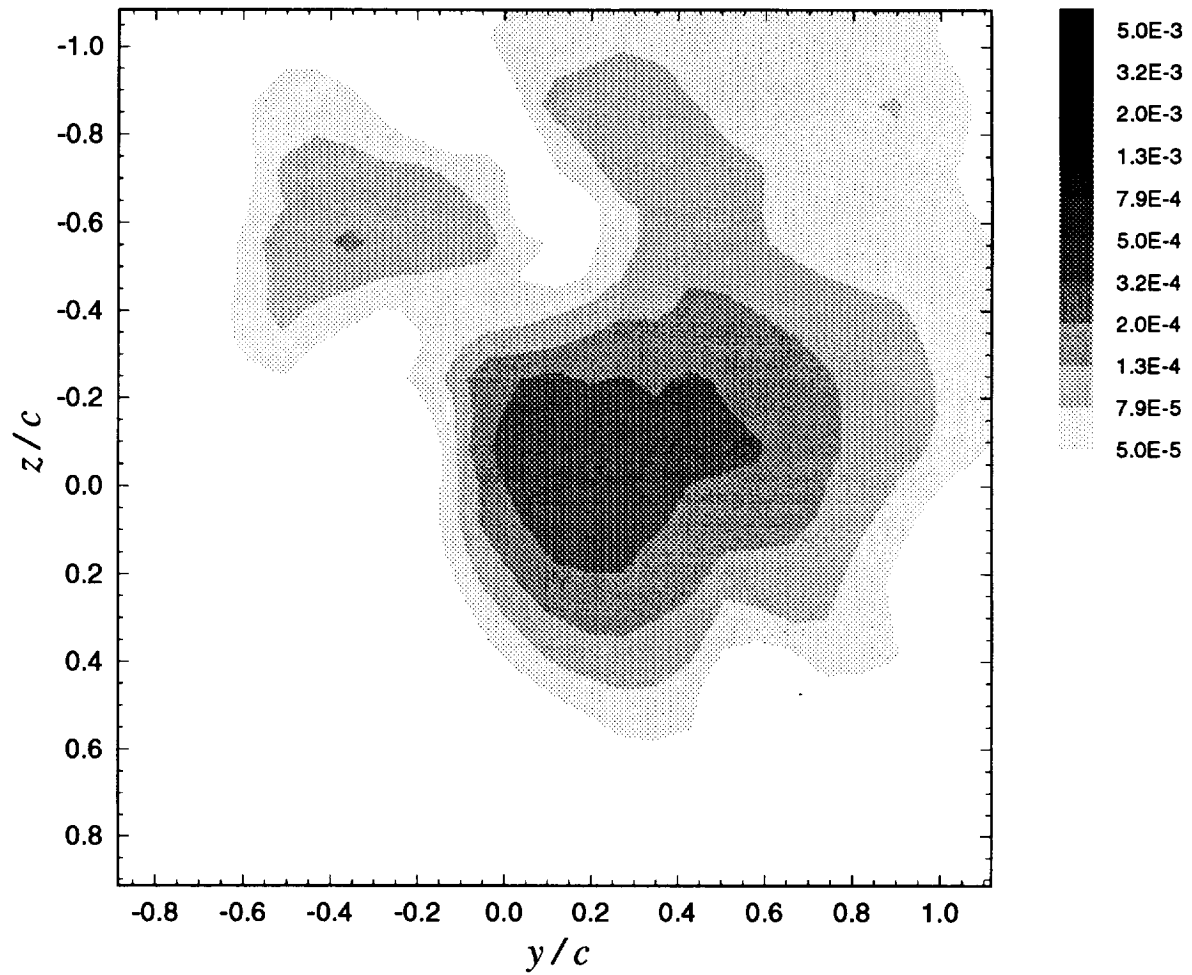


**Figure 3.60g** Contours of axial shear stress magnitude  $(\tau_a / U_{ref}^2)$  for suction side passage of  $\Delta/c = 0.0625$ :  $x/c = 30$ ,  $\alpha_1 = 5^\circ$ ,  $\alpha_2 = 5^\circ$ ,  $d/c = 0.3125$

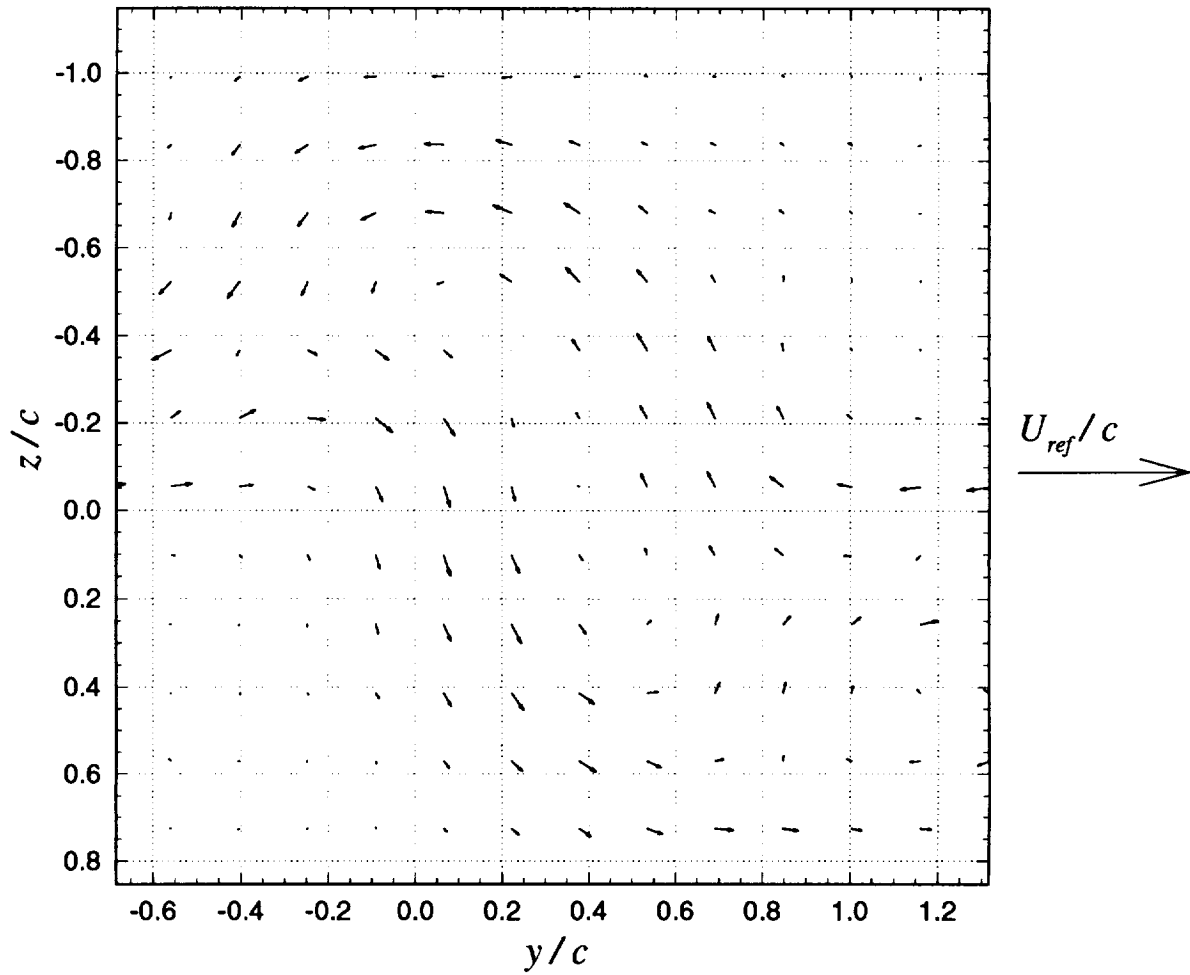


**Figure 3.61a** Mean cross-flow vorticity vectors ( $\Omega_y \cdot c / U_{ref}$ ,  $\Omega_z \cdot c / U_{ref}$ ) for vortex centerline stagnating on blade leading edge ( $\Delta = 0$ ):  $x/c = 30$ ,  $\alpha_1 = 5^\circ$ ,  $\alpha_2 = 5^\circ$ ,  $d/c = 0.3125$



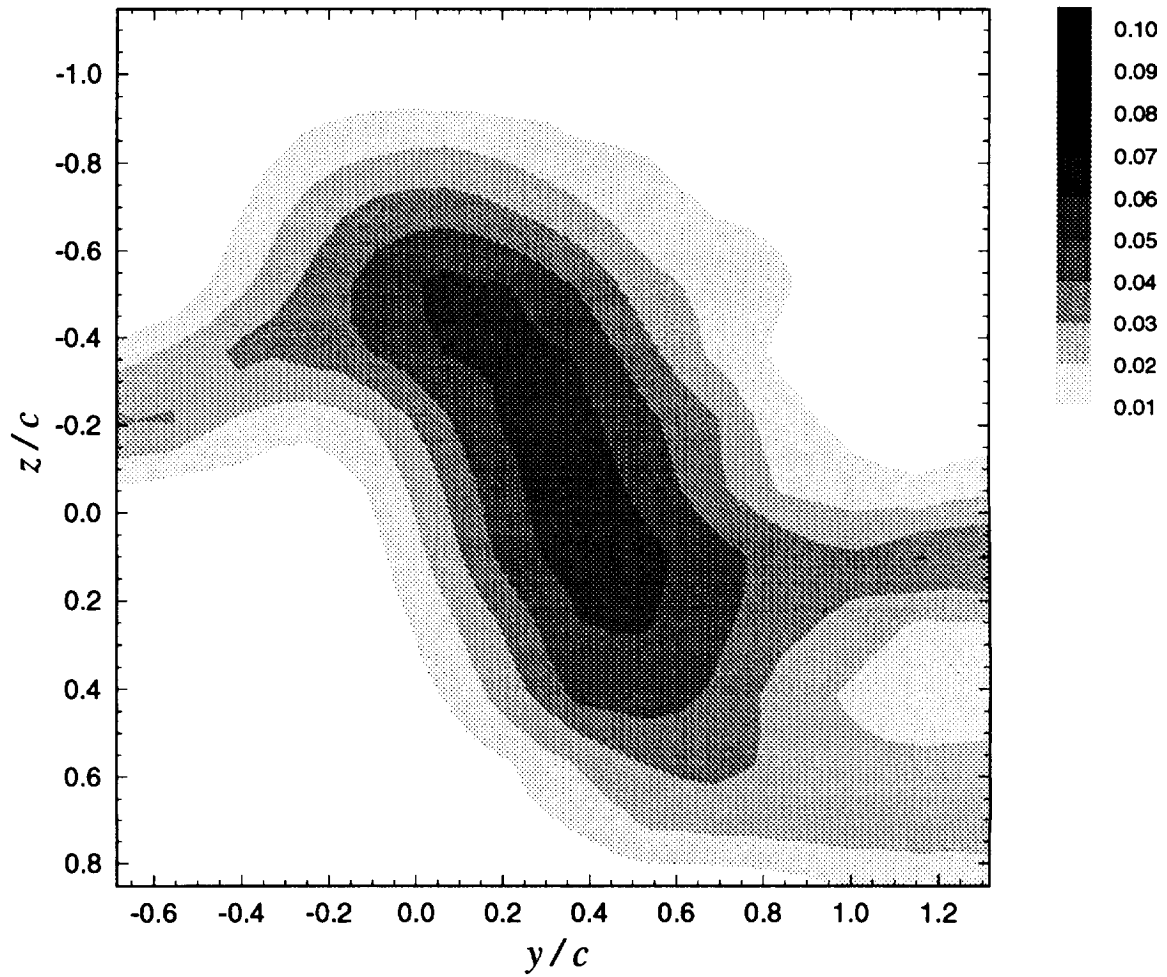


**Figure 3.61b** Contours of mean axial velocity deficit  $((U_{ref} - U) / U_{ref})$  for vortex centerline stagnating on blade leading edge ( $\Delta = 0$ ):  $x/c = 30$ ,  $\alpha_1 = 5^\circ$ ,  $\alpha_2 = 5^\circ$ ,  $d/c = 0.3125$

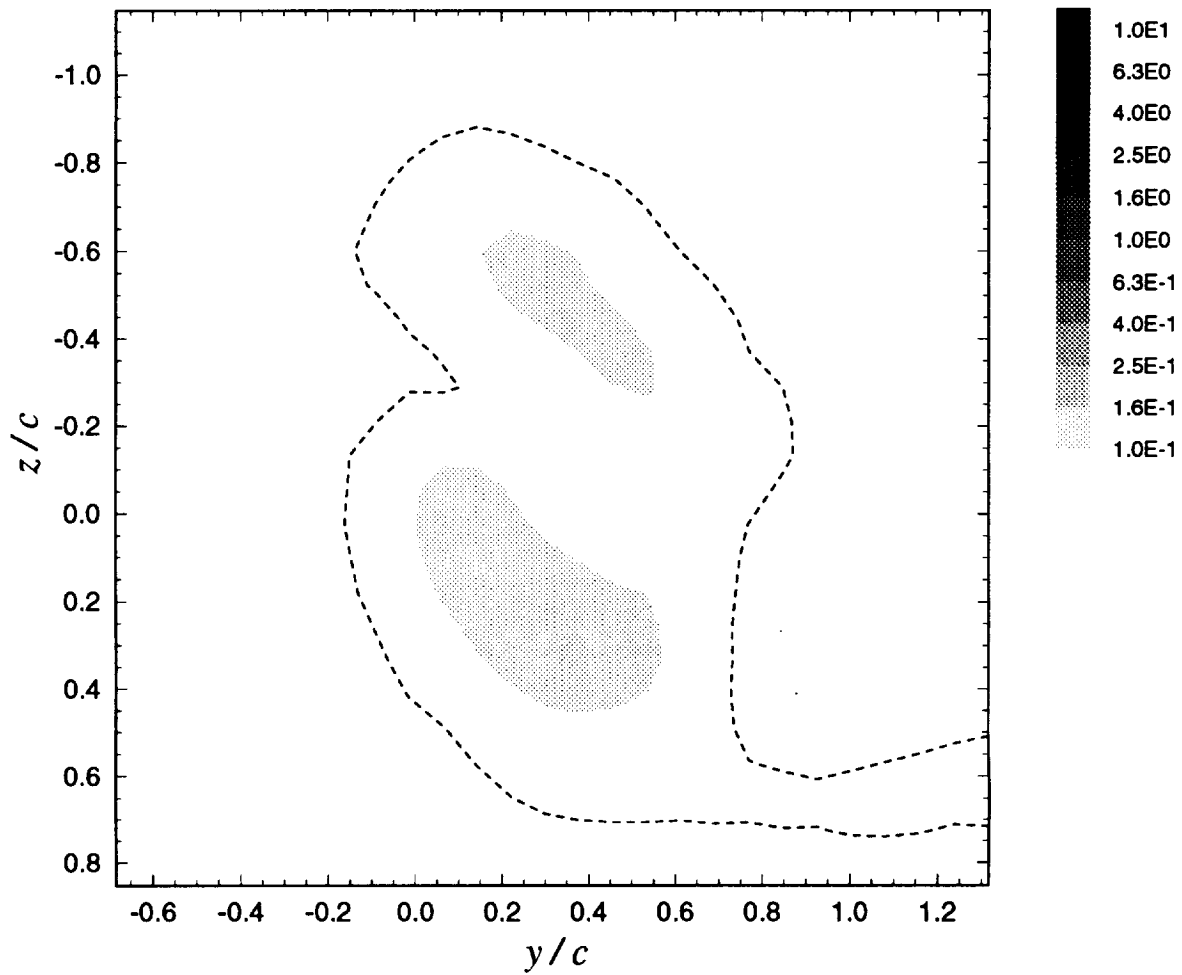


**Figure 3.61c** Contours of mean axial vorticity ( $\Omega_x \cdot c / U_{ref}$ ) for vortex centerline stagnating on blade leading edge ( $\Delta = 0$ ):  $x/c = 30$ ,  $\alpha_1 = 5^\circ$ ,  $\alpha_2 = 5^\circ$ ,  $d/c = 0.3125$ . Dashed contour line is core edge estimate.

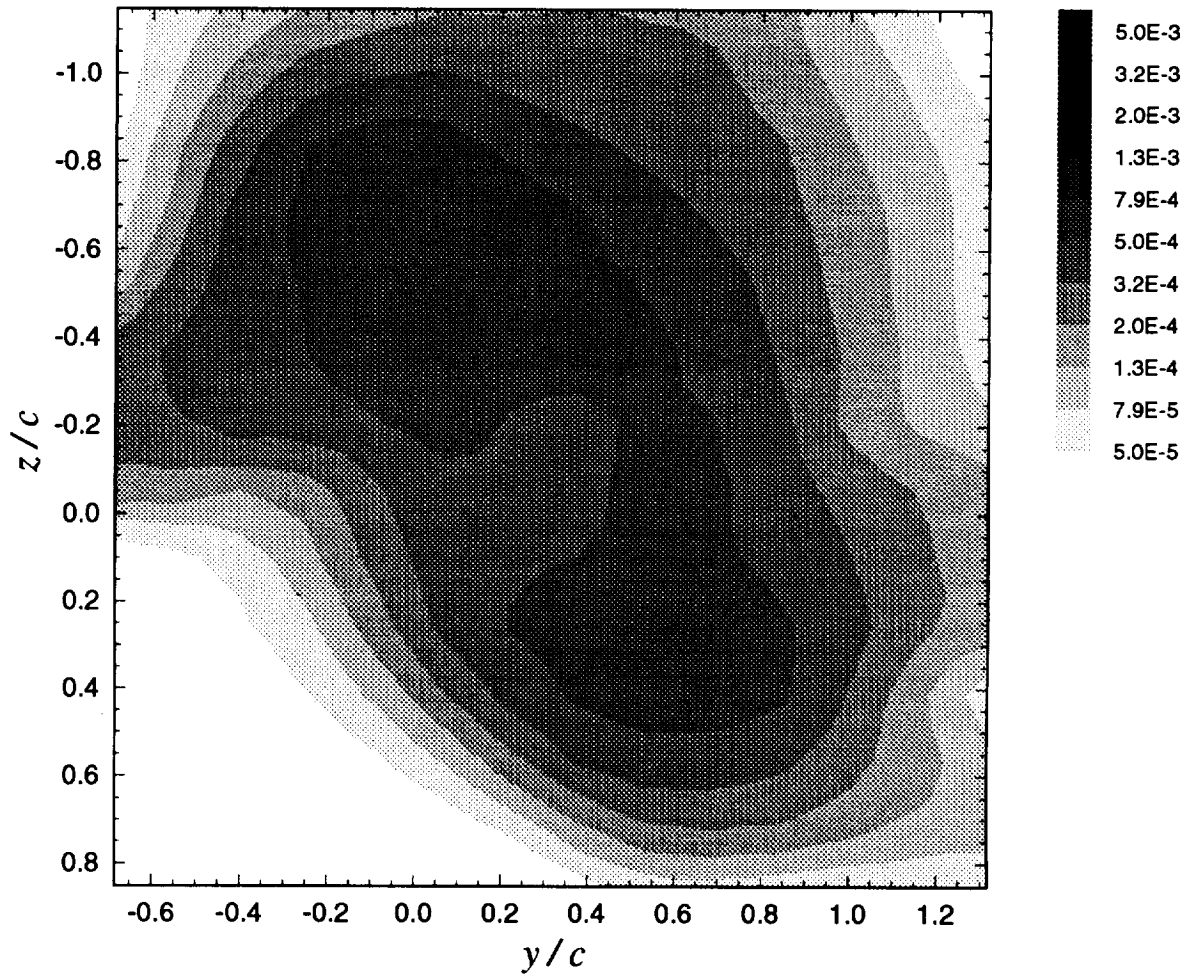


**Figure 3.61d** Contours of axial normal turbulent stress ( $\overline{u'^2} / U_{ref}^2$ ) for vortex centerline stagnating on blade leading edge ( $\Delta = 0$ ):  $x/c = 30$ ,  $\alpha_1 = 5^\circ$ ,  $\alpha_2 = 5^\circ$ ,  $d/c = 0.3125$

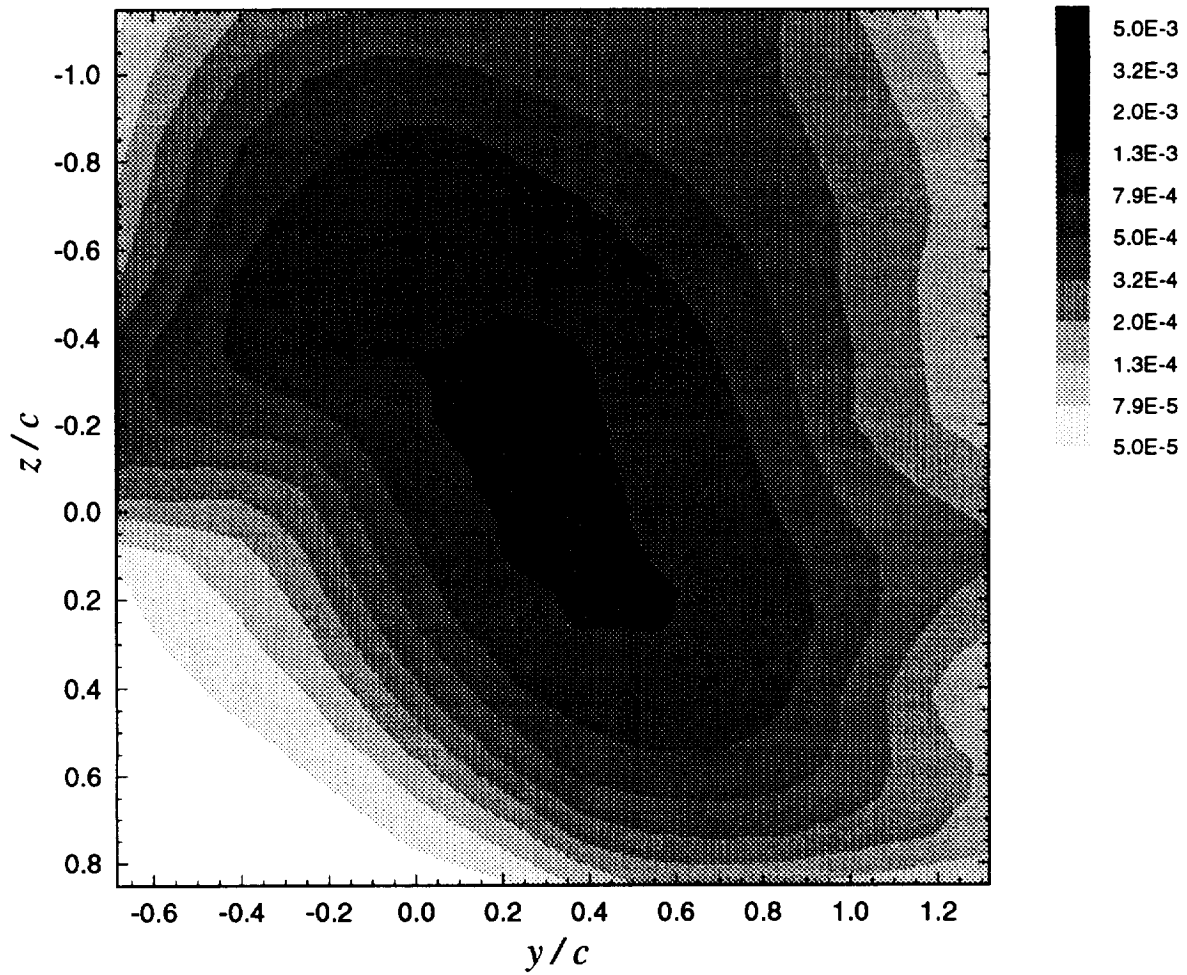


**Figure 3.61e** Contours of summed cross-flow normal turbulent stresses  $(\overline{v^2} + \overline{w^2}) / U_{ref}^2$  for vortex centerline stagnating on blade leading edge ( $\Delta = 0$ ):  $x/c = 30$ ,  $\alpha_1 = 5^\circ$ ,  $\alpha_2 = 5^\circ$ ,  $d/c = 0.3125$

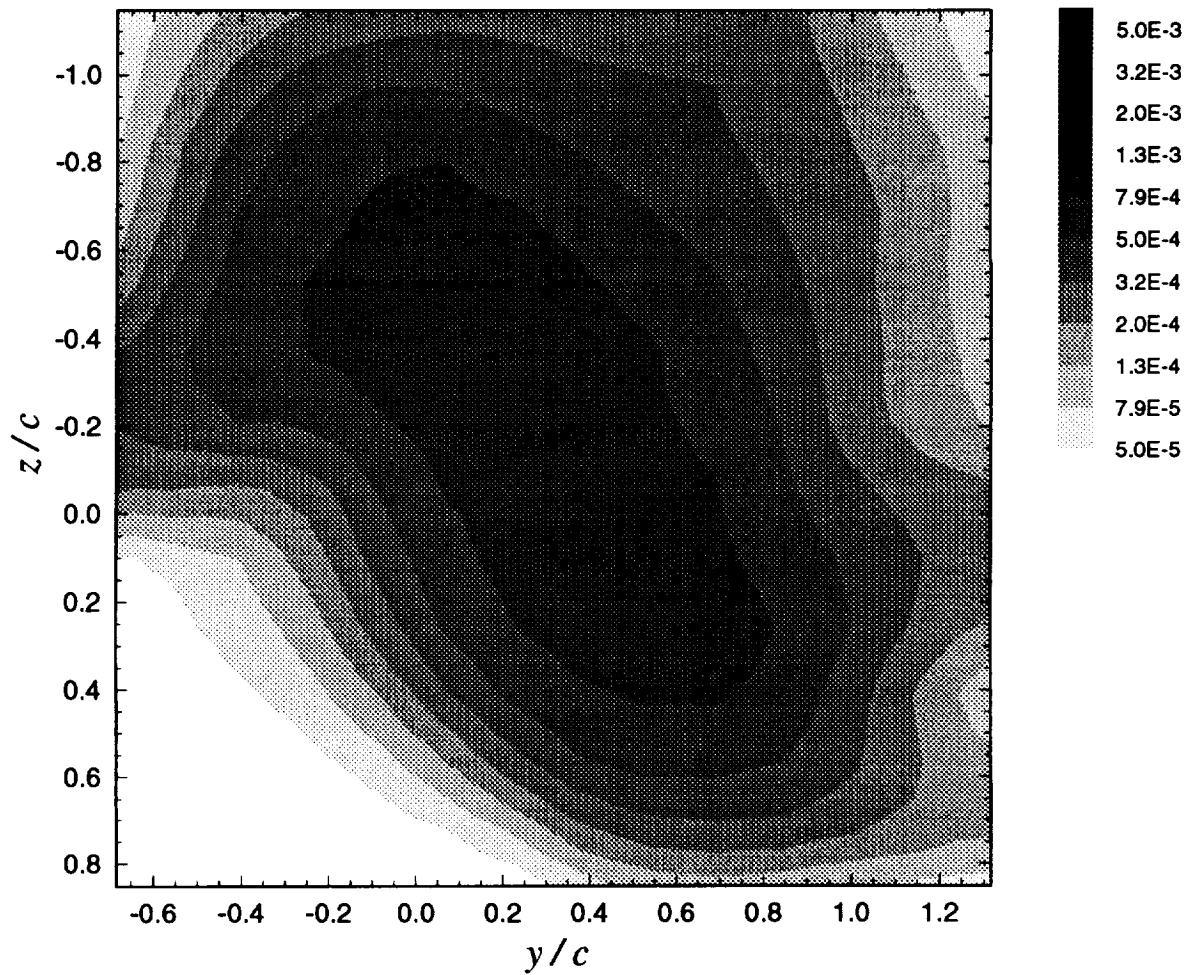


**Figure 3.61f** Contours of turbulent kinetic energy ( $k / U_{ref}^2$ ) for vortex centerline stagnating on blade leading edge ( $\Delta = 0$ ):  $x/c = 30$ ,  $\alpha_1 = 5^\circ$ ,  $\alpha_2 = 5^\circ$ ,  $d/c = 0.3125$

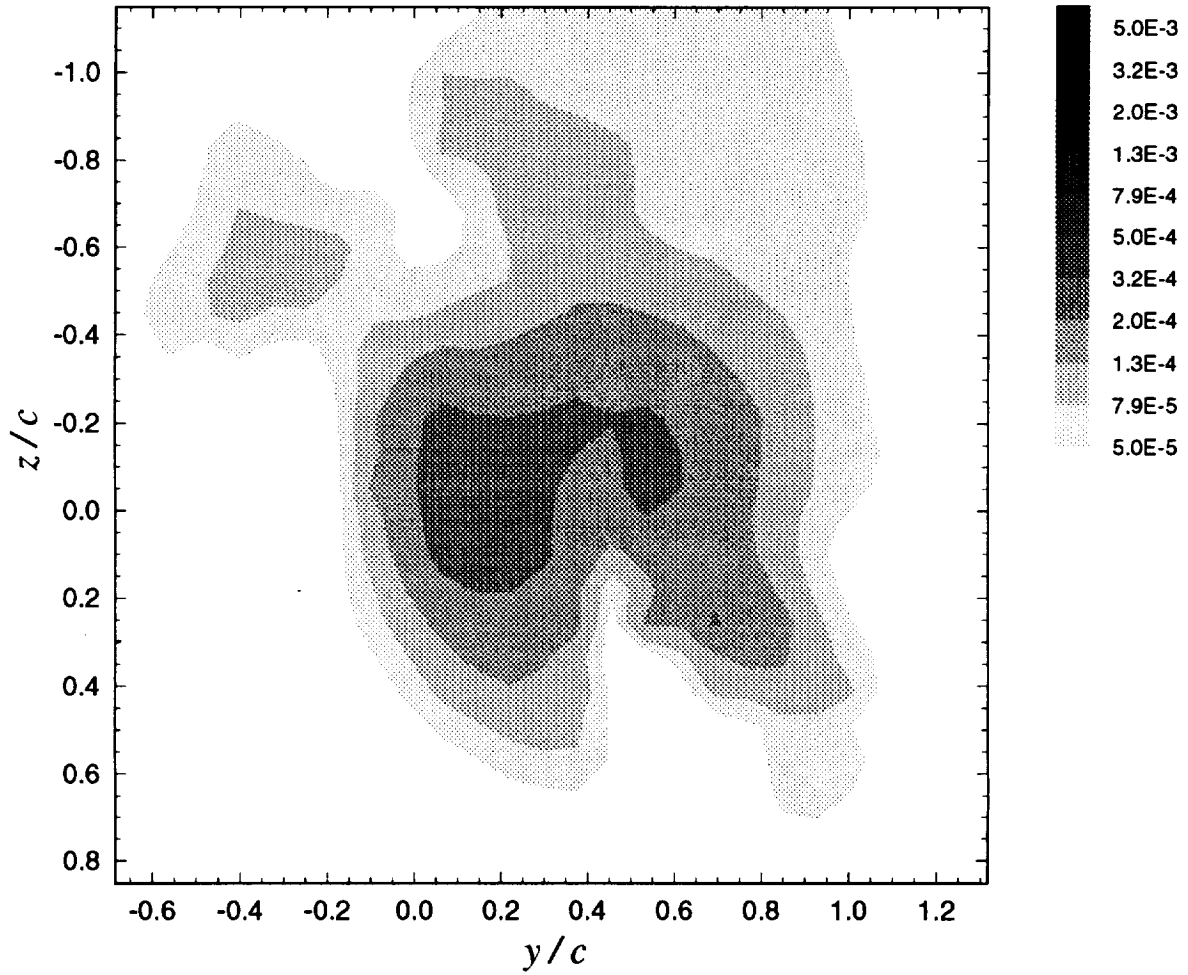


**Figure 3.61g** Contours of axial shear stress magnitude  $(\tau_a / U_{ref}^2)$  for vortex centerline stagnating on blade leading edge ( $\Delta = 0$ ):  $x/c = 30$ ,  $\alpha_1 = 5^\circ$ ,  $\alpha_2 = 5^\circ$ ,  $d/c = 0.3125$

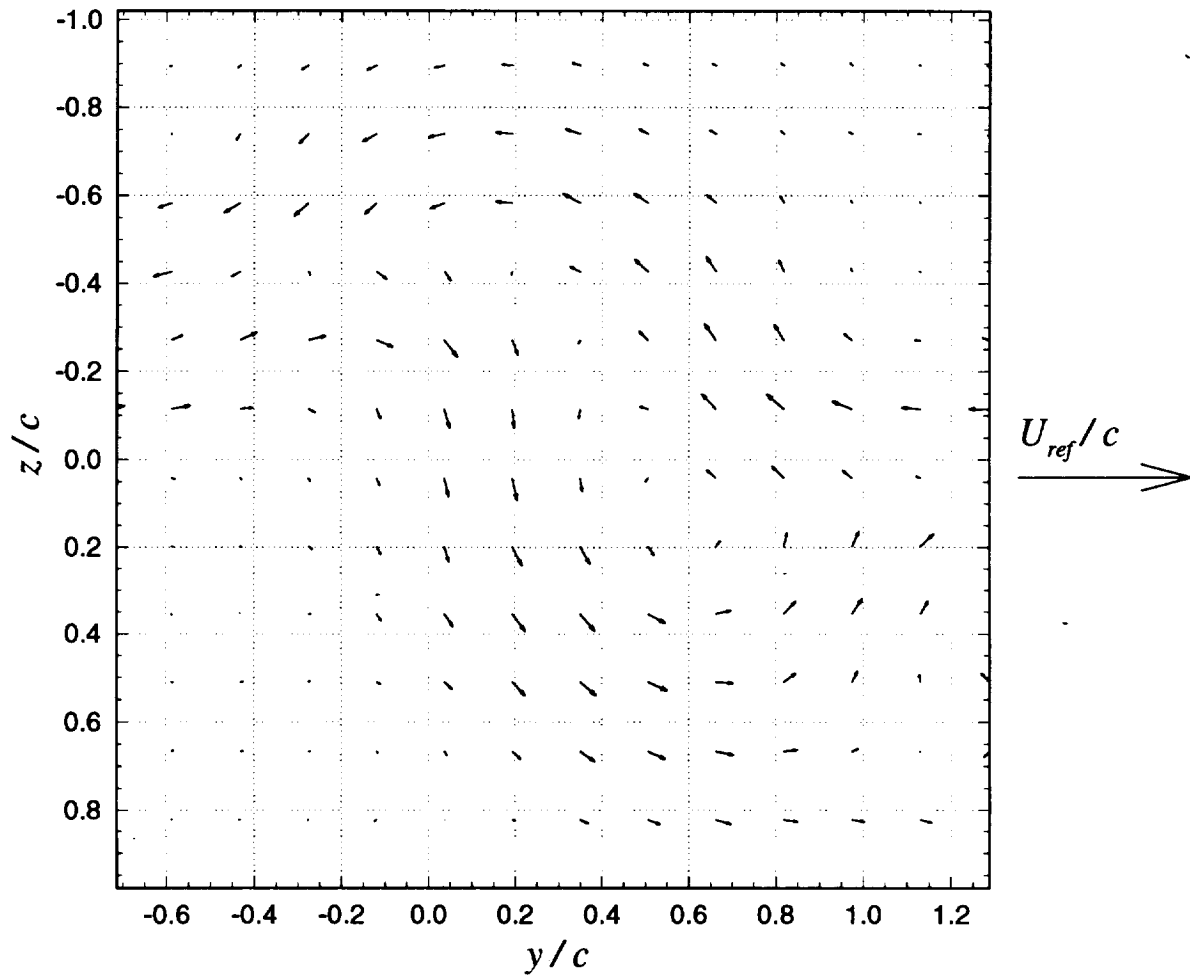


**Figure 3.62a** Mean cross-flow vorticity vectors ( $\Omega_y \cdot c / U_{ref}$ ,  $\Omega_z \cdot c / U_{ref}$ ) for suction side passage of  $\Delta/c = -0.0625$ :  $x/c = 30$ ,  $\alpha_1 = 5^\circ$ ,  $\alpha_2 = 5^\circ$ ,  $d/c = 0.3125$

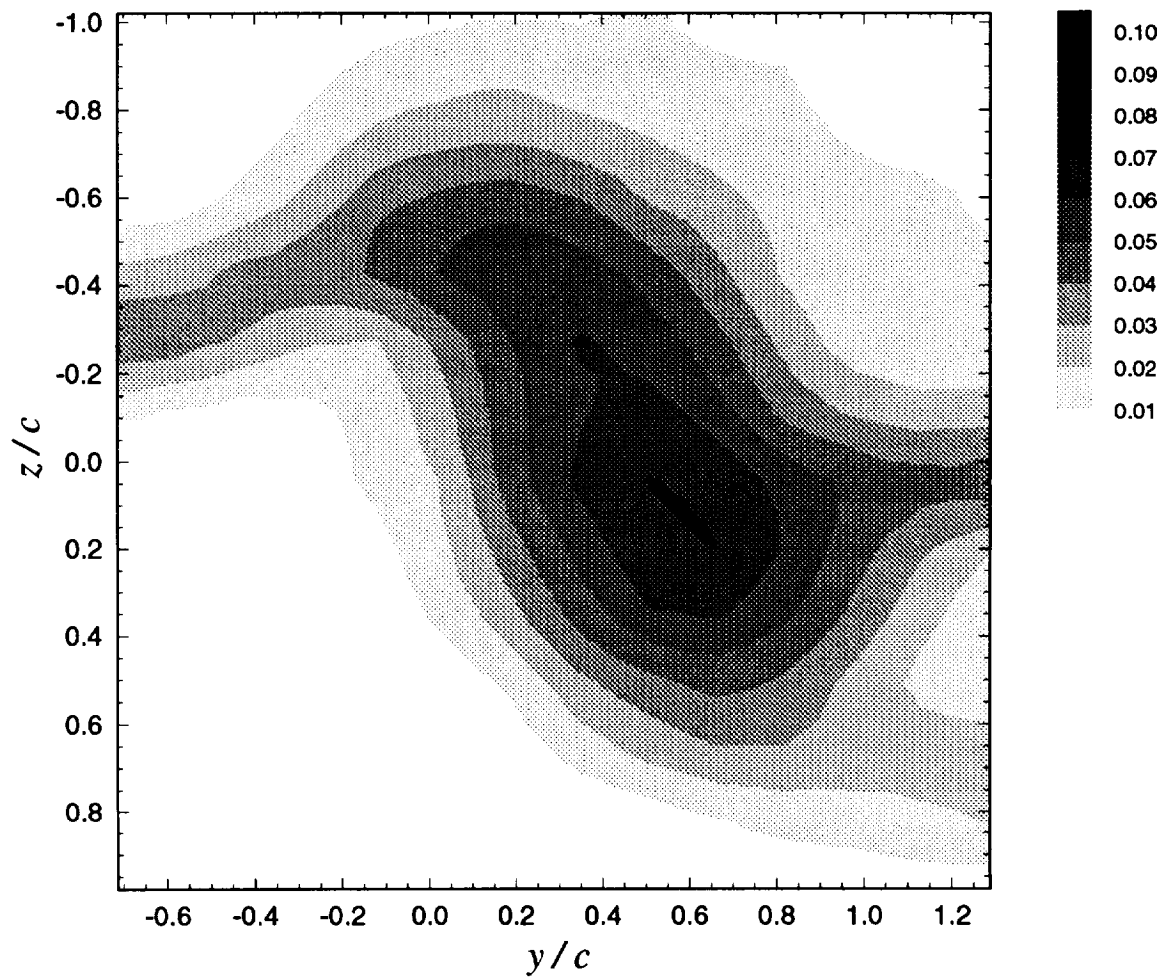


**Figure 3.62b** Contours of mean axial velocity deficit  $((U_{ref} - U) / U_{ref})$  for suction side passage of  $\Delta/c = -0.0625$ :  $x/c = 30$ ,  $\alpha_1 = 5^\circ$ ,  $\alpha_2 = 5^\circ$ ,  $d/c = 0.3125$



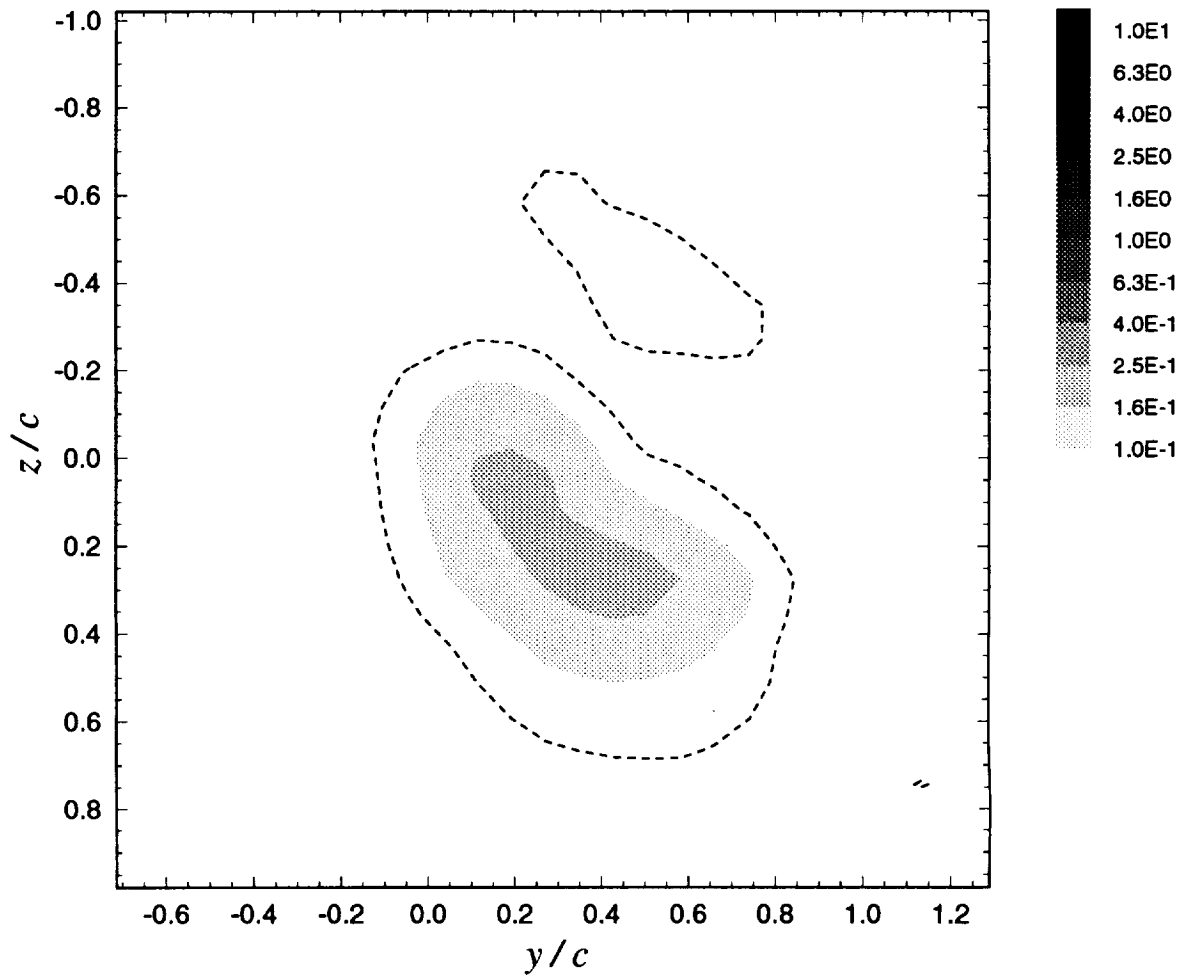


**Figure 3.62c** Contours of mean axial vorticity ( $\Omega_x \cdot c / U_{ref}$ ) for suction side passage of  $\Delta/c = -0.0625$ :  $x/c = 30$ ,  $\alpha_1 = 5^\circ$ ,  $\alpha_2 = 5^\circ$ ,  $d/c = 0.3125$ . Dashed contour line is core edge estimate.

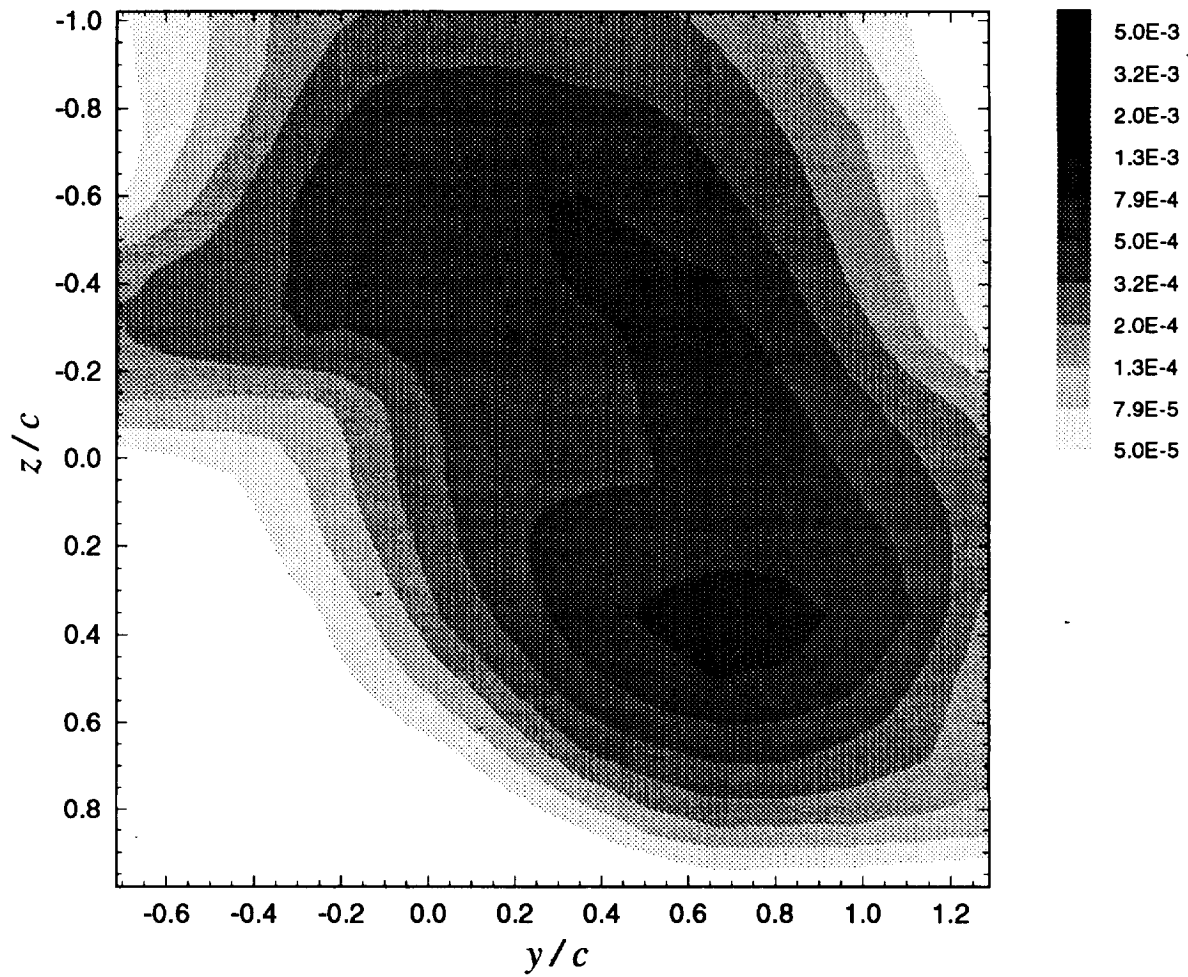


**Figure 3.62d** Contours of axial normal turbulent stress ( $\overline{u^2} / U_{ref}^2$ ) for suction side passage of  $\Delta/c = -0.0625$ :  $x/c = 30$ ,  $\alpha_1 = 5^\circ$ ,  $\alpha_2 = 5^\circ$ ,  $d/c = 0.3125$

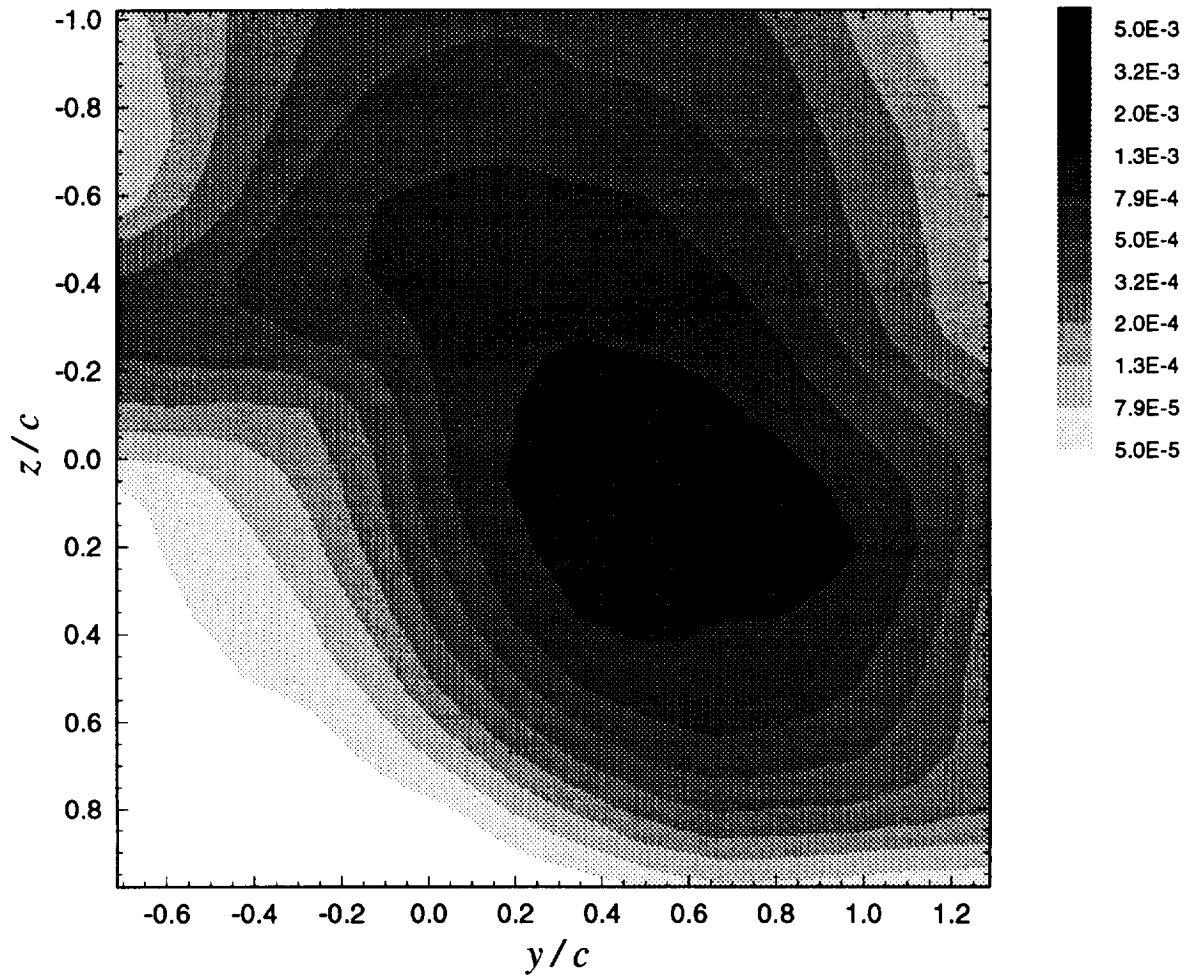


**Figure 3.62e** Contours of summed cross-flow normal turbulent stresses ( $(\overline{v^2} + \overline{w^2}) / U_{ref}^2$ ) for suction side passage of  $\Delta/c = -0.0625$ :  $x/c = 30$ ,  $\alpha_1 = 5^\circ$ ,  $\alpha_2 = 5^\circ$ ,  $d/c = 0.3125$

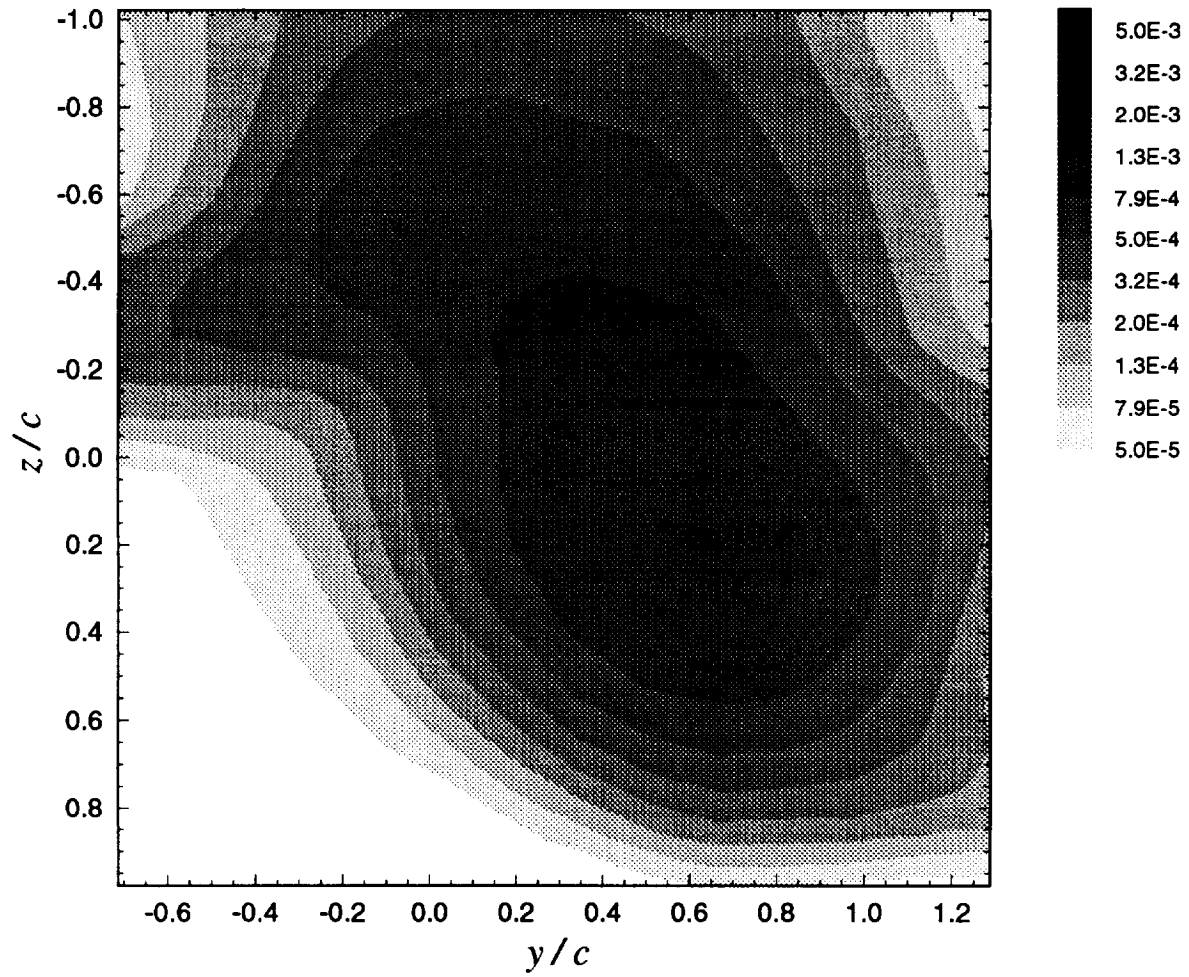


**Figure 3.62f** Contours of turbulent kinetic energy ( $k / U_{ref}^2$ ) for suction side passage of  $\Delta/c = -0.0625$ :  $x/c = 30$ ,  $\alpha_1 = 5^\circ$ ,  $\alpha_2 = 5^\circ$ ,  $d/c = 0.3125$

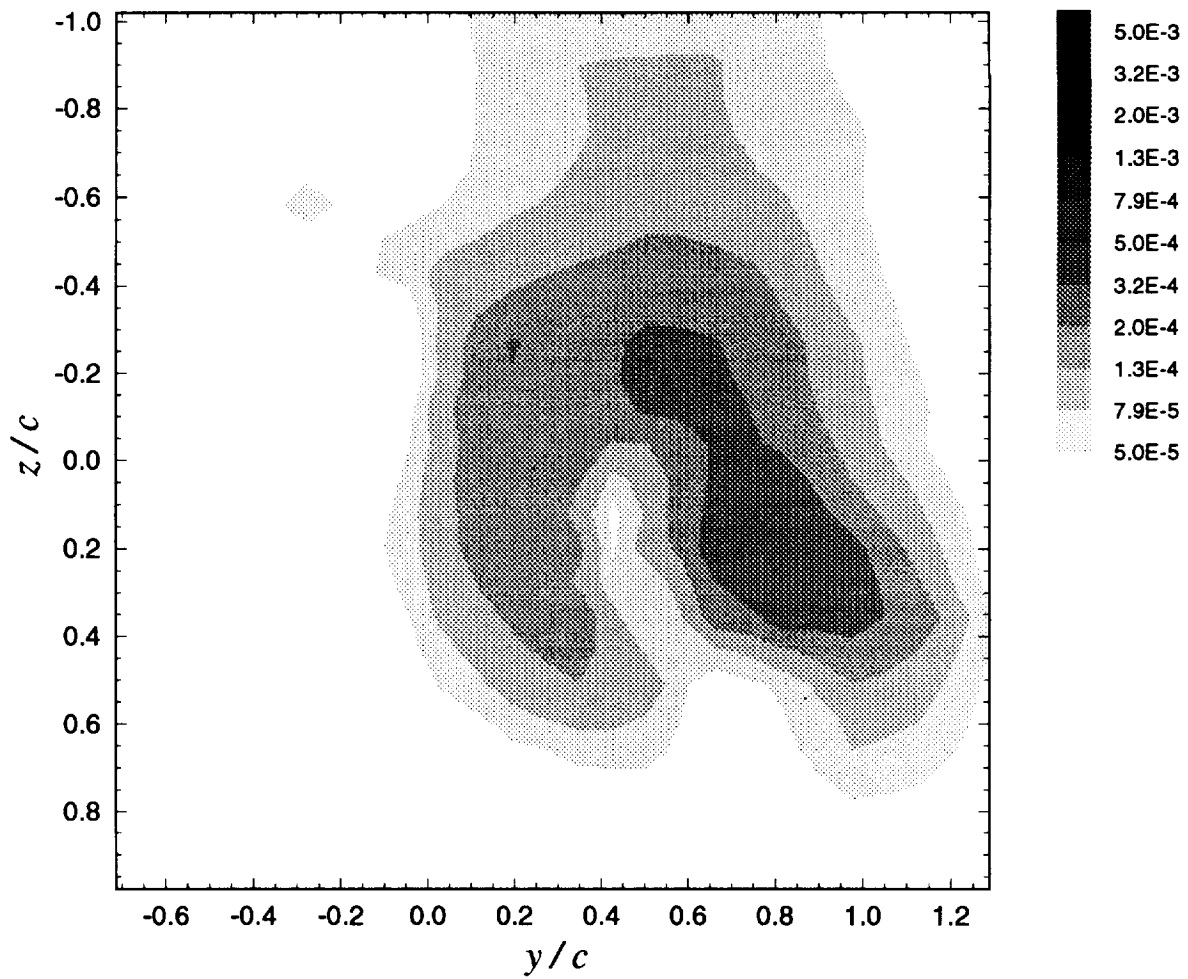


**Figure 3.62g** Contours of axial shear stress magnitude  $(\tau_a / U_{ref}^2)$  for suction side passage of  $\Delta/c = -0.0625$ :  $x/c = 30$ ,  $\alpha_1 = 5^\circ$ ,  $\alpha_2 = 5^\circ$ ,  $d/c = 0.3125$

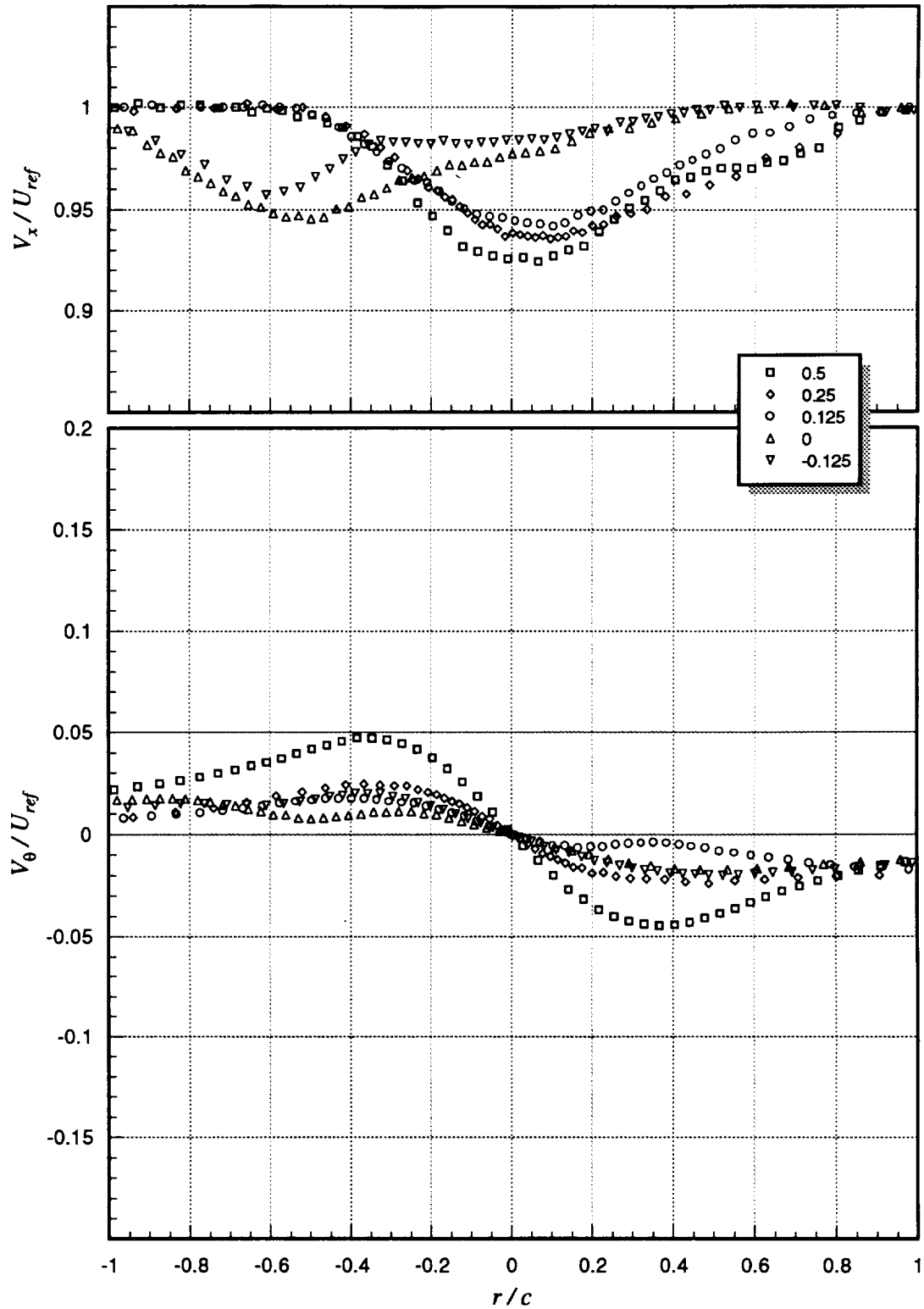


**Figure 3.63** Mean axial ( $V_x$ ) and tangential ( $V_\theta$ ) velocities (measured along  $z$ -wise profiles through the vortex core center) as a function of blade–vortex separation ( $\Delta$ ):  $x/c = 30$ ,  $\alpha_1 = 5^\circ$ ,  $\alpha_2 = 5^\circ$ ,  $d/c = 0.3125$ . Legend lists  $\Delta/c$  values.

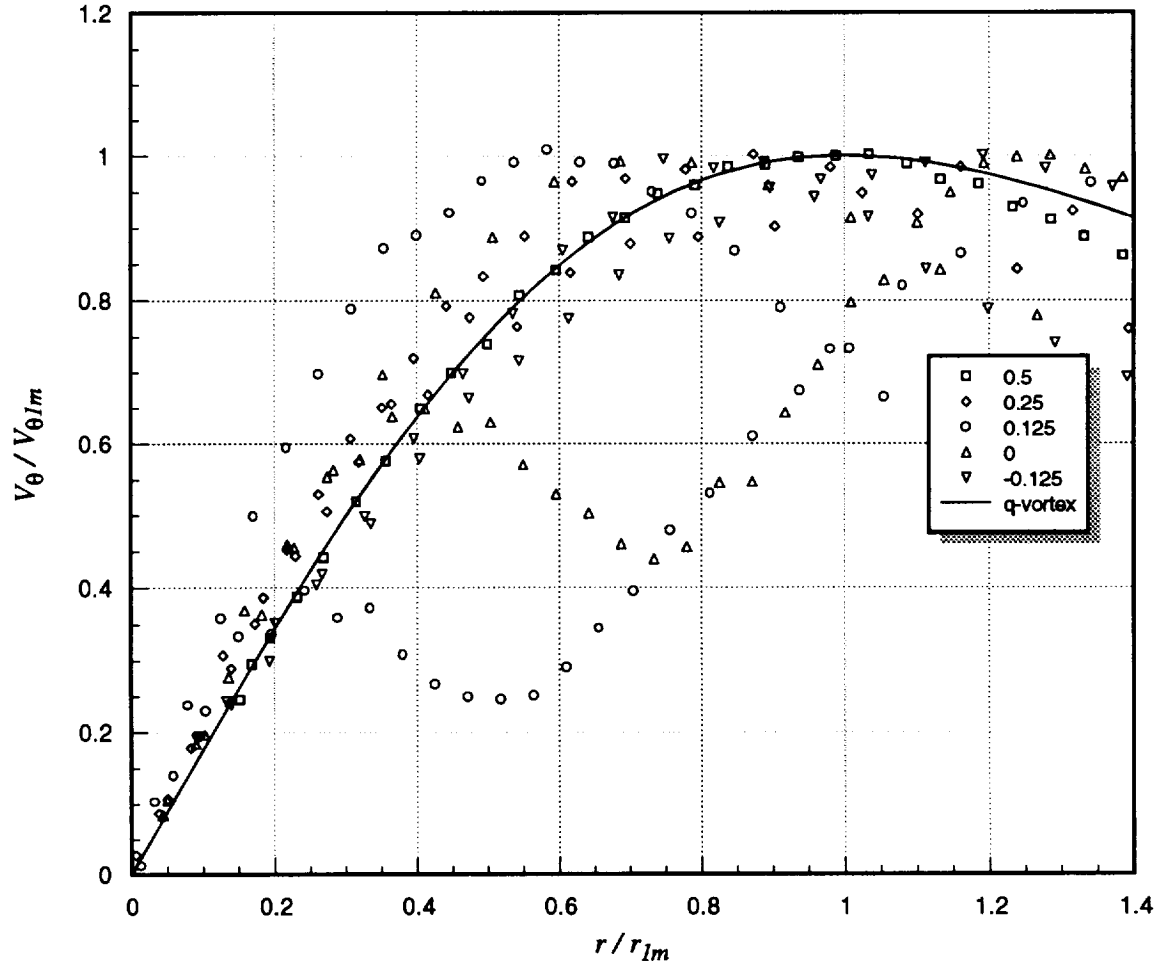


**Figure 3.64** Mean tangential ( $V_\theta$ ) velocities (measured along  $z$ -wise profiles through the vortex core center), normalized on measured peak tangential velocity ( $V_{\theta 1m}$ ), as a function of blade–vortex separation ( $\Delta$ ):  $x/c = 30$ ,  $\alpha_1 = 5^\circ$ ,  $\alpha_2 = 5^\circ$ ,  $d/c = 0.3125$ . Legend lists  $\Delta/c$  values.

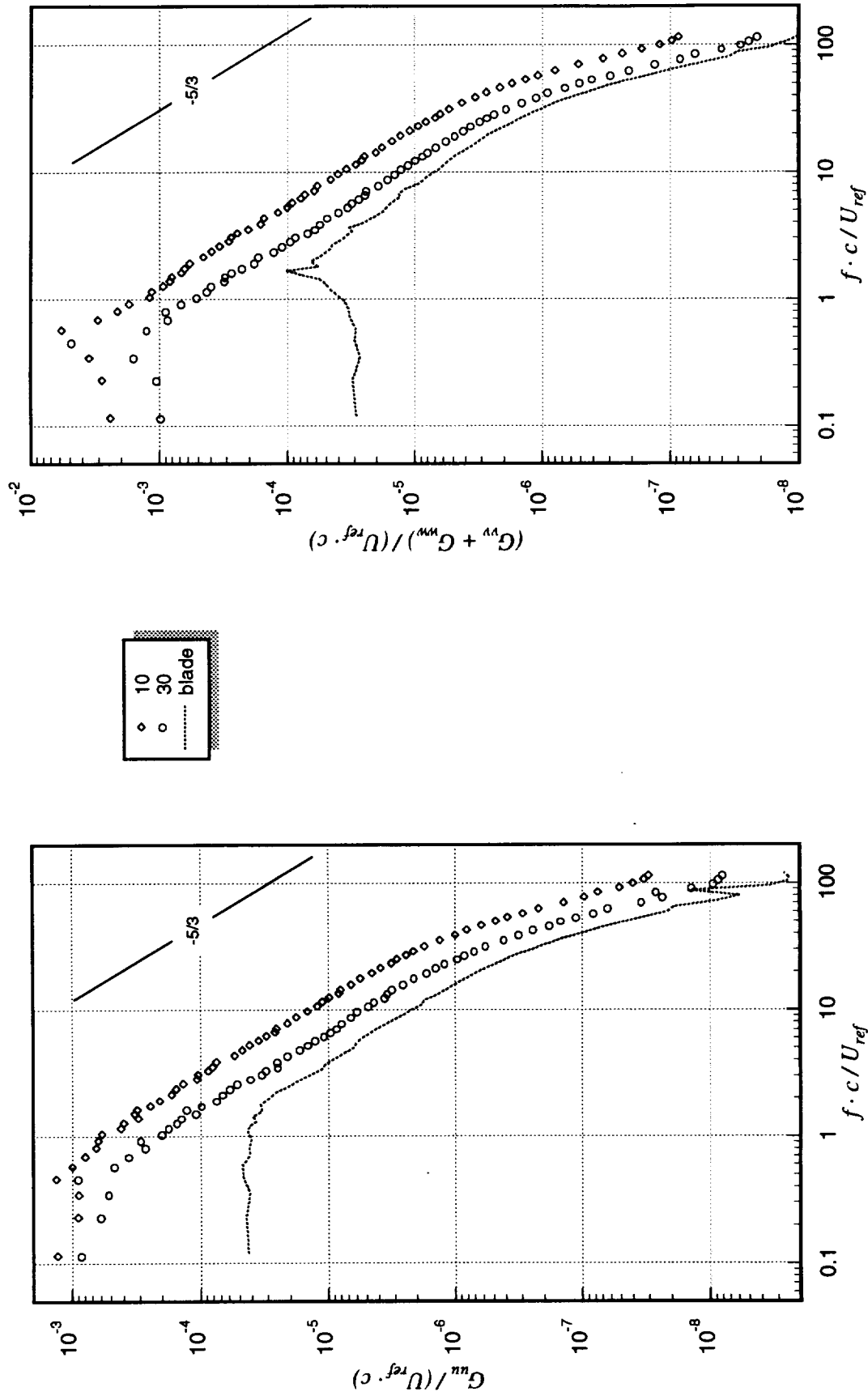


**Figure 3.65** Core center velocity autospectra for undisturbed vortex ( $x/c = 10$ ) and for suction side passage of  $\Delta/c = 0.5$  measured at  $x/c = 30$ :  $\alpha_1 = 5^\circ$ ,  $\alpha_2 = 5^\circ$ ,  $d/c = 0.3125$ . Legend lists  $x/c$  values. Autospectra measured in undisturbed portion of interaction blade wake at  $x/c = 30$  also included (marked as “blade” in legend).



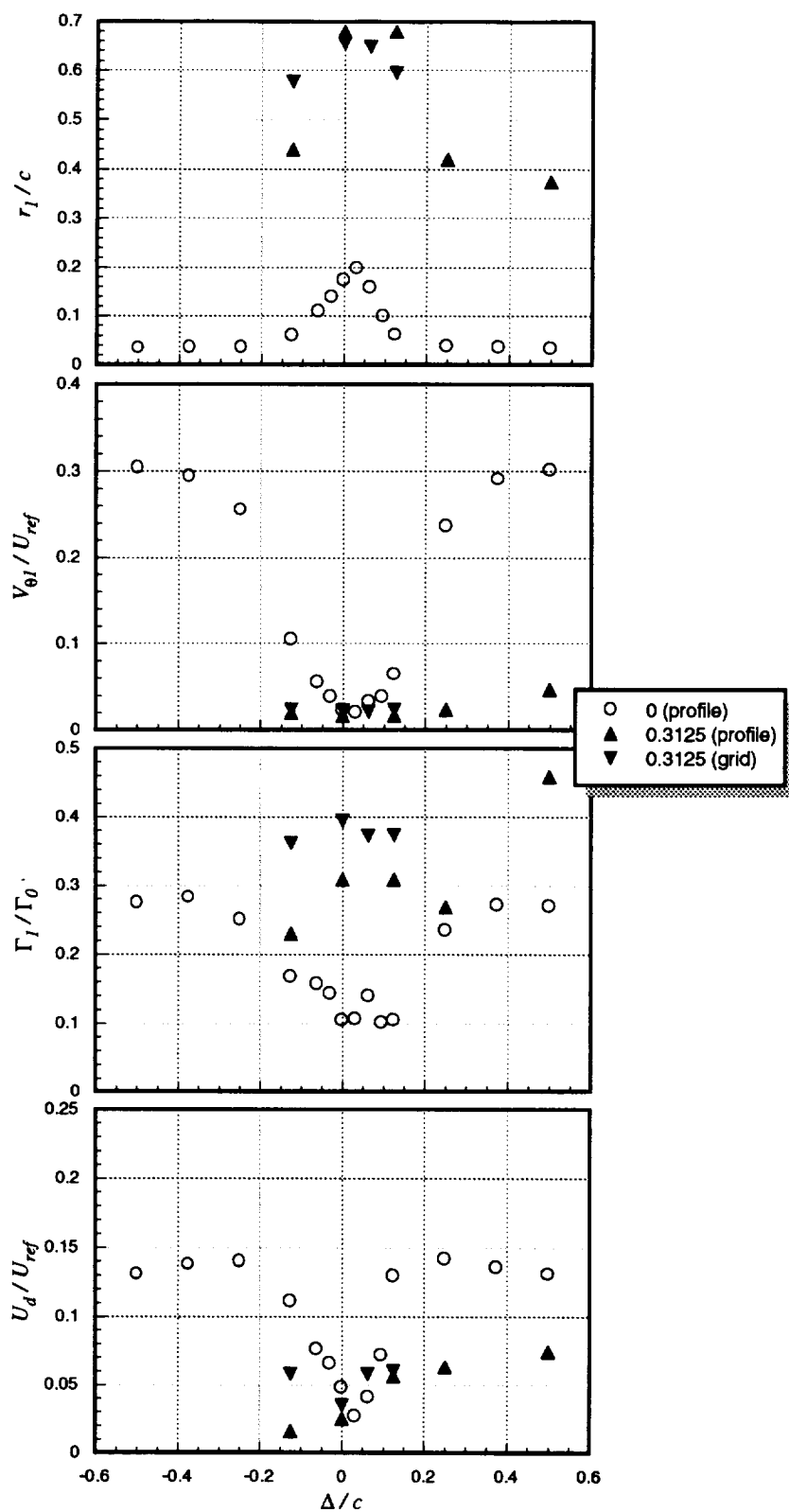


**Figure 3.66** Core parameters (radius,  $r_l$ ; peak tangential velocity,  $V_{\theta l}$ ; circulation,  $\Gamma_l$ ; and axial velocity deficit,  $U_d$ ) as a function of blade–vortex separation ( $\Delta$ ) for different spoiler diameters ( $d$ ):  $x/c = 30$ ,  $\alpha_l = 5^\circ$ ,  $\alpha_2 = 5^\circ$ . Legend lists  $d/c$  values (source of parameters also specified).

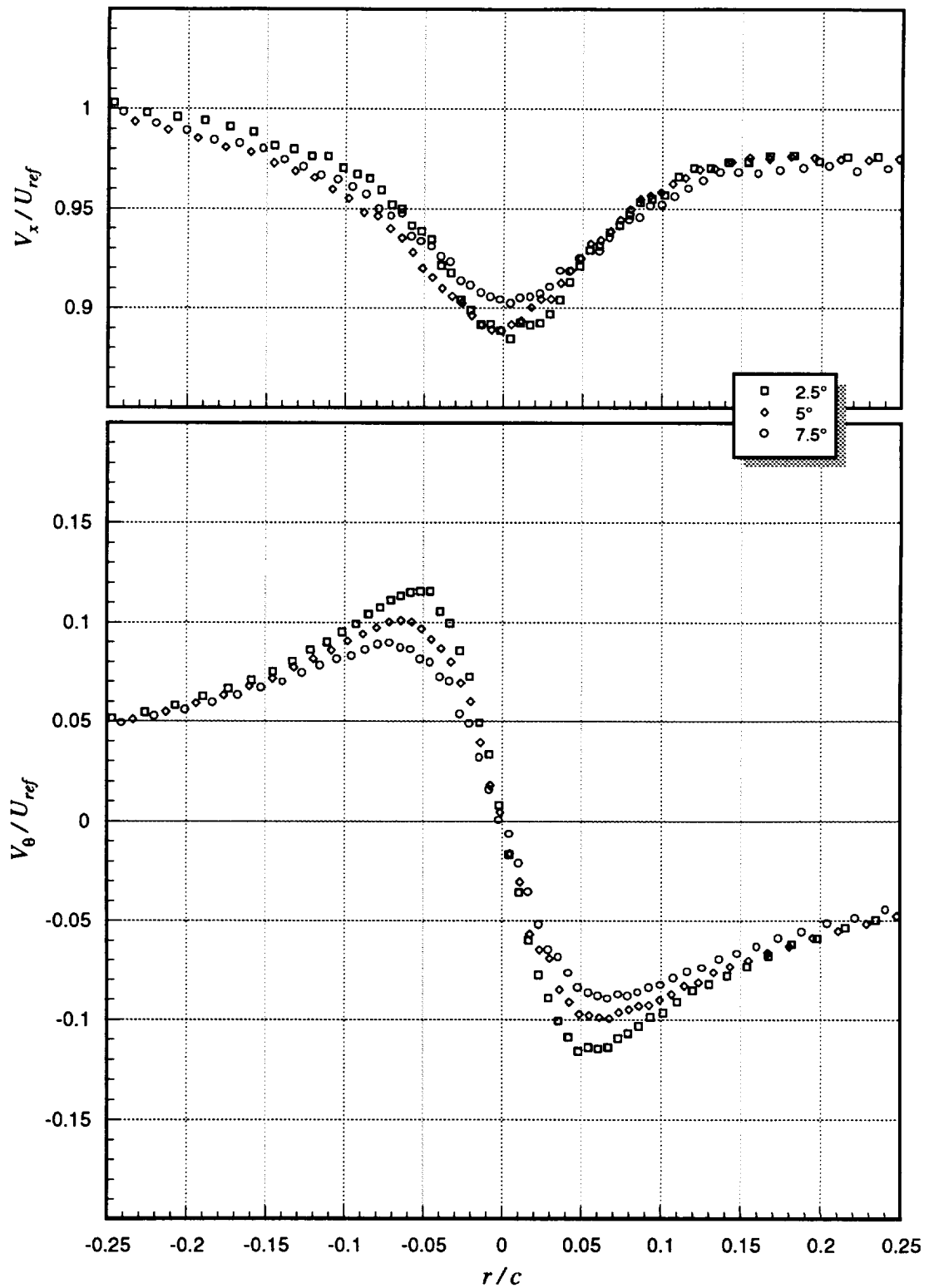


**Figure 3.67** Mean axial ( $V_x$ ) and tangential ( $V_\theta$ ) velocities (measured along  $z$ -wise profiles through the vortex core center) as a function of blade angle of attack ( $\alpha_2$ ) for pressure side passage of  $\Delta/c = -0.125$ :  $x/c = 30$ ,  $\alpha_1 = 5^\circ$ , no spoiler. Legend lists  $\alpha_2$  values.

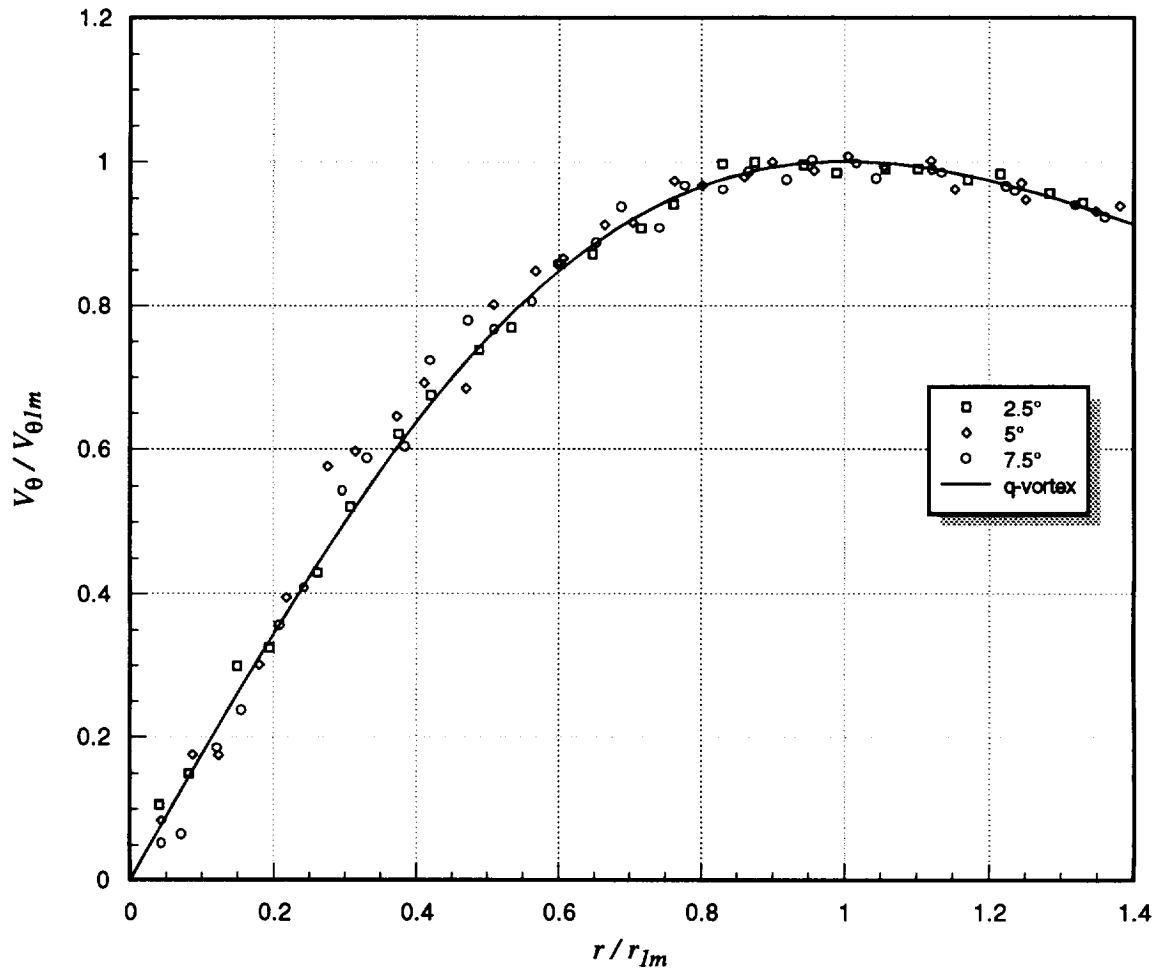


**Figure 3.68** Mean tangential ( $V_{\theta}$ ) velocities (measured along  $z$ -wise profiles through the vortex core center), normalized on measured peak tangential velocity ( $V_{\theta 1m}$ ), as a function of blade angle of attack ( $\alpha_2$ ) for pressure side passage of  $\Delta / c = -0.125$ :  $x / c = 30$ ,  $\alpha_1 = 5^{\circ}$ , no spoiler. Legend lists  $\alpha_2$  values.

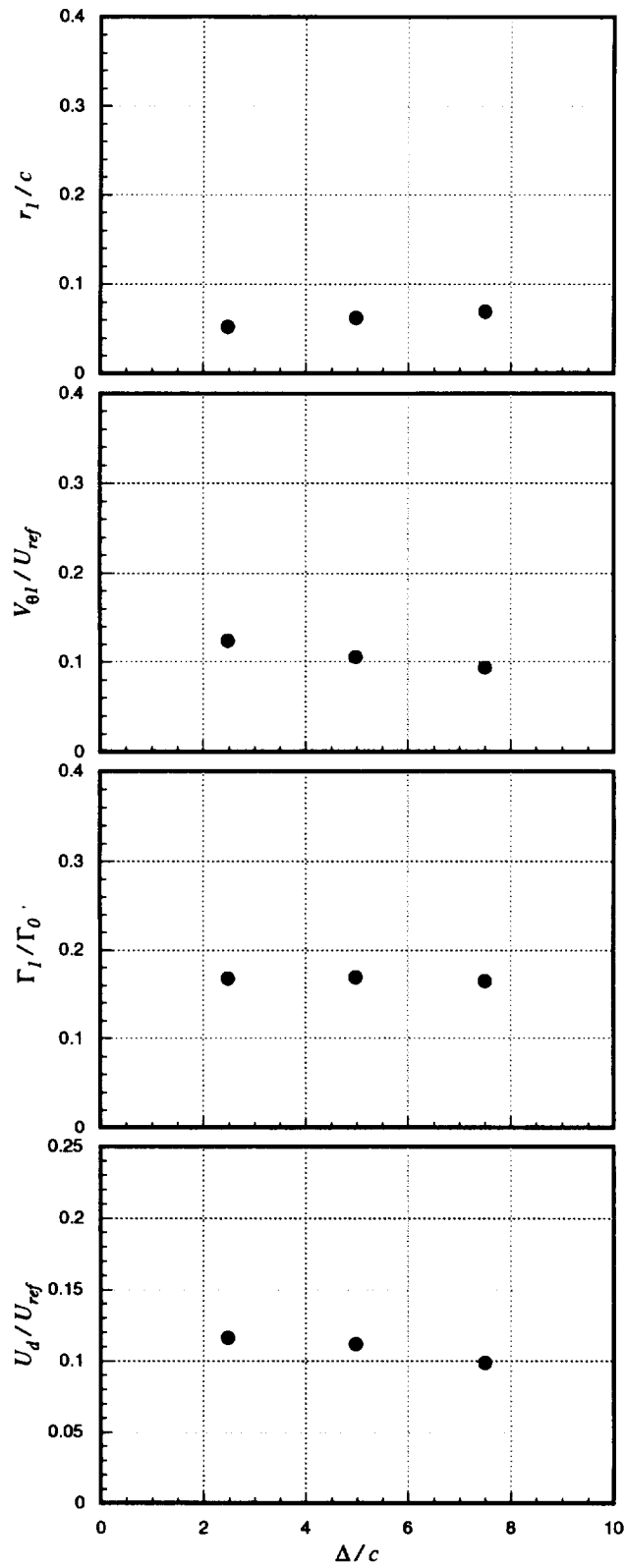


**Figure 3.69** Core parameters (radius,  $r_l$ ; peak tangential velocity,  $V_{\theta l}$ ; circulation,  $\Gamma_l$ ; and axial velocity deficit,  $U_d$ ) as a function of blade angle of attack ( $\alpha_2$ ) for pressure side passage of  $\Delta/c = -0.125$ :  $x/c = 30$ ,  $\alpha_l = 5^\circ$ , no spoiler

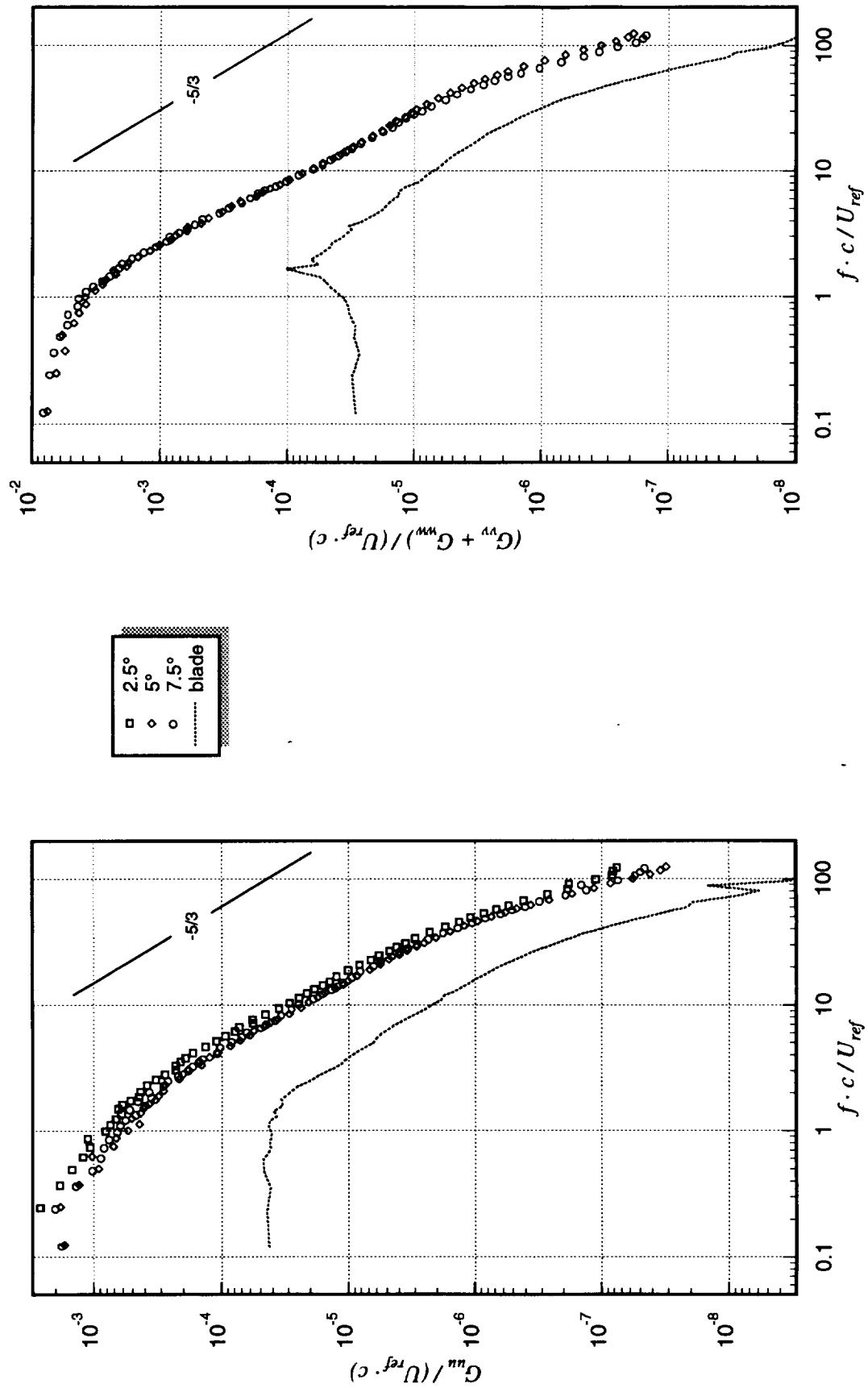
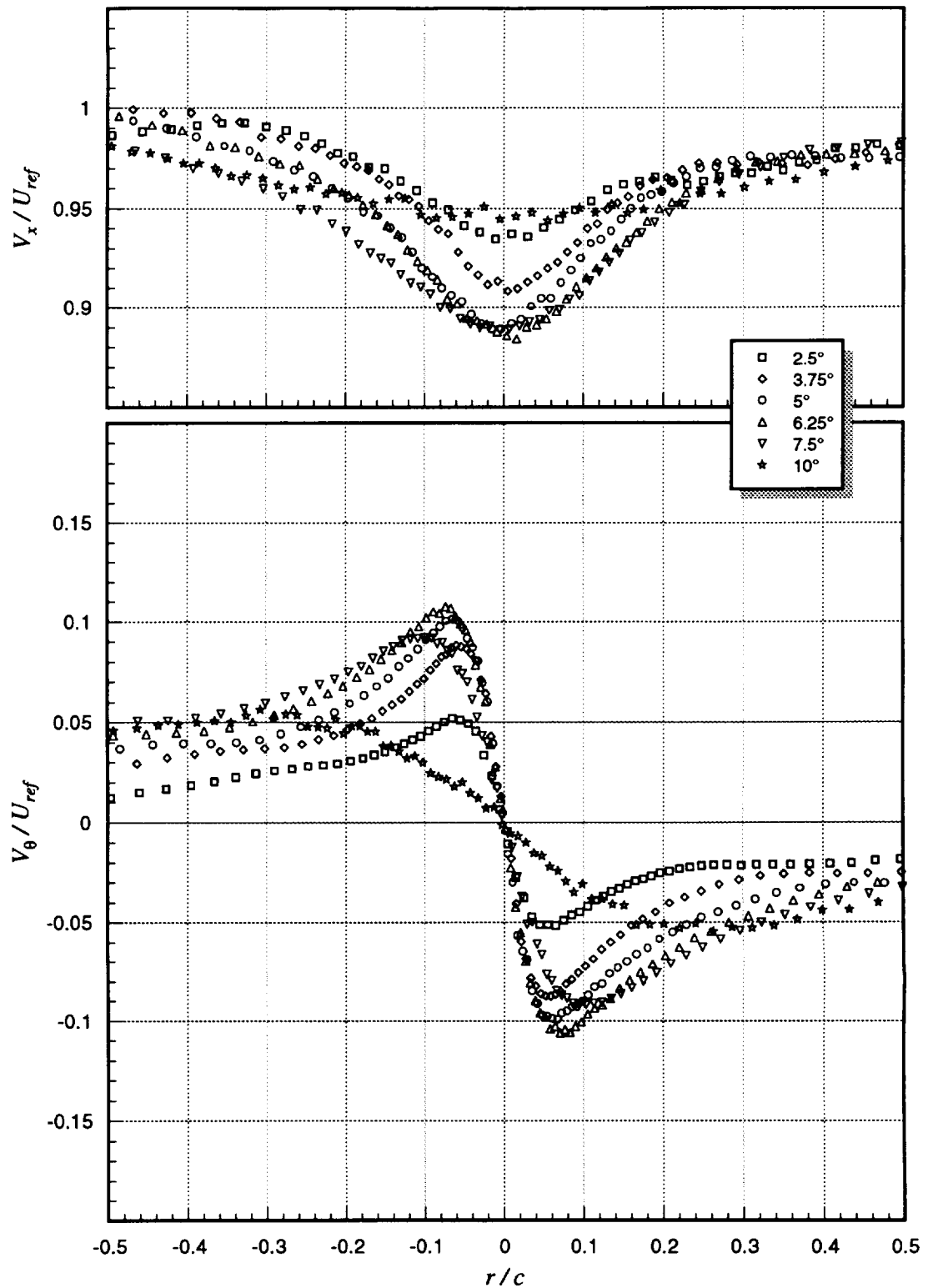
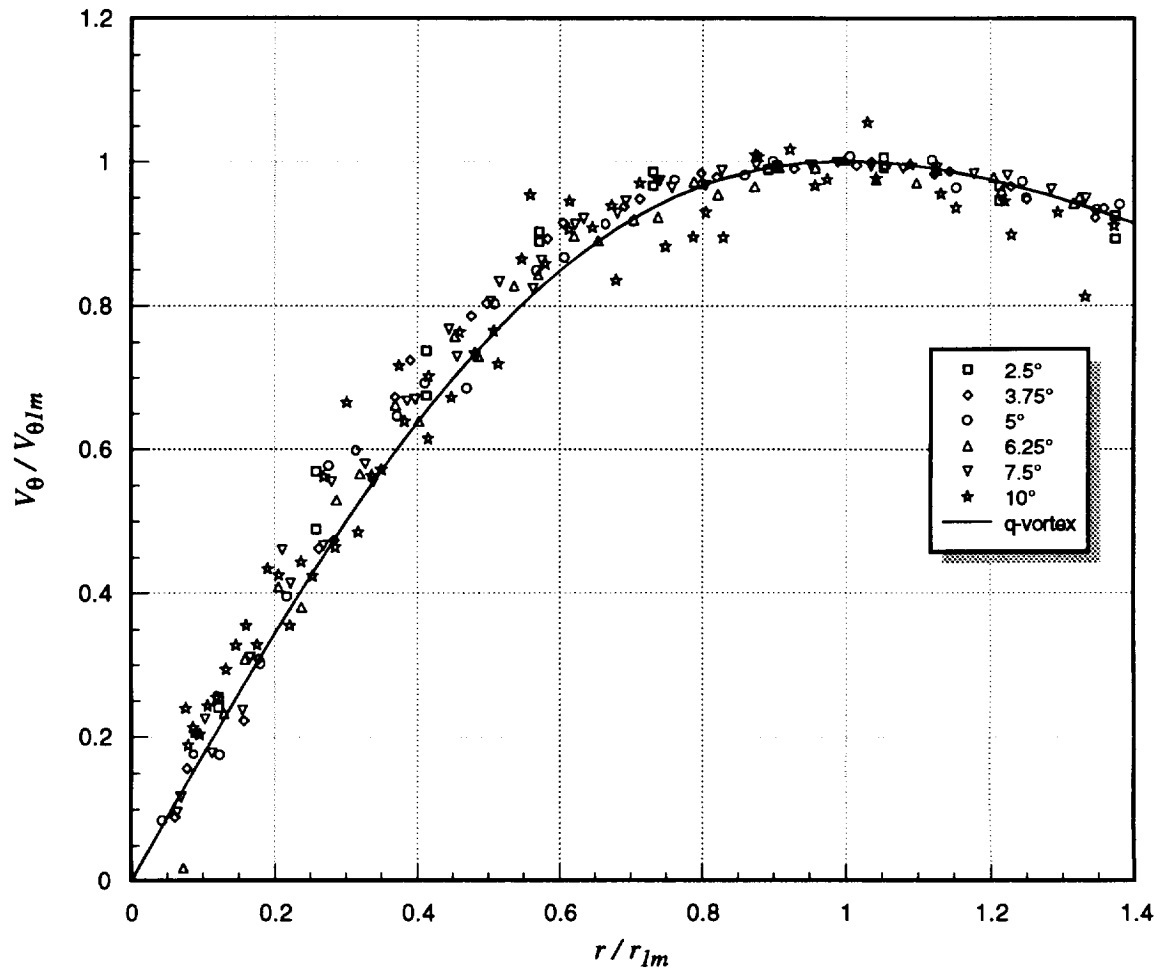


Figure 3.70 Core center velocity autospectra as a function of blade angle of attack ( $\alpha_2$ ) for pressure side passage of  $\Delta/c = -0.125$ :  $x/c = 30$ ,  $\alpha_1 = 5^\circ$ , no spoiler. Legend lists  $\alpha_2$  values. Autospectra measured in undisturbed portion of interaction blade wake at  $x/c = 30$  with  $\alpha_2 = 5^\circ$ , also included (marked as “blade” in legend).



**Figure 3.71** Mean axial ( $V_x$ ) and tangential ( $V_\theta$ ) velocities (measured along  $z$ -wise profiles through the vortex core center) with generator and blade at equal angles of attack ( $\alpha_1 = \alpha_2$ ) for pressure side passage of  $\Delta/c = -0.125$ :  $x/c = 30$ , no spoiler. Legend lists  $\alpha_1 = \alpha_2$  values.



**Figure 3.72** Mean tangential ( $V_\theta$ ) velocities (measured along  $z$ -wise profiles through the vortex core center), normalized on measured peak tangential velocity ( $V_{\theta 1m}$ ), with generator and blade at equal angles of attack ( $\alpha_1 = \alpha_2$ ) for pressure side passage of  $\Delta / c = -0.125$ :  $x / c = 30$ , no spoiler. Legend lists  $\alpha_1 = \alpha_2$  values.

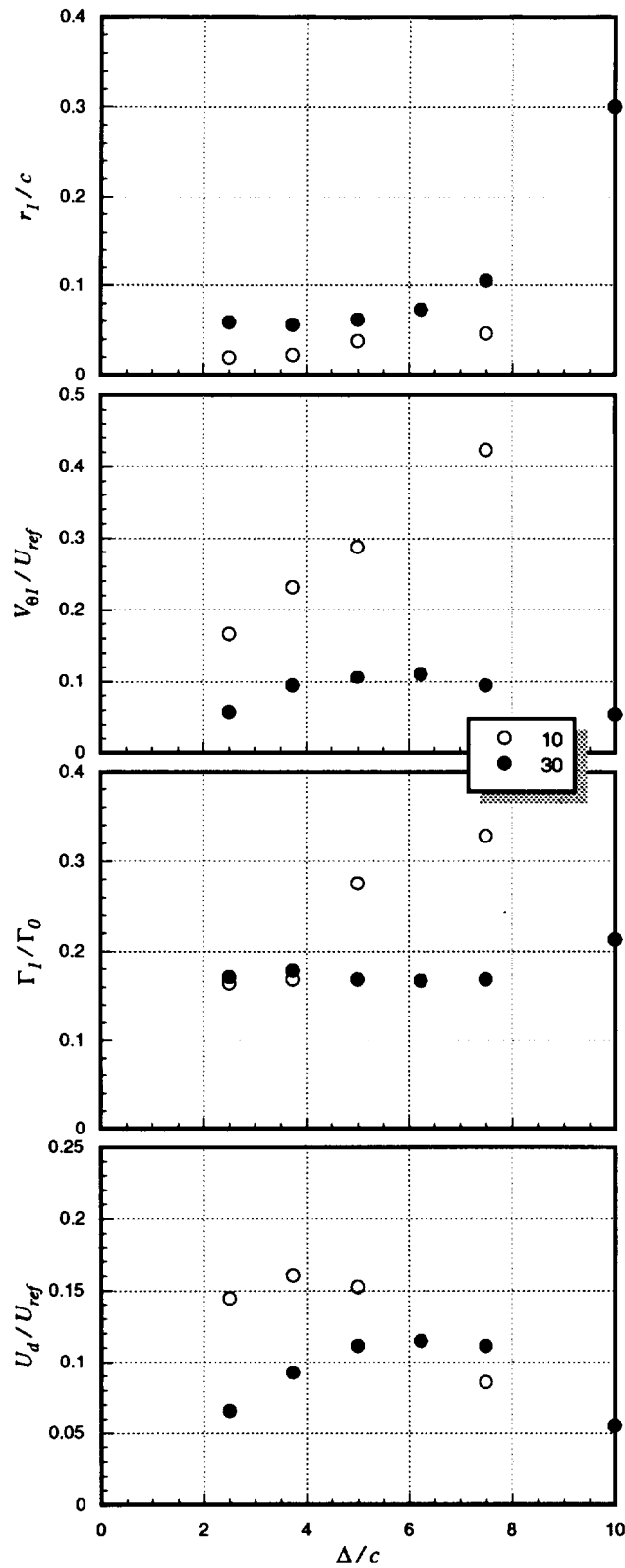


**Figure 3.73** Core parameters (radius,  $r_I$ ; peak tangential velocity,  $V_{\theta I}$ ; circulation,  $\Gamma_I$ ; and axial velocity deficit,  $U_d$ ) with generator and blade at equal angles of attack ( $\alpha_1 = \alpha_2$ ) for pressure side passage of  $\Delta/c = -0.125$ :  $x/c = 30$ , no spoiler. Undisturbed values measured at  $x/c = 10$  also shown. Legend lists  $x/c$  values.



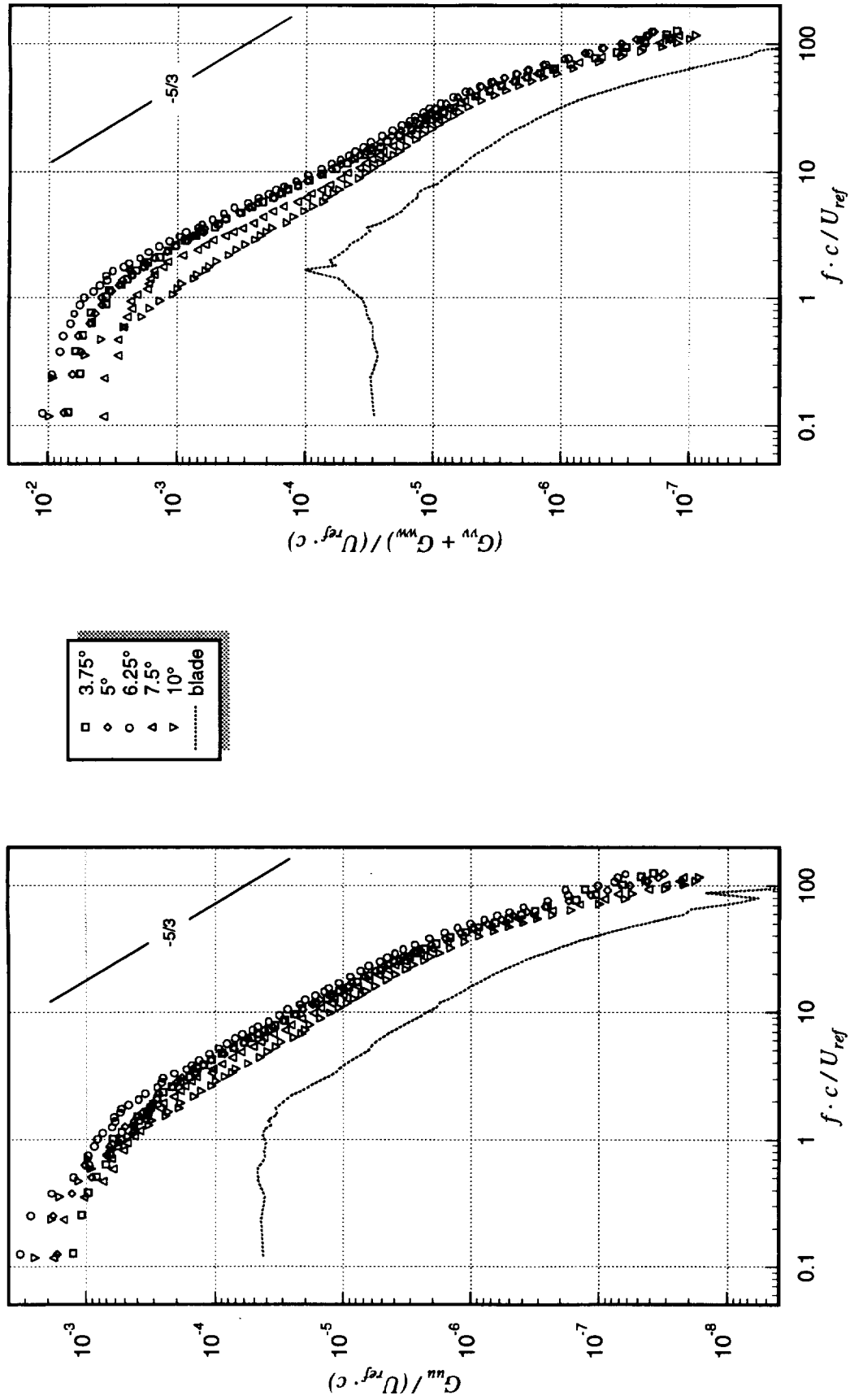


**Figure 3.74** Core center velocity autospectra with generator and blade at equal angles of attack ( $\alpha_1 = \alpha_2$ ) for pressure side passage of  $\Delta/c = -0.125$ ;  $x/c = 30$ , no spoiler. Legend lists  $\alpha_1 = \alpha_2$  values. Autospectra measured in undisturbed portion of interaction blade wake at  $x/c = 30$  with  $\alpha_2 = 5^\circ$ , also included (marked as “blade” in legend).

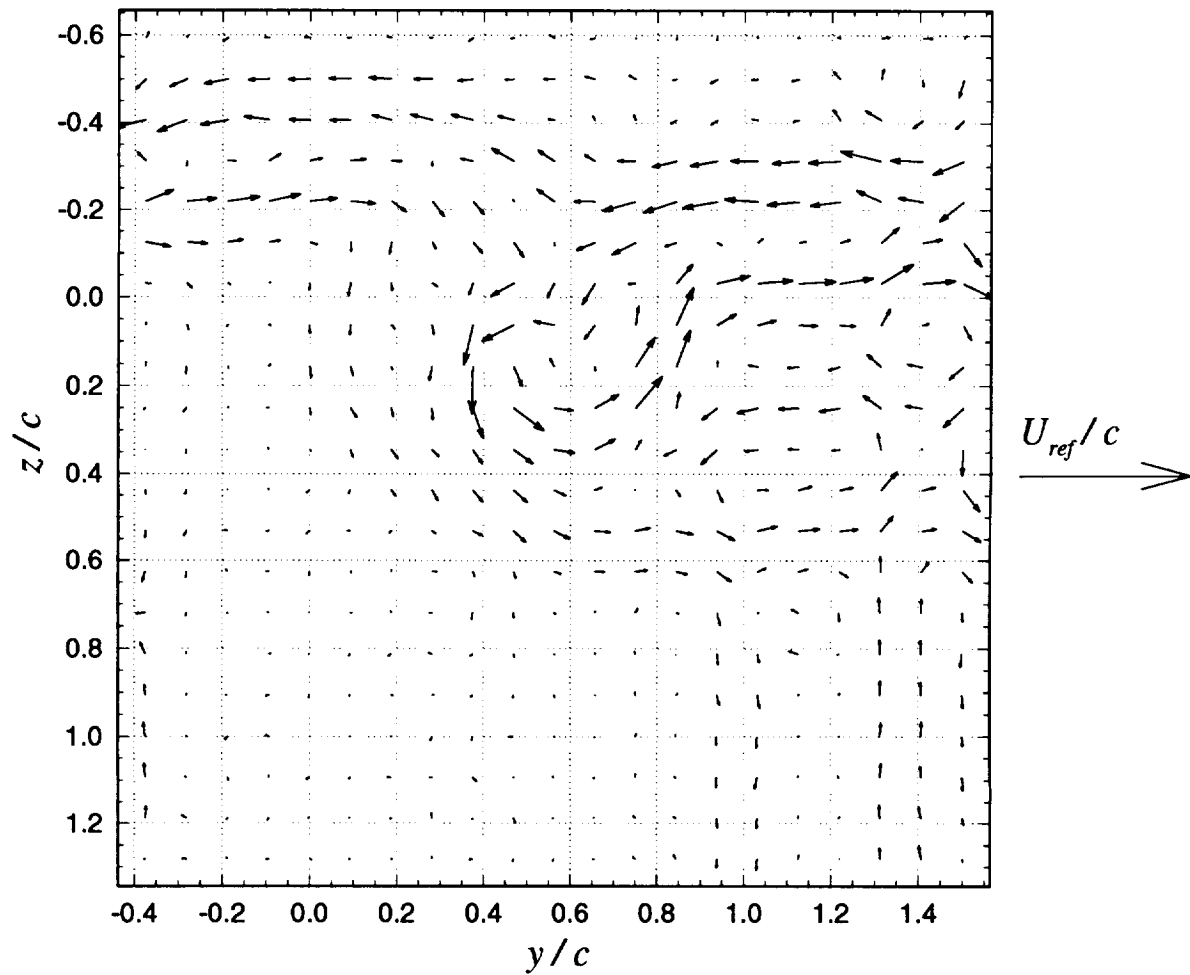


**Figure 3.75a** Mean cross-flow vorticity vectors ( $\Omega_y \cdot c / U_{ref}$ ,  $\Omega_z \cdot c / U_{ref}$ ) for pressure side passage of  $\Delta/c = -0.125$ :  $x/c = 30$ ,  $\alpha_1 = 2.5^\circ$ ,  $\alpha_2 = 2.5^\circ$ , no spoiler

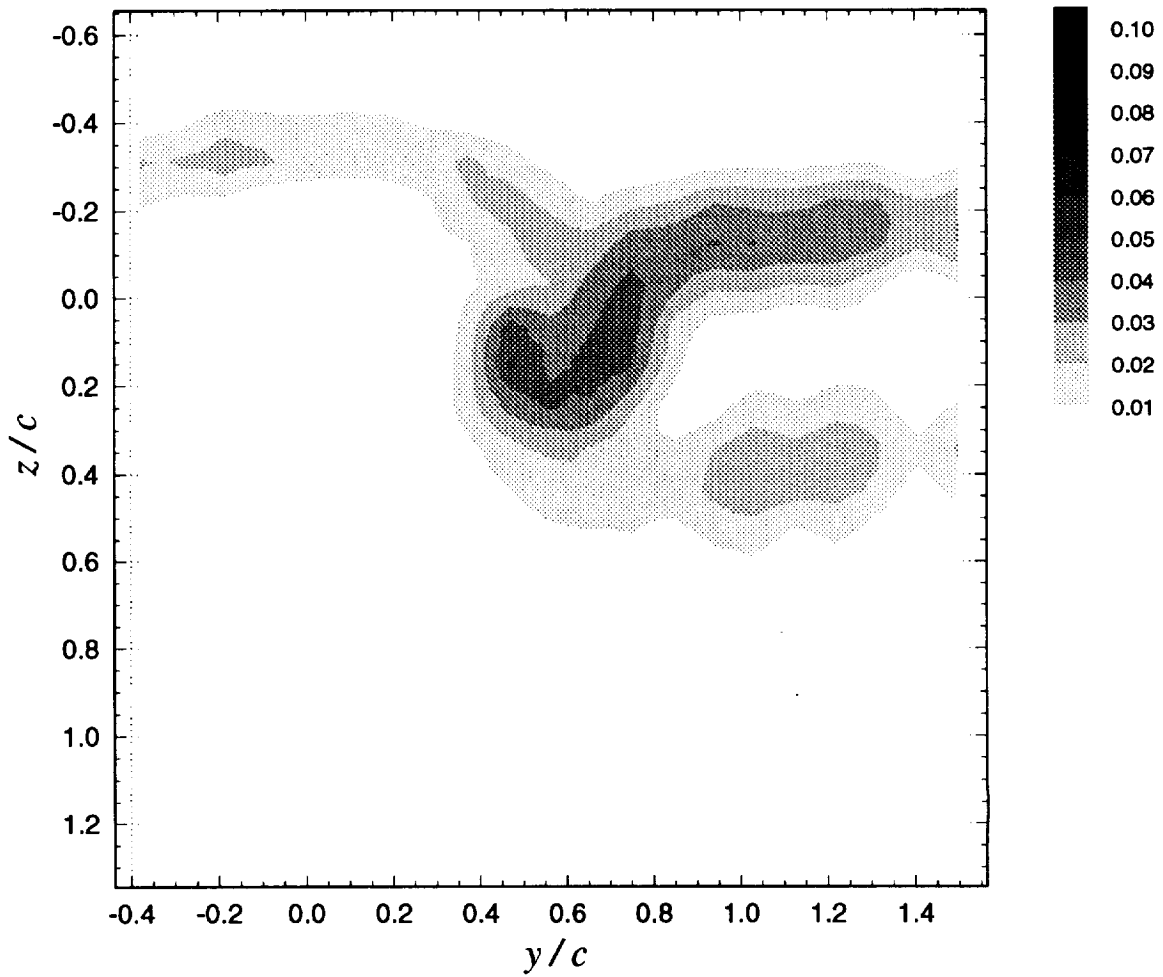


**Figure 3.75b** Contours of mean axial velocity deficit  $(U_{ref} - U) / U_{ref}$  for pressure side passage of  $\Delta/c = -0.125$ :  $x/c = 30$ ,  $\alpha_1 = 2.5^\circ$ ,  $\alpha_2 = 2.5^\circ$ , no spoiler

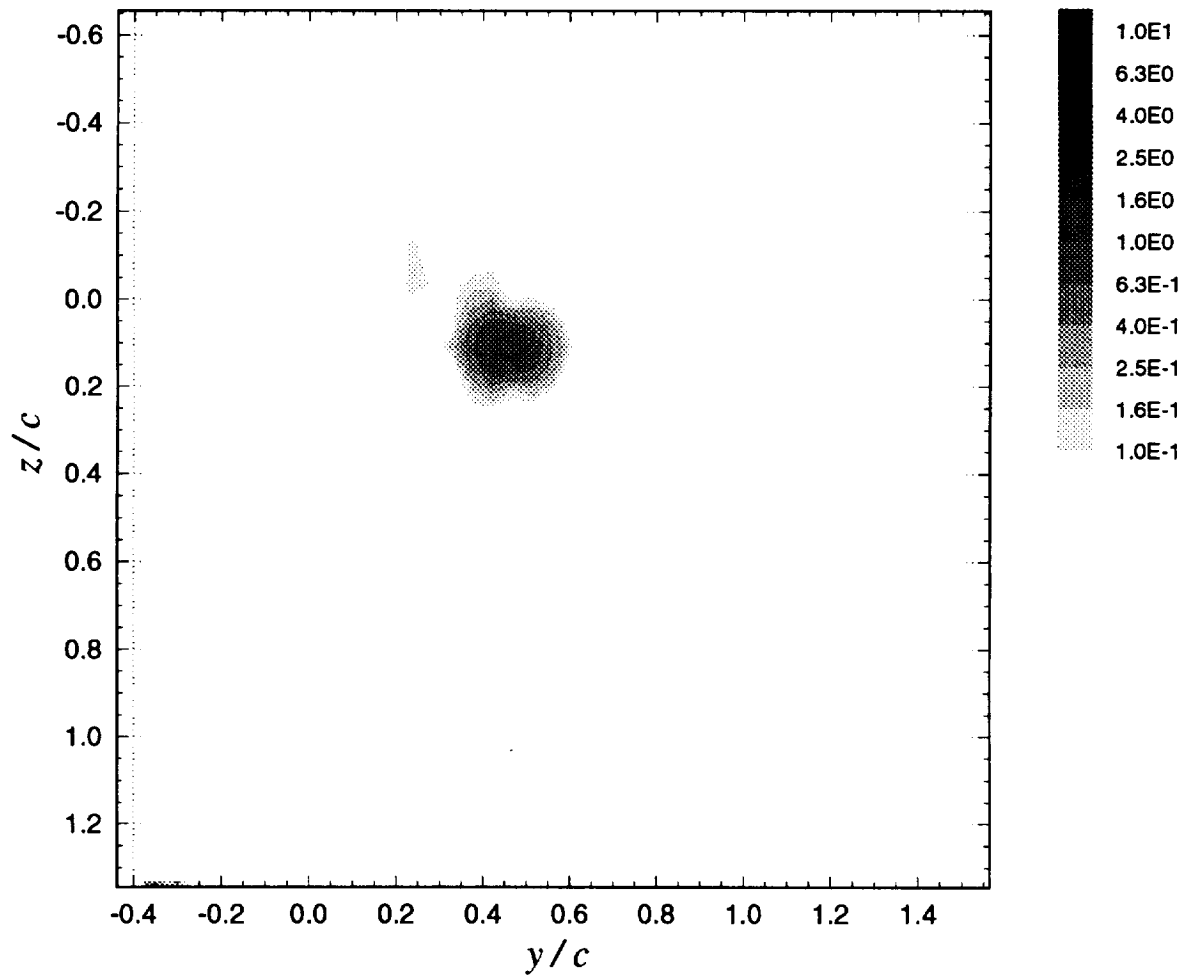


**Figure 3.75c** Contours of mean axial vorticity ( $\Omega_x \cdot c / U_{ref}$ ) for pressure side passage of  $\Delta/c = -0.125$ :  $x/c = 30$ ,  $\alpha_1 = 2.5^\circ$ ,  $\alpha_2 = 2.5^\circ$ , no spoiler

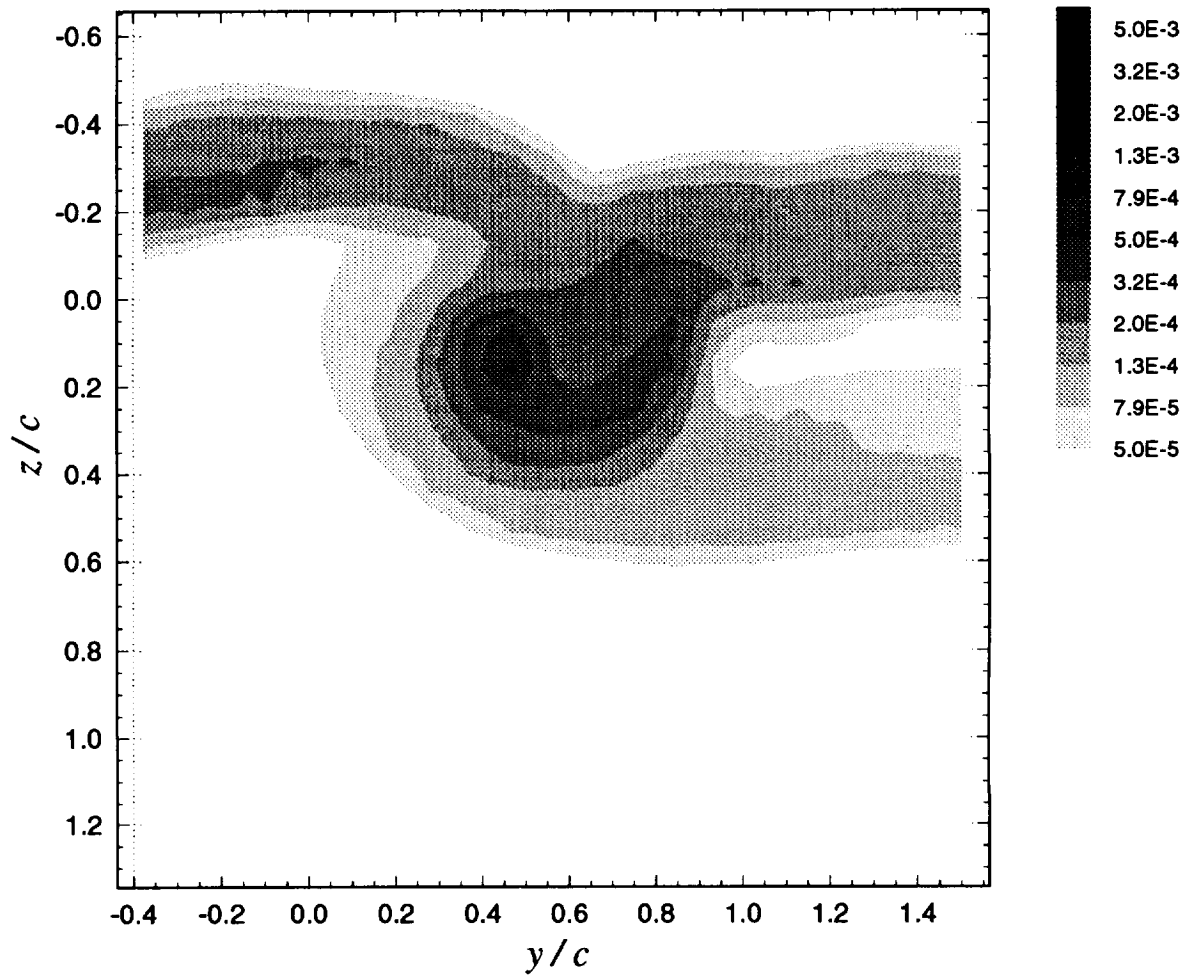


**Figure 3.75d** Contours of axial normal turbulent stress ( $\overline{u^2} / U_{ref}^2$ ) for pressure side passage of  $\Delta/c = -0.125$ :  $x/c = 30$ ,  $\alpha_1 = 2.5^\circ$ ,  $\alpha_2 = 2.5^\circ$ , no spoiler

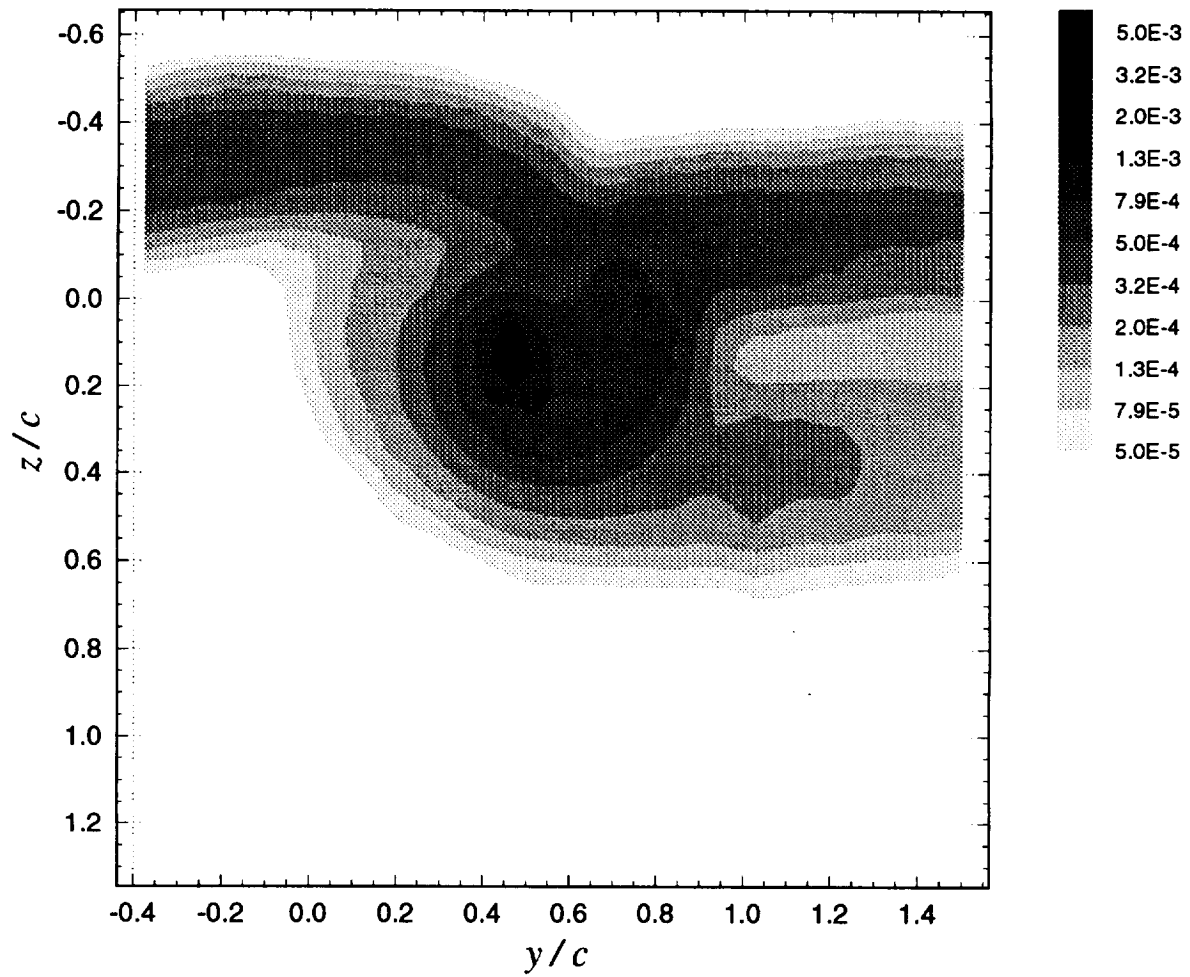


**Figure 3.75e** Contours of summed cross-flow normal turbulent stresses  $(\overline{v^2} + \overline{w^2}) / U_{ref}^2$  for pressure side passage of  $\Delta/c = -0.125$ :  $x/c = 30$ ,  $\alpha_1 = 2.5^\circ$ ,  $\alpha_2 = 2.5^\circ$ , no spoiler

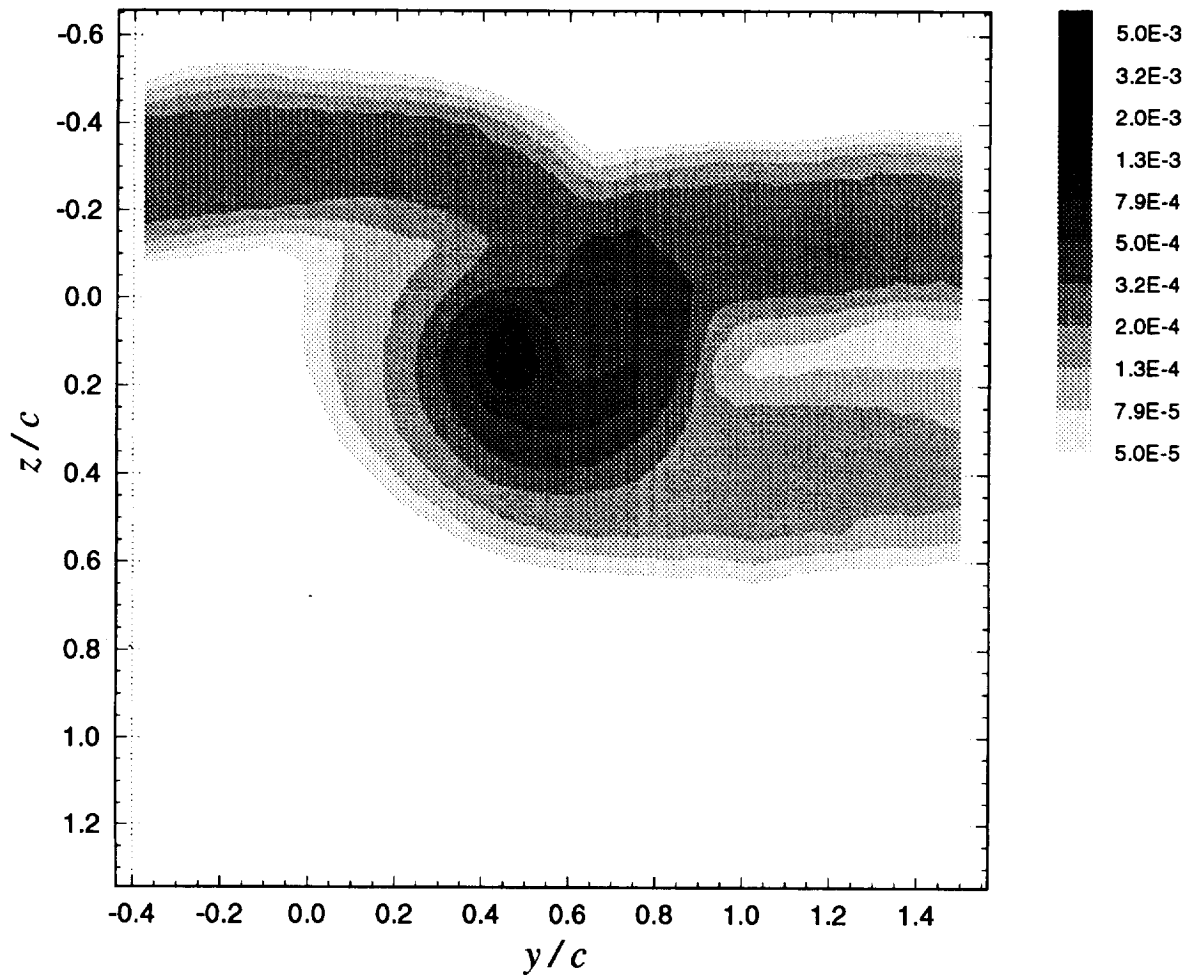


**Figure 3.75f** Contours of turbulent kinetic energy ( $k / U_{ref}^2$ ) for pressure side passage of  $\Delta/c = -0.125$ :  $x/c = 30$ ,  $\alpha_l = 2.5^\circ$ ,  $\alpha_2 = 2.5^\circ$ , no spoiler

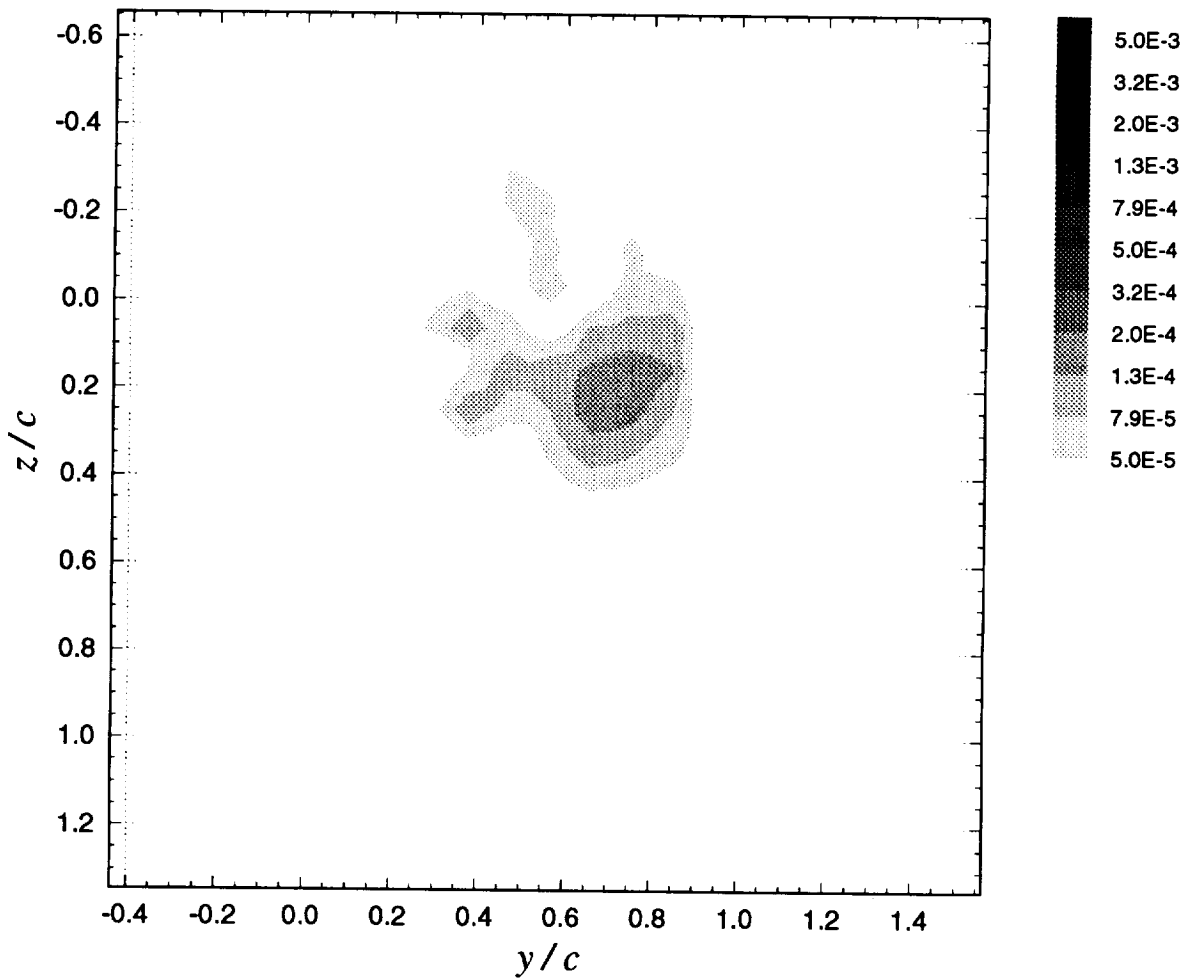


**Figure 3.75g** Contours of axial shear stress magnitude  $(\tau_a / U_{ref}^2)$  for pressure side passage of  $\Delta/c = -0.125$ :  $x/c = 30$ ,  $\alpha_l = 2.5^\circ$ ,  $\alpha_2 = 2.5^\circ$ , no spoiler



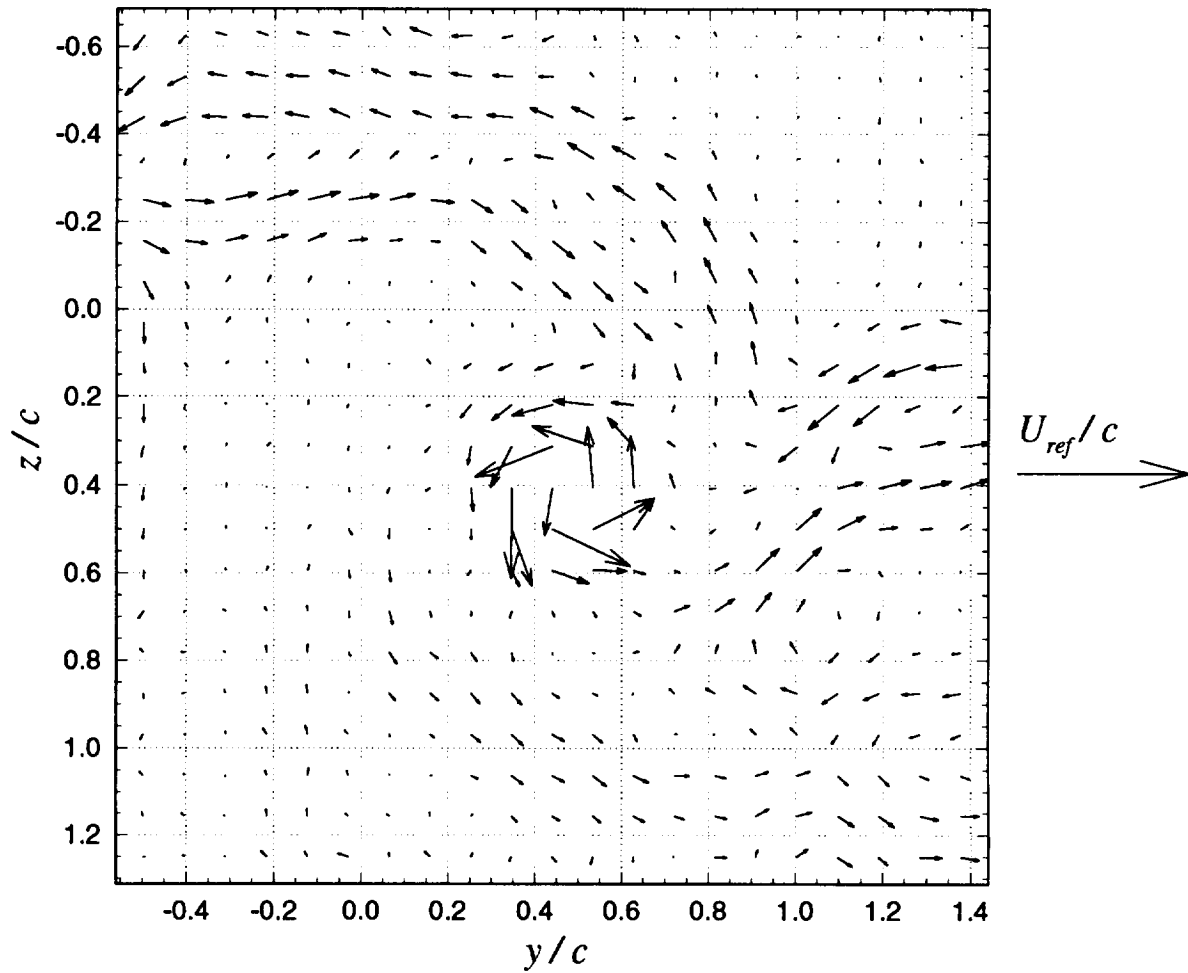


**Figure 3.76a** Mean cross-flow vorticity vectors ( $\Omega_y \cdot c / U_{ref}$ ,  $\Omega_z \cdot c / U_{ref}$ ) for pressure side passage of  $\Delta/c = -0.125$ :  $x/c = 30$ ,  $\alpha_1 = 7.5^\circ$ ,  $\alpha_2 = 7.5^\circ$ , no spoiler

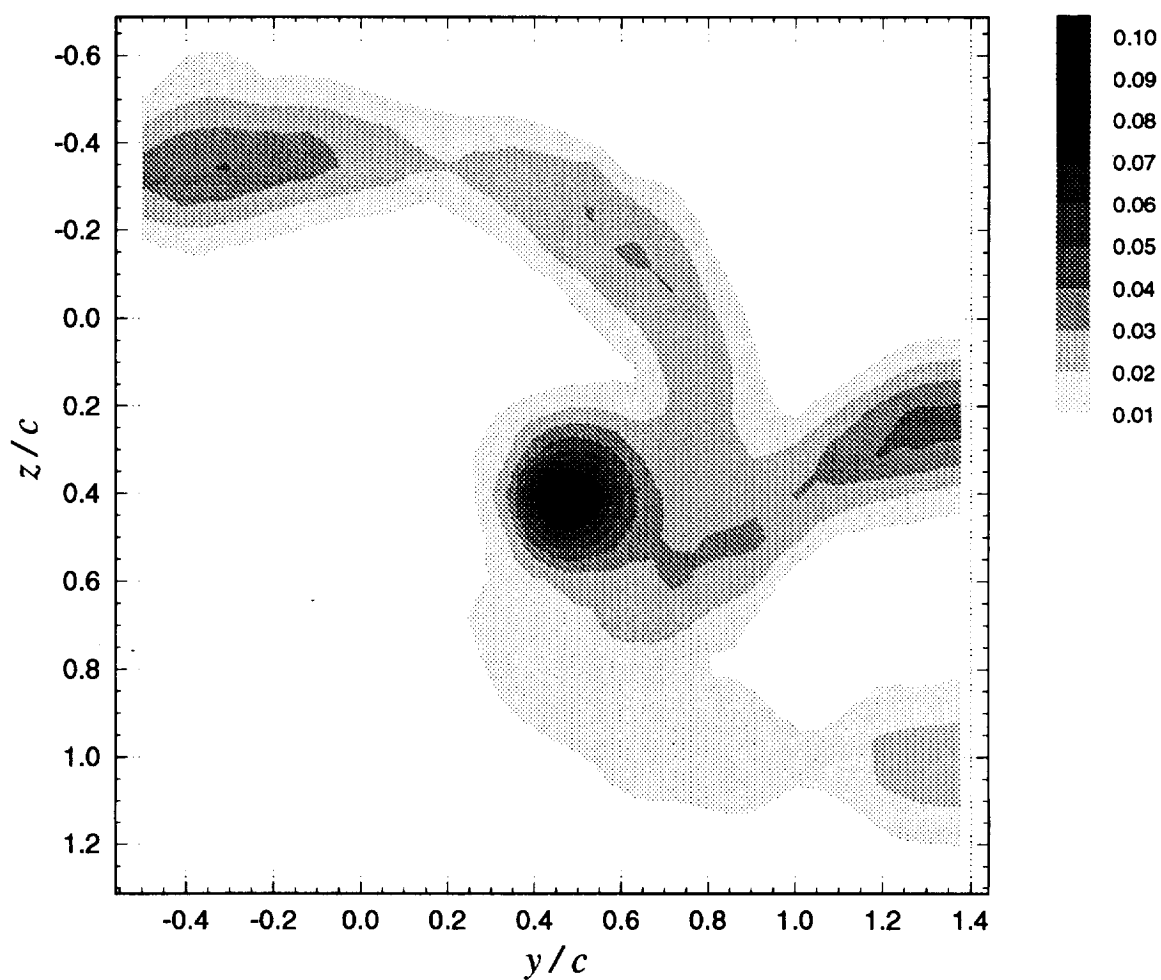


**Figure 3.76b** Contours of mean axial velocity deficit  $(U_{ref} - U) / U_{ref}$  for pressure side passage of  $\Delta/c = -0.125$ :  $x/c = 30$ ,  $\alpha_1 = 7.5^\circ$ ,  $\alpha_2 = 7.5^\circ$ , no spoiler

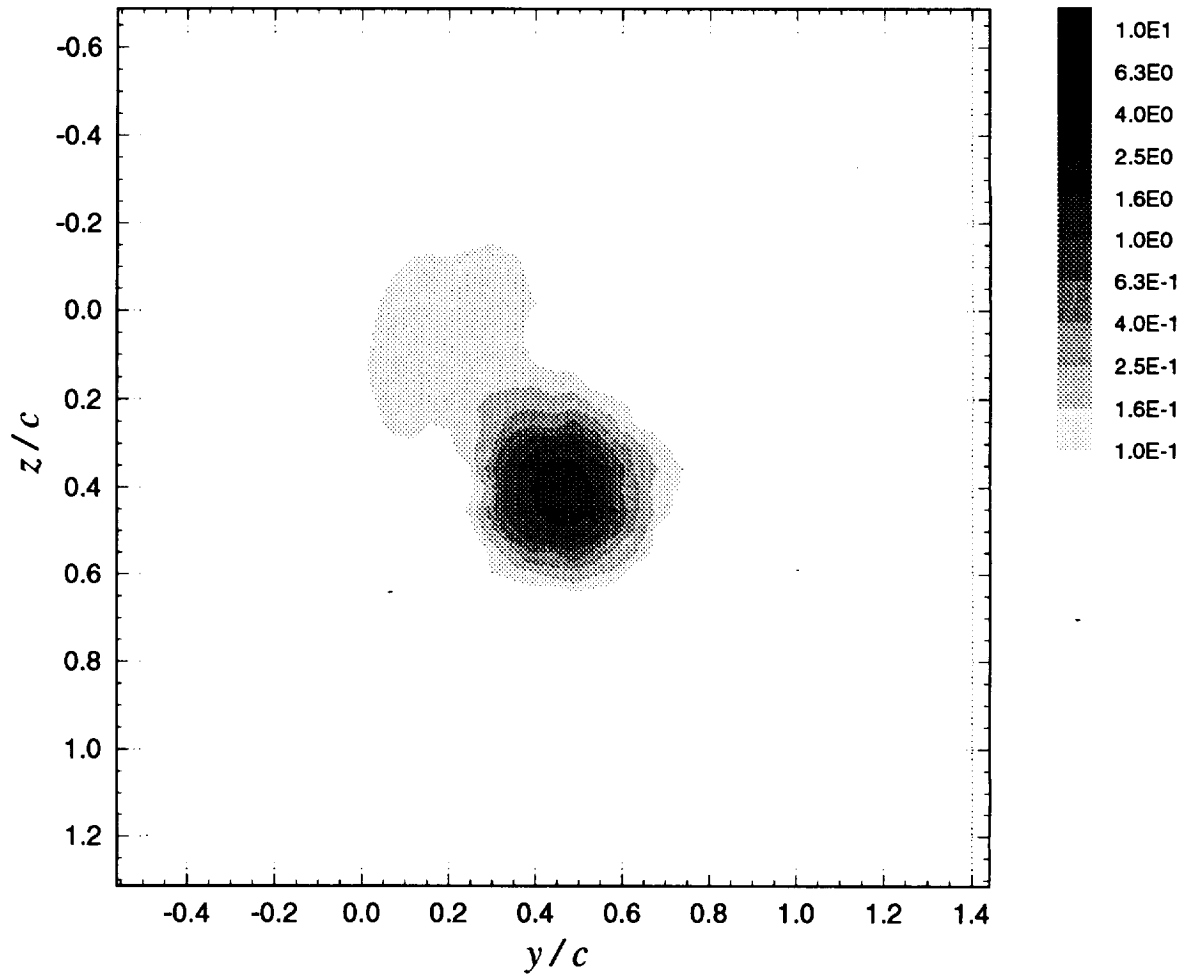


**Figure 3.76c** Contours of mean axial vorticity ( $\Omega_x \cdot c / U_{ref}$ ) for pressure side passage of  $\Delta/c = -0.125$ :  $x/c = 30$ ,  $\alpha_l = 7.5^\circ$ ,  $\alpha_2 = 7.5^\circ$ , no spoiler

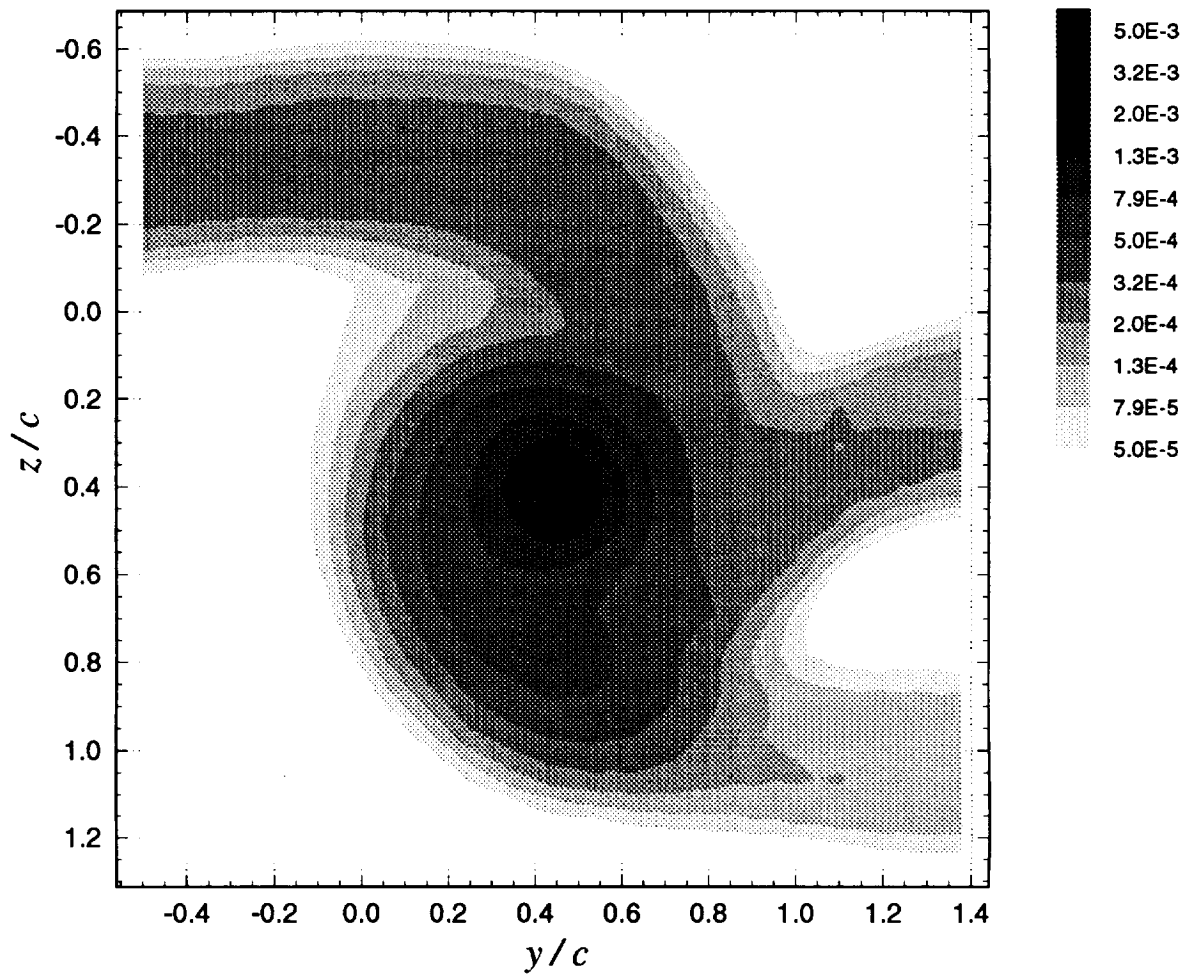


**Figure 3.76d** Contours of axial normal turbulent stress ( $\overline{u^2} / U_{ref}^2$ ) for pressure side passage of  $\Delta/c = -0.125$ :  $x/c = 30$ ,  $\alpha_1 = 7.5^\circ$ ,  $\alpha_2 = 7.5^\circ$ , no spoiler

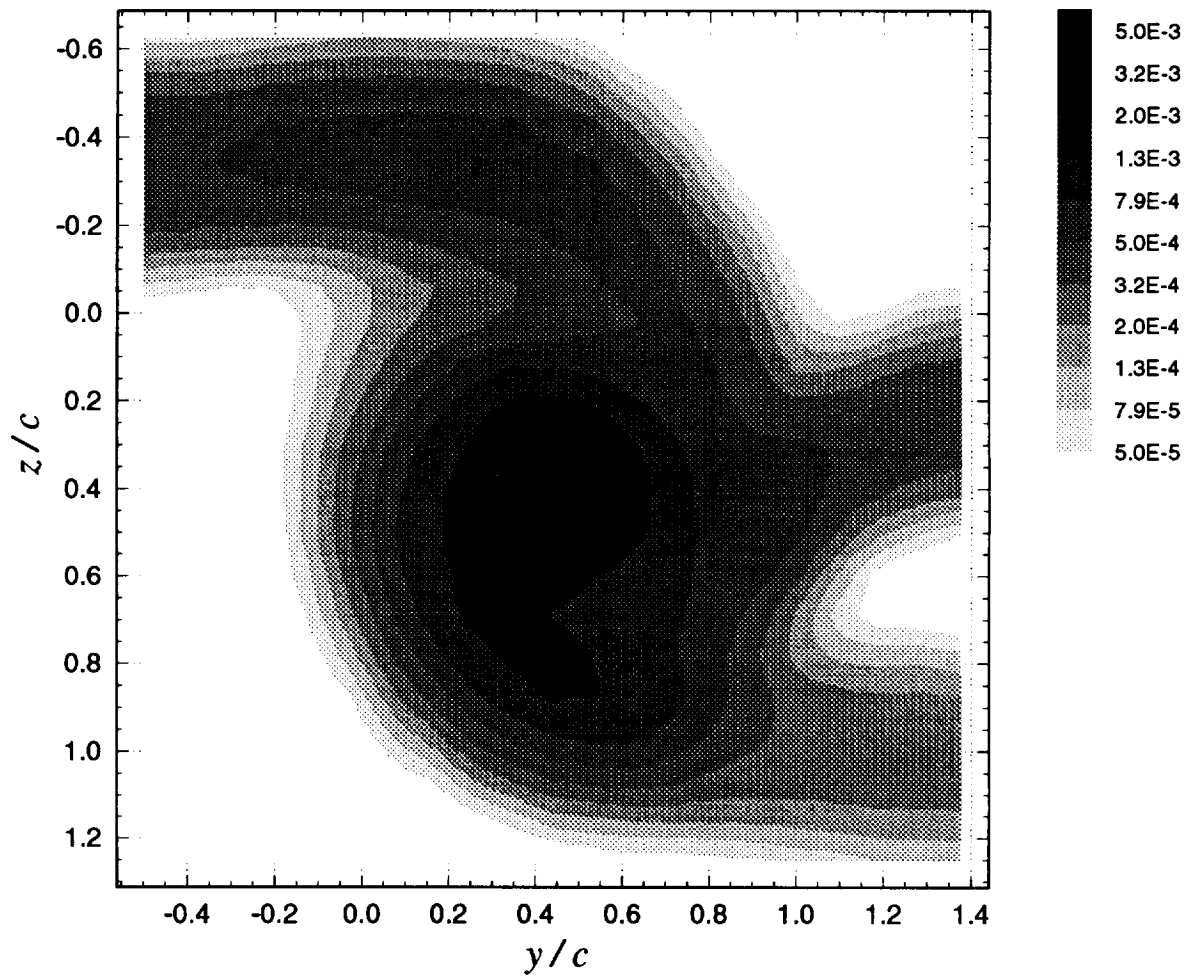


**Figure 3.76e** Contours of summed cross-flow normal turbulent stresses  $(\overline{v^2} + \overline{w^2}) / U_{ref}^2$  for pressure side passage of  $\Delta/c = -0.125$ :  $x/c = 30$ ,  $\alpha_1 = 7.5^\circ$ ,  $\alpha_2 = 7.5^\circ$ , no spoiler

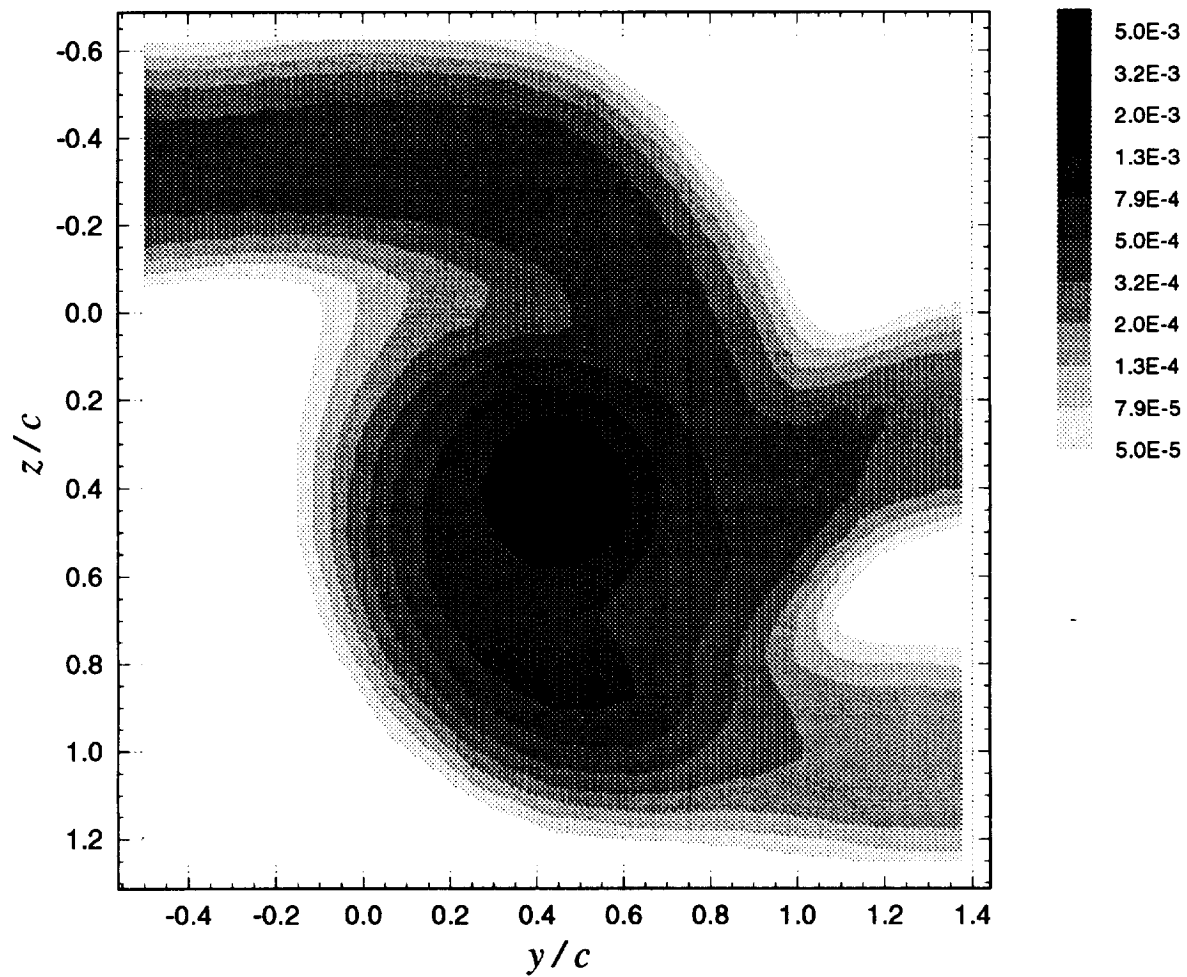


**Figure 3.76f** Contours of turbulent kinetic energy ( $k / U_{ref}^2$ ) for pressure side passage of  $\Delta/c = -0.125$ :  $x/c = 30$ ,  $\alpha_1 = 7.5^\circ$ ,  $\alpha_2 = 7.5^\circ$ , no spoiler

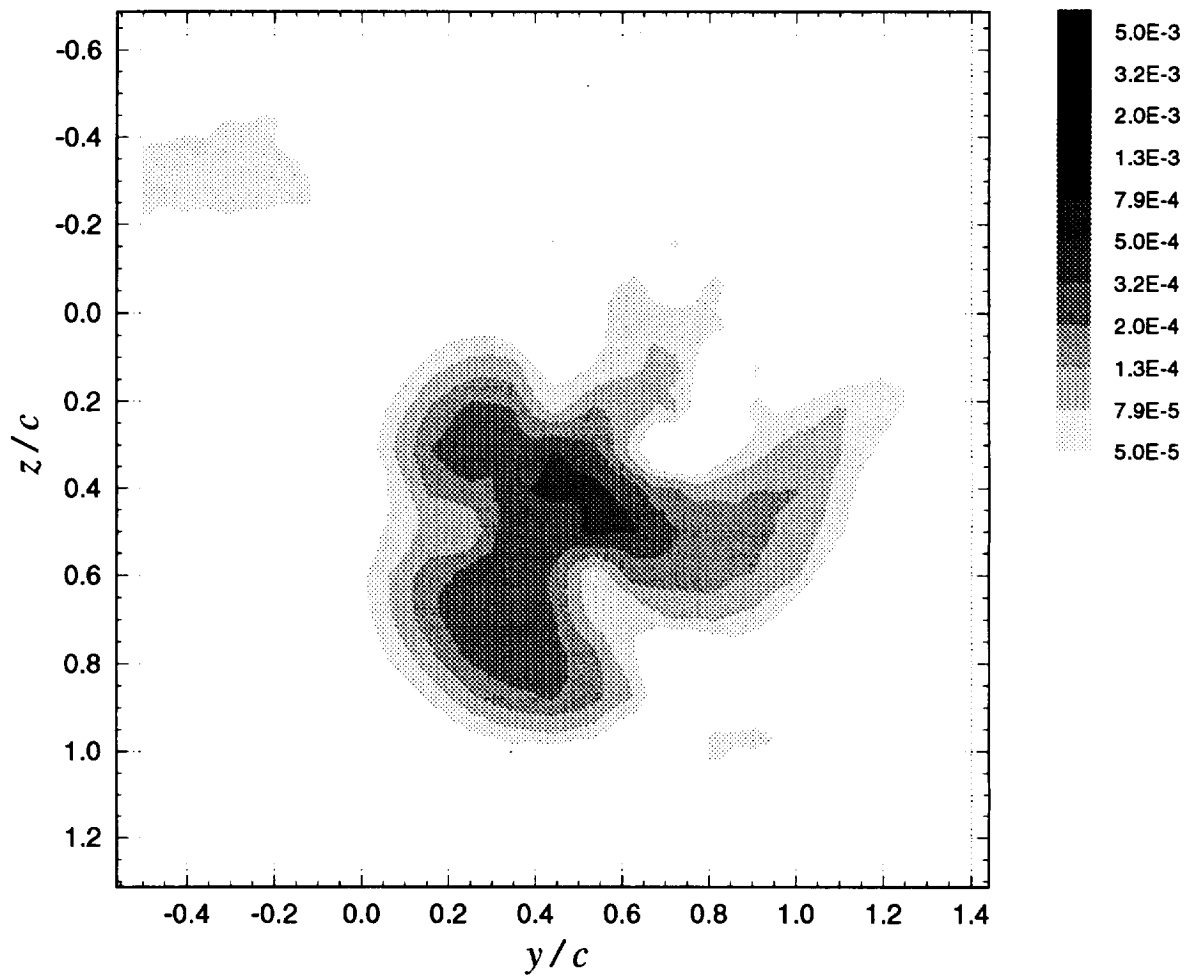


**Figure 3.76g** Contours of axial shear stress magnitude  $(\tau_a / U_{ref}^2)$  for pressure side passage of  $\Delta/c = -0.125$ :  $x/c = 30$ ,  $\alpha_1 = 7.5^\circ$ ,  $\alpha_2 = 7.5^\circ$ , no spoiler

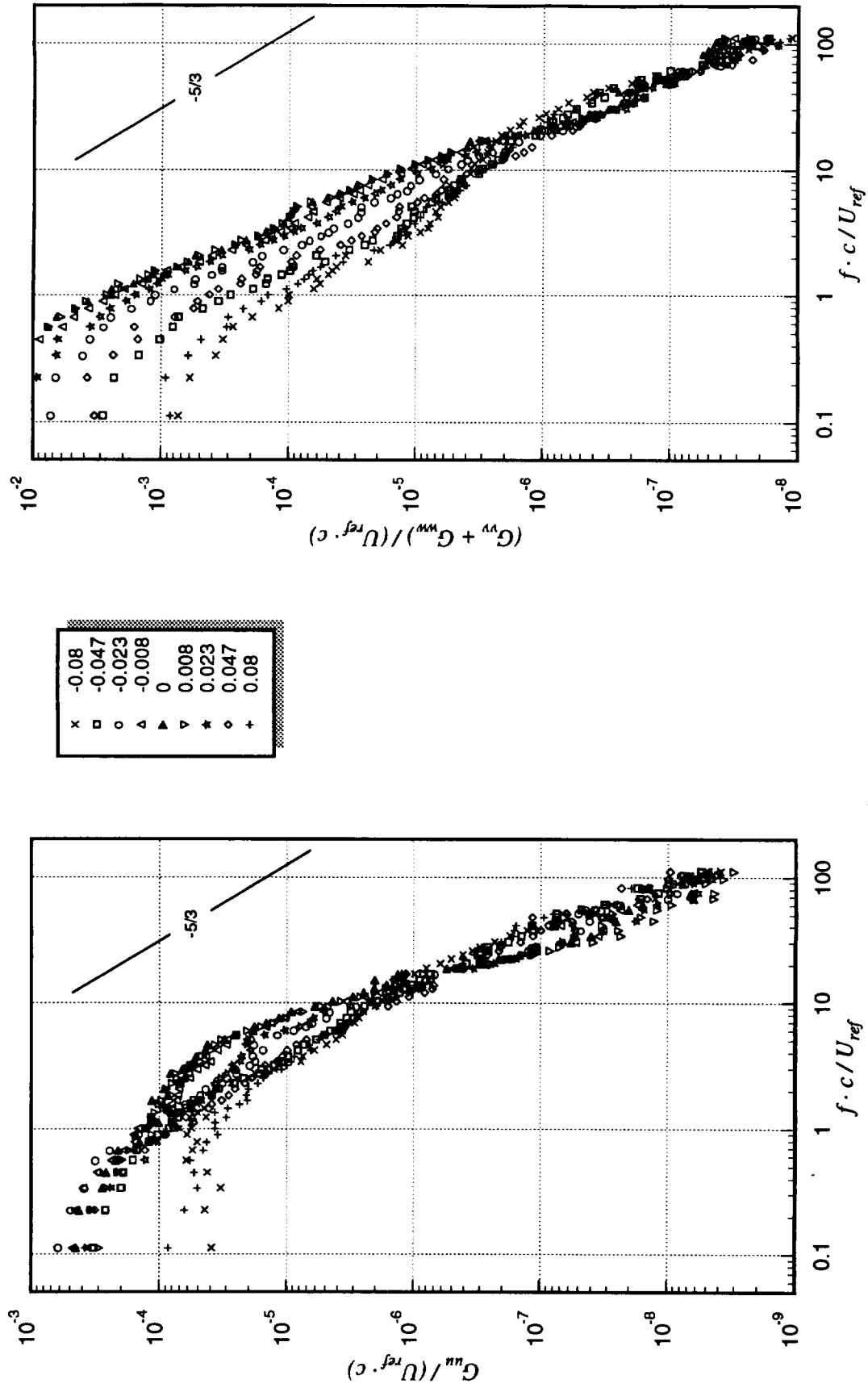


**Figure 3.77a** Velocity autospectra measured along z-wise profiles through the vortex core center:  $x/c = 30$ ,  $\alpha_1 = 5^\circ$ ,  $\alpha_2 = 0^\circ$ , no spoiler,  $\Delta/c = 0.375$ . Legend lists  $r/c$  values ( $r_1/c = 0.037$ ).



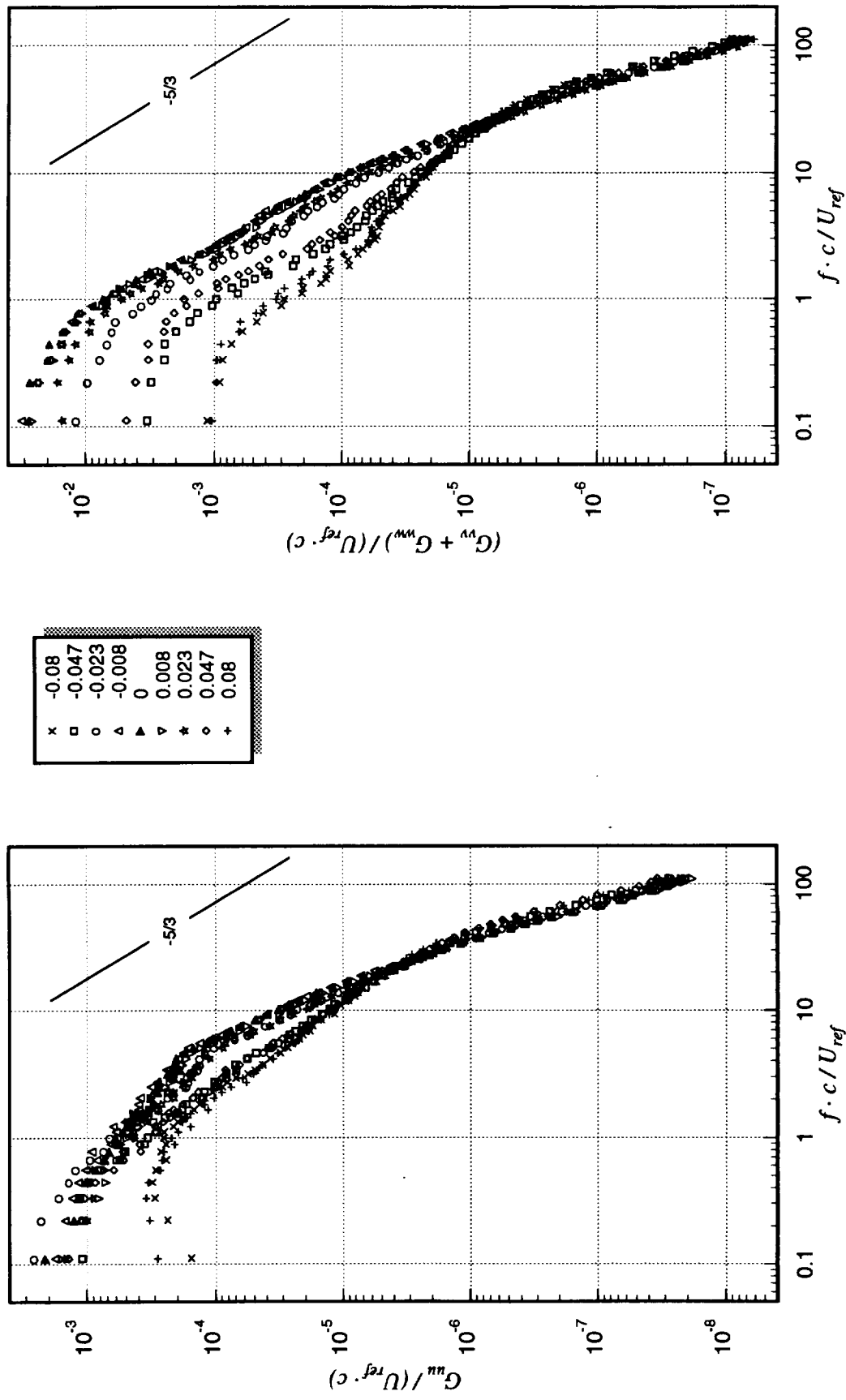


**Figure 3.77b** Velocity autospectra measured along z-wise profiles through the vortex core center:  $x/c = 30$ ,  $\alpha_1 = 5^\circ$ ,  $\alpha_2 = 0^\circ$ , no spoiler,  $\Delta/c = 0.25$ . Legend lists  $r/c$  values ( $r_1/c = 0.038$ ).

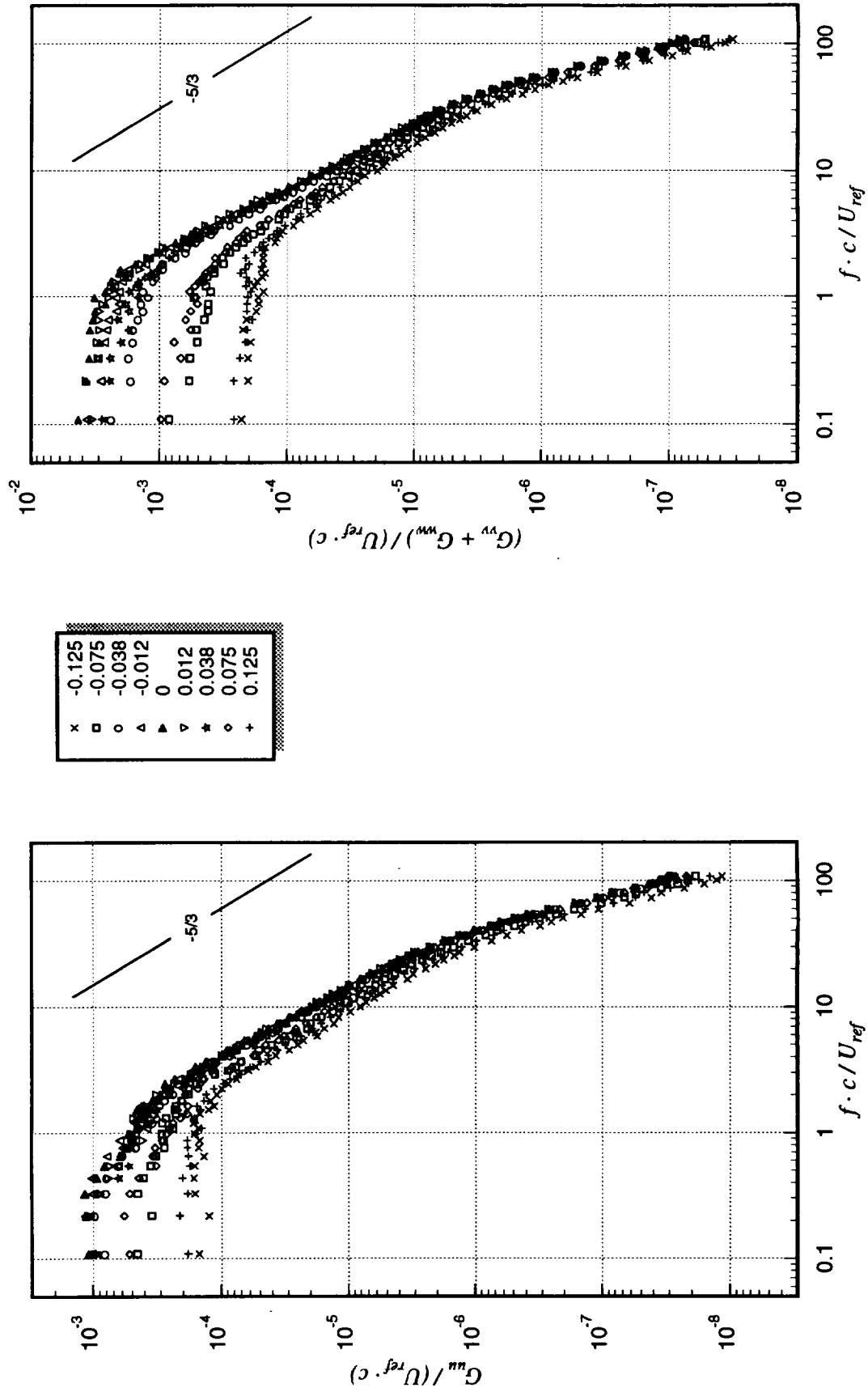


**Figure 3.77c** Velocity autospectra measured along  $z$ -wise profiles through the vortex core center:  $x/c = 30$ ,  $\alpha_1 = 5^\circ$ ,  $\alpha_2 = 0^\circ$ , no spoiler,  $\Delta/c = 0.125$ . Legend lists  $r/c$  values ( $r_1/c = 0.071$ ).

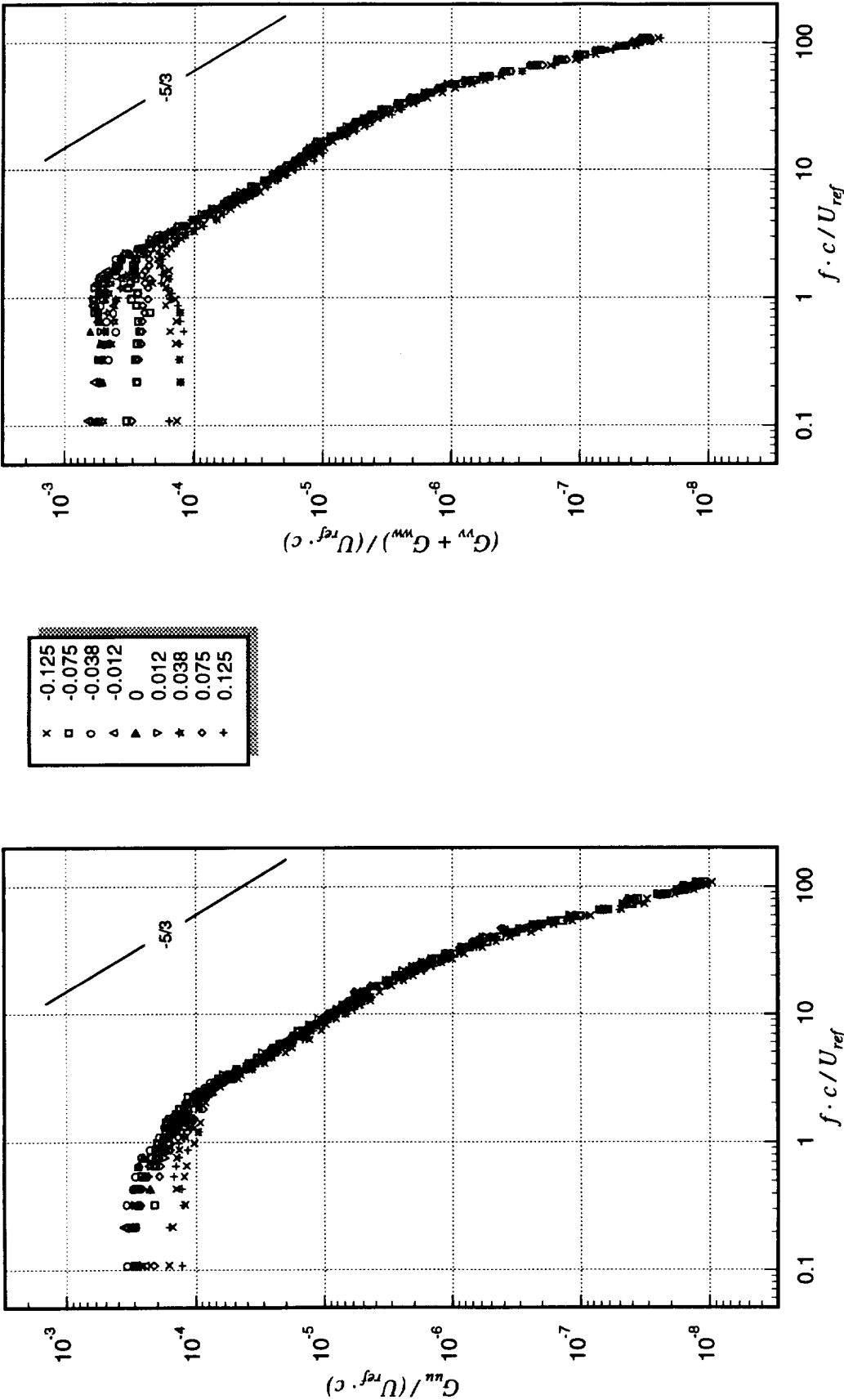


**Figure 3.77d** Velocity autospectra measured along z-wise profiles through the vortex core center:  $x/c = 30$ ,  $\alpha_1 = 5^\circ$ ,  $\alpha_2 = 0^\circ$ , no spoiler,  $\Delta/c = 0.0938$ . Legend lists  $r/c$  values ( $r_1/c = 0.109$ ).

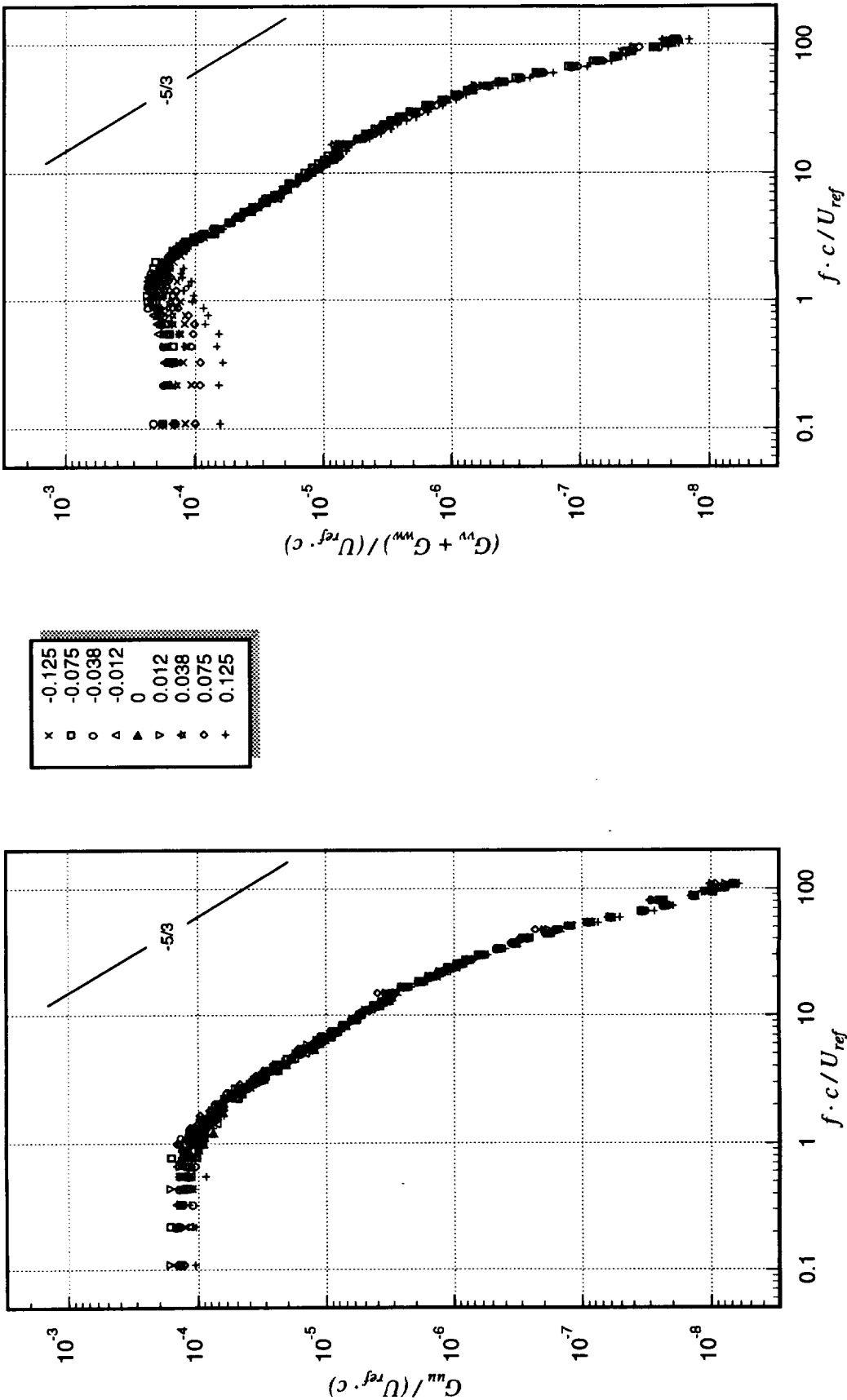
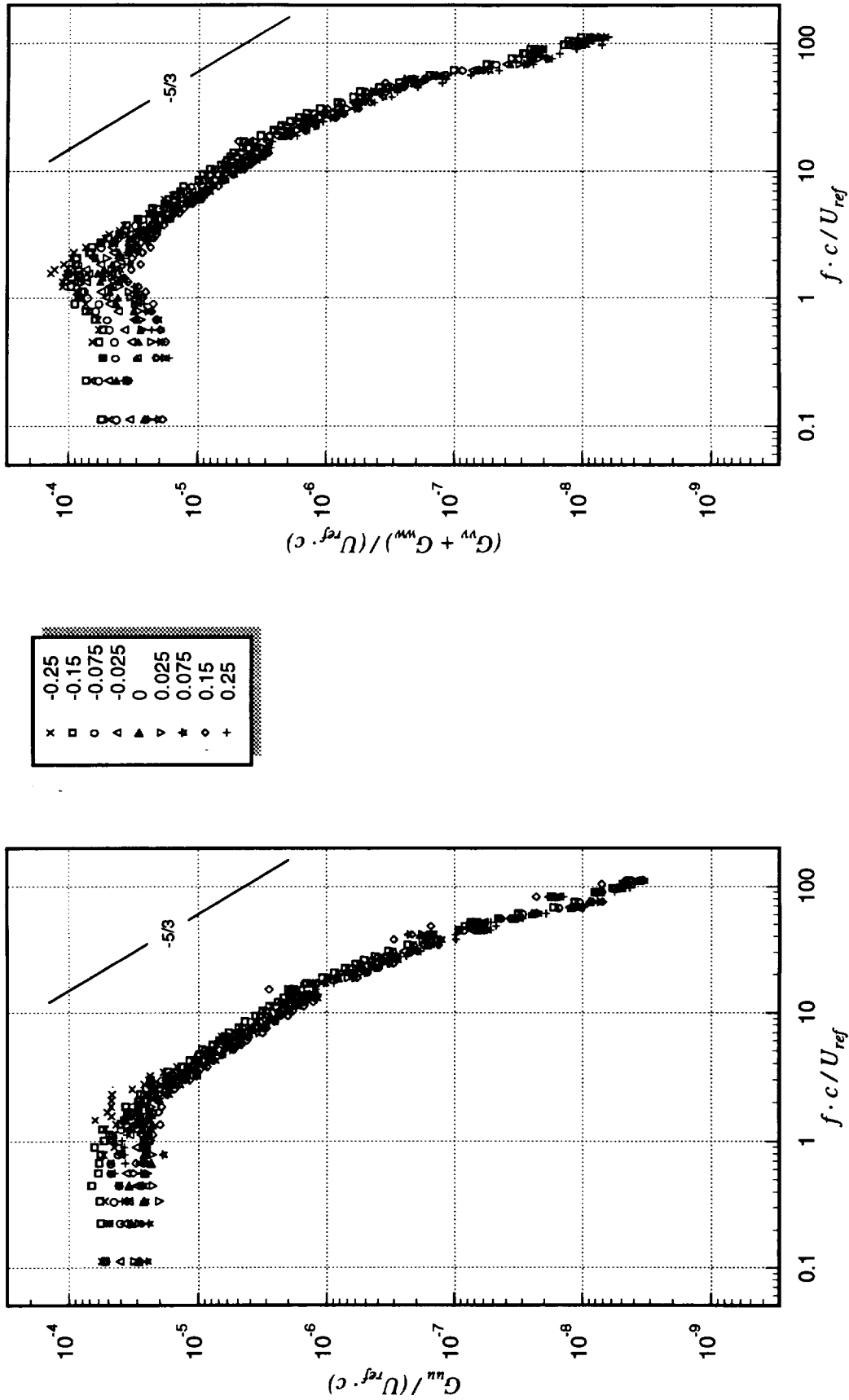
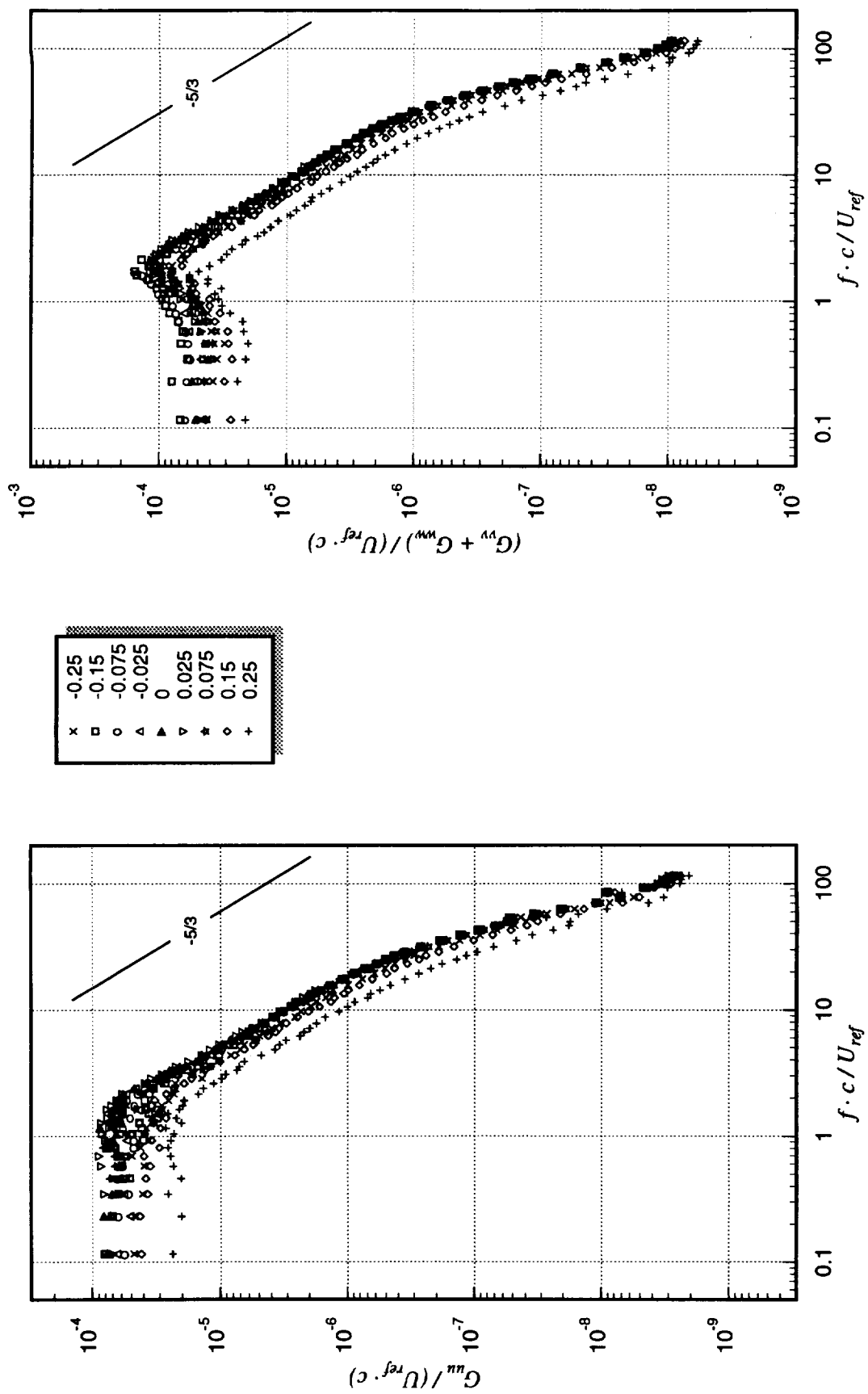


Figure 3.77e Velocity autospectra measured along z-wise profiles through the vortex core center:  $x/c = 30$ ,  $\alpha_1 = 5^\circ$ ,  $\alpha_2 = 0^\circ$ , no spoiler,  $\Delta/c = 0.0625$ . Legend lists  $r/c$  values ( $r_1/c = 0.146$ ).



**Figure 3.77f** Velocity autospectra measured along z-wise profiles through the vortex core center:  $x/c = 30$ ,  $\alpha_1 = 5^\circ$ ,  $\alpha_2 = 0^\circ$ , no spoiler,  $\Delta/c = 0.0312$ . Legend lists  $r/c$  values ( $r_1/c = 0.595$ ).



**Figure 3.77g** Velocity autospectra measured along z-wise profiles through the vortex core center:  $x/c = 30$ ,  $\alpha_1 = 5^\circ$ ,  $\alpha_2 = 0^\circ$ , no spoiler,  $\Delta/c = 0$ . Legend lists  $r/c$  values ( $r_1/c = 0.580$ ).

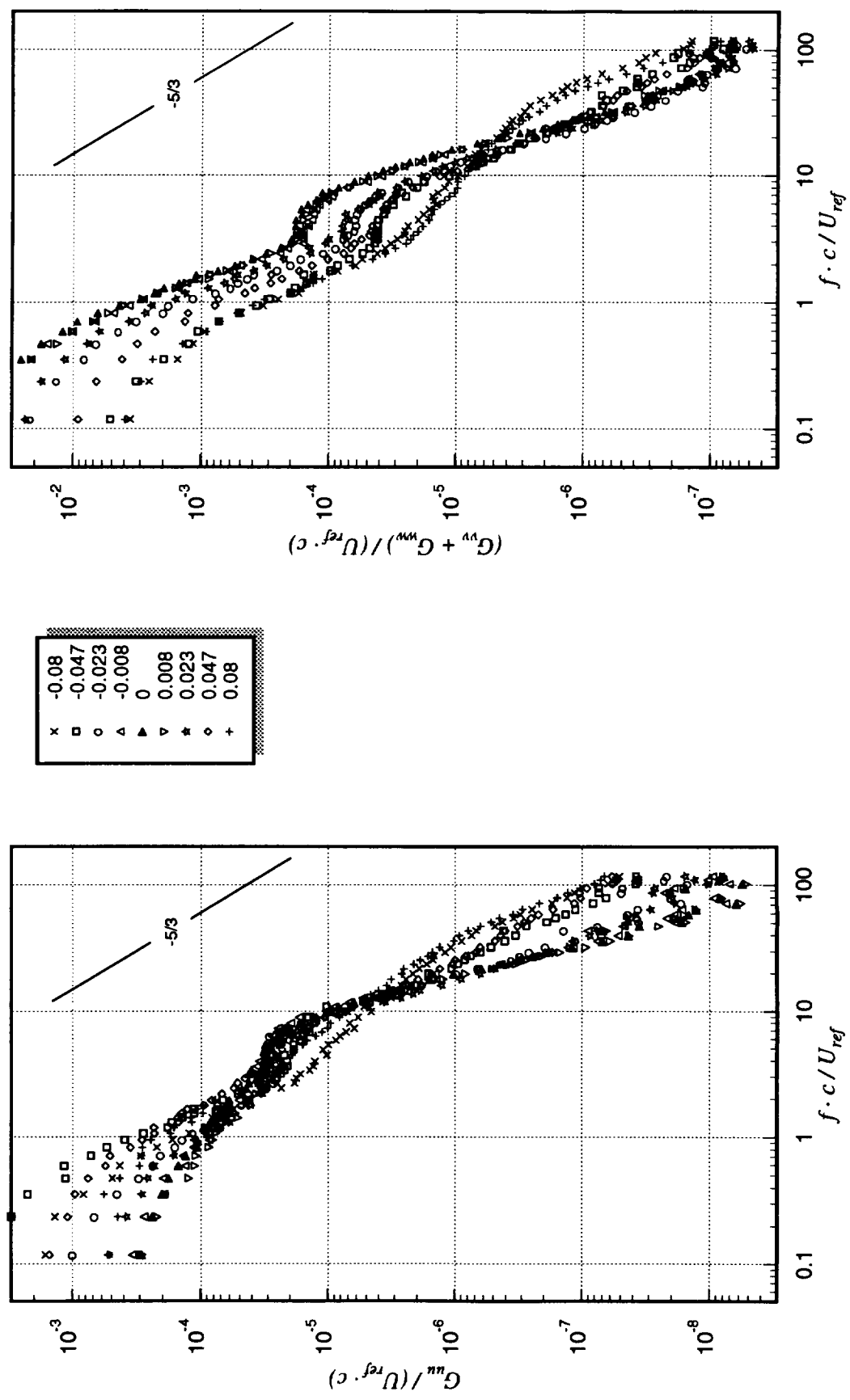
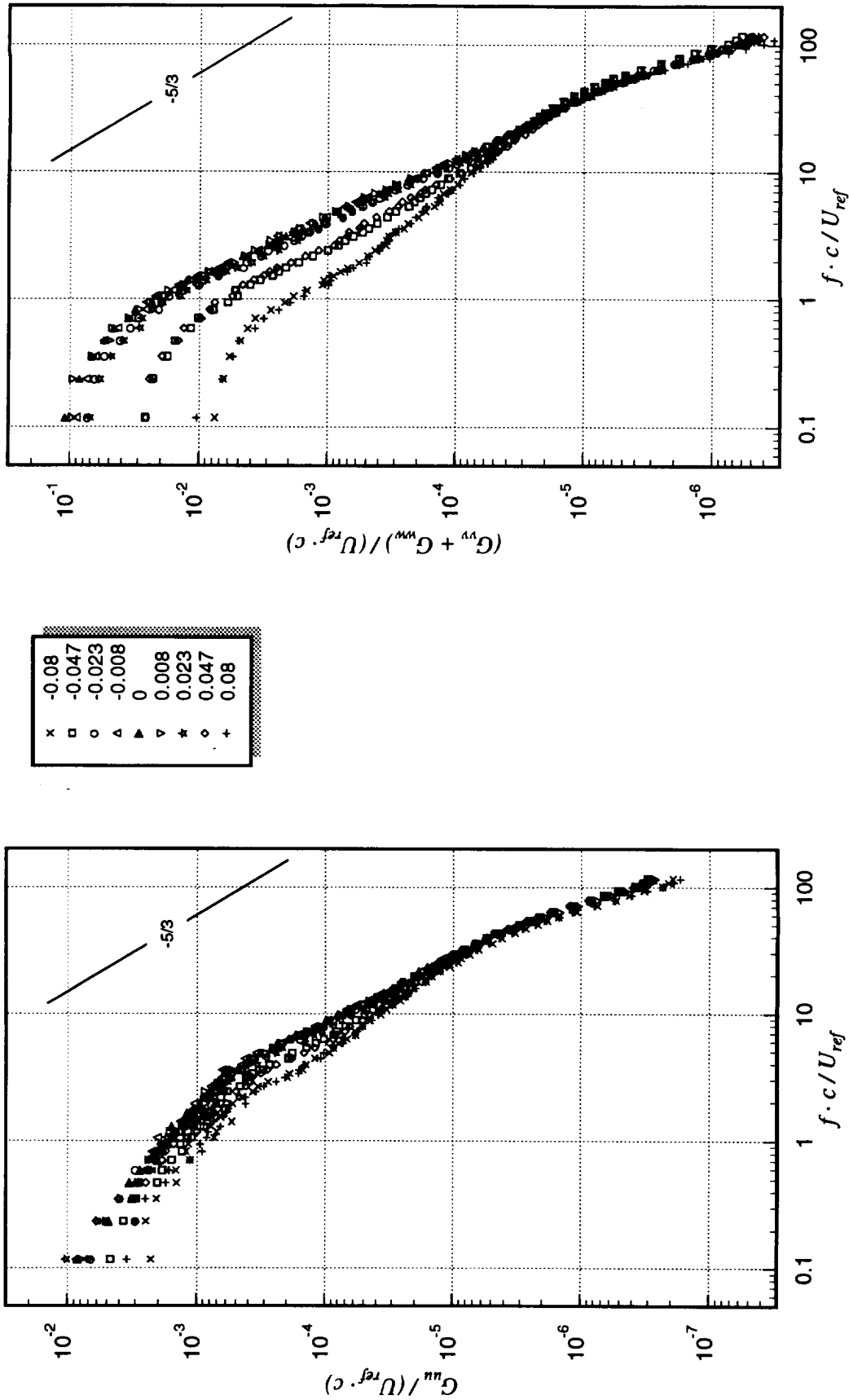


Figure 3.78a Velocity autospectra measured along z-wise profiles through the vortex core center:  $x/c = 30$ ,  $\alpha_1 = 10^\circ$ ,  $\alpha_2 = 5^\circ$ , no spoiler,  $\Delta/c = 0.5$ . Legend lists  $r/c$  values ( $r_1/c = 0.053$ ).



**Figure 3.78b** Velocity autospectra measured along z-wise profiles through the vortex core center:  $x/c = 30$ ,  $\alpha_1 = 10^\circ$ ,  $\alpha_2 = 5^\circ$ , no spoiler,  $\Delta/c = 0.25$ . Legend lists  $r/c$  values ( $r_1/c = 0.053$ ).



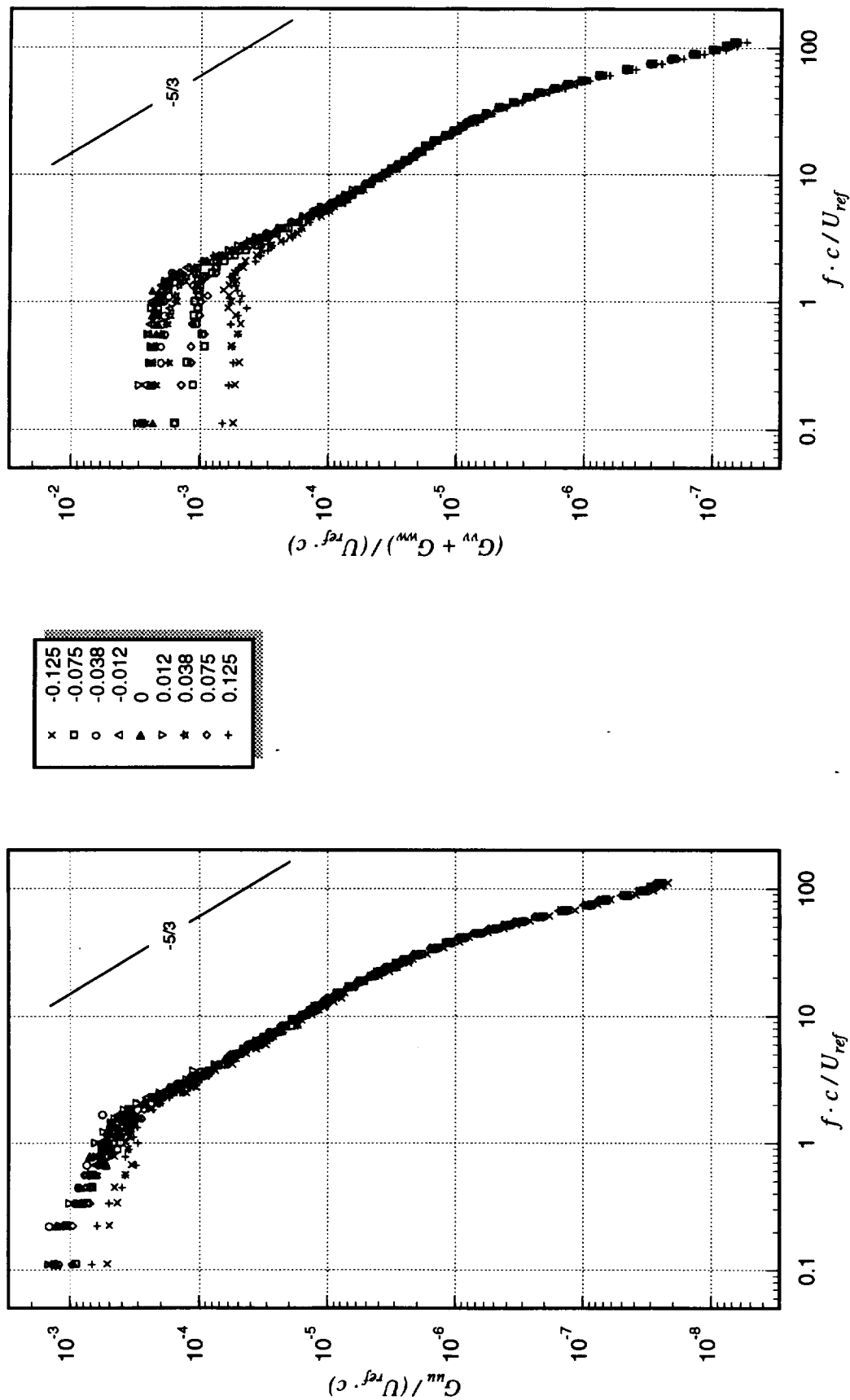
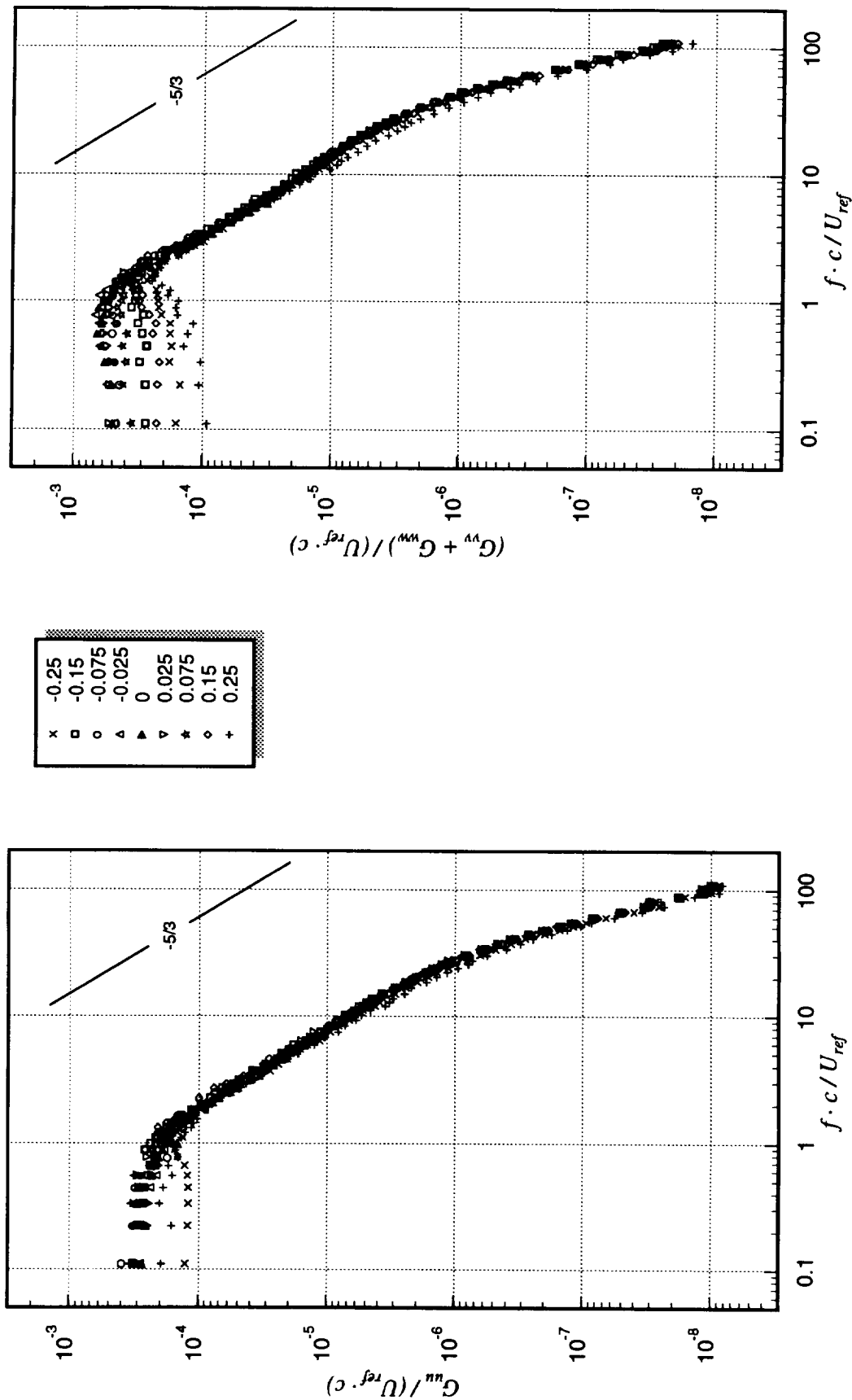
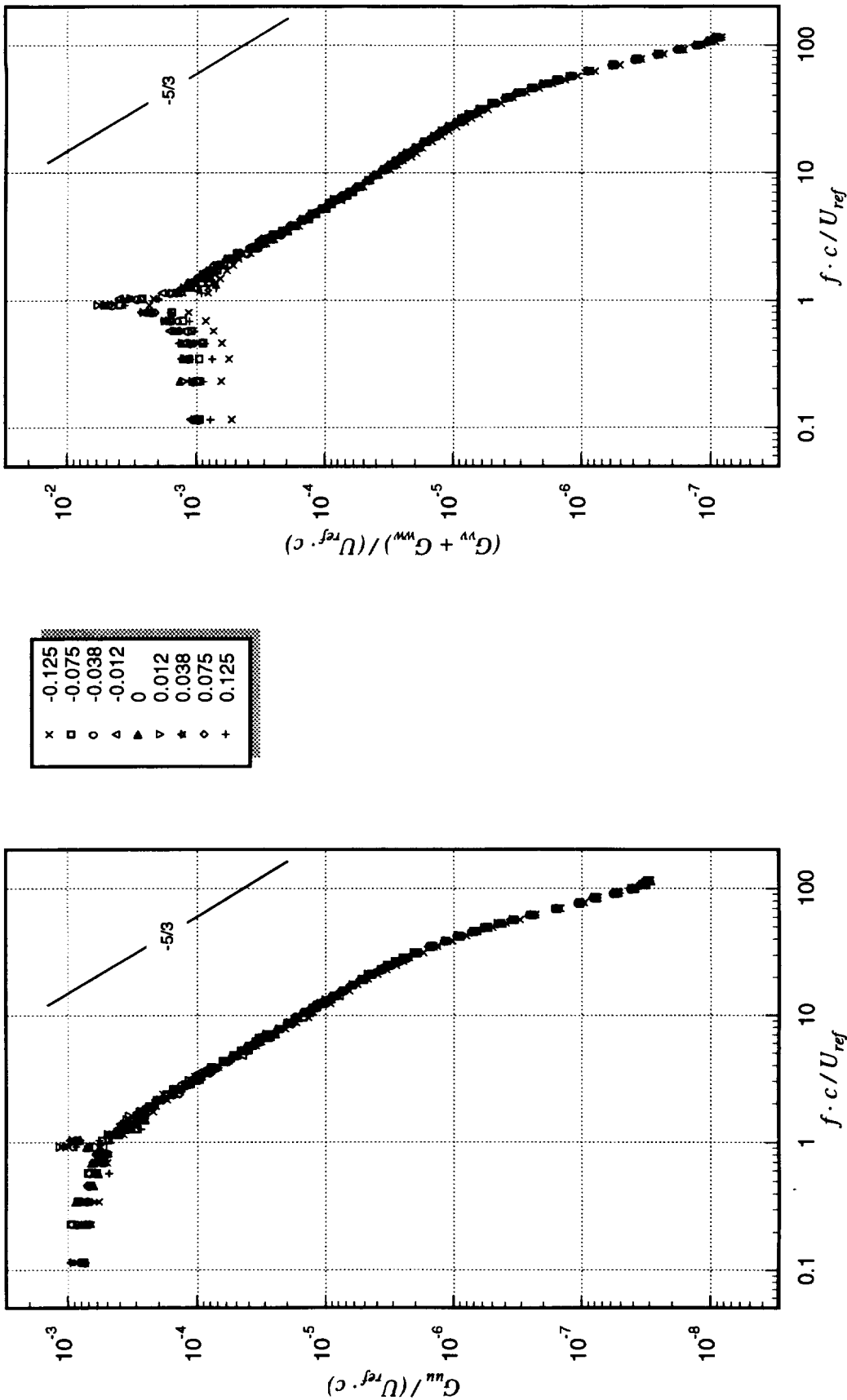


Figure 3.78c Velocity autospectra measured along z-wise profiles through the vortex core center:  $x/c = 30$ ,  $\alpha_1 = 10^\circ$ ,  $\alpha_2 = 5^\circ$ , no spoiler,  $\Delta/c = 0.125$ . Legend lists  $r/c$  values ( $r_1/c = 0.119$ ).



**Figure 3.78d** Velocity autospectra measured along z-wise profiles through the vortex core center:  $x/c = 30$ ,  $\alpha_1 = 10^\circ$ ,  $\alpha_2 = 5^\circ$ , no spoiler,  $\Delta/c = 0.0625$ . Legend lists  $r/c$  values ( $r_1/c = 0.2$ ).



**Figure 3.79a** Velocity autospectra measured along z-wise profiles through the vortex core center:  $x/c = 10$ ,  $\alpha_1 = 5^\circ$ ,  $d/c = 0.2125$ . Legend lists  $r/c$  values ( $r_1/c = 0.178$ ).

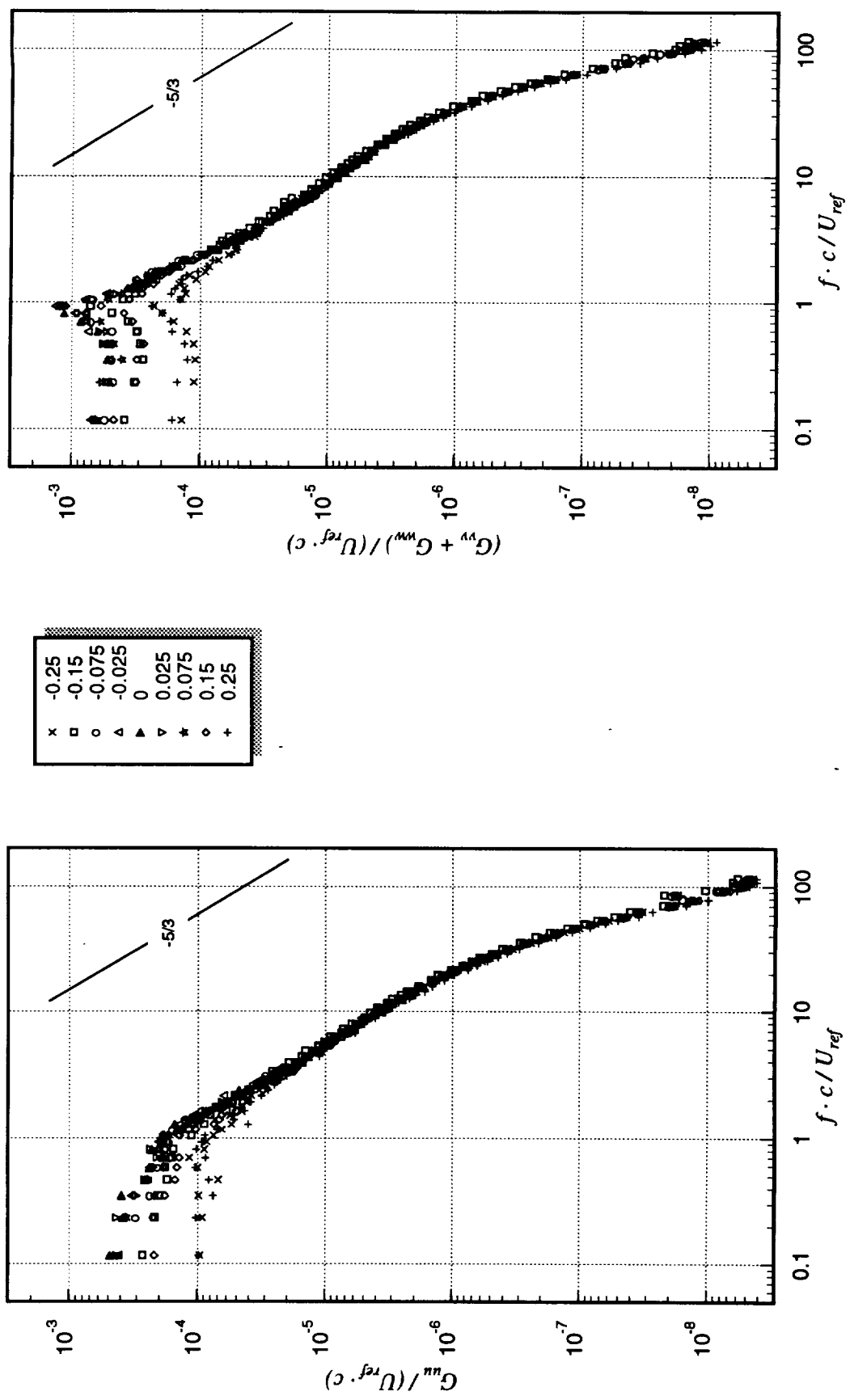


**Figure 3.79b** Velocity autospectra measured along z-wise profiles through the vortex core center:  $x/c = 30$ ,  $\alpha_1 = 5^\circ$ ,  $\alpha_2 = 5^\circ$ ,  $d/c = 0.2125$ ,  $\Delta/c = 0.5$ . Legend lists  $r/c$  values ( $r_1/c = 0.216$ ).

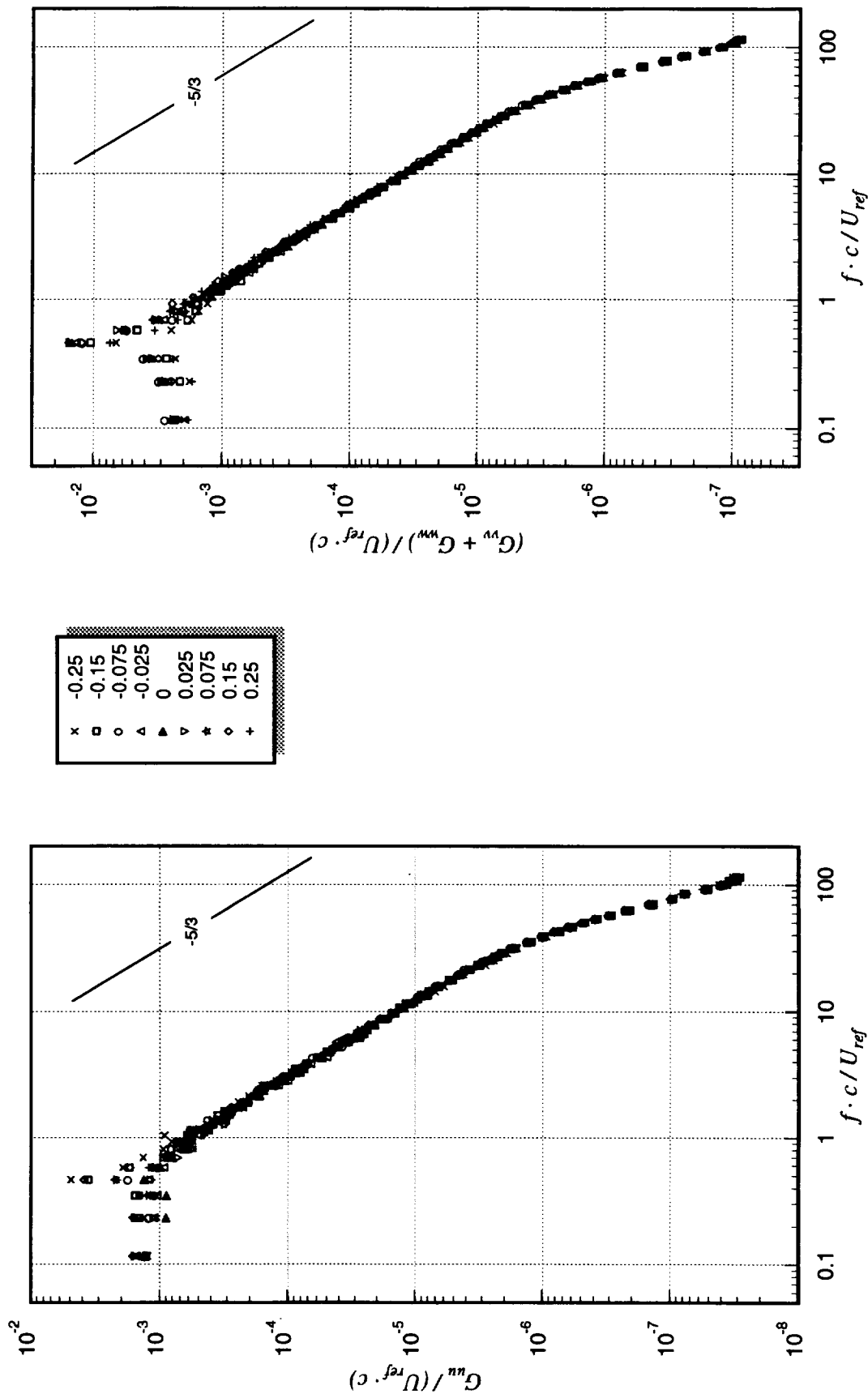
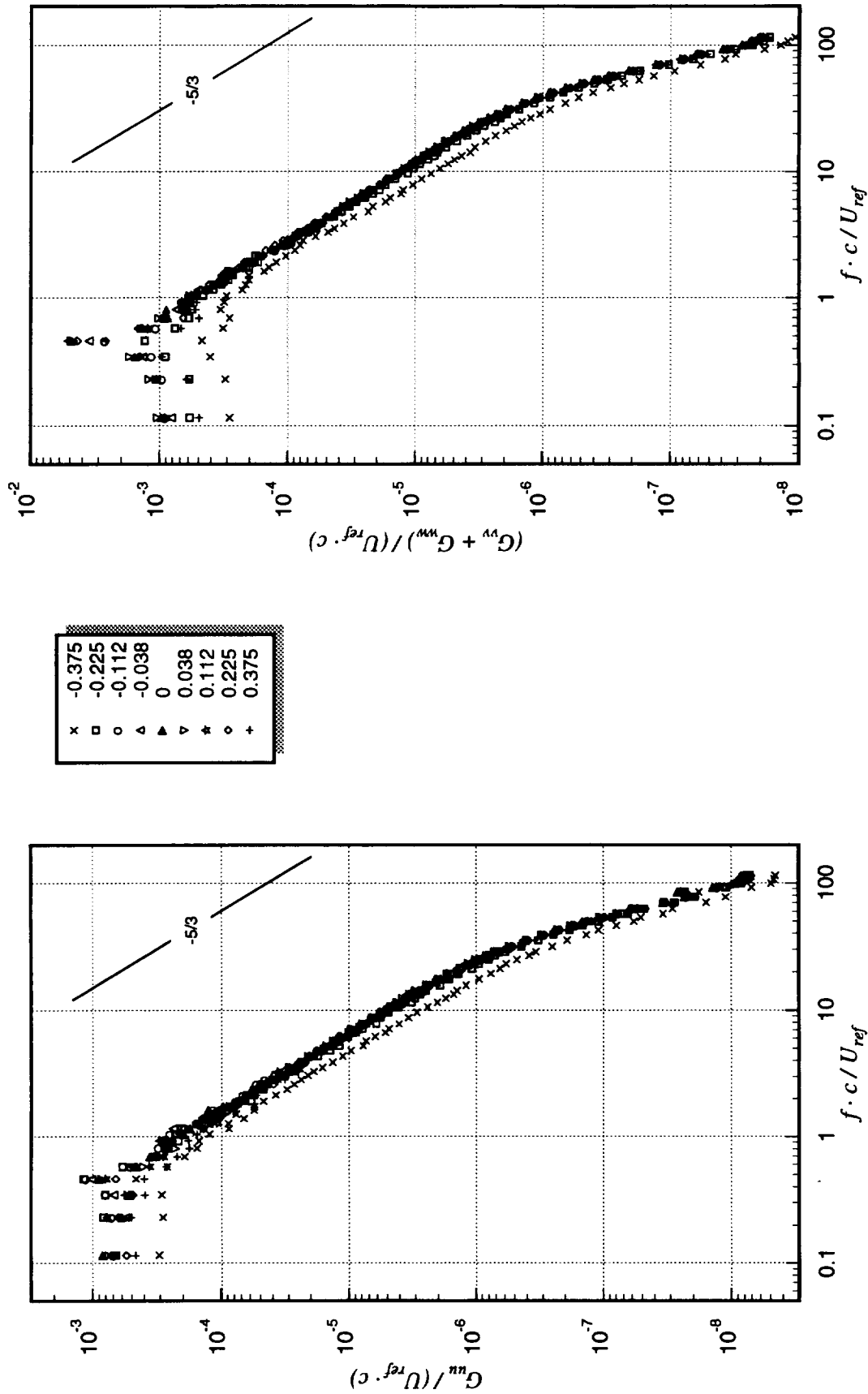
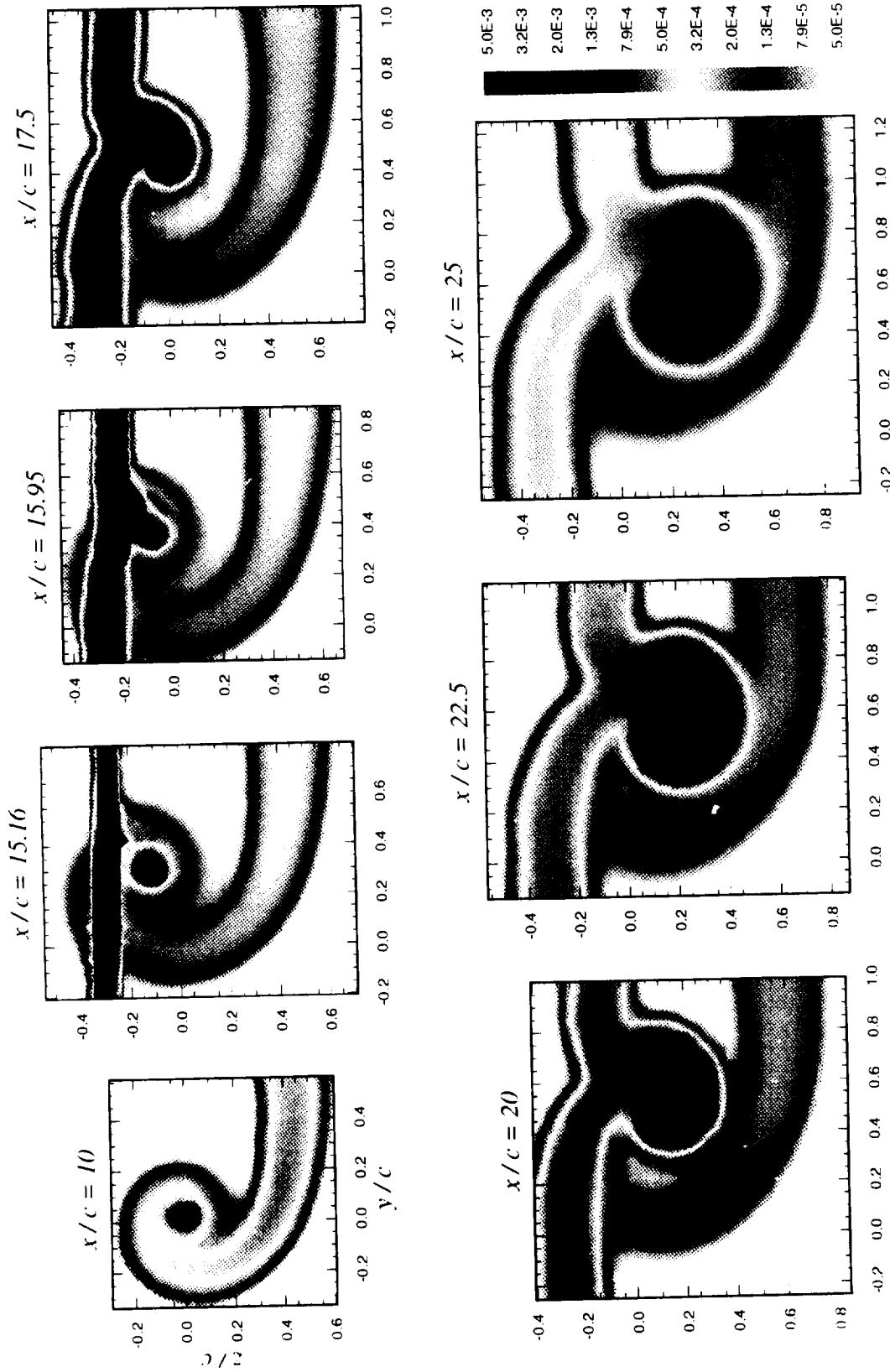


Figure 3.80a Velocity autospectra measured along z-wise profiles through the vortex core center:  $x/c = 10$ ,  $\alpha_I = 5^\circ$ ,  $d/c = 0.3125$ . Legend lists  $r/c$  values ( $r_I/c = 0.395$ ).



**Figure 3.80b** Velocity autospectra measured along z-wise profiles through the vortex core center:  $x/c = 30$ ,  $\alpha_1 = 5^\circ$ ,  $\alpha_2 = 5^\circ$ ,  $d/c = 0.3125$ ,  $\Delta/c = 0.5$ . Legend lists  $r/c$  values ( $r_1/c = 0.375$ ).



**Plate 3-1** Contours of turbulent kinetic energy ( $k / U_{ref}^2$ ) for pressure side passage of  $\Delta/c = -0.125$  as a function of  $x/c$ :  $\alpha_1 = \alpha_2 = 5^\circ$ , no spoiler

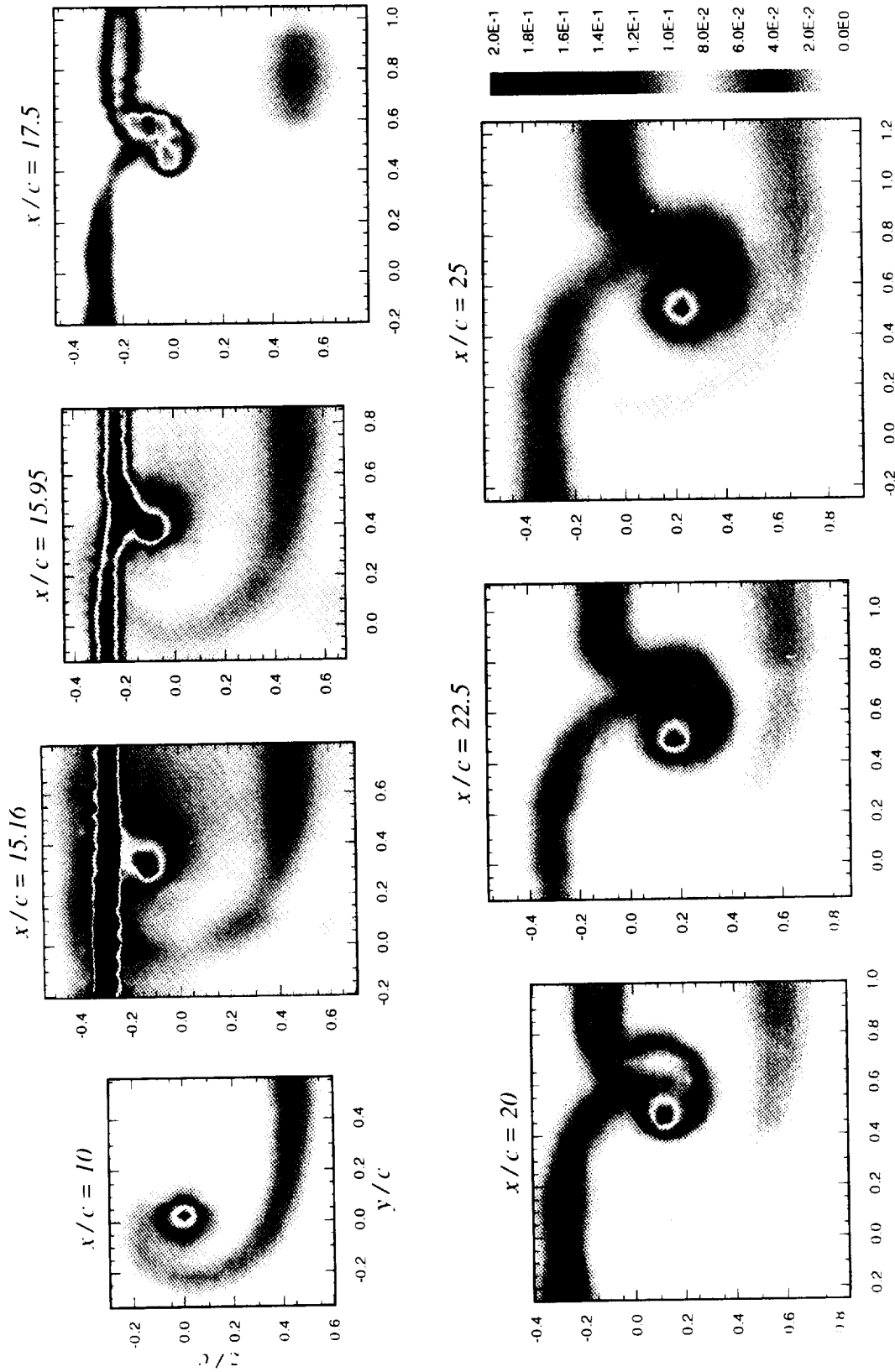


**Plate 3-2** Contours of mean axial velocity deficit  $((U_{ref} - U) / U_{ref})$  for pressure side passage of  $\Delta / c = -0.125$  as a function of  $x / c$ :  $\alpha_1 = \alpha_2 = 5^\circ$ , no spoiler



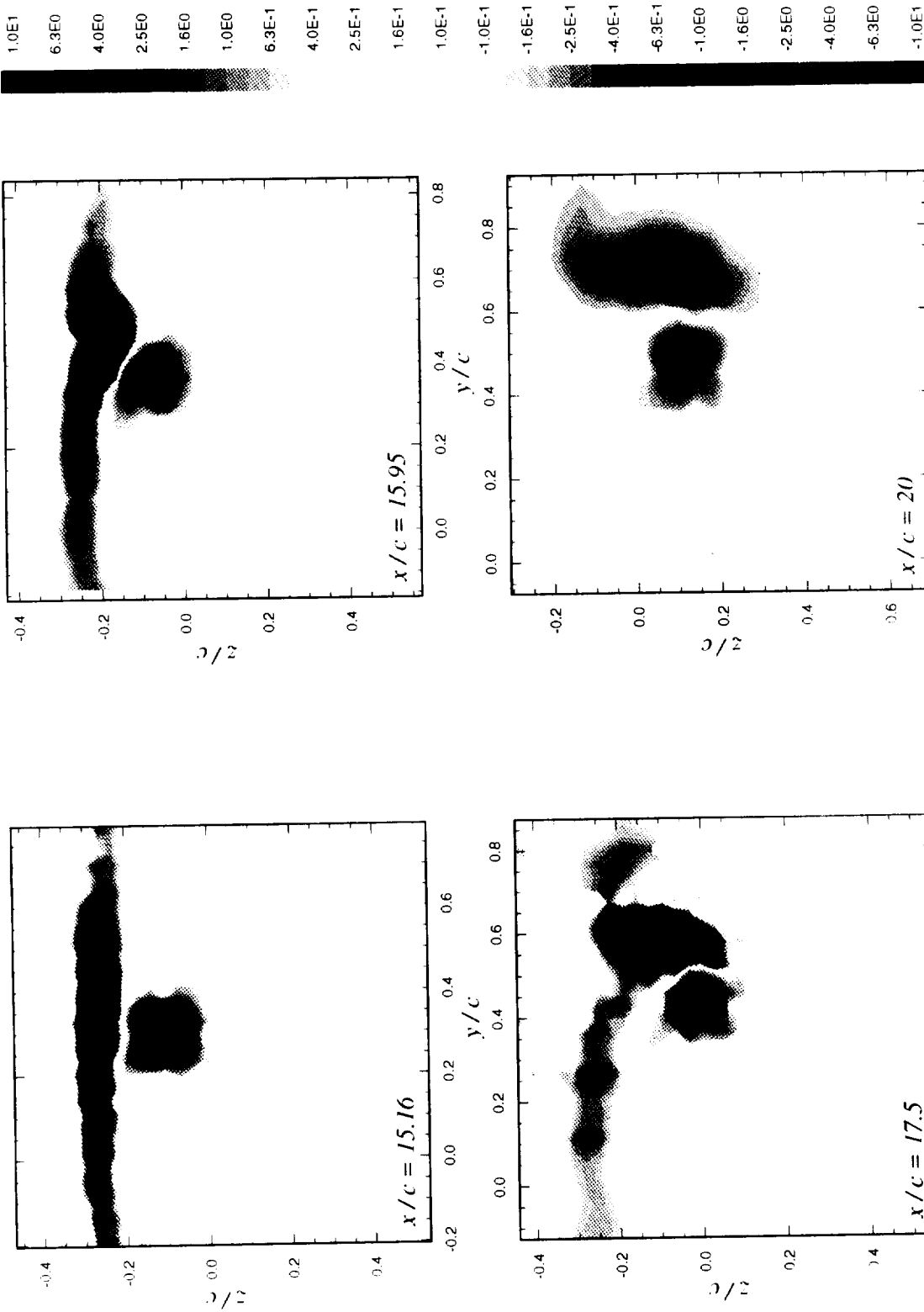


**Plate 3-3** Contours of mean axial vorticity ( $\Omega_x \cdot c / U_{ref}$ ) for pressure side passage of  $\Delta/c = -0.125$  as a function of  $x/c$ :  $\alpha_1 = \alpha_2 = 5^\circ$ , no spoiler

## 4. THEORETICAL MODELING

### 4.1 Correlation of core parameters

In this section we examine and attempt to find an empirical model for the functional relationship controlling the size and strength of the disturbed tip vortex downstream of a perpendicular blade–vortex interaction in terms of its initial properties and the strength of the interaction. Knowledge of this function is needed in prediction methods for impulsive parallel BVI noise so they may take into account the effects of prior perpendicular interactions.

#### 4.1.1 Data summary

To make this task manageable it is necessary to characterize the initial and disturbed vortex in terms a few parameters. As shown in section 3, most of the tangential velocity profiles are very similar if normalized on core radius ( $r_l$ ) and peak tangential velocity ( $V_{\theta l}$ ) making these parameters an obvious choice. Where possible, measurements made at  $x / c = 10$  (four chord lengths upstream of the blade leading edge location) were used to determine the initial core parameters ( $r_{l0}$ ,  $V_{\theta l0}$ ). Given the very slow streamwise development expected of the undisturbed core (discussed in section 3.2.1), it is reasonable to assume these parameters are independent of streamwise position upstream of the blade. Initial core parameters are listed in table 4.1 for all the measurement conditions. Note that measurements were not made at  $x / c = 10$  for generator angles of attack of  $6.25^\circ$  and  $10^\circ$  without spoiler. The values for  $6.25^\circ$  appearing in the table were obtained by interpolating the values for  $5^\circ$  and  $7.5^\circ$ . The values for  $10^\circ$  were obtained by

assuming them to be the same as those measured 15 chord lengths downstream of the blade trailing edge ( $x/c = 30$ ) for the largest blade–vortex separation ( $\Delta/c = 0.5$ ). Effects of the interaction upon the vortex at this separation were thought to be minimal as was the streamwise decay of the vortex between  $x/c = 10$  and 30.

The initial size and strength of the vortex were controlled using the angle of attack of the generator ( $\alpha_1$ ) and the size of the spoiler ( $d$ ) mounted on its tip. We would expect the size and strength of the disturbed vortex also to be a function of the blade–vortex separation ( $\Delta$ ), the blade angle of attack ( $\alpha_2$ ) and distance downstream of the blade (characterized by  $x/c$ ).

Figure 4.1 illustrates the development of the disturbed vortex with downstream distance. Data are shown for two blade–vortex separations ( $\Delta/c = \pm 0.125$ ), all other factors being held constant ( $\alpha_1 = 5^\circ$ ,  $\alpha_2 = 5^\circ$ , no spoiler). For about 2.5 chord lengths downstream of the blade trailing edge the core parameters change little from their initial values. The peak tangential velocity then begins to decay, shortly followed by growth of the core radius. As discussed in section 3.3, these changes occur because the negative vorticity shed by the blade makes the vortex core unstable. Large eddy simulations of a Taylor vortex (which also has a similar region of negative vorticity surrounding its core) show the form of this instability and the turbulence it generates (Sreedhar and Ragab [45]). Interestingly they also show decay of the peak tangential velocity beginning with a decrease in core radius. Later, the core radius begins to grow as it becomes turbulent, much like what is seen here.

Figure 4-2 shows the effects of blade angle of attack ( $\alpha_2 = 0^\circ$  and  $5^\circ$ ) on the parameters of the disturbed vortex at a fixed distance downstream of the blade ( $x/c = 30$ ). Data are shown as

functions of blade–vortex separation, other factors being constant ( $\alpha_1 = 5^\circ$ , no spoiler). As previously discussed, these data show an increase in vortex core size and a reduction in the peak tangential velocity with decrease in the magnitude of the blade–vortex separation with these effects being largely independent of blade angle of attack. The only significant effects of blade angle of attack are seen in the core radius for blade–vortex separations less than the initial core size ( $0.037c$ ). These are probably insignificant considering the profiles are not well defined by the parameters here (see figure 3.42) and the velocity gradients involved are very small—making it difficult to determine the core radius anyway.

The effects of initial vortex strength ( $\alpha_1 = 10^\circ$  and  $5^\circ$ ) on the disturbed vortex at a fixed distance downstream of the blade ( $x / c = 30$ ) are shown in figure 4.3. Data are again shown as functions of blade–vortex separation, other factors being constant ( $\alpha_2 = 5^\circ$ , no spoiler). At first sight, the effects of the interaction appear more heavily dependent upon the generator angle of attack. At all blade–vortex separations where a comparison is possible, the core radius and peak tangential velocity are greater with the generator at  $10^\circ$  than at  $5^\circ$ . However, if we normalize these parameters on their undisturbed values then the effects of the generator angle of attack appear much weaker (figure 4.4).

Figure 4.5 shows the effects of initial vortex core size controlled by spoiler size ( $d / c = 0$ ,  $0.2125$ , and  $0.3125$ ) on the disturbed vortex at a fixed distance downstream of the blade ( $x / c = 30$ ). Data are shown as functions of blade–vortex separation, other factors being constant ( $\alpha_1 = 5^\circ$ ,  $\alpha_2 = 5^\circ$ ). As the initial core radius is increased, the effects of the interaction are felt in the disturbed vortex at larger blade–vortex separations. The effects of the interaction upon the core

radius do not scale upon either the undisturbed radius, or do they add to the undisturbed radius (figure 4.6). These, and the equally intractable effects upon the peak tangential velocity may be a consequence of the fundamental change in the nature of the interaction that occurs as the vortex core size is increased. For small core radii the core becomes embedded in the blade wake, stimulating its growth and decay. For larger radii, however the blade splits the core, and part of the blade wake becomes embedded in the core.

Combining all of the above data reveals a useful correlation between the initial and disturbed states of the vortex. Figure 4.7 shows  $V_{\theta I} / V_{\theta I0}$  as a function of  $r_{I0} / r_I$ . If the tangential velocity profile of the vortex core were self similar, and the core circulation were constant, then we would expect  $V_{\theta I} / V_{\theta I0}$  and  $r_{I0} / r_I$  to be equal to each other; and thus all the points in figure 4.7 to lie on a straight line of slope 1. This obviously does not happen, presumably because the core circulation is reduced by the negative vorticity it absorbs from the blade wake. However, there is still a correlation between  $V_{\theta I} / V_{\theta I0}$  and  $r_{I0} / r_I$  described approximately by the curve given in equation 4.1.

$$\frac{V_{\theta I}}{V_{\theta I0}} = 0.3 \cdot \left( \frac{r_{I0}}{r_I} \right) + 0.7 \cdot \left( \frac{r_{I0}}{r_I} \right)^3 \quad (4.1)$$

The additional cubic term suggests that core may decay partly as a Taylor vortex (consistent with the above discussion). The Taylor vortex has a core of positive vorticity surrounded by a ring of equal negative vorticity and thus generates no net circulation (much like the negative vorticity shed from the blade and the positive portion of the core vorticity which it cancels). Self-similar Taylor vortices decay such that  $V_{\theta I} \sim r_I^{-3}$  (see Uberoi [46]).

#### 4.1.2 Modeling

In this section we develop an empirical model for the effects of perpendicular BVI on vortex parameters. If we make use of equation 4.1, only a model for the core radius is needed. Bearing in mind the complexity of this flow and the large number of independent variables involved, however, finding such a model is a long process of trial and error. Some of the most obvious, physically justifiable models simply do not work (e.g. assuming the core grows as the square root of  $x$  from the point where it first comes into contact with the blade wake). A total of 11 different models were developed and tested. The following produced by far the best agreement with measurements. Even though this model was obviously not developed *a priori*, it does include some flow physics and thus might be expected to have some predictive capability beyond the range of the experimental data.

Figures 4.8 and 4.9 show idealizations of the flow structure downstream of the blade and its evolution with downstream distance. Two scenarios are presented, one where the core is small compared to blade-vortex separation (figure 4.8), and one where it is large (figure 4.9). These idealizations assume the wake is wrapped into an annulus around the core center by the rotation of the vortex. In reality, of course, a double spiral will be formed but the negative vorticity that initiates the transition and growth of the core will be contained only in the inner most (roughly annular) part of the spiral.

The wake annulus is assumed to sit at a radius  $\Delta$ , the initial separation of the core center and blade wake center. Its half-width  $L$  is assumed to grow as the square-root of streamwise distance i.e.:

$$\frac{L}{c} = k \cdot \sqrt{\frac{x - x_o}{c}} \quad (4.2)$$

where  $c$  is blade chord,  $x_o$  the origin of wake growth, and  $k$  a constant. Given the results of previous studies of two-dimensional wakes we might expect  $k$  to be related to the momentum thickness  $\theta$  of the blade wake as:

$$k = \sqrt{\frac{k_I \cdot \theta}{c}} \quad (4.3)$$

where  $k_I$  would be a more fundamental constant.

Progressing downstream the wake grows and overwhelms the core, stimulating its growth and decay. We assume that core decay begins once the wake annulus has grown to the core center, i.e. at the streamwise location,

$$\frac{x_i}{c} = \left( \frac{\Delta / c}{k} \right)^2 + \frac{x_o}{c} \quad (4.4)$$

For small  $|\Delta|$  this location may be upstream of the blade trailing edge, in which case we set

$$\frac{x_i}{c} = \frac{x_{te}}{c} \quad (4.5)$$

where  $x_{te}$  is the trailing edge location.

The manner in which the core then grows is assumed dependent on whether it is larger or smaller than the (now circular) cross section of the idealized wake. If the core is embedded in the wake one might expect it to grow in proportion with the wake disc, i.e. as

$$\begin{aligned} \frac{r_l}{r_{lo}} &= 1 & x &\leq x_i \\ \frac{r_l}{r_{lo}} &= \frac{L + |\Delta|}{L_{x_i} + |\Delta|} & x &> x_i \end{aligned} \quad (4.6)$$

for  $r_{lo} \leq L_{x_i} + |\Delta|$ , where  $L_{x_i}$  is the wake width at  $x_i$  and  $r_{lo}$  is the undisturbed core radius (assumed constant with  $x$ ). If the wake is embedded in the core one might expect the growth of the wake disc to add to the core radius (i.e. that part of the core outside the wake disc continues not to grow), i.e. as

$$\begin{aligned} r_l &= r_{lo} & x &\leq x_i \\ r_l &= L - L_{x_i} + r_{lo} & x &> x_i \end{aligned} \quad (4.7)$$

for  $r_{lo} \leq L_{x_i} + |\Delta|$ .

This model requires two inputs ( $r_{lo}$  and  $V_{\theta lo}$ ) characterizing the initial state of the vortex and produces two outputs ( $r_l$  and  $V_{\theta l}$ ) characterizing the disturbed state at the  $x / c$  location specified. There are two empirical constants  $k$  and  $x_o$ . Setting these to 0.07 and 14.5 (0.5c upstream of the blade trailing edge) produced optimum agreement with the measurements. This agreement is illustrated in figures 4.10 through 4.13 which compare the measured data of figures 4.1–4.3 and 4.5 with the model predictions. The model seems to do well in predicting the streamwise growth of core radius and decay of peak tangential velocity seen in figure 4.10 and the variations of core radius and peak tangential velocity seen as a function of  $\Delta$  in figure 4.11. The effects of vortex strength (figure 4.12) and core size (figure 4.13) are also reasonably well modeled. Weakness of the model include its inability to predict asymmetric behavior about  $\Delta = 0$



(figures 4.10 and 4.11) and inaccuracy in the predictions of peak tangential velocity for the case with the vortex generator at 10° angle of attack (figure 4.12b).

## 4.2 Vortex circulation theory (VCT)

### 4.2.1 Derivation

The first step in this theory is to determine the strength of the vortex sheet shed from the blade. This could be done in any of a number of ways. The simplest (though probably not most accurate) is to use Prandtl's lifting line theory modified to account for the non-uniform inflow. It is assumed that the effects of the non-uniform inflow with respect to the shed vorticity are the same as those of a twist on the blade; with the twist angle distribution ( $\alpha_v(y)$ ) being equal to the angle of attack distribution produced by the vortex.

For example, the situation shown in figure 4.14 is assumed equivalent to a uniform flow impinging on a blade with an angle of attack  $\alpha(y) = \alpha_2(y) + \alpha_v(y)$  where  $\alpha_2$  is the actual angle of attack of the interaction blade. From the geometry shown in figure 4.15,  $\alpha_v(y)$  is calculated from the initial vortex circulation distribution ( $\Gamma_i(r)$ ) as

$$\alpha_v(y) = \arctan\left(-\frac{w}{U_\infty}\right) \cong \frac{\Gamma_i(r)}{U_\infty} \cdot \frac{y_v - y}{2\pi \cdot r^2}, \quad (4.8)$$

where  $y_v$  is the y-location of the vortex center and  $r$  is radial distance from the vortex center to the point on the blade located by  $y$ , i.e.

$$r = \sqrt{\Delta^2 + (y_v - y)^2}. \quad (4.9)$$

Note that we are assuming that the blade has no influence on its inflow.

The lifting line theory equations used to compute the shed vortex sheet strength distribution from  $\alpha(y)$  depend on the configuration. In the present situation of an full-span blade mounted between wind-tunnel walls as shown in figure 4.15, the relationship between  $\alpha(y)$  and the circulation distribution on the blade ( $\Gamma_b(y)$ ) is

$$\alpha(y) = \frac{\Gamma_b(y)}{\pi \cdot U_\infty \cdot c} + \frac{1}{4\pi \cdot U_\infty} \cdot \int_{-\infty}^{\infty} \left( \frac{\frac{d\Gamma_b}{dy'}}{y - y'} \right) \cdot dy' \quad (4.10)$$

where  $y'$  is a dummy variable for  $y$ . The reflections provided by the walls will result in the  $\Gamma_b(y)$  being periodic over  $2s$ , where  $s$  is the height of the wind tunnel section. Under these conditions the solution to this equation is

$$\Gamma_b(y) = s \cdot U_\infty \cdot \left[ A_0 \frac{\pi \cdot c}{s} + \sum_{n=1, \dots, \infty} \left( \frac{A_n}{\frac{s}{\pi \cdot c} + \frac{n \cdot \pi}{4}} \right) \cdot \cos\left(\frac{n \cdot \pi}{s} \cdot (y - h)\right) \right] \quad (4.11)$$

where  $h$  the distance from its lower wall to the origin of  $y$ . The  $A_n$ 's are coefficients in the Fourier cosine series for  $\alpha(y)$ :

$$\alpha(y) = A_0 + \sum_{n=1, \dots, \infty} A_n \cdot \cos\left(\frac{n \cdot \pi}{s} \cdot (y - h)\right). \quad (4.12)$$

(Note that this is quite different that the solution for a finite-span blade in external flow.) The strength of the vortex sheet shed from the blade ( $\gamma(y)$ ) is thus

$$\gamma(y) = \frac{d\Gamma_b}{dy} = -\pi \cdot U_\infty \cdot \left[ \sum_{n=1, \dots, \infty} \frac{n \cdot A_n}{\left( \frac{s}{\pi \cdot c} + \frac{n \cdot \pi}{4} \right)} \cdot \sin\left( \frac{n \cdot \pi}{s} \cdot (y - h) \right) \right] \quad (4.13)$$

Note that the vortex sheet strength is independent of the mean angle of attack of the blade, reflected in  $A_0$ .

The second step in the theory is to model how this vortex sheet becomes incorporated into the vortex. To do this we use a method similar to Betz's theory. We assume that the vorticity contained by an incremental portion of the vortex sheet lying at a distance  $r$  from the vortex center, remains at this distance but becomes distributed into an annulus. The final circulation distribution in the vortex ( $\Gamma_f(r)$ ) is therefore given by

$$\Gamma_f(r) = \Gamma_i(r) + \delta\Gamma(r) \quad (4.14)$$

where  $\delta\Gamma(r)$ , the additional circulation provided by the vortex sheet is given by

$$\delta\Gamma(r) = \int_{y_1(r)}^{y_2(r)} \frac{d\Gamma_b}{dy} dy = (\Gamma_b(y_2) - \Gamma_b(y_1)) \quad (4.15)$$

for  $r > \Delta$  where

$$y_1(r) = -\sqrt{r^2 - \Delta^2} \quad (4.16)$$

and

$$y_2(r) = \sqrt{r^2 - \Delta^2} . \quad (4.17)$$

#### 4.2.2 Comparison with experimental data

There are two things worth noting first about the results of this derivation. One is the vorticity shed from the full-span blade—and thus the combined circulation distribution—is dependent only on the magnitude of the blade–vortex separation, i.e. it is the same for either pressure or suction side passage. The experimental data presented in sections 3.3.2 and 3.4.1 indicate that there are some differences between pressure and suction side passages. Possible contributors to these differences are hypothesized, but this inviscid analysis is obviously not capable of accounting for any of these complex viscous effects. The second observation immediately apparent from the results of the derivation, is the shed vorticity is not dependent upon the blade angle of attack. Experimental data shown in figure 3.42 and discussed in section 3.4.4 shows that the core parameters appear to be largely independent of the blade angle of attack; thereby supporting this inviscid analysis since changes to the core occur have been shown to occur primarily due to its interaction with the shed vorticity.

Calculations of the combined circulation distribution were made for the case where the vortex produced by the generator blade at  $5^\circ$  passes the interaction blade at  $\Delta / c = 0.125$ . The measured velocity distribution of the vortex at  $x / c = 10$  was used to calculate the angle of attack distribution experienced by the full-span blade. The vortex was assumed to pass the blade midway between the tunnel walls ( $y_v + h = \frac{1}{2}s$ ). The predicted circulation distribution of the full-span blade and the resulting shed vorticity distribution are shown in figure 4.16. Figure 4.17 compares the predicted final circulation distribution with the measured circulation distributions (calculated from velocity profiles through the core) for the following conditions:  $\alpha_1 = \alpha_2 = 5^\circ$ ,  $\Delta / c = -0.125$ ,  $x / c$

= 10, 15.95, 17.5, and 20. The results from two theoretical calculations are shown in each figure. One calculation was done without limiting the change in lift coefficient ( $\Delta C_{Lmax}$ ) experienced by the full-span blade. The second calculation imposed a limit on  $\Delta C_{Lmax}$  of 0.2. The idea of imposing a limit was based on the work of Ham [18] (discussed in section 1.5) which suggests that the spanwise pressure gradient supplied by the vortex limits, through flow separation, the amount of loading which can be induced on the blade. For typical helicopter rotor blade–vortex interactions, this limits the maximum incremental lift coefficient to less than 0.3. Figure 4.17 shows that without imposing the limit, the theory severely over-predicts the change in the circulation distribution; but with a limit on  $\Delta C_{Lmax}$  of 0.2, the theory approximates the distribution fairly well. The measured distribution at  $x / c = 20$  is not well represented because, the vortex core has become turbulent. This results in turbulent diffusion of vorticity which is not accounted for by the theory. An interesting feature resulting from imposing the  $\Delta C_{Lmax} = 0.2$  limit is the span of negative shed vorticity predicted by the vortex circulation theory increases from about  $0.9c$  to  $1.7c$  (see figure 4.16). Vorticity contours measured at  $x / c = 15.16$  (figure 3.15d) show that the negative vorticity region extends beyond one chord, supporting the imposition of a limit.

While it is satisfying to see some agreement between the predictions and measurements close to the blade, future improvements to the model are needed to increase the accuracy of its predictions further downstream. Some way needs to be found to model the diffusion of vorticity. One possibility is to make use of the similarity in the form of the core tangential velocity profiles measured downstream of the blade—many of which were found similar to a q-vortex. A second possibility is to use some elements of the core parameter model presented in section 4.1.

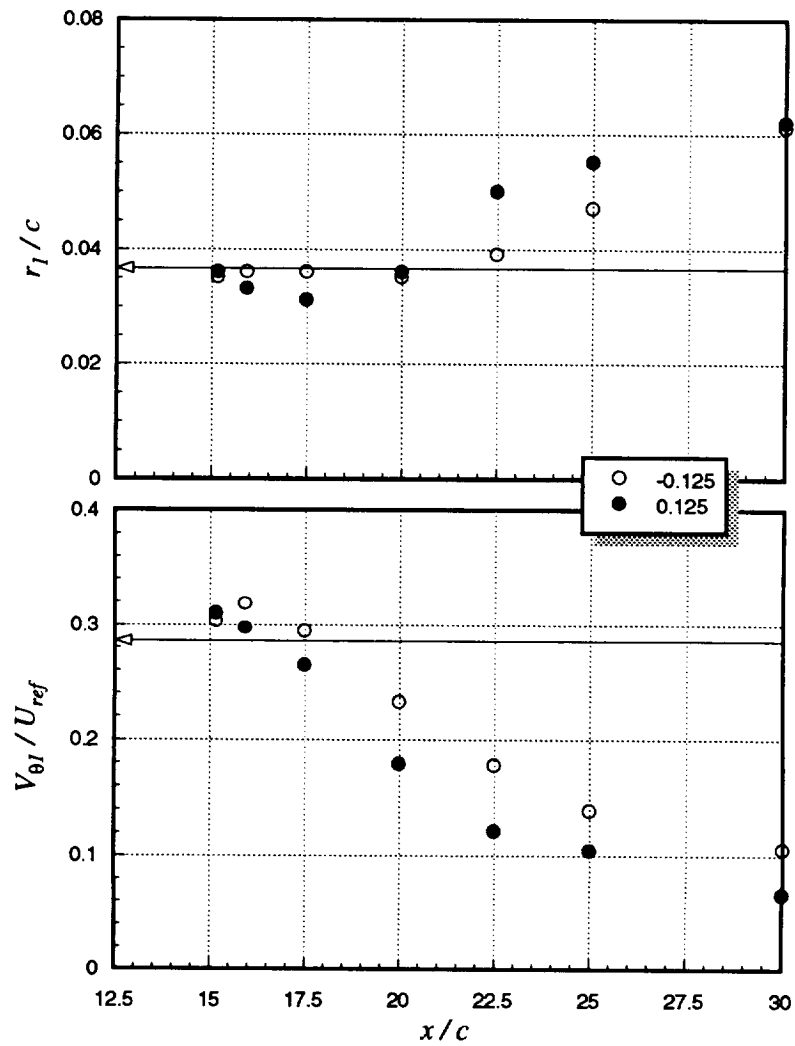


**Figure 4.1** Core parameters (radius,  $r_l$ ; and peak tangential velocity,  $V_{\theta 1}$ ) as a function of downstream distance ( $x$ ) for both suction ( $\Delta/c = 0.125$ ) and pressure side ( $\Delta/c = -0.125$ ) passage:  $\alpha_1 = 5^\circ$ ,  $\alpha_2 = 5^\circ$ , no spoiler. Legend lists  $\Delta/c$  values.

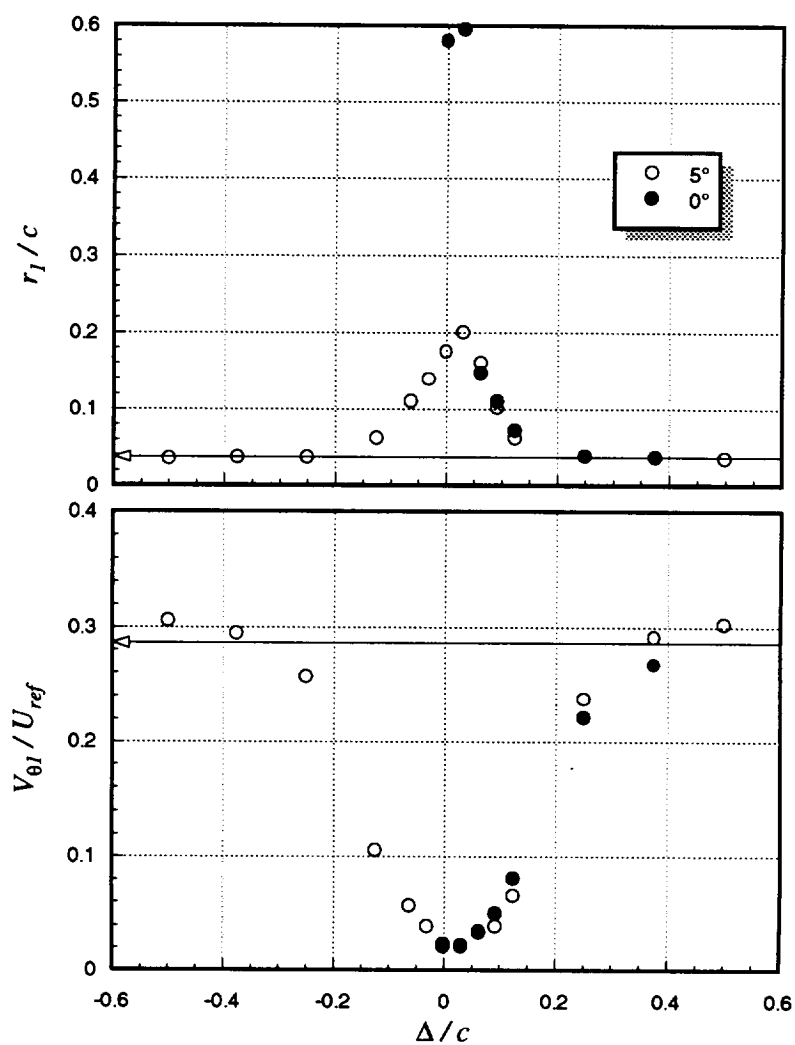


**Figure 4.2** Core parameters (radius,  $r_1$ ; and peak tangential velocity,  $V_{\theta 1}$ ) as a function of blade-vortex separation ( $\Delta$ ) for different blade angles of attack ( $\alpha_2$ ):  $x/c = 30$ ,  $\alpha_1 = 5^\circ$ , no spoiler. Legend lists  $\alpha_2$  values.

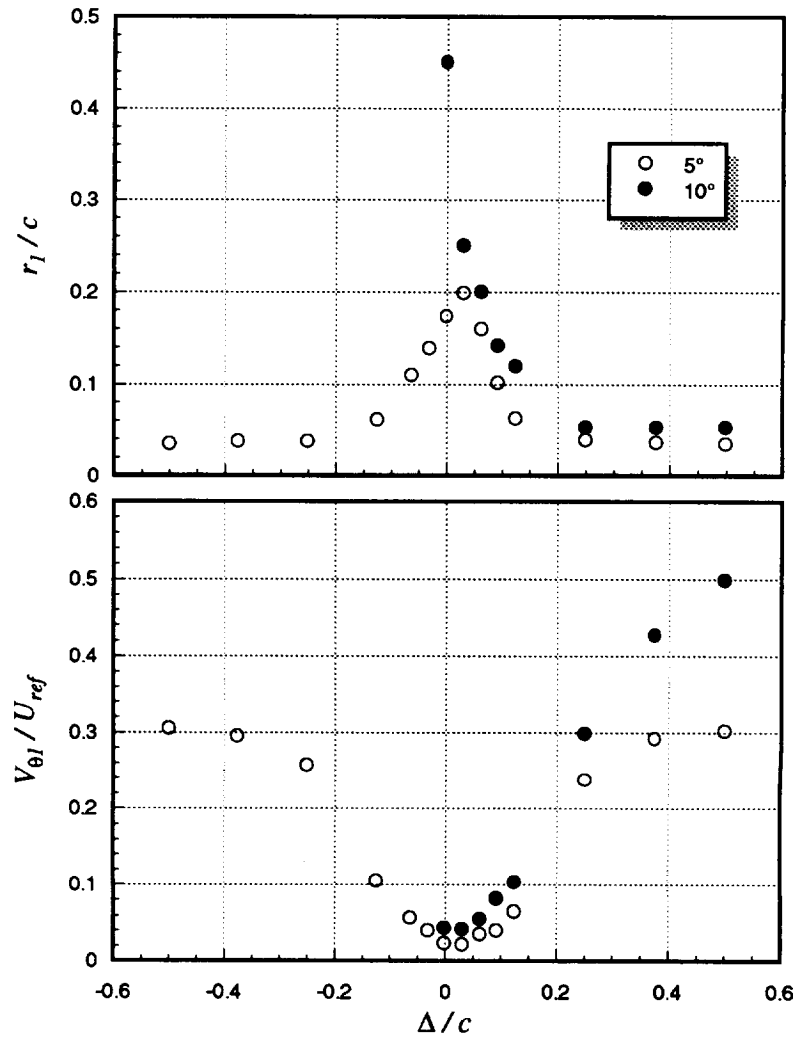


**Figure 4.3** Core parameters (radius,  $r_l$ ; and peak tangential velocity,  $V_{\theta l}$ ) as a function of blade-vortex separation ( $\Delta$ ) for different initial vortex strengths (controlled by  $\alpha_l$ ):  $x/c = 30$ ,  $\alpha_2 = 5^\circ$ , no spoiler. Legend lists  $\alpha_l$  values.



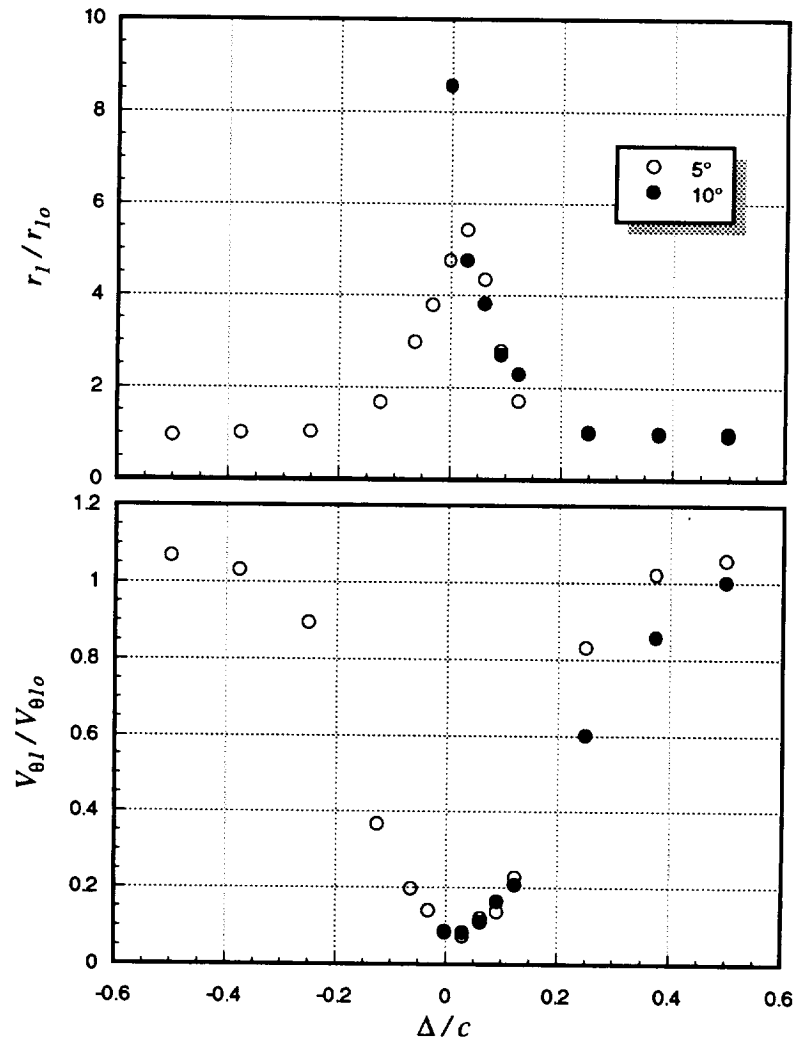


**Figure 4.4** Normalized core parameters (radius,  $r_l / r_{lo}$ ; and peak tangential velocity,  $V_{\theta l} / V_{\theta lo}$ ) as a function of blade-vortex separation ( $\Delta$ ) for different initial vortex strengths (controlled by generator angle of attack,  $\alpha_1$ ):  $x / c = 30$ ,  $\alpha_2 = 5^\circ$ , no spoiler. Legend lists  $\alpha_1$  values.

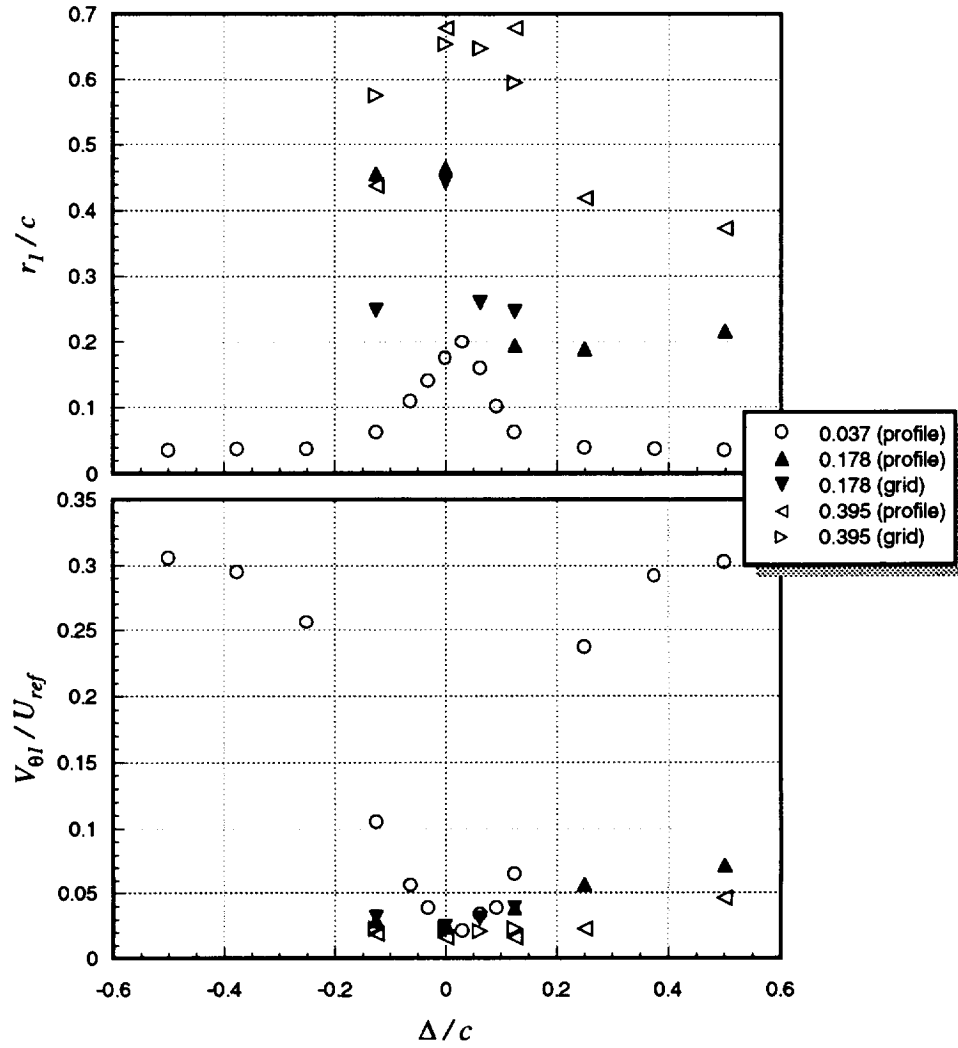


**Figure 4.5** Core parameters (radius,  $r_l$ ; peak tangential velocity,  $V_{\theta l}$ ; circulation,  $\Gamma_l$ ; and axial velocity deficit,  $U_d$ ) as a function of blade–vortex separation ( $\Delta$ ) for different undisturbed core radii ( $r_{l0}$ ):  $x/c = 30$ ,  $\alpha_1 = 5^\circ$ ,  $\alpha_2 = 5^\circ$ . Legend lists  $r_{l0}/c$  values, (source of parameters also specified).

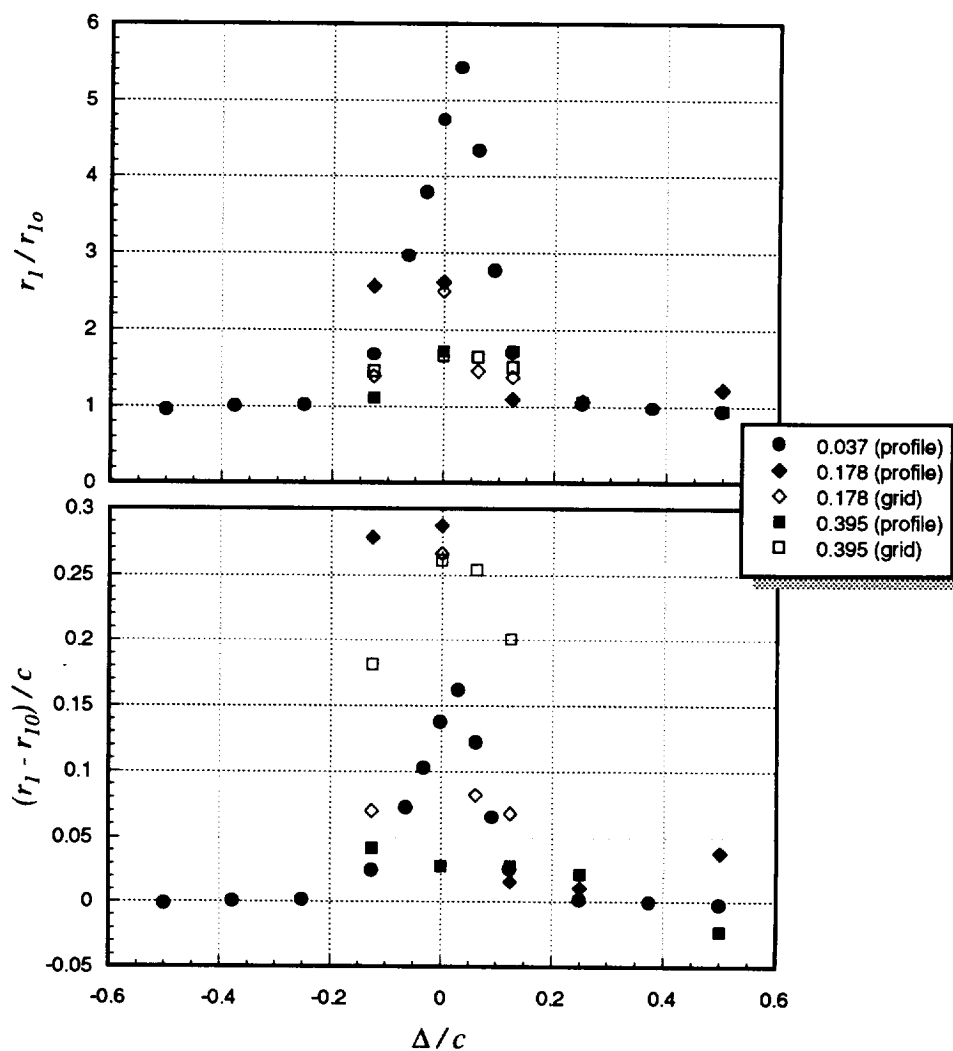


**Figure 4.6** Normalized core parameters (radius,  $r_1/r_{1o}$ ; and peak tangential velocity,  $V_{\theta 1}/V_{\theta 1o}$ ) as a function of blade-vortex separation ( $\Delta$ ) for different undisturbed core radii ( $r_{1o}$ ):  $x/c = 30$ ,  $\alpha_1 = 5^\circ$ ,  $\alpha_2 = 5^\circ$ . Legend lists  $r_{1o}/c$  values, (source of parameters also specified).

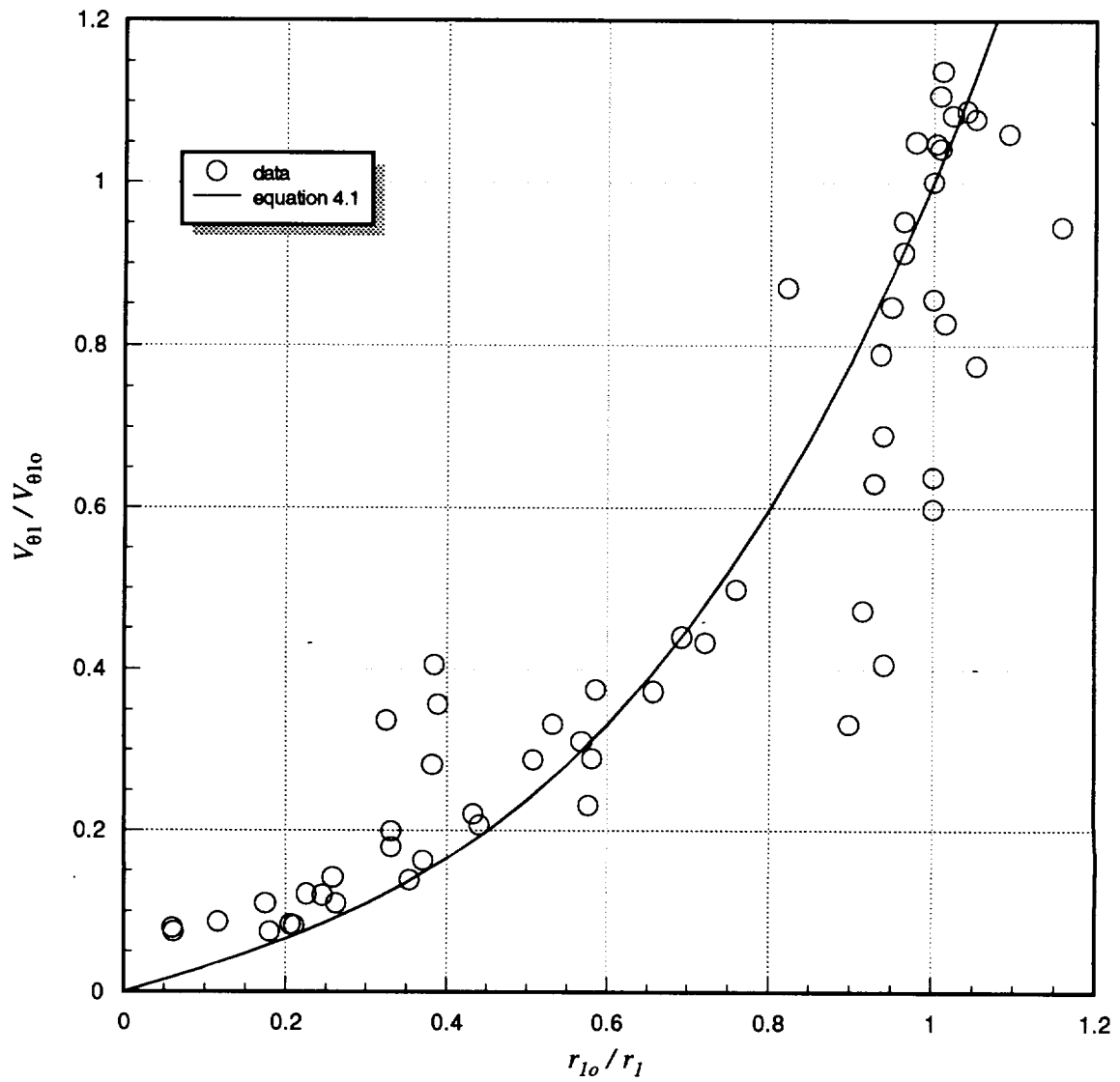


**Figure 4.7**  $V_{\theta 1} / V_{\theta 1o}$  as a function of  $r_{1o} / r_1$  for all data compared with curve fit described by equation 4.1

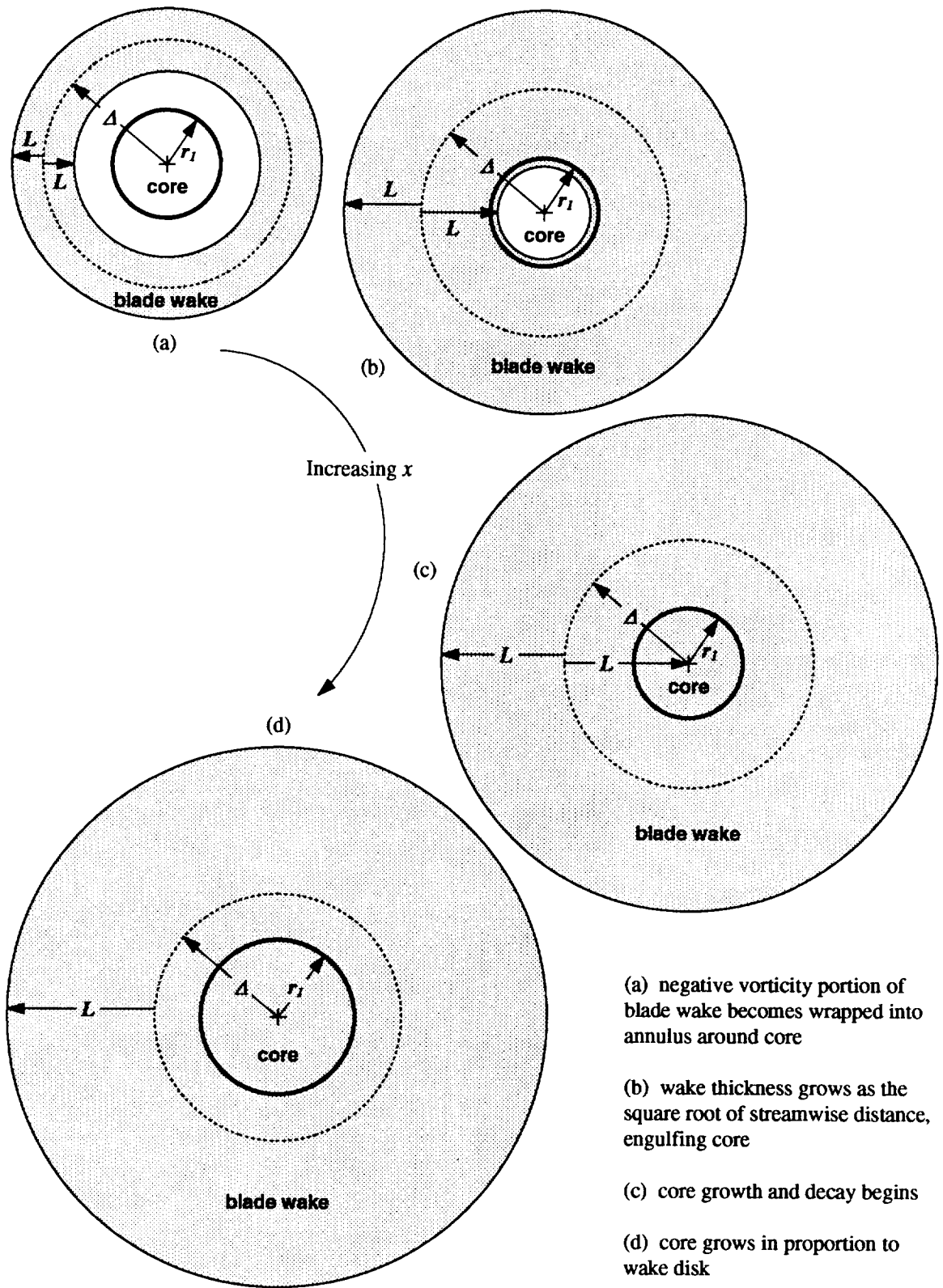


**Figure 4.8** Illustration of idealized core development for core radius small compared to the blade-vortex separation

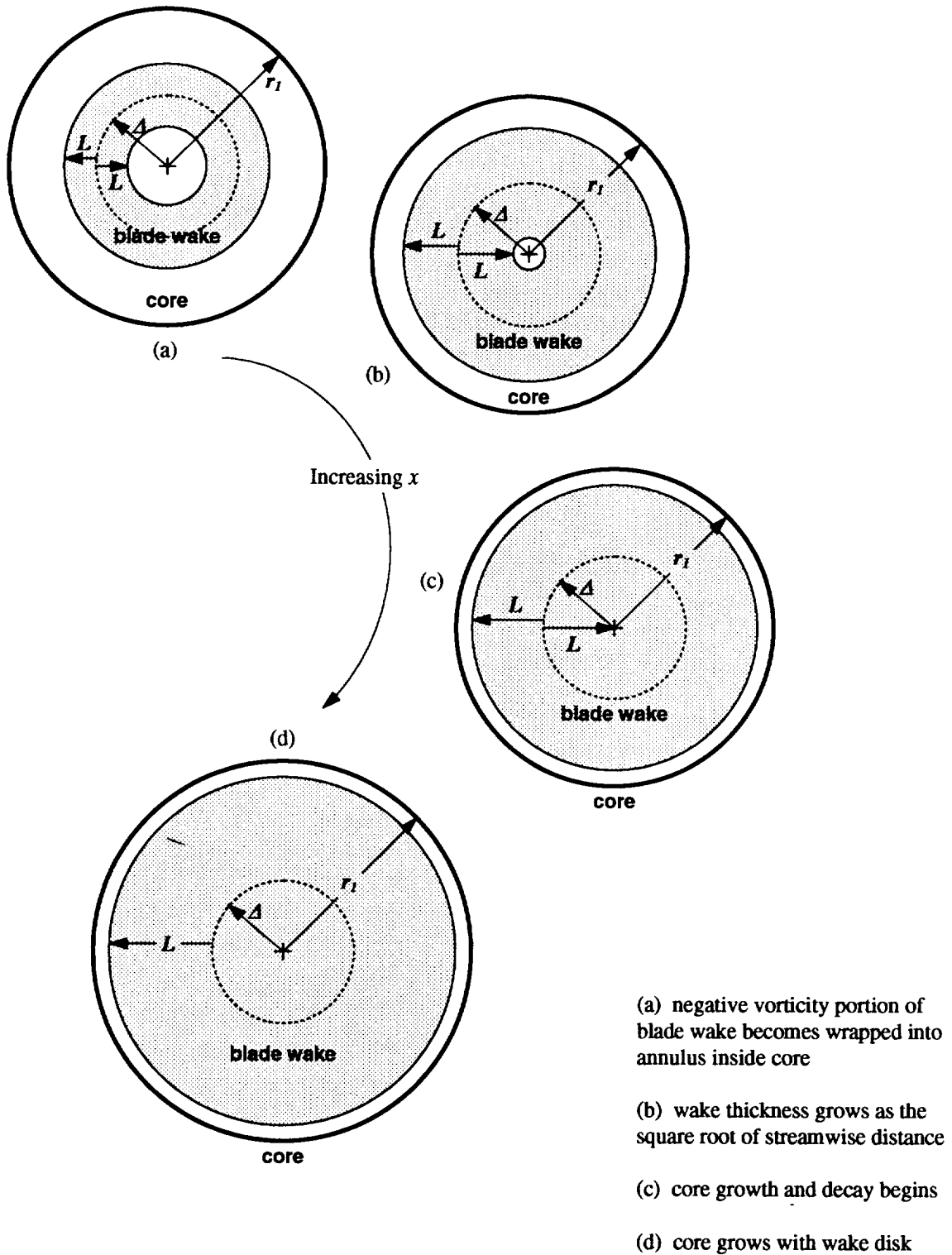


**Figure 4.9** Illustration of idealized core development for core radius large compared to the blade-vortex separation

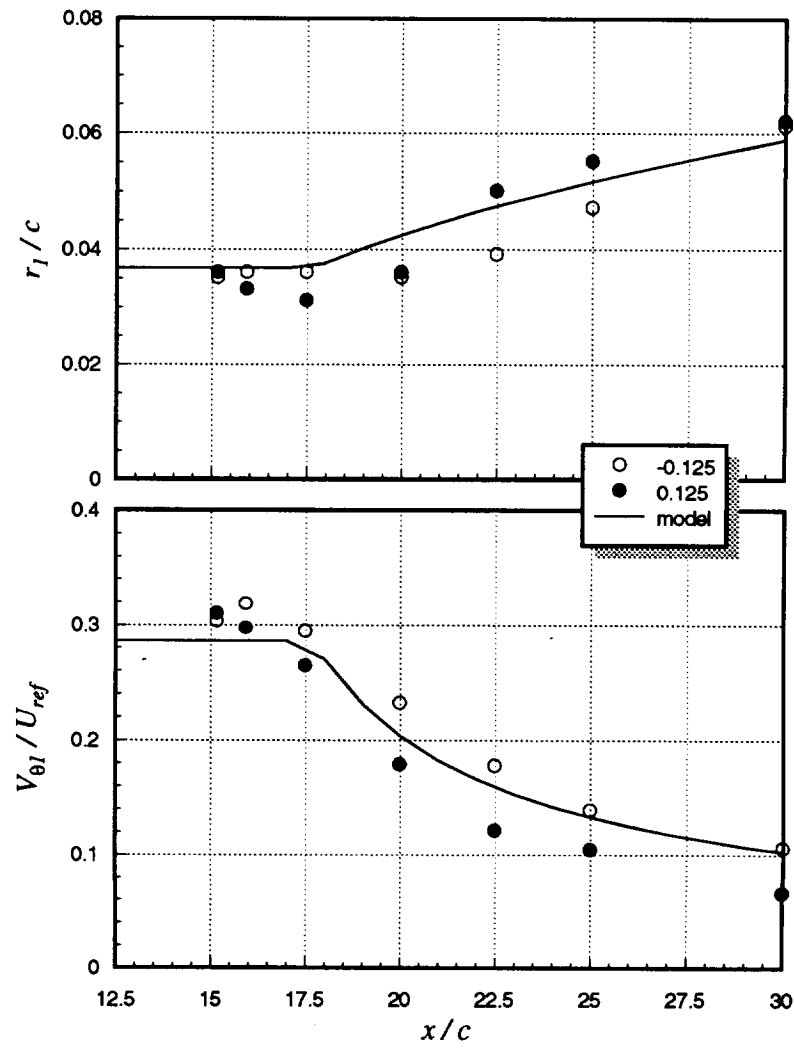


**Figure 4.10** Core parameter model described in section 4.1.2 compared to measured data:  $\alpha_1 = 5^\circ$ ,  $\alpha_2 = 5^\circ$ , no spoiler. Legend lists  $\Delta/c$  values.

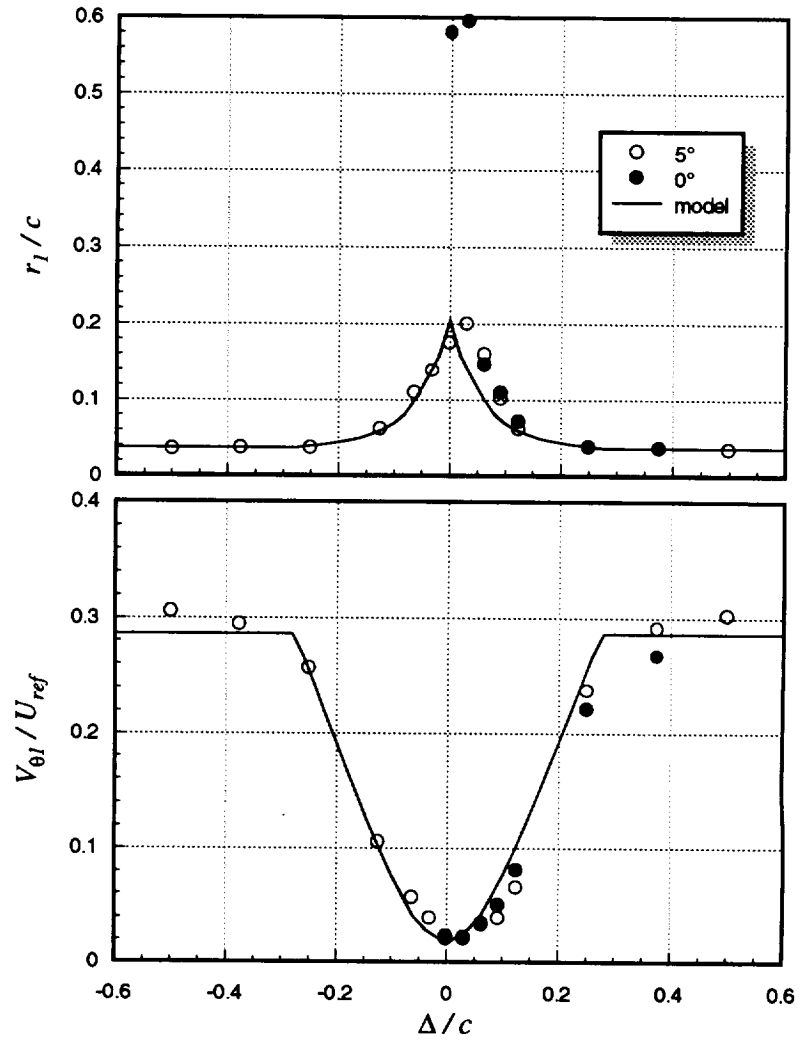


**Figure 4.11** Core parameter model described in section 4.1.2 compared to measured data:  $x / c = 30$ ,  $\alpha_l = 5^\circ$ , no spoiler. Legend lists  $\alpha_2$  values.



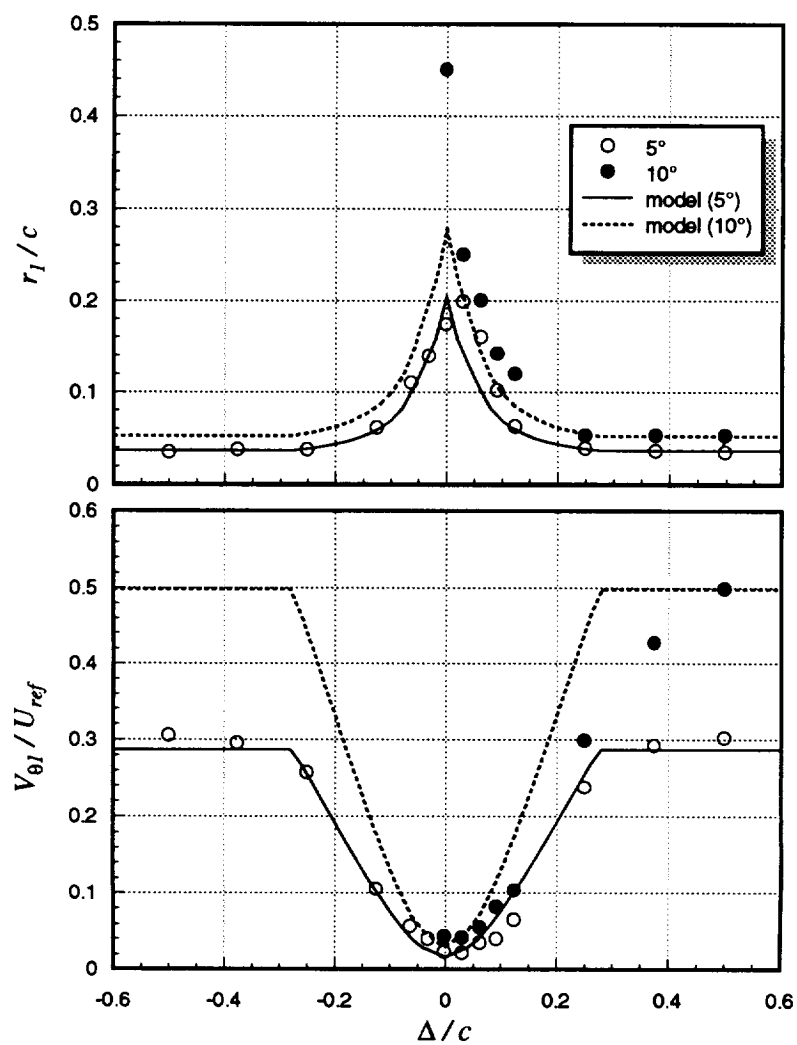


**Figure 4.12** Core parameter model described in section 4.1.2 compared to measured data:  $x / c = 30$ ,  $\alpha_2 = 5^\circ$ , no spoiler. Legend lists  $\alpha_l$  values.

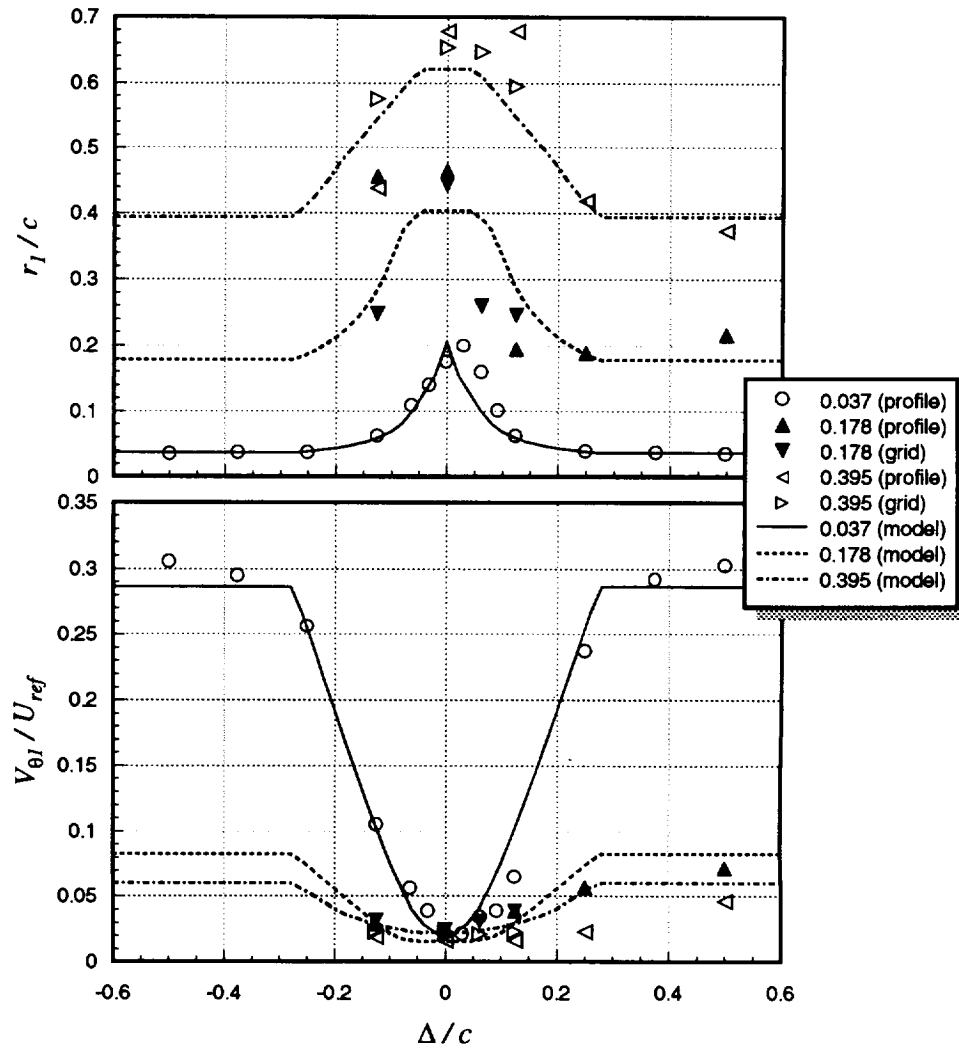


**Figure 4.13** Core parameter model described in section 4.1.2 compared to measured data:  $x/c = 30$ ,  $\alpha_1 = 5^\circ$ ,  $\alpha_2 = 5^\circ$ . Legend lists  $r_{l0}/c$  values, (source of parameters also specified).

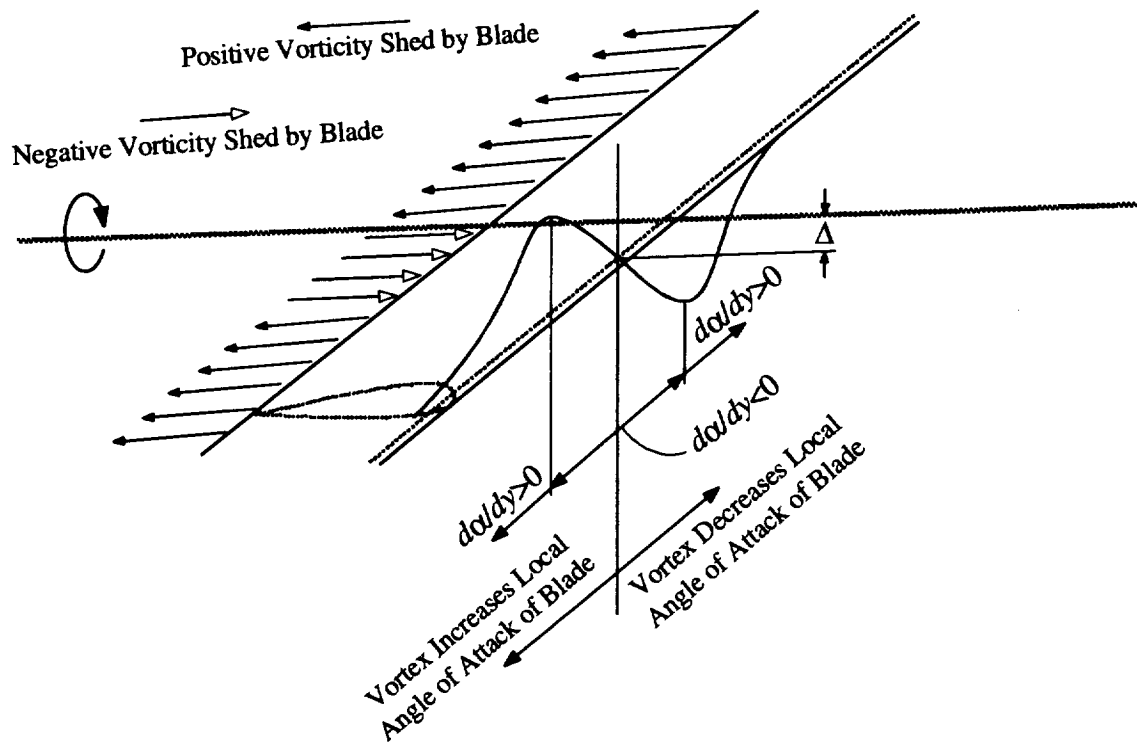


**Figure 4.14** Idealized perpendicular blade–vortex interaction

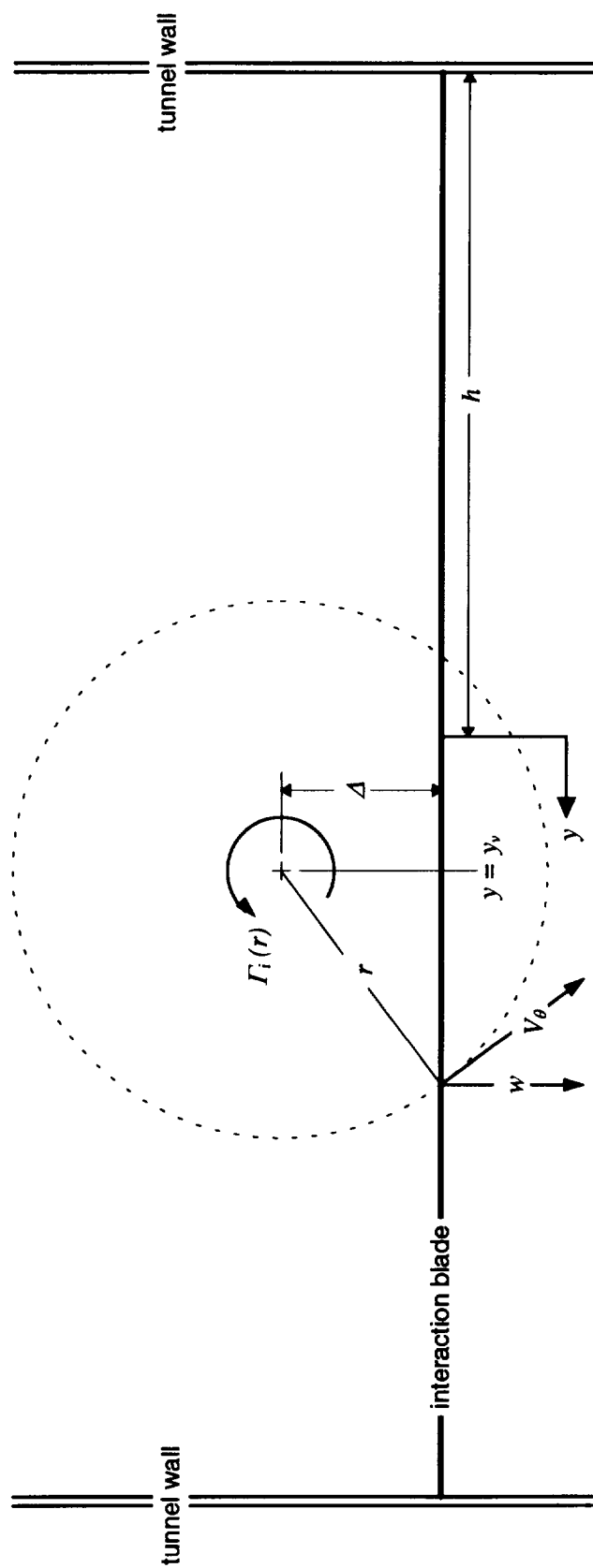


**Figure 4.15** Configuration referred to in derivation of vortex circulation theory (VCT)

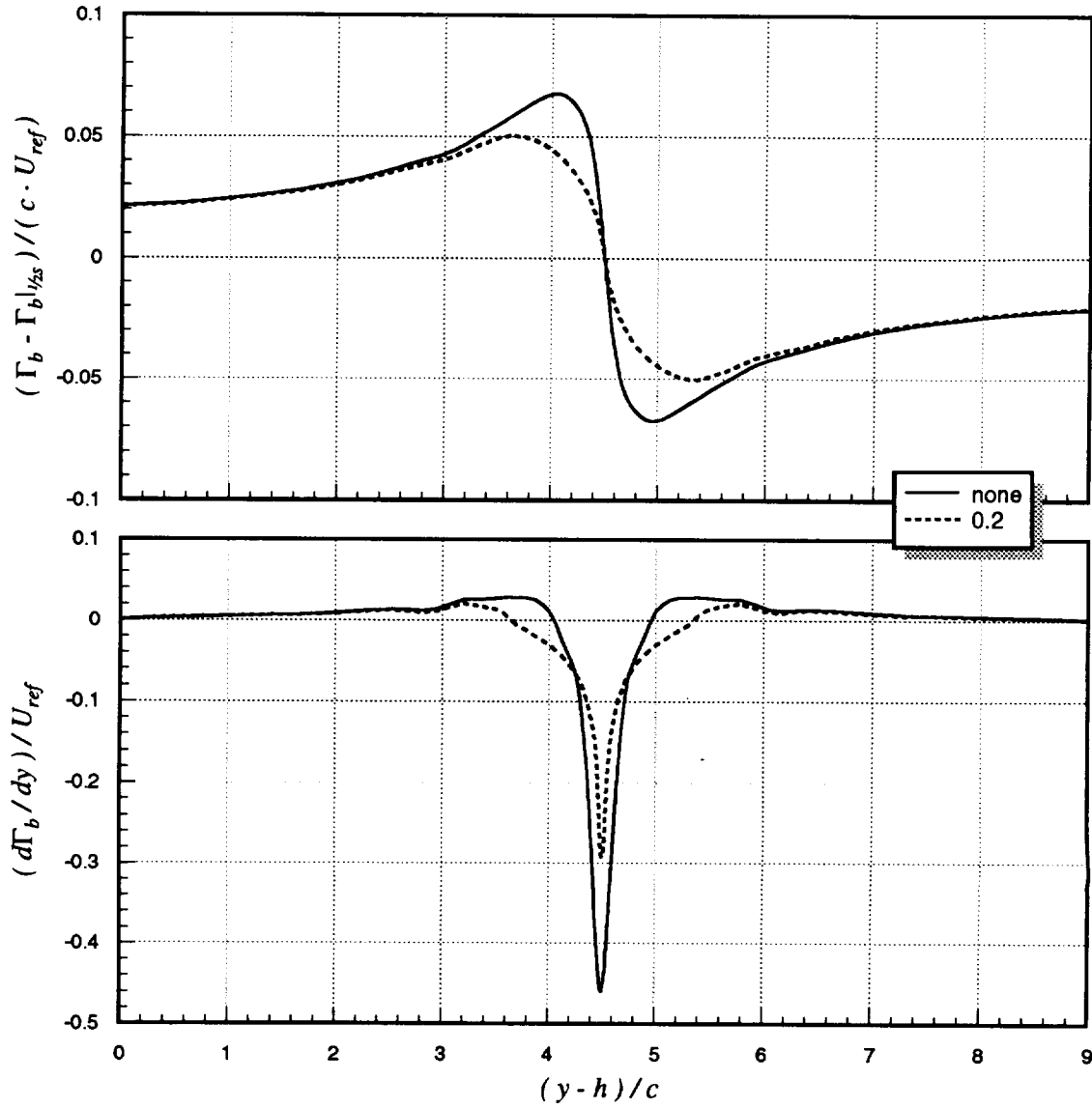


**Figure 4.16** Change in circulation distribution on full-span blade  $(\Gamma_b - \Gamma_b|_{1/2s})$  and shed vorticity distribution  $(d\Gamma_b / dy)$  due to interacting vortex predicted by vortex circulation theory (VCT):  $\alpha_i = 5^\circ$ ,  $|A/c| = 0.125$ , no spoiler. Legend lists  $\Delta C_{Lmax}$  values.

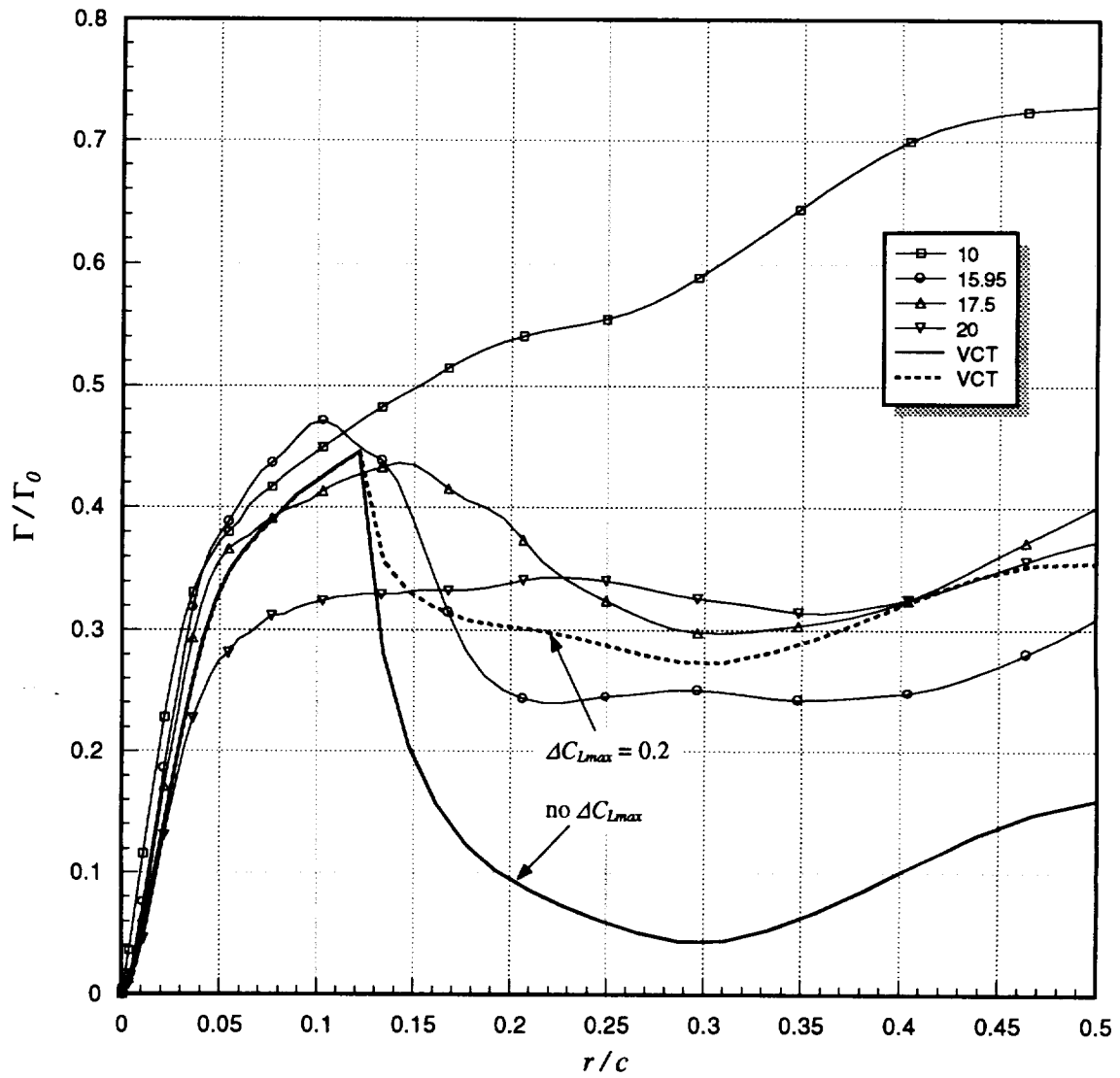


**Figure 4.17** Circulation distributions predicted by vortex circulation theory (VCT) compared to measured distributions:  $\alpha_1 = \alpha_2 = 5^\circ$ ,  $\Delta/c = -0.125$ , no spoiler. Legend lists  $x/c$  values.

## 5. CONCLUSIONS

The perpendicular interaction of a streamwise vortex with an infinite span blade was studied in incompressible flow. Interactions were produced using two rectangular NACA 0012 blades of 0.203m chord. The vortex generator blade was mounted in the wind tunnel test section as a half wing with 0.879m extending into the flow, and the interaction blade which completely spanned the test section was mounted 14 chords downstream. Three-component velocity and turbulence measurements were made using a sub-miniature four sensor hot-wire probe. Vortex core parameters (radius, peak tangential velocity, circulation, and centerline axial velocity deficit) were determined as functions of blade-vortex separation, streamwise position, blade angle of attack, vortex strength (controlled by generator angle of attack), and vortex size (controlled by the size of a circular spoiler attached to generator tip). Grids of velocity measurements and velocity spectra were also taken to provide insight into the fluid dynamics governing the flowfield. All measurements were made at a chord Reynolds number of 530,000.

Velocity measurements were made without the interaction blade to document the undisturbed structure and development of the undisturbed tip vortex. Without the spoiler attached, measurements indicate that the vortex core is laminar surrounded by the turbulent wing wake wrapped in a loose spiral. None of the core parameters vary significantly over the measured streamwise length consistent with laminar diffusion.

With the interaction blade installed, the passing vortex induces an angle of attack distribution on the blade which varies along its span, resulting in negative vorticity being shed into

the blade wake. For a blade-vortex separation several times the core radius, the vortex core passes the blade with hardly any effect. It is not until further downstream where the vortex core and blade wake begin to interact that significant changes in the vortex structure are seen. The interaction with the negative vorticity region in the blade wake causes the vortex core to become unstable and turbulent resulting in a dramatic magnification of the size and intensity of the turbulent part of the flowfield. At the same time the core radius increases and the peak tangential velocity decreases with the effect being greater for smaller separations. These effects are largely independent of blade angle of attack. Also, if these parameters are normalized on their undisturbed values, the effects are only weakly dependent on vortex strength.

To apply the core parameter data beyond the specific measurement conditions, an empirical model was developed which has some rudimentary physical basis, implying a usefulness beyond a simple curve fit. A combined circulation theory was also developed which predicts the distribution of vorticity shed in the blade wake, and the changes it causes in the circulation distribution of the vortex



## 6. REFERENCES

- [1] Landgrebe, A. J., "The wake geometry of a hovering helicopter rotor and its influence on rotor performance," 28th Annual National Forum of the American Helicopter Society, Washington, D.C., May 1972, Preprint No. 620.
- [2] Simons, I. A., Pacifico, R. E., and Jones, J. P., "The movement, structure, and breakdown of trailing vortices from a rotor blade," Proceedings from CAL/USAAVLABS Symposium, 1966.
- [3] Johnson, W., "A comprehensive analytical model of rotorcraft aerodynamics and dynamics, part 1, analysis and development," NASA TM-81182, June 1980.
- [4] Preisser, J. S., Brooks, T. F., and Martin, R. M., "Recent studies of rotorcraft blade-vortex interaction noise," *Journal of Aircraft*, Vol. 31, No. 5, September-October 1994, pp. 1009-1015.
- [5] George, A. R., "Helicopter noise: state-of-the-art," *Journal of Aircraft*, Vol. 15, No. 11, November 1978, pp. 707-715.
- [6] Hoad, D. R., "Helicopter model scale results of blade-vortex interaction impulsive noise as affected by tip modification," 36th Annual Forum of the American Helicopter Society, Washington, D.C., May 1980.
- [7] Egolf, T. A. and Landgrebe, A. J., "Helicopter rotor wake geometry and its influence in forward flight, volume 1—generalized wake geometry and wake effect on rotor airloads and performance," NASA CR-3726, October 1983.
- [8] Widnall, S. E. and Wolf, T. L., "Effect of tip vortex structure on helicopter noise due to blade-vortex interaction," *Journal of Aircraft*, Vol. 17, No. 10, October 1980, pp. 705-711.
- [9] Hardin, J. C. and Lamkin, S. L., "Concepts for reduction of blade/vortex interaction noise," *Journal of Aircraft*, Vol. 24, No. 2, February 1987, pp. 120-125.
- [10] Srinivasan, G. R., McCroskey, W. J., and Baeder, J. D., "Aerodynamics of two-dimensional blade-vortex interaction," AIAA Paper 85-1560, AIAA 18th Fluid Dynamics and Plasmadynamics and Lasers Conference, Cincinnati, Ohio, July 1985.
- [11] Tadghighi, H., Hassan, A. A., and Charles, B., "Prediction of blade-vortex interaction noise using airloads generated by a finite-difference technique," *Journal of the American Helicopter Society*, October 1992, pp. 38-47.

- [12] Lee, D. J. and Smith, C. A., "Distortion of vortex core during blade/vortex interaction," AIAA Paper 87-1243, AIAA 19th Fluid Dynamics, Plasma Dynamics, and Laser Conference, Honolulu, Hawaii, June 1987.
- [13] Brooks, T. F., Marcolini, M. A., and Pope, D. S., "Main rotor broadband noise study in the DNW," *Journal of the American Helicopter Society*, Vol. 34, No. 2, 1989, pp. 3-12.
- [14] Devenport, W. J., Glegg, S. A. L., and Sharma, G., "Turbulence measurements in trailing vortices for B.W.I. noise prediction," Report to NASA Langley under grant NAG-1-1119, 1992.
- [15] Glegg, S. A. L., "The prediction of blade-wake interaction noise based on a turbulent vortex model," AIAA 12th Aeroacoustics Conference, San Antonio, TX, April, 1989.
- [16] Ham, N. D., "Some preliminary results from an investigation of blade-vortex interaction," *Journal of the American Helicopter Society*, April 1974, pp. 45-48.
- [17] Johnson, W., "Application of a lifting-surface theory to the calculation of helicopter airloads," 27th Annual Forum of the American Helicopter Society, Washington, D.C., May 1971.
- [18] Ham, N. D., "Some conclusions from an investigation of blade-vortex interaction," *Journal of the American Helicopter Society*, October 1975, pp. 26-31.
- [19] Patel, M. H. and Hancock, G. J., "Some experimental results of the effect of a streamwise vortex on a two-dimensional wing," *Aeronautical Journal*, April 1974, pp. 151-155.
- [20] Hancock, G. J., "Aerodynamic loading induced on a two-dimensional wing by a free vortex in incompressible flow," *The Aeronautical Journal of the Royal Aeronautical Society*, Vol. 75, June 1971, pp. 413-416.
- [21] Paterson, R. W., Amiet, R. K., and Munch, C. L., "Isolated airfoil-tip vortex interaction noise," *J. Aircraft*, Vol. 12, No. 1, January 1975, pp. 34-40.
- [22] Phillipe, J. J. and Armand, C., "ONERA aerodynamic research on helicopters," *Rotorcraft Design*, AGARD CP-223, January, 1978.
- [23] Seath, D. D. and Wilson, D. R., "Vortex-airfoil interaction tests," AIAA Paper 86-0354, AIAA 24th Aerospace Sciences Meeting, Reno, NV, January 1986.
- [24] Müller, R. H. G., "Special vortices at a helicopter rotor blade," *Journal of the American Helicopter Society*, October 1990, pp. 16-22.

- [25] Kalkhoran, I. M., Wilson, D. R., and Seath, D. D., "Experimental investigation of the perpendicular rotor blade-vortex interaction at transonic speeds," *AIAA Journal*, Vol. 30, No. 3, March 1992, pp. 747-755.
- [26] Devenport, W. J., Glegg, S. A. L., Wittmer, K. S., and Rife, M. C., "Perpendicular blade vortex interaction and its implications for helicopter noise prediction," Report VPI-AOE-214, VPI&SU, Blacksburg, VA, 1994.
- [27] Devenport, W. J., Rife, M. C., Liapis, S. I., and Follin, G. J., "The structure and development of a wing-tip vortex," *Journal of Fluid Mechanics*, in press, 1995.  
See also: Devenport, W. J., Rife, M. C., Liapis, S. I., and Follin, G. J., "Turbulence structure and scaling in trailing vortices," AIAA Paper 95-0588, 33rd Aerospace Sciences Meeting and Exhibit, Reno, NV, January 1995.
- [28] Choi, K. and Simpson, R. L., "Some mean-velocity, turbulence, and unsteadiness characteristics of the VPI&SU Stability Wind Tunnel," Report VPI-AOE-161, VPI&SU, Blacksburg, VA, 1987.
- [29] Reynolds, G. A., "Experiments on the stability of the Blasius boundary layer," MS thesis, VPI&SU, 1979.
- [30] Weisser, C. M., "Controlling trailing tip vortices," AIAA 1995 Mid-Atlantic Student Conference, George Washington University, NASA Langley Campus, April, 1995.
- [31] Wood, N. B., "A method for the determination and control of the frequency response of a constant-temperature hot-wire anemometer," *Journal of Fluid Mechanics*, vol. 67, 1975, pp. 769-786.
- [32] Kovasznay, L. S. G., Physical Measurements in Gas Dynamics and Combustion, Princeton University Press, Princeton, 1954, p. 227.
- [33] Vukoslavcevic, P. and Wallace, J. M., "Influence of velocity gradients on measurements of velocity and streamwise vorticity with hot-wire X-array probes," *Review of Scientific Instruments*, vol. 52, no. 6, June 1981, pp. 869-879.
- [34] Bearman, P. W., "Corrections for the effect of ambient temperature drift on hot-wire measurements in incompressible flow," *DISA Information*, no. 11, May 1971, pp. 25-30.
- [35] Mathioudakis, K. and Breugelmans, F. A. E., "Use of triple hot wires to measure unsteady flows with large direction changes," *Journal of Physics E: Scientific Instruments*, vol. 18, 1985, pp. 414-419.

- [36] Tutu, N. K. and Chevray, R., "Cross-wire anemometry in high-intensity turbulence," *Journal of Fluid Mechanics*, vol. 71, pt. 4, 1975, pp. 785-800.
- [37] Browne, L. B. W., Antonia, R. A., and Chua, L. P., "Calibration of X-Probes for turbulent flow measurement," *Experiments in Fluids*, vol. 7, 1989, pp. 201-208.
- [38] Leuptow, R. M., Breuer, K. S., and Haritonidis, J. H., "Computer-aided calibration of X-probes using a look-up table," *Experiments in Fluids*, vol. 7, 1988, pp. 201-208.
- [39] Döbbeling, K., Lenze, B., and Leuckel, W., "Computer-aided calibration with a quadruple hotwire probe," *Experiments in Fluids*, vol. 8, 1990, pp. 257-262.
- [40] Batchelor, G. K., "Axial flow in trailing line vortices," *Journal of Fluid Mechanics*, vol. 20, 1964, pp. 645-658.
- [41] Moore, D. W., and Saffman, P. G., "Axial flow in laminar trailing vortices," *Proceedings of the Royal Society of London A*, vol. 333, 1973, pp. 491-508.
- [42] Betz, A., "Behavior of vortex systems," NACA TM 713, June 1933, pp. 237-253.
- [43] Rossow, V. J., 1973, "On the inviscid rolled-up structure of lift-generated vortices," *Journal of Aircraft*, vol. 10, no. 11, November 1973, pp. 647-650.
- [44] Donaldson, C. duP., Snedeker, R. S., and Sullivan, R. D., "Calculation of aircraft wake velocity profiles and comparison with experimental measurements," *Journal of Aircraft*, vol. 11, no. 9, September 1974, pp. 547-555.
- [45] Sreedhar, M. K., and Ragab, S. A., "Large eddy simulation of a longitudinal vortex," AIAA Paper 94-0529, 32nd Aerospace Sciences Meeting and Exhibit, Reno, NV, January 1994.
- [46] Uberoi, M. S., "Mechanisms of decay of laminar and turbulent vortices," *Journal of Fluid Mechanics*, vol. 90, 1979, pp. 241-255.

**7. APPENDIX**

**CONTROLLING TRAILING TIP VORTICES**

**BY CHRISTOPHER M. WEISSER**

**Spring 1995 Undergraduate Research Project**

**Virginia Polytechnic Institute and State University**

**Advisor: Dr. William Devenport**

**May 8, 1995**

# CONTROLLING TRAILING TIP VORTICES

Christopher M. Weisser\*

*Department of Aerospace and Ocean Engineering  
Virginia Polytechnic Institute and State University  
Blacksburg, VA.*

## **Abstract**

Experiments have been performed on the trailing tip vortex from a rectangular NACA 0012 airfoil. Studies have shown that the vortex is insensitive to the introduction of a probe and subject to only small wandering motions. Therefore, significant velocity measurements could be made using hot-wire probes.

This study was undertaken to formulate an empirical prescription for obtaining a given core size based on a set of wing-tips. These wing-tips were designed such that they vary in only one-dimension. This was done such that a change in the core size could be related to only one parameter. The main interest of this investigation was to find a set of wing-tips that would increase the vortex core size to a desired level and reduce the intensity of the core. It was also important that the increasing the core size have no effect on the lift of the entire wing section. After numerous trials of different design wing-tips, a circular tip-plate was found to yield the desired results.

Spectral decomposition was used to separate the wandering characteristics from the velocity fluctuations due to turbulence. Spectral analysis was also used to determine the development of the core structure at the measurement point.

## **1. Nomenclature**

$\alpha$	angle of attack
$\Gamma$	circulation around wing
$\rho_{\text{ref}}$	free-stream density
AR	aspect ratio of the unmodified wing
c	chord length
q	dynamic pressure
r	vertical distance from core center
u	normal velocity component
$U_{\text{ref}}$	free-stream velocity
w	tangential velocity component

## **2. Introduction**

Aircraft trailing vortices have become of great interest to the aviation industry in recent years. The

aircraft industry is taking precautions in avoidance of wake-aircraft interactions while the helicopter industry is interested reducing the noise associated with the vortices. Due to this insight, a considerable amount of research is being performed to better understand the trailing tip vortex to control the vortex core size. Studies such as those performed by Marchman and Uzel at Virginia Polytechnic Institute and State University and Heyson, Riebe, and Fulton at the NASA Langley Research Center include the use of variable wing-tips to change the size of the vortex. These wing-tip modifications have concluded varying degrees of success. The modifications used include wing-tips such as endplates, decelerating chutes, and extensions.

## **3. Experimental Procedure**

An experimental investigation of the effects of seventeen wing-tips on a NACA 0012 wing section's trailing vortex was performed in the Virginia Tech Open Circuit Wind Tunnel. The tunnel has a three foot by two foot test section and the test section spans twenty-two feet. Figure 1 shows an internal view of the test section and the tunnel setup. Measurements were taken at a distance of ten chord lengths downstream of the wing's trailing edge.

Measurement data was reduced from a calibrated quad-wire hot wire anemometer. The hot-wire probe was used to measure the three components of velocity of the trailing vortex. The quad-wire consists of two orthogonal X-wire arrays within a total volume of  $0.1 \text{ mm}^3$ . The quad-wire was operated using four Dantec 56C17/56C01 anemometer units. The anemometer outputs were read by an IBM AT compatible computer through an Analogic 12 bit HSDAS-12 A/D converter buffered by 4 x 10 buck-and-gain amplifiers. The four wires were calibrated in the freestream by using King's Law to correlate the wire output voltages with the cooling velocities.

A traversing gear was mounted around the exterior of the tunnel to allow horizontal and vertical movement of the probe through the test section. The

\* Undergraduate Student, Student member AIAA

probe was mounted to a probe stem, shown in Figure 2, which was in turn mounted to the traversing system. This allowed for the determination of the vortex core center that is where the profiles were taken.

The wing used in this experimental investigation was a rectangular planform, 8-inch chord, aluminum, NACA 0012 wing section four feet in length. This wing is similar to the wing that was used in References 2 and 4. For the measurements of this experiment, the boundary layer was tripped using 0.5 mm diameter glass beads glued in a random pattern between the 20% and 40% chord locations. The wing was mounted horizontally in the open circuit wind tunnel. The mounting apparatus allowed the wing to be set at any desired aspect ratio and angle of attack. For this investigation an aspect ratio of 2.5 and an angle of attack of  $5^\circ$  was chosen. The  $5^\circ$  angle of attack provided a strong vortex that was simpler to measure and the aspect ratio of 2.5 guaranteed that there would be no vortex wall interaction at ten chord lengths downstream. All tests were run at the same angle of attack and at a dynamic pressure of 1.44 inches of water, or a chord Reynolds Number,  $U_\infty c/\nu$ , of 335,000.

The wing modifications were held on the wing using an adapter. The adapter was an aluminum, 8 inch NACA 0012 wing section two inches in span. The adapter had a two inch slot at the quarter chord and mid-thickness to house the subwing wing-tips. The adapter also held two 16/32" tapped holes for mounting of the other wing-tips.

Sixteen wing modifications were used as well as the plain wing case. These wing modifications were grouped into five categories: 1) elliptical tips, 2) full-endplates, 3) flat-plate subwings, 4) half-endplates, and 5) circular tip-plates. Thirty-six wing-tips were originally made with one varying parameter of each set. All the wing-tips were mounted to the end of the wing, except for the circular tip-plates that were mounted perpendicular to the flow at the tip of the trailing edge. The number of wing-tips tested of each set was determined based on the effectiveness of the design of the wing-tip.

The first set of wing-tips were of the elliptical tip design and are shown in Figure 3. These tips were made of wood and were sanded into a rectangular ellipse shape to satisfy the ellipse equation below.

$$\frac{x^2}{a^2} + \frac{y^2}{b^2} = 1 \quad (1)$$

These wing-tip profiles were created using a template with an accuracy of  $\pm 0.02$  inches. They vary in span from one-quarter to two inches with a chord of eight inches with holes to match those of the adapter for mounting.

The endplate design wing-tips are shown in Figure 4. They were constructed of one-eighth inch, aluminum sheet metal. These wing-tips had a chord length of eight inches and introduced no twist or camber. The wing-tips had a semicircular leading edge and a blunt trailing edge. The wing-tips of this category ranged in height from one-quarter to four inches. These wing-tips had counter-sunk holes to match that of the adapter.

The subwings, shown in Figure 5, were constructed of one-sixteenth inch, steel sheet metal and varied in span from one-half to five inches, each having a chord of two inches. The subwings were mounted at mid-thickness such that the half-chord of the subwing matched with the quarter chord of the wing. These subwings were held in place by a set screw on the adapter wing section.

The next two wing-tips were constructed during testing in the search for a wing-tip that produced satisfactory results. The first of which was a half-endplate design shown in Figure 6. This wing-tip was constructed the same as the full endplate above except the bottom of the plate was cut to the shape of a NACA 0012 half section. Only two of these were constructed before moving on to the next style of wing-tip. The sizes of these two tips were three-quarters of an inch and one and three quarters of an inch in height from the chord line.

The final wing-tip tested was the circular tip-plate shown in Figure 7. This circular plate was constructed of one-sixteenth inch sheet metal and was attached to an adapter mounted on the tip of the wing section like that of the endplate design. The adapter allowed the tip-plate to be mounted perpendicular to the trailing edge of the wing with the center of the circular plate was just inboard of the wing-tip. The tips ranged in diameter from one to three inches.

#### 4. Results and Discussion

The core size data from this investigation can be seen in Figures 8 - 17 as the ratio of the tangential velocity profiles,  $w/U_{ref}$ , versus the vertical distance,  $y$  in inches, at ten chord lengths downstream of the wing. The plots show the peak tangential velocity, represented by the upper lower peaks. The vortex core size can be noted by the horizontal distance between the two peaks. Also plotted are the normal velocity profiles with the same  $y$  in inches along the horizontal axis and  $u/U_{ref}$  on the vertical. These plots can be

useful in determining whether the vortex core was found.

Figure 8 shows the tangential velocity profile for the Elliptical wing-tips plotted against the plain wing case. From this plot, one notes that the peak tangential velocity increases slightly with increasing wing-tip size. The peak-to-peak distance that represents the vortex core size is slightly decreasing. This change is fairly small and, unfortunately, is not the direction of interest. Figure 9 shows the normal velocity profiles that conclude that the core centers were indeed found.

Figures 10 and 11 show similar plots for the Endplate wing-tips. In this plot, the tangential velocity decreases, which is the desired case. However, the core size remains almost constant, decreasing only slightly with the increasing height of the endplates. Therefore, this design does not satisfy the requirements of this research either.

The Subwing wing-tip produced interesting results that can be seen in Figure 12. The subwing designs show a little improvement over the previous two cases. The tangential velocity component does indeed decrease as compared to the plane wing for all the cases. However, as the size increased from approximately a 1" subwing, a second vortex core was measured. This is denoted from the dip in tangential velocity before the first peak, and immediately following the second vortex peak. This is most profound in the 3" Subwing case. With a small subwing, the two vortex cores had time to merge by 10c downstream, the distance at which the measurements were taken. However, the larger the subwing, the larger the second core became until there was not enough distance between the wing and 10c for the two cores to merge. Because of this, it was difficult to deduce whether the subwing was producing the desired results. The normal velocity profile also demonstrates the dual vortex cores shown in Figure 13.

During testing, the idea of a half-endplate was introduced. This idea was thought to allow the flow to circulate freely from the under-side of the wing while not permitting it to form the vortex on the top side due to the interference of the plate. The results of these wing-tips can be seen in Figures 14 and 15. Unfortunately, these tips showed the same results as the full endplates. The half-endplates decreased the tangential velocity flow but did not increase the vortex core size.

One last attempt to increase the vortex core size was made by designing a circular tip-plate attached at the tip of the wing, perpendicular to the flow. The idea behind this wing-tip was to burst the vortex core as it began to develop. The results were

astounding and can be seen in Figure 16. Not only did the core size increase but, the tangential velocity decreased at an unbelievable rate. In fact, the tangential velocity ratio becomes astonishingly small with the 3" circular tip-plate. At the same time, the vortex core size grew to over six inches. The normal velocity profiles were plotted again in Figure 17 to confirm that the vortex center was found. From this plot, one can see that the centers were indeed found within some degree of accuracy. The three inch tip-plate was the least accurate. The miss of the core center can be explained by the large amount of turbulence at the center of the core. This turbulence made it difficult to determine the correct center.

In summary of all the tip modifications used, Figure 18 shows the trends in vortex core size with the increasing component of the wing-tip. As shown, there is no real change in the size of the vortex core for the subwings, elliptical tips, endplates, or half-endplates. It is rather fair to say that the small changes are well within the experimental error of this investigation. The one trend that stands out above all the others is the circular tip-plate. Its core size increases almost linearly with increasing diameter.

It is very important that when changing the vortex core size, that the lift developed by the wing not be disturbed. In an attempt to determine the lift on the wing, the circulation was calculated for all the circular tip-plates used above. Where the circulation is calculated as shown in Equation 2 and is directly related to the lift by Equation 3 below:

$$\Gamma = 2\pi r w \quad (2)$$

$$l = \rho_{\infty} U_{\infty} \Gamma \quad (3)$$

The results of this calculation can be seen in Figure 19. As shown, there is no major change in the circulation around the wing as compared to the plain wing case. This is apparent due to the similarity of the peak circulation at the left and right endpoints. This demonstrates that this wing-tip is fully effective in enlarging the vortex core size while not harming any lift on the wing. The only question remaining about this design of wing-tip is whether the drag induced by the circular tip-plate is less than or greater than the trailing vortex drag of the plane wing.

Analysis of the spectral measurements was made and can be seen in Figures 20 - 27. The spectral measurements show us some interesting information about these flows; however the exact reasons for these results are somewhat unknown. The plots are in the form of  $G_{uu}$  or  $G_{vv} + G_{ww}$  normalized with respect to  $U_{ref}$



and  $c$  plotted against  $f$  normalized with respect to  $c/U_{ref}$ .

Figures 20 and 21 show the spectral plots of the Endplate wing-tips. As shown, the slope of the curve is approximately -3. This is almost standard with respect to most trailing vortex wakes. This can most likely be described as unsteady laminar flow. The same results were found for the subwings and half-endplates shown in Figures 22 - 25. The circular tip-plates yield interesting results again. As shown in Figures 26 and 27, the slope is approximately -5/3. This is very different from the previous cases and was not expected. This may be caused by the turbulent nature of the flow caused by these plates. Further study is required to fully understand the flow behind these circular tip-plate wing-tips.

### **5. Conclusions**

This study has concluded that wing-tips do have an impact on the size and strength of a vortex core. It has also been concluded that different design wing-tips have distinct effects on the vortex core. Of all the design tips tested in this research project, the circular tip-plate wing-tip design has proven to be the most valuable. The circular tip-plate design does in fact increase the vortex core size without harming the lift on the wing.

The spectral plots have shown interesting results and it would be interesting to know why this occurs. More research is needed on this subject for the exact empirical relation between the vortex core size and the plate diameter. Further study is also needed to deduce the lift and drag information associated with this wing-tip design.

### **6. Acknowledgments**

I would like to thank Dr. William Devenport, Mr. Ken Whittmer, and Mr. Mark Engel of Virginia Polytechnic Institute and State University for their guidance through this project. Financial support for some of the instrumentation and supplies used in this study was provided by NASA Langley through grant NAG-1-1539.

### **7. References**

1. Bertin, J.J. and Smith, M.L., *Aerodynamics for Engineers*, Second Edition, Prentice Hall, New Jersey, 1989, pp. 96-7.
2. Devenport, W.J., Rife, M.C., Liapis, S.I., and Follin, G.J. "Turbulence Structure and Scaling in Trailing Vortices." 33rd Aerospace Sciences Meeting & Exhibit, Reno, NV, January 9-12, 1995. Paper AIAA 95-0588.

3. Heyson, H.H., Riebe, G.D., and Fulton, C.L., "Theoretical Parametric Study of the Relative Advantages of Winglets and Wing-Tip Extensions," NASA TP-1020, 1977.
4. Marchman, J.F., III and Uzel, J.N., "Effects of Several Wing Tip Modifications on a Trailing Vortex," *Journal of Aircraft*, Vol. 9, No. 9, September 1972, pp. 684-686.

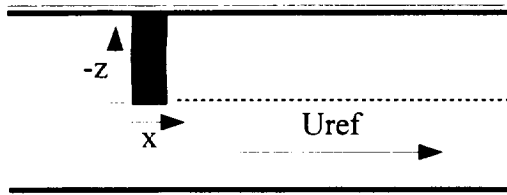


Figure 1: Internal Tunnel Layout.

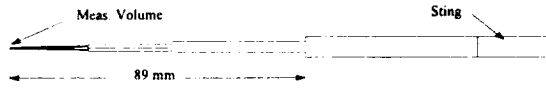


Figure 2: Hot Wire Probe and Sting

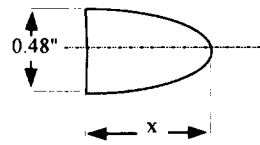


Figure 3: Elliptic Wing-Tip

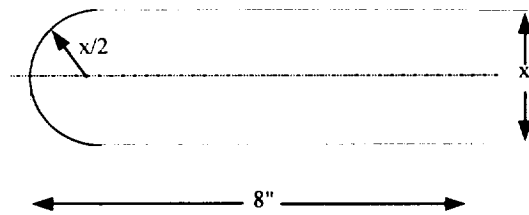


Figure 4: Endplate Wing-Tip

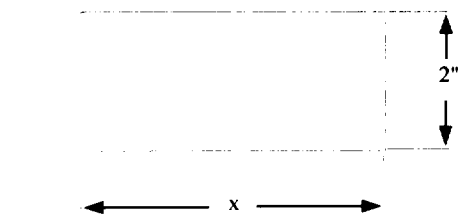


Figure 5: Subwing Wing-Tip

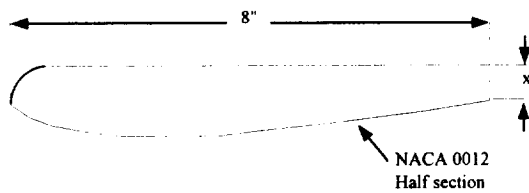


Figure 6: Half-Endplate Wing-Tip

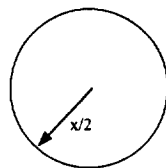


Figure 7: Circular Tip-Plate Wing-Tip

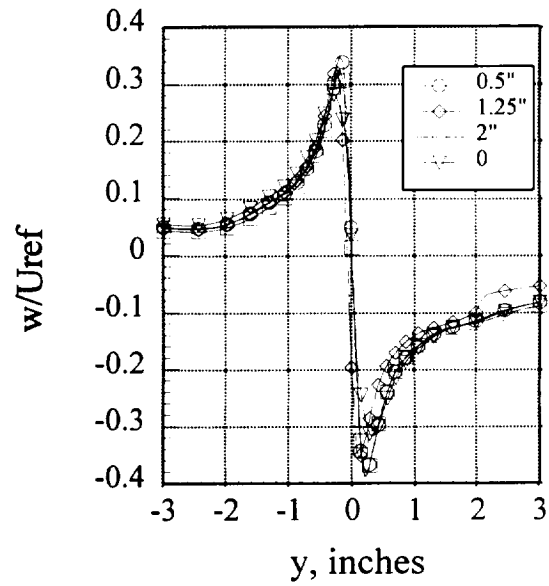


Figure 8: Tangential Velocity Profile for Elliptical Wing-Tips.

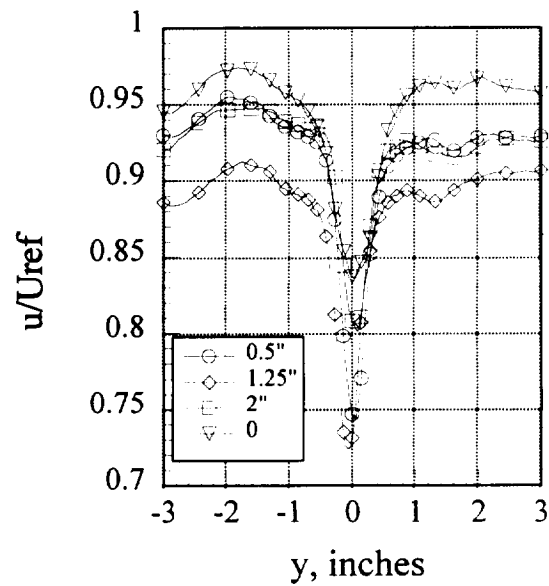


Figure 9: Normal Velocity Profiles for Elliptical Wing-Tips.

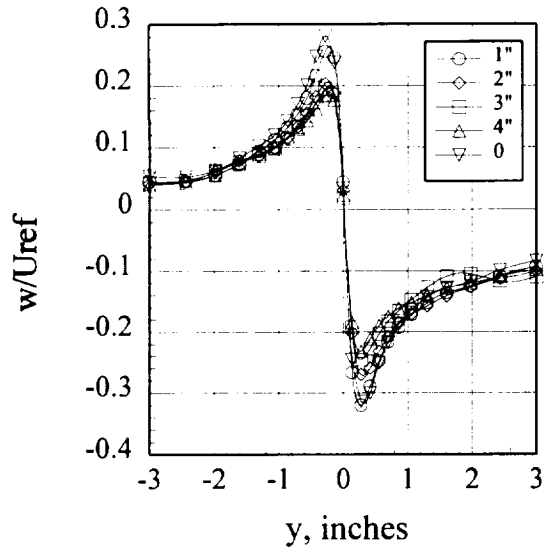


Figure 10: Tangential Velocity Profile for Endplate Wing-Tips.

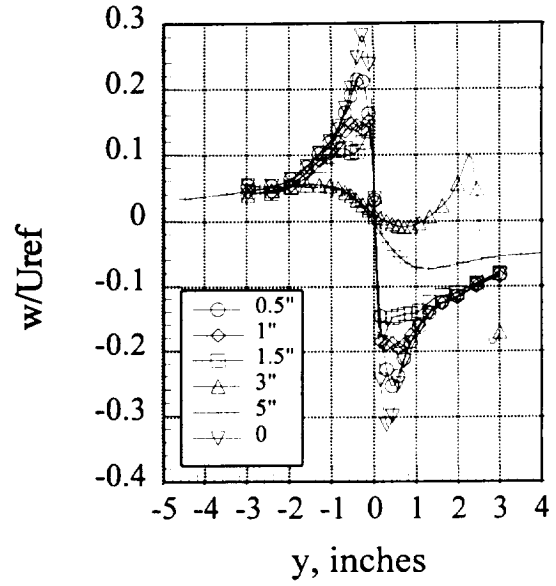


Figure 12: Tangential Velocity Profile for Subwing Wing-Tips.

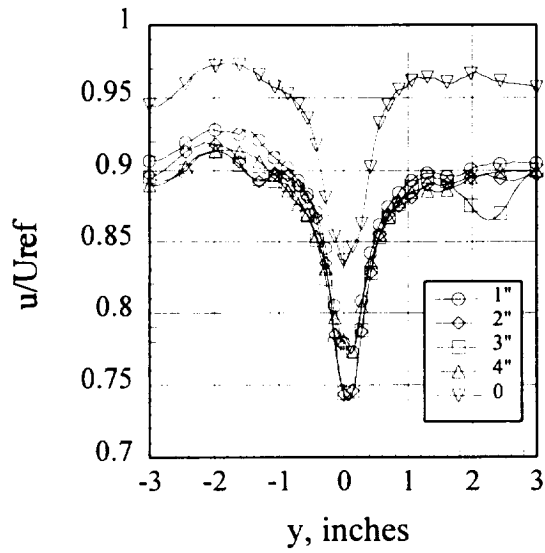


Figure 11: Normal Velocity Profile for Endplate Wing-Tips.

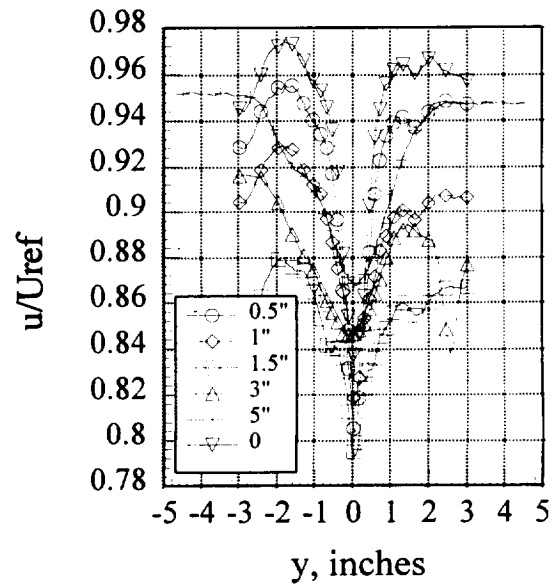


Figure 13: Normal Velocity Profile for Subwing Wing-Tips.

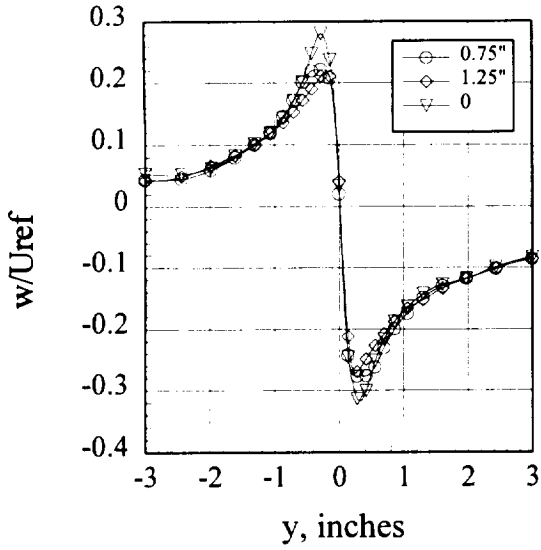


Figure 14: Tangential Velocity Profile for Half Endplate Wing-Tips

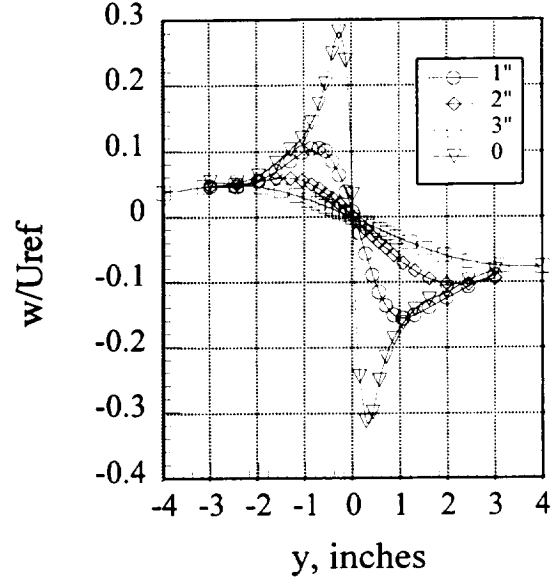


Figure 16: Tangential Velocity Profile for Circular Tip-Plate Wing-Tips.

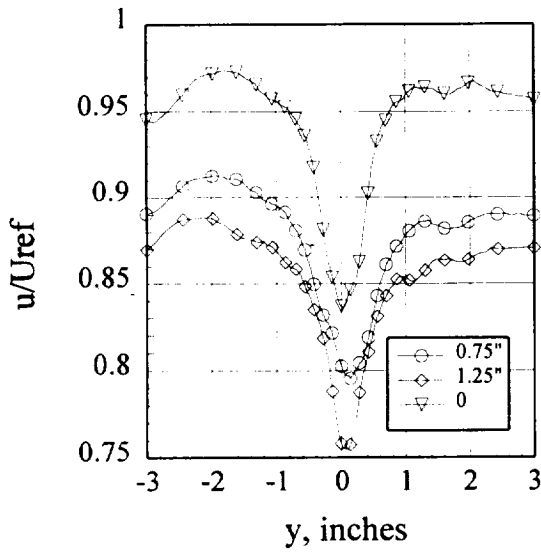


Figure 15: Normal Velocity Profile for Half Endplate Wing-Tips.

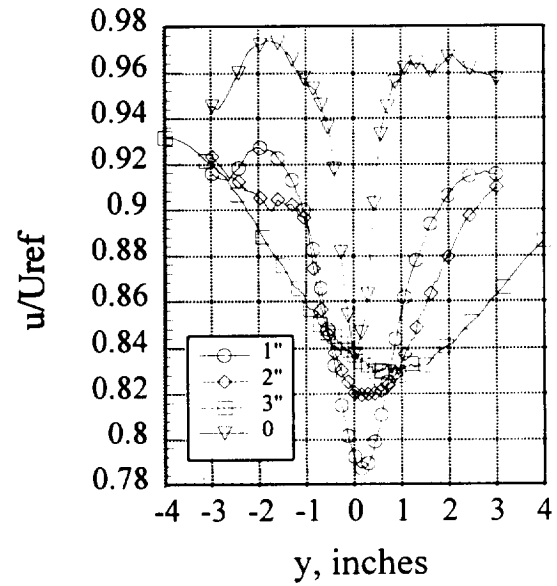


Figure 17: Normal Velocity Profile for Circular Tip-Plate Wing-Tips.

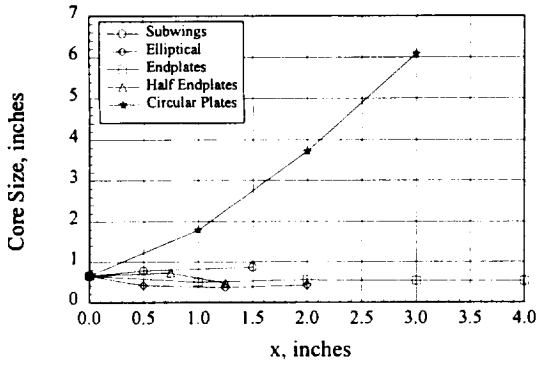


Figure 18: Comparison of Vortex Core Size Results.

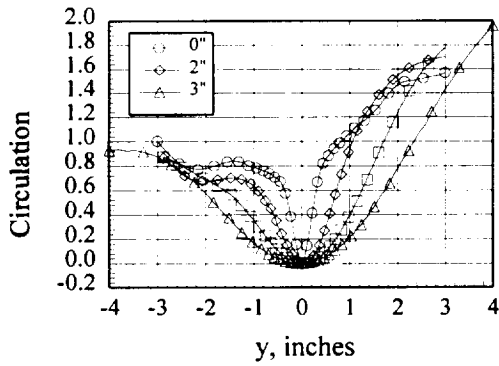


Figure 19: Circulation Plot for Circular Tip-Plate.

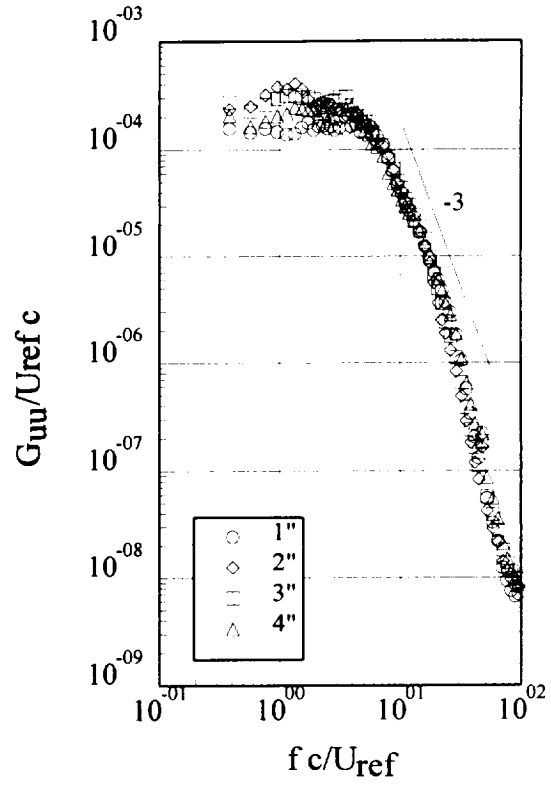


Figure 20: Spectral Analysis for Endplates.

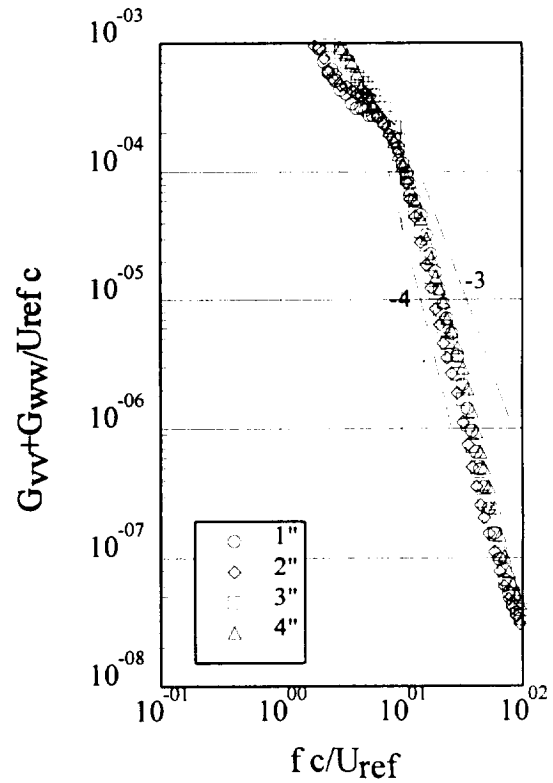


Figure 21: Spectral Analysis for Endplates.

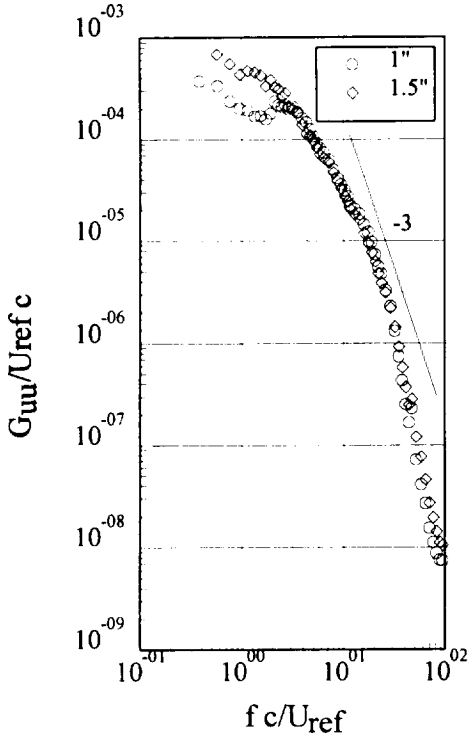


Figure 22: Spectral Analysis for Subwings.

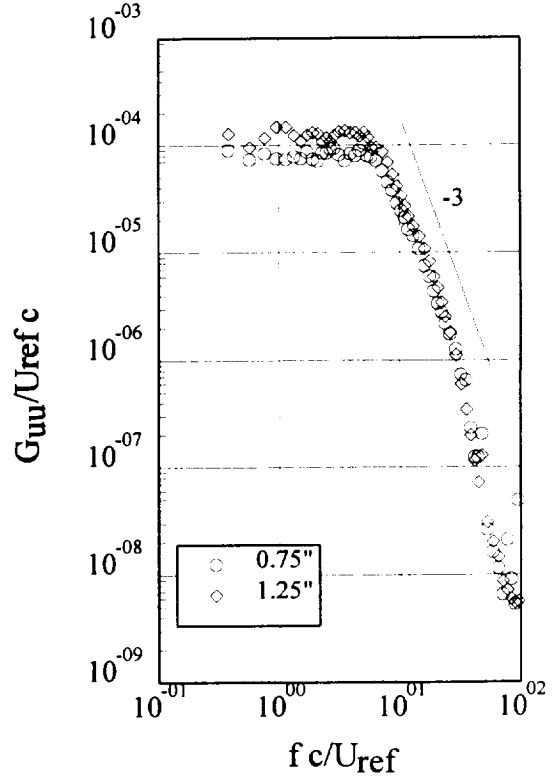


Figure 24: Spectral Analysis for Half-Endplate

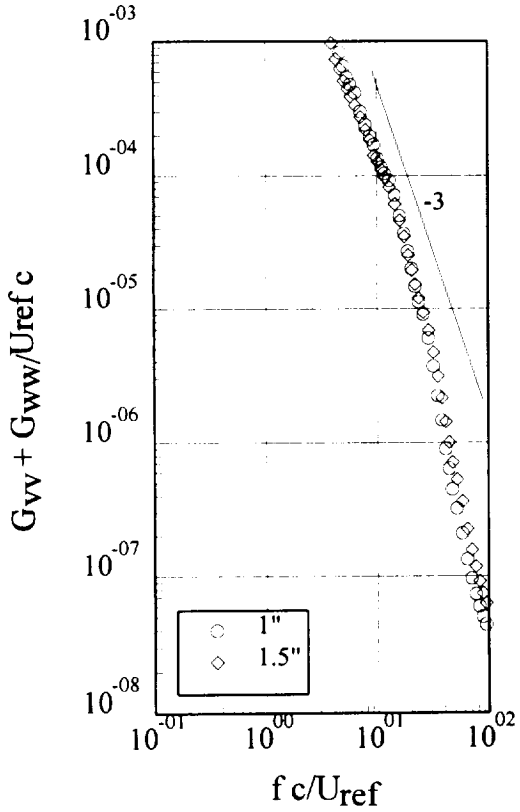


Figure 23: Spectral Analysis for Subwing

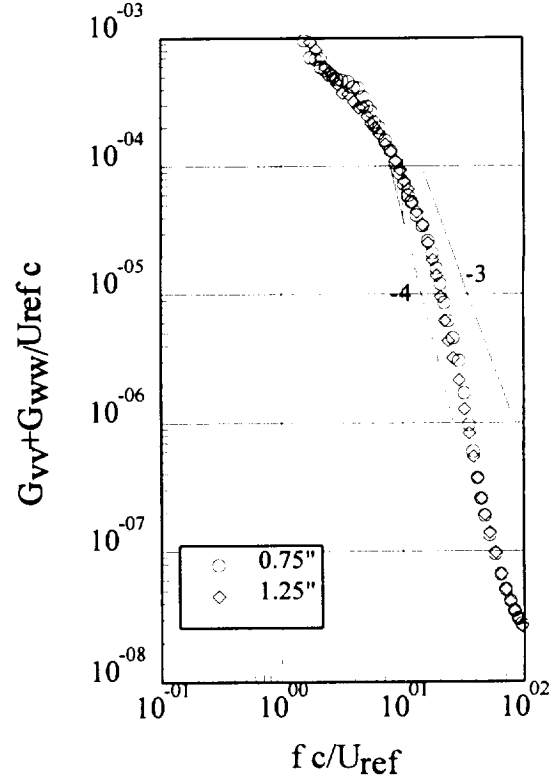


Figure 25: Spectral Analysis for Half-Endplate